Printed in the United States of America. Available from
National Technical Information Service
U.S. Department of Commerce
5285 Port Royal Road, Springfield, Virginia 22161
NTIS price codes—Printed Copy: A15 Microfiche A01

ORNL--5843

DE83 000213

ORNL-5843
Dist. Category UC-20

Contract No. W-7405-eng-26

MASTER

FUSION ENERGY DIVISION

ANNUAL PROGRESS REPORT

PERIOD ENDING DECEMBER 31, 1981

Date Published - September 1982

Prepared by the
OAK RIDGE NATIONAL LABORATORY
Oak Ridge, Tennessee 37830
operated by
UNION CARBIDE CORPORATION
for the
DEPARTMENT OF ENERGY

Reports previously issued in this series are as follows:

ORNL-2693	Period Ending January 30, 1959
ORNL-2832	Period Ending July 31, 1959
ORNL-2926	Period Ending January 31, 1960
ORNL-3011	Period Ending July 31, 1960
ORNL-3104	Period Ending January 31, 1961
ORNL-3239	Period Ending October 31, 1961
ORNL-3315	Period Ending April 30, 1962
ORNL-3392	Period Ending October 31, 1962
ORNL-3472	Period Ending April 30, 1963
ORNL-3564	Period Ending October 31, 1963
ORNL-3652	Period Ending April 30, 1964
ORNL-3760	Period Ending October 31, 1964
ORNL-3836	Period Ending April 30, 1965
ORNL-3908	Period Ending October 31, 1965
ORNL-3989	Period Ending April 30, 1966
ORNL-4063	Period Ending October 31, 1966
ORNL-4150	Period Ending April 30, 1967
ORNL-4238	Period Ending October 31, 1967
ORNL-4401	Period Ending December 31, 1968
ORNL-4545	Period Ending December 31, 1969
ORNL-4688	Period Ending December 31, 1970
ORNL-4793	Period Ending December 31, 1971
ORNL-4896	Period Ending December 31, 1972
ORNL-4982	Period Ending December 31, 1973
ORNL-5053	Period Ending December 31, 1974
ORNL-5154	Period Ending December 31, 1975
ORNL-5275	Period Ending December 31, 1976
ORNL-5405	Period Ending December 31, 1977
ORNL-5549	Period Ending December 31, 1978
ORNL-5645	Period Ending December 31, 1979
ORNL-5674	Period Ending December 31, 1980

CONTENTS

FIGURES

TABLES

INTRODUCTION

The Fusion Program of the Oak Ridge National Laboratory (ORNL) is a major component of the U.S. national fusion program, and it encompasses nearly all aspects of magnetic fusion research. The program includes the collaborative efforts of staff from ORNL, Union Carbide Corporation Nuclear Division (UCC-ND), private industries, universities, and other fusion laboratories. There have been numerous advances, and many subprograms have been successfully completed. This report, which summarizes the information obtained during 1981, is issued as the *Fusion Energy Division Annual Progress Report*; for completeness, however, it includes the approximately 15% of the ORNL Fusion Program not located in the Fusion Energy Division.

Areas in which the Fusion Program carries out its work include experimental and theoretical research on two magnetic confinement concepts, the ELMO Bumpy Torus (EBT) and the tokamak; theoretical and engineering studies, initiated this year, on a third concept, the stellarator; the development of the essential technologies for heating and fueling fusion plasmas, of the superconducting magnets that will be used to confine plasmas, and of the materials needed in fusion devices; the development of diagnostic tools and techniques; the assembling of databases on atomic physics and radiation effects; the physics and engineering of present-generation devices; the design of future devices; and the assessment of the environmental impact of magnetic fusion power. The interactions between these activities and their integration into a single program are major factors in the success of each activity, and one goal of the ORNL Fusion Program is to maintain this balance among confinement, technology, and engineering activities.

The EBT Program at ORNL comprises two major elements: the EBT-Scale (EBT-S) experiment and the EBT Proof-of-Principle (EBT-P) project. The EBT-S device was operated with up to 200 kW of power at 28 GHz and achieved electron temperatures of ~1 keV at densities of ~10^{12} particles per cubic meter. Ion cyclotron heating (ICH) was applied in a collaborative program with McDonnell Douglas Astronautics Company, and substantial heating of tail ions was achieved with 20 kW of power. This work dominated the first half of the year and provided data essential to the EBT-P checkpoint review in August. A major program following the review was in laser fluorescence spectroscopy. The velocity distribution of impurity ions was measured for the first time, showing that the source was wall sputtering. The preliminary design for the EBT-P device was 95% complete at the end of the year, and McDonnell Douglas Astronautics Company, the industrial participant in the project, was given verbal authorization to proceed with detailed design. In addition to the design effort, the EBT-P project includes research and development (R&D) activities for the magnet system, the microwave system, and other machine systems. In the magnet system program, two development coils for EBT-P were fabricated and tested at ORNL. Initial testing of microwave power distribution components was performed under the microwave system program, and a laboratory facility for low power, 60-GHz testing was completed. The machine systems program was initiated this year and encompasses all other technologies required for EBT-P development. As part of the EBT Program, the Division manages the Department of Energy (DOE) Gyrotron Development Program. Both companies involved in this program, Varian Associates, Inc., and Hughes Aircraft Company, successfully operated 60-GHz pulsed gyrotrons at peak powers of 200 kW during 1981.

The ORNL Tokamak Program expanded this year to include physics optimization studies for the design of an Advanced Toroidal Facility (ATF-1) to replace the Impurity Study Experiment (ISX-B) tokamak in the mid-1980s. The ATF-1 activity is aimed at identifying the optimal toroidal configuration for a Fusion Demonstration Plant (FDP). Various stellarator options are being addressed; the ATF-1 is envisioned as a current-free stellarator with possible extension to a tokamak/stellarator hybrid. The ongoing experimental program on ISX-B focused on high beta plasma operation, with studies to investigate

why the volume-averaged beta does not increase linearly with applied beam power. It was determined that the deterioration of confinement was correlated with an increased electron energy loss. In addition, studies on impurity transport, the effects of toroidal field ripple, and electron cyclotron heating (ECH) were continued. Pellet fueling was demonstrated with a prototype centrifugal injector in ISX-B, and pumped limiter tests confirmed the results of a simple model of the ballistic particle collection principle.

In the ORNL Plasma Theory Program, the ATF-1 activity is supported through a study group formed this year to assess confinement in stellarators and torsatrons. The group is building on previous work and models developed in the study of tokamaks. A new configuration, the Symotron (for symmetric modular torsatron), is being pursued. EBT theory this year was focused on understanding the EBT-S plasma and improving the various subsystem models. Particular emphasis was placed on ICH and beta effects. Theoretical studies continue to support the possibility of attaining reactor-relevant beta. Tokamak theory was focused on finding and evaluating explanations for deteriorating confinement at high power levels. Advances were made in the understanding of resistive MHD behavior. Other areas of effort included the use of a variational moments method in place of MHD equilibrium calculations, spatially resolved transport analysis of fueling and beam heating dynamics, and modeling of low ripple bundle divertors, pumped limiters, and MHD equilibria.

Technology development for plasma heating and fueling continued to advance during 1981. In the Advanced Positive Ion Source (APIS) Program, R&D activity in two areas, long pulse plasma generators and accelerators, was geared to the development of the long pulse, multimegawatt neutral beam injection systems that will be required for future experiments such as the Mirror Fusion Test Facility upgrade, MFTF-B. The R&D activity was supported by theoretical studies. Direct energy recovery was also studied experimentally and theoretically. Negative ion beams have been generated using an extensively modified ion source, and a conceptual beam line incorporating a negative-ion-based source was designed and studied. In pellet injector development, efforts concentrated on construction of the advanced mechanical injector (AMI) and advanced pneumatic injector (API) test facilities. The AMI facility was completed and initial tests verified the functionality of the various subsystems. A prototype 4-pellet pneumatic injector was successfully tested and delivered to the Princeton Plasma Physics Laboratory, where it was installed on the Poloidal Divertor Experiment. A radio frequency (rf) technology program was established in October 1981 in response to the growing interest in rf heating for magnetic fusion devices.

Superconducting magnet development continued with strong interactions between the Large Coil Program (LCP) and the Magnetics and Superconductivity (M&S) Section. Development proceeded on the six coils — three from the United States and one each from Japan, Switzerland, and Euratom — that will be tested in the Large Coil Test Facility (LCTF). Technical problems delayed all six coils. Construction of the LCTF continued on schedule. The M&S Section carried out R&D in support of the LCP and also made progress in the 12-T coil projects and in the development of advanced superconductors. The two development coils for EBT-P were fabricated and successfully tested, and a 12-T facility magnet, the Coil Winding Test Experiment, was placed in service.

The ORNL Fusion Materials Program made advances in the development of materials for fusion reactors. Neutron irradiation studies of a variety of alloys were carried out in the High Flux Isotope Reactor and the Oak Ridge Research Reactor at ORNL and in the Experimental Breeder Reactor at Idaho National Engineering Laboratory. The Plasma-Materials Interactions Program addressed issues relating to plasma edge phenomena in fusion devices and the interaction of the plasma with exposed surfaces through experiments on ISX-B and EBT-S. Issues emphasized in 1981 were edge flux measurements, hydrogen recycling studies, and advanced limiter experiments.

Diagnostic development work was carried out in close association with ISX-B and EBT-S. Measurements were made of the Faraday rotation of the polarization of far-infrared (FIR) laser radiation by the plasma magnetic fields. Other activities included development of FIR lasers and of neutral particle analyzers.

The atomic physics activity combines theory and experiment to investigate excitation-autoionization and collisional electron transfer. The results are employed in plasma modeling and are disseminated by the Controlled Fusion Atomic Data Center.

In the neutron transport activity, experiments are made to provide the data necessary for verifying analytic methods. Cross sections are obtained for use in fusion reactor neutronics calculations. The Radiation Shielding Information Center serves the international fusion community by maintaining a technical database on radiation transport.

The advanced system studies effort includes the Fusion Engineering Design Center (FEDC) and the Fusion Environmental Assessment Program. The FEDC is a centralized laboratory/industry design team hosted by ORNL and charged with the development of the device to follow the Tokamak Fusion Test Reactor. During 1981, the FEDC staff developed a baseline design for the Fusion Engineering Device. The Fusion Environmental Assessment Program was established in 1979 to assist DOE in developing the documents required by the National Environmental Policy Act as the national fusion program advances into engineering development. In 1981, the technical basis for a generic environmental impact statement on fusion power was developed and documented.

During the past year, the ORNL Fusion Program has made many significant contributions to the evolution of magnetic fusion towards a viable energy source. It is a pleasure to be associated with the staff of the Fusion Energy Division, other ORNL divisions, UCC-ND, and associated industries, universities, and fusion laboratories who collaborated in this program and contributed to its achievements.

O. B. Morgan

O. B. Morgan, Jr., Director
Fusion Energy Division

John Sheffield

J. Sheffield, Associate Director
Fusion Energy Division

1. EBT RESEARCH AND DEVELOPMENT

L. A. Berry, EBT Experimental Section Head

A. L. Boch, EBT-P Project Manager

C. M. Loring, Gyrotron Development Program Manager

F. W. Baity	H. O. Eason	T. L. Mann[11]
J. K. Ballou[1]	R. S. Edwards[4]	H. C. McCurdy
D. B. Batchelor[2]	O. C. Eldridge[10]	M. W. McGuffin
D. D. Bates[3]	D. A. Everitt[8]	T. J. McManamy[6]
P. G. Beasley[4]	W. M. Fletcher[5]	J. R. Miller[1]
D. L. Bible[3]	C. L. Garren[9]	D. R. Overbey[2]
F. M. Bieniosek[3]	J. C. Glowienka	L. W. Owen[9]
J. A. Blair[6]	D. C. Greenwood[3]	T. L. Owens[7]
J. S. Brodkowicz[7]	S. L. Hall[9]	J. H. Pfannmuller[7]
A. Y. Broverman[8]	E. A. Hallock[5]	D. A. Rasmussen
R. A. Brown[8]	W. R. Hamilton[8]	R. K. Richards
R. L. Brown[1]	G. R. Haste	C. R. Schaich
R. D. Burris[9]	C. L. Hedrick[2]	S. S. Shen[1]
D. B. Campbell[8]	A. L. Henderson[7]	L. Solensten[5]
P. G. Clark[8]	D. L. Hillis	J. D. Stout[8]
J. A. Cobble	S. Hiroe	L. W. Swain
R. J. Colchin	E. F. Jaeger[2]	J. S. Trieb[9]
M. R. Conner[7]	H. D. Kimrey	T. C. Tucker[3]
K. D. Cook[8]	A. Komori	N. A. Uckan[2]
W. A. Davis	S. G. Larson[8]	T. Uckan
R. J. DeBellis[7]	R. L. Livesey	T. L. White
R. D. Donaldson	J. W. Lue[1]	J. B. Wilgen
R. A. Dory[2]	S. R. Maddox[7]	R. E. Wintenberg[3]
R. A. Wright[8]	K. G. Young[2]	

1. Magnetics and Superconductivity Section.
2. Plasma Theory Section.
3. Instrumentation and Controls Division.
4. Management Services Section.
5. Rensselaer Polytechnic Institute, Troy, New York.
6. UCC-ND Purchasing.
7. McDonnell Douglas Astronautics Company, St. Louis, Missouri.
8. UCC-ND Engineering.
9. UCC-ND Computer Sciences.
10. Tokamak Experimental Section.
11. General Dynamics-Convair Division, San Diego, California.

I. EBT RESEARCH AND DEVELOPMENT

ABSTRACT. Investigations of the ELMO Bumpy Torus (EBT) magnetic confinement concept continued. Experiments on the EBT device, in both its initial (EBT-I) and scaled (EBT-S) configurations, Title I design for the EBT Proof-of-Principle (EBT-P) device, and management of gyrotron development comprised the major activities in this area.

EBT-S ran throughout the year, with short downtimes for diagnostic changes and improvements. The first half of the year emphasized plasma confinement and ion cyclotron heating (ICH) studies in preparation for the EBT-P checkpoint review, which was held in August. Runs were made at power levels of <200 kW. A comprehensive set of plasma data was amassed that included detailed power and pressure scans. Results included electron temperatures of ~1 keV at densities of ~10^{18} particles per cubic meter, and electron confinement appeared to be classical. ICH experiments were successful in launching propagating waves and in heating tail ions with powers of up to 20 kW.

After the EBT-P checkpoint review, experiments focused on absolute measurement of the neutral aluminum impurity density using laser fluorescent scattering. For the first time in a plasma device, the velocity distribution of impurity atoms was measured, proving that the source was wall sputtering. The last month of the year was dedicated to detailed ICH experiments. Up to 110 kW of power in 5-ms pulses was applied in the C-mode, and 80-kW pulsed operation was achieved in the I-mode.

The EBT-P project completed several significant milestones during 1981. Title I (preliminary) design for EBT-P was 95% complete at year's end. Preliminary design reviews were held for each of the eight device systems, and individual system design reports and drawings were prepared by McDonnell Douglas Astronautics Company (MDAC) and reviewed by ORNL. Verbal authorization to proceed with detailed (Title II) design was given to MDAC on all systems, and a request for proposals was released for the detailed design of the cryogenic system. Title I reports and drawings will serve as the baseline for the Title II design.

In addition to the plant and capital equipment design effort, the EBT-P project includes research and development (R&D) activities required to develop the technology needed for the device. The principal device R&D programs are magnet system development, microwave system development, and machine systems development.

The magnet system development program, which is to provide the technical base for the detailed design and fabrication of the EBT-P mirror coils, obtained significant results during the year. Two development coils were fabricated at ORNL, and initial open dewar tests were performed on both coils. The coils operated successfully at full field corresponding to the 90-GHz upgrade for EBT-P, with simulated x-ray heating imposed at the design level of 10 W. These coils are being assembled into development magnet dewars by General Dynamics-Convair Division (GD). A test facility for testing the two development magnets and a GD prototype magnet is currently under construction at ORNL.

The microwave system R&D program, which has as its objective the development of the high power microwave components that are required to distribute power from the gyrotrons to the plasma, is also in progress at ORNL. Initial testing of some of these elements was performed on EBT-S during the year. A laboratory facility completed this year provides capability for low power testing of components at 60 GHz. Calculational methods were developed for analyzing the performance of microwave distribution system components; the methods were verified against EBT-S experimental data and applied to evaluate EBT-P design alternatives.

The machine systems R&D program, which encompasses all technologies required for the development of EBT-P other than the magnet and microwave systems, was initiated this year. A test limiter built by MDAC will be installed on EBT-S to study limiter effects on the plasma.

The ORNL Gyrotron Development Program continued to manage the development of gyrotron tubes by two industrial subcontractors, Varian Associates, Inc., and Hughes Aircraft Company. A 200-kW, 28-GHz gyrotron developed through this program was operated at 340 kW with 37% efficiency in 1981. Efforts to develop pulsed and continuous wave (cw), 200-kW, 60-GHz gyrotrons are under way at Varian and Hughes. Both companies operated pulsed 60-GHz tubes this year, and significant progress was made toward the goal of a gyrotron capable of producing 200-kW cw power at 60 GHz. In late 1981, Varian began testing the first experimental steady-state (cw) axisymmetric 60-GHz tube.

1.1 EBT RESEARCH

1.1. ICRH Experiments

F. C. Baity, W. A. Davis, T. L. Owens

1981 saw considerable emphasis on heating experiments in the ion cyclotron range of frequencies (ICRF) on EBT-S. The installation of the antenna and matching circuit is shown in Fig. 1.1. Exploratory surveys of plasma loading on the antenna, wave propagation, ion heating, and effects on plasma confinement were carried out over a wide range of operating conditions.

The antenna and the matching circuit were modified during the year to improve the power handling capability and frequency response. Experiments were performed at 20 kW cw and 100 kW pulsed at 30 MHz under best conditions. The frequency range of the system was increased to 15-50 MHz. New power sources were added to provide 100 kW cw up to 20 MHz and 1.5 kW cw, 4 kW pulsed from 30 to 50 MHz. A 20-kW transmitter covering the range from 30 to 60 MHz was ordered from Continental Electronics Manufacturing Company and will be operational in mid-1982.

Diagnostic improvements included installation of a set of ten Faraday-shielded loop probes around the torus and the addition of a charge exchange analyzer on the antenna cavity.

The results of the ICRF experiments are described in detail in Refs. 1 and 2. The main findings may be summarized as follows.

(1) Antenna loading increases with frequency and with ambient pressure throughout the range examined. The maximum loading in the T-mode was ~70% for a deuterium plasma. Loading in a hydrogen plasma was 10-20% less than for deuterium, in general.

(2) Wave propagation closely follows predictions for a plasma-filled cylindrical waveguide with a uniform axial magnetic field. For EBT-S, in a deuterium plasma in the C-mode, propagation begins about 25 MHz. In the T-mode, propagation does not begin until about 35 MHz. The onset frequencies for hydrogen plasmas are still higher: 35 MHz and 45 MHz, respectively. No evidence of high Q eigenmodes has been observed.

(3) Energetic ion tails are produced during ICRF heating. The total energy in the tail increases with increasing frequency, pressure, and power. The distribution of ion energy around the torus follows the same general behavior as the wave propagation. The measurements are not sufficiently refined to allow determination of the ion power balance; however, the observed heating is anomalous. Figure 1.2 shows the ion distribution function deduced from a charge exchange analyzer, four cavities away from the antenna, for several applied ICRF power levels up to 15 kW at a frequency of 30 MHz for a 95% deuterium plasma. The figure shows that both the density and the temperature of the energetic ion tail component increase substantially with increasing applied power.

(4) The only effects of the ICRF power (up to 20 kW) on core plasma confinement are slight reductions in density (~15%) and ambipolar potential (~30%). No change is observed in impurity levels or electron temperature.

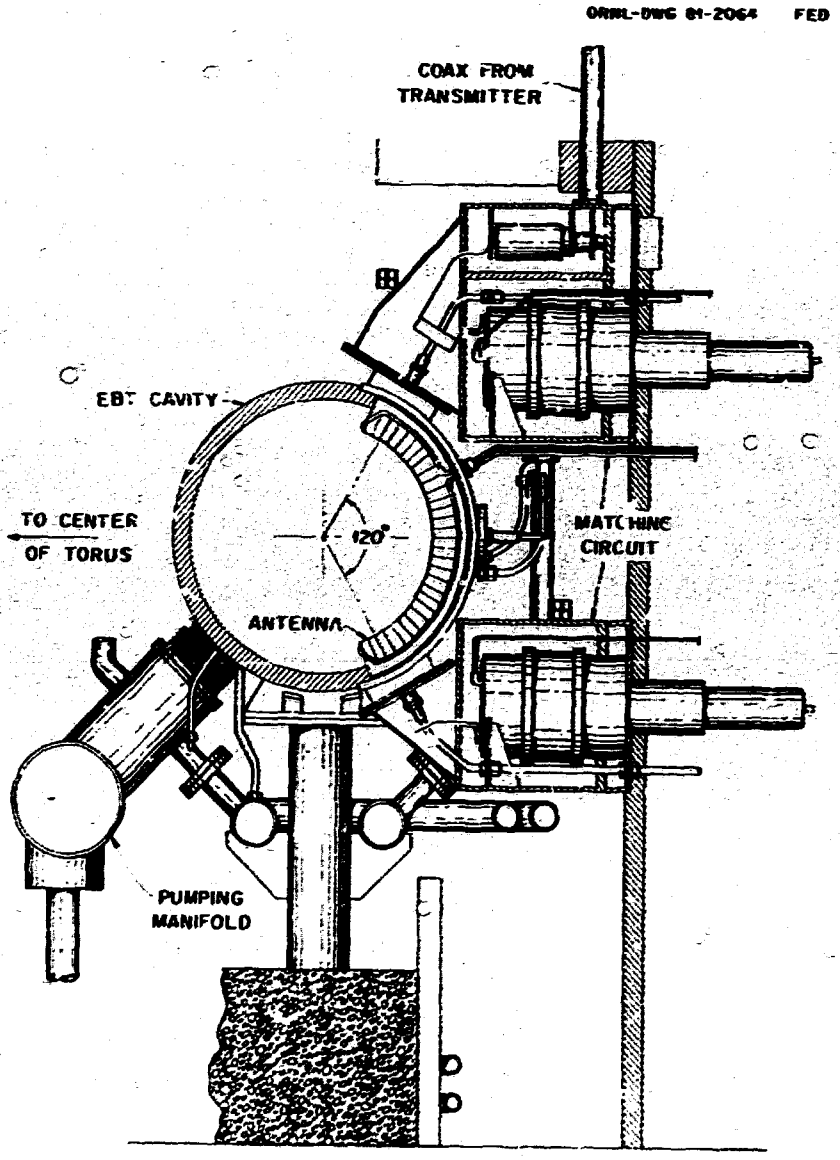

Fig. 1.1. Sectional view of the ICRF antenna and matching circuit installed on EBT.

(5) Anomalous increases in the relativistic electron ring beta are observed during ICRF heating in the T-mode. The trends closely follow those of the ion heating, except that the ring enhancement is uniform around the torus when wave propagation is present. Measurements with a hard x-ray spectrometer show an increase in both the temperature and the density of the ring.

1.1.2 Charge Exchange Measurements

W. A. [illegible]

Charge exchange measurements have continued with the aim of obtaining a better understanding of the systematic variation of ion properties with electron cyclotron heating (ECH) power and with torus pressure. In addition, considerable effort was devoted to charge exchange measurements during ICH experiments.

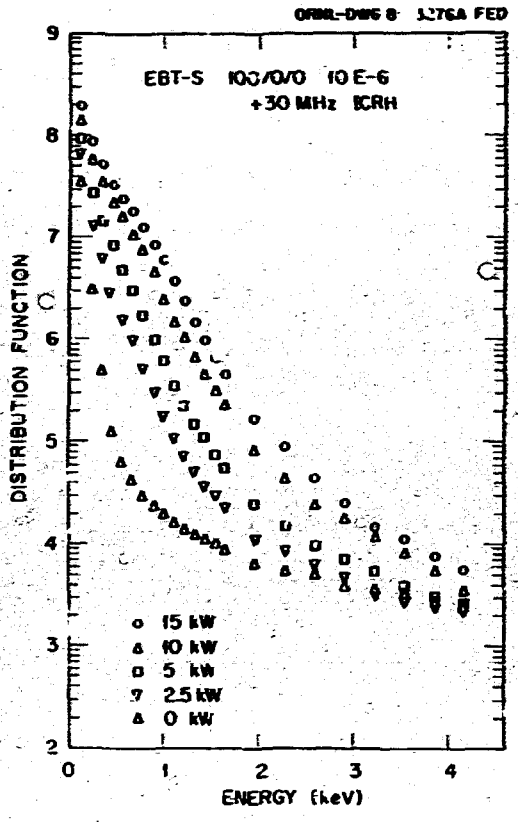

Fig. 1.2. Ion distribution function measurements during ICH at 30 MHz for several applied power levels up to 15 kW. The plasma conditions (EBT-S T-mode) for these data were as follows: ECH, 100 kW at 28 GHz; ambient neutral pressure, 1×10^{-5} torr (95% deuterium); midplane magnetic field on axis, 7 kG.

The ICH work is summarized in Sect. 1.1.1. In support of that effort, the single-chord nitrogen stripping cell analyzer with velocity filter was moved from cavity E1 to cavity W3, where the ICH antenna is located. The 4-chord nitrogen analyzer was then returned to cavity E1 for use with the ICH experiments.

Doppler width measurements of H_α radiation, detailed in Sect. 1.1.8, show a component of neutral hydrogen with a temperature of 10-20 eV, which (if assumed to be formed by charge exchange) has a line density n_f nearly equal to the line density n_e measured by soft x rays, microwave interferometry, and spectroscopy. Ion heating from Coulomb collisions with electrons heated by ECH power gives ion temperatures of 5-20 eV, depending on the plasma density and the particle confinement times. These results imply that the spectra recorded by the charge exchange diagnostics are not those of the bulk plasma but are ion tail components. This is consistent with the fact that the analyzer does not normally collect data below 100 eV and that the observed "temperature" components have low densities compared to n_e.

The observed spectra show a non-Maxwellian distribution that may be characterized by two main ion "temperature" components. One has a "temperature" of 60-100 eV with an integrated density product $n_i n_0 \ell \lesssim 6 \times 10^{12}$ cm^{-5}. The other component has a higher "temperature" of 200-350 eV but a much lower density. The "temperatures" of these tail components show no strong dependence on ECH power or torus pressure. The higher "temperature" tail is only obvious at torus pressures from the middle of the T-mode to the T-M transition.

The densities of these tails are strongly dependent on the torus pressure and the ECH power, as shown in Figs. 1.3 and 1.4. (The boxes in these two figures represent the range of different numbers of measurements at the various operating points.) The results in Fig. 1.3 are for a low pressure of 4.7×10^{-6} torr, which at the higher powers is very near the T-M transition. As the power is raised the relative densities of the two ion components rise, with that of the higher "temperature" component rising most dramatically. Figure 1.4 shows the steep rise in density of the high energy tails as the torus pressure is lowered through the T-mode toward the low pressure T-M transition at a constant input of 100 kW of 28-GHz ECH power.

1.1.3 Electron Density Measurements with a 9-Channel Microwave Interferometer

T. Uehara

The mean electron line density $\bar{n}_e$ is measured at various radii with a 9-channel,

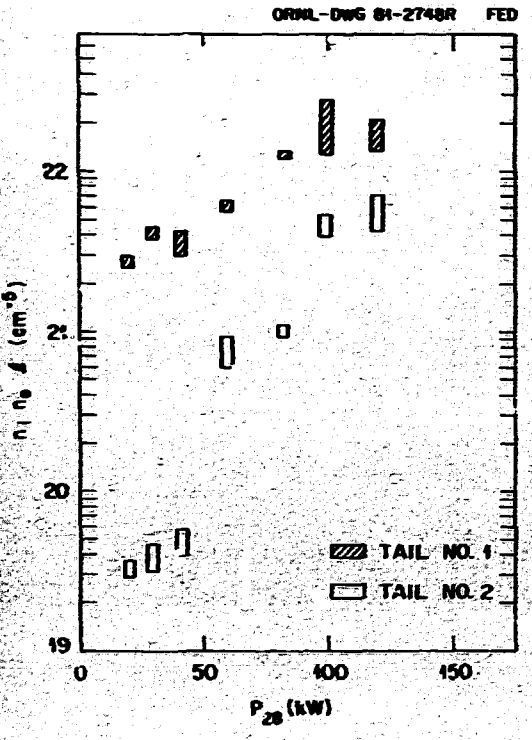

Fig. 1.3. Line-averaged $n_i n_0 \ell$ measurements vs torus pressure for the two observed "temperature" components for EBT-S operation at 100 kW of 28-GHz ECH power.

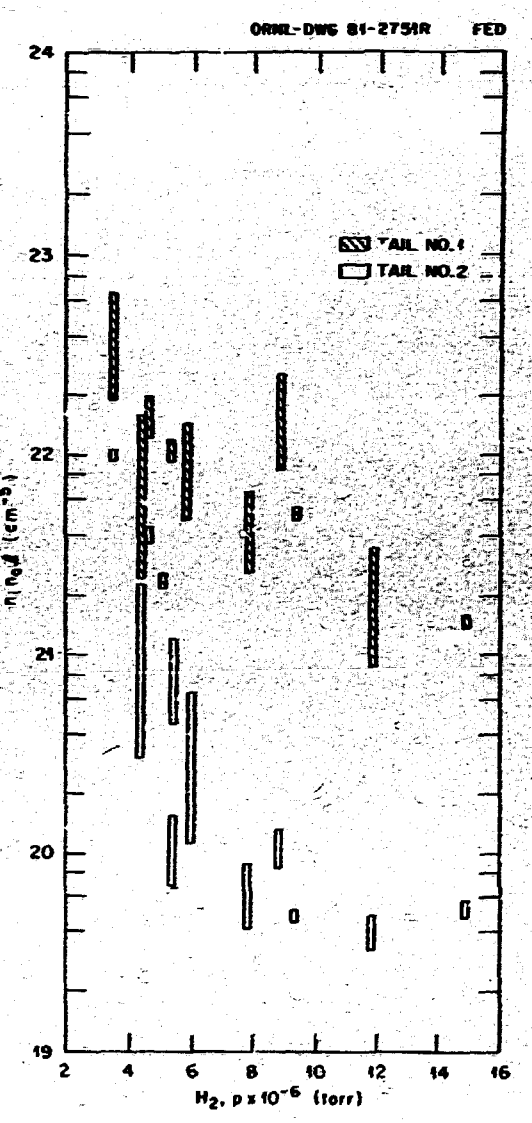

Fig. 1.4. Line-averaged $n_i n_0 \ell$ measurements vs 28-GHz ECH power. These data are for low pressure operation of EBT (4.7×10^{-6} torr), which at the higher power levels is near the T-M transition.

70-GHz microwave interferometer. The microwave beam is injected into the EBT cavity vertically through a standard gain horn that has a metallic lens for better directivity. The locations of the channels are shown in Fig. 1.5. From the chord-averaged phase shift data, the central density n(r=0) and its profile are obtained by an Abel inversion technique. From the high power microwave power experiments up to 200 kW at 28 GHz in EBT-S, the following observations are made about the electron density.

(1) The line-averaged (through the plasma center, r = 0) electron density increases with microwave power P_μ (Fig. 1.6).
(2) The density profile n(r) changes with the pressure p_0 and power as shown in Fig. 1.7.

The effective size of the plasma, $\ell_{eff} = \bar{n}\ell/n(r=0)$, a measure of the changing profile, decreases as the power increases or as the pressure decreases. However, the density scale length is almost constant for controlled power and pressure combinations, as shown in Fig. 1.8.

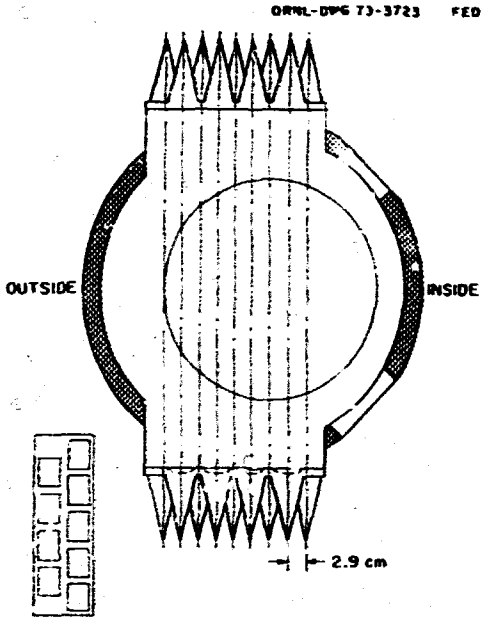

Fig. 1.5. Cutaway view of the 70-GHz, 9-channel microwave interferometer cavity on EBT-S.

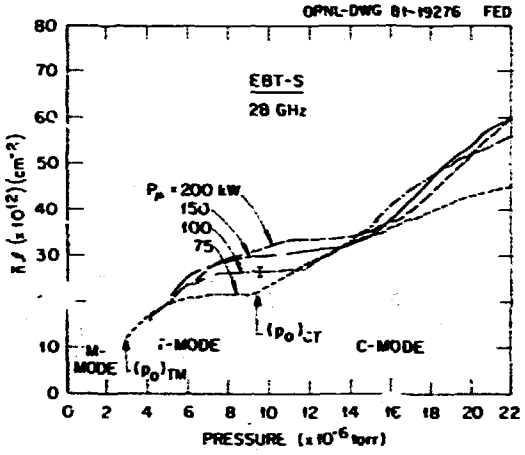

Fig. 1.6. Variations of the electron line density $\bar{n}\ell$ with pressure p_o and applied 28-GHz microwave power P_μ. The line density increases with the microwave power, and for a given power level it stays almost constant in the T-mode.

(3) The variation of $\bar{n}\ell$ with P_μ for constant scale length pressure cases [i.e., p_o $(p_o)_{TM}$ and p_o $(p_o)_{CT}$] is shown in Fig. 1.9. Within the experimental error bars of the measurements, the power scaling is given by $\bar{n}\ell \propto P_\mu^{0.5\pm0.1}$, which is consistent with the prediction of the neoclassical scaling.

1.1.4 Neoclassical Core Electron Confinement Scaling in EBT-S

T. Imai, K. A. Werley, J. H. Miller, K. A. Molvik

Recent high power microwave experiments in EBT-S at power levels through 200 kW at 28 GHz cover a broad parameter range (density, temperature, potential well, etc.). The operating window (T-mode) increases with power, and the plasma characteristics change significantly with operating parameters (power and pressure). Because the density profiles are observed to change with these parameters, zero-dimensional (0-D) comparisons with theoretical expectations for the complete data set are not possible. However, it is shown that for controlled power and pressure combinations, scale lengths and $e\phi/T_e$ are constant and the electron transport in EBT-S scales neoclassically; the power balance ($P_\mu \propto n^2/T_e^{0.5}$, see Fig. 1.10) and particle balance (τ_E/τ_p = constant, see Fig. 1.11) are consistent with neoclassical predictions.

1.1.5 Thomson Scattering

F. A. Hoffman

A limited amount of data was obtained with a new 25-J ruby laser system for electron measurements in EBT-S. The quality of the data was such that less was learned about the electrons than about what further improvements would be necessary. It was discovered that an input lens with a 2-m focal length cannot be used because of laser dump damage. (That lens had been selected to minimize the average spot size of the focused beam in the domain of the 20-cm scan.) At the same time, it was observed

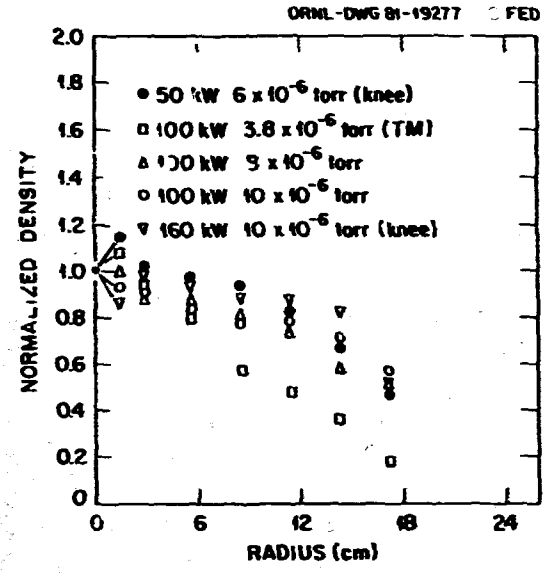

Fig. 1.7. Radial profiles of electron density, normalized to the central value n(r=0), for various combinations of P_μ and p_0.

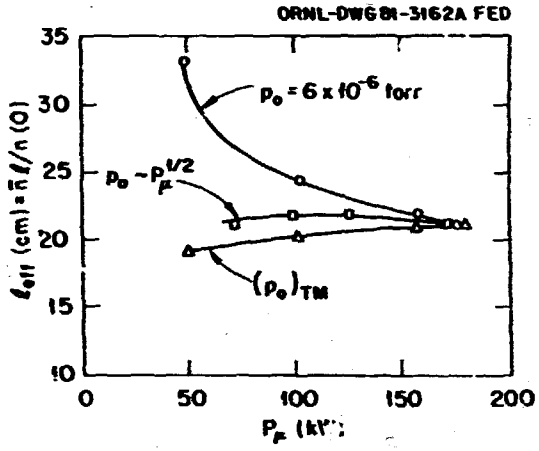

Fig. 1.8. Effective density scale length $\ell_{eff} \equiv \bar{n}\ell/n(r=0)$ as a function of microwave power. ℓ_{eff} stays almost constant for pressures of $p_0 \sim p_\mu^{0.5}$ and $(p_0)_{TM}$ (controlled pressure points).

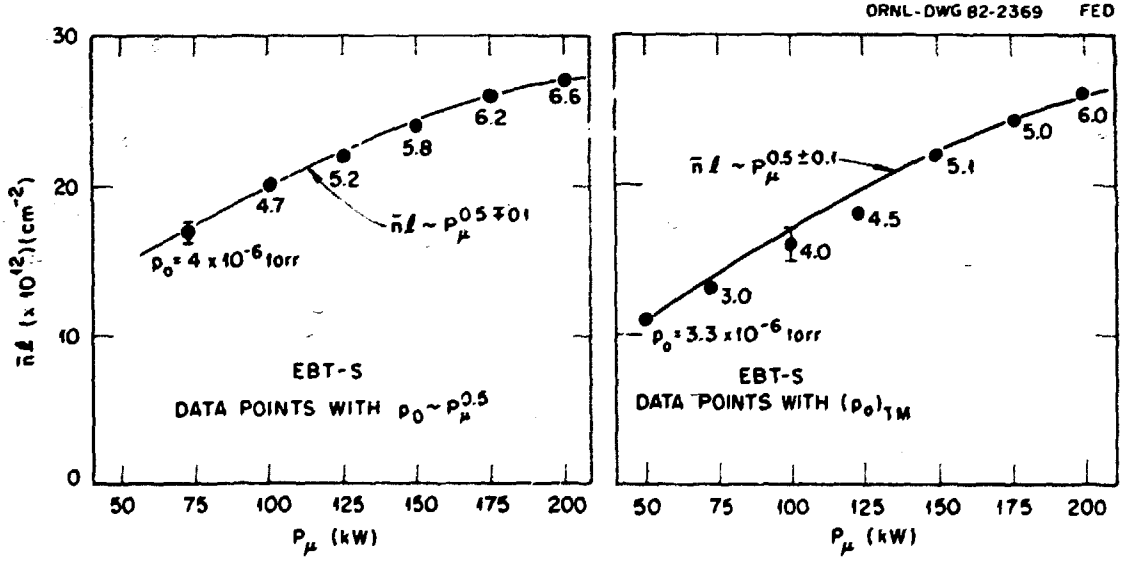

Fig. 1.9. Scaling of electron line density with the microwave power, $\bar{n}\ell \sim p_\mu^{0.5 \pm 0.1}$, for data points with controlled pressures.

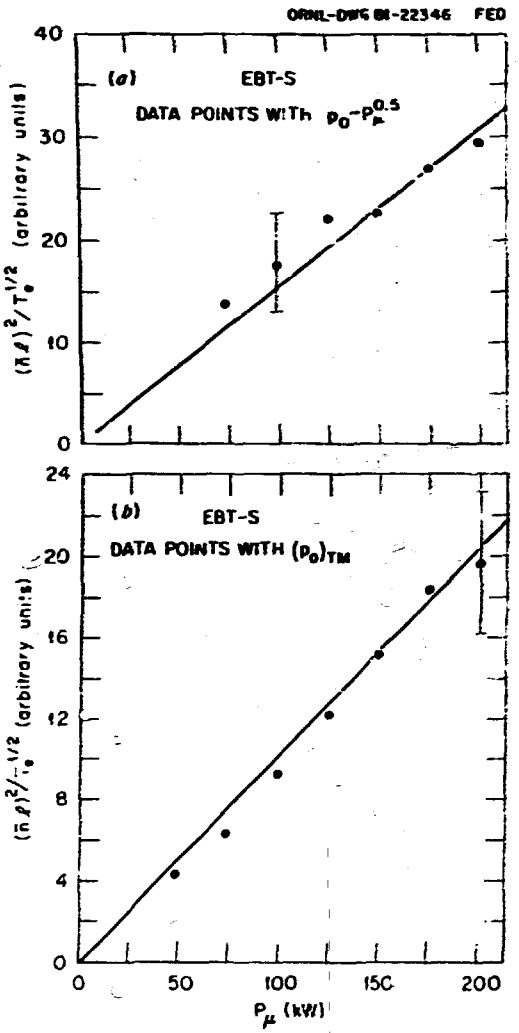

Fig. 1.10. The relationship between microwave power and electron line density and temperature indicates that $P_\mu \sim (\bar{n}\ell)^2/T_e^{0.5}$ for data points with constant scale length [$p_0 \sim P_\mu^{0.5}$ and $(p_0)_{TM}$], which indicates that the power balance is neoclassical.

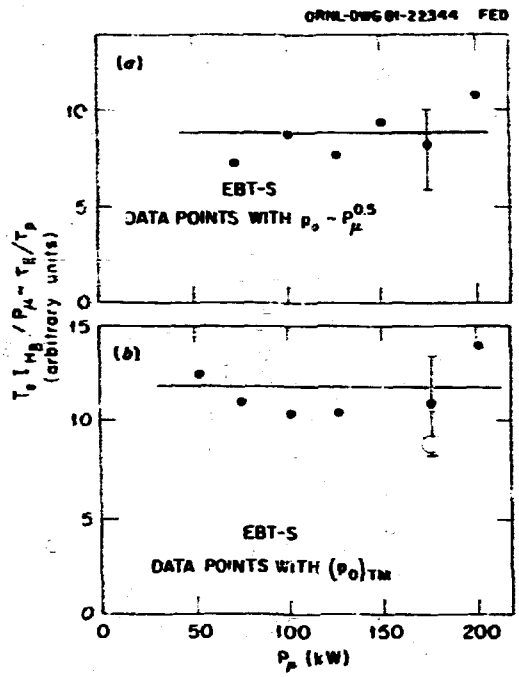

Fig. 1.11. The ratio of electron energy confinement time to particle confinement time τ_E/τ_p, which is experimentally observable through $T_e I_{H_\beta}/P_\mu$, is consistent with the neoclassical scaling for constant scale lengths. Here, $I_{H_\beta} \sim n n_0$, and n_0 is the neutral particle density.

that plasma light is still a severe problem in the outer data channels (720-750 nm) even with a reduction of the spectrometer slit width to 0.5 mm. This may be due in part to the increasing harshness of the plasma environment as the microwave power has increased. So far, the signal-to-noise ratio in the outer channels is much less than one, and it has not been possible to corroborate the temperatures indicated by soft x-ray measurements.

Improvements made during the year include the replacement of most optical components with nonbrowning, antireflection coated materials and a rearrangement of the detector configuration. For the latter, a sixth data channel was added, and a block was inserted to mask the aluminum multiplet at 704-706 nm. Since the plasma light is very low in the adjacent channels, the block is apparently working very well.

Design and fabrication have been completed on a replacement for the microwave-absorbing water window. The new viewing window consists of a Suprasil vacuum window, protected by a flap (with a ferrofluidic feedthrough), and a so-called "egg crate" microwave cutoff screen. Cold tests indicate nearly 30-dB attenuation of 28-GHz power, while visible radiation is 90% transmitted at normal incidence.

1.1.6 *Abstract of* Hard X-Ray Measurements of the Hot Electron Rings in EBT-S[5]

D. L. Hillis

A thorough understanding of the hot electron rings in EBT-S is essential to the bumpy torus concept of plasma production, since the rings provide bulk plasma stability. The hot electrons are produced via electron cyclotron resonant heating (ECRH) using a 28-GHz cw gyrotron, which has operated up to power levels of 200 kW. The parameters of the energetic electron rings are studied via hard x-ray measurement techniques and with diamagnetic "pickup" coils. The hard x-ray measurements have used collimated NaI(Tl) detectors to determine the electron temperature T_e and electron density n_e for the hot electron annulus. Typical values are T_e = 400-500 keV and n_e = 2-5 x 10^{11} cm^{-3}. The total stored energy of a single energetic electron ring as measured by diamagnetic pickup loops approaches ~40 J and is in good agreement with that deduced from hard x-ray measurements. By combining the experimental measurements from hard x rays and from the diamagnetic loops, an estimate can be obtained for the volume of a single hot electron ring. The ring volume is determined to be ~2.2 liters, and this volume remains approximately constant over the T-mode operating regime. Finally, the power in the electrons scattered out of the ring is measured indirectly by measuring the x-radiation produced when those electrons strike the chamber walls. The variation of this radiation with increasing microwave power levels is found to be consistent with classical scattering estimates.

1.1.7 *Abstract of* Electron Confinement Studies on EBT-S Using Soft X-Ray Techniques

D. L. Hillis, G. R. Haste

Soft x-ray bremsstrahlung measurements have been performed on the EBT-S plasma to determine the electron temperature T_e and electron density n_e using a calibrated Si(Li) detector over a wide range of operating conditions. The steady-state plasma of EBT-S is heated solely by microwaves using a cw gyrotron that can operate at power levels up to 200 kW. From the soft x-ray measurements, both electron temperature and density are found to increase at higher microwave power levels. For operation at microwave power levels of 200 kW, T_e approaches 1 keV while n_e approaches 1.2 x 10^{12} cm^{-3}. In general, confinement properties are found to improve with increased microwave power. The data are compared with neoclassical transport scaling, and the electron transport is found to be collisionless ($\nu/\pi < 1$) as well as neoclassical.

1.1.8 A Measurement of the Ion Temperature Using the Wings of the H_α (D_α) Spectral Line

R. K. Richards

Just as a charge exchange energy-analyzing diagnostic can determine the ion temperature from the shape of the energy spectrum of neutrals leaving the plasma, a spectroscopic measurement of the energy spectrum of neutrals within the plasma can be used to estimate the ion temperature. A particle balance within the plasma for the neutrals produced by charge exchange $n_0(cx)$ on a background neutral population $n_0(Bkg)$ gives

$$\frac{n_0(cx)}{n_0(Bkg)} \sim n_i \ell \sigma_{cx},$$

where n_i is the ion density, ℓ is the plasma diameter, and σ_{cx} is the charge exchange cross section. For the conditions in EBT, this ratio is in the range 0.01-0.1. A Doppler broadening measurement of the H_α (D_α) profile shows the existence of a neutral component with a fractional density in this range. The temperature of this component varies with plasma conditions between 8 and 18 eV. Correcting for a neutral temperature reduction due to wall recycling yields ion temperatures of 10-20 eV. Estimates of $n_i \ell$ for this component are typically ~2 x 10^{13} cm^{-2}, which is

in good agreement with the measurements of n_e from the microwave interferometer. Since the majority of the particles at these low energies cannot be detected with a charge exchange diagnostic, the charge exchange results will yield only the energy in the ion tail. This effect would explain the discrepancy between the value of $n_e n_{0_i}$ determined by a spectroscopic measurement and that of $n_i n_{0_i}$ determined by the charge exchange measurement.

1.1.9 Study of Aluminum Impurity Ions and the Ambipolar Potential in EBT

*R. H. Rhyne, E. F. Jaeger**

A previous spectroscopic study of impurity densities and their spatial profiles[7] has shown low charge states of aluminum existing in the core of the EBT plasma. Present studies indicate that the higher charge states are nonexistent. The particle confinement time for aluminum must then be very short and can be estimated by comparing densities of the existing charge states. For example, the lifetime for Al^{+3} is determined by these density measurements, $\tau_{Al^{+3}} \sim 40$ μs. Such a lifetime is smaller than the electron confinement time by several orders of magnitude and suggests a large flux of aluminum and an influence on the ambipolar potential as a consequence.[7] Doppler broadening measurements of the aluminum impurity indicate that it has an anomalously high temperature [$T(Al^{+3}) \sim 600$ eV].

A correlation of aluminum temperature and potential well depth has been observed and is shown in Fig. 1.12. This correlation appears between the potential and the temperature of the highest observable charge state with the scaling

$$\frac{Ze\phi}{kT} \sim 2.5 ,$$

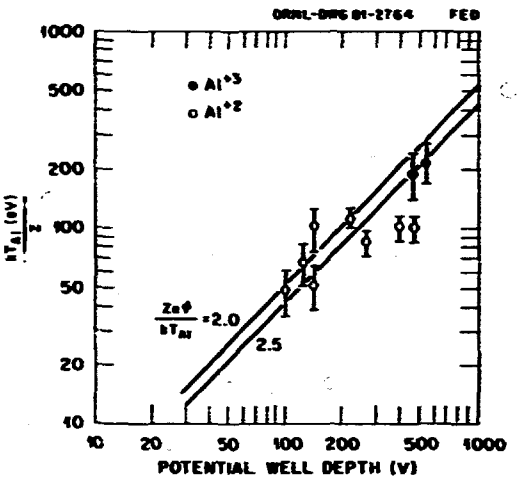

Fig. 1.12. The correlation of aluminum temperature, normalized by its charge state, with the potential well depth.

1.1.10 Synchrotron Radiation in EBT

*T. Uehara, H. A. Uehara**

The energy spectrum of the synchrotron radiation emitted by the relativistic ring electrons in EBT has been calculated for various classes of anisotropic ring electron distribution functions.[8] Calculations have been carried out for present (EBT-I/S) and planned (EBT-P) experiments. The ring temperatures in EBT-I and EBT-S are ~200 keV and ~500 keV, respectively. The projected ring temperature in EBT-P is ~1000-1500 keV. The calculations indicate that the radiation spectrum monotonically decreases and becomes almost flat at high frequencies, as observed in the experiments[10] (see Fig. 1.13). With increasing temperature and anisotropy, the total emission increases, the slope of the spectrum decreases, and the peak of the spectrum moves to a higher frequency. The ratio of the extraordinary wave intensity to the ordinary wave intensity decreases with temperature, but it increases with anisotropy (see Fig. 1.14). Calculated spectra and relative intensity levels of EBT-I and EBT-S are found to be in reasonable agreement with the experimental

*Plasma Theory Section.

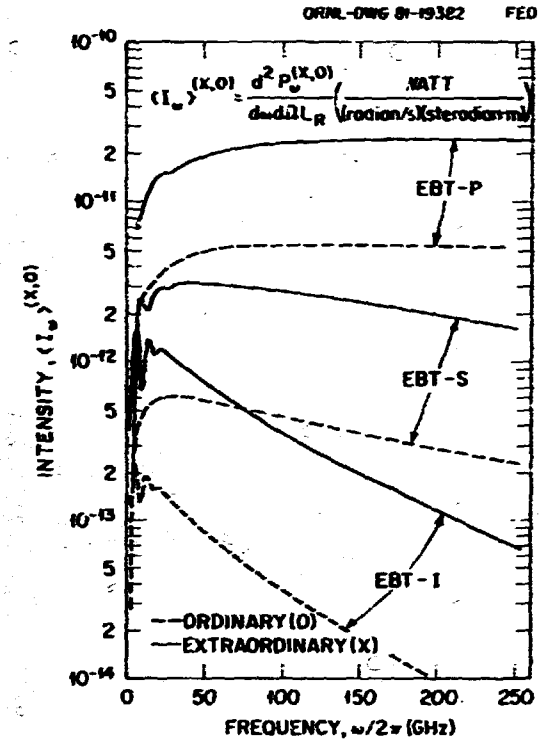

Fig. 1.13. Synchrotron radiation spectrum of the hot electron rings of EBT-I, EBT-S, and EBT-P. The extraordinary and ordinary wave intensities are shown for the isotropic Maxwellian distribution.

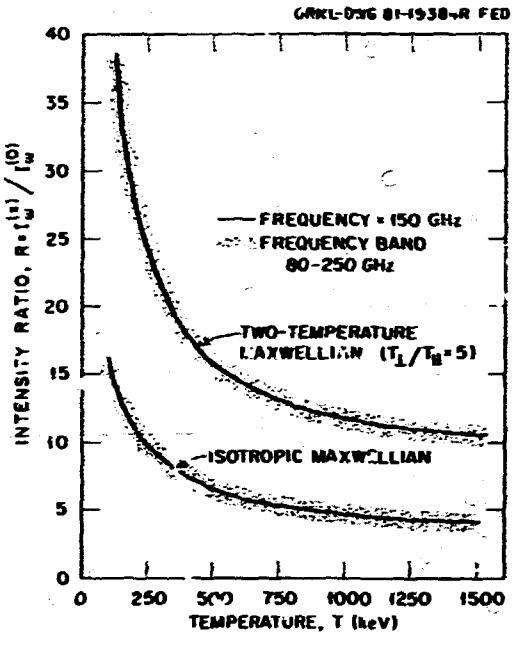

Fig. 1.14. Computed variation of the ratio of extraordinary wave intensity to ordinary wave intensity with temperature and anisotropy. The solid curve is for 150 GHz. Variation of the ratio within the frequency range 80-250 GHz is shown with a shaded band.

measurements.[10] For a Maxwellian ring electron distribution function, the total radiation power loss P_{rad} (in watts) can be estimated from

$$P_{rad}/V_r = 1.55 \times 10^5 \beta_r B_r^4 K_3(mc^2/T_r)/K_2(mc^2/T_r) ,$$

where K_2 and K_3 are the Hankel functions

$$K_3/K_2 \cong 1 + 2.5(\gamma - 1) + \frac{1.5(\gamma - 1)^2}{\gamma - 0.3} ;$$

$$\gamma = 1 + T_r/mc^2 ,$$

and V_r (in cubic meters), β_r, B_r (in Tesla), and T_r are volume per ring, ring beta, vacuum magnetic field at the ring location, and ring temperature, respectively. In Table 1.1, using typical EBT-I/S and EBT-P ring parameters, the estimated radiation power per ring is given. Both measurements and calculations show that synchrotron losses are low in EBT-I and EBT-S. However, in future experiments (EBT-P, reactor, etc.), radiation losses will play an important role in determining the ring power balance.

Table 1.1. The estimated radiation power loss for EBT-I, EBT-S, and EBT-P hot electron rings

	EBT-I	EBT-S	EBT-P
B_r (T)	0.32	0.5	1.0
T_r (keV)	200	500	1000
β_r (%)	18	24	20
V_r (m^3)	0.2×10^{-2}	0.2×10^{-2}	0.6×10^{-2}
P_{rad} (W)	1.3	20	1525

1.1.11 Modulated Electron Ring Measurements

T. B. Wilgen, D. L. Fitts

Formation, heating, and loss processes for an energetic electron ring can be investigated by modulating the ECH power applied to the EBT device. For these measurements, the power to a single EBT cavity is square-wave modulated at a very low frequency, 0.2-0.5 Hz, and the resulting periodic formation and decay of the electron ring in that cavity are monitored using diamagnetic loops, hard x rays, and synchrotron radiation diagnostics.

The analysis of the dynamic response of the ring is greatly simplified if the loss processes of the ring do not change with time (as the ring decays, for example). The dominant classical energy loss processes, drag cooling by the toroidal plasma electrons and classical scattering, depend primarily on the density of the toroidal plasma at the location of the ring. For this reason, only a single EBT cavity is modulated. The remaining cavities are powered continuously and serve to sustain constant plasma density in the modulated cavity; therefore, constant classical drag and scattering of the ring electrons is expected. Interferometer measurements in the modulated cavity verify that this approach is reasonably successful, as the line-averaged density changes by only 5-8% as the power is modulated At present, such a ring modulation experiment can only be done on EBT-I, where the power to individual cavities is controlled by a ferrite device with a switching time of 8 ms. EBT-S does not have a similar switching capability.

The time variation of the hard x-ray signal from a modulated ring is shown in Fig. 1.15, where the hard x-ray count rate is plotted on a logarithmic scale as a function of time. The time dependence of the applied power is also indicated. The time variation of the synchrotron radiation, measured at a frequency of 94 GHz, is shown in Fig. 1.16. Similar data are acquired from the diamagnetic loops. In Fig. 1.16, the synchrotron signal does not decrease to zero when the applied power is

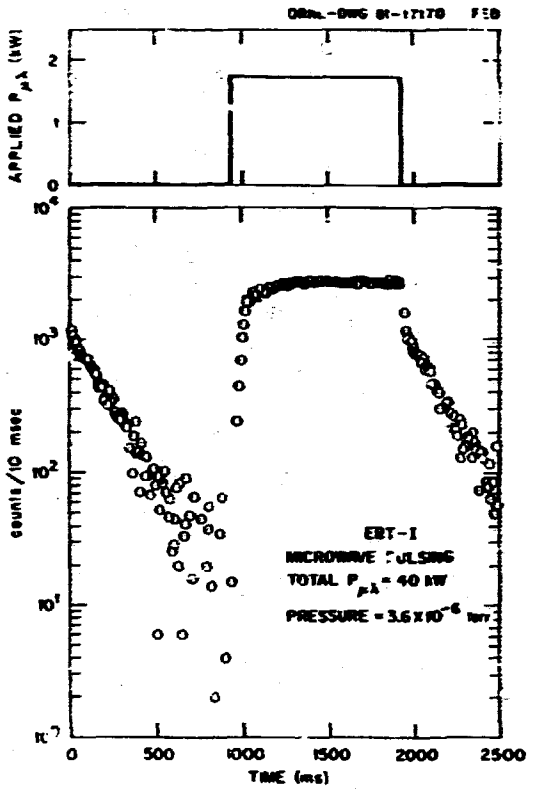

Fig. 1.15. The hard x-ray (E > 80 keV) count rate on a logarithmic scale as a function of time. The modulation of the applied power is also shown for reference.

switched off. Although the residual radiation is largely attributable to the rings in adjacent cavities, it is also possible that a weak residual ring (~10% of the original ring) still remains in the cavity. It is evident that the characteristic time scale of the rings is on the order of a few tenths of a second, and that total equilibrium is not established for several seconds. It might also be noticed that the formation process proceeds much more rapidly than the decay.

The signals recorded from the various ring diagnostics are processed on the assumption that the waveforms are exponential in shape. The formation and decay are analyzed separately and summarized by an e-folding time, which is assigned on the basis of a best fit to an exponential. In some instances, such as the

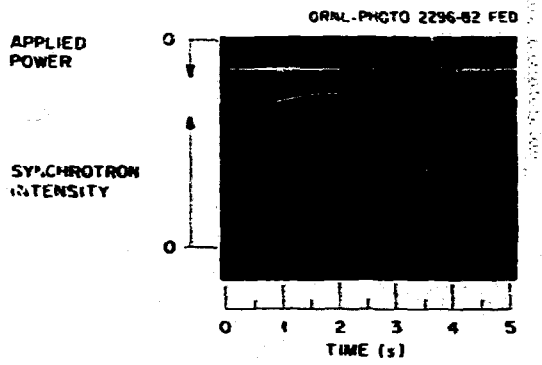

Fig. 1.16. Waveforms showing the time evolution of the applied power and the synchrotron radiation (94 GHz) when the power is square-wave modulated.

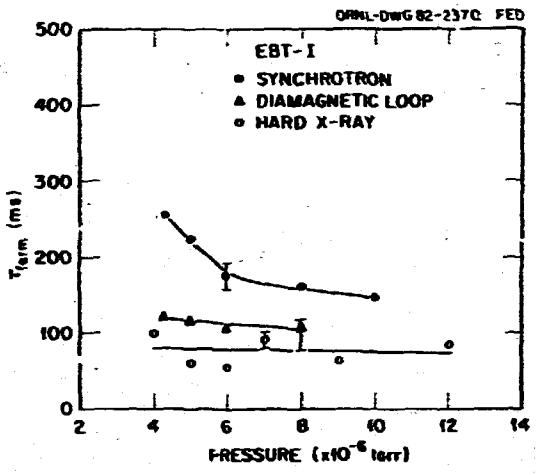

Fig. 1.17. Characteristic electron ring formation times, as measured by the diamagnetic, hard x-ray, and synchrotron diagnostics, vs the neutral gas pressure for EBT-I operation.

decay of the synchrotron radiation, the measured waveforms are almost exactly exponential in shape and the data are easily reduced. However, in the case of the diamagnetic loop, the data are significantly modified because the diamagnetic field must diffuse through the vacuum vessel wall. No attempt was made to correct the data for this effect. The best estimates for the decay time of the skin currents induced in the vacuum vessel wall by the diamagnetic field are in the range of 30 ms, which is not completely negligible.

The reduced data describing the formation of the ring are shown in Fig. 1.17, where the characteristic formation times inferred from the various ring diagnostics are plotted as a function of the neutral gas pressure. Similar data corresponding to the decay of the electron ring are shown in Fig. 1.18. The hard x-ray data were acquired during operation with 40 kW of power at 18 GHz, while the synchrotron and diamagnetic data correspond to 50-kW operation. Because the results are only weakly power-dependent, this difference can be neglected. With the exception of the synchrotron data, the characteristic times do not change substantially as the neutral gas pressure is varied. It is apparent, however, that there are consistent differences between the various diagnostics. Generally, the characteristic times inferred from the hard x-ray and diamagnetic data are comparable, whereas those inferred from the synchrotron measurements are longer by a factor of 2. This is comprehensible, however, when it is realized that each of the diagnostics has a different ring parameter dependence and represents a different

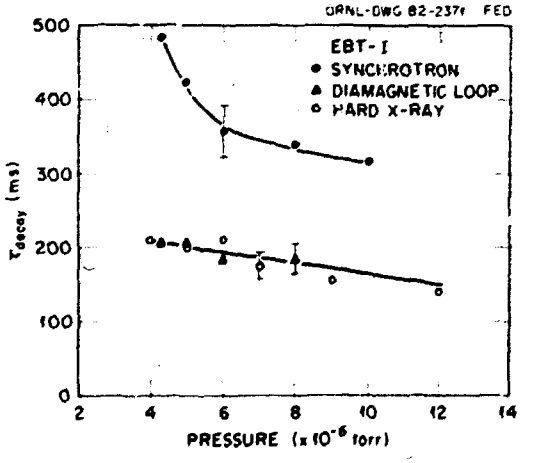

Fig. 1.18. Characteristic ring decay times, as measured by the various ring diagnostics, vs the neutral gas pressure for EBT-I operation.

moment of the energy distribution of the electron ring. Finally, the formation of the ring proceeds more quickly than the decay by roughly a factor of 2.

Of the two processes, formation and decay, the decay of the ring is more easily analyzed and can readily be compared with predictions based on classical ring loss processes. For this purpose, it is assumed that the electron ring temperature is 160 keV and that the magnetic field at the ring location is 3.2 kG. Using data from the multichannel microwave interferometer, the density of the toroidal plasma at the location of the ring is approximately 2.5×10^{11} cm^{-3}. In this case, classical drag cooling, scattering, and synchrotron radiation add up to an energy loss of 155 keV/s per electron, which corresponds to a classical energy decay time of 1.0 s. As can be seen from the data of Fig. 1.17, the stored energy of the ring, as measured by the diamagnetic loop, decays with a characteristic e-folding time of 200 ms. Although uncertainties in both the measured and calculated decay times must be taken into account, it appears that the electron rings of EBT-I decay significantly faster than expected on the basis of classical losses.

1.1.12 Microwave Interferometer Measurements at 140 GHz

R. F. [illegible], J. R. Wilson

A 2-mm microwave interferometer (f = 140 GHz), on loan from the Impurity Study Experiment (ISX), was installed on EBT and compared with the standard single-channel 4-mm interferometer (f = 70 GHz). The 2-mm interferometer was located two cavities away from the 4-mm system. A comparison of the phase shifts measured during pressure scans in EBT-I operation is shown in Fig. 1.19, where the 2-mm phase shift is plotted versus the 4-mm phase shift. Since the ratio of the interferometer frequencies is exactly 2:1, the 2-mm phase shift is expected to be exactly half of the 4-mm phase shift. Differences between the two measurements are quite small, corresponding to 10° for the 4-mm interferometer or 5° for the 2-mm system. Similar results were obtained for EBT-S operation, but in this case thermal drifts of the 2-mm system made the comparison difficult. The agreement between the two measurements indicates that it is very unlikely that errors in the standard single-channel 4-mm interferometer will exceed 10°. Assuming a path length of ℓ = 30 cm, this corresponds to a maximal uncertainty of $\pm 0.5 \times 10^{11}$ cm^{-3} for the measured line-averaged density.

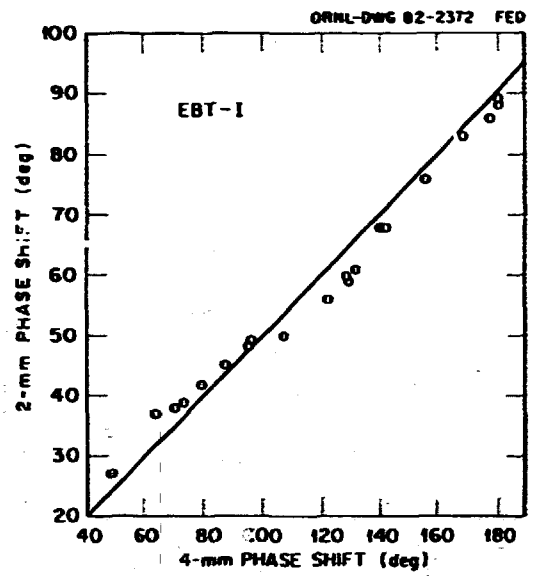

Fig. 1.19. The phase shift measured with a 2-mm interferometer vs the phase shift measured with a 4-mm system. The various data points were taken from three pressure scans during EBT-I operation.

1.1.13 Synchrotron Radiation Diagnostic Development

J. D. Tataronis,* D. G. Wang,* J. R. Wilson

A synchrotron radiation diagnostic has been under development at the University of Maryland. The objective is to measure the parameters of the EBT electron rings, with the initial

*University of Maryland, College Park, Maryland.

measurements to provide information on the density, energy, and parallel velocity distribution of the energetic electrons.

Because multiple reflections from the vacuum vessel walls are a nontrivial complication in the interpretation of measurements at high harmonics of the electron cyclotron frequency, considerable development has been undertaken to achieve optimal viewing optics. The quasi-optical viewing system that has been adopted uses a mirror-lens arrangement to isolate direct radiation from the ring.[11,12] By reflecting the viewing beam back on itself, the mirror enables double-pass viewing of the ring and at the same time allows the viewing port to be used as a viewing dump. The calibrated millimeter wave radiometers, which will be used to measure the absolute intensity and the polarization state of the radiation at frequencies of 80 and 138 GHz, have been received and are presently in use at the University of Maryland on a test setup that uses a retired EBT cavity to simulate the actual measurement.

In addition, supportive theoretical work has led to the development of simplified analytic expressions to describe the parameter dependences of synchrotron radiation from the relativistic electrons.[12,13] It is anticipated that these expressions will be useful in interpreting the forthcoming measurements on the EBT device.

1.1.14 Heavy Ion Beam Probe Experiments

K. A. Connor, F. M. Bieniosek, J. R. Goyer,* G. A. Hallock, R. L. Hickok, Jr.,* L. Solensten*

Experiments performed with the heavy ion beam probe during the past year have further demonstrated the similarity between data obtained under EBT-I and under EBT-S operating conditions. For example, the total detected Cs^{+2} signal profiles show that the plasma radius is somewhat larger in the C-mode than in the T-mode. Also, field errors can short out the potential well structure in the T-mode. While all the basic profile features have been observed now for both EBT-I and EBT-S, some difficulties were encountered in obtaining the scaling of the well with heating power and pressure. A detailed study of the transition from C- to T-mode showed the formation of the well at the C-T boundary in both cases. However, there were errors in the data for EBT-S that are related to system alignment and loading in the high voltage regions; the errors indicate that for the higher energy beams needed in EBT-S measurements better system control is required. Major modifications to the beam probe system are now under way to rectify this situation.

The EBT heavy ion beam probe is sensitive to the electron temperature and density in the core plasma, the surface plasma, and the hot electron rings. Since the sensitivity is not the same for all three electron distributions, it is possible to determine some of the gross properties of each by comparing their relative signal strengths. In particular, for EBT-I operation, it is possible to pulse the 18-GHz microwave power in the beam probe cavity and observe changes in the total detected signal. In normal operation, i.e., for potential measurements, the measurement is made with Cs^{+2} secondary ions, but increased sensitivity results when Cs^{+3} is used.

The location of the resonance surface has been shown to determine the size of the core plasma, as determined from potential profiles and profiles of Cs^{+2} signals obtained with the beam probe.[14] A complementary study has now been made with Cs^{+3}, showing that the hot electrons also move as expected. Figure 1.20 displays the results of three pulsed ring experiments (1 s on, 1 s off) at field currents of 4000, 5000, and 7250 A. The hatched regions correspond to the position of the second harmonic, and the crosshatched region corresponds to the fundamental resonance. The measurements were made at the bottom of the

*Rensselaer Polytechnic Institute, Troy, New York.

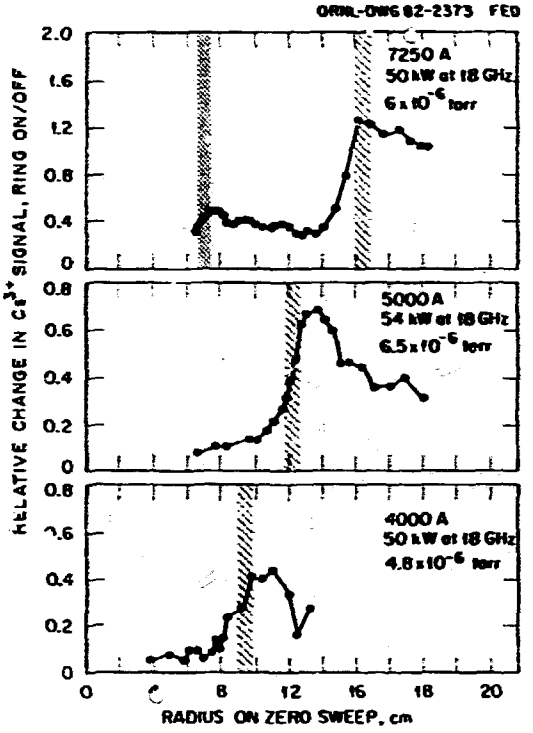

Fig. 1.20. Radial profile of the relative change in the Cs^{+3} signal for ring turnoff experiments with I_T = 4000, 5000, and 7250 A.

plasma, but measurements at the top show the same characteristics; namely, the peak relative change in the Cs^{+3} signal occurs near the second harmonic resonance location. The effect of the pulsed ring is less than 10% in the core. It is much larger in the surface plasma because the difference in relative sensitivity between the hot electrons and the surface plasma is greater than that between the hot electrons and the core. This fact distorts the apparent shape of the ring. Neglecting temperature gradients in the background plasma, the thickness of the ring is roughly 5-8 cm for both the 4000- and 5000-A cases. Although the background electron temperature is not well known in this region, the presence of any positive temperature gradient would reduce the thickness of the ring, as interpreted from these data, by 1-3 cm.

The 7250-A case is a fundamentally different heating topology, in which the magnetic field is high enough to move the fundamental resonance for 18 GHz into the midplane. The largest observed difference in the Cs^{+3} signal was still near the second harmonic, despite the fact that it was near the outer edge of the plasma. In contrast to the lower field cases, the relative change in the signal did not drop to 10% inside the second harmonic, but remained close to 40% up to the first harmonic surface. Inside the fundamental surface, there was no signal at all because of the very low electron temperature in this heating configuration. Similar hollow profiles were observed on the relative changes of the Cs^{+2} signal. The 7250-A profile shows heating from the fundamental surface nearly to the wall. Hence, the position of the hot electron ring is not clear from this experiment.

1.1.15 Observations of Low Frequency Plasma Fluctuations in EBT

A. Komori

In the EBT plasma, two types of low frequency fluctuations have been identified in the dc frequency range up to 1 MHz: a drift-type fluctuation and an interchange instability. The latter, which leads to an unstable toroidal plasma, is prominently excited in the outer plasma along the hot electron ring. In the proper neutral pressure regime, the hot electron rings prevent these two fluctuations from growing and permit the establishment of a stable toroidal plasma.

1.1.16 *Abstract of* Experimental Hot-to-Warm Electron Density Ratio for Instability Threshold in the ELMO Bumpy Torus[15]

O. Hiroe, L. A. Berry, R. J. Colchin, J. C. Glowienka, G. R. Haste, D. L. Hillis, T. Uehan

The hot-to-warm electron density ratio is determined for the onset of instabilities that spontaneously grow in the region of large stored energy in EBT. When this ratio exceeds ~0.5, the instability becomes conspicuous as

an oscillation on the microwave interferometer signal. When the microwave power and ambient pressure are varied, the ratio remains constant in spite of changes in the density, temperature, and beta value. The stable region in a beta diagram increases when the microwave power increases.

1.1.17 *Abstract of* Nonstandard Heating Experiments in EBT[16]

J. C. Glowienka, W. A. Davis, D. L. Hillis, T. Uckan, F. M. Bieniosek, L. Solensten

The magnetic design of EBT-I/S provides a flexible environment in which to examine various ring and core plasma ECH scenarios. The heating occurs when the ECH power, available at three discrete frequencies (10.6, 18, and 28 GHz), is in resonance with local harmonics of the electron cyclotron frequency. The resonance locations can be moved in a continuous fashion in the cavity sectors by changing the toroidal magnetic field over the range of 0-1.4 T. In an EBT, the bumpy magnetic equilibrium is stabilized by the high beta, hot electron rings formed in the field bumps by proper choice of microwave heating frequency and magnetic geometry. The most commonly used heating geometry for ECH is the standard resonance configuration (SR) wherein a fundamental resonance exists across the mirror coil throats for bulk plasma heating and a second harmonic resonance exists in an annular region in the cavity midplane for ring heating. Reported here are the results of two nonstandard heating experiments. In one, the fundamental ECH resonance at either 10.6 or 18 GHz was placed at the usual ring position in an attempt to generate rings solely with fundamental heating; this is the fundamental resonance configuration (FR). In a second experiment, an attempt was made to heat the ring and core separately by forming the ring as above with 10.6 GHz and then heating the core with the fundamental and second harmonic of 28 GHz; this is the separately coupled ring and toroidal core heating configuration (SCRATCH). In both cases, the hot electron annuli were formed and stabilized the core plasma as in the SR experiments. In FR, the rings formed at the second harmonic and no significant potential structures were found. In SCRATCH, either a potential well or a potential hill could be formed (see Fig. 1.21). In both heating regimes, significant ion heating above that found in standard heating experiments was found.

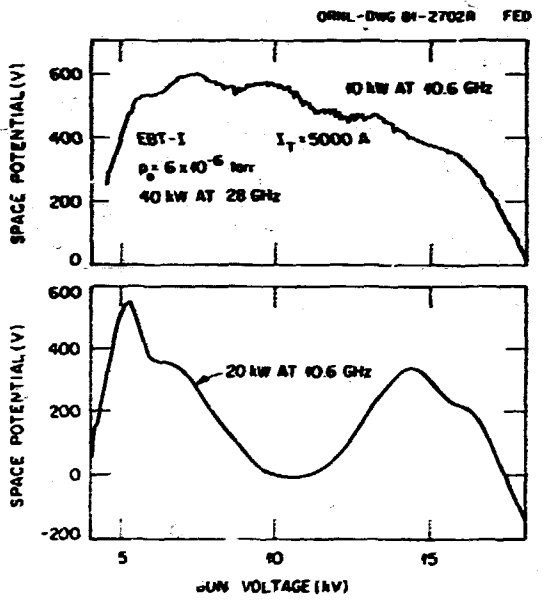

Fig. 1.21. Comparison of two plasma potential profiles in SCRATCH using the same ECH power at 28 GHz (50 kW) but different levels of 10.6-GHz power (10 kW vs 20 kW).

1.1.18 Ring Diamagnetic Diagnostics: Perpendicular Energy

*K. H. Carpenter**

The concentric cylindrical current sheet model that has been used to provide a calibration for the diamagnetic flux loops' perpendicular energy signal has been studied extensively.[17] The calibration results obtained

*University of Missouri, Rolla, Missouri.

using this simple model are quite insensitive to the model parameters (a fact attributed in part to the arrangement of the pickup loops, which resemble Helmholtz coils); this should imply that similar calibration results would be obtained with other models. A test of this hypothesis has been carried out in studies using a magnetohydrodynamic (MHD) equilibrium model in bumpy cylinder geometry. Calculations using a modification of an available EBT equilibrium code[18] have shown results for the perpendicular energy calibration that are in essential agreement with those obtained using the current sheet model.[19-21] This MHD equilibrium model automatically provided a more realistic geometry, along with a self-consistent treatment of drift current effects and local magnetic flux density. These two factors had been the major points on which the current sheet model had been questioned.

1.1.19 Ring Diamagnetic Diagnostics: Ring Geometry

R. D. Dimmick, W. C. Griffith,* F. W. Prohaska,* W. C. Turner*

Although the ring diamagnetic flux linking the perpendicular energy pickup loops is almost completely insensitive to ring geometry, some information on ring geometry can be obtained from measurements of the diamagnetic field strength at the outside of an EBT cavity.[22] A magnetometer based on ferromagnetic resonance in small spheres of yttrium iron garnet (yig) has been developed to provide such measurements with a precision of a few hundredths of a gauss.[23] Generator current fluctuations and plasma fluctuations limit the accuracy of the data, but with generator current compensation incorporated in the instrumentation, diamagnetic field variations as small as 0.05 G can still be observed. Data taken with the field probe located on the outer wall of the horizontal midplane of an EBT cavity yielded field values in agreement with the perpendicular energy signals and the current sheet model. With reasonable assumptions for all current sheet model parameters but one, this last geometrical parameter is determined by the field measurement.[20] Field measurements taken with the field probe relocated to the cavity wall on the inside of the torus (diametrically opposed to the first location) also yielded agreement with the perpendicular energy and the current sheet model – but with a different set of model parameters. This points out a lack of axisymmetry in the rings, which has been anticipated. The details of this asymmetry and their interpretation will be the subject of further study.

1.1.20 EBT-S Microwave System Development

H. O. Barrow, T. L. White, D. D. Bates, N. M. Wellington

Routine operation of the 28-GHz, 200-kW, cw gyrotron ECH system on EBT-S continued, and further development was undertaken to improve the efficiency and reliability of operation, especially at higher power levels. Plasma operation at 200-kW cw gyrotron output was initially achieved in May, thus enabling timely acquisition of desired EBT scaling data for the EBT-P checkpoint review in August.

Detailed calorimetric measurements of the 28-GHz power losses in the overmoded transmission and distribution system showed that the average efficiency of delivery of gyrotron output power to the EBT toroidal vessel is slightly over 70%. About one-third of this dissipative loss occurs in lumped elements that are included to improve impedance matching for the $TE_{0,1}$ gyrotron interaction mode. An additional third of the transmission loss appears as I^2R losses in the 6.35-cm-diam (2.5-in.) circular waveguide, and the final third appears as I^2R losses in the large toroidal manifold used for power division and distribution. As expected, the system is slightly dispersive, and variations both in the total fractional losses and in the distribution of losses are

*University of Missouri, Rolla, Missouri.

observed in response to the small frequency changes that accompany variations in gyrotron output power.

To improve the performance and efficiency of the toroidal manifold used to divide and distribute the power to the 24 mirror confinement regions, the diameters of the circular output coupling apertures through which 28-GHz power is coupled to EBT-S were enlarged. The larger apertures produce stronger coupling to the lossy plasma, thereby reducing the level of stored 28-GHz energy in the manifold. This leads to improved impedance matching to the input waveguide from the gyrotron and to improved transmission efficiency of the manifold through reduction of losses.

1.1.21 *Abstract of* Analysis of Mixed-Mode Microwave Distribution Manifolds[22]

T. L. White

The 28-GHz microwave distribution manifold used in the EBT-S experiments consists of a toroidal metallic cavity, the dimensions of which are much greater than a wavelength, fed by a source of microwave power. Equalization of the mixed-mode power distribution to the 24 cavities of EBT-S is accomplished by empirically adjusting the coupling irises that are equally spaced around the manifold. The performance of the manifold to date has been very good, but no analytical models existed for optimizing manifold transmission efficiency or for scaling this technology to the EBT-P manifold design. The present report develops a general model for mixed-mode microwave distribution manifolds based on isotropic plane wave sources of varying amplitudes, which are distributed toroidally around the manifold. The calculated manifold transmission efficiency for the most recent EBT-S coupling iris modification is 90%. This agrees with the average measured transmission efficiency. The model also predicts the coupling iris areas required to balance the distribution of microwave power while maximizing transmission efficiency. In addition, losses in waveguide feeds connecting the irises to the cavities of EBT are calculated using an approach similar to the calculation of manifold losses. The model will be used to evaluate EBT-P manifold designs.

1.1.22 *Abstract of* Vacuum System Problems of EBT, a Steady-State Fusion Experiment[23]

R. L. Livesey

The EBT is a 24-sector, steady-state, fusion energy research device with plasma production and heating provided by microwave sources. The microwave heating is provided by klystrons, which deliver up to 60 kW of 18-GHz power and 30 kW of 10.6-GHz power, and by a cw gyrotron, which has operated at power levels up to 150 kW. Preliminary experiments with ICRH have added up to 10 kW of 30-MHz steady-state rf power. The large amount of microwave power used in heating the plasma of EBT produces a number of problems which have impacted the vacuum vessel design. Special attention has been directed toward the elimination of microwave propagation to elastomer surfaces. Various problems dealing with the maintenance of this unique vacuum vessel operated in a microwave environment will be discussed. Particular emphasis will be placed on how these problems have been addressed on EBT.

1.1.23 *Abstract of* Intrinsic Engineering Problems for ELMO Bumpy Torus-Scale[24]

D. A. Everitt, H. O. Eason, R. L. Livesey, T. L. White

The reduction in engineering problems stemming from EBT's large aspect ratio and steady-state operation has made the EBT concept an attractive alternative to the tokamak concept. However, EBTs have their own unique engineering problems. Microwave containment, hard x-ray shielding, aluminum sputtering, and steady-state heat dissipation are the major concerns for the EBT-S experiment. The most difficult of these is the containment of high power microwaves in an all-aluminum vacuum vessel sealed with O-rings. Since O-ring

materials readily absorb microwave power, a special O-ring gland was designed for protection. Careful attention must be paid to this seal to prevent microwave arcs and O-ring damage. For diagnostic access, a variety of microwave reflectors and absorbers have been designed to protect equipment and personnel. Water jackets and other lossy mediums have been designed to absorb microwave power where reflection has not been practical. In addition, all diagnostics that protrude into the microwave environment must be designed to preclude sharp edges and small cracks where microwave arcs may occur. The creation of hard x rays within EBT-S has added to the engineering problems. Radiation hardening of flexible nylon water lines is evident and has caused some loss-of-coolant incidents in the mirror coils. Obviously, personnel and sensitive diagnostic equipment must be protected. Aluminum sputtering creates another unique engineering problem. Glass viewing ports must be designed with shutters to prevent accumulation of sputtered aluminum, and rf insulators must be protected from sputtered material to preserve their integrity. In addition, the thin layer of aluminum tends to peel off or flake, and these flakes fall into areas where they can cause microwave arcing and other problems. Finally, the move to higher power and higher frequency microwave energy is beginning to tax present cooling schemes on EBT-S. This could be a serious obstacle in the road to even higher injected powers.

1.1.24 EBT Split Mirror Coils

R. H. Hunter

The proposed design for the split mirror coils for EBT-S was improved during 1981. These coils are intended to replace four of the ordinary coils on EBT-S to permit experiments to be done in the mirror, or high field, region. The principal design criterion for the split coils is that they be as nearly identical — mechanically, electrically, magnetically, and thermally — to the ordinary coils as possible. If this criterion is met, the new coils could be interchanged with the ordinary coils with no changes other than the new access to the coil throats. In this section, the new design is described and compared with the ordinary coils.

Coils

The new design makes use of a concept first proposed by Luton.[25] In this concept the crossovers are not formed by bending the conductor but are machined from a solid copper block, through which the water passage is drilled and to which the conductor is soldered. Advantages of this technique include more reliable insulation in the crossover region and fewer void spaces, or regions without conductor, in the coil.

Cases

The new coil case will have three 2- by 15-cm ports on the midplane. It will be machined from a solid aluminum forging, in contrast to the ordinary coil cases, which are made in two sections and then welded together. The two halves of the split coil will be wound in place in grooves in the coil case. This type of construction allows the material in the coil throat to be thinner than it is in the ordinary coil case. The result of the thinner throat, plus the added layer of conductor on the inner portion of the coil, is that the clear bore diameter of the new cases is reduced by 0.36 cm.

Magnetics

While the magnetic field produced by these split coils is not identical to that produced by the ordinary coils, the two appear to be very similar except near the windings. Since it is difficult to assess the impact of the difference in the magnetic fields directly, another property of the field is used to compare the two. The longitudinal invariant of particle motion, $J = \int v_{\parallel} ds$, can be shown to be proportional to $\oint(1 - B/B_t)ds$ evaluated along the flux line, where B_t is the field value where the particle turns. Particles tend to drift along surfaces

of constant J known as drift surfaces. Evaluation of the drift surfaces in a cavity bounded by ordinary coils and in a cavity bounded by split coils shows that the drift surfaces are very similar in the two. The greatest difference occurs for particles that turn in the coil throat, near the windings. The intersections of these drift surfaces with the midplane are shown in Fig. 1.22 for these particles.

Conclusions

The new design appears to be feasible to construct, to result in magnetic fields that are sufficiently close to the present magnetic

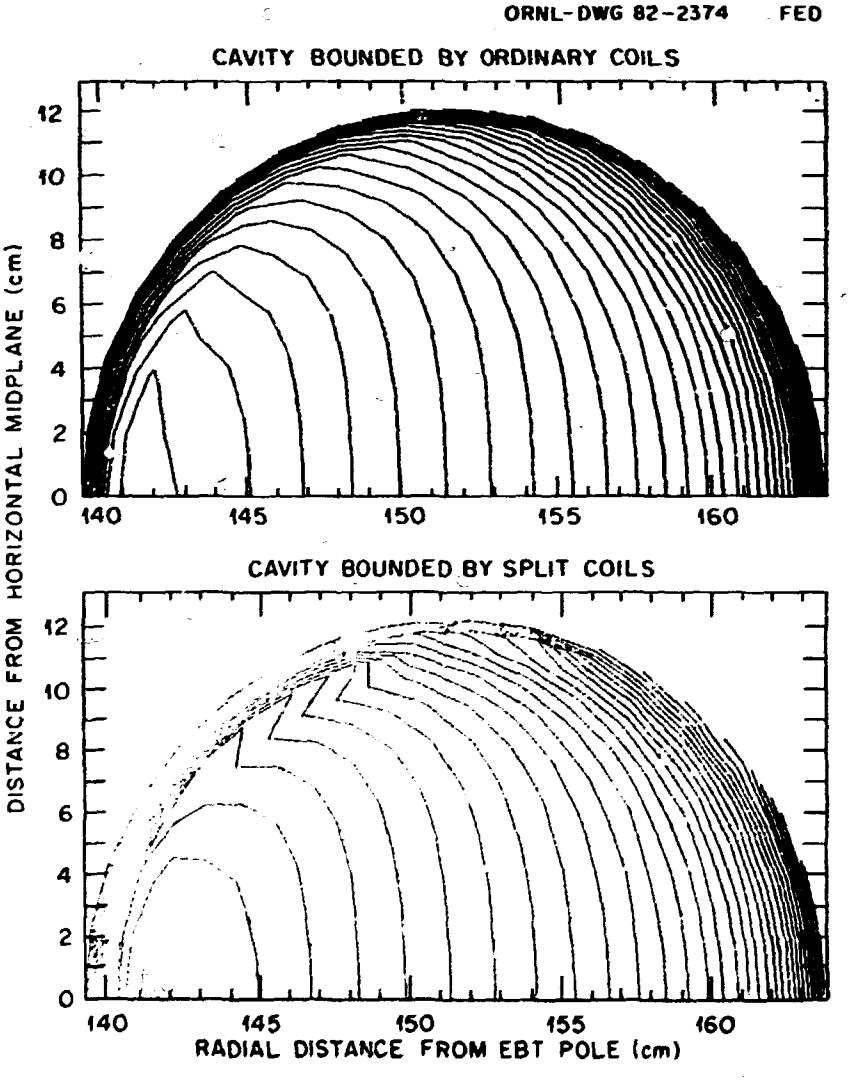

Fig. 1.22. Drift surfaces in cavities bounded by ordinary coils and by split coils. The value of the turning magnetic field has been chosen so as to maximize the difference between the two sets of curves.

fields, and to have clear bores only slightly smaller than those of ordinary coils.

1.1.25 Bundle Divertor Study

A study contract with the Fusion Power Systems Department of Westinghouse Electric Corporation was established in 1980 for the design of a bundle divertor for EBT-S. This work was completed in 1981, and reports[26] have been issued.

The first phase of the contract focused on magnetic field conceptual designs; toroidal and bundle divertors were considered in detail. The magnetic field configuration of choice was the toroidal divertor, and the second phase of the study focused on a mechanical design that can fit into the existing EBT-S machine without large modifications. A conceptual design was evolved that is compatible with EBT even if aspect ratio enhancement (ARE) coils are added. This design included considerations of force, heat loads, and pumping. An entirely satisfactory solution to the pumping problem was not found, in large part because of the microwave environment of the divertor chamber. Initial operation using turbopumps was envisioned. It was estimated that another 18 months of detailed design and manufacture would be required to construct the toroidal divertor system.

1.1.26 Aspect Ratio Enhancement

As a general statement, confinement in an EBT depends on the square of the aspect ratio, i.e., $n \propto A$, where $A = R/a$ with R the major radius of the device and a the radius of a coil. It has been shown, however, that use of any of a number of different types of auxiliary coils improves the confinement or, in effect, enhances the aspect ratio.[7] Perhaps the simplest system is one that simply increases the mirror ratio.

An approach to implementing this configuration on EBT-S is illustrated in Fig. 1.23, where, in addition to the toroidal field coils, two Helmholtz-like ARE coils are shown. They are wound in slots that are machined into the microwave cavities because cooling lines, generator buses, coil supports, and a host of other components severely restrict the available space outside the cavity envelope.

A prototype cavity was installed in late 1980 to test compatibility with the microwave environment and with the ring and core plasmas. Unfortunately, there was a factor of 2 reduction in the ring energy as measured by diamagnetic loops. Figure 1.24 illustrates this drop for runs while the ARE cavity was in place and after it was taken out. This drop is unacceptable and has forced consideration of alternative designs.

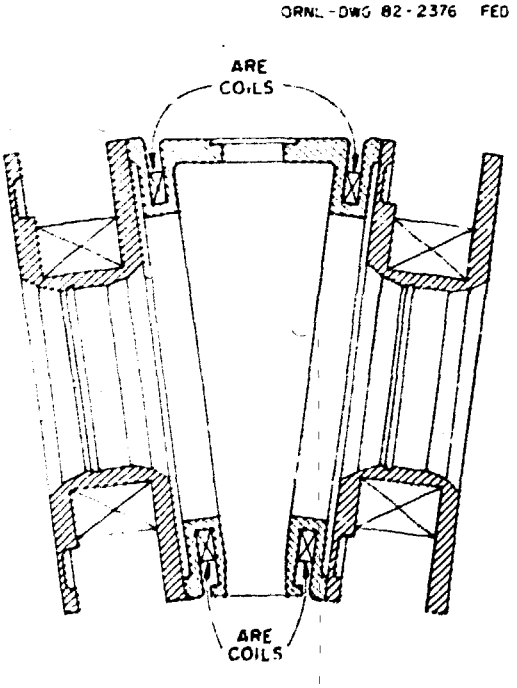

Fig. 1.23. Equatorial section of EBT-S ARE cavity.

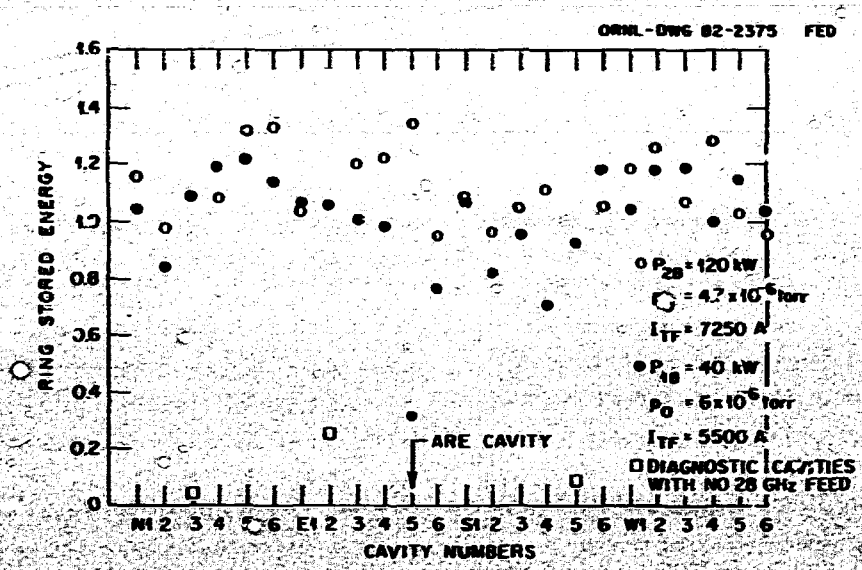

Fig. 1.24. Ring stored energy for runs with (●) and without (○) the presence of the ARE cavity. The runs shown are typical of all runs made during the respective time periods, and the differences in microwave frequency and power, filling pressure, and toroidal magnetic field are not important.

Three options will be considered:

(1) reducing the depth of the intrusion by using smaller coils with higher current density,

(2) attempting to install a set of coils outside the microwave cavities, and

(3) using iron pole piece inserts.

A decision as to which approach is best will be made in mid-1982.

In order to obtain information for the evaluation, a subcontract was placed with Westinghouse Electric Corporation to develop the iron pole piece concept (which was first advanced in Westinghouse's EBT-P Phase I study). This work was summarized in Ref. 28. Briefly, the conclusions were: (1) iron pole pieces can improve particle drift surfaces by an amount equivalent to an aspect ratio enhancement of 20-30% (the definition of the ARE factor is somewhat arbitrary) and (2) there are no essential engineering or physics problems associated with the iron system. The decision among the various approaches will be based on cost, schedule, flexibility, and performance.

1.2 EBT-P PROJECT

A. L. Hoch, J. K. Ballou, A. Y. Broverman, R. A. Brown, R. S. Edwards, W. H. Fletcher, W. R. Hamilton, C. M. Loring, H. C. McCurdy, T. J. McNamara, J. D. Stout, D. W. Swain

1.2.1 Introduction

Recent DOE policy on the development of fusion energy has placed increased emphasis on the testing of alternate concepts to permit comparisons with tokamaks and mirrors in the mid-1980s. In December 1978, DOE selected the EBT concept as one of the alternate concepts to be advanced through a proof-of-principle experiment. The EBT-P device is a R&D facility intended to advance the EBT magnetic confinement fusion concept to the proof-of-principle level. Specific objectives of EBT-P are:

- to extend EBT plasma parameters into the range where they can be reliably scaled to the reactor regime, to validate scaling laws, and to demonstrate that a power-producing EBT reactor is a viable concept, and

to determine whether core plasmas with intermediate values of beta can be stably confined.

The responsibility for technical management of the EBT-P project, including the supporting R&D activities, is assigned to ORNL. The project is being conducted in three phases. Phase I, project definition, was completed in October 1979. Phase II, the design, fabrication, and installation of the device, is now in progress. Phase III, operations, is scheduled to begin in 1985.

Before Phase I began, a memorandum of agreement (MOA) was completed to document the agreements between DOE and ORNL on plans and responsibilities for initiating the project. An important aspect of the MOA was the intention that industry have a major role in the definition, design, fabrication, and experimental operation of the device.

Phase I project definition studies were completed in October 1979 by four industrial teams (Ebasco Services, Inc., Grumman Aerospace Corporation, MDAC, and Westinghouse Electric Corporation) and ORNL. Using the information derived from the project definition studies, ORNL prepared a proposed reference design for EBT-P[23] that was approved by DOE in early 1980. This approved reference design was used as the basis for soliciting proposals to design and build EBT-P from the four industrial teams. In September 1980, MDAC was selected as the Phase II industrial participant to design and construct EBT-P in the Oak Ridge Valley Industrial Park. Principal subcontractors are General Dynamics-Convair Division (GD) and Gilbert Associates, Inc. (GAI).

In October 1980, MDAC was awarded a letter subcontract to begin Title I engineering design, and Phase II of the EBT-P project was officially under way. The initial project baseline definition was completed late in 1980 and called for $86 million in capital funds and $59.1 million in operations support, with April 1985 as the target date for completion of Phase II.

1.2.2 Design Description

EBT-P is to be designed and built by MDAC on a 4.45-hectare (11-acre) site at the Oak Ridge Valley Industrial Park. The MDAC-funded facility, estimated to cost $10 million, will include an administration building, a test center building containing the EBT-P device and its enclosure, a mechanical equipment building, and an outdoor power supply pad. Figure 1.25 presents an artistic rendering of the proposed facility.

The EBT-P device is housed in a bilevel concrete enclosure, arranged as shown in Fig. 1.26, which provides adequate x-ray shielding to reduce external exposure levels to safe limits. The upper level of the enclosure houses the device, its support structure, and the overhead superstructure for ancillary equipment. The lower level contains mainly the microwave generating and support equipment.

The projected plasma parameters for EBT-P are shown in Table 1.2. EBT-P is a toroidal device with a 4.5-m major radius and 36 sectors, each comprising a mirror cavity, a coil vacuum liner, and a superconducting mirror coil. The toroidal vacuum vessel consists of alternating mirror cavity and coil vacuum liner sectors, which form the vacuum boundary. Four actively cooled, replaceable limiters are positioned in each mirror cavity to intercept scattered electrons and bremsstrahlung and thus prevent excessive heating and erosion of the toroidal vessel walls.

The steady-state plasma is contained by the magnetic field generated by the pool-boiling NbTi superconducting coils, each contained in a separate vacuum dewar. A shield is provided at the base and sides of each coil to protect it from x-radiation. Power is supplied to the mirror coils from a high current dc power supply through gaseous-helium-cooled leads connected in series.

The plasma will be stabilized and heated by the injection of up to 0.4 MW of microwave power at 28 GHz and up to 1.2 MW at 60 GHz into the

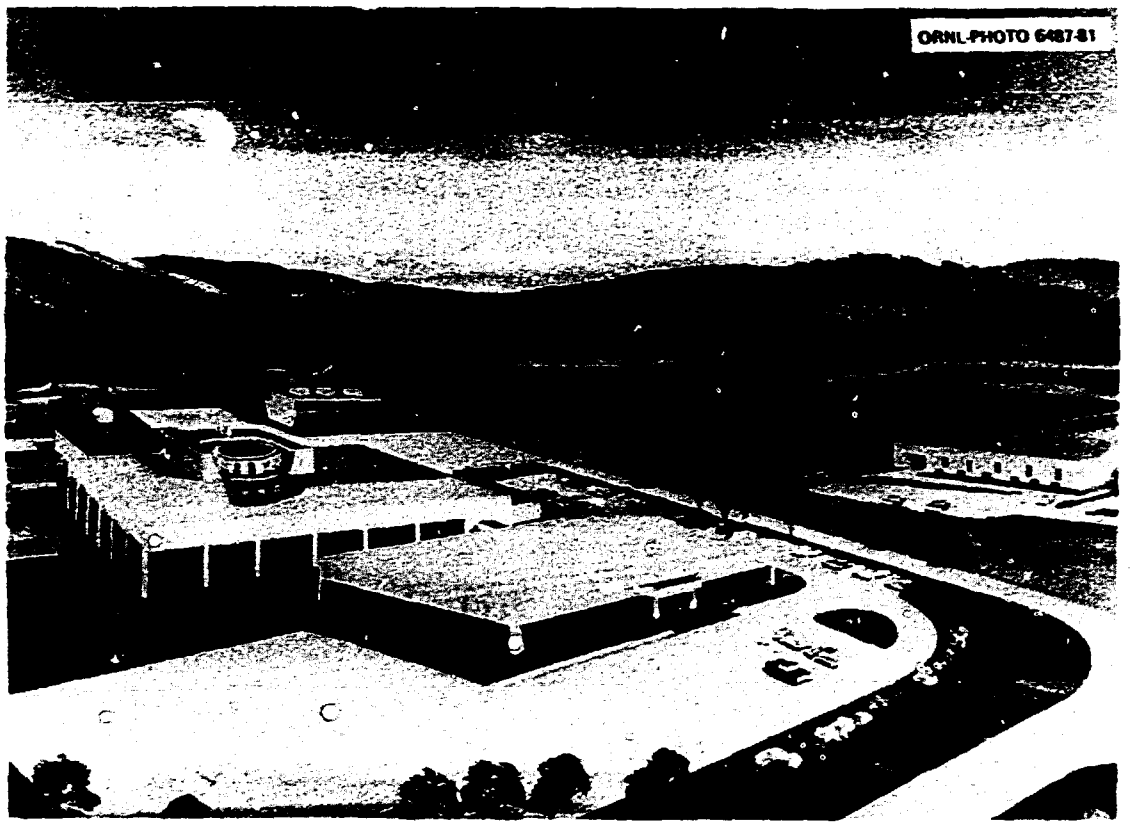

Fig. 1.25. Perspective of EBT-P facilities located in Oak Ridge Valley Industrial Park (photo courtesy of Gilbert Associates, Inc.).

toroidal vessel. Microwave power is transmitted uniformly from gyrotron power sources (located in the lower level) to the toroidal vessel via an overmoded, segmented manifold system with symmetrical connections to each mirror cavity.

Primary pumping of the toroidal vacuum vessel is accomplished with five turbomolecular pumps located on mirror cavities around the torus periphery. A roughing system is used for initial pumpdown of the vacuum vessel and coil dewars and for foreline pumping of the turbomolecular pumps. Primary pumping of the coil vacuum dewars is accomplished with four turbomolecular pumps attached to a common manifold, which serves all 36 dewars. The torus pumping system is shielded from microwave power by a water-cooled, perforated copper plate in each pumping port.

The entire torus and magnet structure is cantilevered from a structural concrete bucking ring designed to structurally restrain the magnetic loading and dead weight of the torus. A superstructure above the device serves as a platform for mounting mirror coil electrical components, cryogenic and vacuum manifolds, waveguides, and other ancillary equipment.

Liquid helium and nitrogen are supplied to the device for cooling the superconducting mirror coils and gyrotron magnets. The closed-loop liquid helium system delivers saturated liquid helium from the refrigeration/liquefaction equipment via a vacuum-jacketed, super-insulated distribution system. The open-loop liquid nitrogen system supplies liquid nitrogen from a storage dewar to the device; the waste gaseous nitrogen is vented to the atmosphere.

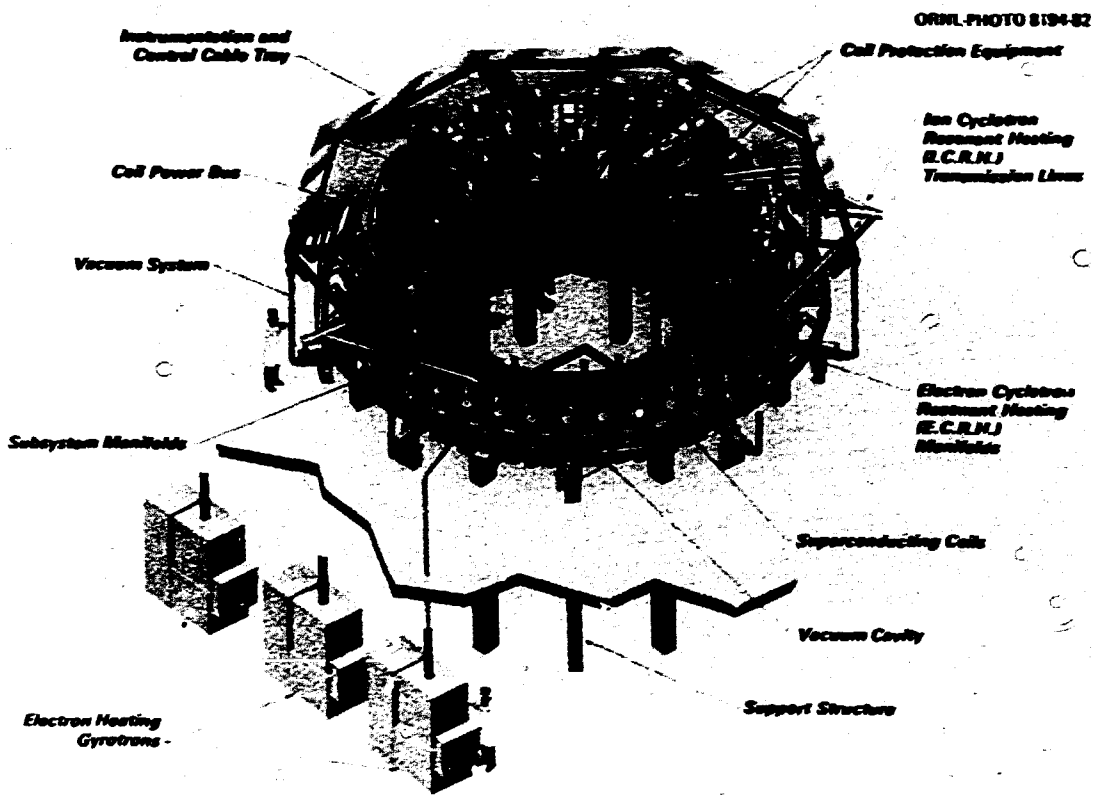

Fig. 1.26. Perspective of EBT-P device (photo courtesy of McDonnell Douglas Astronautics Company).

Table 1.2. Projected EBT-P plasma parameters

Parameter	Startup	Base	Upgrade
N_{coils}	36	36	36
R (m)	4.5	4.5	4.5
B_{res} (T)	2.1	2.1	3.2
n (cm^{-3})	1.0×10^{13}	1.5×10^{13}	3×10^{13}
T_e (keV)	2.0	5.0	7.5
T_i (keV)	0.4	2.5	5.0
Core beta (at annulus) (%)	1.5	5.0	8.0
τ_{Ee} (ms)	30	60	60
$n\tau_{Ee}$ (cm^{-3}-s)	3×10^{11}	1×10^{12}	2×10^{12}
P_{ECRH} (MW)	0.8	1.2	?
	0.4	0.4	?
P_{ICRH} (MW)	0	1.0	?

All densities and temperatures are nominal values with a nominal 30% uncertainty.

Additional ICH power, ECH at 90 GHz, operation at higher fields, and ARE coils will be used to attain the upgrade parameter objectives.

A semiautomatic instrumentation and control (I&C) system is provided to ensure sequential and orderly startup and operation of the device and to furnish adequate data to verify the operation. The I&C system includes data acquisition, device system, and safety instrumentation.

The device is designed to allow future upgrades that will extend performance parameters toward the conditions necessary for containing a fusion reactor plasma. Future upgrades include additional ICH and ECH power, ECH at 90 GHz and correspondingly higher magnetic field, and ARE coils.

1.2.3 Technology Development

Successful realization of EBT-P requires significant advances in certain areas of technology. The ongoing EBT-S experimental program will be essential in extending the technology by providing important operating experience and serving as a test-bed for subsystems and components. Other needs will dictate development efforts specifically for EBT-P. Two major subsystems, the superconducting magnet system and the microwave system, were identified early in the program as requiring intensive development efforts, and development programs for these components have been initiated.

The magnet development program, which is to provide the technical base for detailed design and fabrication of the EBT-P mirror coils, consists of the fabrication, testing, and verification of magnet performance on two development coils and a prototype unit. Testing of these units will take place in a coil test facility at ORNL. The magnet development effort is described in Sect. 7. The magnet development program is being conducted jointly by ORNL, MDAC, and GD.

The microwave system R&D program consists of the development of the high power microwave sources and components that are required to generate and distribute power to the plasma. Development of the microwave sources is being carried out as a part of the DOE National Gyrotron Program and is described in Sect. 1.3. Development of the microwave distribution system components is a joint ORNL/MDAC effort.

In addition, a machine system R&D program was initiated this year for the development of other technologies required for EBT-P.

1.2.4 Progress in 1981

The EBT-P project achieved several significant milestones during 1981. The preliminary (Title I) design phase for EBT-P was approximately 95% complete at year's end. Preliminary design reviews were held for each of the eight device systems, and Title I design reports for the individual systems were prepared by MDAC. Approximately 80 Title I drawings were prepared by MDAC and submitted to ORNL for review/approval during the year. Also during this period, the baseline cost estimate was continually updated to reflect changes in the baseline design. Nineteen design changes were proposed during the year, and four major changes were implemented: the toroidal vessel will be a stainless steel vessel with metal seals, rather than an aluminum vessel with elastomer seals; the pumping system will use turbomolecular vacuum pumps, rather than cryosorption pumping; the primary support structure will be made of concrete, rather than stainless steel; and the device enclosure will be constructed of normal aggregate concrete, rather than high density barite concrete. The first two changes were dictated by the effects of the harsh x-ray environment on nonmetallic seals, and the last two were incorporated to reduce costs.

Several important project documents were prepared by MDAC, including a configuration management plan, a project management plan, a procurement plan, a preliminary safety analysis report, a preliminary quality assurance plan, a set of Title I design criteria, a work breakdown structure dictionary, and a preliminary manufacturing plan. MDAC also performed a number of trade studies and analyses during Title I design.

All device systems are currently in limited Title II design. Official approval for Title II

design will be given once the final Title I report volumes are received and approved by ORNL (probably in March 1982). The request for proposals for design of the cryogenic system was released to eight prospective bidders, including foreign suppliers.

Detailed design of the MDAC-funded facility is about 60% complete. Baseline schedules call for initial facility construction to begin in February 1982 and for the device design, construction, and checkout (Phase II) to be completed in time to start the experimental test phase (Phase III) by May 1985. However, the latest guidance from DOE dictates that no construction or procurement will be initiated during FY 1982 and FY 1983 and that the effort during this period will include only Title II design and development activities. This stretchout of approximately 21 months requires a replanning of project activities and will, of course, have a significant impact on the cost and schedule. It is anticipated that construction/procurement funds will be available in FY 1984.

Several important achievements have also been made in the technology development area. Two development coils, fabricated by ORNL, were open-dewar-tested at ORNL. Both coils operated successfully at full field corresponding to the 90-GHz upgrade for EBT-P, with simulated x-ray heating imposed at the design level of 10 W. This effort is described in more detail in Sect. 7. These coils are currently at GD for complete assembly into magnets and installation in individual vacuum dewars. These two magnets will then be returned to ORNL for testing, along with a GD prototype, in a magnet test facility at ORNL. Construction of the magnet test facility is approximately 75% complete.

Developmental testing of high power microwave components was performed this year in the ORNL microwave test facilities, including the EBT-S device. A laboratory facility was completed that provides capability for low power testing of components at 60 GHz. Calculational methods were developed for analyzing the performance of microwave distribution system components; the methods were verified against EBT-S experimental data and applied to evaluate EBT-P design alternatives. In a related activity, significant progress was made toward the goal of a gyrotron capable of producing 200-kW cw power at 60 GHz. In late 1981 Varian began testing the first experimental steady-state (cw) axisymmetric 60-GHz tube. This effort is a part of the DOE National Gyrotron Program and is described in Sect. 1.3.

1.3 GYROTRON DEVELOPMENT PROGRAM

The ORNL Fusion Energy Division manages the development portion of the DOE National Gyrotron Development Program. The objective of the ORNL program is to operate a coordinated, timely program in industry to develop millimeter wave power generators (gyrotron tubes) for use in plasma heating systems. The program manages the efforts of two industrial subcontractors, Varian Associates, Inc., and Hughes Aircraft Company; performs supporting analytical and material development work; and cooperates with gyrotron R&D activities at other laboratories, including the basic gyrotron research at the Massachusetts Institute of Technology (MIT) and the Naval Research Laboratory (NRL).

Gyrotron tubes operating at 28 GHz are currently in use on EBT-S and ISX at ORNL, on the Tandem Mirror Experiment upgrade at Lawrence Livermore National Laboratory (LLNL), and on experiments in England, Italy, and Japan. They will also be used on EBT-P and on LLNL's Mirror Fusion Test Facility upgrade (MFTF-B). Systems operating at 60 GHz are planned for EBT-P, MFTF-B, the Poloidal Divertor Experiment at Princeton Plasma Physics Laboratory (PPPL), and the Doublet III tokamak at General Atomic Company. Power required for these systems is in the range of 0.4-2 MW. Longer-range plans, for such devices as EBT-P and the Advanced Toroidal Facility at ORNL, Alcator-C at MIT, the Tokamak Fusion Test Reactor at PPPL, and the Fusion Engineering Device, indicate that multimegawatt systems with frequencies from 90 to 150 GHz will be required in the future.

The program at Varian that developed the 28-GHz gyrotrons now in use was completed in 1980 with the successful operation of a 200-kW, cw, 40-50% efficient gyrotron. A tube of this design was operated at 340 kW with 37% efficiency in 1981.

A program to develop the 60-GHz, 200-kW, pulsed and cw gyrotrons needed for the next phase of fusion experiments is under way at Varian and Hughes. During 1981, 60-GHz pulsed tubes were operated by both companies. At Varian, three experimental pulsed tubes were operated at a peak power of 200 kW for 100 ms. At lower peak power, 10-kW average power was achieved. At Hughes, the first experimental pulsed tube operated at a peak power of 160 kW with a 15-μs pulse length (equipment limited) and an average power of 15 W. Varian's first 60-GHz cw tube produced 70 kW for a few minutes early in 1982. The 60-GHz, 200-kW cw gyrotron development effort is expected to be completed in 1983; the completion in August 1983 of a high power test facility that can run 200-kW, pulsed or cw tubes at Hughes will aid in this effort.

Studies in collaboration with Hughes, Varian, and the ORNL Engineering Technology and Metals and Ceramics divisions began this year to determine the cyclic thermal fatigue life of the electron beam collector. A collaborative program with MIT and the Metals and Ceramics Division is in progress to measure the relevant electrical and mechanical properties of candidate microwave window materials.

It is expected that work in progress at MIT and NRL will result in improved efficiency and megawatt-level power in future developmental gyrotrons. The possibility of beginning an industrial program to develop 1-MW, cw, 60- or 100-GHz gyrotrons is under consideration.

REFERENCES

1. T. L. Owens, F. W. Baity, W. A. Davis, O. C. Eldridge, D. L. Hillis, and J. H. Mullen, "Heating Experiments in the Ion Cyclotron Range of Frequencies on EBT-S," to be published in Nuclear Fusion.
2. F. W. Baity, J. C. Glowienka, D. L. Hillis, and T. L. Owens, "Enhancement of EBT Ring Parameters During Ion Cyclotron Heating," in *Hot Electron Ring Physics: Proceedings of the Second Workshop*, CONF-811203, Oak Ridge, Tennessee (in press).
3. T. Uckan, Rev. Sci. Instrum. 52, 21 (1981).
4. T. Uckan, L. A. Berry, D. L. Hillis, and R. K. Richards, *Core Electron Confinement Scaling in EBT-S*, ORNL/TM-8117, Oak Ridge, Tennessee (1982).
5. D. L. Hillis, *Hard X-Ray Measurements of the Hot Electron Rings in EBT-S*, ORNL/TM-8179, Oak Ridge, Tennessee (1982).
6. D. L. Hillis and G. R. Haste, *Electron Confinement Studies on EBT-S Using Soft X-Ray Techniques*, ORNL/TM-8256, Oak Ridge, Tennessee (1982).
7. N. H. Lazar et al., Nucl. Fusion 19, 571 (1979).
8. R. K. Richards and E. F. Jaeger, *Proceedings of the Workshop on Ambipolar Potential Formation and Control in Bumpy Tori and Mirrors*, CONF-810511, Oak Ridge, Tennessee (1981), p. 167.
9. T. Uckan and N. A. Uckan, *Synchrotron Emission from the Ring Electrons in EBT*, ORNL/TM-8026, Oak Ridge, Tennessee (1982).
10. J. B. Wilgen and T. Uckan, "Synchrotron Emission Measurements from the Hot Electron Rings in EBT," in *Hot Electron Ring Physics: Proceedings of the Second Workshop*, CONF-811203, Oak Ridge, Tennessee (in press).
11. Z. S. Wang, G. D. Tsakiris, and D. A. Boyd, Bull. Am. Phys. Soc. 26, 996 (1981).
12. D. Winske, D. A. Boyd, and G. D. Tsakiris, "Analytic Expressions for Synchrotron Radiation from EBT," in *Hot Electron Ring Physics: Proceedings of the Second Workshop*, CONF-811203, Oak Ridge, Tennessee (in press).
13. D. Winske, D. A. Boyd, and G. D. Tsakiris, Bull. Am. Phys. Soc. 26, 996 (1981).
14. F. M. Bieniosek and K. A. Connor, "Sensitivity of Heavy Ion Beam Probe to Hot Electrons in EBT," in *Hot Electron Ring*

Physics: Proceedings of the Second Workshop, CONF-811203, Oak Ridge, Tennessee (in press).

15. S. Hiroe, L. A. Berry, R. J. Colchin, J. C. Glowienka, G. R. Haste, D. L. Hillis, and T. Uckan, "Experimental Hot-to-Warm Electron Density Ratios for Instability Threshold in the ELMO Bumpy Torus," in *Hot Electron Ring Physics: Proceedings of the Second Workshop*, CONF-811203, Oak Ridge, Tennessee (in press).
16. J. C. Glowienka, W. A. Davis, D. L. Hillis, T. Uckan, F. M. Bieniosek, and L. Solensten, *Nonstandard Heating Experiments in EBT*, ORNL/TM-8180, Oak Ridge, Tennessee (1982).
17. K. H. Carpenter, R. A. Dandl, and M. W. McGuffin, *Calibration of a Diamagnetic Diagnostic for Stored Energy of High Temperature Electron Annuli in ELMO Bumpy Torus (EBT)*, ORNL/TM-7076, Oak Ridge, Tennessee (1982).
18. G. B. Nelson and C. L. Hedrick, Nucl. Fusion 19, 283 (1979).
19. K. H. Carpenter, *Research Support for Plasma Diagnostics on ELMO Bumpy Torus — Investigation of Diamagnetic Diagnostics for the Electron Rings*, ORNL/Sub-7676-1, Department of Electrical Engineering, University of Missouri, Rolla, Missouri (1981).
20. K. H. Carpenter, "Comparison of Flux-Energy Calibrations for Diamagnetic Diagnostic of EBT Electron Rings from MHD and Current Sheet Models," paper presented at the IEEE International Conference on Plasma Science, Santa Fe, New Mexico, May 18-20, 1981.
21. K. H. Carpenter and M. K. DaSilva, *Research Support for Plasma Diagnostics on ELMO Bumpy Torus — Study of Diamagnetic Measurements for the Electron Rings and Instrumentation of a Diamagnetic Diagnostic System*, ORNL/Sub-7676-2, Department of Electrical Engineering, University of Missouri, Rolla, Missouri (1981).
22. T. L. White, *Analysis of Mixed Mode Microwave Distribution Manifolds*, ORNL/TM-8127, Oak Ridge, Tennessee (1982).
23. R. L. Livesey, "Vacuum System Problems of EBT," to be published in the Journal of Vacuum Science and Technology.
24. D. A. Everitt, H. O. Eason, R. L. Livesey, and T. L. White, "Intrinsic Engineering Problems for ELMO Bumpy Torus-Scale," paper presented at the Ninth Symposium on Engineering Problems of Fusion Research, Chicago, Illinois, October 26-29, 1981.
25. *Thermonuclear Division Semiannual Progress Report for Period Ending October 31, 1967*, ORNL-4238, Oak Ridge, Tennessee, pp. 127-32.
26. W. C. Brenner, G. Gibson, E. M. Iwinski, L. P. May, F. S. Malick, and D. A. Sink, *Phase I, EBT-D Diverter Project: A Study of the Feasibility of Installing a Toroidal Ge Ramble Diverter in EBT-D*, WFPS:TME-81-020, Fusion Power Systems Department, Westinghouse Electric Corporation, Pittsburgh, Pennsylvania (1981); W. C. Brenner, R. Chianese, G. Gibson, F. M. Heck, E. M. Iwinski, A. Y. Lee, F. S. Malick, D. A. Sink, and R. W. Stooksberry, *Phase II, EBT-D Diverter Project: Engineering Design of a Toroidal Diverter for the EBT-D Fusion Device*, WFPS:TMF-81-026, Fusion Power Systems Department, Westinghouse Electric Corporation, Pittsburgh, Pennsylvania (1981).
27. L. W. Owen and N. M. Uckan, *Optimization of EBT Reactor Operation*, ORNL/TM-7729, Oak Ridge, Tennessee (1981).
28. *Feasibility of Iron Coil Plugs for Aspect Ratio Enhancement of EBT-S*, WFPS:TN-81-079, Fusion Power Systems Department, Westinghouse Electric Corporation, Pittsburgh, Pennsylvania (1981).
29. A. L. Boch et al., *EBT-I Preconceptual Reference Design Summary*, ORNL/TM-7191, Oak Ridge, Tennessee (1980).

2. TOKAMAK EXPERIMENTS

M. J. Saltmarsh, Section Head

J. L. Dunlap, Associate Section Head

O. B. Adams[1]	R. H. Fowler[2]	M. S. Lubell[13]	J. R. Reagan[2]
D. E. Arnurius[1]	J. E. Francis, Jr.[3]	V. E. Lynch[2]	W. J. Redmond
M. B. Baer[1]	W. A. Gabbard	J. F. Lyon	J. B. Roberto[6]
S. C. Bates	W. L. Gardner[2]	C. H. Ma[10]	J. A. Rome[3]
J. D. Bell[2]	D. H. Gray[1]	J. M. Madison[5]	S. D. Scott
E. T. Blair[2]	S. L. Halsted	L. A. Massengill	S. S. Shen[13]
C. E. Bush	P. C. Hanna[2]	J. T. Mihalczo[5]	D. J. Sigmar[3]
B. A. Carreras[3]	J. H. Harris	S. L. Milora[6]	J. E. Simpkins
L. A. Charlton[2]	R. E. Hill[1]	P. K. Mioduszewski	K. A. Stewart[3]
R. E. Clausing[4]	J. T. Hogan[3]	J. A. Moore[1]	D. W. Swain[16]
O. C. Cole[5]	W. A. Houlberg[3]	J. K. Munro[2]	C. E. Thomas
T. B. Cook[6]	H. C. Howe[3]	M. Murakami	T. C. Tucker[2]
W. A. Cooper[3]	D. P. Hutchinson[10]	L. E. Murray	R. L. Wall[1]
E. C. Crume, Jr.[3]	R. C. Isler	A. P. Navarro[14]	J. A. White[1]
R. A. Dory[3]	T. C. Jernigan	G. H. Neilson	R. M. Wieland[2]
G. R. Dyer	R. L. Johnson[1]	B. E. Nelson[1]	W. R. Wing
P. H. Edmonds	S. Kasai[11]	C. W. Nestor, Jr.[2]	S. P. Withrow[6]
O. C. Eldridge	H. E. Ketterer[3]	J. A. O'Toole[15]	A. J. Wootton
L. C. Emerson[4]	R. R. Kindsfather	D. R. Overbey[3]	R. A. Wright[9]
A. C. England	P. W. King	V. K. Paré[5]	W. L. Wright[1]
J. C. Ezell[7]	A. G. Kulchar[12]	J. E. Phelps[5]	R. B. Wysor[1]
R. D. Foskett[6]	R. L. Langley	N. S. Ponte[9]	J. L. Yarber
C. A. Foster[3]	E. A. Lazarus	T. F. Rayburn	R. A. Zuhr[6]

1. UCC-ND Engineering.
2. UCC-ND Computer Sciences.
3. Plasma Theory Section.
4. Metals and Ceramics Division.
5. Instrumentation and Controls Division.
6. Solid State Division.
7. Management Services Section.
8. Foster-Miller Associates, Oak Ridge, Tennessee.
9. Plasma Technology Section.
10. Physics Division.
11. Japan Atomic Energy Research Institute, Tokai, Japan.
12. The University of Tennessee, Knoxville, Tennessee.
13. Magnetics and Superconductivity Section.
14. Junta de Energia Nuclear, Madrid, Spain (former visiting scientist at ORNL).
15. Grumman Aerospace Corporation, Bethpage, New York.
16. EBT Experimental Section.

2. TOKAMAK EXPERIMENTS

ABSTRACT. The activities of the tokamak group during 1981 centered around two major efforts, the experimental program on the Impurity Study Experiment (ISX-B) tokamak and the physics optimization studies for the design of an Advanced Toroidal Facility (ATF-1) to replace ISX-B in the mid-1980s. In both these areas, a close and effective cooperation with the Plasma Theory Section has been crucial.

The goals of the experimental program are primarily directed toward resolution of the physics and technology issues relevant to a tokamak-based Fusion Engineering Device (FED), with particular emphasis on what is currently the most important of the physics issues — high beta plasma operation. Using intense neutral beam injection, with a maximum total beam power P_b of 2.5 MW from two coinjectors, ISX-B has achieved volume-averaged beta $\langle\beta\rangle$ of ~2.5% and central beta $\beta(0)$ of ~9%. However, at high beam power the increase in $\langle\beta\rangle$ is not linear with applied beam power. Recent ISX-B experiments have been aimed at understanding this response.

To characterize the problem more clearly, ISX-B experiments focused on systematic single-parameter scans involving change in only one of the main operational parameters (toroidal field B_T, plasma current I_p, electron density $\bar{n}_e$, and P_b). Both circular and noncircular plasmas were employed, with and without gettering. The overall results confirmed the earlier empirical scaling, $\beta_p I_p^{1/2} \propto P_b^{1/3}$, implying that the global confinement time scales as $\tau_E^* \propto I_p^{3/2} P_b^{-2/3}$. In B_T scans, the poloidal beta β_p and τ_E^* remain constant, while $\langle\beta\rangle$ varies by a factor of ~4. The fact that τ_E^* is independent of $\langle\beta\rangle$ indicates that beta itself is not relevant to the observed deterioration of confinement. Plasma current scans confirm the $I_p^{3/2}$ scaling of τ_E^*, and this scaling has motivated the upgrade of the poloidal field power supply for higher I_p operation. Detailed confinement analysis is carried out with a profile analysis code based on Thomson scattering, which properly incorporates high beta geometrical effects such as Shafranov shift and plasma elongation. The analysis indicates that the deterioration of confinement is most strongly correlated with increasing electron energy loss, although ion energy, particle confinement, and parallel momentum confinement are also degraded.

The magnetohydrodynamic (MHD) activity (as observed by Mirnov loops and soft x-ray detector arrays) at relatively low β_p is best described as a β_p distortion of the $m = 1; n = 1$ mode that drives other helicities through toroidal and nonlinear coupling; however, both B_T and I_p scans show that confinement is not governed by this phenomenon. The theory also predicts that as β_p increases, resistive ballooning modes become dominant. The effects of resistive ballooning modes on confinement are currently under investigation. Fluctuation measurements will be extended using a variety of methods, such as microwave scattering, far-infrared (FIR) Faraday rotation/interferometry, and ion beam probe measurements.

Toroidal plasma rotation is another candidate for driving the deterioration of confinement. The rotation velocities (~10^7 cm/s) estimated from spectroscopic measurements are on the order of the ion thermal velocity and suggest that substantial effects on energy confinement might be expected. Dramatic differences in density clamping and impurity transport between coinjection and counterinjection are observed and suggest that particle transport may be strongly affected by rotation. Thus, investigation of momentum transport may provide insight into a central transport phenomenon. Preparations are being made for experiments with controlled momentum input (via balanced beams) and measurements of the rotation-induced electric field with a heavy ion beam probe.

Along with the emphasis on the high beta work, a broad range of other studies has continued. Impurity transport studies in discharges with coinjection and counterinjection have shown evidence for beam-driven impurity flow reversal effects. The effects of periodic toroidal field ripple have been investigated by comparing plasma characteristics with either 9 or 18 toroidal field (TF) coils energized. The observed enhancement of transport is consistent with, or slightly higher than, that

predicted theoretically. Electron cyclotron heating (ECH) studies of preionization and bulk heating effects were pursued in collaboration with Princeton Plasma Physics Laboratory (PPPL) and the University of Tennessee. The pellet fueling program demonstrated the use on a tokamak of a prototypical centrifugal injector capable of producing 150 pellets per second. Pumped limiter tests of the principle of ballistic particle collection were completed, confirming the applicability of a simple model for the process. In the plasma-materials interaction program, deposition probes were used to investigate the fluxes of both deuterium and impurities in the plasma edge region, and hydrogen recycle studies in collaboration with the Georgia Institute of Technology were continued. Improvements were made in the FIR interferometry/Faraday rotation system, and a successful test of a low energy (≤50-eV) charge exchange analyzer was completed, both in collaboration with the diagnostic development group in the Physics Division.

In the coming year many of these programs will be enhanced by significant improvements and additions to the facilities. The beta and shaping studies will be pursued with an increased plasma current capability, an improved Thomson scattering system, the addition of a counterinjection beam line to investigate the effects of plasma rotation, and a number of diagnostics to explore MHD and fluctuation effects. The ECH program will continue in collaboration with the Naval Research Laboratory (NRL), using the NRL 300-kW, 35-GHz gyrotron for current drive, startup, and bulk heating studies. In the area of particle control, a new 4-pellet injector from the Plasma Technology Section will be installed, as will two pumped limiter modules that are being developed with Sandia National Laboratories. In collaboration with Rensselaer Polytechnic Institute (RPI), an ion beam probe will be mounted on ISX-B to investigate the transport effect of the radial electric field. A new pulsed laser fluorescence system will be used in the plasma-materials program for measuring impurity fluxes in the edge region, and further expansion of the Faraday rotation diagnostic is anticipated.

The ATF activity supports the efforts within the U.S. program to identify the optimum toroidal confinement concept for future application in a Fusion Demonstration Project (FDP). In this context, toroidal confinement encompasses configurations with closed nested flux surfaces of the tokamak/stellarator class. The objective is to construct a facility in the middle to late 1980s that will investigate beta limits and transport in a flexible steady-state device. The ATF-1 is envisaged as a current-free stellarator, with possible later extension to a hybrid tokamak/stellarator. At present, various stellarator options are being assessed. The physics optimization studies have included calculation of vacuum magnetic surfaces, particle orbits, and MHD equilibrium and stability properties. In parallel, engineering assessments are in progress for continuous-coil torsatron configurations, as well as for modular stellarators and an ORNL-developed modular torsatron. A final choice of coil configuration is expected in mid-1982 so that initial procurement and fabrication can begin in 1983.

2.1 THE ISX-B EXPERIMENTAL PROGRAM

2.1.1 High Beta Confinement with Neutral Beam Injection

Introduction

S. C. Bates, J. D. Bell, C. E. Bush, W. A. Cooper, J. L. Dunlap, P. H. Edmonds, H. C. Howe, D. P. Hutchinson, R. C. Isler, E. A. Lazarus, J. F. Lyon, C. H. Ma, M. Murakami, L. E. Murray, G. H. Neilson, D. R. Overbey, V. K. Paré, J. B. Reagan, M. J. Saltmarsh, S. D. Scott, K. A. Stewart, C. E. Thomas, D. M. Thomas,* R. M. Wieland, W. R. Wing, A. J. Wootton

High beta studies in 1981 focused on systematic single-parameter scans involving changes in only one of the main operational parameters (B_T, I_p, $\bar{n}_e$, and P_b). The overall results confirmed earlier empirical scaling results, which suggested that $\beta_p I_p^{1/2} \propto P_b^{1/3}$, indicating that β_p (rather than $\langle\beta\rangle$) "saturates" with P_b.[1] This implies

$$\langle\beta\rangle \propto I_p^{3/2} P_b^{1/3} / B_T^2 (1 + \kappa^2) ,$$

as shown in Fig. 2.1, or equivalently a global confinement time† derived from the poloidal equilibrium measurement,[2] $\tau_E^* \propto I_p^{3/2} P_b^{-2/3}$ for $P_b >> P_{OH}$ (where P_{OH} is the ohmic heating power). These scans also resulted in a number of noteworthy parameter dependences.

(1) As B_T was varied from 0.75 to 1.4 T, β_p and τ_E^* remained constant, while $\langle\beta\rangle$ decreased from 2.4 to 0.6%. The independence of τ_E^* on $\langle\beta\rangle$ is consistent with confinement not limited by ideal MHD modes.

(2) The observed strong dependence of τ_E^* on I_p and the relative independence of τ_E^* on $\bar{n}_e$ are in sharp contrast with the usual scalings observed in ohmically heated discharges.

(3) Beta values achieved with elongated discharges are similar to those with circular discharges, and τ_E^* in elongated discharges is larger (by factors of $\approx\kappa$) than that in circular discharges with fixed P_b, B_T, and $q_\psi(a)$. However, these statements must be qualified by noting that the available range of both external (1.1-1.6) and internal (1.1-1.3) elongations is somewhat limited.

Since beam power does appear to be delivered to the plasma (e.g., from an analysis of the charge exchange fluxes), the nonlinear dependence of beta on beam power is a consequence of degrading confinement with increasing beam power. Electron and ion energy confinement (τ_{Ee} and τ_{Ei}) have been evaluated in a MHD equilibrium-consistent geometry (including internal flux shift and elongation) using the variational moments analysis[3] incorporated with (1) Thomson scattering profile measurements, (2) classical beam deposition and slowing-down calculations, and (3) an ion power balance with an enhancement factor for neoclassical heat conduction adjusted to match the measured central ion temperature (T_i). The T_i profile so calculated is not significantly different from $T_e(R)$ under typical high beta conditions. On the other hand, the power lost through the ion channel is less than that lost through the electron channel (30±10% versus 70±10% of P_b). Therefore, τ_{Ee} is typically smaller by a factor of 2 than τ_{Ei}, a result which emphasizes the problem of electron confinement. As P_b increases from 0 to 2.5 MW, τ_{Ee} (as well as τ_E) decreases from 2 to 0.5

---

*University of Texas, Austin, Texas.

†$\tau_E^* \equiv (W_e + W_i + W_f)/P_b$, which approximates the more conventional gross energy confinement time (τ_E), since $W_e + W_i >> W_f$ and $P_b >> P_{OH}$.

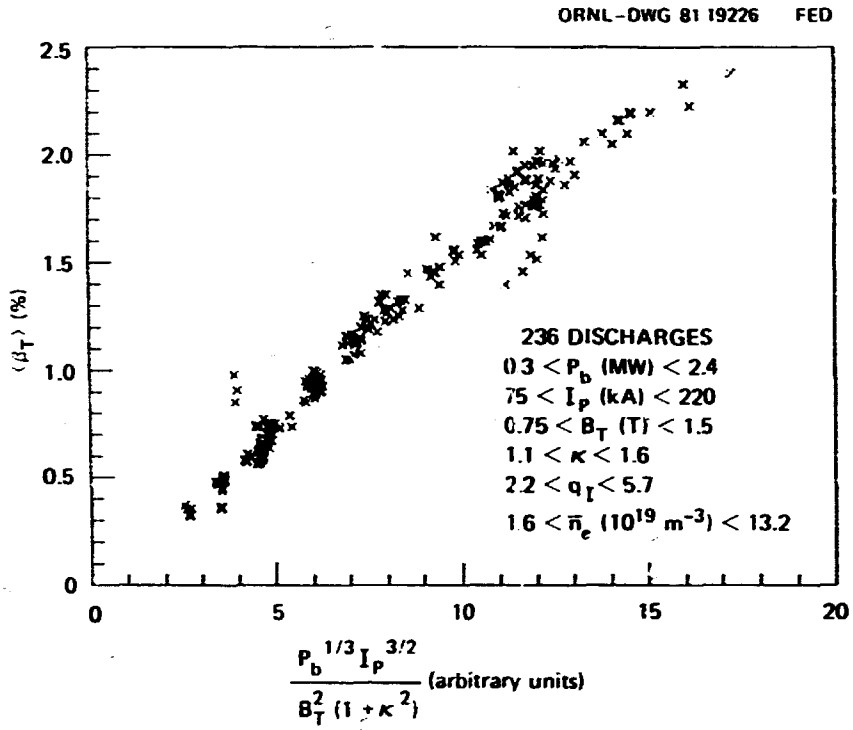

Fig. 2.1. ISX-B empirical scalin

times the Alcator scaling. Scalings of τ_{Ee} with other parameters are similar to those of τ_E^* discussed above (see Fig. 2.2).

The increased energy loss rate at high beam power cannot reasonably be accounted for by increases in radiation and convective losses. Two other candidates are discussed: effects of MHD activity and plasma rotation.

The observed MHD activity is dominated by the high poloidal beta distortion of the m = 1;n = 1 mode, as evidenced by the close correlation of the observed oscillations with calculations based on the theoretical mode structure. In B_T scans, the intensity of the mode changed as predicted by the theory (i.e., strong oscillations at low B_T diminished as B_T rose), while the confinement time remained constant. In I_p scans, the MHD activity and τ_E both increased as I_p increased. Therefore, we conclude that this mode structure, in particular the theoretically predicted overlapping islands outside q = 1, is not a

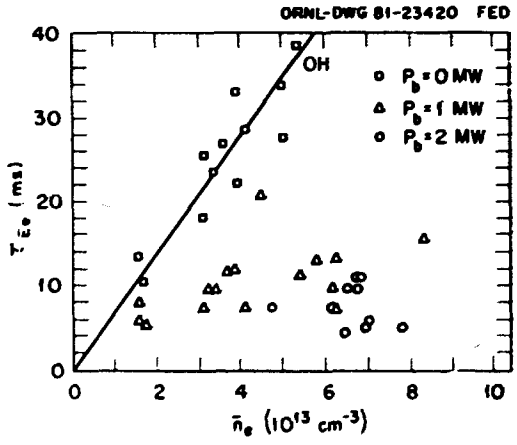

Fig. 2.2. Deterioration of electron energy confinement with increasing beam power.

significant loss factor and that this mode is not responsible for saturation of $\tau_p I_p^{1/2}$. However, higher n pressure-driven modes, which are predicted by the same theory, still remain a candidate.

Inferred toroidal plasma rotation velocities $v_\phi(0)$ are $\sim 1 \times 10^7$ cm/s under typical high beta conditions. Because the inferred parallel momentum confinement is anomalous ($\tau_\phi \sim$ 5-10 ms τ_{Ee}) and $v_\phi(0)$ approaches the ion thermal velocity at the center, direct effects on ion energy confinement are expected. Dramatic differences in density clamping and impurity transport between coinjection and counter-injection were observed and suggest that particle transport may be strongly affected by rotation. Therefore, investigation of momentum transport may provide a better understanding of central transport phenomena.

In summary, the observed scaling ($\beta_p I_p^{1/2} \propto p_b^{1/2}$) implies deteriorating energy confinement. The mechanism for the deterioration of τ_{Ee}, τ_{Ei}, τ_p, and τ_ϕ has not been identified. The observed $m = 1, n = 1$ mode is not responsible, but pressure-driven modes with $n > 1$ remain a possibility and should be measured. Rotation effects are expected, and experiments with balanced beams will help resolve this possibility. It is not yet clear whether the deterioration is a beam-specific or a high poloidal beta effect.

High beta profile and MHD equilibrium analysis of ISX-B plasmas

L. A. Charlton, J. L. Dunlap, E. A. Lazarus, J. K. Munro, M. Murakami, G. H. Neilson, V. K. Paré, S. D. Scott, K. A. Stewart, C. E. Thomas, R. M. Wieland, A. J. Wootton

MHD equilibrium analysis has been coupled with the traditional profile analysis of ISX-B discharges in order to (1) obtain a mapping of the magnetic surfaces, including variations of the shift and elongation, consistent with high poloidal beta configurations and (2) provide the most accurate model possible for theoretical stability analyses. A variational moments technique is used to solve the Grad-Shafranov equation[3] with the boundary specified by poloidal magnetic probe measurements and the pressure profile by Thomson scattering, charge exchange, and FIR interferometer data, together with classical fast ion calculations. The ion component of the required pressure profile comes from a detailed treatment of the ion power balance, using a neoclassical χ_i multiplier to yield a central ion temperature in agreement with ion temperature diagnostics.

The toroidal current profile $I(\rho)$, where $\rho = r/a$, must also be specified; the choice is important for stability analysis because it directly determines the q profile. While more direct measurements are not available, there do exist data directly related to $I(\rho)$: the location of the $q = 1$ surface, obtained from soft x-ray array data, and moments of the toroidal current distribution,[5] obtained from magnetic data. We construct the profile so that the calculated equilibrium agrees with these data. As a check, the external multipole fields required to sustain the resulting configuration are calculated and compared with the actual fields provided by the poloidal field (PF) coils.

To illustrate this technique for choosing $I(\rho)$, we consider a moderate beta case, in which the plasma current was kept constant for ~80 ms to allow time for penetration. Figure 2.3 illustrates the pressure profile, along with the midplane current density (j_ϕ) and q profiles used to model this case; Table 2.1 shows that parameters calculated from this equilibrium agree well with those obtained from the magnetic data. Figure 2.3 further indicates that the assumed current profile corresponds very nearly to that obtained assuming a resistive equilibrium (i.e., RE_ϕ constant over the cross section).

Abstract of MHD Instability with Neutral Beam Heating in the ISX-B Tokamak

J. L. Dunlap, B. A. Carreras, V. K. Paré, J. A. Holmes, S. C. Bates, J. D. Bell, H. R. Hicks,* V. E. Lynch, A. P. Navarro*

We describe observations of MHD instability with neutral beam heating in the ISX-B tokamak and the theory specifically developed to support these experiments. The observed MHD activity is explained by the resistive model presented but is not responsible for the

*UCC-ND Computer Sciences.

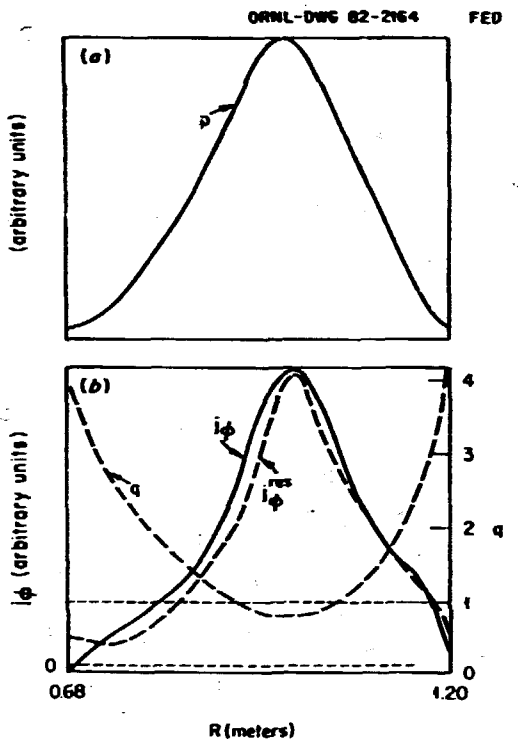

Fig. 2.3. (a) Pressure and (b) current density and q profile used in equilibrium modeling of case described in Table 2.1.

Table 2.1. Comparison of measured and modeled magnetic equilibrium parameters with I_p = 185 kA, B_t = 1.22 T, κ = 1.4, $\langle a \rangle$ = 1.5 cm, β_p = 1.74, ℓ_i = 1.1, and q_a = 4.5

	Measured	Modeled
Moments of j_ϕ[a]		
y_1	4.46 cm	4.36 cm
y_2	-9.56 cm	-9.35 cm
Multipole fields		
Vertical	629 G	640 G
Quadrupole	291 G/m	299 G/m
Poloidal coil currents		
Inner	10.0 kA	9.9 kA
Outer	15.7 kA	15.9 kA
Shaping	0 kA	0.1 kA

[a] $y_n = \mathrm{sgn}(Y_n)|Y_n|^{1/n}$, where $Y_n = I_p^{-1} \int dS_\phi j_\phi r^n \cos n\theta$.

observed degradation of confinement. Increasingly important n > 1 pressure-driven modes are predicted by the theory for the higher experimental β_p values, but there is no experimental verification of their presence.

2.1.2 Impurity Transport and Behavior

Reduced impurity radiation in ISX-B plasmas heated by coinjection

C. E. Bush, M. Murakami, D. R. Overbey, B. Thomas, Jr., R. M. Wieland*

Introduction. Theoretical studies indicate that neutral beam injection heating can also be used to control impurities in tokamak plasmas. These theories depend either on momentum or plasma rotation introduced[6,7] by the beams or on the use of beams to drive the Pfirsch-Schlüter ion current.[8] In either case, conditions are predicted under which impurities may be expelled from the plasma, i.e., impurity flow reversal. On ISX-B, experimental support for beam-induced impurity flow reversal is provided by radiometric and spectroscopic data for a group of independent though consistent experiments. The radiometric measurements of impurity radiation were made using uncollimated pyroelectric detectors and an array of 12 collimated detectors.[9] The experiments include ohmically heated discharges, coinjection- and counterinjection-heated discharges, and discharges with and without deliberate but controlled impurity contamination.

Experiments. Controlled amounts of contamination were introduced into ISX-B plasmas either by gas puffing (argon, neon, nitrogen) or by vaporization of metallic impurities (such as titanium, aluminum, and iron) using a laser blowoff system. With ohmic heating alone, there is a relatively slow but steady increase in radiated power with time into the discharge; this is suggestive of a gradual

*UCC-ND Computer Sciences.

accumulation of intrinsic impurities. When titanium is injected at ~100 ms into the ohmically heated discharge, radiative losses increase from 20% just before impurity injection to ~40% of the total ohmic input, P_{OH}, just before current rundown (~190 ms). Based on data from the radiometer array, a large fraction of the increased radiation is from the core plasma. Except for a short burst of impurity radiation just after titanium injection, the radiative loss from the outer regions of the plasma, i.e., the outer ~7 cm, returned to and remained at the level it was before titanium injection. At the same time, the volume emission in the 8- to 10-cm-diam core plasma continues to increase up to the time of current rundown. When titanium is injected about 20 ms prior to neutral beam injection (P_b ~ 1 MW), there is an initial increase in impurity radiation up to the time of beam turnon; this is followed by a moderately fast decrease (~50 ms) after turnon, which apparently indicates the expulsion of accumulated impurities from the core plasma.

A dramatic difference in time evolution of the profiles of impurity radiation from intrinsic impurities is observed for coinjection and counterinjection. Counterinjection appears to enhance the rate of increase, and coinjection apparently retards and actually reduces the impurity radiation from the core plasma. These effects appear to be obvious when radiometer data, such as those in Figs. 2.4 through 2.7, are used as the basis for comparing coinjection and counterinjection. Figures 2.4 and 2.5 show the time evolution of chordal intensity profiles for counterinjection and coinjection, respectively. In both cases ~1 MW of beam power is injected. The intensity profile for the counterinjection case evolves rapidly, becoming highly peaked at the center, t ~ 185 ms. At ~190 ms the plasma goes unstable, resulting in a sharp perturbation in total energy flux to the walls. Also indicative of a disruption are a spike on the loop voltage signal, a sharp drop in the soft x-ray monitor signal, and a sharp rise in MHD

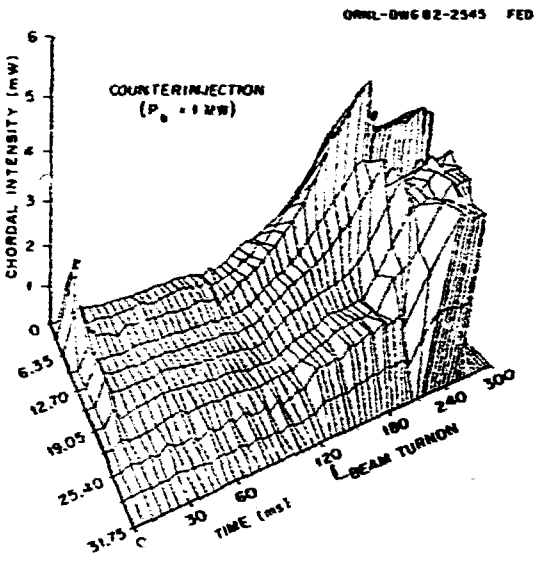

Fig. 2.4. Time evolution of chordal intensity profile for counterinjection with P_b = 1 MW of H^0 beam into a deuterium plasma. Time-resolved profile data from the array of 12 collimated radiometers are available for each discharge; however, here the data have been averaged over several discharges. Beam turnon is at t = 120 ms.

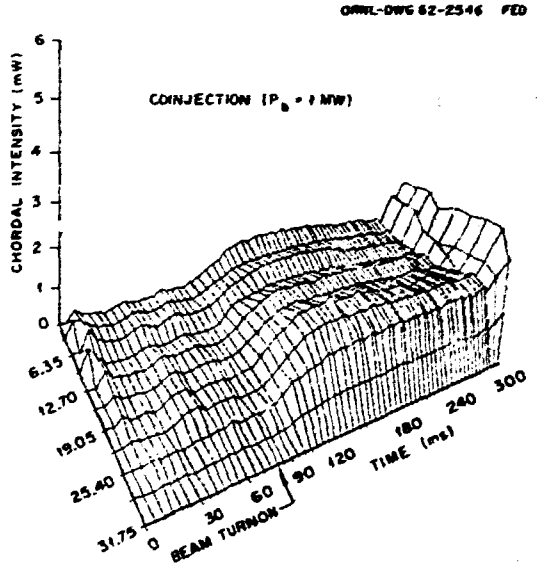

Fig. 2.5. Time evolution of chordal intensity profile of impurity radiation emission for coinjection-heated discharge; P_b = 1 MW of H^0 beam into a deuterium plasma. Beam turnon is at t = 80 ms.

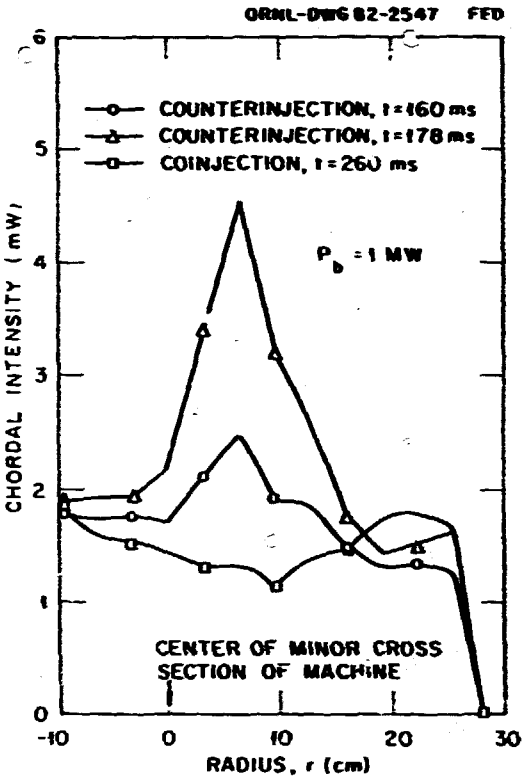

Fig. 2.6. Chordal intensity profile data for t = 160 ms and t = 178 ms in the counterinjection case and t = 260 ms in the coinjection case of Figs. 2.4 and 2.5. The machine center, R_0 = 93 cm, is at r = 0.

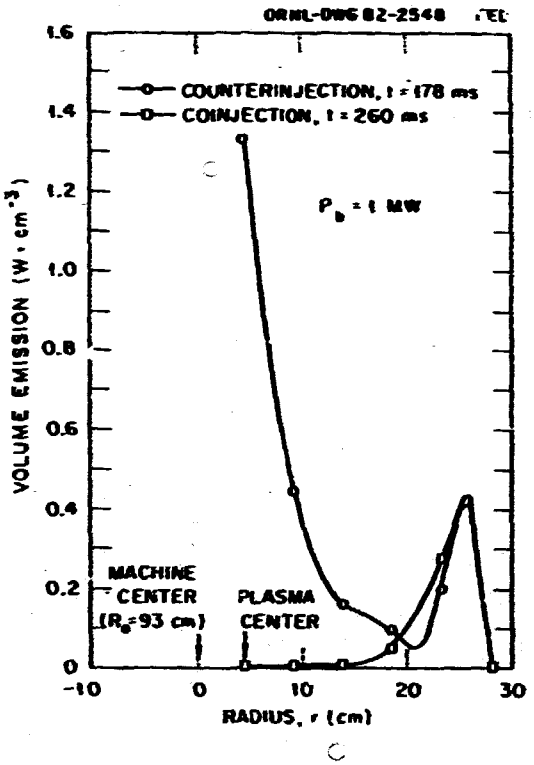

Fig. 2.7. Volume impurity emission profiles for the counterinjection case at t = 178 ms and for the coinjection case at t = 260 ms. Intensity data are inverted using flux surface distributions provided by the ZORNOC code (which makes use of data from an array of magnetic pickup coils). The machine center, R_0 = 93 cm, is at r = 0. The shift of the inner flux surface for both cases is ~4.5 cm toward the outside.

activity, which remains until the discharge terminates catastrophically at t ≅ 280 ms. These examples are relatively typical of coinjection and counterinjection in the sense that something of an equilibrium in the radiation profile is established for the coinjected case, while profiles for counterinjection continue to evolve at a significant rate until an inevitable disruption.

Figure 2.6 shows chordal intensity profiles for discrete times into the two discharges, times well after beam turnon but before any significant perturbations. Inverted profiles, i.e., the radial dependences of volume impurity radiation emission, are given in Fig. 2.7 for the coinjection case at t ≅ 260 ms and for the counterinjection case at t ~ 178 ms. For the coinjection case, the volume emission is peaked close to the edge of the plasma, with ~70% of the total radiation loss, P_{rad}, emitted from a ~5-cm-thick shell at the plasma edge and an insignificant amount from within the inner half-radius of the plasma. On the other hand, for the counterinjection case the emission is peaked at the center of the discharge, with ~25% of P_{rad} coming from the inner half-radius of the plasma. Though there is already significant peaking of the emission profile for counterinjection at t = 160 ms, the total radiated power, P_{rad} ~ 240 kW, is the same as for the coinjection case. Also, the central electron densities were the same,

$n_e(0) \sim 7 \times 10^{13}$ cm^{-3}, and the central electron temperatures, $T_e(0)$, were 600 eV and 800 eV for counterinjection and coinjection, respectively. However, the radial T_e and n_e profiles were significantly different for the two cases, with fairly broad, flat profiles for coinjection and significantly peaked profiles for counterinjection.

Finally, with controlled injection of impurities the timings of increases or decreases of radiative losses are clearly associated with the introduction of the impurity into the plasma and the turnon of the neutral beams. On the other hand, even though intrinsic impurities are continually introduced into the plasma by interactions with walls and limiters during the course of the discharge, the effects of coinjection and counterinjection on the resulting radiative losses appear to be similar to those observed for deliberate contamination. In both cases, however, electron density and temperature profiles and spectroscopic measurements of line radiation must be considered in detail before conclusions are drawn about the extent to which the observations based on the radiometric data are due to beam-induced impurity accumulation or to impurity flow reversal.

Impurity transport and plasma rotation

R. C. Isler, L. E. Murray

Studies of impurity transport started in 1980 have continued, with the addition of observations on impurities that are introduced rapidly by the laser blowoff technique. Also, plasma rotation measurements, which come into play in the theories of neutral-beam-driven processes, have been started.

We summarize a large part of the work with abstracts of published results. A description of some of the most recent data follows.

Abstract of Impurity Sources and Accumulation in Ohmically Heated ISX-B Discharges[10] *(R. C. Isler, S. Kasai, L. E. Murray, M. J. Saltmarsh, M. Murakami).* Spectroscopic observations on the ISX-B tokamak indicate that most of the metallic impurities come from the wall in ohmically heated discharges in which the plasma is kept centered in the vacuum chamber. These impurities appear to accumulate during the quasi-steady-state part of the discharge if the working gas is deuterium but not if it is hydrogen.

Abstract of Influence of Neutral Beam Injection on Impurity Transport in the ISX-B Tokamak[11] *(R. C. Isler, L. E. Murray, S. Kasai, D. E. Arnurius, S. C. Bates, E. C. Crume, J. L. Dunlap, P. H. Edmonds, E. A. Lazarus, M. Murakami, V. K. Paré, M. J. Saltmarsh, D. W. Swain, C. E. Thomas).* Observations of radiation from iron and from argon used as a test gas indicate that coinjection inhibits impurity accumulation in the interior of the ISX-B tokamak discharges, but counterinjection enhances accumulation. These results agree qualitatively with recent theoretical calculations.

Abstract of Charge Exchange Excitation and Recombination of Oxygen in the ISX-B Tokamak *(R. C. Isler, L. E. Murray, S. Kasai, J. L. Dunlap, S. C. Bates, P. H. Edmonds, E. A. Lazarus, C. H. Ma, M. Murakami).* Several spectral lines produced by charge transfer of neutral beam hydrogen atoms with completely ionized oxygen have been detected in the ISX-B tokamak and have been used to compute the absolute concentrations of O^{8+}. Charge exchange recombination is found to have a minor effect on the total radiative losses, but enhanced transport during neutral beam injection appears to raise the oxygen radiation from the interior of the discharges by factors of 3 to 5. This result may reflect an increase of anomalous transport rates that could account for the density "clamping" often observed with injection.

Recent results

Impurity transport studies have been extended this year by using the laser blowoff technique to inject titanium rapidly into

tokamak discharges so that the subsequent temporal evolution can be monitored. Figure 2.8 shows several stages in the time behavior of titanium introduced into an ohmically heated plasma. The initial rapid increase in the signals following injection is produced as the titanium is transported inward and ionized to successively higher stages. If the titanium were subsequently being transported out of the plasma in a period much shorter than the length of the discharge, the radiation from all of the ionization stages would decay simultaneously. It is seen, however, that although the emissions from Ti XVIII and Ti XIX do begin to decrease after about 180 ms, the signals from the lower stages, Ti XIV and Ti XV, are actually rising during this period. It is tempting to ascribe this behavior solely to recombination as the plasma cools owing to the rise of deuterium concentration during the shot and not to transport of the impurities. Figure 2.9 shows both a temperature and a density profile at 150 ms during the shot, as well as the evolution of the central values of these quantities throughout the discharge. It is seen that the plasma is, indeed, cooling, at least from 100 ms onward. At 150 ms, when the electron temperature and density profiles were recorded, a total titanium profile was inferred from a numerical modeling calculation that matched calculated and experimental line-integrated spectral signals [Fig. 2.9(b)]. In order to test the hypothesis that little of the titanium actually disappears from the plasma during the discharge, we have calculated the signals expected if this distribution were to remain fixed after 150 ms. The comparison between the experiment and a calculation assuming corona equilibrium is shown in Fig. 2.10. The agreement is close enough to substantiate the supposition that almost none of the titanium

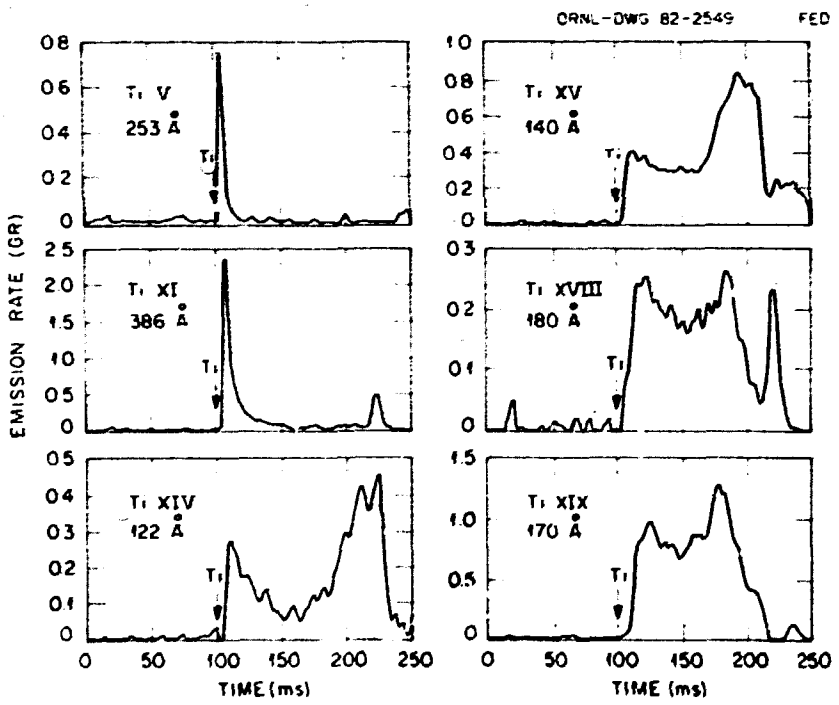

Fig. 2.8. Emissions from several ionization stages of titanium injected into an ohmically heated discharge by the laser blowoff method.

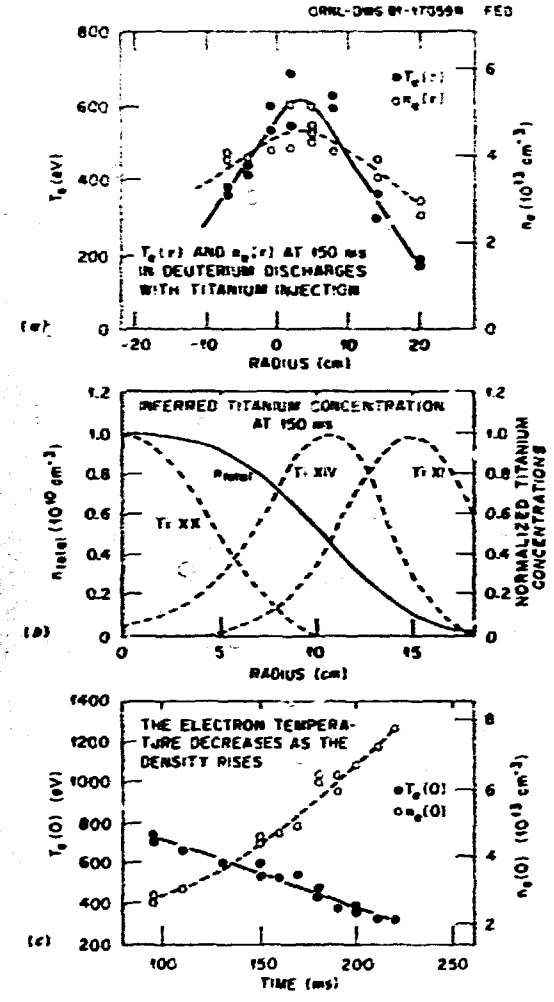

Fig. 2.9. Plasma parameters for an ohmically heated discharge with titanium injection. (a) Electron temperature and density profiles at 150 ms. (b) Inferred titanium profiles at 150 ms. (c) Time evolution of the central electron temperature and density.

actually leaves the plasma. This long-term confinement in ohmically heated ISX-B discharges substantiates previous results obtained using silicon.[13] In contrast, if the impurity is injected during neutral beam heating, it is confined in the center for only about 12 ms, as shown in Fig. 2.11. This confinement time is most likely the same as the confinement time of the deuterium ions and indicates that anomalous processes may well dominate the coinjected discharges.

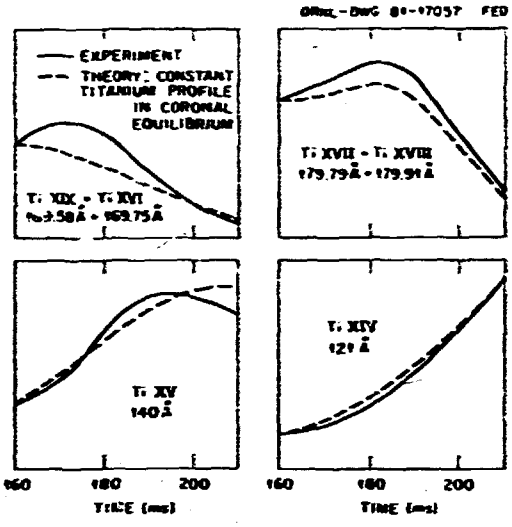

Fig. 2.10. Comparison of experimental and theoretical line emissions in a cooling plasma.

Recent theories indicate that both the momentum transferred to the plasma particles[6] and the induced plasma rotation[14] can affect the transport of impurities. We have begun to make measurements of the plasma rotation in order to correlate these theories and the experiments. The investigations are still in a preliminary stage, but initial toroidal rotation studies have been performed. The experimental arrangement is shown in Fig. 2.12. A visible spectrometer and a set of mirrors are positioned so that observations can be made either normal to the magnetic field lines or at an angle of about 30° to the field lines in either the upstream or the downstream direction. A vibrating mirror is positioned in front of the exit slit of the spectrometer. This mirror permits about 10 A of the spectrum to be scanned in approximately 10 ms. The plasma rotation is measured by detecting the Doppler shift of impurity lines in the near-ultraviolet region, usually in the third- or fourth-order spectrum. The C V line at 2271 A is intrinsically bright in the discharge and can be used to measure the rotation at a plasma radius of about 22 cm. In order to observe the rotation nearer the center, we

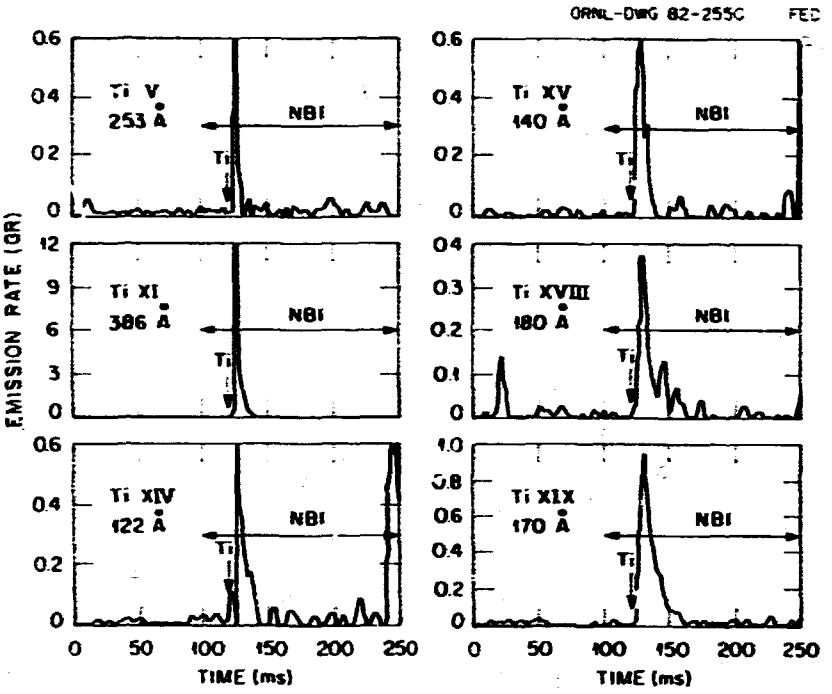

Fig. 2.11. Spectral emissions observed if titanium is introduced into a plasma heated with coinjected neutral beams.

have tried to employ forbidden transitions of Ti XV and Ti XVII, but the intrinsic signals are not bright enough. It is necessary to use the laser blowoff device to seed the plasma with enough titanium to produce signals of adequate strength. Even so, it is quite difficult to make the measurements because of the short confinement time in coinjection discharges. It is necessary to introduce the titanium before the neutral beams are turned on so that its concentration can build up to a useful level. In general, this type of operation permits the rotation to be explored for about 30 ms after the beams are turned on; the signal becomes very small after this time as the titanium disappears from the plasma. Rotation results are shown in Figs. 2.13 and 2.14, and Table 2.2 summarizes all of the results obtained to date.

Major endeavors for the coming year are to extend the scope of the rotation experiments to a wide variety of plasma conditions and to attempt correlations with both experimental and theoretical results related to neutral beam modifications of heat and impurity transport.

2.1.3 Particle Control

Pumped limiter studies

P. K. Mioduszewski, P. H. Edmonds

Continuous removal of both heat and particles will be a vital necessity in future steady-state fusion devices. The pumped limiter/mechanical divertor seems to be an attractive concept to combine these two tasks. Various schemes of pumped limiters are being explored on ISX, with a final goal of furnishing the ATF with a pumped limiter to handle heat removal and particle control in quasi-steady state. The ORNL pumped limiter development is planned in three stages: scoping studies on ISX-B, operation of a full-size pumped limiter for particle control on ISX-B, and operation of a quasi-steady-state pumped limiter on ATF.

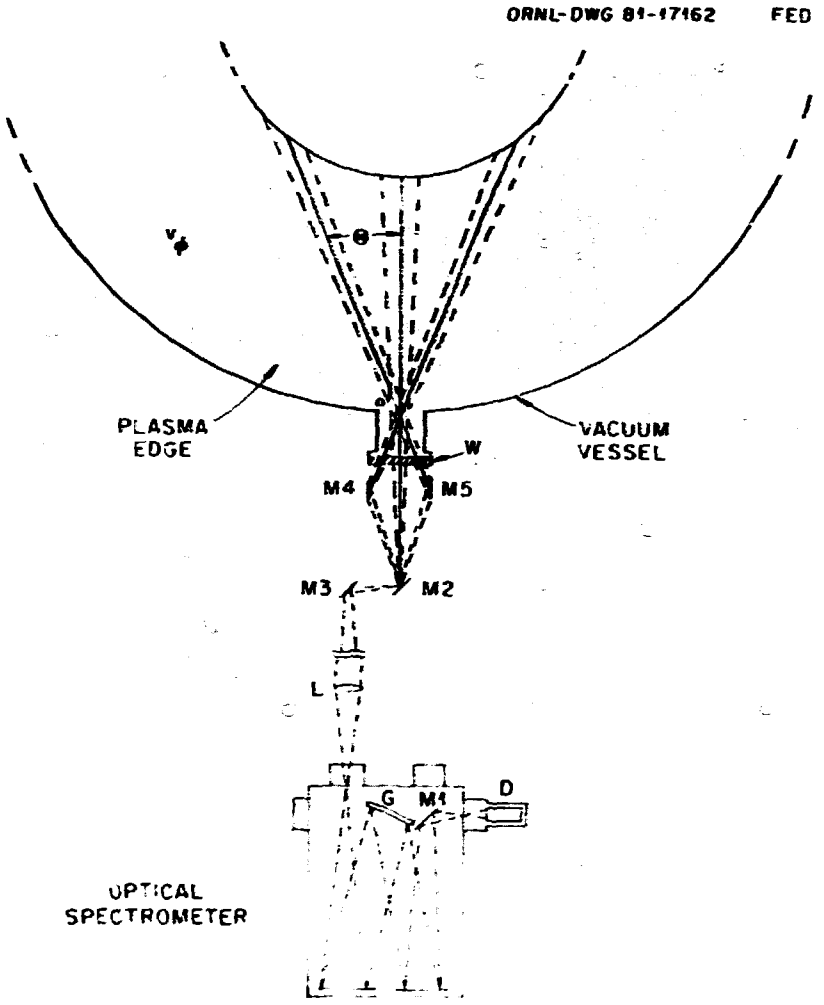

Fig. 2.12. Experimental arrangement for plasma rotation measurements.

The primary objective of the pumped limiter scoping studies on ISX-B is to explore the importance of ballistic effects on the particle collection efficiency.[15] To test the basic concept, a probe-type limiter has been inserted into ISX. The experimental setup is shown schematically in Fig. 2.15. The probe consists of two separate, electrically isolated blades that intercept the scrapeoff plasma perpendicularly.

A certain fraction of the plasma particles reflected from one of the blades is collected by a tube at the outer end, and the pressure rise in this tube is measured. When the ion saturation current to the limiter blade is measured simultaneously, a correlation can be found between the incident particle flux and the pressure buildup in the tube. Both limiter blades are equipped with thermocouples, so that the total energy deposited during the discharge can be measured.

The particle collection efficiency of this arrangement is calculated to be 10% of the incident flux. The pressure rise in the collection tube, the ion saturation current to the limiter blade, and the average energy flux

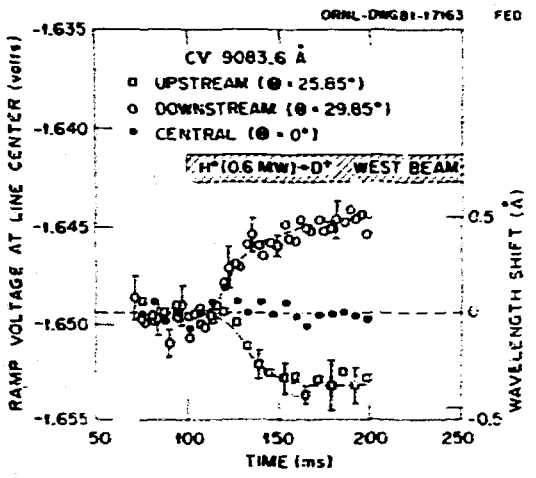

Fig. 2.13. Spectral shifts of the 2271-Å, C V line for three different angles of observation.

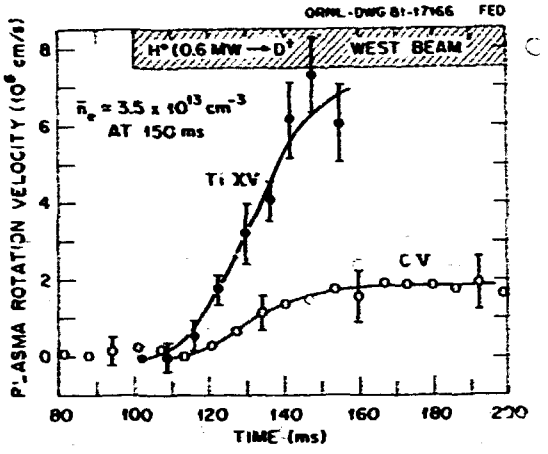

Fig. 2.14. Rotation velocities of carbon and titanium ions as a function of time after the neutral beams are turned on.

Table 2.2. Summary of plasma rotation measurements

	P_b (MW)	$\bar{n}_e$ (cm^{-3})	$T_e(0)$ (eV)	$T_i(0)$ (eV)	$v_\perp$ (cm/s) Ti XV	Ti XVII	C V
Coinjection	1.0	3.2×10^{13}		960	5.35×10^5		1.6×10^5
	0.95[a]	1.9×10^{13}		862	9.4×10^4		1.1×10^5
	0.7[b]	2.6×10^{13}	650	392	1.48×10^5		0.33 10^6
	0.7	3.1×10^{13}	650		3.72×10^4		
	0.7	3.9×10^{13}	620		2.11×10^5		
	0.6	2.9×10^{13}		633[c]	5.86×10^5		1.75×10^5
Counterinjection	1.0	4.5×10^{13}	550	463	12.4×10^4	14.2×10^5	

[a] 8 kG, 18 TF coils.

[b] 8 kG, 9 TF coils.

[c] Neutron.

density were measured as functions of the distance from the main limiter into the scrapeoff layer. Figure 2.16 shows the measured profiles. All data have been taken on the electron drift side of the limiter. At a line-averaged plasma density $\bar{n}_e = 2 \times 10^{13}$ cm^{-3}, the ion saturation current to the limiter blade was 12.5 A. This corresponds to an average flux incident on the limiter of 8×10^{18} cm^{-2}·s^{-1}. The density buildup n in the tube has been estimated for equilibrium between the incident particle flux Γ_{in} and the escaping thermal flux,

$$(n\bar{v}/4)_{mol} = (2\Gamma_{in})_{atom} , \qquad (2.1)$$

where $\bar{v}$ is the velocity of the thermalized particles and the factor 2 accounts for the recombination into molecules. Assuming a 10% collection efficiency, the maximum density

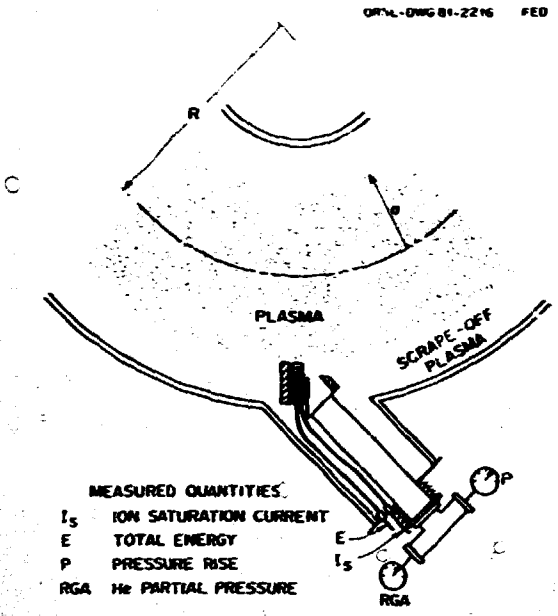

Fig. 2.15. Experimental arrangement for pumped limiter scoping studies on ISX-B.

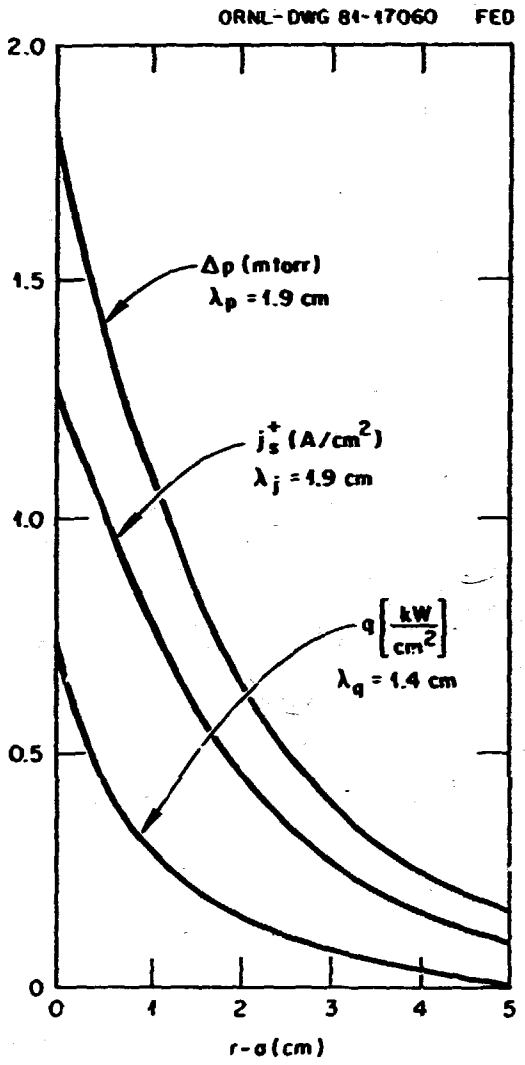

Fig. 2.16. Pressure rise in the collection tube, ion saturation current to the limiter blade, and average energy flux density as functions of distance from the main limiter into the scrapeoff layer. All data are taken on the electron drift side of the limiter.

according to Eq. (2.1) is 4.8×10^{13} cm^{-3} and the corresponding pressure p is 1.4 mtorr. Comparison with the measured 1.8 mtorr indicates that the actual collection efficiency must have been 13%, i.e., slightly higher than computed.

The energy deposition to the limiter blades was measured with thermocouples to give an average power deposition per shot, and the electron temperature at the plasma edge was measured by Thomson scattering to be 40 eV. It is then possible to evaluate density and temperature profiles in the scrapeoff layer by means of the equations

$$j_{sat}^{+} = ne\sqrt{\frac{2kT_e}{\pi m_i}} \text{ (in A/cm}^2\text{)} \qquad (2.2)$$

and

$$q = \gamma(j_{sat}^{+}/e)kT_e \text{ (in W/cm}^2\text{)} , \qquad (2.3)$$

where T_e = 40 keV (at r = a) and γ is the heat transmission coefficient, which is assumed to be 7-17 for normal deuterium discharges.

For the present case of ohmically heated discharges, with $\bar{n}_e = 4 \times 10^{13}$ cm^{-3}, these equations give γ = 14, and the electron density at the plasma edge $n_e(a) = 2.5 \times 10^{12}$ cm^{-3}. The calculated density and temperature profiles have an approximately exponential falloff,

with e-folding lengths of λ_n = 2.3 cm and λ_T = 4.8 cm, respectively.

For the second stage of the pumped limiter development, a pumped mushroom limiter has been designed that can take the full power load and can serve as the primary plasma limiter. Assuming a recycling coefficient of 0.9 and a pumping efficiency of 5%, the total particle exhaust should be sufficient to demonstrate particle control in ISX. First results are expected in the second half of 1982.

Surface pumping with getters

J. E. Simpkins, P. H. Edmonds, P. Mioduszewski

Titanium gettering has been used successfully in ISX, as in other tokamaks, to control impurities and reduce recycling of hydrogenic species.[16] In a standard getter cycle, titanium is sublimated from two Varian Ti-balls for 0.5 h at a rate of 0.1 g/h. This leaves about 70% of the wall with a titanium coverage of >1 monolayer and about 7% of the wall with a coverage of >10 monolayers. The resulting initial pumping speeds observed for hydrogen were: a static pumping speed of 3×10^3 liter/s at $p = 4 \times 10^{-6}$ torr and an average dynamic pumping speed of 4×10^4 liter/s for a 0.25-s gas pulse. After 30 shots, the dynamic pumping speed dropped by an order of magnitude.

While the titanium film following one getter cycle should be saturated with hydrogen after about ten discharges, oxygen pumping should last longer, because hydrogen can be displaced by the more reactive oxygen.

Whether the direct control of the oxygen by the titanium getter or the control of hydrogen recycling plays the dominant part in the gettering effect may be determined by comparing titanium gettering with chrominum gettering. While sufficiently thick titanium layers pump large amounts of hydrogen via diffusion, the hydrogen pumping capacity of chromium is only about one monolayer adsorbed on the surface. For future deuterium-tritium (D-T) devices, the use of chromium for surface pumping can help to avoid the accumulation of large quantities of tritium in the gettered walls.

Initial laboratory experiments were conducted to compare titanium and chromium gettering for some of the gases of interest in fusion research.[17] An ultra high vacuum (UHV) chamber with about 1000 cm^2 of active getter surface was used to compare the pumping of chromium and titanium films. After the getter film was deposited, the working gas (hydrogen, oxygen, or nitrogen) was admitted to the system through calibrated leaks, and the corresponding partial pressure was monitored with a quadrupole mass filter as a function of time. The resulting pressure versus time curves reveal the initial pumping speed as well as the capacity of the getter film. Initial results show that oxygen is pumped at least as well by chromium as by titanium. In contrast, hydrogen was pumped by titanium in quantities of many monolayers due to diffusion into the deposited film, whereas the amount of hydrogen pumped by the chromium corresponded to approximately one monolayer. This behavior is shown in Fig. 2.17.

Effects of titanium gettering on plasma confinement

A. J. Wootton

Two methods of particle control have been discussed: the pumped limiter and gettering. However, the limiter experiments performed on ISX-B to date were not expected to influence the gross plasma behavior because of the small limiter area and the lack of pumping. Therefore, this section is devoted to the effects of titanium gettering on plasma parameters.

Recycling of the working gas is monitored by noting the external gas feed required to produce a given density. Results show that, following a standard getter cycle, hydrogen (or deuterium) recycling is reduced for about ten discharges. This corresponds to the time required to convert all the deposited titanium to a hydride.

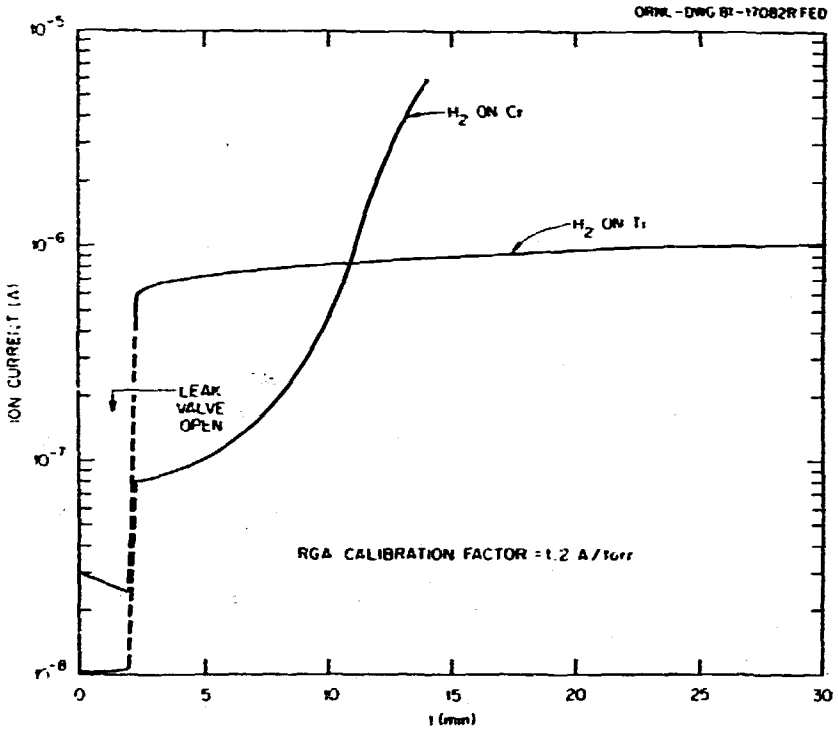

Fig. 2.17. Comparison of titanium and chromium gettering for hydrogen gas in ISX-B.

Impurity levels are monitored by the total radiated power and by impurity line emission rates. These show a reduced radiated power (from oxygen), lasting for ~100 discharges after a getter cycle. This corresponds to the time required for the hydrogen in the saturated film to be replaced by the more active oxygen. In ohmically heated discharges, the radiation from iron is reduced and that from titanium is increased, in agreement with a model in which charge exchange neutral sputtering at the vessel walls is the dominant source for metal impurities.

One of the objectives of gettering was to increase the operational space ($1/q_\psi$, $\bar{n}_e R/B_\phi$) available. Figure 2.18 shows this space, with each point representing the maximum density and the corresponding q_ψ achieved during a given discharge. Ohmically heated and beam-heated plasmas with circular and elongated cross sections are distinguished. For circular discharges, $\bar{n}_e R/B_\phi \leq 25 \times 10^{14}\ q_\psi^{-1}$ (mks units), but for elongated cross sections, $\bar{n}_e R/B_\phi \leq 10 \times 10^{19}\ m^{-2}T^{-1}$ seems more appropriate. In both cases, densities significantly higher than those expected from extrapolating results on other machines have been attained.

An analysis of data taken both before and after gettering was initiated indicates that the gross energy confinement time, τ_E^* [(total energy in plasma)/(total input power)], has been affected. As is well known, gettering and the consequent reduction of low Z impurities increase τ_E^* for ohmically heated plasmas. To investigate effects in beam-heated discharges, a phenomenological expression $\tau_E^*(PH) = kI_p^{3/2}P_T^{-2/3}$ must be used for normalization. This expression, in which P_T is the input power, has been derived since gettering was initiated. A graph of $\tau_E^*/\tau_E^*(PH)$ versus shot number then

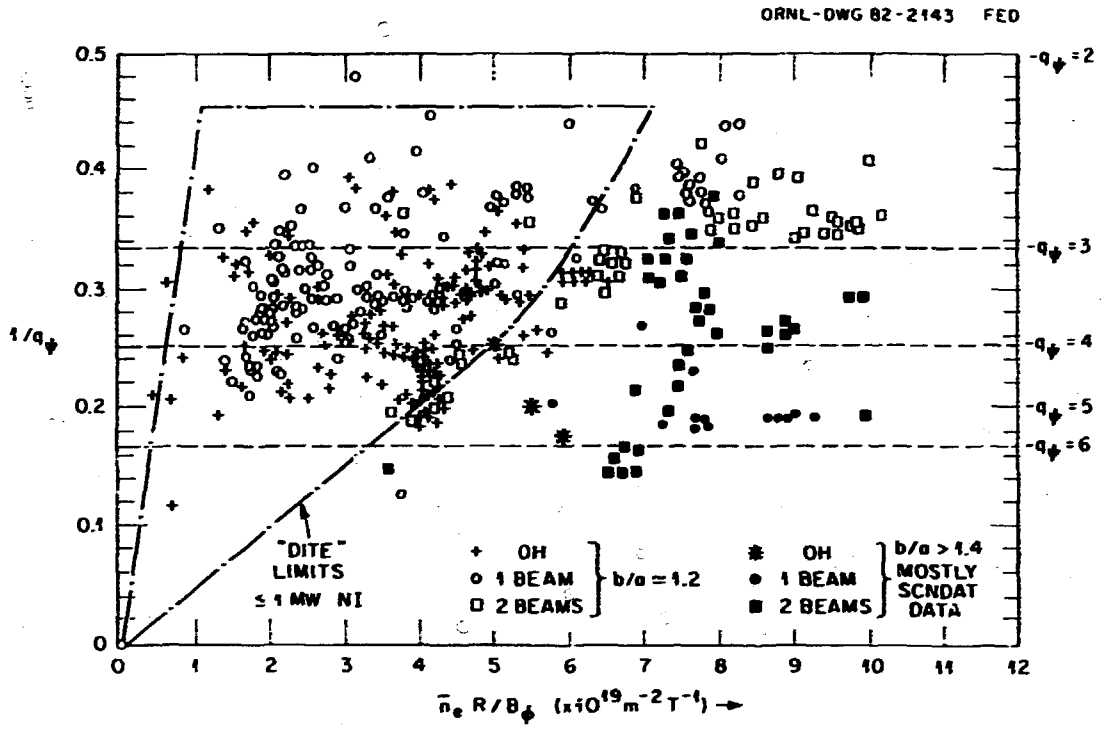

Fig. 2.18. Extension of operational space made possible through gettering.

shows the surprising result that the "constant" k was reduced by 30% when gettering was initiated. This suggests that the reduction of the low Z impurity concentration is responsible for the reduced confinement. Experiments undertaken since gettering began, with nitrogen added as an impurity, support this suggestion. Figure 2.19 shows τ_E^* versus τ_E^*(PH) for ~350 discharges. Those produced with additional impurity levels have τ_E^* ~40% higher than those without; that is, τ_E^* returns to the value obtained before gettering.

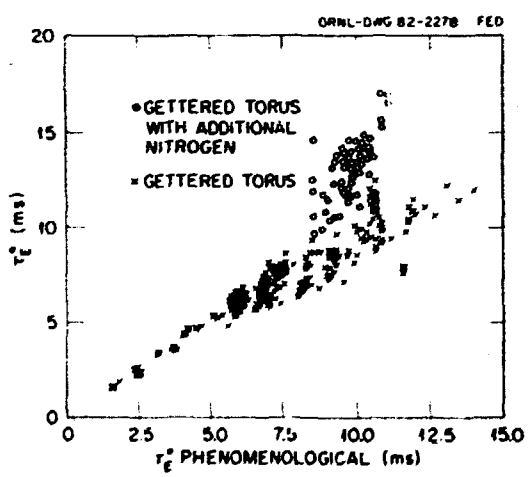

Fig. 2.19. Effects of gettering on gross energy confinement time.

The ISX-B bundle divertor experiment

T. C. Jernigan, D. H. Gray, J. A. O'Toole, R. B. Wysor

The ISX-B Bundle Divertor Project has been under way since FY 1979. A major design review was held in November 1979, and the panel recommendations were incorporated in the design, which was completed in the first quarter of FY 1981. Fabrication of hardware was completed during the third quarter of FY 1981. The divertor itself, which was designed and fabricated by the staff at the

Massachusetts Institute of Technology (MIT), was tested and delivered in the fourth quarter of FY 1981. Most modifications to the tokamak have been completed, but installation of the divertor coil and pumping chamber has been delayed due to programmatic considerations. Additional tasks remaining include TF coil modifications for the force restraint system, programming of the programmed controller, and installation of instrumentation.

2.1.4 Ripple Studies

Periodic ripple studies on ISX-B

S. D. Scott, J. F. Lyon, S. L. Halsted, E. A. Lazarus, R. H. Fowler, L. E. Murray, C. E. Thomas, R. M. Wieland

The experimental program for periodic ripple studies was described in last year's annual report. The effect of periodic ripple on fast ion losses, ion thermal transport, plasma rotation, and other plasma parameters is determined by comparing similar beam-heated plasmas with either 9 or 18 TF coils energized. During 1981, the deterioration of plasma confinement due to ripple was studied over a range of plasma parameters, using improved diagnostic capabilities for measurements of ion temperature and plasma rotation.

Fast ion losses. Changes in the fast ion population were inferred from changes in the charge exchange neutral flux, measured by a pair of toroidally scanning, mass discriminating neutral particle analyzers (see Fig. 2.20). As with all charge exchange measurements, the results are difficult to interpret, due to the chord-integrated nature of the measurement and the steepness of the neutral density radial profile. A complication of the analysis unique to the 9-TF-coil experiment arises from the shift of an ion's pitch angle by ripple during a single transit between energized TF coils [$\Delta(v_{\parallel}/v) \cong (\Delta B/B)^{1/2} \sim (2\delta)^{1/2}$, where δ is the peak-to-average ripple]. This shift generates a discontinuity in the neutral flux as a function of viewing position between measurements obtained by a neutral particle analyzer viewing the bottom of a ripple well and those obtained by a neutral particle analyzer viewing the top. The 9-coil charge exchange spectra shown in Fig. 2.20 have been corrected for this shift. There is severe depletion of the ripple-trapped ions, particularly at low energy, but at most a very small effect is seen on passing ions, as expected. Because most tangentially injected (passing) ions slow down considerably before pitch angle scattering into banana-trapped or ripple-trapped orbits, these results indicate that ripple should cause only a modest reduction in beam power delivered to ions and electrons in the ISX-B 9-coil experiment. Monte Carlo orbit calculations[18] of neutral injection and subsequent fast ion thermalization, using the plasma parameters achieved in the transport study discussed below, suggest that ripple reduced the power delivered to the ions by 35% and the power delivered to the electrons by 17%.

Ripple-induced thermal transport. The deterioration of ion energy confinement due to ripple was evaluated by comparing the ion temperature performance in similar beam-heated discharges (~1-MW $H^0 \rightarrow D^+$) with 9 and 18 TF coils. Ion temperature was measured by the charge exchange analyzers, using a diagnostic neutral beam to localize the source of charge exchange neutrals to the plasma center. The charge exchange ion temperature decreased significantly in the 9-coil discharges relative to the 18-coil discharges, as shown in Table 2.3. However, neutron emission decreased only 20% in the 9-coil discharges, indicating a negligible decrease in ion temperature. This discrepancy has been resolved by the discovery that the neutron emission is not representative of ion temperature in beam-heated plasmas with central ion temperatures less than 600 eV (see Sect. 2.1.6). Therefore, it is concluded that ripple does cause a serious degradation of ion energy confinement in the 9-coil configuration.

A one-dimensional, steady-state simulation of the ion power balance for the 9-coil and 18-coil discharges, using the ZORNOC[19,20]

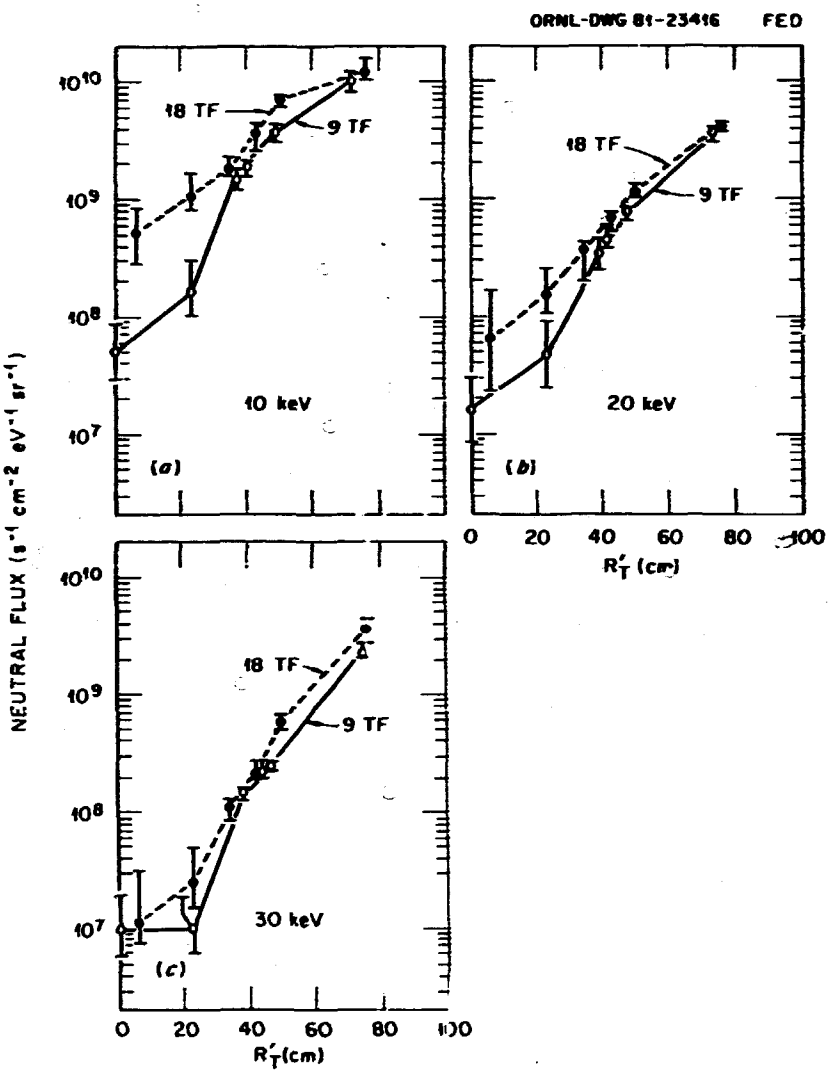

Fig. 2.20. Comparison of fast neutral flux for discharges with 9 and 18 TF coils as a function of viewing position at 10, 20, and 30 keV. R_T' is the tangency radius of the sightline, defined as the minimum distance from the sightline to the torus center. It is related to the parallel velocity of the viewed neutral particles by $v_{\parallel}/v = R_T'/R$, where R is the major radius of the birth point of the charge exchange neutral. For this figure, R_T' has been corrected to account for the variation in pitch angle due to ripple over a single transit through a ripple well. Ripple-trapped particles are viewed for $R_T' \lesssim 35$ cm. These measurements were obtained in discharges with $I_p = 120$ kA, $\bar{n}_e = 3.0 \times 10^{13}$ cm^{-3}, $P_b = 1.1$ MW, and $E_b = 32$ keV. Measurements in other discharges indicate that the depletion of the fast neutral flux from the ripple-trapped region becomes more severe at lower energy (5 keV).

Table 2.3. Range of plasma parameters studied in the ISX-B periodic ripple experiments with 9 TF coils and nominal plasma parameters achieved during neutral beam injection with 9 and 18 TF coils

	Range studied	Nominal values	
	9 TF coils	18 TF coils	9 TF coils
$\bar{n}_e$ (cm^{-3})	2.3-4.9 x 10^{13}	4.3 x 10^{13}	3.5 x 10^{13}
I_p (kA)	110-160	134	135
P_b (MW)	0.0-1.9	1.0	1.0
$T_i(0)$ (eV)	260-420	620	325
$T_e(0)$ (eV)	580-800	720	645
τ_{Ei} ($r \leq 17$ cm) (ms)	5.0-7.8	13.6	5.6
τ_{Ee} ($r \leq 17$ cm) (ms)	5.0-10.0	7.0	6.2

tokamak data analysis code, indicates that the theoretical ripple thermal transport coefficients (ripple trapping, with the boundary layer correction, and ripple plateau) must be multiplied by a factor greater than 1, typically 2 to 3, to reproduce the measured central ion temperatures. However, the uncertainty in ion temperature and (to a lesser extent) the uncertainty in neoclassical transport yield approximately a factor of 3 uncertainty in the ripple transport inferred from experiment. Consequently, these experiments do not demonstrate conclusively that ripple transport is greater than predicted theoretically. Furthermore, a recent reanalysis of the 1980 ripple experiments indicates that the ripple multiplier was nearly equal to unity for those experiments, despite a correction to the ion temperature to account for charge exchange measurements obtained without a diagnostic neutral beam.

Taken together, the 1980 and 1981 9-coil ripple experiments corroborate ripple transport theory to the extent that theory predicts a serious degradation of ion energy confinement in the 9-coil configuration and such a degradation was observed. The ripple transport appears to be within a factor of 1-3 of theoretical predictions, with an uncertainty of the same order (factor of ~3). Further experiments are planned on the ISX-B tokamak, with emphasis on (1) understanding the causes of the discrepancy between the 1980 and the 1981 results and (2) increasing the neutral beam power so as to increase the ion temperature and the magnitude of ripple transport relative to neoclassical transport.

Plasma rotation. The toroidal rotation velocity during neutral beam injection in 9-coil plasmas was lower than the velocity achieved in 18-coil plasmas. The rotation velocities were inferred from the Doppler shift of Ti XV line radiation, which originated near the plasma center. Figure 2.21 shows the time history of plasma rotation velocity for a 9-coil and an 18-coil discharge, as a function of time after turnon of the neutral beam. The rotation velocity is reduced from approximately 9 x 10^6 cm/s (18 coils) to 1.5 x 10^6 cm/s (9 coils), with an uncertainty of ±1.5 x 10^6 cm/s.

The experimental momentum confinement time can be determined by dividing the momentum in the plasma core ($r < a/2$) by the rate of beam momentum input to the plasma core. The latter quantity is calculated by ZORNOC, using a

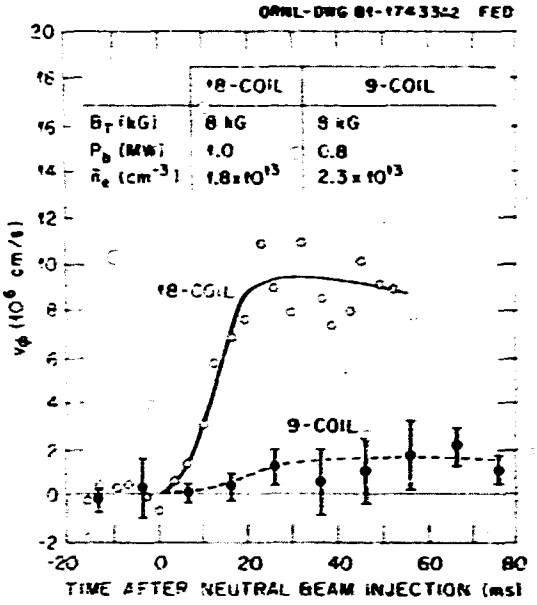

Fig. 2.21. Time history of the beam-induced toroidal plasma rotation in the 9-coil and 18-coil configuration as measured by the Doppler shift of the Ti XV line radiation.

Monte Carlo beam neutrals deposition code and a Fokker-Planck slowing-down code. The measured rotation velocity in the 18-coil discharge implies a momentum confinement time of 5-7 ms. As previously observed on the Princeton Large Torus (PLT),[21] this confinement time is at least an order of magnitude shorter than would be expected from charge exchange damping or from classical or neoclassical momentum diffusivity. The corresponding momentum damping time for the 9-coil discharge is 1.1 ms. Theory predicts that ripple will enhance the damping of toroidal momentum through the ripple-induced nonambipolar particle flux, leading to a momentum confinement time $\tau \sim \rho_p^2/D_\perp$, where ρ_p is the poloidal gyroradius and $D_\perp$ is the ripple particle diffusion coefficient.[22] The measured damping time agrees reasonably well with a simple calculation of the theoretical damping time, which includes diffusion from the ripple trapping mechanism (with the boundary layer correction) and from the ripple plateau mechanism. The uncertainty in the theory-experiment comparison is approximately a factor of 3, arising primarily from uncertainty in the measurement of plasma rotation velocity.

Experimental test of ripple injection

The ripple-enhanced neutral beam injection technique proposed by Jassby and Goldston[23] may permit the effective heating of large, dense plasmas with beams of moderate energy ($E_0 \sim$ 100 keV). Briefly, the method consists of injecting the heating beam vertically into a magnetic ripple well with a strong vertical gradient. Neutrals ionized at the plasma edge $\vec{B} \times \vec{\nabla}B$ drift vertically to the plasma center because they have insufficient parallel velocity to escape from the well. Beyond the plasma center, the ripple becomes sufficiently weak that rotational transform eliminates the well entirely, causing all ripple-injected ions to assume banana or passing orbits. During 1981 the first experimental tests of the ripple injection principle were performed. The experiments investigated three key physics issues that will determine the feasibility of ripple-assisted neutral beam injection: (1) enhancement by ripple of the penetration of the ions to the plasma center, (2) subsequent confinement of the fast ions as they slow down, and (3) the effect of the ripple perturbation on the background plasma.

For these experiments, a pair of eyeglass-shaped coils capable of producing a ripple well (or "hill") of 1% on axis at B_T = 12 kG, toroidally localized to ±40°, was attached to the TF coils, approximately 60 cm below the plasma midplane (see Fig. 2.22). A 15.9-keV, 1.4-A deuterium diagnostic neutral beam located at a major radius of 104 cm was injected vertically into the center of the ripple well. The population of fast injected ions was monitored by two scanning charge exchange analyzers, during similar ohmically heated discharges with and without a ripple well generated by the auxiliary coils. Ripple contours for this experiment and contours of the ripple parameter δ^*, which measures the

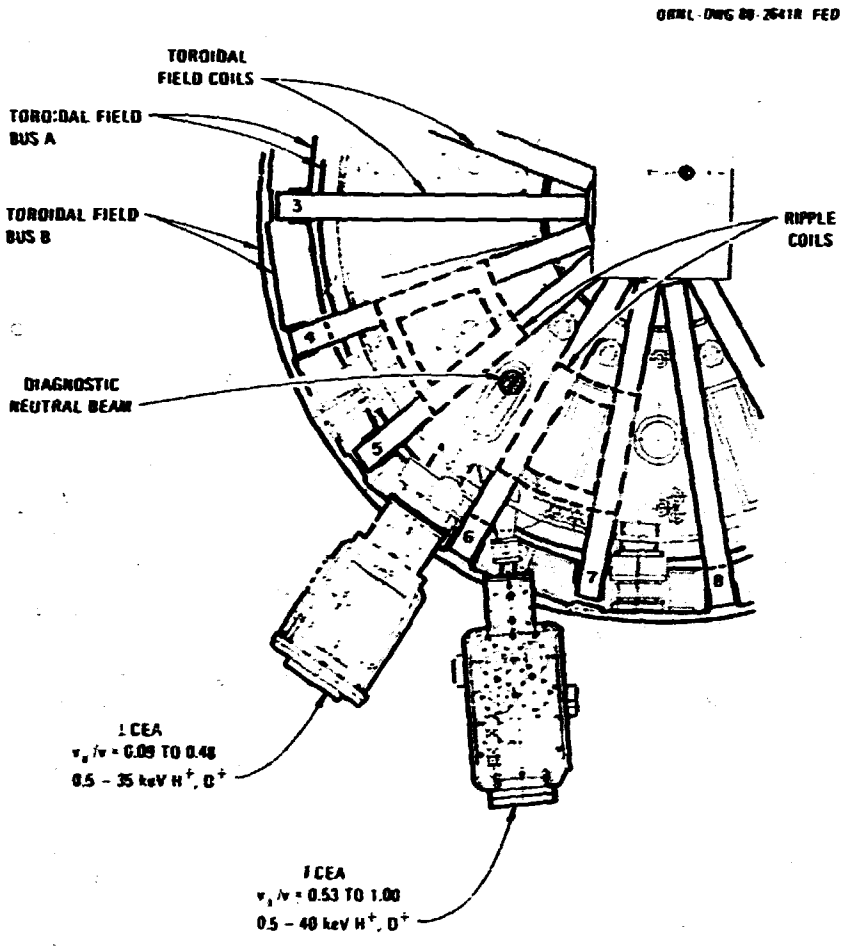

Fig. 2.22. Plan view of the ISX-B ripple injection experiment, showing the locations of the two neutral particle analyzers, the diagnostic neutral beam, and the ripple coils. The perpendicular charge exchange analyzer (⊥CEA) also scans vertically from Z = -6 cm to Z = +35 cm.

ratio of magnetic field strength variation along a field line due to rotational transform to the variation arising from ripple, are shown in Fig. 2.23. The ripple well is eliminated in the region $\alpha^* > 1$. As required for effective ripple injection, there was a symmetric trapping region ($\alpha^* > 1$) a few centimeters above the horizontal midplane, but no symmetric trapping region below the horizontal midplane. Very similar plasma conditions were obtained in discharges with and without ripple ($\bar{n}_e = 4.7 \times 10^{13}$ cm^{-3}, $I_p = 150$ kA, $B_T = 11.3$ kG).

Enhanced penetration of ripple-injected fast ions to the plasma center was clearly evident in the charge exchange spectrum measured along a sightline in the horizontal midplane that passed through the ripple well, as shown in Fig. 2.24. The neutral flux was a factor of 3 to 10 times larger in discharges with ripple than in discharges with no ripple. As predicted by theory, there was no enhanced penetration when the direction of the ripple was reversed, producing a magnetic "hill," or when the magnitude of the ripple well was decreased to the point where a second symmetric

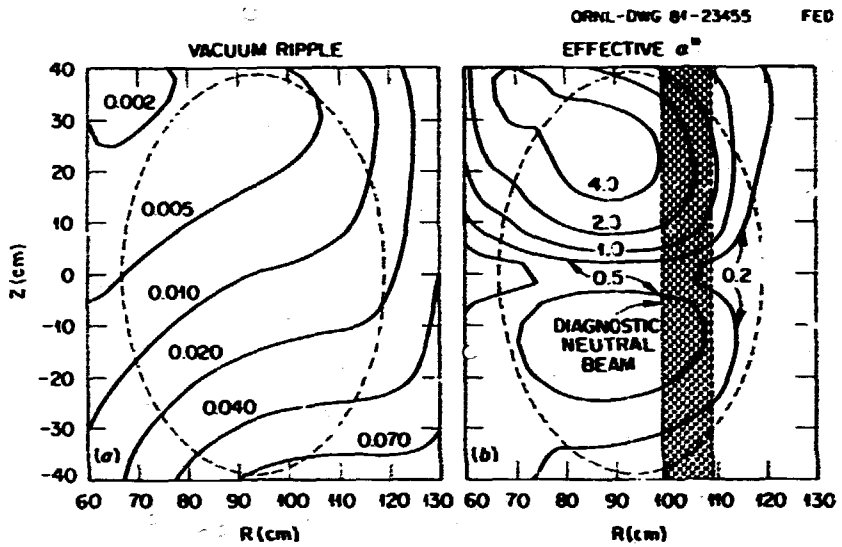

Fig. 2.23. (a) Peak-to-average ripple contours (ε) produced by the ripple coils. (b) Effective α* contours calculated from the ripple and plasma equilibrium. The ripple well is eliminated for α* > 1.

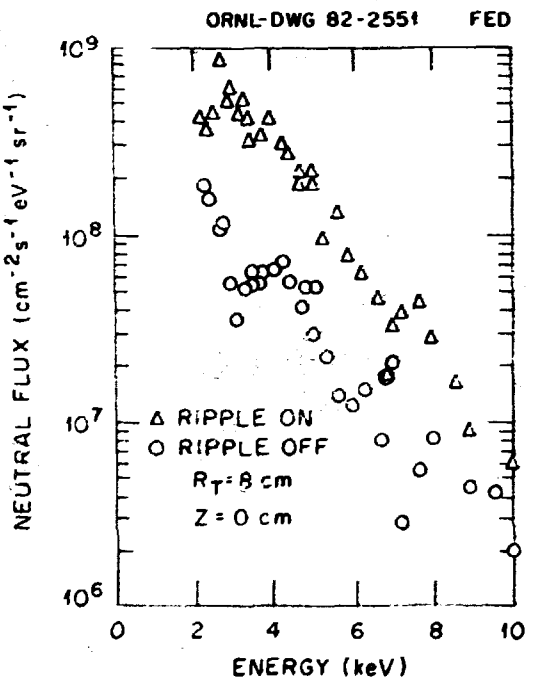

Fig. 2.24. Measurement of the fast neutral flux along a nearly perpendicular sightline in the horizontal midplane with and without a 1% (on-axis) ripple well. The plasma parameters for this discharge were $\bar{n}_e = 4.7 \times 10^{13}$ cm^{-3}, $I_p = 150$ kA, elongation = 1.5, $T_e(0) = 420$ eV, and $T_i(0) = 300$ eV.

trapping region ($\alpha^* > 1$) formed below the horizontal midplane in the path of the diagnostic beam. The results of a toroidal and vertical scan of the fast neutral flux were also consistent with enhanced penetration of the ripple-injected ions.

The feasibility of ripple injection is also contingent upon good confinement of the fast ions once they penetrate to the plasma center. Analytical theory and Monte Carlo simulations,[23] which indicate that 100- to 150-keV ions would be well confined in a large tokamak, predict a rapid loss of the full energy (15.9-keV) deuterons or protons in ISX-B due to a ripple-induced radial drift. The reasons for this expected loss are excessive neutral beam energy, relative to the plasma density and radius, and nonoptimal location of the diagnostic neutral beam for this experiment ($R_{opt} = 93$ cm). Both the charge exchange spectra and measurements of the D-D neutron yield (which is dominated by collisions between the fast beam-injected deuterons and the thermal deuterons) were consistent with poor confinement of the full energy fast ions. Along the sightline for Fig. 2.24, the neutral

flux decreased by an order of magnitude, from 14.5 keV to 11.6 keV. Neutron production increased by 20% in discharges with ripple, whereas an increase of approximately a factor of 2 would have been observed if all of the 15.9-keV fast deuterons were confined down to an energy of 13.5 keV. Monte Carlo simulations of the fast ion orbits, summarized in Table 2.4, show that with ripple on, 76% of the injected power at 15.9 keV is deposited on the limiter. Of 150 beam neutrals injected by the code, not one thermalized.

The ripple injection theory and Monte Carlo calculations predict improved confinement of the lower energy beam components (8.0 keV and 5.3 keV). Experimentally, the neutral flux increased smoothly with decreasing energy below 10 keV, consistent with reasonably good confinement of the ions. However, direct comparison with theory is difficult due to the chord-integrated nature of the charge exchange measurement and the steepness of the neutral density radial profile.

Additional experiments measured the effect of a single ripple well on the confinement of ions produced by the primary tangential heating beams. Along a nearly perpendicular sightline lying inside the ripple well that viewed the ripple-trapped and deeply banana-trapped populations, a strong depletion of the fast neutral flux was observed when the ripple coils were turned on, and the depletion increased with ripple strength.[24] This depletion is consistent with the theoretical expectation of a ripple-induced loss of energetic banana-trapped ions. In a separate experiment, the fast neutral flux along more tangential sightlines (corresponding to $v_{\parallel}/v = 0.77$ and $v_{\parallel}/v = 0.53$ at the plasma center) was nearly unaffected by a 0.6% on-axis ripple well. In this experiment, there was only a small decrease (<5%) in the ion temperature as indicated by the charge exchange and neutron diagnostics. This favorable result provides encouraging evidence that a small ripple well does not cause a loss of fast passing ions or a serious enhancement of thermal transport; however, it must be confirmed at the higher ripple required for successful ripple injection.

Table 2.4. Fraction of diagnostic beam power deposited on the limiter P_{lim} as a function of energy during the ripple injection experiment, calculated by a Monte Carlo orbit simulation, with plasma parameters of $\bar{n}_e = 4.7 \times 10^{13}$ cm^{-3}, $I_p = 150$ kA, elongation = 1.5, and $T_e(0) = 420$ eV

Deuteron energy (keV)	Ripple	P_{lim}
15.0	On	0.76
15.0	Off	0.58
7.5	On	0.48
7.5	Off	0.44
5.0	On	0.23
5.0	Off	0.38

2.1.5 Electron Cyclotron Heating

Introduction

A. C. England, T. B. Elder, C. C. Eldridge, J. C. Ezell, H. Hsuan,* A. J. Kulchar, C. M. Loring,† W. R. Russell,‡ J. B. Wilgen§*

During 1981, both ECH experiments and ECH preionization (ECH/PI) experiments were performed in ISX-B. These experiments are reported below. The experiments used a Varian triple miter bend gyrotron (VGA-8000), operating at a frequency of 28 GHz with a window output power of ≤100 kW for pulses up to 100 ms. Another 28-GHz axisymmetric Varian gyrotron (VGA-8050) with higher power (≤200 kW) and a shorter pulse length (≤40 ms) was to have been installed. However, this gyrotron suffered a vacuum failure and was not used. Plans for a future experiment using a NRL 35-GHz gyrotron

*Princeton Plasma Physics Laboratory, Princeton, New Jersey.
†EBT-P Project.
‡Management Services Section.
§EBT Experimental Section.

with a power of ~200 kW and a pulse length of 20-40 ms are discussed at the end of this section.

Heating experiments

The 28-GHz gyrotron was found to have an output power at the window of <100 kW. Subsequent measurements indicated that <70 kW of power was delivered to a calorimeter at the far end of the waveguide, roughly at the plasma position. This loss was found to be correlated with a bad waveguide mode mixture. Mode patterns were observed by inserting ordinary paper or thermofax paper across a waveguide under operation. The regions of high electric field strengths caused color changes and charring of the paper. Examples of these patterns are shown in Fig. 2.25.

With this sort of mode pattern, the Wengenmroth[25] polarizer would clearly be ineffective, and we could only assume that a mixture of ~50% ordinary and ~50% extraordinary radiation was broadcast into the plasma. As discussed in Ref. 26, the antenna was on the high field side on the midplane and was set to introduce the radiation at an angle of 60° to the magnetic field, an optimum angle for absorption and bulk heating. A number of attempts were made at bulk heating, as reported in last year's annual report.[26] During 1981, a measurable temperature rise was observed. The operating window was found to be very narrow. The magnetic field was set for resonance very close to the axis (10.2 kG). The plasma current had to be kept low enough (80 kA) to avoid masking the ECH effect, but

ORNL-PHOTO 8137-82

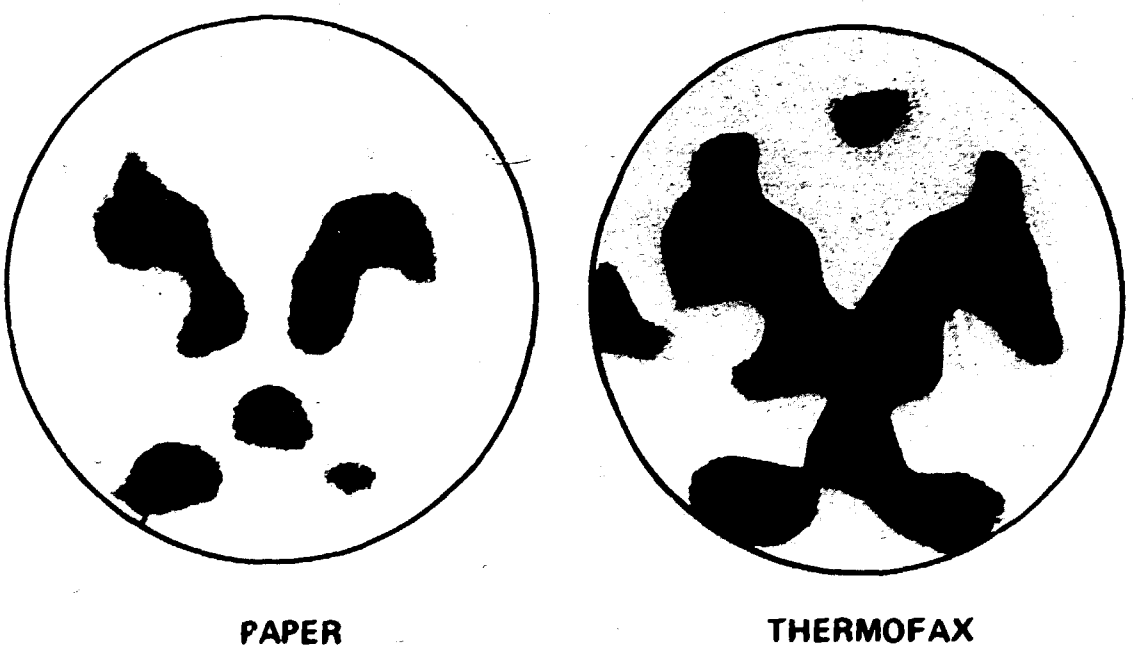

Fig. 2.25. Photographs of paper placed across waveguide at gyrotron. Dark areas show regions of high energy density. The gyrotron was pulsed for 10-50 ms, depending on the paper and the operating conditions. The patterns clearly indicate that the circular electric modes (e.g., $TE_{0,1}$, $TE_{0,2}$, ...) are not dominant and that the mode mixture is not optimum for long-distance transmission.

also high enough to provide an electron temperature, T_e, adequate for good single pass absorption. An initial value of T_e = 600 eV was sufficient, and the measured temperature rise was 370±110 eV. The plasma density had to be low (~6×10^{12} cm^{-3}) to provide accessibility and to keep the total number of particles small. Due to the low density, only a central temperature could be measured by Thomson scattering.

During this experiment the loop voltage was observed to drop ~30% (Fig. 2.26) in rough agreement with the temperature rise. The density also dropped as in the previous ISX-B experiment at 35 GHz[27] and in the JFT-2 experiment at 28 GHz.[28] There is still no satisfactory understanding of this density drop, which was observed on both the laser measurement and the 2-mm interferometer.

Without profile data, only a rough energy balance could be made. However, if 70 kW entered the plasma, then between 35% and 70% of this power was deposited in the plasma.

No heating effect was observed for off-axis (B ≠ 10.2 kG) heating, and there was no evidence of profile broadening or instability suppression. However, due to the low power, these effects would not be easily observed.

The electron cyclotron emission (ECE) showed strong effects. Detectors at the first, second, and third harmonic all showed signals much stronger than those expected from the laser measurement, and it appears that the ECH is enhancing a superthermal tail. In some cases (Fig. 2.27), the ECE increased after the ECH pulse was over. There are two possible explanations for this: (1) the parallel energy of the superthermal tail is converted into perpendicular energy by some mechanism (not yet identified) or (2) the heating location is off-resonant (and not in the detection band of the ECE devices) and drifts spatially into resonance after the ECH pulse ends. The heating of superthermal electrons is discussed in Ref. 29.

The process causing this radiation peak has an apparent threshold. There is a critical dependence on the length of the ECH pulse. Theoretical work is continuing on the explanation of the measurements.

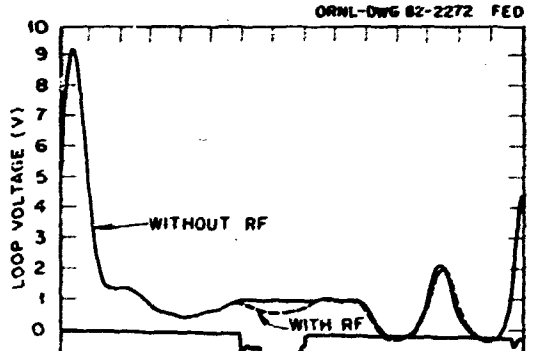

Fig. 2.26. The upper trace shows the loop voltage as a function of time for shots with (dotted) and without (solid) ECH. The trace has been smoothed by a Gaussian filter to remove spikes due to power supply noise and feedback. The lower trace shows the rf power monitor. The monitor signal is inverted, and the voltage reduction is ~30%.

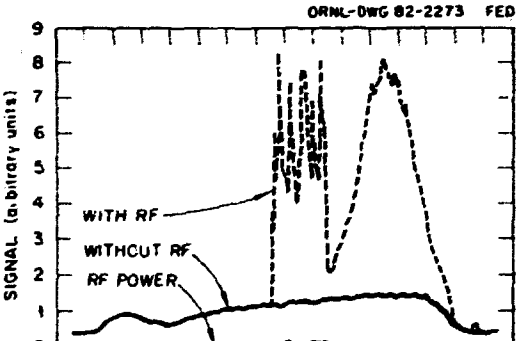

Fig. 2.27. The upper trace shows the second harmonic electron cyclotron emission with (dotted) and without (solid) ECH as a function of time. The trace with ECH shows a strong signal during the ECH pulse and also a larger signal building up after the rf pulse. The lower trace shows the rf power monitor.

It was interesting to note that the fundamental ECE detector occasionally displayed other anomalous behavior. It was set to look at frequencies just above the 28-GHz gyrotron frequency with a high pass waveguide filter. Subsequent measurements showed that the gyrotron occasionally put out significant power at 29 GHz, 30 GHz, and 31 GHz, thus completely swamping the fundamental emission.

Preionization experiments

The ECH/PI studies continued, with the Varian gyrotron supplying approximately 70 kW of 28-GHz microwave power to the plasma. The capacitor bank voltages used for breakdown and ohmic heating, the toroidal magnetic field, and the times of the radio frequency (rf) pulse were varied. Many of the experiments confirmed previous work at 35 GHz[30] and extended these measurements.[31] The volt-second savings and the rate of rise of the current depend on the magnetic field in a nonlinear way. The maximum volt-second savings occurred when the field was adjusted for resonance near the outside of the tokamak (Fig. 2.28).

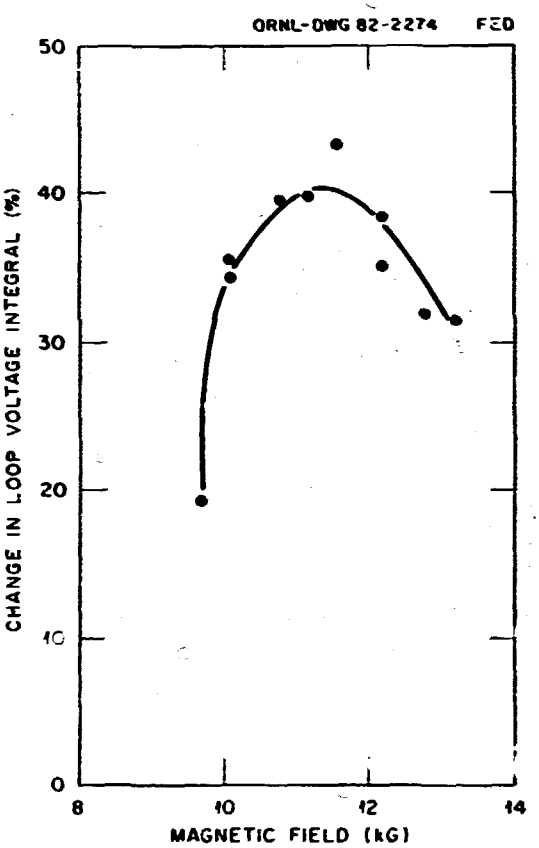

Fig. 2.28. The reduction in the loop voltage integral vs the main magnetic field. Note that the maximum is displaced from the position where the resonance would be on axis (10 kG) to a higher field of ~11.5 kG, indicating that the optimum condition is with the resonance at a larger major radius.

The length of the rf pulse before the capacitor banks fired was varied. Figure 2.29 shows that the volt-second savings increased monotonically with pulse width. However, the percentage of reduction in the loop voltage saturated after ~5 ms.

The rate of rise of current, dI/dt, appears to saturate with pulse length and field. The length of the rf pulse after the capacitor bank fires has no effect on the plasma, as was previously observed.[30] Curiously, rf pulses that ended 20 ms before the capacitor banks fired produced a noticeable reduction in loop voltage, indicating that the ECH/PI produced a long-lived plasma component.

The upper and lower limiter currents were also studied. The current between the limiter and the liner was measured by a commercial current probe. The dependence of the limiter current on the error fields was observed. Specifically, for large error fields (produced by current in the inner and outer poloidal field windings without plasma current) there is a large limiter current. The current flows vertically in the sense calculated for the curvature drift ($\vec{B} \times \nabla \vec{B}$). The current changes sign when the toroidal field is reversed, but the magnitude changes dramatically, an effect probably due to differences in the error fields. Although visible light increases rapidly with the application of ECH/PI power, the limiter current rises with a time constant

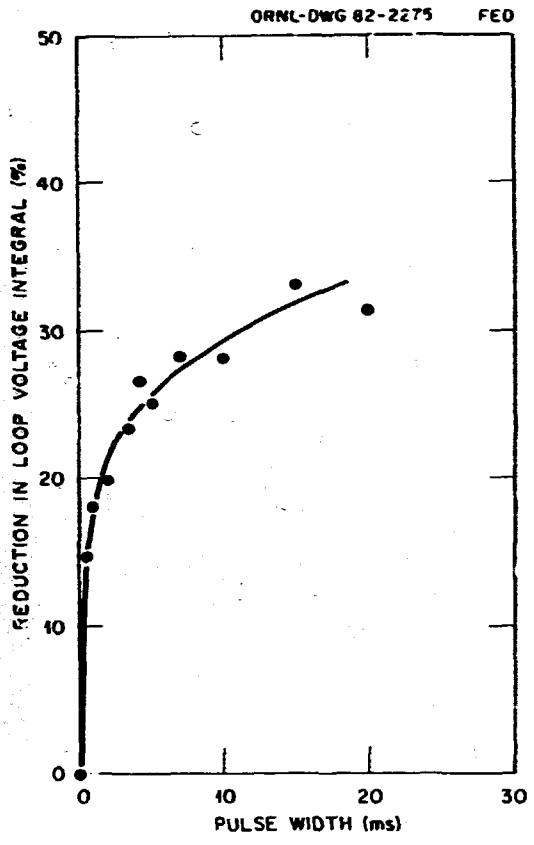

Fig. 2.29. The reduction in the loop voltage integral with pulse width. Note the rapid rise for the first few milliseconds.

of ~5 ms. The current decreases with increasing gas pressure. Comparisons between these measurements and theory[32] are in progress.

Some preliminary measurements of edge plasma temperatures were made with a Langmuir probe. These show a very cold (~1- to 3-eV), low density (~1 × 10^{12}-cm^{-3}) plasma near the wall of ISX, in disagreement with previous measurements on ISX-B with 35-GHz preionization.[30] Spectroscopic measurements of electron temperature were inconclusive due to irreproducibility of the data. This is probably evidence of turbulence or gross plasma motion. A Runge-Kutta program, similar to a program already written by Sprott,[33] is now being prepared to model these processes.

Future experiments

During 1982, another gyrotron from NRL will be brought to ORNL for further ECH experiments. The new gyrotron will be a considerable improvement over the one brought here in 1979. The frequency is the same, 35 GHz, but the new tube will have an output of ~300 kW for pulse lengths of 20-40 ms. The output will be in the TE_{04} mode, and this will be converted to TE_{01} for transmission to the tokamak.[34] A rotating antenna is now being designed to launch the power from the high field side at the midplane. The radiation will be polarized. The first priority experiments will be current drive, with lower priorities including bulk heating, profile modification, MHD suppression, preionization, second harmonic heating, etc. Experiments are expected to start in the fall of 1982.

2.1.6 Diagnostics

Neutron measurements on ISX-B

S. D. Scott, J. T. Mihalczo

A systematic discrepancy between the central ion temperature deduced from charge exchange (T_{CX}) and the ion temperature obtained from measurements of the thermonuclear neutron production rate (T_n) during H^0 injection into D^+ plasmas has been observed on ISX-B.[35] Typically $T_{CX} > T_n$, but at low ion temperature ($T_i < 600$ eV) the reverse condition holds, $T_n > T_{CX}$. Recent analysis has established that the ion temperature inferred from the neutron production rate is relatively insensitive ($\Delta T_n < 10\%$) to uncertainties in the radial profiles of plasma density and ion temperature and to uncertainties in the depletion of deuterium density near the plasma center that results from fueling by the hydrogen beam. Charge exchange measurements of the deuterium concentration $R \sim [n_D/(n_D + n_H)]$ at $r \sim 8$ cm during H^0 injection (1.7 MW) indicate that $R \sim 0.8$.

However, one mechanism has been identified theoretically that causes the ion temperature

inferred from the neutron emission rate to be higher than the actual ion temperature during neutral injection into low temperature plasmas (T_i < 600 eV).[36] Under these conditions, neutron production is dominated by collisions between thermal deuterons and a very small population of fast deuterons created by (1) the minute isotopic fraction (1.5×10^{-4}) of deuterons in the nominal H^0 heating beam (2) infrequent large angle collisions between the H^+ fast (beam) ions and thermal deuterons. This mechanism will be studied experimentally during 1982 by injecting a H^0 neutral beam containing 1% deuterium into a D^+ plasma.

Charge exchange measurements on ISX-B

S. D. Scott, C. L. Hailted, J. F. Lyon, J. T. Mihalczo, G. H. Neilson

Diagnostic status. The ISX-B charge exchange diagnostics consist of two scanning, mass- and energy-selecting neutral particle analyzers and a vertically directed diagnostic neutral beam (DNB). The momentum energy analyzer (MEA) views chords in the horizontal midplane with tangency major radii R_t (smallest major radius of the viewing chord) ranging from 49 to 93 cm. The velocity filter analyzer (VFA) scans both toroidally (R_t = 6-45 cm) and vertically [Z(R = 93 cm) = -6.6 to +35 cm]. The DNB allows local charge exchange measurements of the central ion temperature to be obtained.

Comparison of central ion temperature measurements. Before the DNB was available, the central ion temperature was calculated by a "model fit" numerical code[37] that accounts for many effects associated with the chord-integrated nature of the charge exchange measurement, such as the steep radial profile of the neutral density and the reionization of the charge exchange neutrals along the line of sight. To obtain a localized measurement of the central ion temperature, the charge exchange flux is measured in similar discharges with and without a DNB to enhance the central neutral density. The ion temperature is then calculated directly from the difference spectrum, $\phi(E) = \phi(\text{DNB on}) - \phi(\text{DNB off})$, after a straightforward correction for reionization is applied. In Fig. 2.30, the ion temperature

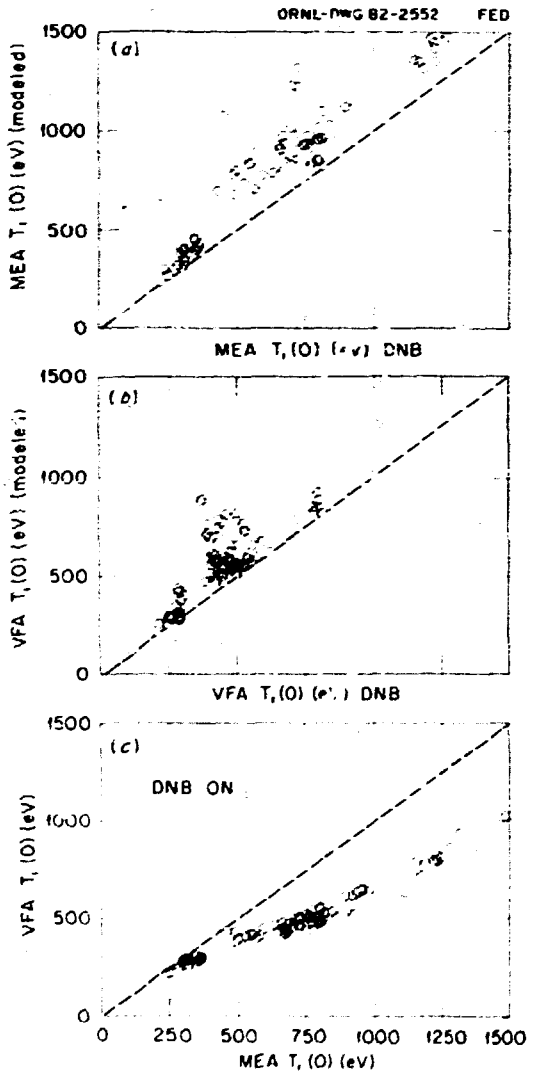

Fig. 2.30. (a) Comparison of the central ion temperature calculated by the model fit code to that measured with the DNB by the MEA. The dashed line represents the locus of equal temperatures, and the dotted line represents the best fit to the data. (b) Comparison of calculated central ion temperature with that obtained from the VFA. (c) Comparison of the ion temperature as measured by the VFA and MEA charge exchange diagnostics using the DNB to enhance the central neutral density.

obtained with the DNB is compared to that calculated by the modeling code for both neutral particle analyzers. The model fit calculation of central ion temperature is considered to be the less credible measurement, because it is sensitive to assumptions about the shape of the ion temperature radial profile, the neutral density radial profile, and the energy range over which the code fits the measured neutral particle flux. Typically, the modeling code overestimates the central ion temperature by 25%, although the discrepancy may be considerably greater (<70%) in some high density discharges. A regression analysis indicates that the discrepancy increases with plasma density.

The ion temperature measured with the DNB by the MEA diagnostic along a predominantly tangential sightline (R_t = 72 cm) and that measured by the VFA diagnostic along a nearly perpendicular sightline (R_t = 8 cm) are compared in Fig. 2.30(c). The apparent ion temperature is considerably lower along the more perpendicular (VFA) sightline. Approximately 15-20% of the discrepancy can be attributed to instrument-specific errors. There is evidence, not yet conclusive, that the remainder is caused by beam-induced toroidal plasma rotation, which Doppler shifts the charge exchange energy spectrum. The evidence consists of the observations that (1) both neutral particle analyzers tend to record a higher ion temperature in beam-heated discharges when they are rotated from a more perpendicular to a more tangential viewing orientation; (2) the central ion temperature measured by the VFA diagnostic along a perpendicular sightline using the DNB agrees reasonably well with the temperature inferred from neutron production, T_n, at high ion temperature, while the temperature measured by the MEA diagnostic (R_t = 72 cm) is substantially higher than T_n; and (3) scaling of preliminary spectroscopic measurements of the toroidal rotation velocity in discharges with high power injection indicates that rotation velocities on the order of 1.4×10^7 cm/s may be attained. These studies will be continued in 1982 by reversing the positions of the neutral particle analyzers.

Two-dimensional imaging of x-ray emission density in ISX-B

V. K. Paré, A. P. Navarro, J. L. Dunlap, J. D. Bell, S. C. Bates, C. W. Nestor, Jr.

Three arrays with a total of 80 slit-collimated, semiconductor, soft x-ray detectors were installed so as to view the ISX-B plasma in a poloidal plane. The detector currents, each proportional to a line integral of emitted x-ray power density, are amplified, recorded by a computer data acquisition system, and processed by a generalized Abel inversion method[38] to yield maps of the emission density in the plane. Since contours of constant emission density are assumed to be on magnetic surfaces, the internal magnetic geometry can be seen. Figure 2.31 shows the arrangement of the arrays and the lines of sight of the individual detectors.

The reconstruction of the emission density from its line integrals is very sensitive to errors in the detector signals; thus, great care is required in calibration of the system and in removal of dc offsets and electromagnetic interference. During the year we were able to do reconstructions using data from the side and top (180° and 270°) arrays.

Figure 2.32(a) shows the reconstructed emission distribution from a beam-heated shot. An $m = 1$ mode is present but is not readily apparent in the plot. To make it visible, we did a second reconstruction [Fig. 2.32(b)] from detector signals averaged over one cycle of the mode rotation and subtracted it from the first. The result, representing the contribution of the mode, is shown in three-dimensional (3-D) form in Fig. 2.32(c) and as a contour plot in Fig. 2.33.

We expect that further improvement in calibration techniques, precise measurement of the collimation geometry, and shielding of the detectors against ultraviolet light will enable us to employ all three arrays in imaging and analysis of internal MHD modes.

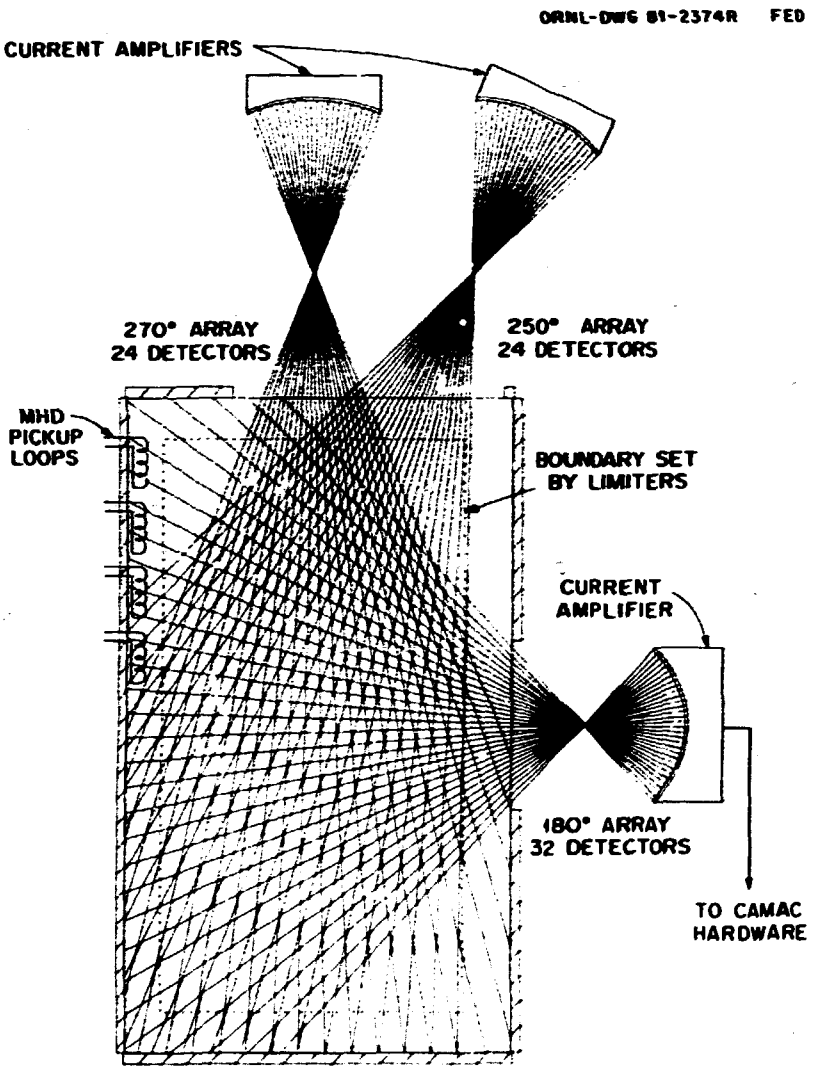

Fig. 2.31. Arrangement of x-ray arrays on ISX-B

2.1.7 Tokamak Operations and Technology

Tokamak operations

G. R. Dyer, P. H. Edmonds, W. A. Gabbard, H. E. Ketterer, D. R. Overbey, C. E. Parker, T. F. Rayburn, J. R. Reagan, W. J. Redmond, R. K. Rowell,* M. J. Saltmarsh, J. L. Yarber*

Comparison of statistics with 1979 and 1980 shows that the continuing projection of four experimental days per week is very close to the achieved number (Table 2.5). The total number of shots fired was 11,806, an average of 76 shots per day. The distribution of shots among the various program elements is shown in Table 2.6. There is a significant increase in the percentage for setting up an operation when compared to the previous years. This mostly reflects the difficulty of ascribing a particular shot to any one category but also indicates a significant change in the experiment, in that much more time was spent

*Y-12 Maintenance Division, Research Services Department.

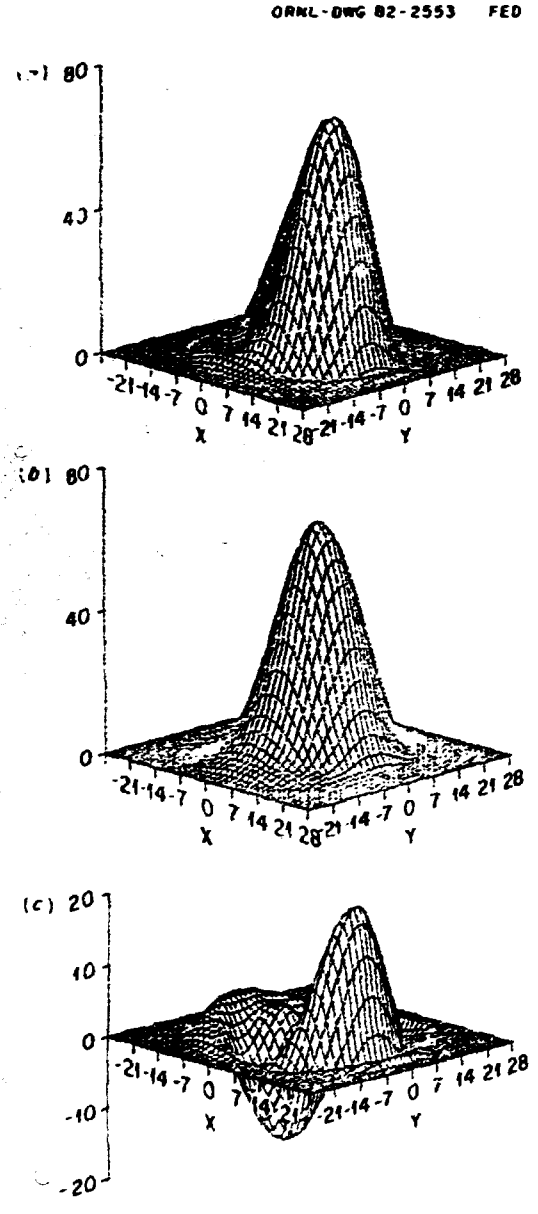

Fig. 2.32. (a) Emission density at a single time point, reconstructed using data from two arrays. (b) Reconstruction from data averaged over a cycle of m = 1 MHD mode rotation. (c) Difference between (a) and (b). X and Y are horizontal and vertical coordinates, respectively, in centimeters from nominal plasma center.

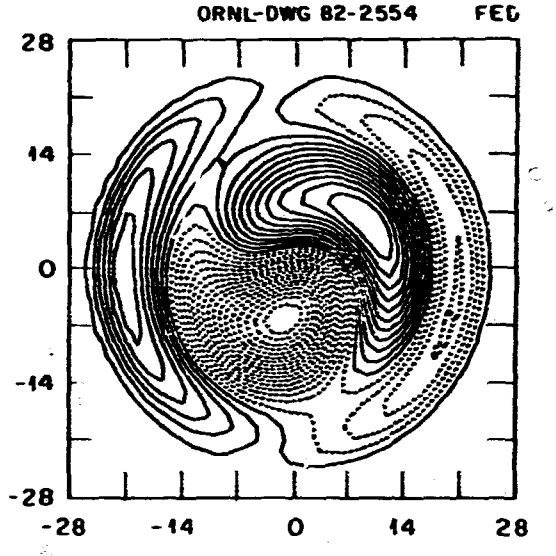

Fig. 2.33. Contour plot of emission density for the mode reconstruction of Fig. 2.32(c). Dashed contours represent negative values.

in attempting to expand the operating envelope and in exploring the operating envelope than was spent in detailed documentation of discharges. The operating history for 1981 is shown in Fig. 2.34. Surprisingly, no downtime included an entire working week.

Relatively few major problems were experienced during the year. A large amount of time was devoted to improving the reliability of the feedback system. An ongoing problem for most of the year was caused by the high voltages induced around the torus by a disruption. The latest fix was to install a spark gap across the back bias windings, and this seems to have solved the problem.

During the last three months of the year, the tokamak was shut down for the installation of (1) the new multipoint Thomson scattering system, (2) the bundle divertor, and (3) a reinforcement system for the TF coils. On

Table 2.5. ISX-B operational days for 1981

Projected days available (4 days/week)	202
Days lost to scheduled shutdowns (October-December)	46
Days available for operation	156
Days of actual operation	156
Net days lost	0

Table 2.6. Distribution of tokamak shots by program objectives for 1981

Program	Number of shots	Percent of total
General plasma experiments (setup, baseline, and exploration)	4673	40
High beta program		
Circular plasma	2118	18
Noncircular plasma	979	8
ECH studies	423	4
Ripple studies	814	7
Impurity transport (includes rotation experiments)	1351	11
Pellet injection	118	1
Surface physics	348	3
Machine tests	982	8

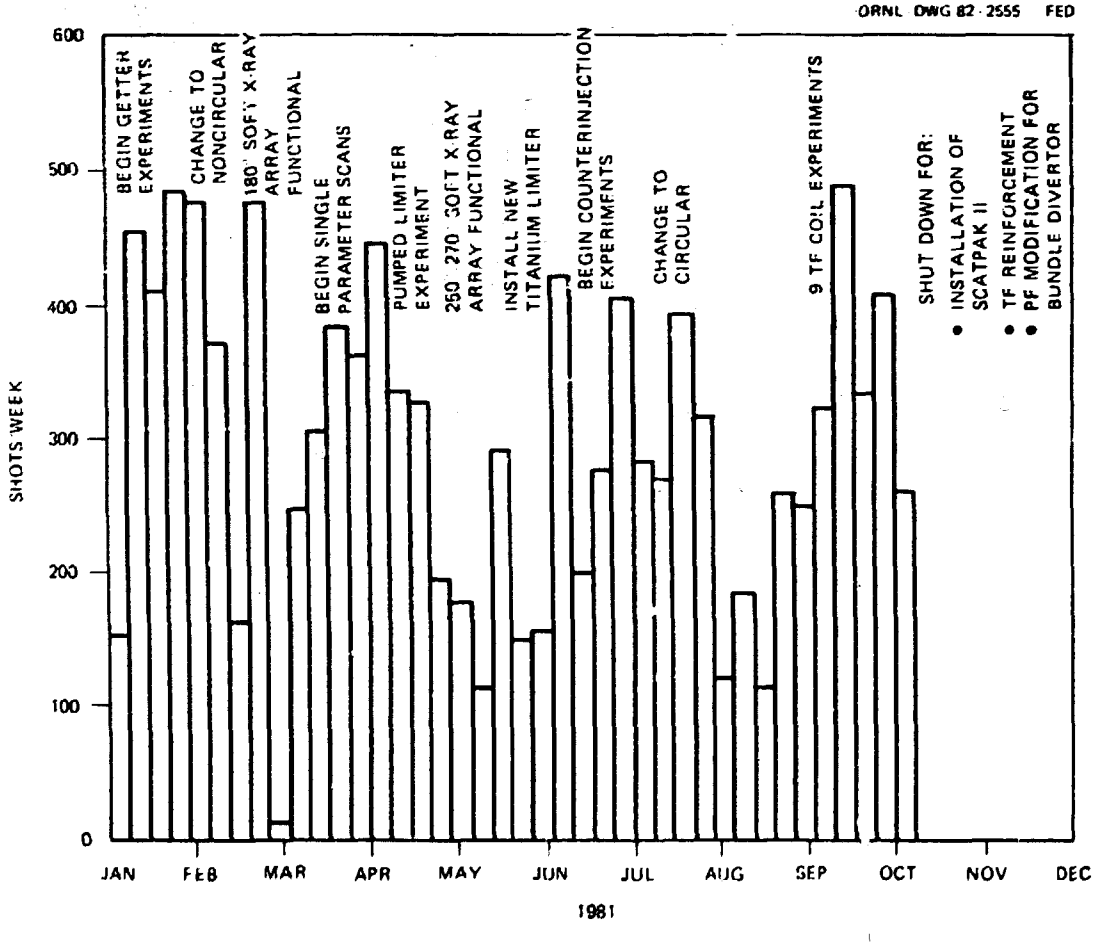

Fig. 2.34. Operating history of ISX-B for 1981.

completion of the modifications to the poloidal field coil system, the bundle divertor installation was halted, leaving the very large access port available for other diagnostics.

ISX-B neutral beam lines

E. F. Bates, O. C. Cole, P. H. Edmonds, P. C. Efthimion, E. A. Hasenzahl

Beam line description.[39] Neutral hydrogen beams provide the plasma heating for the beta studies that are being done on ISX-B. Nearly 3 MW of power has been injected into the plasma by two separate beam lines operated simultaneously. Injection of the beams is tangential and slightly inside the plasma axis for maximum absorption. The 100-A, 30-cm-diam ion sources and associated beam line hardware were developed by the Plasma Technology Section at ORNL[40] and have been slightly modified to meet tokamak operating requirements. The other major parts of the ISX-B beam systems are a helium liquefaction and supply system and two 6-MW, pulsed, dc power supplies, described in previous annual reports.[41-43]

Beam line operation. Neutral beam injection experiments were performed throughout the year until ISX-B was shut down for modification in October. Failures in components of the 6-MW power supplies and the beam conditioning calorimeter mechanisms caused limits on the available beam power, but only short shutdowns occurred. Minor manufacturing defects in the power supplies resulted in faults that were repaired as part of a continuing major in-house effort to improve the long-term performance of these supplies. Part of this work consists of maintaining switchgear that has now significantly exceeded its design lifetime.

Neutral beam operation has reached the stage at which availability of the beams is not a factor in tokamak program planning. The beams are used on a routine basis at injected power levels up to 2 MW. Higher power operation of approximately 2.5 MW has been achieved with greater difficulty and less reliability; total power of up to almost 3 MW was achieved in isolated instances. This situation should improve further as the more slowly developing problems and minor deficiencies are corrected.

Beam line computerization program. A multifaceted beam line computerization effort continued during the year.[44] This work includes data acquisition, analysis, and storage and equipment control. A microprocessor-controlled CAMAC system continued to monitor and display beam line calorimetric measurements. Experiments also demonstrated the feasibility of a CAMAC station floating at high voltage and communicating by fiber optic links. New equipment, including a PDP11/34 and additional CAMAC hardware, was acquired for further work.

In June it was decided to fully automate conditioning and injection of the beams in order to minimize the need for beam line operating personnel. The system was installed while manual operation was in progress. The computer-operated controls were made to be parallel to the manual controls; each one could be selectively activated. Computer operation and individual control were phased in gradually as the programs and hardware proved workable. Operation was uninterrupted during this process. The PDP11/34 provided control over standard CAMAC hardware and simple controls modification. By the October shutdown, the system[45,46] was performing conditioning and injection of both beam lines for total power levels up to 2 MW entirely automatically on a routine basis.

Liquid helium system. The helium liquefaction system supplied all the needs of the beam lines throughout the operating year. Final correction of manufacturing defects, coupled with an improved vacuum system and a 1000-liter liquid reserve dewar, allowed problems to be solved without affecting beam operation. Gas recovery had to be temporarily abandoned pending installation of new piping because of impurity fouling of the system. The system works satisfactorily but will be further improved.

Work in progress. In response to plasma physics questions concerning the effects of beam-induced plasma rotation on confinement, work is in progress on a third beam line, equivalent to the existing beam lines but injecting in an opposite direction. The three beam lines will share the use of the present high voltage power supplies. The third beam line is expected to become available late in the summer of 1982.

ISX-B data system

K. B. Wong, J. D. Bell, E. C. Blair, P. C. Haste, D. C. Hamer,* D. B. Overbey, J. B. Rogers, K. A. Stewart

Data system highlights from 1981 include the following:

- installation of a new immediate display system in the control room,
- development of an automatic computer control system for the ISX-B neutral injectors,
- operation of the 3-array x-ray detector system and reconstruction of the first tomographic images of the ISX-B plasma,
- implementation of a new extended ISX data access subroutine, XISX, which returns data in physics units or as analyzed results, and
- completion of an internal analysis of the future needs and directions of the data system and a review by DOE of the conclusions of this analysis.

The year was primarily one of evolutionary rather than revolutionary change; as implied by these highlights, there were developments in all areas of the data system. A few of the most interesting are discussed in depth.

One of the most visible changes in the data system during 1981 was the replacement of the PDP12 as an immediate display with a system based on a dual processor (PDP11/34), a shared disk, and a stroke vector, refreshed CRT display system. The ISX data system [and its predecessor, the Oak Ridge Tokamak (ORMAK) data system] has always included an immediate (oscilloscope-like) display as a guide to operations. This display was formerly provided by a PDP12, using its built-in CRT. However, as the number of diagnostic data channels and the level of diagnostic sophistication grew, the capability of the PDP12 was outgrown. It was capable of recording, for display, 24 channels of data on each shot and of storing the current and two preceding shots. It thus stored a total of 72 channels, of which any two could be displayed simultaneously. The display was fully interactive but could only provide numerical values as raw data, with no conversion to physics units.

By contrast, the replacement system provides access to 160 channels on each shot. Twenty-four channels can be displayed simultaneously and any two of these can be inspected at high (and variable, via a zoom capability) resolution. The 24 simultaneously displayed channels are divided into three groups. Any group can be associated with any of the five most recent shots or with one of two reference shots. A reference shot may be any shot available on the spooling disk, which typically means any of the last 600 to 1200 shots. Finally, the data curve's readout is provided as converted physics units.

Supporting this display requires most of the resources of a PDP11/34, which represents the second processor of the dual-processor, shared-disk system described in the 1980 annual report. The first CPU serves purely as a data acquisition processor; it sets up and then reads transient recorders, receives data files from two front-end PDP8/e computers, creates spool files of all these data on an RP06 (200-megabyte) disk drive, and finally transmits all the data to the PDP10. The second processor has read-only access to the shared disk. After each shot it waits for the new data files to be written on this disk; then it reads them and updates the display. The standard RSX-11M operating system does

*DCC-ND Computer Sciences.

not support such shared access, so a local modification was made to the disk driver software so that it no longer regarded a busy status as an error condition.

The second major development of 1981 was the successful automation of the process of controlling the ISX-B neutral injectors. This task first required the provision of a computer interface to all the beam line diagnostic readouts and operator control inputs. Second, it required unusually sympathetic cooperation between the programmer in charge and the beam line operation crew. Finally, it required careful thought and study on both sides to elucidate the thought processes used by a beam operator to arrive at a fully conditioned, operating beam ready for injection into the tokamak. This program is still undergoing development and improvement. However, even at its present stage of development it is capable of initiating beam line operation, conditioning a source and beam up to a 1-MW power level, and providing two such beams to the tokamak without operator intervention. The program constantly monitors its own past behavior (averaging over the ten previous conditions) and attempts to improve the delivered beam power.

The 1980 annual report described the use of the Perkin-Elmer 8-32 computer system to acquire data from MHD loop detectors surrounding the plasma. During the past year this system has been expanded to acquire data from three sets of collimated x-ray detectors (see Sect. 2.1.6). These arrays have overlapping, fan-shaped detector lines that allow a partial tomographic reconstruction of the x-ray emission from the plasma cross section. Since data from each detector are sampled and recorded as time-series data (typically 8000 samples at a 140-kHz rate), each sampling frame can potentially yield an x-ray image. The evolution of these images will provide one of the few tools available for studying the internal behavior of the plasma as it approaches a disruption or is pushed toward higher beta. The system can acquire over 1.5 megabytes of data on each shot; this quantity doubles if a background shot is taken. Enough preprocessing is done between shots to determine whether the data are acceptable and worth further study. If the answer is yes, a permanent data file is created that also stores all necessary calibration and configuration data.

In the past, the files stored on the PDP10 have always been simply files of raw data. Calibration constants have been needed to interpret these data, and the calibrations have been circulated to persons interested in interpreting the data. In 1981, the system was upgraded by including the necessary calibration coefficients with the data. Data are still stored as raw integers, but now each channel has an associated descriptor that converts the data into physics units. To allow users to take advantage of this, an extended version of the ISX data access subroutine was added to ISXLIB on the PDP10. This subroutine, called XISX, returns channels of data in the appropriately scaled physics units (e.g., volts, kiloamperes, or particles per cubic centimeter). In addition, it is aware of the existence of pseudo-channels (with negative channel numbers) that contain analyzed or reduced data.

Developments in electronic instrumentation

D. E. Dunn, J. M. Mellon, J. A. Moore, J. E. Phelps

During 1981, the ISX electronics group entered into agreements with the ORNL Instrumentation and Controls (I&C) Division and the General Engineering staff of UCC-ND to allow personnel from these groups to work in the Fusion Energy Division with Tokamak Experimental Section (TES) personnel on instrumentation problems. Under this arrangement, J. E. Phelps from I&C and J. A. Moore from General Engineering were added to our group. General Engineering also agreed to provide drafting and circuit layout support for TES. These arrangements are part of a continuing effort to use the technical expertise of the

entire Nuclear Division in solving fusion problems.

Advances in switching transistor technology during the past year made it possible to design a switching power regulator that can replace the present transistor array in the ISX outer power supply. The new regulator circuit is designed to operate at twice the terminal voltage of the present system and thus will allow better control of plasma position and current than is now possible. A small-scale prototype of the proposed circuit was built and tested during 1981, and potential difficulties with the full-scale system were identified and corrected. Work is under way on the complete system.

An optically isolated analog signal link design was completed in collaboration with General Engineering personnel. This design can be built in versions with bandwidths to 500 kHz and with either fiber optic coupling up to 5 m long or with an integrated circuit optical coupler for ground loop or low voltage isolation. The several versions available fill needs for shunt amplifier/isolators, high voltage isolation of diagnostic signals from beam line electronics, and general ground loop isolation of diagnostic signals on the present ISX machine. In addition, the concept is ready for implementation on future fusion experiments, where essentially all signals from the machine enclosure must be isolated from the experimental area. A paper covering part of this work was presented at the Ninth Symposium on Engineering Problems of Fusion Research.[1]

Several new instruments were designed for the ISX operating system during 1981. A group of analog modules, including a triggered ramp generator, an analog signal gating module with both logic and amplitude threshold control circuits, summing amplifiers, and signal conditioning (filtering, polarity control, and gain adjustment) modules, was completed for the plasma positioning control system. A digitally delayed pulse generator with CAMAC-readable delay settings was designed; plans are to use this instrument as a replacement for the present experiment control timer, as well as for general experimental and diagnostic applications. A high frequency filament supply was added to the fast ionization gage to allow its use in high ambient magnetic fields. Design work on a digitally loaded, CAMAC-controlled analog function generator was completed this past year, and a prototype is being tested. This module will be used in the gas puff and plasma position control systems.

In the area of general diagnostic instrumentation, development included improvements on the calorimeter for the Thomson scattering laser and a light pulse generator for calibration of the photomultiplier array in the new Thomson scattering diagnostic. A new high voltage (±150-V output) operational amplifier was designed for a scanning ion microscope used in surface physics studies. An analog function generator was added to the collection of general-purpose instrumentation available to the experimental staff.

In addition to developing new designs, the electronics staff provided the usual consultation and specialized diagnostics and repair services necessary for the continuation of the experimental program in the tokamak group. A union strike during the summer made it necessary for the professional staff to provide maintenance services essential for operation of ISX. In spite of several electrical and electronic problems, the staff was able to keep the machine operational for the duration of the strike.

2.2 THE ATF-1 PROGRAM

T. C. Jernigan, J. F. Lyon, B. A. Carreras, J. H. Harris, B. D. Nelson, J. A. Rome, M. R. Baer, R. A. Dory, R. H. Fowler, L. Garcia, R. L. Johnson, V. E. Lynch, P. F. Maddox,† J. Sheffield,‡ T. C. Tucker*

The ATF-1 device is expected to further the toroidal confinement concept by testing beta limits and collisionless transport in a

*University of Madrid, Spain.

†UCC-ND Computer Sciences.

‡Associate Division Director, Fusion Energy Division.

current-free stellarator configuration, with possible later extension to a tokamak/stellarator hybrid. The general device parameters under consideration are major radius R ~ 1.75-2 m, coil radius ~ 0.5 m, and magnetic field B ≤ 2 T. The moderate aspect ratio (A = R/$\bar{a}$ = 6-12) is intermediate between that of conventional tokamaks (A = 3-4) and that of stellarator-torsatron configurations (A = 10-20) to complement the existing toroidal confinement program, to provide adequate well depth and shear, and to provide relevance for tokamak/stellarator hybridization. It is expected that high power auxiliary heating [neutral beams and perhaps ion cyclotron resonant heating (ICRH)] will provide high beta capability and that low collisionality (ν_i^* ~ 1-0.1) will test plateau and ripple transport in an ISX-B-scale device. ATF-1 will be capable of steady-state operation and could therefore test steady-state technology, including particle and impurity control systems, heating systems, and fueling systems. Superconducting coils are being evaluated for ATF-1.

2.2.1 ATF-1 Design Approach

The ATF-1 studies are in the final stage of feasibility studies; selection of the coil configuration parameters is expected to take place in the summer of 1982. To select the best configuration, a wide range of stellarator-torsatron configurations is being evaluated and compared using several physics and engineering criteria. These criteria include (1) vacuum field flux surface topology and rotational transform (ι = 1/q) profiles, (2) guiding center orbit containment, (3) existence of stable, 3-D, finite beta MHD equilibria, (4) stability to ideal and resistive MHD interchange and ballooning modes, and (5) results from engineering studies assessing forces, cooling, and access for proposed configurations.

These criteria are applied in an iterative and interactive manner to optimize each configuration. The optimization procedure is as follows.

(1) Select configuration parameters.
(2) Calculate vacuum magnetic surfaces, the radius $\bar{a}$ of the last closed surface, $\iota(r)$, $\int dl/B$ variation on each surface, etc.
(3) Iterate on configuration parameters until a desired vacuum configuration is obtained.
(4) Calculate guiding center orbits for this configuration and evaluate fast ion confinement for neutral beam heating efficiency and thermal ion step sizes in ψ (flux) for transport estimates.
(5) Revise configuration parameters for better orbit confinement and return to step 2.
(6) Calculate 3-D MHD equilibrium/stability properties for maximum attainable $\langle\beta\rangle$.
(7) Revise configuration parameters for better high $\langle\beta\rangle$ behavior and return to step 2.
(8) Perform an engineering study of mechanical configuration and calculate forces (on support structure), access (for diagnostics and heating), and coil size (to determine minimum bend radii, cooling, and choice of material).
(9) Revise configuration parameters for better engineering properties and return to step 2.

The development of some of the tools used in this optimization procedure is described in Sect. 4.3 of this report. Their application to the ATF-1 design study is discussed below.

2.2.2 Magnetic Configuration Studies

The configurations studied for ATF-1 have magnetic surfaces with moderate aspect ratios (R/$\bar{a}$ = 6-12), large mean radii ($\bar{a}$ ≈ 25-30 cm) of the last closed flux surface, substantial rotational transform (ι_{max} > 0.5), and magnetic shear and/or well. Some configurations also feature small variations of $\int dl/B$ on flux surfaces and a helical magnetic axis. All coil systems have outward radial forces and good access for diagnostics and quasi-tangential neutral beam injection.

The types of configurations studied include (1) $\ell = 2$ continuous torsatrons with modulated winding laws, (2) modular stellarators with identical, rotated, toroidally deformed coils, (3) modular torsatrons with identical, nonrotated, helically deformed coils of the type shown in Fig. 2.35, both with and without a helical axis, (4) the "snake" geometry,[48] and (5) the existing Heliotron-E and Wendelstein VII-A configurations. The constraints on forces and access precluded consideration of a classical stellarator. The Heliotron-E and Wendelstein VII-A studies are used to compare our calculations on these configurations with those of other groups.

Although filamentary coils are used to study these configurations and their variants, all systems have coil separations and bend radii that are practical from an engineering viewpoint. The continuous-coil torsatron configurations under study are characterized by a helical coil winding law of the form $\varphi = (\ell/m)(\theta - \alpha \sin \theta)$, where φ is the toroidal angle, θ is the poloidal angle, ℓ is the number of windings, m is the number of toroidal periods, and α is the poloidal modulation of the helical winding. The initial reference configuration for this type, with $\ell = 2$, $m = 10$, $\alpha = 0.2$, and coil aspect ratio $A = 3.5$, had $\iota(0) = 0.1$, $\iota(a) = 0.6$, a mean radius $\bar{a} = 0.32$ m, and a 3.5% magnetic well. An improved (higher $\langle\beta\rangle$ limit) continuous-coil torsatron configuration, with $\ell = 2$, $m = 10$, $\alpha = 0$, and $A = 4.5$, has $\iota(0) = 0.3$, $\iota(a) = 0.9$, $\bar{a} = 0.26$ m, and a 1% magnetic well. These two configurations are compared in Fig. 2.36. The addition of an external toroidal field, an imbalance of the two helical winding currents, or a variation of the vertical field permits variations of $\bar{a}$ and $\iota(r)$.

ORNL-DWG 82-2556 FED

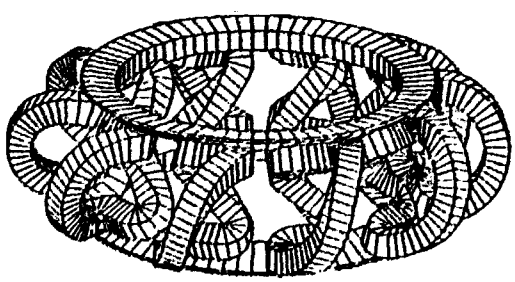

Fig. 2.35. Reference modular torsatron configuration with $\ell = 2$, $m = 10$, $R_0 = 1.75$ m, and $B_T = 2$ T.

The modular stellarator configurations under study have N identical, rotated TF coils, where the jth coil is deformed toroidally by[49] $\Delta_j(\theta) = d \sin[s\ell(\theta - \theta_j)]$, where $\theta_j = (2\pi/\ell)(m/N)j$ and the harmonic enhancement factor $s > 1$ in the region near the coil deflection nodal points in order to increase the rotational transform. The reference configuration, with $m = 4$, $N = 24$, $A = 4.5$, $s = 2$ at the positive node, and $s = 1$ at the negative node, has $\iota(0) = 0.6$, $\iota(\bar{a}) = 0.3$, $\bar{a} = 0.30$ m, and a 1% magnetic well. With a weak (12%) antiparallel toroidal field added, the rotational transform increases to $\iota(0) = 0.7$ and $\iota(\bar{a}) = 0.5$, while $\bar{a}$ decreases.

Modularization of the torsatron configuration presents a problem, because there is a net toroidally directed current in the helical windings of a torsatron that does not occur in the stellarator. We have developed a new configuration, the symmotron (for symmetric modular torsatron), which uses identical, nonrotated modular coils, one per field period. Figure 2.35 shows an $m = 10$ symmotron with circular coils on the top and bottom of the torus interior to cancel the toroidally directed windbacks of the modular coils. A variety of magnetic surface configurations can be produced by modulating the helical winding pitch (as in the continuous-coil torsatron), by winding the helix on a noncircular cross section, and by varying the radial location of the compensating circular windings.

2.2.3 Guiding Center Orbit Studies

Each configuration is analyzed for fast ion confinement (heating) and thermal ion step

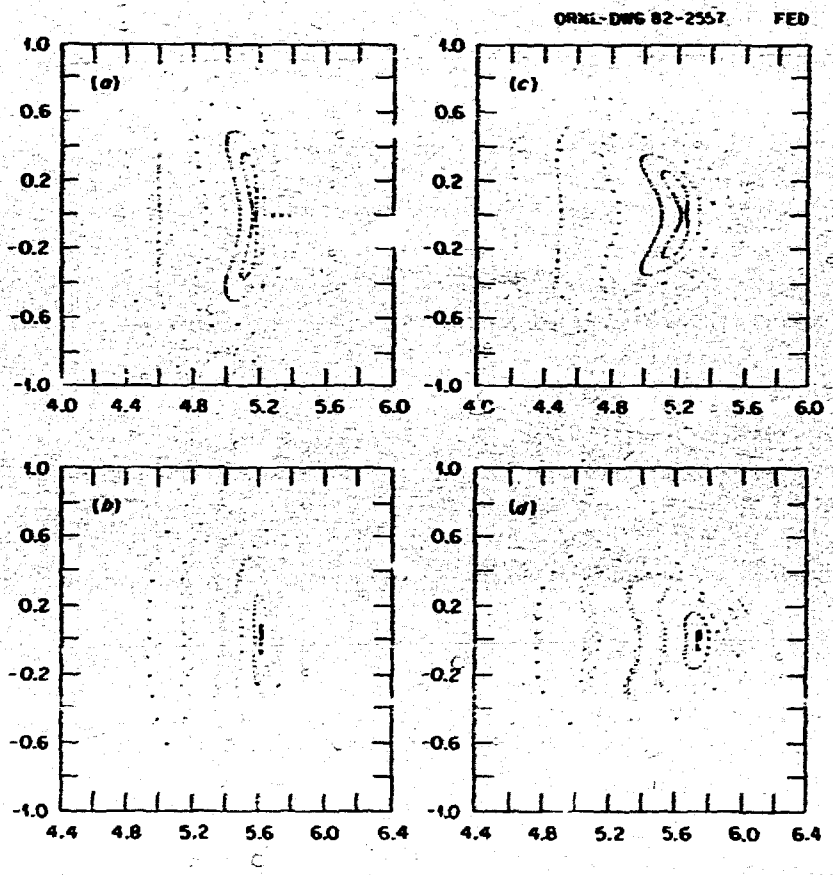

Fig. 2.36. Magnetic surfaces at $\zeta = 0$ (left) and $\zeta = \pi/m$ (right) for continuous torsatrons with $m = 10$, $\iota(0) = 0.1$, and $\langle\beta\rangle \approx 1\%$ (top) and with $m = 12$, $\iota(0) = 0.3$, and $\langle\beta\rangle \approx 4\%$ (bottom).

size $\Delta\psi$ (transport). Up to 1000 monoenergetic ions randomly distributed in $v_\parallel/v$ and space, which fall within the last closed 3-D flux surface, are followed for ~20 toroidal transits, using vacuum fields generated from a large number of linear current filaments that approximate the coil configuration. Calculations are made both in spatial coordinates and in field line coordinates ψ (flux), χ ($= \int B\, dl$), and a field line label θ_0. A Fourier transform representation of the magnetic field[50] in θ_0 is used for following both monoenergetic orbits and Monte Carlo calculations (which include electric fields, slowing down, and pitch angle scattering) and for analysis of the harmonic content of the magnetic field configuration.

The orbit studies indicate that direct losses of 30-keV H^+ in 2-T fields are ~20% for $|v_\parallel/v| < 0.5$ but are only ~1-4% for $|v_\parallel/v| > 0.5$, as would occur with quasi-tangential neutral beam injection. Three-dimensional Monte Carlo calculations of the birth distribution of injected fast particles have also been made to obtain better loss estimates. For particles below 5 keV, a 1-kV potential generally has more effect on losses than do the configuration parameters. In these cases, ~1% of all 1-keV protons are lost, and the average step size $\Delta\psi$ is $\sim 1/15(\psi_{wall} - \bar{\psi})$. In all cases, helically trapped particles make up the major loss population. The harmonic spectrum of modular systems is much fuller than that of continuous-coil torsatrons, which may enhance helical trapping and thus account for the generally poorer orbit confinement in these systems.

2.2.4 Equilibrium and Stability Studies

Since $\langle\beta\rangle$ limits are more sensitive to configuration parameters than is particle confinement, equilibrium and stability assessment is emphasized in the configuration optimization studies. Two parallel approaches are followed: (1) averaged MHD equations based on the stellarator expansion and (2) the full 3-D calculations. In the first approach, equilibria are obtained by solving a two-dimensional (2-D) Grad-Shafranov equation, which results from spatial averaging over a helical field period.[51] A reduced set of MHD equations is used for the stability studies for low n modes. In the averaged reduced equations, the magnetic field contains the contributions from both the external helical current and the plasma current. In addition, the curvature term is also modified by the averaged curvature of the external helical field. For intermediate mode numbers ($1 \ll n \ll m$), a ballooning mode equation along the effective averaged magnetic field is obtained that takes into account the averaged helical curvature term arising from the external windings.

For the full 3-D calculations, a modified version of the Chodura-Schlüter code[52] has been used. Starting with the vacuum magnetic field and a specified plasma pressure profile as initial conditions, the code minimizes the plasma potential energy $W = \int[B^2/2 + p/(\gamma - 1)]dV$, subject to the constraints of div B = 0, mass conservation, and magnetic flux conservation. Particular features of the Chodura-Schlüter code are Cartesian coordinates, Eulerian formulation, and boundary conditions specified on a square box (now generalized to exclude conductors and more closely follow the plasma boundary). Depending on $\iota(r)$ and the pressure profile, β limits arise from equilibrium failure or large-scale instabilities. The equilibrium limitations are due to a large shift of the magnetic axis, which can cause an internal separatrix, or to magnetic island formation, which can lead to destruction of magnetic surfaces, or both. For continuous-coil torsatrons, bifurcation of the magnetic axis occurs for low $\iota(0)$ even for $\langle\beta\rangle < 1\%$, as shown in Fig. 2.36 (*top*). For $\iota(0) > 0.3$, bifurcation does not occur, and equilibria with good magnetic surfaces are found with $\langle\beta\rangle$ values above 4%. An example, with $\iota(0) = 0.3$, $\iota(a) = 0.9$, and m = 12, is shown in Fig. 2.36 (bottom). If $\iota(0) > 0.5$, a $\langle\beta\rangle$ limit below 4% results, caused by instabilities rather than equilibrium limitations.

Simple $\ell = 2$ modular stellarators with a moderate number of TF coils (N ~ 15-30, with A = 3-4.5 and m = 3-6 periods) have a relatively high rotational transform per period ($\iota/m \approx 0.1$). Equilibria with good magnetic surfaces are not found for $\langle\beta\rangle > 1\%$ unless ι/m is reduced, and then these equilibria are unstable due to the low shear of these configurations. For snake configurations, equilibria with $R/a = \infty$ are found for all $\langle\beta\rangle$ values considered (1-5%). However, for $R/a = 6$, equilibria are not found even at low $\langle\beta\rangle$ values unless a fixed conducting boundary is assumed near the plasma edge.

2.2.5 Engineering Design Studies

Engineering design studies are in progress to develop design concepts for the ATF-1 device. Areas being explored in detail include (1) magnetic fields and forces with finite cross-section coils and (2) conductor designs; cooling, winding, and structural concepts; and stress levels. The engineering studies have identified a number of critical areas that may have a significant impact on ATF-1 considerations, including (1) minimum bend radius for the coils, (2) maximum force levels, (3) coil winding complexity, (4) cooling requirements for water-cooled coils, and (5) water-cooled versus superconducting coils. Of these, the minimum bend radius, which requires a small conductor cross section, and the requirement for continuous cooling, which favors large cooling passages and short lengths for increased flow, are the requirements most in conflict. In addition, the

effects of magnetic field errors and required tolerances during construction will be examined in these studies.

The basic design assumptions are that the coils can be operated in a steady state at 2 T and that access will be designed to accommodate tangential neutral beam heating and to allow flexible diagnostic arrangements. Initial operation will be pulsed, using existing power supplies, neutral beam systems, and cooling systems at ORNL. Upgrades of these systems will eventually allow steady-state operation at 2 T with multimegawatt plasma heating.

Figure 2.37 shows the design developed for the reference continuous-coil torsatron case. The parameters for this case are $\ell = 2$, $m = 10$, $R_0 = 1.75$ m, $a = 0.5$ m, and $B_T = 2$ T. Each coil has 16 turns, dissipates 23 MW, and requires 160 liter/s of cooling water. The self-magnetic forces of helical coils are primarily taken by the stainless steel coil cases with additional periodic support rings. Self-centering forces of the TF coils are taken by a bucking cylinder. Forces between the TF coils and the helical coils are taken by the vacuum vessel. A reference design for a modular torsatron (shown in Fig. 2.35) is being developed. The parameters for this case are $\ell = 2$, $m = 10$, $R_0 = 1.75$ m, $a_{coil} = 0.5$ m, and $B = 2$ T. Superconducting coils are being considered for this case because of the sharp bends required in the coils.

A reference design for a modular coil stellarator is shown in Fig. 2.38. For this design, the parameters are $N = 24$, $B_T = 2$ T, $a = 0.5$ m, $R_0 = 2.25$ m, $\ell = 2$, $m = 6$, and coil deflection = 0.12 m. Each coil has 16 turns, dissipates 2.5 MW, and requires 20 liter/s of cooling water. In this design the vacuum vessel and four of the coils form a removable module. Forces are again primarily taken in the coil cases. However, in this design the vacuum vessel takes both the overturning forces and the centering forces.

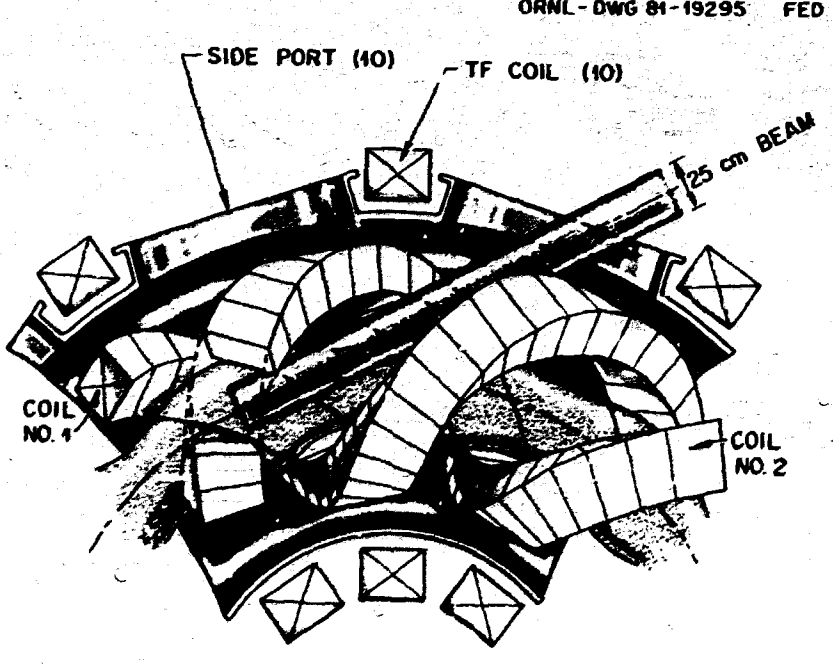

Fig. 2.37. The ATF-1 reference torsatron. Shown are the two helical coils inside the vacuum vessel. A set of TF coils for configuration modification is also shown, together with a possible neutral beam injection path. Not shown are the vertical field coils and the ohmic heating system. The system parameters are $\ell = 2$, $m = 10$, $R_0 = 1.75$ m, and $B_T = 2$ T.

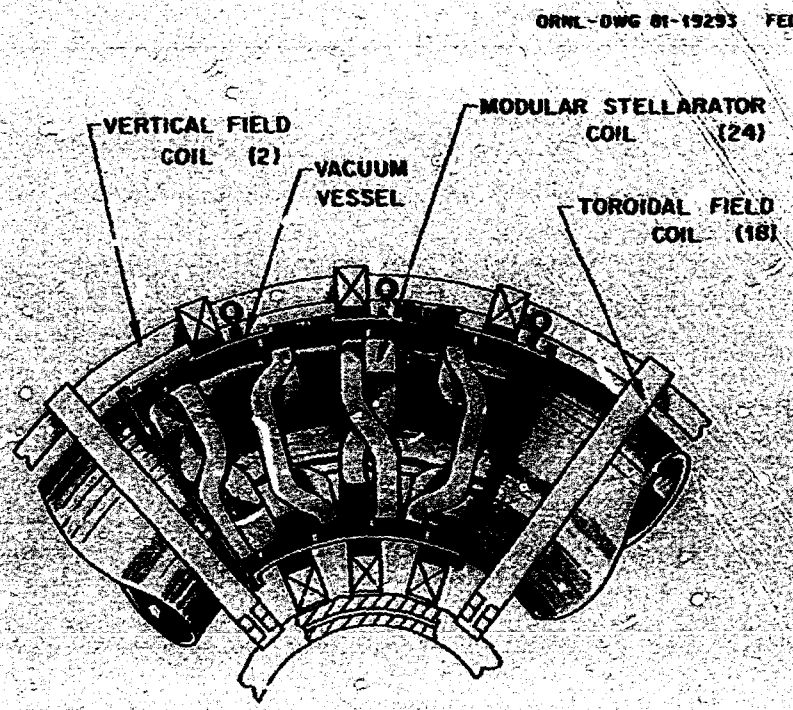

Fig. 2.38. A modulator stellarator system for ATF-1, showing the modular stellarator coils, the TF coils, and the vertical field coils. The ohmic heating system is not shown. The parameters for this design are $\ell = 2$, $m = 6$, $R_0 = 2.25$ m, $N = 24$ coils, and $B_T = 2$ T.

REFERENCES

1. D. W. Swain et al., Nucl. Fusion 21(11), 1409-23 (1981).
2. D. W. Swain and G. H. Neilson, "An Efficient Technique for Magnetic Analysis of Tokamak Equilibria," submitted to Nuclear Fusion.
3. L. L. Lao et al., Phys. Fluids 24(8), 1431-41 (1981).
4. J. L. Dunlap, B. A. Carreras, V. K. Paré, J. A. Holmes, S. C. Bates, J. D. Bell, H. R. Hicks, V. E. Lynch, and A. P. Navarro, Phys. Rev. Lett. 48, 538 (1982).
5. L. E. Zakharov and V. D. Shafranov, Sov. Phys.-Tech. Phys. 18, 151-56 (1973).
6. W. M. Stacey and D. J. Sigmar, Nucl. Fusion 19, 1665 (1979).
7. K. H. Burrell, *Neutral-Beam Induced Alteration in Impurity Transport: Summary of Experiments and a Possible Theoretical Explanation*, GA-A16387, General Atomic Company, San Diego, California (1981). The list of references in this report includes most of the theoretical literature on the subject.
8. F. L. Hinton, *Impurity Flow Reversal in Tokamaks Without Momentum Input*, IFSR 43 (DOE/ET/53088-43), Institute for Fusion Studies, University of Texas, Austin, Texas (1981).
9. C. E. Bush, R. C. Isler, J. M. Madison, and D. R. Overbey, "Power Losses from the ISX-B Tokamak," p. 56 in *Fusion Energy Division Annual Progress Report for Period Ending December 31, 1979*, ORNL-5645, Oak Ridge, Tennessee.
10. R. C. Isler, S. Kasai, L. E. Murray, M. J. Saltmarsh, and M. Murakami, Phys. Rev. Lett. 47, 333 (1981).

11. R. C. Isler et al., Phys. Rev. Lett. 47, 649 (1981).
12. R. C. Isler et al., Phys. Rev. A 24, 2701 (1981).
13. K. H. Burrell et al., Nucl. Fusion 21, 1009 (1981).
14. K. H. Burrell, T. Ohkawa, and S. K. Wong, Phys. Rev. Lett. 47, 511 (1981).
15. P. Mioduszewski, B. H. Edmonds, and J. Sheffield, "Advanced Limiters for ISX," to be published in the Journal of Vacuum Science and Technology.
16. P. H. Edmonds, P. M. Mioduszewski, J. E. Simpkins, and A. J. Wootton, "Gettering Experience in ISX, or Titanium is Good for Your Health," to be published in the Journal of Vacuum Science and Technology.
17. J. E. Simpkins and P. Mioduszewski, "Comparison of Ti and Cr Gettering," to be published in the Journal of Vacuum Science and Technology.
18. The Monte Carlo code was kindly provided by R. J. Goldston of PPPL and modified by R. H. Fowler for these calculations. It is described by R. J. Goldston et al., J. Comput. Phys. 43, 61-78 (1981).
19. B. Zurro, R. M. Wieland, M. Murakami, and D. W. Swain, *ZORROC: A 1-1/2-D Tokamak Data Analysis Code for Studying Noncircular High Beta Plasmas*, ORNL/TM-7146, Oak Ridge, Tennessee (1980).
20. R. M. Wieland, H. C. Howe, E. A. Lazarus, M. Murakami, and C. E. Thomas, Oak Ridge National Laboratory, "A Thomson Scattering Based Analysis Method for ISX-B Plasmas Using MHD Geometry" (unpublished, 1981).
21. S. Suckewer, H. P. Eubank, R. J. Goldston, J. McEnerney, N. R. Sauthoff, and H. H. Towner, Nucl. Fusion 21(10), 1301 (1981).
22. K. T. Tsang and E. A. Frieman, Phys. Fluids 19(5), 747 (1976).
23. D. L. Jassby and R. J. Goldston, Nucl. Fusion 16, 613 (1976).
24. J. S. Lyon et al., "Ripple Studies," p. 42 in *Fusion Energy Division Annual Progress Report for Period Ending December 31, 1979*, ORNL-5645, Oak Ridge, Tennessee.
25. R. D. Wengenroth, IEEE Trans. Microwave Theory Tech. MTT-26, 332 (1978).
26. A. C. England et al., "Electron Cyclotron Heating on ISX-B at 28 GHz," p. 64 in *Fusion Energy Division Annual Progress Report for Period Ending December 31, 1980*, ORNL-5674, Oak Ridge, Tennessee.
27. R. M. Gilgenbach et al., Phys. Rev. Lett. 44, 647 (1980).
28. C. P. Moeller, in *Proc. 4th Topical Conf. on RF Plasma Heating* (University of Texas, Austin, Texas, 1981), p. D1-1.
29. O. C. Eldridge, W. Nakano, and A. C. England, in *Proc. Joint Varenna-Grenoble International Symposium on Heating in Toroidal Plasmas* (1978), Vol. 1, p. 203.
30. R. M. Gilgenbach et al., Nucl. Fusion 21, 319 (1981).
31. A. G. Kulchar et al., in *Proc. IEEE 1981 Int. Conf. on Plasma Science* (IEEE, New York, 1981), p. 142.
32. S. K. Borowski, University of Michigan, private communication.
33. D. A. Sheppard, S. C. Prager, and J. C. Sprott, Bull. Am. Phys. Soc. 26, 1034 (1981); J. C. Sprott, University of Wisconsin, private communication.
34. J. Levine and M. Read, Naval Research Laboratory, private communication.
35. J. T. Mihalczo, "Neutron Measurements on ISX-B," p. 77 in *Fusion Energy Division Annual Progress Report for Period Ending December 31, 1980*, ORNL-5674, Oak Ridge, Tennessee.
36. S. D. Scott, doctoral dissertation, Massachusetts Institute of Technology, March 1982.
37. G. H. Neilson, *Charge Exchange Measurements of Ion Behavior in the ISX-B Tokamak*, ORNL/TM-7333, Oak Ridge, Tennessee (1980).
38. A. P. Navarro, V. K. Paré, and J. L. Dunlap, Rev. Sci. Instrum. 52, 1634 (1981).
39. S. C. Bates et al., *ISX-B Neutral Beamlines and the Beam Target Experiment*, ORNL/TM-7452, Oak Ridge, Tennessee (1980).

40. M. M. Menon et al., *PLT Neutral Beam Injection Systems*, ORNL/TM-6658, Oak Ridge, Tennessee (1979).
41. L. A. Berry et al., pp. 63-65 in *Fusion Energy Division Annual Progress Report for Period Ending December 31, 1977*, ORNL-5405, Oak Ridge, Tennessee.
42. H. C. McCurdy et al., pp. 29-32 in *Fusion Energy Division Annual Progress Report for Period Ending December 31, 1978*, ORNL-5549, Oak Ridge, Tennessee.
43. P. H. Edmonds et al., "ISX-B Neutral Ion Beam Lines and System Upgrade," pp. 52-54 in *Fusion Energy Division Annual Progress Report for Period Ending December 31, 1979*, ORNL-5645, Oak Ridge, Tennessee.
44. P. H. Edmonds, B. Sherrill, and J. W. Pearce, *Computer-Controlled Data Acquisition System for the ISX-B Neutral Injection System*, ORNL/TM-7282, Oak Ridge, Tennessee (March 1980).
45. P. C. Hanna, *Computer Control of the ISX-B Neutral Injection Beamlines*, ORNL/CSD/TM-177, Oak Ridge, Tennessee (1982).
46. S. C. Bates and P. C. Hanna, *Automation of the ISX-B Neutral Beams*, to be published as an ORNL/TM.
47. G. R. Dyer, in *Proc. 9th Symp. on Engineering Problems of Fusion Research* (IEEE, New York, 1981), pp. 1026-29.
48. S. Yoshikawa, Institute for Advanced Studies, and T. K. Chu, Princeton Plasma Physics Laboratory, private communication (1981).
49. T. K. Chu, H. P. Furth, J. L. Johnson, C. Ludescher, and K. E. Weimer, IEEE Trans. Plasma Sci. PS-9, 228 (1981).
50. A. H. Boozer, *Establishment of Magnetic Coordinates for a Given Magnetic Field*, PPPL-1775, Princeton Plasma Physics Laboratory, Princeton, New Jersey (1981).
51. H. R. Strauss, Plasma Phys. 22, 733 (1980).
52. R. Chodura and A. Schlüter, J. Comput. Phys. 41, 68 (1981).

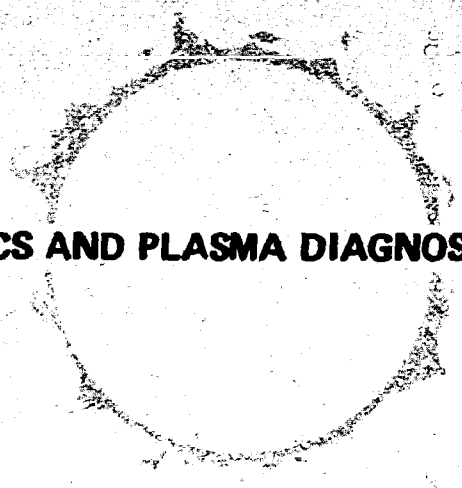

3. ATOMIC PHYSICS AND PLASMA DIAGNOSTIC DEVELOPMENT

D. H. Crandall,[1] Section Head

I. Alvarez[2]
C. F. Barnett[1]
D. S. Belic[3]
C. Bottcher[1]
C. Cisneros[2]
G. H. Dunn[3]
R. A. Falk[3]
H. B. Gilbody[4]
D. C. Gregory[1]
D. C. Griffin[5]
P. M. Griffin[1]
P. M. Hafford[6]
J. W. Hale[1]
T. G. Heil[7]
D. P. Hutchinson[1]
H. J. Kim[1]
M. I. Kirkpatrick[1]
C. H. Ma[1]
E. W. McDaniel[8]
R. H. McKnight[9]
F. W. Meyer[1]
T. J. Morgan[10]
F. M. Ormby[11]
R. A. Phaneuf[1]
M. S. Pindzola[12]
T. R. Price[13]
P. A. Staats[1]
D. M. Thomas[13]
E. W. Thomas[8]
K. L. Vander Sluis[1]

---

1. Physics Division.
2. Summer participant, Instituto de Fisica, Mexico.
3. Collaborator, Joint Institute for Laboratory Astrophysics, Boulder, Colorado.
4. Consultant, Queen's University, Belfast, Northern Ireland.
5. Consultant, Rollins College, Winter Park, Florida.
6. Information Division.
7. Collaborator, University of Georgia, Athens, Georgia.
8. Consultant, Georgia Institute of Technology, Atlanta, Georgia.
9. Consultant, National Bureau of Standards, Gaithersburg, Maryland.
10. Consultant, Wesleyan University, Middletown, Connecticut.
11. Section secretary.
12. Consultant, Auburn University, Auburn, Alabama.
13. Guest, University of Texas, Austin, Texas.

3. ATOMIC PHYSICS AND PLASMA DIAGNOSTIC DEVELOPMENT

ABSTRACT. The atomic physics and plasma diagnostic development activities are pursued within the Physics Division in support of the ORNL Fusion Program.

The diagnostic development work is closely associated with the Impurity Study Experiment (ISX-B) and with the ELMO Bumpy Torus-Scale (EBT-S). The atomic physics activities are pursued independently of fusion plasma devices but rely on low energy beams of ions, atoms, and electrons, as well as on significant computing facilities.

Current diagnostic development activities have concentrated on measuring the Faraday rotation of the polarization of far-infrared (FIR) laser radiation by plasma magnetic fields (and thus by plasma current). It is essential to measure the electron density along the same plasma chords simultaneously with the Faraday rotation observations. A 5-channel density interferometer/Faraday rotation diagnostic is being implemented on ISX-B, based on lasers, light transport, and light detection devices developed within this activity.

Other diagnostic activities include development of FIR lasers that can study electron density fluctuations at low frequencies in EBT-S and ISX-B. Also, the activity has had a long association with neutral particle analyzers. A recently constructed analyzer has been used to study the low energy (50- to 500-eV) H^0 flux to ISX-B walls — with and without neutral beams.

The experimental atomic physics activity relies on beams of multicharged ions (impurities); of H^0, H^+, and H^-; and of electrons that are employed in crossed-beam configurations and in beams passing through gas targets (including thermal H^0 ovens). Recent electron-ion beam experiments have demonstrated that ionization of impurity ions can be dominated by excitation-autoionization, which is not included in standard models of ionization. For example, measurements show that for Ti^{+3} the ionization cross section (and rate) is increased 10-fold by inner-shell excitation-autoionization near the ionization threshold. The theoretical studies within this activity are developing numerical, quantum calculations that predict these effects and can be employed to generate the large number of cross sections needed for ionization balance considerations in high temperature plasmas.

Another area of significant progress within the atomic physics activity is the study of collisional electron transfer from H^0 to impurity ions. Current experiments employing a laser-based ion source have extended measurements for C^{+q} and O^{+q} ($q = 3$-6) colliding with H^0 down to energies below 100 eV/amu and have found that the low energy cross sections do not follow any simple scaling rules. Again, the theoretical activity is developing numerical, quantum calculations that can predict most of the observed results. The experimental and theoretical results for carbon and oxygen ions are being employed within the Fusion Energy Division for modeling ion distribution and radiation in the plasma scrapeoff region where the low energy electron transfer has a dramatic influence.

The Controlled Fusion Atomic Data Center collects and recommends atomic data for fusion applications. The center publishes a bimonthly newsletter, maintains and publishes an extensive, categorized bibliography of atomic collisions, and produces tables of recommended atomic collision cross sections. A current compilation on electron impact excitation of iron ions recommends cross sections for about 1000 individual transitions that are important in plasma modeling and diagnostic observations. The recommended cross sections are selected from detailed quantum calculations, which are believed to be significantly more reliable than the Gaunt factor formula predictions generally used in plasma studies.

3.1 EXPERIMENTAL ATOMIC PHYSICS

3.1.1 Electron-Ion Collisions

D. C. Gregory, D. H. Crandall, R. A. Phaneuf, C. Cisneros, G. H. Dunn, R. A. Falk, D. S. Belic

Significant new results have been obtained at ORNL for both electron impact excitation and electron impact ionization cross sections during this report period through the collaborative efforts of ORNL and the Joint Institute for Laboratory Astrophysics (JILA), Boulder, Colorado.

The cross section for emission of 186-nm (3p → 3s) radiation from Al^{+2} after electron impact has been measured from threshold to 400 eV. These measurements include direct excitation of the 3p level and cascade from higher levels. In Fig. 3.1 the measured emission cross sections are compared with

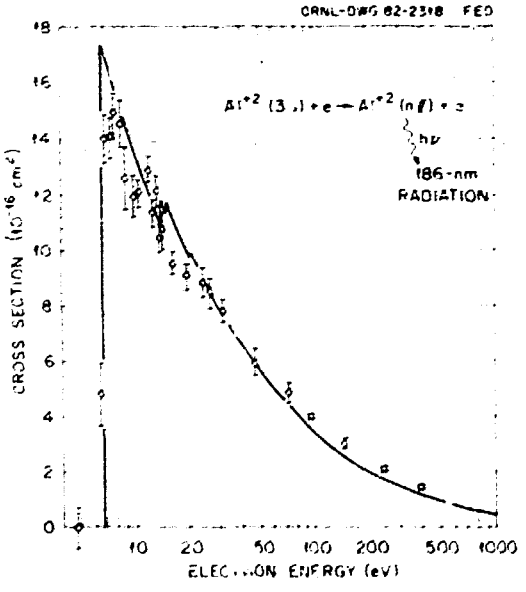

Fig. 3.1. Electron impact excitation of Al^{+2} producing 3p-3s radiation at 186 nm. Data points are present experimental measurements with 1 standard deviation of relative uncertainty. Solid curve is distorted-wave theory by Mann[1] with cascade population of 3p level included.

distorted-wave calculations by Mann,[1] which add direct and cascade excitations of the 3p level. The overall agreement between theory and experiment is quite good and is highly encouraging for application of this theory. The experimental data suggest an unresolved ($\Delta E \approx$ 2 eV experimental) resonance structure near 10-14 eV, which is not predicted by the theory in this case but has been predicted for the isoelectronic Mg^+ case in coupled state theory.[2] Experiments are ongoing at JILA for the Mg^+ case specifically to investigate the predicted resonances.

Measured cross sections for electron impact ionization have been obtained for eight different ions of +3 initial charge. The alkali-like ions Ti^{+3}, Zr^{+3}, Hf^{+3}, and Ta^{+3} all have ionization cross sections that are dominated (roughly by a factor of 10) by excitation of autoionizing levels.[3] This indirect ionization process is not included in most models of ionization but obviously cannot be neglected. The Zr^{+3} case is discussed in Sect. 3.2.1 and is typical of these metallic ions.

The cross sections for ionization of the rare gas ions Ne^{+3}, Ar^{+3}, Kr^{+3}, and Xe^{+3} were also measured. These cases all have ns^2np^3 outer electrons and were not expected to exhibit dominant indirect ionization effects such as excitation-autoionization. Indeed, for Ne^{+3} the Lotz formula fits the experimental data very well, but for Xe^{+3} it is in error by over a factor of 3 (Ref. 4) – presumably due to indirect ionization processes. Figure 3.2 shows the measured cross section for Kr^{+3} and compares the Lotz formula for this case. Near threshold the indirect processes contribute substantially beyond the direct ionization, while at higher energies Lotz overestimates the cross section (in spite of the fact that only one-half of the Lotz contribution by the $3d^{10}$ electrons is included). Table 3.1 gives the ionization rates obtained from the experiments and from the Lotz formula for various Maxwellian temperatures.

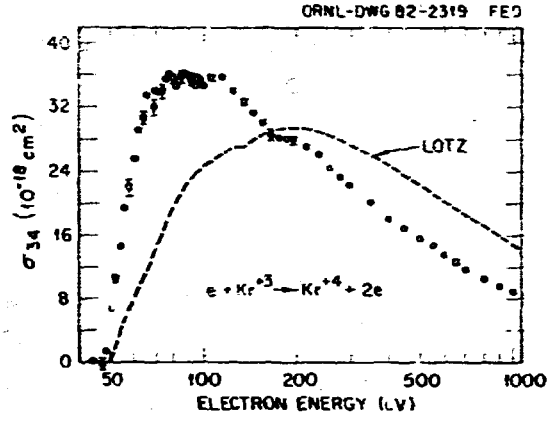

Fig. 3.2. Electron impact ionization of Kr^{+3}. Data points are present experimental measurements with 1-standard-deviation relative error bars (total absolute uncertainty is roughly ±6%). Dashed curve is Lotz formula with $4p^34s^2$ and $3d^{10}$ subshell contributions added, but with only one-half of the d-shell contribution included.

Table 3.1. Kr^{+3} ionization rates

Temperature		Rate (cm^3/s)	
(K)	(eV)	Experimental data	Lotz formula
0.1×10^6	8.6	0.03×10^{-9}	0.03×10^{-9}
0.2×10^6	17.2	1.61×10^{-9}	0.74×10^{-9}
0.4×10^6	34.5	6.85×10^{-9}	4.23×10^{-9}
0.6×10^6	51.7	10.88×10^{-9}	7.88×10^{-9}
1.0×10^6	86.2	15.40×10^{-9}	13.42×10^{-9}
2.0×10^6	172	18.89×10^{-9}	20.41×10^{-9}
4.0×10^6	345	19.09×10^{-9}	24.78×10^{-9}
6.0×10^6	517	18.64×10^{-9}	25.87×10^{-9}
1.0×10^7	862	17.40×10^{-9}	25.92×10^{-9}
2.0×10^7	1723	15.40×10^{-9}	24.28×10^{-9}
4.0×10^7	3447	13.30×10^{-9}	21.51×10^{-9}

3.1.2 Capture to Excited States

P. W. Meyer, P. M. Griffin

We have measured the relative cross section for light emission at 1548 ± 8 Å from the unresolved $(2p)^2P_{1/2,3/2}$ states of the C^{+3} ion formed during electron capture collisions of C^{+4} with helium in the energy range 24-80 keV/amu. These measurements were performed to test the feasibility of optical study in the vacuum ultraviolet (VUV) region of electronic transitions in typical multicharged ions produced by the ORNL-PIG ion source and, at the same time, to check predictions made by existing theoretical calculations[5] of the $(C + He)^{+4}$ quasi-molecular system. The apparatus used in this experiment included an f/4.5 McPherson 234 VUV monochromator together with an EMR 541G photomultiplier to select and detect photons of the desired wavelength. The relative cross section for emission from the $C^{+3}(2p)^2P$ product ion, shown in Fig. 3.3, was found to have approximately the same energy dependence as the total electron transfer cross section, roughly doubling in magnitude over the measured interval as the energy increases. At 64 keV/amu the relative emission cross section was investigated for H_2 and Xe targets as well as helium. Emission from the ^2P states was found to increase by factors of ~4 and ~6 when the C^{+4} collision partner was changed from He to H_2 and Xe, respectively, while the measured total electron

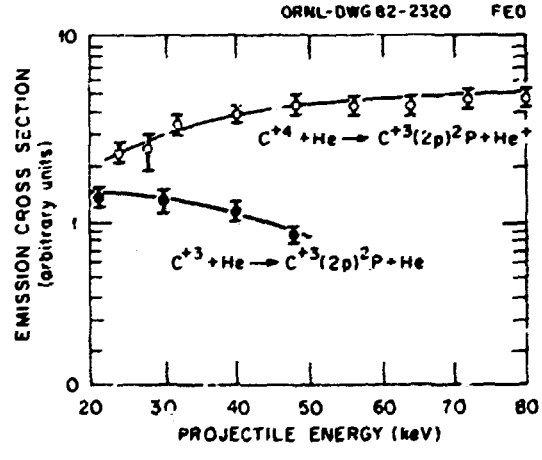

Fig. 3.3. The relative cross section for light emission from C^{+3} $(2p)^2P$ populated by electron transfer from He target atoms to C^{+4} projectiles as a function of projectile energy. Shown also for comparison is the relative emission cross section for the direct excitation reaction C^{+3} + He → $C^{+3}(2p)^2P$.

capture cross sections increased by factors of ~5 and ~8. The higher emission cross sections obtained for H_2 and Xe targets permitted a higher resolution study in which the C^{+3} $(2p)^2P_{1/2,3/2}$ doublet could be partially resolved. For both H_2 and Xe targets it was found that the $^2P_{3/2}$ and $^2P_{1/2}$ states were populated roughly in the ratio of their statistical weights.

Preliminary calibration of the VUV spectrometer by normalization to previously measured absolute cross sections for photon emission at 1075, 1100, 1216, 1493, and 1743 A indicates that, in the measured energy range, the total electron capture cross section is dominated by capture to the $C^{+3}(2p)$ state, confirming coupled-state theoretical calculations for C^{+4} + H. A more definitive calibration in the wavelength range 1100-1800 A, using the Lyman bands of H_2 excited by ArI resonance light at 1066 A, is currently under way.

3.1.3 Low Energy Electron Capture

R. A. Phaneuf, I. Alvarez

Unlike the situation at higher collision energies, electron capture cross sections for highly stripped ions colliding with hydrogen atoms at energies below a few kilo electron volts per atomic mass unit neither scale simply with ionic charge nor exhibit uniform velocity dependences.[6] During such collisions, the electrons in the system have sufficient time to adjust to the slowly varying interatomic field, and a quasi-molecular theoretical description of the collision becomes necessary. In order to evaluate developing theoretical methods, experimental data are needed on simple, few-electron systems involving highly charged ions.

The ORNL pulsed laser ion source and time-of-flight collision apparatus[6,7] have been used to measure total cross sections for electron capture for O^{+q} + H and O^{+q} + H_2 collisions (q = 3-6) at energies ranging from 42 to 726 eV/amu. The O^{+q} ions were produced by bombarding a ThO_2 target in vacuum with intense pulses of CO_2 laser radiation. Ions of selected energy and charge were directed through a calibrated atomic or molecular hydrogen gas target.

Figure 3.4 compares the present measurements with other data[8] and with theory[9,10] for O^{+6} + H and O^{+5} + H collisions. The cross sections are of comparable magnitude and are independent of velocity in the range 300 eV/amu < E < 5000 eV/amu. At decreasing energy, however, the O^{+5} cross section rises abruptly, while the O^{+6} cross section decreases slowly. The theoretical curves are consistent with the qualitative behavior of the cross sections but do not agree in quantitative detail.

Similar measurements are planned for Fe^{+q} + H and Fe^{+q} + H_2 collisions. Also

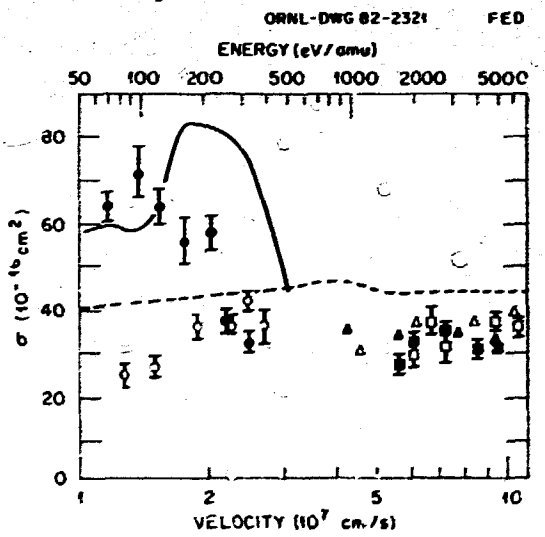

Fig. 3.4. Total electron capture cross sections for O^{+5} + H (solid points and solid curve) and O^{+6} + H (open points and dashed curve). Circles are present data using laser source, and squares and triangles are published and unpublished data of Crandall, Phaneuf, and Meyer[8] using the ORNL-PIG ion source. Solid curve is calculation of Shipsey, Browne, and Olson,[9] and dashed curve is preliminary calculation of Bottcher and Heil.[10] Error flags on data represent reproducibility at 1 standard deviation and are indicative of relative uncertainty. Total systematic uncertainties at good confidence level are estimated to be ±22%.

currently under development is an ion-atom merged-beams experiment, which will facilitate a more precise study of such electron capture collision processes down to energies as low as 1 eV/amu. At these energies, orbiting of the reactants is predicted theoretically in some systems[10] and can result in extremely large electron capture cross sections.

3.2 ATOMIC THEORY FOR FUSION

The atomic theory activity is directed at providing cross sections for collisions involving impurity ions with electrons and hydrogen atoms at collision velocities typical of fusion plasma systems. Current emphasis is on identifying the most reliable theoretical techniques that can still be reasonably applied to calculate the many results needed in plasma modeling and diagnostic interpretation. Electron impact excitation, and particularly excitation-autoionization, has been studied during this report period, with a number of test calculations being compared with experiment. Electron transfer (charge exchange) between C and O ions and H^0 has also been studied with emphasis on energies below 1 keV/amu, characteristic of the plasma scrape-off region where thermal ions of light impurities and atomic hydrogen may coexist.

3.2.1 Electron Impact Excitation and Ionization of Ions

C. Bottcher, D. C. Griffin, M. S. Pindzola

Inner-shell excitation followed by autoionization has been established as an important mechanism influencing total ionization (see Refs. 3, 11, and 12 and citations therein). Experiments, which have been sparse for direct excitation, can study excitation via the excitation-autoionization process. We are developing theoretical approaches for quantal calculations of the relevant excitation cross sections to provide improved ionization cross sections (and rates) and to test excitation theory against experimental measurements. We have been studying transitions of the form $np^6nd^m \rightarrow np^5nd^{m+1}$, which are typically strong dipole allowed transitions with $\Delta n = 0$ but nevertheless often occur at energies just above the ionization threshold. Figure 3.5 shows theoretical and experimental ionization cross sections near threshold for Zr^{+3}. The results are nearly 20 times the usual Lotz prediction at 42 eV due to the excitation

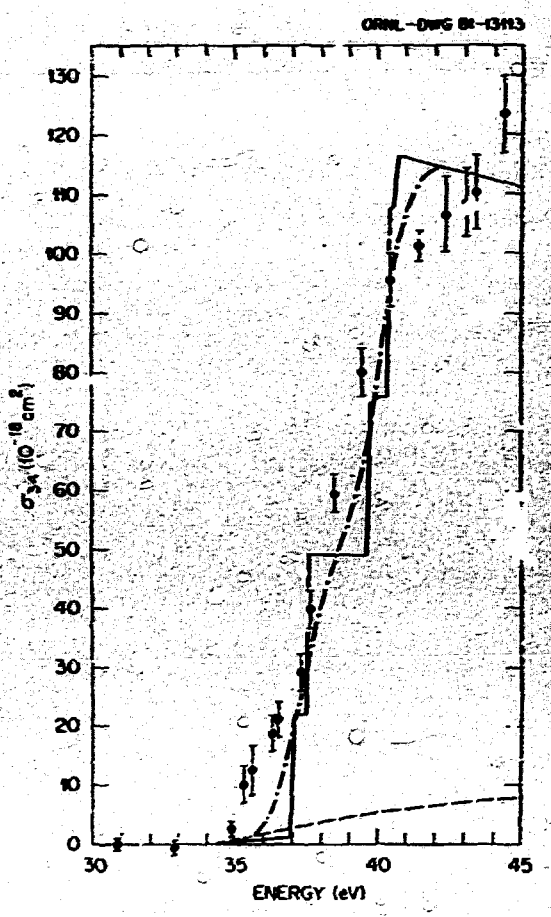

Fig. 3.5. Electron impact ionization of Zr^{+3} near threshold. Dashed curve is Lotz prediction of direct ionization; solid curve includes indirect ionization via excitation-autoionization predicted by distorted-wave theory divided by 2.5; dot-dashed curve is the solid curve convoluted with 2-eV energy spread, typical of the experimental results; solid points are experimental measurements (see Sect. 3.1.1).

contribution from $4p^64d \rightarrow 4p^54d^2$ transitions. The theoretical excitation predictions have been divided by 2.5 to normalize to the experimental results. Thus, while the agreement in shape of the cross section and energy positions of excitation contributions is excellent, the magnitude of the predictions is not satisfactory. A distorted-wave treatment employing dipole-only transition terms and without inclusion of exchange was used for these theoretical results (also for Ti^{+3} and Hf^{+3}, with similar comparison to experiment). Inclusion of exchange, unitarization, and nondipole terms will decrease the excitation cross sections (as it did for sodiumlike ions[11]) but must be tested for these cases and represents a significant increase in the complexity of the calculations.

A further example from the present studies illustrates subtle atomic physics effects that can arise through mechanisms such as excitation-autoionization (see Fig. 3.6). For Fe^{+4} the ground configuration is $3p^63d^4$ with a number of fine-structure, metastable levels of the same configuration within a few electron volts of the lowest ^5D level. If the internal temperature of the Fe^{+4} ions is sufficiently low (about 0.1 eV) only the ground state will be populated, but for higher internal temperatures a number of the metastable levels of the ground $3p^63d^4$ configuration are also populated. Of the 214 levels of $3p^53d^5$ that can be accessed by $\Delta n = 0$, $p \rightarrow d$ excitation transitions, only 22 levels have enough energy to autoionize and none of these has strong transitions coupling it to the (lowest) ground state. However, if the metastable levels of ground configuration are populated, then strong transitions to some of the 22 levels of $3p^53d^5$ are possible. Figure 3.6 shows the predicted ionization cross section within the dipole-only, distorted-wave theory for three internal ion temperatures. For temperatures above 5 eV the cross section does not change significantly. The excitation-autoionization contribution is probably overestimated by the theory, and inclusion of nondipole terms would modify the temperature dependence somewhat, but it is likely that internal ion temperature (initial quantum-state distribution) does influence the Fe^{+4} ionization cross section significantly. For a near-equilibrium plasma, the Fe^{+4} ions would usually have more than 5 eV of internal energy, but this might not always be true.

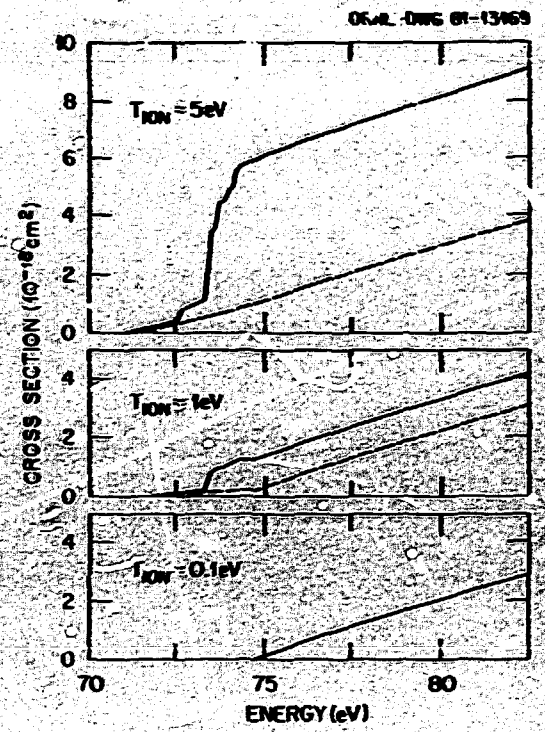

Fig. 3.6. Electron impact ionization of Fe^{+4} near threshold for three different internal temperatures of the ion, which result in differing populations of ground levels. Dashed curves are Lotz prediction of direct ionization, while solid curves have indirect ionization, via excitation-autoionization calculated in distorted-wave theory, added to the Lotz prediction.

The intent of the present theoretical efforts is to properly include some of these subtle effects in the calculational approaches and then to generate the more reliable ionization cross sections that are needed to model and interpret plasma effects.

3.2.2 Electron Capture Theory

C. Bottcher, T. G. Heil

Cross sections are being calculated for electron capture by C^{+q} and O^{+q} ions in hydrogen and will be extended to Fe^{+q} ions. These charge exchange cross sections at low velocity for impurity ions and atomic hydrogen do not obey simple scaling rules. Current experimental (see Sect. 3.1) and theoretical[13] results for C and O ions demonstrate the failure of scaling rules and simple potential curve crossing estimates. For collision energies below 200 eV/amu (velocity of 2×10^7 cm/s) the collision should be treated in a fully quantal, molecular representation. For energies between 200 eV/amu and 20 keV/amu ($2\text{-}20 \times 10^7$ cm/s) the nuclear motion can be described classically, but the fate of the electron during a collision is still controlled by transitions between the adiabatic states of the quasi-molecule.

Calculations for +5 ions of B, C, and O are shown in Fig. 3.7. Striking features of these results are the orbiting behavior of the cross sections at very low energies and their extreme sensitivity to the electronic structure of the projectile. We are able to study isoionic sequences with great facility using our "screened potential method," in which the wave function of the active electron is expanded in base nucleus wave functions and the effect of any inner electrons is relegated to a "screened potential." The physics of Fig. 3.7 is entirely explained by considering three molecular states, $5g\sigma$, $4f\sigma$, and $4d\sigma$: the $5g\sigma$ is the initial $X^{+5} + H(1s)$ channel, while $4f\sigma$ and $4d\sigma$ are final X^{+5} $(n = 4) + H^+$ channels. The electronic energies of these states are plotted in Fig. 3.8: $5g\sigma$ crosses both $4f\sigma$ and $4d\sigma$ around R = 13a. However, the latter crossing is not associated with any significant coupling in the bare nucleus (BH^{+5}) case. The $4d\sigma$ channel only enters when the screened potential is introduced: the couplings are shown to scale for CH^{+5} and OH^{+5}. This subtle effect is the sole cause of the dramatic increase in the cross sections around 100 eV.

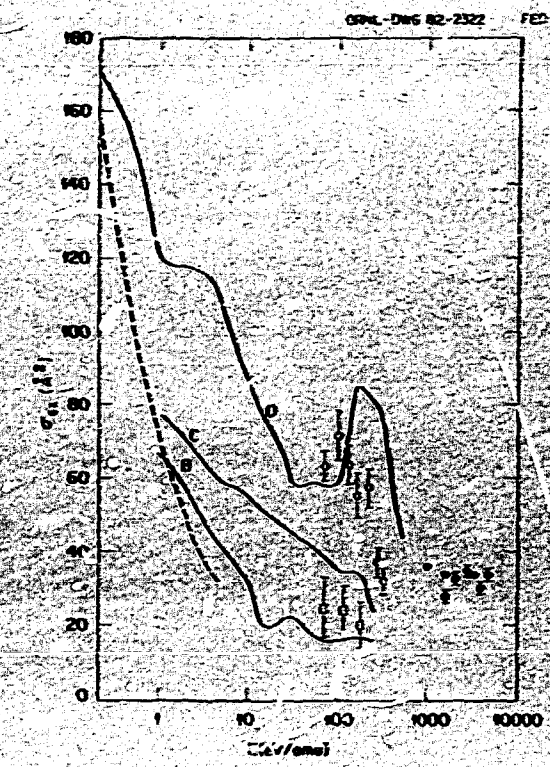

Fig. 3.7. Charge exchange cross sections for ions of charge +5 colliding with H(1s). Key: solid lines, theoretical cross sections for ions of B, C, and O; dashed line, Langevin orbiting cross section; open circles, data of Phaneuf on O; open squares, data of Phaneuf on C; closed circles, ORNL-PIG measurements on O.

Work is in progress on a vectorized version of our close-coupling program, which should open the way to calculations with many more channels.

3.3 CONTROLLED FUSION ATOMIC DATA CENTER

D. E. Crandall, C. F. Barnett, R. B. Gilbody, D. C. Gregory, P. M. Hafford, M. I. Kirkpatrick, E. W. McDaniel, J. H. McKnight, J. W. Meyer, T. J. Morgan, P. M. Ownby, R. A. Phaneuf, M. S. Pindzola, E. W. Thomas

The data center categorizes all publications on atomic collisions and compiles and evaluates atomic data for fusion. The most time-consuming part of the work has been the bibliographical categorization, in which about 3000 entries per year are selected from the total literature

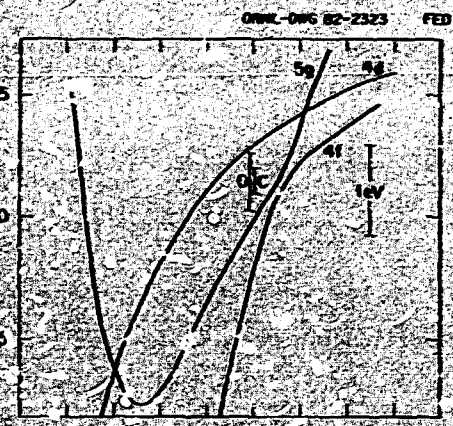

Fig. 3.8. Electronic energies of the 5gσ, 4fσ, and 4dσ states of BH^{+} as functions of internuclear separation. The vertical scale is in hartrees, but an interval of 1 eV is indicated to the right for convenient reference. Vertical bars represent to scale the screened potential coupling between 5gσ and 4dσ for carbon and oxygen (as labeled).

and divided into one or more of 114 process categories within ten areas of collision studies. Author, title, reactants, energy, and category are specified in computer file entries, which can be sorted according to any of the input data.

In addition to their use in ORNL programs, these bibliographies are used by the International Atomic Energy Agency (IAEA) and Japanese data centers, as well as by individual scientists. Copies of the bibliography are published and disseminated throughout the United States and abroad (available through the National Technical Information Service). During this report period, the 1980 bibliography has been published[14] and 1981 entries have nearly been completed.

In a cooperative effort with the Atomic Transition Probabilities Data Center of the National Bureau of Standards (NBS), we have continued publication of the bimonthly newsletter *Atomic Data for Fusion*. The IAEA is also publishing a similar bulletin, which covers bibliographical citations of atomic data. In order to avoid duplication we are helping to supply bibliographic information to the IAEA, and at the same time the ORNL-NBS newsletter is shifting its emphasis toward publication of actual numerical data of current interest for fusion. During this report period we have published an author and subject index for the 1980 newsletter (Vol. 6) and newsletter editions through Vol. 7, No. 4 for 1981.

We are planning a third volume of cross sections and rates for fusion impurity ions. To this end we have completed and published a compilation of electron impact excitation cross sections for iron ions,[15] where data have been selected from the many calculations as the best available values, although they cannot be evaluated in the usual critical sense because no experimental data are available. A compilation of atomic data for oxygen ions covering electron impact excitation and electron capture from hydrogen is in progress as a joint endeavor with the Japanese data center at the Institute of Plasma Physics at Nagoya University.

In December 1981, data center staff participated in a U.S.-Japan Surface Data Review Workshop in Nagoya, Japan. The workshop reviewed the status of particle-surface data relevant to plasma-wall interactions in magnetic fusion and recommended specific studies for the data centers to pursue. A full report of the workshop will be published in 1982.

3.4 PLASMA DIAGNOSTICS

3.4.1 FIR Lasers and Faraday Rotation

D. P. Hutchinson, C. H. Ma, K. L. Vander Sluis, P. A. Staats, T. R. Price

During the past year, we have made several modifications to the ISX-B submillimeter (SMM) wave interferometer[16] to improve the measurement capabilities of the diagnostic. These modifications include: (1) replacement of the

helium-cooled Putley detectors with room temperature Schottky diodes, (2) higher power CO_2 pump lasers (P > 70 W), (3) a CAMAC-based data collection system, (4) the development of an Abel inversion routine to calculate the electron density profile, and (5) a higher frequency Faraday modulator. The Schottky diode detectors, fabricated by the Massachusetts Institute of Technology (MIT) Lincoln Laboratory, are GaAs diodes with a 4λ antenna mounted in a corner cube reflector to concentrate the SMM wave radiation onto the antenna. An f/1 lens is used to focus the radiation emerging from the dielectric waveguide onto the detector. To minimize noise pickup during tokamak discharges, the focusing optics, diode, bias circuit, and first detector amplifier are mounted in a single-shielded enclosure.

The power level of the CO_2 pump lasers has been increased from 30-40 W to approximately 70-80 W by using a new, larger bore, longer, split electrode discharge tube. The increased volume is responsible for the higher power; the split electrode design was used to minimize the high voltage (~15 kV) required to energize the tubes. The mode structure of the CO_2 lasers is controlled by an aperture consisting of a spiral of 0.508-mm (20-mil) wire placed near one end of the laser tube. The spiral aperture prevents off-axis, higher order modes from oscillating. To improve the overall stability of the lasers, the entire system of two CO_2 lasers and two SMM wave lasers has been packaged into a single Invar-stabilized structure.

With the expansion of the interferometer system to five simultaneous channels, a new dedicated data acquisition system has been developed. The data system uses two 8-channel transient recorders operating at a 10-kHz sampling rate. With the memory modules included in the transient recorders, 4096 samples for each channel of density and Faraday rotation data may be recorded. This memory capability is sufficient to record the plasma data for each shot and baselines for at least 50 ms before and after the discharge.

A data analysis code has been developed to reconstruct the asymmetric distribution of the plasma density. A modified Abel inversion technique[17] is employed in the numerical computation. The plasma is assumed to be symmetrical in the z direction (the courdinate parallel to a line passing through the center of the major axis of the tokamak) but may be radially asymmetrical. The spatial profile of the line density is also assumed to be sufficiently smooth to be represented by a fourth-degree polynomial. The code has been employed to analyze the measured line density on ISX-B. In Fig. 3.9, the result of a typical plasma shot is compared with the density profile calculated by a data analysis code (ZORNOC) developed by the ISX-B tokamak group. The code is based on Thomson scattering measurements and is consistent with magnetohydrodynamic (MHD) equilibrium.[18] It can be seen that the two curves appear to be in surprisingly good agreement, considering the approximate nature of the calculation.

A high frequency magneto-optic modulator has been developed for the Faraday rotation experiment. The ferrite modulator originally developed for the Faraday experiment was limited to very low modulation frequencies (4-10 kHz) and was quite lossy (transmission ≈ 30%) at the polarimeter wavelength of 0.393 mm.

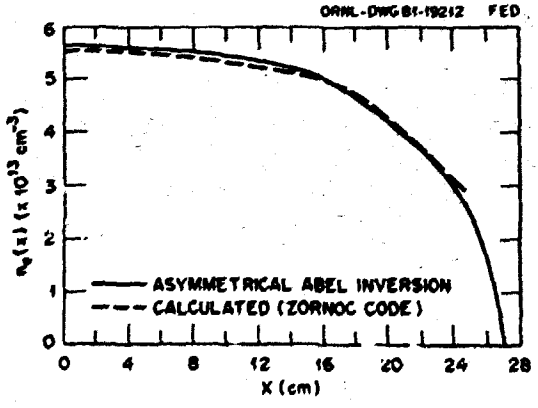

Fig. 3.9. Comparison of the Abel-inverted density profile and the result calculated by the ZORNOC code.

A novel design has led to the construction of a ferrite modulator that has been tested at 125 kHz and exhibits a transmission greater than 50%. A photograph of the modulator is shown in Fig. 3.10. Rather than construct a multiturn coil with high stray capacitance as in our first design, a single turn coil was built to drive the ferrite. This turn was threaded through three iron powder toroidal cores wound with 70 turns each. The cores are wired in series. A 4:1 impedance transformer connects the primary windings to a power amplifier. The primary windings are also in series with a 0.01-μF capacitor to resonate the transformer at 125 kHz. With a rf power of 500 W, we have generated magnetic fields of 0.6-1 kG oscillating at approximately 125 kHz. All of these improved components should be integrated into the ISX-B interferometer system in the spring of 1982.

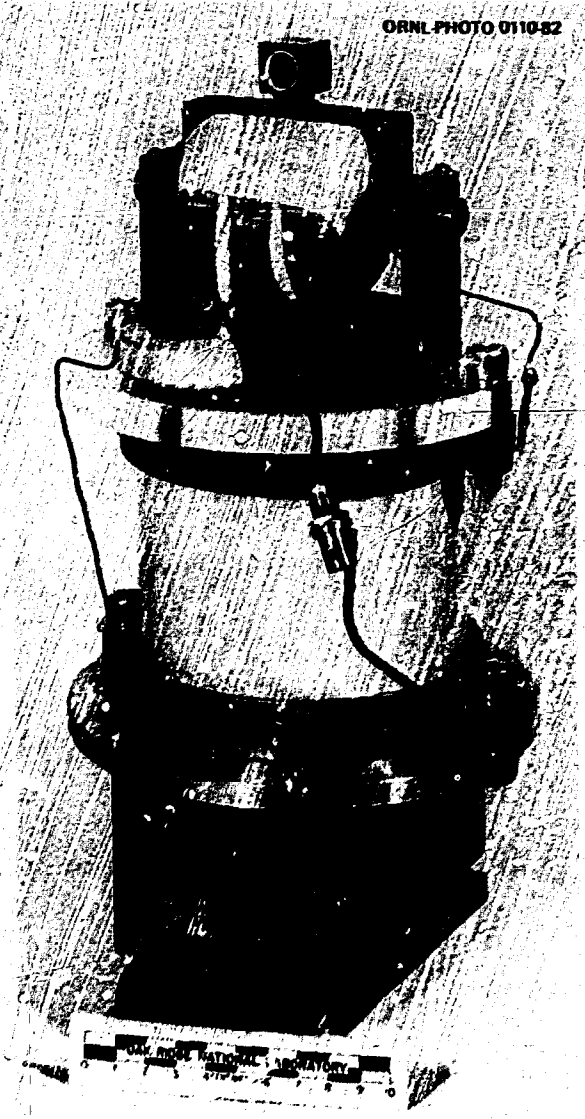

Fig. 3.10. Ferrite modulator.

3.4.2 Low Energy Neutral Particle Spectrometer

D. M. Thomas

A spectrometer capable of observing low energy neutral particles has been designed and installed on ISX-B and has been used to examine the D^0 emission in the range 35-700 eV for a variety of discharge conditions.

A schematic of the diagnostic is shown in Fig. 3.11. After emerging from the tokamak, the neutral particle flux is collimated and enters a cesium vapor cell. A certain fraction of the particles undergo electron capture collisions with the cesium and are converted to negative ions. The conversion efficiency in this energy range is much higher than that of a conventional stripping cell.[19] To spatially confine the cesium vapor and minimize contamination, the charge exchange cell is designed along the lines of a heat pipe.[20] The resulting D^- flux is then energy-analyzed using a 4-channel, high resolution, parabolic electrostatic analyzer that has been optimized for very low energies.

Before installation on ISX-B, the spectrometer was absolutely calibrated in the energy range of interest by using a known monoenergetic D^0 beam from a low energy accelerator, yielding conversion efficiency curves for each channel. For the given viewing geometry and sampling rate ($dA\,d\Omega \approx 2 \times 10^{-2}$ cm^2-sr), one can use these curves to calculate the absolute differential flux, dJ/dE, as a function of energy.

The location of the spectrometer relative to the machine is shown in Fig. 3.12. The

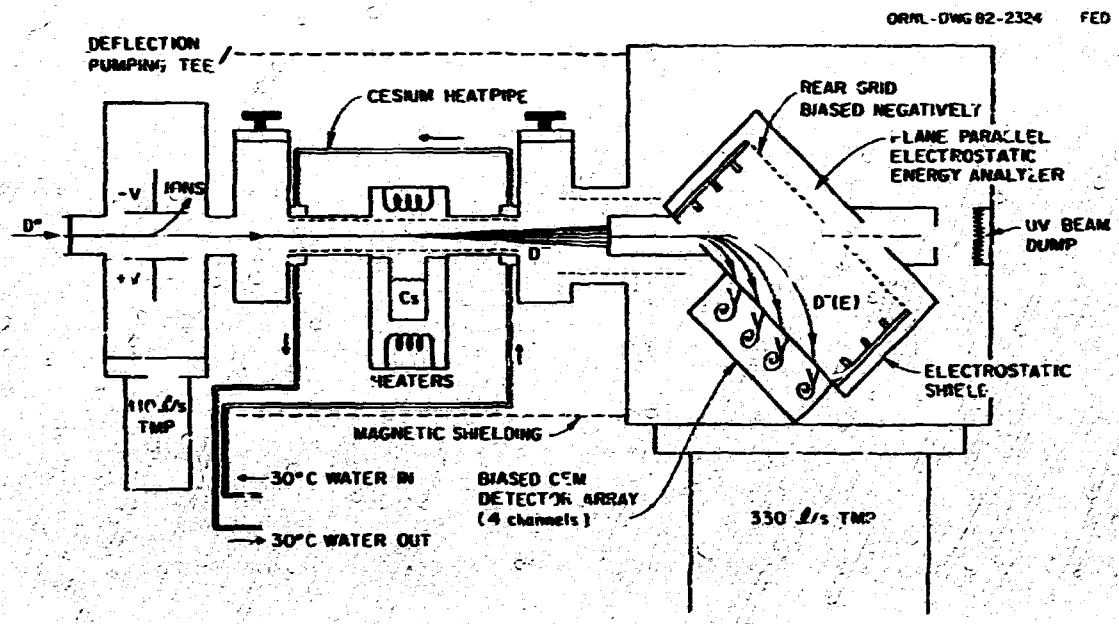

Fig. 3.11. Low energy neutral particle spectrometer as installed on ISX-B.

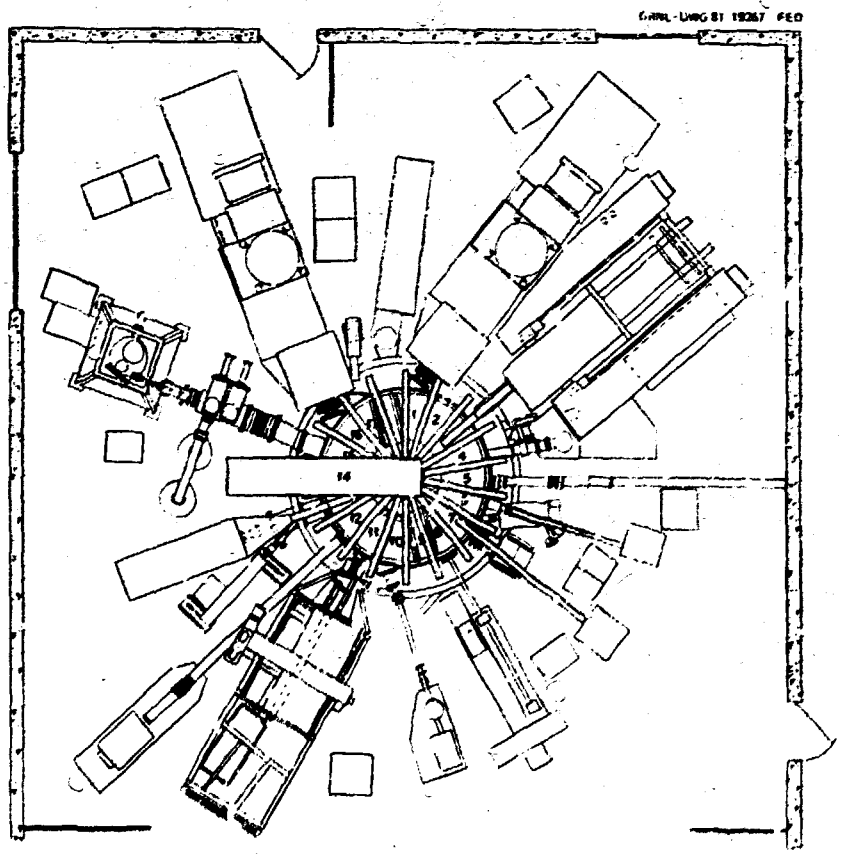

Fig. 3.12. Overhead plan of ISX-B showing location of spectrometer. Limiter is located in sector 14.

flux sampled is emerging in the midplane at an angle of 35° from the normal. Toroidal angles from the limiter, west beam line, and east beam line are 80°, 120°, and 180°, respectively.

Although data reduction is still being performed, the qualitative behavior of the sampled flux may be summarized as follows.

The effect of injecting megawatt levels of neutral beams into typical ohmically heated plasmas is to enhance the particle emission in the range 50-700 eV by between two and five times the existing levels prior to beam turnon. A trickle-down effect may be seen in the rate of increase for different energy settings, with the higher energy channels showing a more rapid increase. There is essentially no difference in the fluxes measured for west beam injection as opposed to east beam, despite the fact that from the viewing geometry the west beam is injecting within 3° of the line of sight of the diagnostic. For staggered injection by both beams, there is very little enhancement of the low energy flux when the second beam starts.

By averaging over several shots while varying the tuning energy, the flux spectrum over the entire instrumental range may be acquired and displayed as a function of time. Since we expect the lower energies to be characteristic of the edge plasma region, as opposed to a chord-averaged sample typical of higher energy charge exchange measurements, we may interpret an effective edge temperature from the logarithmic derivative of the flux. The viewing angle complicates the analysis but mitigates the effects of trapped particles on the measured spectrum. Figure 3.13 shows absolute flux levels versus energy after neutral beam injection and for corresponding ohmically heated discharges.

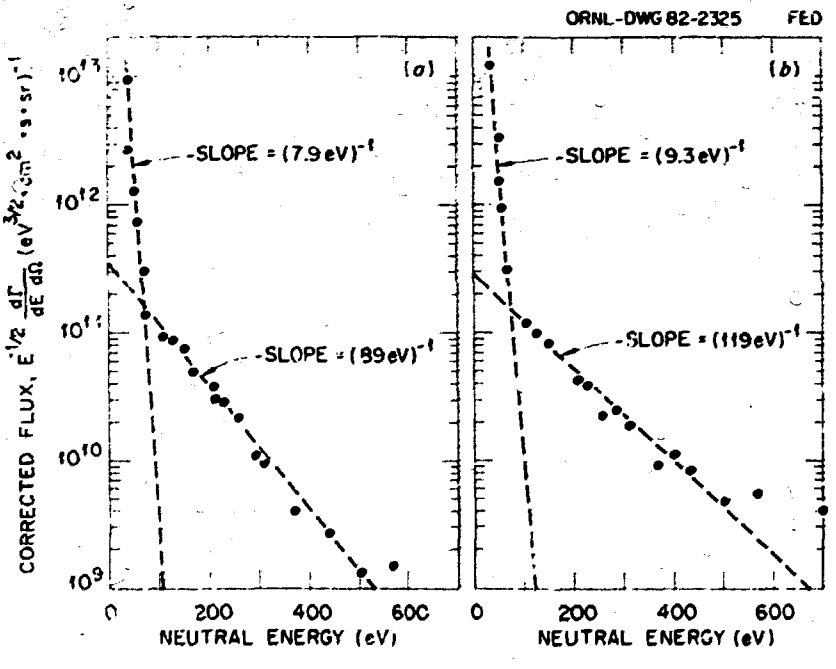

Fig. 3.13. Corrected absolute flux levels during density clamp experiment on ISX-C, with B_T = 12.2 kG, I_p = 150 kA, n_e = 2 × 10^{13} cm^{-3}, and a circular cross section. (a) Flux at 250 ms into discharge. (b) Flux at 250 ms with 0.1 MW of neutral beam injection starting at 120 ms. Both sets of data are well represented by two straight lines consistent with two distinct temperature components of low energy flux.

The spectrometer will be recalibrated using an improved low energy neutral source to verify the calibration and to test the long-term usefulness of this type of diagnostic.

REFERENCES

1. J. B. Mann, Los Alamos National Laboratory, private communication (1981).
2. C. Mendoza, J. Phys. B 14, 2465 (1981).
3. R. A. Falk, G. H. Dunn, D. C. Griffin, C. Bottcher, D. C. Gregory, D. H. Crandall, and M. S. Pindzola, Phys. Rev. Lett. 47, 494 (1981).
4. D. C. Gregory, P. F. Dittner, and D. H. Crandall, *12th Int. Conf. on Physics of Electronic and Atomic Collisions, Abstracts of Contributed Papers* (1981), p. 465.
5. E. J. Shipsey, J. C. Browne, and R. E. Olson, Phys. Rev. A 15, 2166 (1977).
6. R. A. Phaneuf, Phys. Rev. A 24, 1138 (1981).
7. R. A. Phaneuf, IEEE Trans. Nucl. Sci. NS-28, 1182 (1981).
8. D. H. Crandall, R. A. Phaneuf, and F. W. Meyer, Phys. Rev. A 19, 504 (1979); unpublished (1979).
9. E. J. Shipsey, J. C. Browne, and R. E. Olson, J. Phys. B 14, 869 (1981).
10. C. Bottcher, ORNL, and T. G. Heil, University of Georgia, private communication (1981).
11. D. C. Griffin, C. Bottcher, and M. S. Pindzola, Phys. Rev. A 25, 154 (1982).
12. D. C. Griffin, C. Bottcher, and M. S. Pindzola, "Theoretical Calculations of the Contributions of Excitation-Autoionization to Electron Impact Ionization in Ions of the Transition Series of Elements," to be published in Physical Review A.
13. T. G. Heil, S. Butenstock, C. Bottcher, and A. Dalgarno, "Charge Transfer of C^{+3} Ions in Atomic Hydrogen," to be published in Physical Review A.
14. C. F. Barnett, D. H. Crandall, B. J. Farmer, H. B. Gilbody, D. C. Gregory, P. M. Hafford, M. I. Kirkpatrick, E. W. McDaniel, R. H. McKnight, F. W. Meyer, T. J. Morgan, R. A. Phaneuf, M. S. Pindzola, and E. W. Thomas, *1980 Bibliography of Atomic and Molecular Process*, DOE/ER-0118, U.S. Department of Energy, U.S. Government Printing Office, Washington, D.C. (1981).
15. M. S. Pindzola and D. H. Crandall, *A Compilation of Theoretical Electron Impact Excitation Cross Sections for Fe Atomic Ions*, ORNL/TM-7957, Oak Ridge, Tennessee (1981).
16. D. P. Hutchinson, C. H. Ma, P. A. Staats, and K. L. Vander Sluis, Nucl. Fusion 21, 1535 (1981).
17. Y. Yasutamo, K. Migata, S. I. Himeno, T. Enoto, and Y. Ozawa, IEEE Trans. Plasma Sci. PS-9, 18 (1981).
18. B. Zurro, K. Wieland, M. Murakami, and D. W. Swain, *ZORNOC: A 1-1/2-D Tokamak Data Analysis Code for Studying Non-Circular High Beta Plasmas*, ORNL/TM-7146, Oak Ridge, Tennessee (1980).
19. D. Brisson, F. W. Baity, B. H. Quon, J. A. Ray, and C. F. Barnett, Rev. Sci. Instrum. 51, 132 (1980).
20. M. Bacal, A. Truc, H. J. Doucet, H. Laman, and M. Chrétien, Nucl. Instrum. Methods, 114, 407 (1973).

4. PLASMA THEORY

R. A. Dory, Section Head

C. L. Hedrick, Jr., Associate Section Head

D. J. Sigmar,[1] Associate Section Head

D. E. Arnurius[2]
S. E. Attenberger[2]
D. B. Batchelor
C. O. Beasley, Jr.
J. D. Bell[2]
E. T. Blair[2]
S. K. Borowski[3]
T. Breazeale[4]
R. D. Burris[2]
J. D. Callen[5]
B. A. Carreras
L. A. Charlton[2]
G. L. Chen
D. N. Clark[2]
W. A. Cooper
E. C. Crume, Jr.
L. E. Deleanu[2]
P. H. Diamond[6]
W. B. Downum
A. M. El-Nadi[7]
R. H. Fowler[2]
J. E. Francis, Jr.
P. W. Gaffney[2]
L. Garcia[8]
R. C. Goldfinger[2]
M. R. Gordinier[2]
D. E. Greenwood[2]
S. L. Hall[2]
C. E. Hammons
D. E. Hastings
H. R. Hicks[2]
S. P. Hirshman
J. T. Hogan
J. A. Holmes[2]
W. A. Houlberg
H. C. Howe
E. F. Jaeger
C. O Kemper[2]
H. E. Ketterer
L. L. Lao[9]
D. K. Lee[2]
V. E. Lynch[2]
S. R. Maddox[2]
G. S. Massengill
H. K. Meier[10]
K. Molvig[11]
J. K. Munro, Jr.[2]
C. W. Nestor, Jr.[2]
D. R. Overbey
L. W. Owen[2]
J. R. Reagan[2]
J. A. Rome
K. E. Rothe[2]
D. S. Scott[2]
J. Smith[12]
D. A. Spong
C. R. Stewart, Jr.
K. A. Stewart
D. J. Strickler[2]
J. S. Tolliver[2]
K. T. Tsang[13]
N. A. Uckan
W. I. van Rij[2]
H. Weitzner[14]
J. C. Whitson[2]
R. M. Wieland[2]
K. G. Young

---

1. Also adjunct professor of nuclear engineering, Massachusetts Institute of Technology, Cambridge, Massachusetts.
2. UCC-ND Computer Sciences.
3. Student, University of Michigan, Ann Arbor, Michigan.
4. Y-12 Maintenance Division.
5. Consultant, University of Wisconsin, Madison, Wisconsin.
6. Institute for Fusion Studies, University of Texas, Austin, Texas.
7. University of Cairo, Cairo, Egypt.
8. University of Madrid, Madrid, Spain.
9. Now at TRW, Inc., Redondo Beach, California.
10. Now with UCC-ND Computer Sciences.
11. Consultant, Massachusetts Institute of Technology, Cambridge, Massachusetts.
12. Consultant, the University of Tennessee, Knoxville, Tennessee.
13. Now at Science Applications, Inc., Boulder, Colorado.
14. Consultant, Courant Institute of Mathematical Sciences, New York University, New York, New York.

4. PLASMA THEORY

ABSTRACT. The long-standing Theory Section areas, ELMO Bumpy Torus (EBT) Analysis, Tokamak Analysis, and Computing Supoort, were augmented by the formation of a study group for assessing confinement in stellarators and torsatrons. Highlights of the year's activities are as follows.

EBT Theory. Following completion of the EBT Proof-of-Principle (EBT-P) proposal exercises, emphasis has returned to advancing the state of understanding of the EBT-Scale (EBT-S) plasma and improving the broad range of subsystem models. Examples include studies of ion cyclotron resonance heating (ICRH), the sensitivity of the operating point to the ambipolar potential model, the confinement of particles with large gyroradius, aluminum impurity transport, and a survey of the sensitivity of linear microstability theory to simplifying assumptions. Reliability remains an issue for the threshold predictions for ring, core, and mutual instabilities. Core beta values of 10-20% have been estimated, with credit not yet taken for finite Larmor radius effects and axial mode structure. Coupled with this, ring beta values of >20% are needed, and the ratio of core density to ring density must exceed a minimum value. For reactors, this value is uncomfortably high, but axial mode structure again is a mitigating factor not yet properly accounted for. The importance of these thresholds remains to be determined by the experiments.

Tokamak Theory. Finding and evaluating possible explanations for reduced confinement at high power levels has been a major focus. Long wavelength resistive tearing modes are well correlated with observed fluctuations but not with confinement degradation. Shorter wavelength modes and plasma rotation effects remain as good candidates. The drift wave turbulence explanation of anomalous electron thermal conductivity (χ_e) at low beta remains viable, and code calculations have verified and improved the spectral properties used. A variational moments method has supplanted time-consuming magnetohydrodynamic (MHD) equilibrium calculations in many applications. Spatially resolved transport analysis of fueling and beam heating dynamics has replaced the traditional zero-dimensional (0-D) Lawson criterion plots with plasma operation contour (POPCON) plots that summarize the operating characteristics of the International Tokamak Reactor (INTOR), the Fusion Engineering Device (FED), and reactors. Low ripple bundle divertors have been found and pumped limiters modeled. Major advances have been made in MHD modeling, with integrated families of codes to generate equilibria and provide ideal and resistive, linear and nonlinear modeling for large and small values of mode numbers, curvature, and poloidal beta (β_p).

Stellarator Theory. The strong background of tokamak lore and models allowed rapid progress in exploring the relative merits of various continuous and modular stellarator and torsatron configurations. Field line (magnetic surface) and drift orbit analysis and application of an adapted version of the Chodura-Schlüter three-dimensional (3-D) finite element variational equilibrium code have permitted evaluation of particle confinement and beta limits. A new configuration developed at ORNL, the symmotron (symmetric modular torsatron), is being strongly pursued.

Computing Support. The computing network and data acquisition systems continue to keep pace with the state of the art but not so closely as to be experimental or unreliable.

4.1 EBT THEORY

This year has been one of solid accomplishment and one in which a number of new ideas have emerged. These ideas bear directly on the principal physics issues (beta limitations, ion transport, ring physics, etc.) that must be addressed by the entire EBT physics program. The progress in understanding potential stability limitations on core beta and other parameters has been aided by a large number of

contacts outside ORNL (fostered by joint papers, workshops, etc.). New ideas for theoretical models in the areas of transport, heating, and ring physics have arisen in large measure from interaction with the EBT experimental program [particularly the recent higher power electron cyclotron heating (ECH) and ion cyclotron resonant frequency (ICRF) experiments on EBT-S]. Features common to stability and heating theory have been identified, with potentially important impacts on the long-term program. The long-term implications of the theory are crystallized by participation in the EBT-P and EBT reactor design studies.

The past year has been one of transition for EBT theory at ORNL. The early part of the year saw the culmination of a long period of definition and design studies for EBT-P. In the latter part of the year several important insights were obtained and a number of new theoretical calculations were carried out or begun. Many of these calculations are generally applicable to the EBT concept and are aimed at improved models for present experiments (EBT-I/S) as well as for EBT-P and EBT reactors. A number of new ideas and working hypotheses have been developed that provide guidance for the choice of theoretical research. Some of the theory based on these ideas and hypotheses is still very much in the formative stage. Because these new ideas have a large potential impact on the long-term questions confronting EBT physics, we have chosen to indicate some future plans in the material that introduces each of the following subsections.

4.1.1 Stability

A central and long-term issue that must be addressed by the entire EBT physics program is the limitation imposed on core beta by stability considerations. In the past year three potentially dangerous modes have been identified: the core interchange, ring interchange, and compressional Alfvén modes. These modes were originally identified from simplified slab model calculations and provide restrictions on the ratios of core and ring densities and temperatures as well as on core beta. Because these modes were expected to be localized to the radial region occupied by the rings, several radially resolved calculations have been carried out. For low poloidal mode numbers, m, it was found that radial geometric effects (omitted in slab and z-pinch models) have a strong stabilizing effect. For high values of m, the slab and radial calculations agree rather well, but it should be noted that the radial analysis presently omits certain finite gyroradius effects, which preliminary slab calculations indicate are very important.

Particularly for the high frequency modes (ring interchange and compressional Alfvén), the calculations have not yet included the "bumpiness" of an EBT in detail. In particular, calculations of the limits on core beta and of the ratio of core density to ring density presently neglect the fact that the rings do not extend into the mirror throats. Preliminary indications are that this omission leads to overestimating the sources of free energy available to drive these modes and hence gives pessimistic results. To make quantitative statements about these effects will require including the bumpy character of an EBT in these stability calculations. This is a formidable task, because it is necessary to include the various kinetic effects already found to be important as well as additional couplings to shear Alfvén modes.

Abstract of Review of Recent EBT Coupled Ring-Core Stability Theory[1]

D. A. Spong

During the past several years, EBT stability calculations have evolved with respect to treatment of ring-core plasma coupling effects. This evolution began with recognition of the important role of ring compressibility and paramagnetic effects on core beta limits. Since then, models have continued to increase in sophistication, including ring-core frequency

coupling, velocity-space and hot electron distribution function effects, and radially dependent models. Some of these features have resulted in wide variations in predicted plasma performance limitations. A number of the models will be reviewed and assumptions to which they are particularly sensitive will be discussed.

Abstract of Brief Survey of Experimental Investigation of Instabilities in Microwave-heated Plasmas[2]

*H. A. Uckan, G. R. Haste**

Nearly two decades of experimental investigations exist on instabilities in hot electron plasmas in open (simple and minimum-B mirrors) and closed (bumpy tori, EBT, and NCT) geometries. A brief review is given for some, but not all, of the results from these experiments. Also discussed is the observed behavior of the plasma in C-T and T-M transitions in EBT.

Abstract of Numerical Solutions of the EBT Radial Eigenmode Problem[3]

D. A. Spong, J. W. Van Dam,† H. L. Berk,† M. N. Rosenbluth†

The radial structure of eigenmodes in EBT is of interest since both modes which are localized within the annulus and modes which extend into the core plasma have been predicted to be unstable within appropriate parameter regimes. Radially resolved calculations have been done for a z-pinch model which corresponds to a bumpiless, azimuthally symmetric version of EBT. A shooting method is employed which solves 2-point boundary value problems on the inside and outside of the ring and which matches derivatives at the center. Comparison of these results with those of a localized dispersion relation will be discussed.

Abstract of Eigenmode Stability Analysis for a Bumpy Torus[4,5]

J. W. Van Dam,† H. L. Berk,† M. N. Rosenbluth,† D. A. Spong

The analysis of eigenmodes in a bumpy torus yields several stability boundaries that indicate the existence of a parameter regime for generally stable operation consistent with current experiments. However, there is a relatively narrow band of parameters where instability persists.

Abstract of Stability of Hot Electron Plasma in the EBMD Bumpy Torus[6]

K. T. Tsang, C. Z. Cheng‡

The stability of a hot electron plasma in EBT is investigated using two different models. In the first model, where the hot electron distribution function is assumed to be a delta function in the perpendicular velocity, we find a new stability boundary in addition to those discussed by Nelson and by Van Dam and Lee. In the second model, where the hot electron distribution function is assumed to be a Maxwellian in the perpendicular velocity, we find stability boundaries significantly different from those of the first model. Coupling of the Nelson-Van Dam-Lee mode to the compressional Alfvén mode is now possible. This leads to a higher permissible core plasma beta value for stable operation.

Abstract of Analytical Theory of Interchange and Compressional Alfvén Instabilities in EBT[7]

C. Z. Cheng,‡ K. T. Tsang

The local stability of the EBT plasma is analyzed for the long wavelength perturbations in the frequency regime, $\omega \leq \Omega_i$ (Ω_i is ion cyclotron frequency). In addition to the low frequency interchange instability, the plasma can be unstable to the compressional Alfvén wave. Contrary to the previously obtained

*EBT Experimental Section.

†Institute for Fusion Studies, University of Texas, Austin, Texas.

‡Princeton Plasma Physics Laboratory, Princeton, New Jersey.

quadratic dispersion relation in ω for the interchange mode, our dispersion relations for both types of instabilities are cubic in ω. New stability boundaries are found, for the hot electron interchange mode, to relate to the enhanced compressibility of the core plasma in the presence of hot electrons. The compressional Alfvén instability is driven due to the coupling of hot electron magnetic drifts and diamagnetic drift with the compressional Alfvén wave. The stability conditions of these two types of instabilities are opposite to each other.

Abstract of Radial Structure of Instability Modes in the EBT Hot Electron Annulus[8]

D. A. Spong, H. L. Berk, J. W. Van Dam,* M. N. Rosenbluth**

In the EBT device, a hot electron annulus is present near the outside edge of a warm core plasma. Although this provides a localized minimum in B and stabilizes low beta interchange modes of the core plasma, a number of instabilities may still persist in such a configuration. These are: the hot electron interchange mode, the coupling of the ring with compressional Alfvén waves of the core plasma, core plasma pressure-driven modes, and instabilities present in the cold surface plasma region outside the ring. The radial structure of such modes is of interest because both instabilities localized to the ring region and those extending into the core plasma can be present in the appropriate parameter regions. Also, studies of the radial structure are useful in assessing the importance of effects such as finite $k_\perp \rho_i$ and $k_\perp \rho_H$ that are not included in the present theory. Radially resolved calculations have been done for a z-pinch model which corresponds to a bumpiless, azimuthally symmetric version of EBT. A shooting method is employed that matches derivatives of the eigenfunction near the center of the annulus. Relativistic effects are included, and a variety of boundary conditions and core and hot electron models have been considered. Results are discussed for the various modes that are present.

*Institute for Fusion Studies, University of Texas, Austin, Texas.

Abstract of Curvature-Driven Instabilities in a Hot Electron Plasma: Radial Analysis[9,10]

H. L. Berk, J. W. Van Dam,* M. N. Rosenbluth,* D. A. Spong*

The theory of unfavorable curvature-driven instabilities is developed for a plasma interacting with a hot electron ring whose drift frequencies are larger than the growth rates predicted from conventional MHD theory. A z-pinch model is used to emphasize the radial structure of the problem. Stability criteria are obtained for the five possible modes of instability: the conventional hot electron interchange, a high frequency hot electron interchange (at frequencies larger than the ion cyclotron frequency), a compressional instability, a background pressure-driven interchange, and an interacting pressure-driven interchange.

Abstract of On the Stability of Flute Modes in the ELMO Bumpy Torus[11]

A. M. El-Nadi

A radial normal mode analysis is carried out to study the stability of fluid-like flute modes in a simplified model of the EBT. The corresponding stability conditions are obtained.

Abstract of EBT Stability Theory[12]

N. A. Uckan

The first workshop on EBT stability theory was held at Oak Ridge, Tennessee, May 13-14, 1981. It was attended by about 80 participants, most of whom are presently working on stability (theory and/or experiment) relevant to the EBT configuration.

The purpose of the workshop was to provide a forum for (1) discussion and review of the status of EBT stability theory topics and (2) assessment of the various models used and

the importance of modes predicted from these models for the operating regimes of present and future experiments.

The first part of the workshop was devoted to presentations of 15 papers describing the status and various aspects (theory and/or experiment) of EBT stability. The second part of the workshop was devoted to open-session discussions of (1) critical evaluation of existing models and (2) influence of beta limits on reactor performance.

Abstract of The Radial EBT Stability Problem[13]

A. M. El-Nadi, K. T. Tsang

The local theory of electromagnetic modes excited by hot electrons predicts that the stability of an EBT device requires the density ratio of the ring to core electrons to fall in a certain range determined by the operating parameters. In this work we formulate the radial problem which allows us to deal with realistic profiles and then use a shooting method to obtain the stability regimes. We assume that both the hot electron interchange and the compressional Alfvén modes can be localized to the outside of the ring. This is consistent with the local solution in the high mode number limit and allows us to treat the low m case. The mode structure, stability thresholds, and comparison with the experimental results will be presented.

Abstract of Radial Eigenmode Stability for "Bumpiless" EBT[14]

J. W. Van Dam, H. L. Berk,* M. N. Rosenbluth,* D. A. Spong*

The radial eigenmode problem is of interest in the EBT device because there can be unstable modes localized within the thin hot electron annulus region. A model which facilitates analysis of the radial structure is the z-pinch, corresponding to a bumpiless, azimuthally symmetric version of EBT. With this model, we are able to reduce the coupled set of linear partial integrodifferential mode equations (obtained from the momentum transfer equation with the anisotropic pressure calculated kinetically) to an ordinary differential equation in the radial direction.

By integrating across the annulus layer and matching inner and outer solutions, we analytically generate a fourth-order dispersion relation. One of the modes is low frequency and corresponds to the core plasma interchange, known to impose an upper limit on the allowed core pressure. The three higher frequency modes provide additional stability limits on the core density and the annulus pressure. Taken together, these limits indicate that taking into account the radial mode structure leads to a more optimistic outlook for EBT stability.

Numerical solution of the radial differential equation with a shooting code yields results that are consistent with the analytic layer solution. Results for the radial profiles of the eigenmodes and their stability will be presented.

Abstract of Coupling of Hot Electron Interchange and Ion Bernstein Modes in EBT[15]

K. T. Tsang, C. Z. Cheng†

Previous stability studies of hot electron rings and background plasmas in EBT have been pursued in low frequency ($\omega \ll \Omega_{ci}$) and intermediate frequency ($\omega \sim \Omega_{ci}$) with a small Larmor radius approximation ($k_\perp \rho_i \ll 1$).

Present experimental parameters indicate the importance of finite Larmor radius effects and therefore the importance of higher cyclotron harmonics. We derive and analyze the dispersion relation which includes both effects. Our result reduces to those of Nelson and Van Dam and Lee in the appropriate limit. Coupling of the hot electron interchange mode to the compressional Alfvén wave as pointed out by

*Institute for Fusion Studies, University of Texas, Austin, Texas.

†Princeton Plasma Physics Laboratory, Princeton, New Jersey.

El-Nadi is also recovered. However, when the finite Larmor radius is included, further coupling of the compressional Alfvén wave to the cyclotron harmonics is observed to excite a new ion Bernstein instability. This leads to instability channels in the stability diagram. The stability boundary of Nelson, Van Dam, and Lee is connected to the stability boundary due to the ion cyclotron mode at large hot electron beta.

Abstract of Numerical Solutions of the EBT Radial Eigenmode Problem[16]

D. A. Spong, J. W. Van Dam, H. L. Berk,* M. N. Rosenbluth**

The radial structure of eigenmodes in EBT is of interest since both modes which are localized within the annulus and modes extending into the core plasma have been predicted to be unstable within appropriate parameter regimes. Radially resolved calculations have been done for a z-pinch model which corresponds to a bumpiless, azimuthally symmetric version of EBT. A shooting method is employed which solves 2-point boundary value problems on the inside and outside of the ring and matches derivatives at the center. Comparison of these results with those of a localized dispersion relation will be discussed.

Abstract of The Compressional Alfvén Mode for Realistic EBT Plasmas[17]

A. M. El-Nadi

It has been shown that the destabilization effect of the hot electron ring on the compressional Alfvén wave determines the maximum achievable core beta in EBT. This result was obtained by assuming a δ-function velocity distribution for the hot electrons. In this work we examine the realistic case of Maxwellian hot electrons with arbitrary parallel and perpendicular temperatures and compare the obtained core beta limits with previous results.

Abstract of Analysis of EBT Stability[18]

H. L. Berk, M. N. Rosenbluth,* J. W. Van Dam,* D. A. Spong*

Several modes of instability, driven by unfavorable curvature, are possible in a hot electron plasma system such as EBT. A hot electron interchange mode can be stabilized with a sufficient amount of background plasma. However, a compressional Alfvén instability is triggered with too much background plasma. For most parameters a window of stability is possible, but it is possible to choose wave numbers, combined with other physical parameters, for which instability still persists. In addition, the background plasma beta is limited to the Lee-Van Dam limit. However, the background beta can be lower due to various density parameters and finite electron Larmor radius.

4.1.2 Transport

A second major issue for EBT physics is transport. Electron transport is reasonably well understood theoretically, and because electron transport dominates in existing devices, it has been possible to give a reasonably good description of these experiments. The comparison between theory and experiment for ion transport has rested primarily on a somewhat indirect measurement: the ambipolar electric field. This allows a comparison of particle loss rates (ions and electrons must flow out at the same rate in steady state). Energy balance is extremely difficult experimentally because for experiments heated with ECH alone, the ion sources and sinks are typically less than 1% of the total power input to the device. In consequence, not only are the relevant quantities difficult to measure accurately, but also the power balance is susceptible to what might

---

* Institute for Fusion Studies, University of Texas, Austin, Texas.

otherwise be minor effects. The recent ICRF experiments are generally useful for gaining a fuller understanding of the ions. However, power balance calculations are still quite difficult because propagation in EBT-S (in contrast to EBT-P, which will allow propagation at frequencies corresponding to low harmonics of the ion cyclotron frequency) requires frequencies comparable to high harmonics of the ion cyclotron frequency, while heating at these high harmonics is not well understood. Consequently, the power balance for ions in EBT-S with ICRF has uncertainties in both sources and sinks.

For some time the experimental scaling of the ambipolar electrostatic potential has been observed to follow $e\Delta\phi/T_e$ and to be approximately constant (and of order unity). The recent higher power ECH experiments provided part of the impetus for developing a second radially resolved transport code using this empirical scaling. Another reason for this development was that the original code [this year improved to include regions where ∇B (and $\nabla\phi$) is reversed by the rings] typically yielded electric fields scaling with the ion temperature. While both codes yield approximately the same predictions for future devices such as EBT-P, it is clearly desirable to have a first-principles theory of the electric field that agrees with experiment.

The recent higher power ECH experiments on EBT-S showed a substantial increase in $\Delta\phi$. This leads to a considerable reduction in the ion resonant collisionality [$\propto(\Delta\phi)^{-5/2}$]. Accordingly, we have begun to develop new and tractable expressions for the ion transport coefficients that are valid for the full range of resonant ion collisionality (banana to plateau inclusive). Considerable work remains to be carried out because of the dependence on additional parameters. A preliminary analysis has been carried out for these new expressions for resonant ion transport coefficients and appears quite promising. This analysis suggests that for existing experiments, the shape of ϕ is primarily governed by the shape of the magnetic field, but the magnitude (and hence overall scaling) appears to be governed by electrostatic trapping of electrons at the outer edges of the core plasma where ∇B (and $\nabla\phi$) is reversed by the hot electron rings.

These preliminary results are quite different from those obtained earlier using the plateau (highest resonant collisionality) limit for the ion transport coefficients. The underlying reason is that at lower collisionality, the details of ion orbits (e.g., banana width) are more important and cause the electric field to be described in terms of a differential equation (nonlocal) rather than the algebraic equation (local) encountered previously. We reiterate that quantitative calculations require considerably more work: to develop the transport coefficients over the necessary parameter ranges, to analyze the differential equation for the electric field, and finally to incorporate these effects into radially resolved transport calculations. Nonetheless, the work to date is very encouraging because it appears to be a significant step toward a first-principles description of the ambipolar potential with improved agreement with experiment.

Abstract of A Kinetic Model for Neoclassical Transport in EBT with Enhanced Ion Tail[19]

T. S. Tolliver, E. P. Jaeger, C. L. Hedrick

The best currently available transport coefficients for neoclassical transport of ions in EBT in the plateau regime are based on the assumption of a lowest-order ion velocity distribution function that is Maxwellian. Experimental evidence, however, suggests the presence of an enhanced high energy tail on the ion distribution function, and a simple theoretical analysis indicates that an enhanced tail may be a major contributor to neoclassical losses. For a study of these effects, a kinetic model for neoclassical transport is developed assuming isotropic velocity distributions. Three coupled nonlinear integro-differential equations in one velocity dimension

are solved numerically; this includes, for the first time, a self-consistent solution for the lowest-order ion distribution function, which proves to be non-Maxwellian and has an enhanced high energy tail due to electron-ion collisions. It is shown that this non-Maxwellian lowest-order solution leads to higher core ion temperatures and to much larger ion diffusion rates than those obtained when a Maxwellian distribution is assumed.

Abstract of EBT Transport in 2-D Mirror Geometry with Finite Electron Annulus Pressure[20]

E. F. Jaeger, L. L. Lao, L. W. Owen, C. L. Hedrick

Transport equations for the EBT toroidal plasma are averaged along magnetic field lines computed from a two-dimensional (2-D) magnetic equilibrium calculation in mirror geometry. A finite plasma pressure which is peaked off axis approximates the hot electron ring plasma. Previous radial transport calculations have assumed cylindrical geometry with ad hoc magnetic field profiles. Results reported here depend on the value of plasma pressure assumed in the hot electron ring but are relatively insensitive to the degree of anisotropy assumed in the ring pressure. The scaling of confinement parameters with neutral pressure is similar to that observed in the previous one-dimensional (1-D) work.

Abstract of ELMO Bumpy Torus Transport with a Rigid Electron Annulus in Bumpy Cylinder Geometry[21]

E. F. Jaeger, L. L. Lao, L. W. Owen, C. L. Hedrick

Transport equations for the EBT toroidal plasma are averaged along magnetic field lines computed from a 2-D magnetic equilibrium calculation in bumpy cylinder geometry. An anisotropic plasma pressure peaked off axis approximates a rigid, high beta electron annulus which modifies the magnetic field but does not interact with the toroidal plasma. Toroidal plasma pressure is neglected due to low toroidal beta. A local diffusion approximation allows numerical solution of the steady-state transport equations for an isotropic toroidal plasma on a grid of magnetic surfaces, which include both normal and reversed magnetic gradient regions near the electron annulus. The non-Maxwellian ion velocity distribution is neglected. Results depend on the annulus width and pressure distribution. Scaling of energy confinement with neutral pressure is similar to that observed in 1-D cylindrical geometry with ad hoc magnetic profiles.

Abstract of Ambipolar Potential Formation and Control in Bumpy Tori and Mirrors[22]

*N. A. Uckan, R. F. Post**

The Workshop on Ambipolar Potential Formation and Control in Bumpy Tori and Mirrors was held at Oak Ridge, Tennessee, May 11-12, 1981. Attending were approximately 100 scientists from both the U.S.A. and Japan.

The purposes of the workshop were (1) to evaluate the current status of experimental and theoretical understanding of the role played by the ambipolar potentials and (2) to identify processes that influence the formation and control of the ambipolar potentials.

The first part of the workshop was devoted to presentations of 24 papers (divided equally between experiment and theory) along with four reviews. The second part of the workshop was devoted to open-forum discussions of critical topics selected by the workshop participants.

*Lawrence Livermore National Laboratory, Livermore, California.

Abstract of The Ambipolar Potential in EBT, a Theoretical Summary[23]

C. L. Hedrick

In EBT the ambipolar electric field has a profound effect upon single particle orbits and hence upon loss rates. Based upon the experimentally observed ambipolar potential, orbits and loss rates have been calculated. These in turn have been used in transport calculations to calculate density, temperature, and self-consistent electric fields for comparison with experiment.

The gross properties of the EBT-I/S plasmas can be understood in terms of purely hydrogenic, neoclassical transport assuming Maxwellian distributions. The basic elements of these calculations will be reviewed. The agreement with the gross experimental properties using these simplified models is in large part due to the fact that the electron particle and energy losses are both dominant and better understood than the ion losses. The ion losses in EBT-I/S plasmas are complicated by two factors. One is that, because of the relatively small plasma density and mirror radius, impurities (e.g., Al) may substantially modify the ambipolar potential even though their density is very low. The second factor is that Coulomb collisions are a very weak mechanism for heating ions. Thus the ions are susceptible to what otherwise might be negligibly small nonclassical effects.

Recent Fokker-Planck calculations suggest that very small amounts of heating (by fluctuations) can produce an enhanced tail on the ion distribution — as observed experimentally. Single particle orbit calculations suggest a possible mechanism for heating both hydrogen (to produce an enhanced tail) and impurity ions. These calculations also suggest a mechanism for enhanced hydrogen and impurity loss rates. Radially resolved transport calculations indicate that such mechanisms can indeed lead to ambipolar potentials which are in better quantitative agreement with experiment.

These complications in modeling EBT-I/S plasmas should be largely eliminated in EBT-P, where the larger mirror radius and plasma density will shield the plasma from impurities and permit efficient penetration of and direct ion heating by ICRF.

Abstract of Power Requirements for Ion Tail Formation in EBT[24]

J. S. Tolliver, E. F. Jaeger, C. L. Hedrick

Experimental evidence suggests the possible presence of an enhanced high energy tail on the ion distribution function, and a simple theoretical analysis indicates that an ion tail may be a major contributor to neoclassical losses, which in turn influence the ambipolar potential. In order to study these effects, a kinetic model for neoclassical transport is developed using a Fokker-Planck collision operator and assuming isotropic electron and ion velocity distributions. Three coupled nonlinear integrodifferential equations are solved numerically. The solution shows a non-Maxwellian lowest-order ion distribution function. This non-Maxwellian solution leads to higher core ion temperatures and larger ion diffusion rates than those obtained when a Maxwellian distribution is assumed. If the ion tail is further enhanced by a small amount of ad hoc heating, even higher core temperatures and loss rates are obtained.

Abstract of Effects of Fluctuating Electric Fields on Hydrogen and Impurity Ions in EBT[25]

L. W. Owen

The effects of fluctuating poloidal electric fields on the orbits and on the heating and loss rates of ions and impurities in EBT are examined. The equations of motion for particles

confined to a sector midplane are numerically integrated to yield the temporal behavior of the velocity and position coordinates in the presence of the vacuum magnetic field, a realistic steady-state ambipolar electric field, and the sinusoidally varying electric field of a wave propagating in the poloidal direction. It is shown that a wave of modest amplitude and frequency comparable to typical fluctuation frequencies (10-150 kHz) measured in EBT can lead to large excursions in the kinetic energy and radial position of the hydrogen or impurity ion. The possible relevance of the results of these calculations to the behavior of impurity ions as a function of the mass, charge state, fluctuation level, steady-state potential, etc., is discussed.

Abstract of EBT Transport and Ambipolar Potential Formation with Rapid Loss of High Energy Impurity Ions[26]

T. F. Jaeger, R. K. Richards, C. L. Hedrick*

Density profiles for neutral impurity atoms and impurity ions of a single charge state are calculated as functions of radius in a one-and-one-half dimensional ($1\frac{1}{2}$-D) transport calculation for the EBT toroidal plasma. The ion tail is neglected along with the source of electrons due to ionization of neutral impurity atoms. Ad hoc energies and transport rates are assumed for the impurity ions consistent with spectroscopic measurement. Ambipolar transport rates are rederived to include impurity transport in the flux of positive particles, and the electric field is computed self-consistently. Steady-state solutions show potential well depths on the order of the impurity ion temperature divided by its charge. Also, due to the large gyroradius of the impurity ions, viscosity limits shear in the poloidal drift velocity. Thus, potential profiles tend to be more parabolic and the plasma rotates more nearly as a rigid body than would be expected from simple neoclassical theory with no impurities present.

Abstract of Aluminum Impurity Ions and the Ambipolar Potential in EBT[27]

R. K. Richards, E. F. Jaeger*

There is experimental evidence of a correlation between the electric potential and aluminum impurities in EBT. This correlation is observed in the relation between the temperature of the highest aluminum charge state and the potential well depth. The aluminum temperature is determined for each charge state by measuring the Doppler broadening of a characteristic spectral line. Temperatures as large as 650 eV have been found for Al^{+3}. Aluminum densities are derived by measuring the brightness of spectral lines with an absolutely calibrated spectrometer. Typical central values indicate $n_{Al}/n_e \sim 10^{-3}$. The particle confinement time for the aluminum ions is determined by comparing the ratios of aluminum ion densities. Values for the aluminum confinement times are smaller than the electron confinement time by several orders of magnitude ($\tau_{Al} < 100$ μs). This short lifetime suggests a large particle flux of aluminum and the formation of an ambipolar potential as a consequence.

Abstract of Magnetic Field Error Effects on the Ambipolar Potential in EBT[28]

J. D. Callen

Mirror-trapped particles are not significantly affected by field errors because their motion is restricted to a single mirror cell. Toroidally passing particles are shown to drift on surfaces of constant $J^{**} = \oint d\underline{\ell} \cdot [\underline{v}_\parallel + (e/mc)\underline{\tilde{A}}] = J + (e/mc)\tilde{\psi}$, where the loop integral is over one toroidal transit and $\oint d\underline{\ell} \cdot \underline{\tilde{A}} = \oint\oint d\underline{S} \cdot \underline{\tilde{B}} = \tilde{\psi}$ is the magnetic flux function associated with the error field. For small field errors ($\tilde{B}/B \ll \rho_e/r \sim 10^{-4}$) the drift surfaces are nearly the same as those in the ideal system, and the field error effects

* EBT Experimental Section.

are negligible. As the field error is increased into an intermediate range ($10^{-4} \sim \rho_e/R \sim \tilde{B}/B \sim \rho_e/r \sim 10^{-3}$) the passing particle drift surfaces become dominated by the field errors (i.e., $\tilde{\psi}$), and the toroidally passing electrons cause, via a Spitzer-type kinetic equation, particle and concomitant current flow in the direction of the field error ($\tilde{B}$). However, in the intermediate regime this charge flow is small compared to the poloidal charge flow due to the mirror-trapped particles, and hence the field error causes only a slight distortion of equipotentials of the ambipolar potential well — toward those of the field error flux surfaces. For large field errors ($\tilde{B}/B \gtrsim \rho_e/r \sim 10^{-3}$) the field-error-induced charge flow dominates, there are an electric field and current in the direction of the error field ($\tilde{B}$), a potential well (T-mode operation) becomes impossible, and neoclassical transport is drastically modified. Since the field error is small, the current and charge flow are effectively in the toroidal direction but spiral slowly out of the confinement volume in the $\tilde{B}$ direction. The toroidal current causes a poloidal magnetic field structure which can modify the $\tilde{B}$ in the plasma and hence the possibility of forming a potential well. A number of the characteristics predicted by this theoretical model are observed experimentally.

Abstract of EBT Transport and Ambipolar Potential Formation with Rapid Loss of High Energy Impurity Ions[29]

E. F. Jaeger, R. K. Richards, C. L. Hedrick*

Density profiles for neutral impurity atoms and impurity ions of a single charge state are calculated as functions of radius in a 1½-D transport calculation for the EBT toroidal plasma. Ad hoc energies and transport rates are assumed for the impurity ions consistent with spectroscopic measurements. Steady-state solutions show potential well depths on the order of the impurity ion temperature divided by its charge ($e\phi \gtrsim 100$ eV). Also, classical viscosity due to the large gyroradius of the impurity ions limits shear in the poloidal drift velocity. Therefore, potential profiles tend to be more parabolic and the plasma rotates more nearly as a rigid body than would be expected from simple neoclassical theory with no impurities present.

Abstract of 2-D Kinetic Transport Model for EBT[30]

J. S. Tolliver, E. F. Jaeger, C. L. Hedrick

Work has begun on a 2-D kinetic transport model for ions in EBT. This is an extension of earlier work with a 1-D kinetic model. We begin with the drift kinetic equation in general (α,β,ξ) coordinates allowing full 3-D magnetic geometry. This equation is then bounce-averaged, and generalized moments in terms of an average over the infinitesimal volume between two alpha surfaces are taken in order to prove continuity. It is then convenient to transform from (α,β) coordinates to the more useful (ρ,θ) coordinates defined in the midplane and centered at the plasma center. This bounce-averaged drift kinetic equation can then be simplified by Fourier expanding in the variable θ to yield a set of coupled equations in two velocity dimensions (ε,μ) and one space dimension (ρ). The two quantities $\Omega \equiv \langle \vec{\nabla}_D \cdot \nabla\theta \rangle$ and $V_{D\rho} \equiv \langle \vec{\nabla}_D \cdot \nabla\rho \rangle$ are calculated from the longitudinal invariant J using a 3-D EBT vacuum magnetic field. The coupled equations can be solved numerically when a scale length relationship for the space dimension is assumed (i.e., point model in configuration space).

Abstract of Transport Projections from the Experimentally Observed Ambipolar Potential Scaling in EBT[31]

E. F. Jaeger, C. L. Hedrick

In the EBT, the electron-rich toroidal plasma exhibits an ambipolar potential well

* EBT Experimental Section.

with a radially inward pointing electric field. Experiment shows a potential well depth on the order of the electron temperature, but neoclassical transport theory for Maxwellian ions predicts a well depth on the order of the ion temperature. While the classical theory scales favorably for larger machines, there is also interest in making projections based on the experimental scaling. Consequences of this scaling will be discussed in the context of a 1½-D transport model with ad hoc rather than self-consistent electric fields. Since electron and ion fluxes are not necessarily equal in such a model, ambipolar transport rates are inappropriate and the calculation must be reformulated in terms of separate electron and ion transport coefficients. In this case, terms linear in the electric field appear explicitly in the transport equations.

4.1.3 Magnetics and Orbits

Another aspect of ion transport is that the high energy population (tail) is found experimentally to be larger than that given by a single pure Maxwellian. There is some evidence that the temperature of this tail (~250 eV in EBT-S) follows the scaling law $\rho/L \cong 0.05$ (where ρ is the gyroradius and L is the magnetic scale length) and that only the density of the tail is affected by either ICRH or internally generated fluctuations. This scaling law is similar to that obtained for the hot electron rings, but the experimental evidence for this ion tail is far less complete than that for the rings.

The value of 0.05 for ρ/L is comparable to that at which the lore indicated that the magnetic moment, μ, would begin to fluctuate due to finite gyroradius effects. Numerical calculations using the full single particle equations of motion in finite ring beta magnetic fields and (in the case of ions) ambipolar electric fields have been carried out. These calculations indicate that μ does begin to fluctuate appreciably at values of ρ/L comparable to 0.05, as expected from analytic approximations. However, for $\rho/L < 1$ the particles are not immediately lost even if they become untrapped (in contrast to what happens in a single mirror cell). For $\rho/L < 1$, the gross effect is similar to neoclassical diffusion with enhanced pitch angle scattering, rather than being a prompt or direct loss, because the particles tend to follow well-confined drift surfaces.

While it seems clear that the fluctuations in μ due to finite gyroradius are important for understanding the empirical scaling of both the ring and the ion tail, it is still debatable which of the collective processes (heating, transport, fluctuations, etc.) is most affected by these single particle effects. What is clear is that most theoretical models neglect "small" μ fluctuations, which can be large compared to other "small" effects that are currently included. One of the prime candidates for examination in the near future is heating of high energy electrons (with energies comparable to the ring temperature) by ECH including μ fluctuations due to finite gyroradius effects.

Abstract of 3-D Tensor Pressure Equilibria for EBT[32]

L. W. Owen, C. L. Hedrick

Techniques for calculating magnetohydrostatic equilibria with tensor pressure are reviewed. Algorithms for computing 3-D hot electron ring equilibria for EBT with a separable model for the pressure tensor are discussed, as are the numerical methods used in the implementation of those algorithms in a computer code. Some typical results of 3-D equilibrium calculations for EBT-I/S and an EBT reactor conceptual design illustrate the efferts of the relativistic electron annuli on the magnetic field. Two significant additions to the 3-D code are planned for the near term and discussed in this paper. The first concerns the addition of an isotropic pressure component to model the core plasma in EBT. The second is

the inclusion of the flow and electric field terms in the momentum balance equation. A straightforward method of including mass flow due to the $\vec{E} \times \vec{B}$ plasma rotation and a discussion of its possible importance for 3-D equilibria in EBT are presented.

Abstract of Nonadiabaticity and High Energy Particle Orbits in EBT[33]

L. W. Owen, C. L. Hedrick, L. E. Delemare

The scaling of hot electron ring temperatures in EBT and mirror experiments and the results of recent ICH experiments on EBT-S suggest the scaling law $\rho/L \approx 0.05$, where ρ is the gyroradius and L is the magnetic scale length. This is roughly the value at which conservation of the adiabatic invariant μ begins to break down. The behavior of $\mu(t)$ and the particle drift orbits are obtained by numerical integration of the equations of motion. In the absence of electric fields it is shown that nonconservation of μ for $\rho/L \approx 0.05$ is so weak as to have little effect on drift orbits and to affect particle losses only through enhanced pitch angle scattering. Only for particle energies of about five times the temperature do rapid direct losses due to magnetic moment jumps start to become important. The effects of a radial electric field on μ conservation for high energy impurity and hydrogen ions will be reported.

Abstract of Ring Temperature Scaling[34]

N. A. Uckan

During the last two decades the production of high beta, hot electron plasmas with ECH has been amply demonstrated in open and closed geometries. A wide variety of conditions was present in these experiments, with a factor of 2 change in device dimensions and more than an order of magnitude change in magnetic fields (~1-10 kG), ECH frequencies (~6-55 GHz), and hot electron temperatures (~50-1200 keV). An analysis of the data from all the experiments that used a single ECH frequency indicates that the hot electron temperatures do increase with magnetic field strength (or, equivalently, ECH frequency) and scale length. In particular, they all obey $\rho/L \cong$ constant ($\sim 5\text{-}6 \times 10^{-2}$) scaling, where ρ and L are the hot electron gyroradius (relativistic) and the magnetic field scale length, respectively. This is roughly the value at which conservation of the adiabatic invariant μ begins to break down and suggests that the hot electron temperatures are probably limited by nonadiabatic particle behavior. Results, primarily from hot electron ring experiments (ELMO, EBT, NBT, etc.), are discussed, and projections for future experiments are given. It is shown that although in all previous experiments the ring temperature is determined by the ρ/L criterion, EBT-P will be the first experiment unconstrained by this limit.

Abstract of Adiabatic Energy Limit in ECH Hot Electron Plasmas[35]

N. A. Uckan

During the last two decades the production of high beta, hot electron plasmas with ECH has been amply demonstrated in open (simple and min-B mirrors) and closed (bumpy tori, EBT, and NBT) geometries, an effort largely pioneered by R. A. Dandl. A wide variety of conditions was present in these experiments. While most of these experiments (ELMO, PTF, TPM, CIRCE, EPA, EBT, NBT, etc.) have had a similar device size, with the exception of two (INTEREM, STM) that were twice as large, there was an order of magnitude change in magnetic fields (~1-10 kG), ECH frequencies (~6-55 GHz), and hot electron temperatures (~50-1200 keV). An analysis of data from all these experiments indicates that the hot electron energies do increase with magnetic field and frequency and are probably limited by nonadiabatic particle behavior, obeying $\rho/L \cong$ constant ($\sim 5\text{-}6 \times 10^{-2}$) scaling where ρ and L are the hot electron gyroradius (relativistic) and magnetic field scale length, respectively. Results, mostly from hot electron ring experiments (ELMO, EBT, etc.), will be discussed and projections will be given.

Single particle confinement in bumpy tori with noncircular mirror coils

L. W. Owen

Various methods have been proposed for improving single particle confinement in the vacuum magnetic field of a bumpy torus. These include the use of split-wedge mirror coils, axis-encircling aspect ratio enhancement (ARE) coils, and field symmetrization (SYM) coils. The Nagoya Bumpy Torus (NBT) group has recently investigated the effects of using semicircular (D-shaped) mirror coils.

The purpose of the work now under way is to ascertain the effects of noncircular mirror coils on vacuum magnetic field geometry and single particle confinement. Configurations employing rectangular, trapezoidal, D-shaped, and triangular mirror coils are compared to the basic EBT-S configuration with circular coils. Flux lines and mod-B contours in the equatorial plane, mod-B contours in the midplane, and drift orbits for trapped, transitional, and passing particles are evaluated for each configuration. These qualitative comparisons indicate that single particle confinement with noncircular mirror coils is not significantly better than that with circular coils.

4.1.4 Heating

The theory of both ECH and ICRF heating is critical to EBT physics understanding and has received increased emphasis this year. The major efforts this year have been the continuing development of theoretical tools to study ECRH in EBT and application of these tools. A number of improvements have been made in the RAYS geometrical optics code, including an equilibrium model that includes the electron rings, refined relativistic and nonrelativistic damping modules, multicomponent plasma models, and improved ray diagnostics. Considerable effort has been expended in documenting the code for wider use. [The RAYS code is already being used at Princeton Plasma Physics Laboratory (PPPL) for calculations on the Poloidal Divertor Experiment (PDX), and techniques developed for RAYS are incorporated in the Lawrence Livermore National Laboratory (LLNL) ray tracing code.] The 2-region power balance model has been refined and a technique developed for a priori estimating of the average annulus absorptivity. The RAYS code and the power balance model have been used together to make detailed calculations of microwave power deposition in EBT devices.

We have begun a theoretical program to study ion cyclotron heating (ICH) in EBT devices. This includes a kinetic theory of the wave absorption and a numerical calculation of ICRF wave fields in bumpy cylinder geometry. The calculation of the wave fields is complicated by the relatively long wavelengths of the fast and slow Alfvén modes in EBT-S (as opposed to EBT-P), and a numerical approach based primarily on cold plasma theory is being pursued. Very recently the commonality of propagation features for both ICRF and stability theory has suggested supplementary theoretical approaches for other more nearly electrostatic and flutelike modes, which may be important for understanding the ICRF experiments on EBT-S.

Abstract of A Simple Power Balance Model for Microwave Heating in EBT[36]

D. B. Batchelor

A simple model is presented for the production and absorption of ordinary and extraordinary mode energy in various regions of the EBT plasma. The plasma is divided into two regions: (I) the low magnetic field side of the extraordinary mode cutoff and (II) the high field side of the cutoff. Energy balance equations are written for the sources (injection, mode conversion, and tunneling) and sinks (mode conversion, absorption, and tunneling) in each region, and simplified models are introduced to account for each of these processes. Since a typical ray makes several reflections from cavity wall surfaces before being absorbed, additional simplifying assumptions are made that the wave fields are an

isotropic incoherent superposition of plane waves and that the energy density of each mode is uniform in a given region.

It is found that conversion between eigenmodes upon wall reflection and absorption of the extraordinary mode at the fundamental cyclotron resonance are the most rapid processes. The relative fractions of the injected power that is deposited in the various plasma components are typically 25% to the annulus, 22% to the core plasma, and 53% to the surface plasma. The partitioning of energy between the three plasma components is determined largely by geometric characteristics of the walls, the plasma, and the fundamental cyclotron resonant surface. The results are comparatively insensitive to other parameters of the model and are in rough agreement with estimates of power deposition based on experimental data.

Abstract of Theoretical Studies of Electron-Cyclotron Heating in ELMO Bumpy Torus[37]

D. B. Batchelor, R. C. Goldfinger

The basic features of microwave propagation and electron cyclotron damping in EBT devices are investigated to provide an understanding of the heating of the toroidal core plasma component. Linear cyclotron damping calculations are presented for plasmas having parameters typical of EBT-I and parameters projected for EBT-II. It is shown that the extraordinary mode is completely absorbed near the fundamental cyclotron resonance when propagating from the high magnetic field side (mirror throat). For EBT-I parameters, heating by the ordinary mode at the fundamental cyclotron resonance and by both modes at the second harmonic resonance is negligible. For projected EBT-P parameters, the ordinary mode is heavily damped at the fundamental and the extraordinary mode is heavily damped at the second harmonic. Since the right-hand cutoff prevents injected extraordinary mode energy from propagating to the cyclotron resonance, a mechanism must exist outside geometrical optics by which the extraordinary mode reaches resonances. It is argued that this mechanism is the conversion of ordinary mode energy to extraordinary mode in the high field region upon wall reflection.

Studies of wave absorption processes near the second harmonic resonance (where the annulus is observed to form in EBT) are discussed. Calculations of single particle orbits at the second harmonic resonance in a magnetic mirror field and large amplitude wave characteristic of EBT-I are presented. It is shown that the heating is highly pitch angle dependent and that the motion of particles with large initial pitch angle is superadiabatic rather than stochastic, as is assumed by quasi-linear models. The calculations suggest that coherent wave-particle interactions are important in producing the annulus from a population of particles having small initial perpendicular energies.

Abstract of Ray Tracing Studies of Microwave Heating of the Annulus in EBT Devices[38]

D. B. Batchelor, R. C. Goldfinger, H. Weitzner

Electron cyclotron absorption of ordinary and extraordinary waves by the combined core plasma and relativistic annuli has been studied numerically. A fully relativistic damping package has been developed for the RAYS geometrical optics code, which allows the contribution from an arbitrary number of cyclotron harmonics to be included. The rays are traced in finite beta bumpy cylinder plasma equilibria which are obtained from the ORNL 2-D equilibrium code. These results for direct, single pass absorption are combined with results from a statistical model for the deposition of multiply reflected and mode-converted waves to obtain estimates of the power deposited in the core, surface, and annulus plasma components. Self-consistent estimates of the annulus power losses for EBT-I, EBT-S, and EBT-P are obtained using the same ring equilibrium model.

Abstract of Lower Hybrid Heating in EBT[39]

R. C. Goldfinger, A. E. Kritz, D. B. Batchelor*

The absorption of lower hybrid waves by the electron and ion components of EBT plasma is examined. Parameters are chosen for the hot electron annulus and core region which are representative of EBT-S and EBT-P plasmas. The computations are carried out using the RAYS code that was developed to study ECRH in EBT. The electron Landau damping along the ray is computed with the damping calculated relativisticaliy in the regions where the ray passes through the hot annuli. The lower hybrid ray trajectory is traced until mode conversion to an ion Bernstein mode occurs. We find that the potential for heating depends on an appropriate choice of the wave frequency and incident parallel wave number spectrum. In summary, lower hybrid wave power can be used to heat ions in EBT with a careful matching of wave and plasma parameters.

Abstract of Ion Cyclotron Resonance Heating[40]

H. Weitzner, D. B. Batchelor

In the parameter ranges of present experiments, geometrical optics provides a bad representation for the wave-plasma interaction near the ion cyclotron resonance. We provide a more appropriate modeling of the plasma-electromagnetic wave interactions in the range of frequencies near the ion cyclotron frequency and its harmonics. Based on the linearized Vlasov equation, we give expressions for energy absorption of the fundamental and second or third harmonics. We also examine electromagnetic wave mode patterns in the cavity.

Abstract of Microwave Power Deposition in the Annulus and Core Plasma Components of EBT Devices[41]

D. B. Batchelor, R. C. Goldfinger, H. Weitzner

Electron cyclotron absorption of ordinary and extraordinary mode waves by the combined core plasma and relativistic annuli has been studied numerically. A fully relativistic damping package has been developed for the RAYS geometrical optics code which allows the contribution from an arbitrary number of cyclotron harmonics to be included. The rays are traced in finite beta bumpy cylinder plasma equilibria obtained from the ORNL 2-D equilibrium code. These results for direct, single pass absorption are combined with results from a statistical model for the deposition of multiply reflected and mode-converted waves to obtain estimates of the power deposited in the core, surface, and annulus plasma components. Self-consistent estimates of the power requirements for EBT-I, EBT-S, and EBT-P are obtained.

Abstract of TORAY – A Ray Tracing Code for the Analysis of Electron Cyclotron Heating in Toroidal Geometry[42]

A. H. Kritz, H. Hsuan,† R. C. Goldfinger, D. B. Batchelor*

A ray tracing code (RAYS), developed to study wave propagation in EBT, has been modified (TORAY) to study radio frequency (rf) heating and current drive in toroidal geometry. The ray trajectories are obtained by solving the Hamiltonian form of the geometrical optics equations with either time or arc length as a parameter. Ray patterns are initiated similar to those of an actual antenna. A full graphics package has been developed for displaying the behavior of the rays. The ray paths and the dependence of energy deposition on plasma equilibria and microwave parameters are analyzed. In particular, parameters appropriate for the electron cyclotron heating experiments on PDX, ISX-B, Versator, and T-10 are examined. TORAY is structured for convenient linkage with transport MHD and Fokker-Planck codes. This linkage will be utilized to investigate the effect of ECH on transport and tearing mode stability.

*Hunter College, New York, New York.

†Princeton Plasma Physics Laboratory, Princeton, New Jersey.

Abstract of Cyclotron Absorption by the Relativistic Electron Rings in EBT[43]

D. B. Batchelor, R. C. Goldfinger, E. Weitzner

A key element of the EBT concept is the high beta, relativistic electron annuli formed in each sector of the torus by a cyclotron resonant interaction with high power injected microwaves. The local magnetic wells produced by these annuli stabilize the toroidally confined core plasma and enhance its confinement. In this paper we present initial results of a numerical study of electron cyclotron absorption of ordinary and extraordinary mode waves by the annuli in realistic EBT geometry. The calculations are based on the ORNL geometrical optics code RAYS and a recently developed, fully relativistic damping package that involves *no* expansion in T_e/m_ec^2 and allows an arbitrary number of cyclotron harmonics to be included. The rays are traced in numerically computed, finite beta, bumpy cylinder plasma equilibria obtained from the ORNL 2-D equilibrium code. A self-consistent kinetic modeling of the formation and steady-state properties of the annulus is a long-term research effort of which the present work is a part. Here, we have examined the wave absorption characteristics of specified annuli representative of EBT devices and in particular have studied the relative opacity of EBT-I and EBT-P annuli.

4.1.5 EBT Reactors

Finally we turn to the EBT reactor studies, which play an important role in focusing theory and experiment on the long-term goals of the program. The past year has seen renewed emphasis in this area at ORNL. Considerable progress has been made in the areas of magnetic optimization, synchrotron radiation, and ring scaling. The major and long-term questions for an EBT reactor revolve around the limitations placed on core beta and ring dimensions by stability considerations. These considerations have begun to be incorporated as the theoretical models for stability have evolved.

In the coming year, we plan to incorporate these considerations (especially stability). In recognition that the stability models are still evolving, a sensitivity study has been launched to determine the implications for EBT reactors of the possible limitations imposed by the various modes. A systems approach is being employed so that the relevant engineering and physics constraints are incorporated. This involves not only the critically important integration activity, but the development of modules to treat reactor-specific calculations. For example, in studying an EBT reactor it is necessary to incorporate some (but not all) of the geometric details of the magnetic field in order to treat stability and transport adequately. This development will, of course, draw heavily on the codes and analyses previously developed. Conversely, some of the techniques being implemented for the EBT reactor studies appear to be more generally applicable, so that not only the results but also the techniques of the EBT reactor study can influence the entire EBT program.

Abstract of EBT Reactor Magnetics and Particle Confinement[44]

L. W. Owen, H. A. Uckan

Optimization of the vacuum magnetic field of an EBT reactor is investigated. Several methods of improving reactor volume utilization and single particle confinement are analyzed. These include the use of (1) a large number of sectors and/or a large mirror ratio, (2) high field Nb_3Sn or Nb_3Sn/NbTi hybrid mirror coils, (3) split-wedge mirror coils, (4) axis-encircling aspect ratio enhancement (ARE) coils, and (5) recently developed field symmetrizing (SYM) coils. Of these, particle drift orbit and 3-D tensor pressure equilibrium calculations show that the use of SYM coils in conjunction with high field mirror magnets offers the most promise of good plasma performance in reactors that are smaller (by up to 50%) than previous reference designs that did not employ supplementary coils. ARE coils also offer an attractive alternative for

improved confinement, but they do not have many of the advantages of SYM coils, particularly for reactor applications. Split-wedge mirror coils improve volume utilization and trapped particle confinement, but they do not enhance the confinement of transitional and passing particles. High field magnets improve confinement by permitting a larger mirror ratio and a larger plasma radius by virtue of their smaller cross-sectional area and higher current density. The relative merits of each magnetics configuration are discussed, including the effects on single particle confinement, reactor volume utilization, materials requirements, engineering design considerations, and reactor assembly, maintenance, and accessibility.

Abstract of Beta Limits in EBT and Their Implications for a Reactor[5]

*N. A. Uckan, D. A. Spong, D. B. Nelson**

Theoretical models indicate limits on core beta ranging from a few percent to 10-20% depending on the models and/or assumptions. Some of the parameters that enter into these beta limits are the ratio of the ring radial scale length to the average radius of curvature, $\varepsilon = \Delta/R_c$; the ratio of the cold to the hot plasma density, $f_R = n_{cold}/n_{hot}$; the ratios of the hot electron drift frequency to the ion cyclotron frequency, ω_{dh}/ω_{ci}, and to the drift Alfvén frequency, ω_{dh}/kV_A; the ratio of the ring electron temperature to the core ion temperature, T_R/T_i; the ring beta, β_R; etc.

Because of uncertainties in extrapolating results of simplified models to a reactor plasma, the above parameters that influence the beta limits cannot be determined accurately at the present time. Also, reasonable changes within the models and/or assumptions are seen to affect the core beta limits by almost an order of magnitude. Hence, at the present, these limits cannot be used as a rigid (and reliable) requirement for EBT reactor engineering considerations. However, sensitivity studies can be carried out to determine the boundaries of the operating regime and to demonstrate the effects of various modes, assumptions, and models on reactor performance (Q value). First the modes believed to limit the core beta and ring plasma performance are discussed, and the simplifications and/or assumptions involved in deriving these limits are highlighted. Then the implications of these limits for a reactor are given.

Abstract of Physics Issues of an EBT Reactor[6]

N. A. Uckan, EBT Theory Group

The EBT concept provides a unique basis for a steady-state fusion reactor in a favorable geometry, and it has the potential for a high power density with a significant Q value. The similarity of the dimensionless parameters of the present experiments to a reactor-grade plasma and observed confinement characteristics indicate plausible extrapolations and projections for a reactor; however, there are a number of physics (as well as technology) issues to be resolved. There are difficulties in extrapolating results of simplified (and/or untested) theoretical models to an actual closely coupled, hybrid (toroidal core, hot electron ring, surface plasma, etc.) geometry. There are also uncertainties in extrapolating experimental results from low density, low temperature (low beta) plasmas to predict the behavior of a burning plasma.

Basically, the plasma physics areas that influence the operating characteristics of EBTs are the following: (1) particle orbits, equilibrium, and magnetics, (2) stability boundaries of both core and ring plasmas, (3) transport scaling, (4) heating, and (5) ring-core interaction and power balance. In addition to the "conventional" mode of EBT operation, innovative ideas that enhance the reactor performance include (1) the use of supplementary (and/or trim) coils to improve confinement (and/or stability), (2) control of

*Office of Fusion Energy, U.S. Department of Energy, Washington, D.C.

ambipolar potential (and its sign, i.e., positive electric field) to enhance confinement (and to be able to burn alternative fuels, i.e., D-D, etc., in a reasonably sized reactor), and (3) the possibility of "fundamental ring" mode heating to reduce microwave frequency requirements by a factor of 2. This paper reviews each of these areas briefly and discusses their projections to a reactor.

Abstract of Prospects for EBT-R Potential Control[47]

J. R. McNally, Jr.

R. A. Dandl proposed the injection of molecular hydrogen ions into an EBT to control the plasma potential by depositing an unbalanced (net positive) charge in the plasma. Jaeger and Hedrick have demonstrated that such a positive potential in the plasma leads to a stable plasma with an order of magnitude increase in confinement times compared to negative plasmas. The EBT Reactor (EBT-R) will require very high energy H_2^+ (or D_2^+ or DT^+) ions for injection with trapping primarily by the dissociation reaction $H_2^+ + (i,e) \rightarrow H^0 + H^+ + (i,e)$. Scaling from the results of Lee for a 40-coil EBT-P, one finds that ~35-MeV H_2^+ ions would be suitable for injection into an EBT-R. The projected mean free path for 90% H_2^+ dissociation in such an EBT-P scaled up (photographic enlargement) to a 40-coil EBT-R-size device operating at 10^{20} e/m^3 is about 26 m, whereas the average H_2^+ confinement path length exceeds 44 m without electron rings present and 74 m with electron rings present in a 5° × 5° injection window, thus giving more than 90% H_2^+ dissociation in either case. This would provide about 5×10^{17} H^+/s and about 1.6 MW of plasma heating power per injector. Detailed H_2^+ orbit injection and H^+ confinement studies are necessary to ensure that an adequate injection window exists in the proposed 24-coil EBT-R design.

Abstract of Analysis of Field Error Criteria in an EBT Reactor[48]

N. A. Uckan, D. W. Swain, D. K. Lee, T. Uckan,* L. W. Owen, H. R. Gordinier*

A closed field line device, such as an EBT, is very sensitive to small perturbations in the magnetic field. The estimates of the maximum tolerable field errors ($\delta B/B$) for an EBT reactor are derived. Numerical calculations of field errors due to single coil misalignments indicate that the field line closure is most sensitive to angular misalignment of the coils. Errors in absolute spatial positions are found to have very small effects ($\delta B/B \sim 10^{-10}$–10^{-11}) provided that there is no corresponding angular misalignment. Statistical analysis of errors from N coils, assuming the errors in all N coil alignments are randomly distributed in a Gaussian fashion, is found to be in reasonable agreement with the numerical calculations. A specific example for N = 36 is given, which indicates that misalignments of 1 cm in one coil position yield an error $\delta B/B < 10^{-10}$, whereas misalignments of 1° in one coil orientation result in an error $\delta B/B \sim 10^{-4}$. Induced field errors due to ARE and SYM coils are found to be small (within 15% of the mirror field coils).

Abstract of Synchrotron Emission from the Ring Electrons in EBT[49]

T. Uckan, N. A. Uckan*

The energy spectrum of the synchrotron radiation emitted by the relativistic ring electrons in EBT has been calculated for various classes of isotropic and anisotropic ring electron distribution functions. Calculations have been carried out for present (EBT-I/S) and planned (EBT-P) experiments.

*EBT Experimental Section.

The ring temperatures in EBT-I and EBT-S are ~200 and ~500 keV, respectively. The projected ring temperature in EBT-P is ~1000-1500 keV. The calculations indicate that the radiation is predominantly in higher harmonics ($s > \gamma^2/2$) and the radiation spectrum monotonically decreases and becomes almost flat at high frequencies, as observed in the experiments. With increasing temperature and anisotropy, the total emission increases, the slope of the spectrum decreases, and the peak of the spectrum moves to higher frequency. The ratio of the extraordinary wave intensity to the ordinary wave intensity decreases with temperature but increases with anisotropy. Calculated spectra and relative intensity levels of EBT-I and EBT-S are found to be in reasonable agreement with the experimental measurements. Both measurements and calculations show that synchrotron losses are low in EBT-I and EBT-S. However, in future experiments (EBT-P, reactor, etc.), radiation losses will play an important role in determining the ring power balance. Correlations of calculated intensity variations with temperature, density, beta, anisotropy, etc., are given that can be used as a useful tool for comparison of theory and experiment, as well as in the determination of ring properties and scaling of the radiation with ring parameters.

Abstract of Synchrotron Radiation from the Hot Electron Rings in EBT[50]

N. A. Uckan, R. G. Spencer, T. Uckan†*

The spectrum of the synchrotron radiation emitted by the relativistic electron rings in EBT has been formulated. A computer code, CYCLU, has been developed for the numerical calculations for the range of frequencies (especially higher harmonics) and temperatures (~0.1-2 MeV) of interest. The analysis has been carried out for various classes of isotropic (not necessarily Maxwellian) and anisotropic ring electron distribution functions. Calculations include the radial profiles of the ring electron density and temperature (approximated from fits to the experimental data) and include consistent magnetic field modifications (magnetic well due to high beta ring) deduced from the pressure balance. The calculated spectra and emission levels for the Maxwellian distribution are in reasonable agreement with those measured, though detailed comparisons of theory and experiment have not been made. Because of the relativistic temperatures, the radiation is predominantly in higher harmonics. The spectrum of emission for each harmonic indicates broadening of individual lines with large frequency widths that cause pronounced overlapping of harmonics and results in a monotonically decreasing spectrum, as observed in the experiments.

Abstract of Physics of Hot Electron Rings in EBT: Theory and Experiment[51]

N. A. Uckan, C. L. Hedrick, G. R. Haste,‡ P. W. Baity,† D. B. Batchelor, P. M. Bieniosek,‡ L. Bighel,† S. K. Borowski, J. A. Cobble,† R. J. Colchin,† R. L. Copeland,† W. A. Davis,† R. A. Dory, H. O. Eason,† J. C. Glowienka,† D. L. Hillis,† E. F. Jaeger, A. Komori,† P. K. Richards,† D. A. Spong, T. Uckan,† T. L. White,† J. B. Wilgen†

Confinement and scaling characteristics of the high beta, hot electron rings (annuli) in EBT are studied. The rings are produced by ECH and form at the location of the second harmonic resonance. This study examines drift orbits, microwave heating, equilibrium and stability requirements of the hot electrons, and their interaction with the toroidal core plasma. Reasonable agreement is found to

*University of California at Berkeley, Berkeley, California.

†EBT Experimental Section.

‡Rensselaer Polytechnic Institute, Troy, New York.

exist among theoretical predictions, observed ring behavior, measured ring parameters, and power losses. Also analyzed is dimensionless parameter scaling of the rings, which implies favorable reactor performance.

Abstract of Role of Beta Limits on Reactor Q Value in EBT[52]

M. A. Uckan, D. A. Spong

In EBT, there are two principal plasma components: toroidal core plasma, where the fusion reactions occur, and hot electron rings, which are essential to the stability of the overall configuration. The economic viability of an EBT reactor improves significantly if $\beta_{core} > 10\%$, and average "minimum-B" stabilization requires $\beta_{ring} \geq 10\text{-}15\%$. Defining a reactor Q value that is roughly the ratio of the fusion power produced ($\propto \beta_{core}^2 B^4$) to the ring sustaining power [$\propto \beta_{ring} B^4 f(\gamma)$, where γ is a relativistic factor and $f(\gamma)$ has a broad minimum for $\gamma \sim 2\text{-}4$], one can see the relative importance of $\beta_{core}^2/\beta_{ring}$ on the reactor performance and economics. [Alternatively, $Q \propto n_{core} g(\gamma,B)/n_{ring}$.]

Theoretical models indicate limits on core beta ranging from a few percent (as a lower limit) to 10-30%, depending on the assumptions. Basically, one of the key parameters in determining limits on β_{core} is $\epsilon = \delta/R_c$ (stable if $\beta_{core} \leq \alpha\epsilon$ with $\alpha \sim 2\text{-}4$), which is roughly the ring radial scale length divided by "average" radius of curvature. Because of uncertainties in extrapolating results of simplified models to a reactor geometry, ϵ (and α) cannot be determined accurately. Also, reasonable changes within the models and/or assumptions are seen to affect the β_{core} limits by almost an order of magnitude. Hence, these limits, at the present, cannot be used as a rigid (and reliable) requirement for EBT reactor engineering considerations. However, sensitivity studies can be carried out within a reasonable parameter range to demonstrate the effects of various modes, assumptions, and models on a reactor performance. One such study has been carried out and the parametric dependence of Q on the stability boundaries has been obtained.

Abstract of A Global Transport Package for EBT Reactor Design[53]

M. R. Gordinier, N. A. Uckan

A global (0-D) transport package has been developed for the self-consistent analysis of proposed EBT reactor configurations. The model is unconventional in that (1) it allows for arbitrary density and temperature profiles and (2) all relevant physics submodels, including previously legislated parameters (such as the radial ambipolar electric field and the neutral fueling source rate), are evaluated radially. The incorporation of this 1-D information in an overall 0-D model creates a unique amalgam between computational speed and radial sophistication. Both the physics and the numerical aspects of the model will be presented.

Abstract of Optimization of EBT Reactor Magnetics[54]

L. W. Owen, N. A. Uckan

Optimization of the vacuum magnetic field of an EBT reactor is investigated. Several methods of improving reactor volume utilization and single particle confinement are analyzed. These include the use of (1) a large number of sectors and/or a large mirror ratio, (2) high field Nb_3Sn or Nb_3Sn/NbTi hybrid mirror coils, (3) split-wedge mirror coils, (4) axis-encircling ARE coils, and (5) recently developed field SYM coils. Of these, particle drift orbit and 3-D tensor pressure equilibrium calculations show that the use of SYM coils in conjunction with high field mirror magnets offers the most promise of good plasma performance in reactors that are smaller (by up to 50%) than previous reference designs that did not employ supplementary coils. ARE coils also offer an attractive alternative for improved confinement, but they do not have many of the advantages of SYM coils, particularly for reactor applications. Split-wedge mirror coils

improve volume utilization and trapped particle confinement, but they do not enhance the confinement of transitional and passing particles. High field magnets improve confinement by permitting a larger mirror ratio and a larger plasma radius by virtue of their smaller cross-sectional area and higher current density. The relative merits of each magnetics configuration are discussed, including the effects on single particle confinement, reactor volume utilization, materials requirements, engineering design considerations, and reactor assembly, maintenance, and accessibility.

Abstract of Status of the ELMO Bumpy Torus Research[55]

N. A. Uckan

Recent developments in the EBT program of experiment, theory, technology development, and reactor studies are reviewed. A 28-GHz gyrotron has been routinely operated at 200 kW (cw) on EBT-S. Operation through 200 kW shows that the electron transport in EBT-S continues to scale neoclassically. The ring power losses scale classically, and in all ECH devices ring temperatures scale with ρ_{eR}/L (where ρ_{eR} is the ring electron gyroradius and L is the magnetic field scale length). Initial steady-state, fast wave ICH experiments have been successful and show a several-fold increase in energetic ion population. Theoretical analysis of a large number of modes and ring core coupling in stability calculations indicates that a substantial, stable, finite beta operating window is available with $\beta_{core} \sim 10\%$. The coupling of the ring power balance to the core plasma beta limits, based on the present theories, is of concern for reactor optimization, and parametric studies indicate possible operating windows. The technology development for the next device, EBT-P, is progressing well, having achieved operation of the 60-GHz development gyrotron at 125 kW for 60 ms and operation of the two superconducting development magnets (7.4 T, 10,000 A/cm^2) at the design field.

Abstract of The Status of EBT Physics[56]

C. L. Hedrick

The EBT program is currently in transition from the original torus (EBT-I/S) to the next major step, EBT-P. We review the status of physics understanding and indicate the major areas of uncertainty which must be addressed by future research.

The earliest EBT experiments convincingly demonstrated the validity of the idea which motivated the EBT concept: the hot electron rings observed in the earlier ELMO experiments could provide average minimum beta to stabilize the toroidal core plasma against instabilities which hao plagued earlier bumpy tori. In the ten years since the proposal of EBT-I, the stability of the coupled ring and core plasmas has been treated in increasing detail. Nevertheless, it is possible to explain the major features of the experiments in terms of a set of ideas which have remained invariant over the past five years. The present picture is that the core plasma provides the density to stabilize the core, while the rings provide the minimum in beta necessary to stabilize the core plasma. Present theories suggest that stability can exist for core betas which lead to an attractive EBT reactor. The neoclassical theory of transport in EBT has developed to a point where it is in reasonable agreement with experiment. Because electron transport dominates the particle and energy losses in EBT, this is really a statement that electron transport is well understood. Ion transport (and heating) is less well understood, in part because it is subdominant and in part because the heating of ions by Coulomb collisions with electrons is a weak process. Correlations between theory and experiment for ion transport rest in large measure on the ambipolar electric field. Present theory yields radially resolved ambipolar potentials which are in qualitative agreement with experiment. Investigation of what might otherwise be subdominant processes is in progress to improve quantitative agreement, but transport studies would be greatly facilitated by direct ion heating. Standard EBT experiments were heated by a single

frequency of microwave power; the core plasma electrons were heated at the fundamental of the electron cyclotron frequency, and the rings formed where the applied frequency equals the second harmonic of the electron cyclotron frequency. Theoretical calculations of the deposition of power in the core, ring, and cold edge plasmas are in reasonably good agreement with experiment, as is ring power balance. In addition to standard frequency configurations, other configurations have been examined experimentally. Those involving single frequency heating indicate a simple scaling relation for the ring temperature.

While many of the features of EBT physics can continue to be explored in the present torus, the path to a reactor requires a larger torus with higher magnetic field to further explore:

- stability at higher beta,
- transport (particularly for ions),
- ring and core plasma coupling.

The EBT-P device should permit an effective examination of these issues.

4.2 TOKAMAK THEORY

The primary emphases of the ORNL Tokamak Theory Group are improving tokamak devices through confinement analysis of high beta tokamak plasmas and increasing beta through the use of beams, rf heating, pellet injection, and impurity control. Strong emphasis is placed on wall-plasma interactions and edge control. Major efforts in the study of resistive MHD fluctuations and disruptions and in the inclusion of kinetic effects on ballooning modes have added to the knowledge of MHD behavior. Kinetic studies of nonlinear stochastic effects have led to new insights into anomalous heat transfer processes. Collaboration between theorists and experimentalists, particularly in the areas of MHD fluctuations and numerical transport simulation of tokamak discharges, has resulted in major advances in the understanding of high beta plasmas.

This section is divided into six categories:

- ideal and resistive magnetohydrodynamics (MHD stability),
- kinetic modifications of MHD instabilities,
- kinetic theory, anomalous transport, and neoclassical theory,
- energetic particles, including ripple and divertor effects,
- transport simulations and plasma-wall interactions, and
- tokamak reactors.

Work done by theorists in the Tokamak Theory Group in collaboration with tokamak experimentalists is also reported in Sect. 2 of this report, especially MHD instability studies, tokamak modeling, and plasma edge effects.

4.2.1 Ideal and Resistive Magnetohydrodynamics

Equilibria that more closely match those observed experimentally than earlier calculations are being used to determine the MHD stability of the highest $\langle\beta\rangle$ ($\sim$2%) modes in ISX-B. Such equilibria are calculated to be close to marginal stability; they are unstable for toroidal mode number $n = 1$ and stable for poloidal mode number $m = 2$, 3, and 4. Inclusion of tensor pressure induced by neutral beam injection in ISX-B and use of equilibria obtained from Thomson scattering data lead to more accurate resistive MHD stability calculations. Finite beta effects are included in nonlinear studies of resistive tearing modes, and excitation of higher n modes is compared with experiment. The abstracts of papers that follow discuss the individual calculations in more detail.

Abstract of MHD Stability of Noncircular ISX-B Plasmas[57]

L. A. Charlton, R. A. Dory, J. A. Holmes, G. H. Neilson, J. L. Dunlap,* E. A. Lazarus,* R. M. Wieland, D. K. Lee*

It has been previously reported[58] that tokamak equilibria which have ISX-B-like parameters are ideal MHD unstable for circular plasmas at the highest $\langle\beta\rangle$ seen in the ISX-B device. This study is being extended in three ways: (1) the recent high $\langle\beta\rangle$ (~2%) noncircular discharges have been considered; (2) equilibria which more closely match the details of the discharge are being used; and (3) the resistive MHD formalism is being applied. The input profiles for the equilibria are consistent with Thomson scattering data, and a free boundary calculation is being done which allows direct input of the coil currents used on the device and comparison with magnetic measurements.

Although inconsistencies still exist between the equilibria and the data, the ideal growth rates calculated for low n are consistent with marginal stability for the highest $\bar{\beta}$ shots that were modeled.

The use of lower $\bar{\beta}$ equilibria in the resistive MHD codes allowed the calculation of sawtoothing behavior, where such behavior was seen experimentally, and of a continuous m = 1 mode, where such a mode was consistent with the data.

Abstract of Tensor Pressure Tokamak Equilibrium and Stability[59]

W. A. Cooper

We investigate the equilibrium and MHD stability of tokamaks with tensor pressure and examine, in particular, the effects of anisotropies induced by neutral beam injection. Perpendicular and parallel beam pressure components are evaluated by taking moments of a distribution function obtained from the solution of a Fokker-Planck equation that models the injection of high energy neutral beams into a tokamak. We numerically generate D-shaped, beam-induced, tensor pressure equilibria. From these equilibria, we find that the level perpendicular pressure contours can be quite distorted and shifted away from the outer boundary (relative to the flux surfaces), especially with perpendicular injection into broad pressure profile equilibria, and that the level parallel pressure contours undergo a smaller shift that is concentrated in the central core of the plasma. On the other hand, in equilibria with peaked pressure profiles, the pressure contours nearly coincide with the flux surfaces. In addition, a force balance relation, a representation for the poloidal beta (β_p), and the expressions for the current densities are derived from the MHD equilibrium relations for an axisymmetric tensor pressure tokamak.

A double adiabatic energy principle is derived from a modified version of the guiding center plasma energy principle. The asymptotic expansion (in large toroidal mode number n) and subsequent minimization of this energy principle yield an Euler equation from which we obtain a necessary stability criterion for the guiding center plasma to oscillations of large toroidal mode number. If we neglect the terms peculiar to the double adiabatic theory, we obtain a sufficient stability condition for the guiding center plasma. The stabilizing term due to the bending of the field lines is almost equivalent to the corresponding term in ideal MHD. The driving term is modified, however, because the pressures are no longer constant on a flux surface and the additional double adiabatic term is stabilizing. We use a shooting method to examine the stability of tensor pressure equilibria to perturbations of large toroidal mode number. We find that because the double adiabatic term inhibits perturbations in high pressure regions, the difference between the necessary and the sufficient criteria is significant for plasmas

*Tokamak Experimental Section.

susceptible to flute modes that naturally concentrate near the magnetic axis. The difference between criteria is small for ballooning stability because the pressures are weak near the edge of the plasma, where this type of mode concentrates. The critical beta values imposed by stability to ballooning modes are higher for perpendicular beam injection than for parallel beam injection or for corresponding scalar pressure equilibria with comparable pressure profiles. Perpendicular injection causes an inward displacement of the p_i surfaces with respect to the flux contours, and this displacement improves the stability conditions. The difference between the stability limits of broad, as compared with peaked, pressure profile equilibria is large for interchange-unstable plasmas and tends to coalesce for ballooning-unstable plasmas.

Finally, we apply the tensor pressure ballooning mode equation to computed equilibria that model experimentally determined ISX-B discharge profiles with high power neutral beam injection. We predict that the plasma is unstable to flutelike modes in the central core of the discharge as a result of the pressure profile peakedness induced by the beams.

Abstract of Periodic Large Amplitude MHD Activity in Beam-Heated Tokamaks[60]

J. T. Hogan

Using the $\Delta'(W)$ finite island width model we calculate the existence of large amplitude, slow (diffusion) time scale MHD activity in low beta, circular, beam-heated discharges. Large temperature gradients across the forming islands are found to drive an oscillation between 2/1 and 3/2 islands, which alternate in time. Faster (resistive tearing) time scale calculations would predict disruption if the 2/1 and 3/2 islands were to overlap simultaneously.

This "giant" periodic activity emerges from the simulation without a priori assumptions about its existence and is sensitive both to the mechanism for describing transport (as affected by islands) and to the q profile. A similar ansatz-free periodic behavior for the 1/1 sawtooth has been found by Parail and Pereversev,[61] where an alternating hollow j-reconnection cycle leads to periodic behavior. The 2/1-3/2 activity described here occurs under conditions close to disruptivity.

This low beta effect, caused by large beam-induced temperature gradients, joins a number of other beam-specific effects (Ohkawa current modification of the q profile, charge exchange recombination enhancement of radiative losses, rotation-induced modification of flux surface triangularity) which must be distinguished from authentic new high beta (or β_{pol}) phenomena. The period and amplitude are calculated to be affected by pellet deposition modifications to n_e and T_e and by the spatial distribution of the beam-induced current.

Abstract of Nonlinear Destabilization of Tearing Modes[62]

B. A. Carreras, H. R. Rosenbluth, H. R. Hicks*

We have studied the effect of a background of many modes on the growth of a tearing mode. A third-order calculation with a random phase approximation is presented for a static background. In that case, the tearing mode is further destabilized (stabilized) if the values of the nonlinearly driven modes are positive (negative). This explains the destabilization of the (m = 3;n = 2) tearing mode observed in nonlinear 3-D calculations.

Abstract of Resistive MHD Studies of High Beta Tokamak Plasmas[63]

V. E. Lynch, B. A. Carreras, H. R. Hicks, J. A. Holmes, L. Garcia

Numerical calculations have been performed to study the MHD activity of high beta tokamaks

*Institute for Fusion Studies, University of Texas, Austin, Texas.

such as ISX-B. These initial value calculations build on earlier low beta techniques, but the beta effects create several new numerical issues. These issues are discussed and resolved. In addition to time-stepping modules, our system of computer codes includes equilibrium solvers (used to provide an initial condition) and output modules, such as a magnetic field line follower and an x-ray diagnostic code.

The transition from current-driven modes at low beta to predominantly pressure-driven modes at high beta is described. The nonlinear studies yield x-ray emissivity plots which are compared with experiment.

Abstract of Finite Beta Effects on the Nonlinear Evolution of the (m = 1;n = 1) Mode in Tokamaks[64]

J. A. Holmes, B. A. Carreras, H. R. Hicks, V. E. Lynch, K. E. Rothe

The stability and evolution of ISX-B-like plasmas are numerically studied using a reduced set of resistive MHD equations. For a sequence of equilibria stable to ideal modes, the n = 1 mode changes from a tearing branch to a pressure-driven branch as β_p is increased. When this mode is unstable at low beta, it is just the (m = 1;n = 1) tearing mode. Higher n modes also become linearly unstable with increasing β_p; they are essentially pressure-driven and have ballooning character. For low values of beta the instability is best described as a β_p distortion of the (m = 1;n = 1) tearing mode. This mode drives many other helicities through toroidal and nonlinear couplings. As β_p is increased, the growth of the m = 1 island slows down in time, going from exponential to linear before reconnection occurs. If β_p is large enough, the island saturates without reconnection. A broad spectrum of other modes, driven by the (m = 1;n = 1) instability, is produced. These results agree with some observed features of MHD activity in ISX-B, as shown in Fig. 4.1.

Abstract of Rippling Modes in the Edge of a Tokamak Plasma[65]

B. A. Carreras, J. D. Callen, P. W. Gaffney, H. R. Hicks

A promising resistive MHD candidate for the underlying cause of turbulence in the edge of a tokamak plasma is the rippling instability. In this paper we develop a computational model for these modes in the cylindrical tokamak approximation and explore the linear growth and single-helicity, quasi-linear saturation phases of the rippling modes for parameters appropriate to the edge of a tokamak plasma. Large parallel heat conduction does not stabilize these modes; it only reduces their growth rate by a factor scaling as $K_\parallel^{-4/3}$. Nonlinearly, individual rippling modes are found to saturate by quasi-linear flattening of the resistivity profile. The saturated amplitude of the modes scales as m^{-1}, and the radial extent of these modes grows linearly with time due to radial $\vec{E} \times \vec{B}_0$ convection. This evolution is found to be terminated by parallel heat conduction.

Abstract of Nonlinear Analysis of Disruptions in the JIPP T-II Tokamak[66]

H. R. Hicks, B. A. Carreras, J. A. Holmes, V. E. Lynch

A comparison is made between results of the profile control experiments on the JIPP T-II tokamak and those of the time evolution of tearing modes. Over a wide range of conditions, nonlinear initial value tearing mode calculations are consistent with experimental results. In particular, the time scale of soft disruptions, as reflected in the negative voltage spikes, given by the tearing mode analysis agrees with that obtained experimentally.

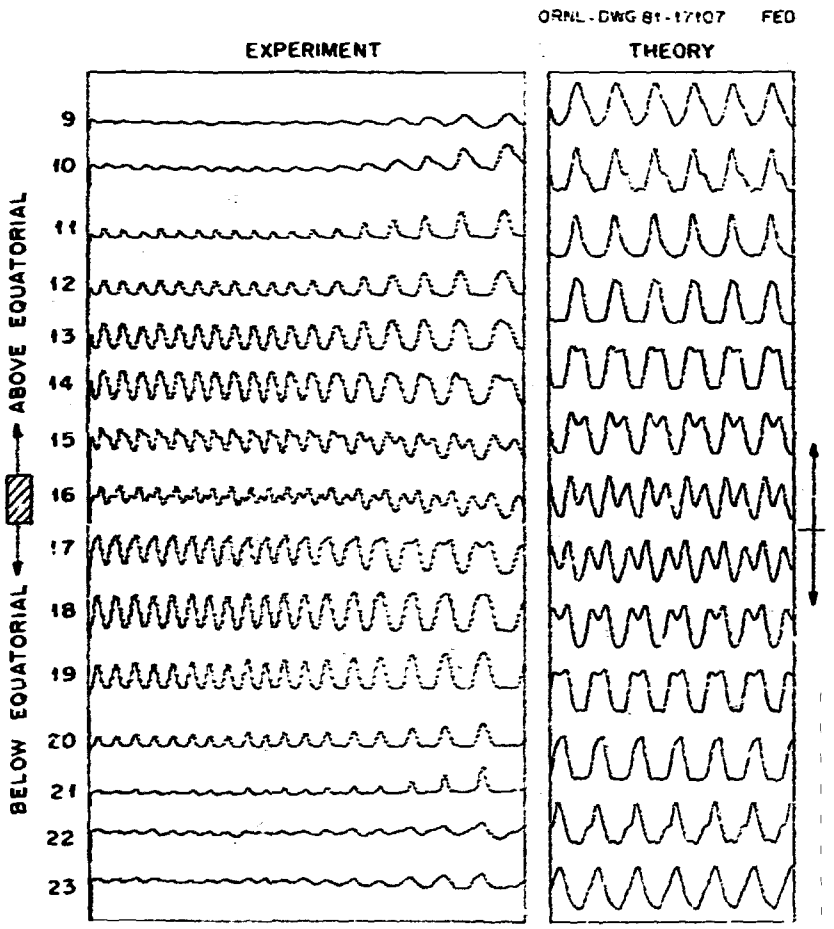

Fig. 4.1. Comparison of $\tilde{x}$ waveforms. (Experimental waveforms are from shot 34600 on ISX-B, for the time from 242 to 243.33 ms.)

Abstract of Resistive Modes in Tokamak-Stellarator Configurations[67]

H. R. Hicks, B. A. Carreras, L. Garcia, J. A. Holmes, V. E. Lynch

The nonlinear evolution of tearing modes is investigated for a range of tokamak-stellarator configurations. The tokamak with a small external rotational transform represents one extreme. It is found that the average method[68] for calculating stellarator corrections is accurate when the toroidal winding number of the helical coil is large, but it yields saturated magnetic island widths which are too small for low toroidal winding numbers. At the other extreme is the low current stellarator, where the fields are dominated by the external coils rather than by the plasma. To numerically study this range of cases, we use a cylindrical configuration with one or more external helical magnetic field components due to external currents. A self-consistent numerical 3-D equilibrium is used as the initial condition.

Abstract of Resistive Modes in a High Beta Tokamak[69]

J. A. Holmes, B. A. Carreras, L. A. Charlton, H. R. Hicks, V. E. Lynch

The stability and evolution of the (m = 1;n = 1) mode in tokamaks having finite beta are studied numerically using a reduced set of resistive MHD equations. Particular attention is given to the effects of beta, q profile, and plasma cross-section shape. The results of these studies agree with the systematics of the observed MHD activity in ISX-B. Detailed comparison of theoretical and experimental x-ray and magnetic loop signals shows excellent agreement.

Abstract of Fast Moment Equation Method for Solving the Grad-Shafranov Equation[70]

H. K. Meier

A set of nested toroidal plasma surfaces can be represented by expressions of the form

$$R = \sum_{n=0}^{\infty} R_n(\psi)\cos n\theta \ ,$$

$$Z = \sum_{n=1}^{\infty} Z_n(\psi)\sin n\theta \ ,$$

where ψ is the poloidal flux function. It is found that with a good choice of poloidal angle θ, only a few harmonics are required. For an elliptical plasma (R_0,R_1,Z_1) are sufficient, and for a D-shaped plasma going to the third harmonic is adequate.

Several methods exist for determining the harmonics; one is straightforward insertion into the Grad-Shafranov equation. Another fast method is to use a variational principle to obtain a set of coupled, second-order, ordinary differential equations for the amplitude.[71] A still faster method is to obtain a set of moment equations by a weighted integration of the Grad-Shafranov equation from the magnetic axis to an arbitrary contour. The integral is zero; i.e.,

$$\int_0^{\psi} d\psi' \oint d\theta G(R,Z)\left(\Delta^*\psi' + 4\pi R^2 \frac{dp}{d\psi'} + f\frac{df}{d\psi'}\right) = 0 \ , \ \ldots \ , \quad (4.2.1)$$

where (R,Z) are functions of ψ' and θ, and (p,f) depend only on ψ'. Two integrations by parts alter the integral so that the Δ^* operator is applied to G rather than ψ. In general, a surface term arises in the process which contains in the denominator J, the Jacobian of the transformation from (R,Z) to (ψ,θ) coordinates. The variational method also has a term containing J in the denominator. For finite beta plasmas there is a large variation in J with θ which leads to serious difficulties for analytical work and time-consuming θ integrations for numerical methods.

A set of G functions for Eq. (4.2.1) can be found which eliminates the surface term. The result is a set of moment equations which depends on the (R_n,Z_n) amplitudes, but not on any of their derivatives, and on another set of functions $H_j(\psi)$, whose derivatives with respect to ψ depend again only on the (R_n,Z_n) amplitudes.

This formulation eliminates the need for any numerical θ integration. It also simplifies analytical work, since there are known representations for the amplitudes that are poor for their derivatives.

4.2.2 Kinetic Modifications of MHD Instabilities

On general theoretical grounds and in particular at ORNL, due to the observations of ISX-B, there has been an awareness that the set of ideal MHD equations is too idealized to describe the experiment. These equations have been generalized to include the finite Larmor radius of the bulk and the beam species, n_i [= (d ln T_i/d ln n)] effects, magnetic drift resonances, and toroidal plasma rotation. Results show that in ISX-B, ballooning modes are stabilized except for rather low mode numbers $n < 10$, even for the highest values of

poloidal beta achieved. Further work on rotation and drift resonance effects is in progress.

Abstract of Finite Larmor Radius Stabilization of Ballooning Modes in Tokamaks[72]

K. T. Tsang

A ballooning mode equation that includes full finite Larmor radius effects has been derived from the Vlasov equation for circular tokamak equilibria. A numerical solution of this equation shows that finite Larmor radius effects are stabilizing.

Abstract of Neutral Beam Effects on Tokamak Ballooning Mode Stability[73]

W. A. Cooper, G. Bateman, D. B. Nelson,† T. Kammash‡*

An equation is derived that gives a necessary, as well as sufficient, stability criterion for the guiding center plasma to instabilities of large toroidal mode number. This equation is applied to D-shaped scalar pressure and beam-induced tensor pressure tokamak equilibria of aspect ratio 3. The tensor and scalar pressure equilibria generated have comparable pressure profiles. The tensor pressure equilibria are valid in the limit that the beam particle injection energy $E_0 >> E_c$ and $(\gamma_{eff} - 1) << 1$, where E_c is the critical energy. The scalar pressure equilibria are valid when $E_0 \leq E_c$. Therefore, the effects of neutral beam injection on the stability of a tokamak are bracketed. It is found that quasi-perpendicular injection induces a displacement of the $p_\perp$ contours with respect to the flux surfaces away from the destabilizing curvature region, which enhances the stability of tensor pressure equilibria over comparable scalar pressure equilibria. Also found is a distinct difference between the necessary and sufficient stability limits when the most unstable modes concentrate in regions of relatively high pressure. Both stability criteria coalesce when ballooning modes, which appear near the edge of the plasma where the pressure is low, dominate.

Abstract of Stabilization of Ballooning Modes by Energetic Particles in Tokamaks[74]

K. T. Tsang, D. J. Sigmar

A ballooning eigenmode equation, taking into account the presence of energetic particles in a tokamak, is derived from the Vlasov equation. The numerical solution of this equation demonstrates that the finite Larmor radius effect of the energetic particles can have a strong stabilizing effect on ballooning modes. This result supports the observed lack of high mode number ballooning instabilities in ISX-B injection experiments.

Abstract of Diamagnetic Drift Stabilization of Ballooning Modes in Tokamak Geometry[75]

W. A. Cooper, K. T. Tsang

The stabilizing impact of the finite thermal ion gyroradius on the ballooning mode stability of realistic axisymmetric toroidal equilibria is examined. The diamagnetic drift frequency effectively stabilizes modes with $n > 30$-50 in ISX-B-like equilibria.

Abstract of Safety Factor Profile Optimization of High n Ballooning Mode Stability of Tokamaks[76]

W. A. Cooper

Conditions of improved stability to high n ideal MHD modes are obtained with equilibria generated by flattening and raising the safety factor (q) profile. Flat q profiles shorten the connection length for high n ballooning modes and diminish the destabilizing impact of the geodesic curvature. High values of q stabilize the residual interchange modes.

---

*Georgia Institute of Technology, Atlanta, Georgia.

†Office of Fusion Energy, U.S. Department of Energy, Washington, D.C.

‡University of Michigan, Ann Arbor, Michigan.

Abstract of Diamagnetic Drift Frequency Effects on Tokamak Ballooning Stability[77]

W. A. Cooper

The stabilizing effect of finite ion diamagnetic drift frequency on ballooning modes in realistic tokamak geometry is investigated. The inclusion of temperature gradient effects can significantly enhance the stability of a tokamak with broad mass density profiles.

4.2.3 Kinetic Theory, Anomalous Transport, and Neoclassical Theory

With a recently developed nonlinear Vlasov (gyrokinetic) code modeling the strong turbulence effects on the electrons with a renormalized orbit propagator, both electrostatic and finite beta electromagnetic drift modes have been investigated. Thus, the self-consistent anomalous transport calculations by Hirshman and Molvig can be rigorously analyzed, leading to relevant quantitative improvements in the use of the renormalized propagator for electron diffusion, inclusion of electron temperature gradients, and recovery of inverse proportionality of electron diffusion with density (Alcator scaling) for the electromagnetic case. Analytically, this theory has been applied to compare its prediction of the anomalous electron heat transport with tokamak experimental results. One finds consistency with the presumption that electromagnetic drift wave turbulence contributes substantially to that anomalous heat loss.

A further frontier effort in strong turbulence theory relates to the spectral analysis of noisy nonlinear maps, leading to a linear equation for the distribution function of the spectrum.

Several contributions to linear kinetic theory have led to publications dealing with kinetic effects on ballooning modes and low mode number radial eigenmodes of the shear Alfvén wave in tokamaks, modes destabilized by particles faster than the Alfvén speed.

In neoclassical theory, a major invited review paper on impurity transport appeared in *Nuclear Fusion*. A special section of this paper is devoted to the effects of momentum input and plasma rotation on impurity confinement. Transport modeling of these effects has started for ISX-B. Inclusion of neutral beam heating effects in neoclassical calculations leads to predictions not observed in ISX-B, implying a neoclassical current much lower than that observed. Neoclassical theory is also used to calculate density profiles used to predict ideal MHD stability in reactor-like regimes.

Abstract of Universal Mode with Diffusive Electrons: Linear Instability and Nonlinear Saturation[78]

C. O. Beasley, Jr., E. Molvig, W. I. van Rij

The effects of spatial electron diffusion on the stability properties of the universal drift mode in a sheared magnetic field are studied using an initial value code, TEDIT.[79] Previous studies of this problem by Hirshman and Molvig relied on an approximation to the electron resonance function equivalent to making a Krook approximation for the spatial diffusion operator, $D\,\partial^2/\partial x^2$. The present work treats the diffusion operator precisely and also allows the treatment of a realistic parallel velocity dependence of the diffusion coefficient, $D = D(v_\parallel)$. For the case of a velocity-independent diffusion coefficient, the qualitative features found by Hirshman and Molvig are observed. The modes with $k_y \rho_i > 1$ destabilize at small values of the diffusion coefficient and saturate at higher values, corresponding to several orders of magnitude in D. There are quantitative discrepancies with the previous work that, near the saturation point, can be accounted for reasonably well by a simple asymptotic theory. However, when the code uses a more realistic form, $D = D_0 \times (v_e/|v_\parallel|)\exp(-v_c^2/v_\parallel^2) + D_c$, where D_c corresponds to the (small) collisional diffusion and D_0 parametrizes the turbulence level, then a quantitative difference is observed. Instability persists down to zero turbulence

levels, $D_0 = 0$. This is essentially a linear instability due to collisional diffusion alone.

Abstract of TEDIT, a Computer Code for Studying the Time Evolution of Drift Instabilities in a Torus[79]

W. I. van Rij, C. O. Beasley, Jr.

TEDIT is an initial value program which calculates the time evolution of drift instabilities in a toroidal plasma with a slab geometry approximation. The linearized electron and ion kinetic equations are advanced in time, so that it is possible to include precisely physical effects which, without further approximation, make the formulation of a tractable eigenvalue problem for the electric and magnetic fields impossible. For example, TEDIT can treat exactly the electron diffusion arising from intrinsic orbital stochasticity or collisions, and it can almost completely relax the small $k_x \rho_i$ approximation for the ion gyrokinetic equation. TEDIT also has electrostatic, finite beta, and adiabatic electron options.

Regardless of the initial conditions, the most unstable eigenmode dominates the long-time solution, at which time the distributions and fields all vary like $\exp(-i\omega t)$. The establishment of this eigenmode and the evaluation of its eigenfrequency ω are achieved by continuing the TEDIT calculation until $\partial[\ln \phi(x,t)]/\partial t$ is independent of x and t. The electrostatic potential ϕ and the vector potential $A_\parallel$ are calculated from quasi-neutrality and Ampère's law, respectively.

Abstract of Numerical Simulation of Finite Beta Nonlinear Drift Modes[80]

C. O. Beasley, Jr., K. Molvig, W. I. van Rij

Using a diffusion operator to model electron stochasticity, we combine Ampère's law with Poisson's equation to calculate finite beta effects on the universal mode. We have therefore relaxed the Krook approximation for the renormalized driving term in the drift kinetic equation and also the assumed proportionality of $A_\parallel$ to ϕ, as done in the analytic calculation. We find that this assumption is not justified, but we nevertheless obtain Alcator-type scaling of the saturation mechanism for these modes, with the enhanced shear damping resulting from the finite beta effects. This is shown in Fig. 4.2 for two different poloidal wave numbers for a given level of stochasticity.

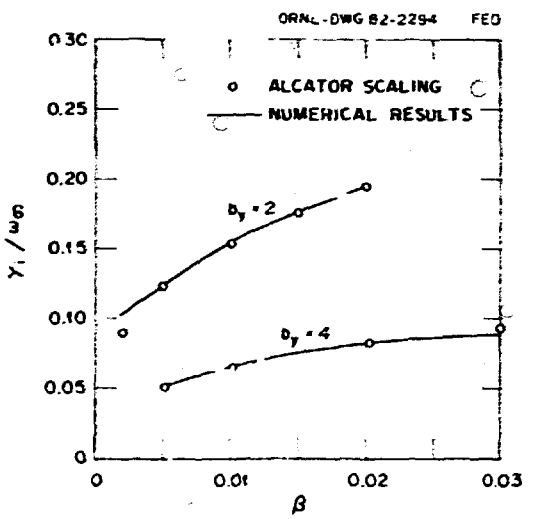

Fig. 4.2. Shear damping as a function of beta.

Abstract of Self-Consistent Spectrum of Electrostatic Drift Wave Fluctuations Due to Electron Phase Space Correlations in a Sheared Magnetic Field[81]

S. P. Hirshman, P. H. Diamond

The spectrum of electrostatic universal mode fluctuations due to electron phase space correlations (clumps) in a sheared magnetic field is self-consistently calculated. The pair correlation equation for electrons in a sheared field is derived and renormalized, and an approximate solution for the correlation function is obtained. Using the density

correlation function as a source term in Poisson's equation, the renormalized dielectric operator is inverted to obtain the turbulent spectrum. Self-consistency is imposed by requiring that the diffusion coefficient derived from the calculated spectrum equal that used to obtain the spectrum originally. The diffusion coefficient obtained in this way is in close agreement with that calculated from 1-point turbulence theory. The calculated spectrum is rapidly convergent for large wave numbers.

Abstract of Spectral Analysis of Noisy Nonlinear Maps[82]

S. P. Hirshman, J. C. Whitson

A path integral equation formalism is developed to obtain the frequency spectrum of nonlinear mappings exhibiting chaotic behavior. The 1-D map, $x_{n+1} = f(x_n)$, where f is nonlinear and n is a discrete time variable, is analyzed in detail. This map is introduced as a paradigm of systems whose exact behavior is exceedingly complex, and therefore irretrievable, but which nevertheless possess smooth, well-behaved solutions in the presence of small sources of external noise. A Boltzmann integral equation is derived for the probability distribution function p(x,n). This equation is linear and is therefore amenable to spectral analysis. The nonlinear dynamics in f(x) appear as transition probability matrix elements, and the presence of noise appears simply as an overall multiplicative scattering amplitude. This formalism is used to investigate the band structure of the logistic equation and to analyze the effects of external noise on both the invariant measure and the frequency spectrum of x_n for several values of $\lambda \in [0,1]$.

Abstract of Destabilization of Low Mode Number Alfvén Modes in a Tokamak by Energetic or Alpha Particles[83]

K. T. Tsang, D. J. Sigmar, J. C. Whitson

With the inclusion of finite Larmor radius effects in the shear Alfvén eigenmode equation, the continuous Alfvén spectrum, which has been extensively discussed in ideal MHD, is removed. Neutrally stable, discrete radial eigenmodes appear in the absence of sources of free energy and dissipation. Alpha (or energetic) particle toroidal drifts destabilize these modes, provided the particles are faster than the Alfvén speed. Although the electron Landau resonance contributes to damping, a stability study of the parametric variation of the energy and the density scale length of the energetic particles shows that modes with low radial mode numbers remain unstable in most cases. Since the alpha particles are concentrated in the center of the plasma, this drift-type instability suggests anomalous helium ash diffusion. Indeed, it is shown that stochasticity of alpha orbits due to the overlapping of radially neighboring Alfvén resonances is induced at low amplitudes, $e_i\phi/T_i \geq 0.05$, implying a diffusion coefficient $D_r^a \geq 4.4 \times 10^3$ cm^2/s.

Abstract of Poloidal Satellite Coupling in Low Mode Number Alpha Particle Instability[84]

D. J. Sigmar, K. T. Tsang, J. C. Whitson

Anomalous outward alpha particle diffusion is an important piece of reactor dynamics. It has been shown previously that the low mode number shear Alfvén wave [with (m,ℓ) chosen such that ℓq - m ≠ 0 everywhere in the plasma] can be destabilized by the alpha density gradient. While the radial eigenmodes in the background plasma are only weakly affected by toroidal corrections, we find that due to the $v_{D\alpha} \sim B \times \nabla B$ velocity of the alpha particles, their response to a fundamental mode number occurs through (m ± 1) in leading order in an expansion in $v_{D\alpha}$. The diagonal response (m) enters only to second order in $(v_{D\alpha}/\omega_A r)$, where ω_A is the Alfvén frequency and r the minor plasma radius. Including the satellites leads to three fourth-order coupled ordinary differential equations for the complex eigenfunctions and eigenvalues. A numerical method has been developed to solve this system and

study its stability properties for a sequence of spreading alpha profiles.

Abstract of Neoclassical Transport of Impurities in Tokamak Plasmas[85]

S. P. Hirshman, D. J. Sigmar

Tokamak plasmas are inherently composed of multiple ion species. This is due to wall-bred impurities and, in future reactors, will result from fusion-born alpha particles. Relatively small densities n_I of highly charged nonhydrogenic impurities can strongly influence plasma transport properties whenever $n_I e_I^2/n_H e^2 > (m_e/m_H)^{1/2}$. The determination of the complete neoclassical Onsager matrix for a toroidally confined multispecies plasma, which provides the linear relation between the surface-averaged radial fluxes and the thermodynamic forces (i.e., gradients of density and temperature and the parallel electric field), is reviewed. A closed set of 1-D moment equations is presented for the time evolution of thermodynamic and magnetic field quantities which results from collisional transport of the plasma and 2-D motion of the magnetic flux surface geometry. The effects of neutral beam injection on the equilibrium and transport properties of a toroidal plasma are consistently included.

Abstract of Temperature Dependence of the Electron Thermal Conductivity Coefficient Inferred From Neutral Beam Injection[86]

S. P. Hirshman, K. Molvig

It is shown that the radial variation of the electron-ion temperature ratio induced by neutral beam injection in PLT could account for the observed spatial dependence of the electron thermal conductivity coefficient. Quantitative evaluations using the experimental temperature and electron thermal conductivity (χ_e) profiles show consistency of the measured data with the temperature scaling of a finite beta drift wave turbulence model and also demonstrate the failure of a simple electron temperature power law scaling for χ_e.

Abstract of Plateau Diffusion Coefficient for Arbitrary Flux Surface Geometry[87]

H. K. Meier, S. P. Hirshman, D. J. Sigmar, L. L. Lao

A relatively simple but accurate representation has been developed for magnetic flux surfaces; it is valid for finite beta and it describes configurations with both ellipticity and D-shape. This representation has been applied to the computation of the diffusion coefficient in the plateau regime.

Abstract of Neoclassical Current Effects in Neutral-Beam-Heated Tokamak Discharges[88]

J. T. Hogan

There is a long-standing prediction from neoclassical theory that strong contributions to the toroidal current should be driven by friction between trapped and passing particles when β_{pol} exceeds $\sqrt{R/a}$ in a tokamak. A number of neutral beam heating experiments can now produce such parameters, and it is of interest to calculate the behavior which should occur in this regime to determine the feasibility of using such a "bootstrap" current as a steady-state tokamak current source. It is found that the neoclassical current should be large enough to reverse the external loop voltage for typical experimental parameters (ISX-B, in particular) in cases where the total current is fixed and to produce a detectable excess of total current above the preprogrammed (demand) value in cases where the loop voltage is regulated. Other manifestations of such a current should be either a sharp rise in the central q value (producing a cessation of internal m = 1 and m = 2 MHD activity), with an enhancement by two orders of magnitude of ion thermal conductivity (due to the formation of a hollow current density profile and a consequent drop in local values of the poloidal magnetic field in the central plasma region), or an enhanced tendency for disruption (arising from magnetic reconnection in hollow profile equilibria). Since these gross manifestations are absent in a wide range of experiments on

ISX-B, as reported earlier, the conclusion is that the neoclassical current, if present, can have a value no larger than 25% of its theoretically calculated value. Since the neoclassical particle (Ware) pinch is strongly related to the neoclassical current in the theory (Onsager reciprocity), the existence of the particle pinch is thus called into question.

Abstract of Neoclassical Resistive q(ψ)-Conserving Tokamak Equilibria[89]

*L. A. Charlton, D. B. Nelson**

In previous studies of the plasma properties required to give resistive equilibrium and preserve ideal MHD stability, it was found that for the highest $\tilde{\beta}$ stable equilibria, a hollow temperature profile resulted.[90] Since alpha particles should preferentially leave their energy at the pressure peak in a reactor-like plasma, these hollow temperature profiles would appear to be inconsistent with such a plasma. Spitzer resistivity (with and without neoclassical corrections[91]) was used. For a well-behaved reactor (i.e., one not beset with turbulence or other anomalous transport phenomena), a full neoclassical treatment would be appropriate because of the low collisionality. Starting with neoclassical theory, a differential equation for the density (with electron temperature as input) can be found which gives the density profile required for resistive equilibrium satisfying $\partial q/\partial t = 0$. This differential equation has been used to seek regions of parameter space where resistive equilibrium, ideal MHD stability, and reactorlike temperature profiles can simultaneously be found. The only parameter region found so far has $T_i > T_e$ and corresponds in some sense to the "hot ion mode,"[92] which is unfortunately strongly affected by losses from field ripple.[93] So far, then, the search for resistive equilibria stable to ideal modes at moderately high beta has not led to completely acceptable configurations.

4.2.4 Energetic Particles

Work in the area of energetic particles included constrained ripple optimization of tokamak bundle divertors, ISX-B ripple studies (toroidal field ripple, bundle divertors, ripple injection), examination of counter-injection into ISX-B, and orbit topology for charge exchange analysis. A fundamental paper on alpha particle thermalization with large banana widths appeared in *Nuclear Fusion*.

Abstract of Numerical Simulations of the Bundle Divertor[94]

T. C. Howe, A. J. Wootton†

A 1-D transport model has been used to calculate the effect of a bundle divertor on a tokamak plasma. A parallel loss term is included to simulate the flow along field lines to the divertor. This term includes the magnetic geometry and effects of an electrostatic sheath at the target.

The exhaust efficiency is determined by the competing processes of perpendicular transport and parallel flow. To explain the experimental results obtained on DITE it is necessary for the diffusion coefficient D to increase with minor radius. Both $D = k/n_e$ and $D = k[1 + 10(r/a)^2]/\bar{n}_e$ predict the results within experimental errors. The latter form is preferred because it can also predict the observed density profiles in high density, nondiverted plasmas in ISX-B. The former expression results in profiles which are too broad.

The plasma source term is determined from recycling at the walls and limiters and from the external gas input. To explain the density decay experiments on DITE, and also the small additional external gas feed required when the divertor is operated, the recycling

*Office of Fusion Energy, U.S. Department of Energy, Washington, D.C.

†Tokamak Experimental Section.

coefficient from the titanium limiter must be ~0.5.

Attempts have been made to predict the effects of the ISX-B bundle divertor. Using the same model which correctly predicts the experimental results from DITE, particle exhaust efficiencies of 10% and energy exhaust efficiencies of 25% are found. However, a different functional form of D can reduce these efficiencies by a factor of ~2, while leaving the predicted profiles unchanged within typical experimental errors. The difference between the two cases is in the magnitude of the source term, emphasizing the need for experimental measurements of the total ionization source.

Abstract of Constrained Ripple Optimization of Tokamak Bundle Divertors[95]

L. M. Hively, J. A. Rome, V. E. Lynch, J. F. Lyon,† R. H. Fowler, Y-K. M. Peng,* R. A. Dory*

Magnetic field ripple from a tokamak bundle divertor is localized to a small toroidal sector and must be treated differently from the usual (distributed) toroidal field (TF) coil ripple. Generally, in a tokamak with an unoptimized divertor design, all of the banana-trapped fast ions are quickly lost due to banana drift diffusion or to trapping between the 1/R variation in $|\vec{B}| \equiv B$ due to the divertor.

Studying the full 3-D shape of the B surfaces allows quick evaluation of many inferior designs. For designs which eliminate any large maxima in B, low on-axis ripple is a good indicator of avoiding deleterious effects due to the divertor. However, this must be achieved while satisfying many engineering constraints.

A computer code has been written to optimize automatically on-axis ripple subject to these constraints, while varying up to nine design parameters. Optimum configurations have low on-axis ripple (<0.2%) so that, now, most banana-trapped fast ions are confined. Only those ions with banana tips near the outside region ($|\theta| < 45°$) are lost. However, because finite-size TF coils have not been used in this study, the flux bundle is not expanded.

Abstract of Fast Ion Thermalization in Noncircular Tokamaks with Large-Banana-Width Effects[96]

L. M. Hively, G. H. Miley,* J. A. Rome*

Fusion product thermalization and heating are calculated on the assumption of collisional slowing-down. The present analytical model describes fast ion orbits and their distribution function in realistic, high beta, noncircular tokamak equilibria. The Fokker-Planck equation is bounce-averaged over the large-banana-width orbits after the variables have been transformed to the constants-of-motion space. First orbit losses, trapping effects, and slowing-down drifts are fully treated. By solving a 3-D (+ time) partial differential equation, it is possible to obtain an invariant of the slowing-down process, μ/E = (magnetic moment)/energy = const, and explicit expressions for the slowing-down drifts. Large-banana-width effects give rise to a net co-going alpha particle current. The large-banana-width orbits smear the energy deposition over large regions of the plasma. This causes the in situ heating rates to be 20-25% above the flux-surface-averaged rates on axis but enhances the edge heating ≥10-fold over in situ deposition. While this result implies reduced alpha ash accumulation on axis, the reduced heating rate makes startup and maintenance of ignition more difficult.

---

*Fusion Engineering Design Center.
†Tokamak Experimental Section.

Abstract of Using a Constants-of-Motion Space to Clarify Measurements Involving Energetic Ion Orbits in Tokamaks[97]

J. A. Rome, J. F. Lyon, R. H. Fowler*

In tokamaks with low plasma current energetic ion guiding center orbits can have large deviations from a poloidal flux surface. Analyses of the fast ion orbit topology in a local constants-of-motion space (ε,μ,P_ϕ) and in a more physical space ($R,v_\parallel/v,\varepsilon$) are used to define the wall loss regions, the trapped particle regions, and the various types of fast ion orbits that must be taken into account in interpreting high energy charge exchange or neutron measurements in tokamaks.

Abstract of FLP: A Field Line Plotting Code for Bundle Divertor Design[98]

C. Puchti†

A computer code was developed to aid in the design of bundle divertors. The code can handle discrete toroidal field coils and various divertor coil configurations. All coils must be composed of straight line segments. The code runs on the PDP10 and displays plots of the configuration, field lines, and field ripple. It automatically chooses the coil currents to connect the separatrix produced by the divertor to the outer edge of the plasma and calculates the required coil cross sections. Several divertor designs are illustrated to show how the code works.

4.2.5 Transport Simulations and Plasma-Wall Interactions

A variety of sophisticated transport codes exists. These codes facilitate the data analysis needed by the experimental group and are used in specific ISX-B transport modeling, generic tokamak plasma modeling, and specialized reactor modeling for exploring the approach to ignition and reactor operating space. Results of studies using these codes in ISX-B discharge studies, including effects of beam-induced currents or toroidal flow, are given in this section. The implications of high power level injection, with respect to the disappointingly slow growth of beta with increased power, are discussed.

Abstracts of several papers dealing with transport modeling of impurity control and effects of low energy electron capture collisions at the plasma edge are given here. The effects of neutral beams are included. The impurity transport code IMPTAR, capable of treating noncoronal effects, multiple charge states, and impurity-impurity collisions, now contains an upgraded state-of-the-art oxygen atomic physics model, which can successfully model the argon puff experiment in ISX-B.

Abstract of Developments in Tokamak Transport Modeling[99]

W. A. Houlberg, S. E. Attenberger, L. L. Lao

A variety of numerical methods for solving the time-dependent fluid transport equations for tokamak plasmas is presented. Among the problems discussed are techniques for solving the sometimes very stiff parabolic equations for particle and energy flow, treating convection-dominated energy transport that leads to large cell Reynolds numbers, optimizing the flow of a code to reduce the time spent updating the particle and energy source terms, coupling the 1-D flux-surface-averaged fluid transport equations to solutions of the 2-D Grad-Shafranov equation for the plasma geometry, handling extremely fast transient problems such as internal MHD disruptions and pellet injection, and processing the output to summarize the physics parameters over the potential operating regime for reactors. Emphasis is placed on computational efficiency in both computer time and storage requirements.

---

*Tokamak Experimental Section.

†Student, Cornell University, Ithaca, New York.

Abstract of Transport Study of ISX-B Flux-Conserving Tokamak Heating Scenarios[100]

*L. A. Charlton, R. A. Dory, D. J. Sigmar, D. W. Swain**

Theoretically, one way to achieve high $\bar{\beta}$ in advanced devices is through a flux-conserving tokamak (FCT) sequence of equilibria. The recent achievement of high $\bar{\beta}$ in the ISX-B device[101] by strong beam heating (such that $\tau_E \ll \tau_s$, the classical skin time, was satisfied) suggests a detailed numerical study and comparison with the earlier analytic FCT theory in order to better understand the heating process and possible $\bar{\beta}$ limits. For the resistive diffusion of $q(\psi)$ the 1-D theory of Nelson and Grad[102,103] is used. Energy and particle transport are described by simple equations containing radially varying heat and particle sources and appropriate bulk confinement times. These transport equations are coupled with a free boundary equilibrium code capable of time-dependent shaping of the flux surfaces and plasma current, with the plasma position kept constant. Results confirm the existence of approximately flux-conserving regimes for ISX-B-like parameters, as long as only classical field diffusion processes are admitted.

Abstract of Effects of Flow and Beam-Induced Current on ISX-B Free Boundary Equilibrium[104]

J. K. Munro, Jr., J. T. Hogan, G. H. Neilson†

Toroidal flow or beam-induced currents could have a significant effect on equilibrium in ISX-B high beta experiments. Flow velocities in the relevant range (5×10^6 cm/s < v_ϕ < 4×10^7 cm/s) would increase the triangularity and hence tend to stabilize ballooning interchange modes. Current density profiles, if broadened by the beam-induced current, however, would degrade tearing stability owing to concomitant steep edge gradients. A 1½-D transport code[105,106] has been modified to describe the ISX-B free boundary equilibrium in greater detail. Code comparisons with ISX-B magnetic data will be presented for both circular and D-shaped configurations.

Abstract of Rotation and Island Effects in Tokamaks with High Power Neutral Beam Heating[107]

J. T. Hogan

The study of beta limits in tokamaks with neutral injection has disclosed a slower-than-hoped-for growth in beta as injected power is raised. While attention is focused on the stimulation of new modes to explain this possible saturation (e.g., hybrid tearing/ballooning), it should be reemphasized that neutral injection can introduce important new effects at high power level which are unrelated to beta. We discuss two of these,

(1) the effect of toroidal flow on equilibrium and stability, and
(2) new MHD behavior resulting from large beam-produced temperature gradients,

and present results for typical parameters of the ISX-B tokamak.

Abstract of Halo Neutral Population in Beam-Heated Discharges[108]

G. G. Kelley‡ J. T. Hogan

Parasitic thermal ("halo") neutrals, produced by charge exchange trapping of injected neutral beams, can degrade heating efficiency through enhanced charge exchange loss and impurity recombination radiation. We present an improved estimate for the magnitude of the halo neutral density in noncircular ISX-B high power discharges. The neutral atom section of the NFREYA beam deposition and orbit code[109] has been coupled with a 3-D Monte Carlo code description of halo neutral

*EBT Experimental Section.
†Tokamak Experimental Section.
‡Consultant, Kingston, Tennessee.

transport. Preliminary calculations suggest a significant increase in the flux-surface-averaged halo density with respect to earlier treatments. This effect could be important in orbit following codes for nonsymmetric configurations; the "Russian roulette chamber loading" for charge exchange will be biased incorrectly in a flux-averaged treatment.

Abstract of Transport Modeling of Impurity Control by Direct Momentum and Inertial Effects[110]

D. J. Sigmar, H. C. Howe

The unidirectional momentum input due to beams has been shown to affect impurity transport in tokamaks in two distinct ways. One is due to the direct effect on the momentum balance[111] of the beam source, the other to the centrifugal effect of the ensuing plasma rotation.[112] Rough 0-D analytic criteria are known for impurity flux reversal by each method separately and with respect to each other.[85]

In this paper, a 1½-D transport code with appropriate recycling boundary conditions is used to model both effects in an ISX-B-like plasma. The background plasma is modeled comprehensively (i.e., including beam deposition and anomalous electron transport), but impurity transport is restricted to neoclassical theory. Rather than assuming a specific momentum drag mechanism, impurity reversal is studied as a function of the drag frequencies.

Abstract of The Effects of Low Energy Electron Capture Collisions ($H_0 + C^{n+}$) on the Particle and Energy Balance of Tokamak Plasmas[113]

J. T. Hogan

To illustrate the way in which atomic data provide enlightenment in the search for understandable (and thus extrapolatable) confinement models, we consider electron capture collisions involving H_0 and multiply charged ions. In this discussion attention will be given to applications of data involving $H_0 + C^{n+} \rightarrow H^+ + C^{(n-1)+}$ reactions with energy 10 eV to 2 keV. This energy range is typical of the plasma edge in present devices. The reasons for choosing only carbon for discussion are as follows.

(1) As a result of recent theoretical and experimental progress, some reported at this conference, the electron capture rates for the full suite of charge states ($C^{2+} \rightarrow C^{6+}$) of interest in the plasma edge may be estimated for the first time.

(2) Electron impact ionization cross sections have been measured for these ions, and the use of semiempirical ionization rates is supported by direct measurement.

(3) The cross sections for electron capture have been found to be sufficiently large that, taken together with the typical measured H^0 concentrations in the edge region, this process is the dominant recombination mechanism for C^{n+} by a wide margin; hence both the dominant ionization and recombination processes may be estimated for the full suite of C^{n+} ions of interest.

(4) This situation does not exist for any other impurity ion of fusion interest: a need exists for data in this energy range for impurity ions found in fusion plasmas.

While it is encouraging to be able to make quantitative estimates for a particular process for the first time, it is not necessarily true a priori that the results will be relevant to fusion. In this case, however, the results have a major impact in several topical areas.

(1) An attempt is being made to fashion a "photosphere," or "cool plasma mantle," around future large fusion plasmas. It would be desirable to create and maintain a radiating zone on the plasma periphery in which power deposited in the plasma core by thermalizing alpha particle reaction products is lost to low Z impurity ions and then radiated from the

plasma. Wall damage (and subsequent introduction of a large number of impurities) would thus be minimized. Since $H_0 + H^+$ charge exchange in the edge region creates an efflux of energetic neutral atoms which can sputter wall atoms into the discharge, it is desired to keep the temperature of the radiative zone well below the maximum in the sputtering yield. (As a typical value, S_{max} occurs at 2 keV for iron.) Thus, we will adopt 350 eV as the upper limit of our temperature range.

(2) Recent high power heating results have been carried out with graphite limiters. The dominant impurity ion in these cases is carbon, and the contribution of carbon radiation to the overall energy balance is significant.

(3) Study of the dynamics of impurity motion has disclosed asymmetries in the emitted light, which could confound collisional (so-called "neoclassical") theory. While a theoretical analysis predicts small asymmetries to result from the theory, quite large asymmetries are measured. The possible role of charge exchange of H_0 with multiply charged impurities in producing this asymmetry has been suggested, but the lack of data has prevented calculation till now.

Abstract of Influence of Neutral Beam Injection on Impurity Transport in the ISX-B Tokamak[114]

R. C. Isler, L. E. Murray,* S. Kasai,† D. E. Arnurius, S. C. Bates,* E. C. Crume, J. L. Dunlap,* L. H. Edmonds,* E. A. Lazarus,* M. Murakami,* V. K. Paré,‡ M. J. Saltmarsh,* D. W. Swain,§ C. E. Thomas**

Observations of radiation from iron and from argon used as a test gas indicate that coinjection inhibits impurity accumulation in the interior of ISX-B tokamak discharges, but counterinjection enhances accumulation. These results agree qualitatively with recent theoretical calculations.

Abstract of An Oxygen Atomic Physics Package for Transport Simulations[115]

E. C. Crume

We have integrated together, within an overall corona model framework, treatments of electron impact ionization, radiative and dielectronic recombination and excitation, and charge transfer between atomic hydrogen and oxygen ions. The treatments of ionization and radiative recombination are more or less standard. Considerable effort was made to incorporate the most recent theoretical and experimental data into the treatments of dielectronic recombination and electron impact excitation. Because of the lack of charge transfer cross-section data for some of the oxygen ions, it was necessary to construct some cross-section curves by interpolation, extrapolation, or comparison with results for species with similar electronic structure. We present results of transport simulations using this package and compare them with results using other models.

Implementation of the reduced charge state method of calculating impurity transport in IMPTAR

E. C. Crume, D. E. Arnurius

We have incorporated in the impurity transport simulation code IMPTAR the method of reduced charge states[85] in order to more efficiently calculate the impurity transport coefficients. A form of the Coulomb logarithm appropriate to the reduced charge state method was introduced. We find that we gain about 25% computing speed in a simulation of a typical ISX-B case compared to the previous approximate method.[116] Significantly, the simulation results are almost identical to those obtained previously, which speaks well for the approximate theory.

*Tokamak Experimental Section.

†Japan Atomic Energy Research Institute, Tokai, Ibaraki, Japan.

‡Instrumentation and Controls Division.

§EBT Experimental Section.

4.2.6 Tokamak Reactors

The work in the tokamak reactor area consists of stand-alone investigations of equilibrium, stability, and transport of individual effects, as well as comprehensive transport code modeling of the time evolution of a tokamak reactor, from startup to steady-state burn control of designs such as the Fusion Engineering Device (FED) and the International Tokamak Reactor (INTOR). Included are studies of plasma assessments for the FED, engineering analyses, approaches to ignition, plasma initiation and current startup, neutral beam heating, studies of limiter design, fueling, and ripple effects. Also discussed is the physics of fusion fuel cycles for a variety of fusion processes.

Abstract of Fusion Energy Division Plasma Assessments for the Fusion Engineering Device[117]

Y-K. M. Peng, P. H. Rutherford,† J. F. Lyon,‡ D. Blackfield,§ S. K. Borowski, D. R. Cohn,§ L. M. Hively,* J. A. Holmes, W. A. Houlberg, B. C. Howe, P. Mioduszewski,‡ K. E. Rothe, M. Murakami,‡ D. J. Strickler,* M. Ulrickson†*

An initial range of plasma assumptions and scenarios has been examined for the U.S. tokamak FED concept. The results suggest that the current FED baseline parameters of $R = 4.8$ m, $B_t = 3.6$ T, $a = 1.3$ m, $b = 2.1$ m (D-shape), and $I_p = 4.8$-5.4 MA are appropriate for achieving its nominal goals of P(fusion) ≥ 180 MW and a plasma $Q \geq 5$ for a pulse length greater than 100 s. However, large uncertainty still exists in the areas of current startup, ion cyclotron wave launching, influence of plasma shape on achievable beta, impurity control, plasma edge transport, and plasma disruption. Various options and remedies have been suggested to alleviate the impact of the uncertainty on the FED design concept. They appear promising because they can be studied experimentally and are not expected to lead to fundamental design modifications of FED.

*Fusion Engineering Design Center.

†Princeton Plasma Physics Laboratory, Princeton, New Jersey.

‡Tokamak Experimental Section.

§Massachusetts Institute of Technology, Cambridge, Massachusetts.

Abstract of Plasma Engineering Analyses of Tokamak Reactor Operating Space[118]

W. A. Houlberg, S. E. Attenberger

We present a comprehensive method for analyzing the potential physics operating regime of fusion reactor plasmas with detailed transport codes. Application is made to the tokamak FED. The relationships between driven and ignited operation and supplementary heating requirements are examined. The reference physics models give a finite range of density and temperature over which physics objectives can be reached. Uncertainties in the confinement scaling and differences in supplementary heating methods can expand or contract this operating regime even to the point of allowing ignition with the more optimistic models.

Abstract of Approach to Ignition of Tokamak Reactors[119]

D. J. Sigmar

Recent transport modeling results for JET, INTOR, and ETF are reviewed and analyzed with respect to existing uncertainties in the underlying physics, the self-consistency of the very large numerical codes, and the margin for ignition. The codes show ignition to occur in ETF/INTOR-size machines if empirical scaling can be extrapolated to ion temperatures (and beta values) much higher than those presently achieved, if there is no significant impurity accumulation over the first 7 s, and if the known ideal and resistive MHD instabilities remain controllable for the evolving plasma profiles during ignition startup.

Abstract of Ignition Studies[120]

W. A. Houlberg

A series of 1½-D transport calculations has been performed for FED parameters and implications made for INTOR through comparison of the parameters. The effects of the flux surface shift on neutral beam penetration and increased toroidal field ripple losses are included self-consistently through the evolving 2-D MHD equilibria in the WHIST transport code.

Ignition occurs at an average density of just under 1.1×10^{14} cm^{-3} using the reference transport model for INTOR, while FED is designed to operate in a driven mode at lower densities. The increased ripple losses for $\langle T \rangle \leq 15$ keV are reflected in the increased supplementary power requirements. The startup power requirements are similar for INTOR and FED. The high power requirements at high $\langle n_e \rangle$ and low $\langle T \rangle$ are indicative of poor beam penetration, but this region can be avoided in the startup sequence. The choice of 175-keV, near-normal injection for INTOR appears to put excessive emphasis on beam penetration for far from optimal startup sequences.

In FED, 200 MW of thermal output corresponds to $\langle \beta \rangle \cong 6\%$, while in INTOR $\langle \beta \rangle \cong 5.3\%$ at the cited operating point of 600 MW because of the higher toroidal field.

Abstract of Plasma Initiation and Current Startup in the FED Tokamak[121]

S. K. Borowski, W. A. Houlberg, Y-K. M. Peng, T. Kammash†*

Initiation of a small radius plasma and its subsequent expansion to full radius are examined as a startup option for the FED. RF breakdown and electron preheating at the upper hybrid resonance layer are also assumed. This promotes the formation of a localized, small radius channel of high conductivity plasma prior to current startup. Using the preheated plasma parameters as initial conditions, the 1½-D transport code WHIST is used to study the time evolution of the plasma density, temperature, and poloidal magnetic field during the current rise phase. Questions concerning the relationship between current ramp rate, skin current formation, and double tearing mode activity are addressed and the limitations on heating, initial plasma minor radius, and impurity content are examined. Preliminary results of these studies will be presented.

Abstract of Optimal Neutral Beam Heating Scenario for FED[122]

L. M. Hively, W. A. Houlberg, S. E. Attenberger*

Optimal neutral beam heating scenarios are determined for FED based on a 1½-D transport analysis. We then examine tradeoffs between neutral beam energy, power, and species mix for positive ion systems. A ramped density startup is found to provide the most economical heating. The resulting plasma power requirements are reduced by 10-30% from a constant density startup. For beam energies between 100 and 200 keV, the power needed to heat the plasma does not decrease significantly as beam energy is increased. This is due to reduced ion heating, more power in the fractional energy components, and rising power supply requirements as beam energy increases. An improved source species mix can provide as much gain in the plasma power requirements as increased beam energy.

Abstract of Physics Considerations for the FED Limiter[123]

H. C. Howe

In this report, we review the physics of the scrapeoff plasma and its interaction with a pumping limiter. The governing equations for heat and particle transport in the scrapeoff are solved analytically with several simplifying assumptions. The assumed scrapeoff

*Fusion Engineering Design Center.
†University of Michigan, Ann Arbor, Michigan.

model is widely used and is presented here for completeness. From the solution, a shape for the limiter is derived which has a uniform heat loading on the front surface. The assumed cross-field transport coefficient is varied to examine the sensitivity of the heat loading to variations in plasma scrapeoff thickness. The heat flux to the limiter leading edge is an extremely sensitive function of variations in scrapeoff thickness, and we argue that uncertainties in the plasma cross-field transport preclude derivation of a believable limiter shape. We also discuss the problems involved with an edgeless, perforated limiter and with a global limiter. Finally, a solution is proposed using a flat plate limiter with the heat flux to the leading edge controlled by major radius motion of the plasma.

Abstract of Numerical Simulation of Fueling in Tokamaks[124]

*S. E. Attenberger, W. A. Houlberg, S. L. Milora**

We describe the numerical simulation of fueling and particle transport in both present and future tokamak plasmas. Models for pellet ablation and plasma density behavior after pellet injection are compared with experimental results in ISX and PDX plasmas and then extended to fusion reactor conditions. The role of fast ion ablation due to intense neutral beam injection and fusion alphas is examined along with pellet size and velocity considerations. In plasmas with high pumping efficiency (which may be obtained with divertor operation), pellet injection can significantly reduce fuel handling requirements and interaction of the plasma with the chamber walls while maintaining more flexibility in control of the density profile than afforded by gas puffing. When fueling is dominated by gas puffing or high recycle from the walls or limiter, control of the fueling and density profiles is reduced while plasma-wall interactions increase.

Abstract of The Effects of Toroidal Field Ripple on Injected Deuterons in the FED Device[125]

R. E. Fowler, J. A. Rome

A Monte Carlo beam deposition and thermalization code is used to assess the effects of toroidal field (TF) ripple on injected fast deuterons in the FED. The code uses realistic geometry for the beam, plasma equilibrium, TF ripple, and vacuum chamber. For injection at an angle of 35° (co) from perpendicular, no particles were ripple-trapped and less than 1% of the injected power went to the wall and the limiter. However, due to the large amounts of computer time required by these programs, only 100 particles were followed in the rippled case, and the results must be regarded as preliminary.

Abstract of Toroidal Field Ripple Conduction Losses in the FED Tokamak[126]

S. E. Attenberger, J. A. Holmes, W. A. Houlberg, S. D. Scott†

Efforts to maximize access in tokamak reactor designs such as the FED have led to an increased emphasis on both theoretical and experimental evaluation of ripple-enhanced plasma losses. We investigate ripple-induced ion thermal losses in the FED design through the impact on total energy confinement time and supplementary heating requirements. To make this assessment, we use the WHIST 1½-D time-dependent transport code to generate plasma operation contour (POPCON) plots.

The ion thermal conduction coefficients are flux-surface-averaged over ripple contours in the R-Z plane so that the effect of the plasma shift is included self-consistently. If the peak-to-average toroidal field ripple at the plasma edge is less than 1%, it has

*Plasma Technology Section.

†Tokamak Experimental Section.

little effect on the total plasma behavior for average plasma temperatures below about 6-8 keV. This indicates that startup power requirements should not be significantly increased by the finite ripple.

In the range 8-12 keV, ripple trapping and ripple plateau ion conduction losses both become comparable to the anomalous electron conduction losses. A peak-to-average toroidal field ripple of 0.7% holds the ignition curve at a moderately high density, but it provides a large, thermally stable region for ignited operation. When the peak-to-average ripple is raised to about 1% at the plasma edge, the ignition curve begins to move to significantly higher densities (and plasma betas).

At temperatures greater than about 12 keV, ripple trapping dominates because of its much stronger temperature dependence. The ripple trapping model, however, must be subjected to greater theoretical and experimental scrutiny.

The magnetic axis shift increases with increasing plasma pressure and therefore primarily affects the ripple-trapping losses. It is in this regime that increased losses are desirable for increasing the thermally stable operating range. If these ripple transport models stand up to further theoretical developments and experimental tests, peak-to-average ripple of 0.7-1% at the plasma edge appears to be more beneficial than deleterious.

Abstract of Physics of Fusion Fuel Cycles[127]

J. R. Wally, Jr.

The evaluation of nuclear fusion fuels for a magnetic fusion economy must take into account the various technological impacts of the various fusion fuel cycles as well as the relative reactivity and the required betas, temperatures, and confinement times necessary for economical steady-state burns. The physics of the various fuel cycles [deuterium-tritium, catalyzed deuterium-deuterium (D-D), D-^{3}He, D-^{6}Li, and the exotic fuels: ^{3}He-^{3}He and the proton-based fuels p-^{6}Li, p-^{9}Be, and p-^{11}B] is reviewed. Topics considered include

(1) fuel costs and required purity,
(2) tritium inventory, burnup, and recycle,
(3) ignition criteria,
(4) neutrons,
(5) condensable fuels and ashes,
(6) radiation losses,
(7) direct electrical recovery prospects, and
(8) fissile breeding prospects.

The advantages and disadvantages of each fuel are also treated. The optimum fuel cycle, from an overall standpoint of viability and potential technological considerations, appears to be catalyzed D-D, which could also support smaller, relatively "clean," lean deuterium-rich ^{3}He satellite reactors as well as fission reactors.

Abstract of Plasma Physics Assessments for the Fusion Engineering Device[128]

Y-K. M. Peng, P. H. Rutherford,† J. F. Lyon‡*

The FED is currently envisioned as a tokamak producing a D-T fusion power of 180 MW over 100 s, driven at a level of $Q > 5$ via ICH at the second harmonic of deuterium. The major device parameters at present are $R = 4.8$ m, $a = 1.3$ m, $(b/a) = 1.6$ (D-shaped plasma cross section), $B_t = 3.62$ T, and I_p up to 6 MA. The plasma engineering analyses during the first six months of FY 1981 have yielded the following major results.

The assumption of a soft beta limit (as suggested by preliminary observations in ISX-B) leads to a maximization of $n\tau$ near $\epsilon\beta_p = 0.6$. For fixed q(edge) and B(max) at the TF coils, a (b/a) of 1.6 leads to a factor of 3 enhancement of $n\tau$. A value of $\langle\beta\rangle = 5.5\%$ can be achieved with $\beta_p = 1.8$, $I_p = 5.4$ MA, and $q = 3.2$. These results are insensitive to uncertainties in the size and β_p scaling of confinement.

*Fusion Engineering Design Center.
†Princeton Plasma Physics Laboratory, Princeton, New Jersey.
‡Tokamak Experimental Section.

Under the standard physics assumptions, a clean FED plasma can operate over a finite domain in $\langle T \rangle$ and $\langle n \rangle$ and satisfy the conditions of $Q \geq 5$, $P(aux) \leq 36$ MW, $\langle \beta \rangle \leq 5.5\%$, and $P(fusion) \leq 200$ MW. The operational domain has a range of 6.5 keV $\leq \langle T \rangle \leq$ 14 keV and 4.5×10^{13} cm^{-3} $\leq \langle n \rangle \leq 12 \times 10^{13}$ cm^{-3}. The design can accommodate a factor of 2 margin in confinement. A power level below 50 MW for 6 s is required for heatup.

Several toroidal belt, pumped limiter concepts have been assessed for particle control. The required particle exhaust rate of 3-6% apparently can be satisfied without excessive heat load on the limiter leading edge. Limiter erosion via sputtering remains a potentially serious problem. Backup impurity control schemes include a simplified poloidal divertor (primary), a compact bundle divertor (secondary), and various nonmagnetic options. A mildly contaminated plasma relying on a modest level of impurity efflux mechanisms may be a workable compromise.

A plasma disruption is assumed to proceed with a thermal quench in about 5 ms followed by a current quench in about 10 ms. By assuming that radiation from ablation-generated impurities halts further thermal damage to the limiter and armor, less than 20% of the plasma heat is deposited over the region of plasma contact.

A simplified poloidal field coil configuration has been obtained for FED. It consists of a superconducting central solenoid, providing a flux swing of over 60 Wb, and pairs of interior copper and exterior superconducting coils. The latter coils carry a total of up to 20 meganpere-turns to produce the external equilibrium field and cancel the stray field from the solenoid.

Our results so far suggest that the current FED baseline concept can achieve its nominal plasma performance goals under a range of reasonable assumptions and eventualities. Effort is continuing to overcome the uncertainties that still exist in impurity control and plasma disruption.

4.3 STELLARATOR THEORY

During 1981, the Theory Section joined other ORNL scientists and engineers in developing models for analyzing possible configurations for an Advanced Toroidal Facility (ATF) to replace the ISX-B tokamak over a time scale of several years. Existing models and codes were modified to incorporate the helical fields of stellarator and torsatron devices. It was possible to do this rapidly because the study of tokamaks with realistic (rippled) external fields, helical collective fields, and divertor geometry had already made it necessary to incorporate nonaxisymmetric (3-D) fields and conductors. The large international effort for analyzing tokamaks during the last decade has enabled some of the work for helical devices to proceed as a straightforward extension. To many areas, the third dimension brings only the complication of more data with more components, while an essential complication is introduced into much of the analysis, as in the constructive determination of equilibria.

In addition, models and codes were acquired from the extensive stellarator literature (see Ref. 129 for a list of relevant references) and from cooperative laboratories in the world fusion program. Examples include the Chodura-Schlüter 3-D MHD equilibrium code from the Max Planck Institute for Plasma Physics, Garching, Federal Republic of Germany, and the HERA 3-D helical cylinder ideal MHD instability code from the Center for Research in Plasma Physics, École Polytechnique of Lausanne, Switzerland. Collaboration was begun with several of these laboratories to reduce unnecessary duplication of effort and to provide accelerated progress in the understanding of stellarator physics.

The development of the theoretical tools used so far is briefly discussed. Discussion of the results of their application is largely deferred because the analysis of the broader prospects for stellarator confinement has just begun. Work during 1982 should result in a set of conclusions that will lead to the choice of a specific design for the ATF device.

In the following sections we sketch the tools that have been developed in the general areas of

- magnetic analysis for externally applied (vacuum) fields,
- study of orbit confinement in vacuum fields,
- equilibrium analysis, and
- stability analysis.

4.3.1 Magnetic Design Tools for Vacuum Field Studies

J. A. Rome, J. H. Harris, R. H. Fowler, V. E. Lynch*

Efficient codes have long been in use for analysis of tokamaks with nonuniformly distributed coils, including bundle divertors. Within the approximation that distributed finite current density conductors can be well represented by sufficient filamentary coils appropriately distributed, the generalization to continuous and modular helical coils was straightforward. The availability of graphics procedures to let the results be visualized and appreciated readily is critical for use of a Biot-Savart law code to calculate magnetic fields.

An example of vacuum field results is shown in Fig. 4.3(a), which shows conductors, and in Fig. 4.3(b), which shows Poincaré plots, for a new type of modular torsatron being analyzed for suitability for an ATF design.

Efficient orbit studies require a compact representation of the 3-D magnetic fields and derivatives. A field-line-based representation is very effective because it allows a Hamiltonian formulation of the guiding center orbits and the resulting control of computation time and accuracy in orbit following. This procedure was sketched by A. H. Boozer[130] and carried out at ORNL to yield the sort of information displayed in Fig. 4.3(c), which shows typical field harmonics present on a given magnetic surface for the configuration of Fig. 4.3(a), and in Fig. 4.3(d), which shows the variation from surface to surface of the principal harmonics. The Fourier analysis is in terms of magnetic coordinates ψ,θ,ϕ of the type leading to field lines that are straight in a θ,ϕ plot. The small number of harmonics required demonstrates the utility of this representation.

*Tokamak Experimental Section.

4.3.2 Drift Orbits in Vacuum Magnetic Fields

*J. A. Rome, R. H. Fowler, V. E. Lynch, J. F. Lyon**

The analysis of particle orbits must eventually take into account the finite beta magnetic fields and the electric field within the plasma. Until the latter can be analyzed, only vacuum fields are studied. However, the use of field line coordinates has improved computational time by a factor of 10 compared to the Biot-Savart law. Furthermore, the confusing and irrelevant helical motion (due to the field structure) is removed from the orbit plots.

4.3.3 Equilibrium Studies

B. A. Carreras, L. Garcia

The method used in the 3-D MHD equilibrium calculations is to minimize the energy $W = \int[(B^2/e) + (P/\gamma - 1)]dV$ with the constraints of $\vec{\nabla} \cdot \vec{B} = 0$, mass conservation, and magnetic flux conservation. The approach used has been to adapt the Chodura-Schlüter code[131] to the CRAY computer at Lawrence Livermore National Laboratory (LLNL), link it to the vacuum magnetic field code used in the configuration studies, and implement several diagnostic codes. Particular features of this code are the use of Cartesian coordinates, Eulerian formulation, and boundary conditions specified on a rectangular box. The initial conditions are the vacuum magnetic field and the plasma pressure distribution. Spatial resolution is the most serious limitation of this code. We have made numerical tests on the sensitivity

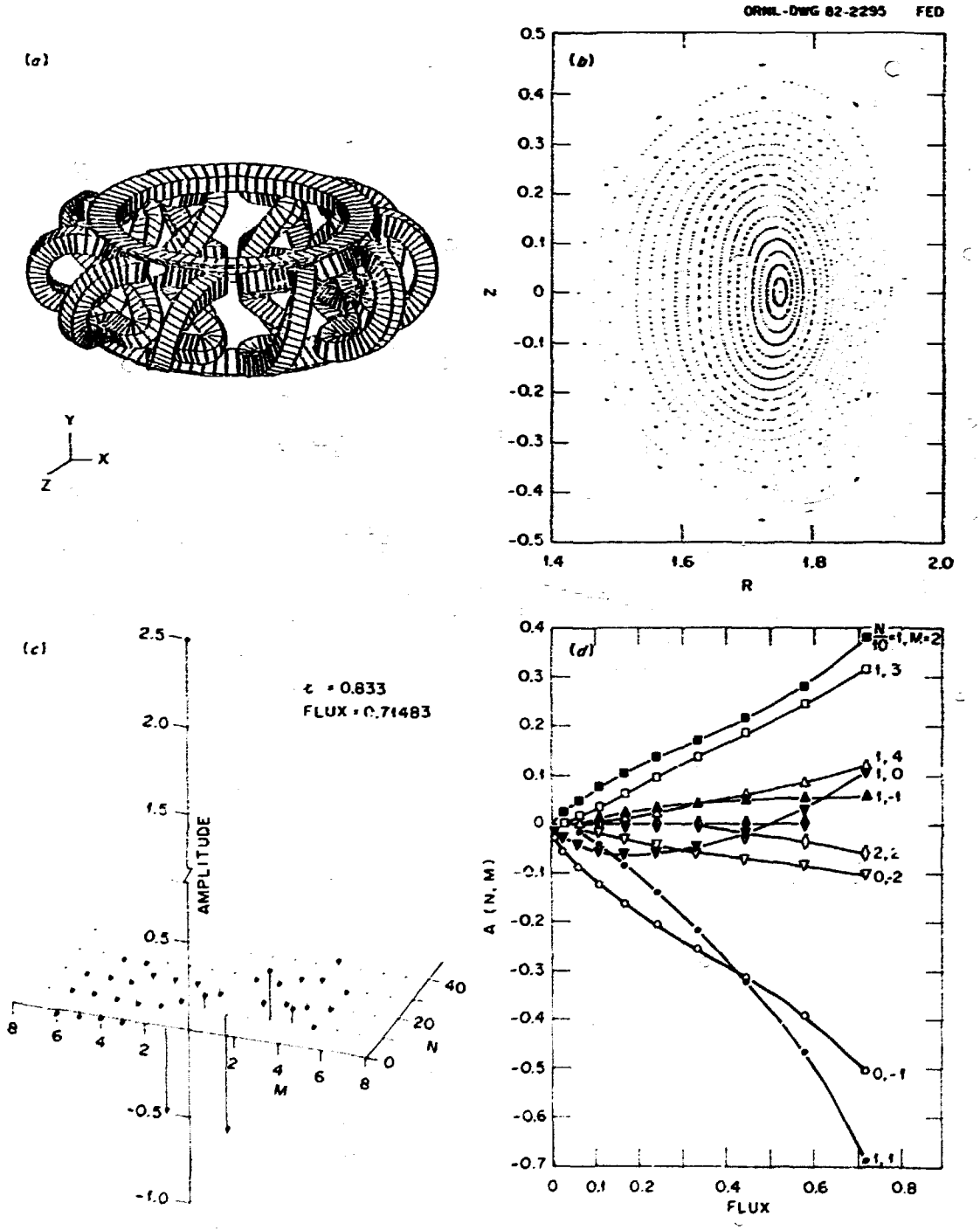

Fig. 4.3. (a) Coil configuration for a new type of modular torsatron. This particular example has $\ell = 2$ and $n = 10$ toroidal field periods. (b) The Poincaré puncture plot of the flux surfaces for this configuration. (c) The Fourier harmonics for a flux surface near the edge of the plasma. N is the toroidal mode number and M is the poloidal mode number. (d) The radial variation of some of the harmonics. The smoothness of these data permits using ψ derivatives, which are needed for orbit following.

of the solution (pressure contours, beta, and shift) to the grid size, and also on the sensitivity of the resulting magnetic field line configuration to the grid size and 3-D interpolation procedures used in the magnetic field line code. We have used grids up to 40 x 40 x 40 points per toroidal half-period, and the results show that the 20 x 20 x 20 grid is more convenient for equilibrium studies.

4.3.4 Stability Analysis

B. A. Carreras, W. A. Cooper, H. R. Hicks, J. A. Holmes

The averaged MHD equations based on the stellarator expansion[132] are used for stability studies. The equilibria are obtained by solving a 2-D Grad-Shafranov equation that results from spatially averaging over a helical field period. A reduced set of MHD equations[133] is used for the stability studies for low n (toroidal mode number) modes. In the averaged reduced equations, the magnetic field contains the contributions from both the external helical current and the plasma current. In addition, the curvature term is also modified by the averaged curvature of the external helical field. For intermediate mode numbers ($1 \ll n \ll$ number of toroidal field periods), a ballooning mode equation along the effective averaged magnetic field is obtained that takes into account the averaged helical curvature arising from the external windings.

4.3.5 Intermediate Mode Number Ballooning Stability Results for a Stellarator-Tokamak Hybrid

W. A. Cooper, B. A. Carreras

The effects of external rotational transform on ballooning modes of intermediate mode number ($1 \ll n \ll m$ = number of field periods) are being studied in stellarator-tokamak hybrids using the averaged MHD equations based on the stellarator and large m expansions (as developed by Strauss[133] and independently by Wakatani). Equilibria for hybrids are obtained numerically for large aspect ratio systems by solving a 2-D Grad-Shafranov equation that has been spatially averaged over the helical field period 2R/m. By linearizing the averaged equation of motion, a ballooning mode equation along the effective averaged magnetic field is obtained. The equation includes an averaged helical curvature term arising from the external windings, in addition to the usual tokamak terms. The stability of several equilibria, with either broad or narrow pressure profiles and tokamak or stellarator-like safety factor (q) profiles (i.e., $q' > 0$ or $q' < 0$) have been examined for $\ell = 2,3$ windings with varying amounts of external transform. It is found that stability beta limits for these ballooning modes are enhanced for $\ell = 2$ systems and virtually unchanged for $\ell = 3$ systems as the externally applied transform is increased for a fixed (total) q profile. The increased value of critical beta for $\ell = 2$ is attributed to the vertical component of the helical curvature (which may increase the plasma well). Tokamaklike q profiles produce somewhat higher values of beta in $\ell = 3$ hybrids (with q fixed at the edge), due to the shorter connection length for the lower central q values for $q' > 0$ profiles. For $\ell = 2$ systems, raising the central value of q (with q fixed at the edge) decreases the maximum stable value of beta due to a decrease in the global shear (i.e., q' decreases).

4.4 COMPUTING SUPPORT

C. E. Hammons

The computing support group provides the Fusion Energy Division with computing resources in two areas: operation of the User Service Center (USC) and development of the experimental data acquisition network. The USC provides (1) access to the large computing systems of the National Magnetic Fusion Energy Computing Center (NMFECC) at LLNL and (2) immediate analysis and storage of experimental

data. The data handling network supports the growing needs of the Division's experimental efforts by providing a rapid, state-of-the-art means of acquiring and storing experimental data. Finally, the group provides input to the DOE Long-Range Automatic Data Processing (ADP) plan on behalf of fusion energy.

4.4.1 User Service Center Operations

C. E. Harmons, D. W. Clark, C. O. Kemper, H. E. Ketterer, G. S. Massengill

The latest version of the DECsystem10 operating system (7.01) was merged with NMFECC software and made operational. The improved reliability of the operating system provided a better user environment in the USC. Similarly, the multiprogramming batch (MPB) system was replaced with the Galaxy/Quasar queuing/batch system, which significantly improved the printing/plotting operations. This was a major change, as it involved all of the NMFECC software.

An additional 512K words of memory was installed and made fully compatible with the KL10 memory bus. This addition brought the memory complement to 1024K words, which has provided relief from excessive swapping. The reduced job swapping has improved the system response time.

A RP07 disk system was ordered to provide data storage needed for the modest increase in usage of the USC. This addition will provide an additional 750K disk blocks of storage for the division staff. The ORNL USC was selected as one of the national test sites for this new technology disk (Winchester).

The latest version of the data acquisition support software used on the USC PDP11/45 system was installed at General Atomic Company (GA) for use in support of Doublet III. This is part of a continuing cooperative effort with GA.

USC accounting was upgraded to a more automated system, and several enhancements and additions were made to the graphics support package. Several terminals were procured to provide the division staff with better access to the USC.

The PDP11/45 front-end processor for the USC was changed to the software system RSX-11M. The PDP11/45 is interfaced via its UNIBUS to the DECsystem10, which provides a 1-megabyte/s data path between the systems. This allows the PDP11/45 to accept spooled data from the USC for printing and plotting while simultaneously routing data from the data acquisition computers attached to Division experiments.

4.4.2 Data Handling Support

EBT-S data handling

R. D. Burris, D. E. Greenwood, S. L. Hall, P. C. Hanna, S. R. Maddox, D. R. Overbey, K. G. Young*

The progress in the computer support system for EBT during 1981 has been chiefly characterized by expansion and improvement. All aspects of the system have been improved, from the data acquisition systems to the DECsystem10 analysis software.

The computer hardware now includes six computers — two PDP11/34s, a PDP11/23, a Nuclear Data 6600, and two PDP8s. One of the 11/34s acts as the center of a star-shaped network, and the other five computers are all connected to it. The two 11/34s are connected via a 1-megabit/s link (DMC-11) and via CAMAC equipment, while all the remaining computers are connected only via CAMAC. All of the links are bidirectional, with the central 11/34 both providing a path to the DECsystem10 and providing such control information as uniform time-of-day ticks and identifying sequence numbers for diagnostic data files. Considerable development was necessary to implement these links.

Several diagnostics were already supported at the beginning of the year, including hard and soft x-ray analysis, charge exchange,

*UCC-ND Computer Sciences.

microwave power distribution, and measurement of fluctuations in the H_α signal. To that list have been added (1) spectroscopy, (2) ICRH studies, (3) studies on confinement time for ions under pulsed ICRH, (4) additional channels of x-ray analysis, (5) error field studies, (6) support for a 9-channel microwave interferometer, (7) support for 16 thermocouples mounted on mirror magnets, and (8) monitoring and power calculation for the 28-GHz microwave power system.

Planning and implementation have begun for additional diagnostics expected within a few months, including (1) a radiometer, (2) an instrumented limiter, (3) a synchrotron emissions system, (4) a residual gas analyzer, (5) data acquisition for use with a diagnostic neutral beam, and (6) extensive revisions to the Rensselaer Polytechnic Institute (RPI) heavy ion beam probe system and support for charge exchange, ICRH, Thomson scattering, and spectroscopy.

There was also considerable revision of the support tasks running in the PDP11/34s, including development of better operator interface tasks (data entering and display), more reliable and effective communications, and improvement in the quality and quantity of data available to the experiment coordinator.

The DECsystem10 end of the EBT system has also received considerable attention. Several modifications to the data retrieval and archiving software were made, and a massive revision is under way. The revision will add many capabilities shown to be important during the 18 months the system has been in use, will make a more appropriate choice of data important enough to be given special status in the system, and will improve the flow of data through the system.

An additional system now under development, with potentially widespread effects, will provide documentation of all of the signals and hardware available to the computer system, so that the state of the machine can more accurately be determined and documented.

ISX data handling

D. R. Overbey, J. E. Francis, K. A. Stewart, R. D. Burris, E. T. Blair, C. O. Kemper, J. R. Reagan

The PDP12 system was replaced by the Sension display system. This PDP11/34-based system provides a much more comprehensive and timely display of data for the ISX experimentalists.

Data acquisition routines to collect data for the plasma rotation diagnostic were developed to acquire two channels of analog information at a 20-kHz data rate and to sample the signals for 200 ms. The low energy charge exchange diagnostic and the ECH plasma heating data acquisition systems were also developed to acquire from one to eight channels of analog data, each at a 1-kHz data rate, and to sample the signal for one second. The infrared camera data acquisition system was moved from a PDP8 to a PDP11 system.

The software for the MHD/PIN array diagnostic was installed on the Perkin-Elmer (P-E) 8/32 along with the SCATPAK II diagnostic development support. The vector-to-raster converter for the P-E 8/32 was installed along with the Advanced Graphics II package. A comprehensive user's and operator's manual for the P-E 8/32 system was produced and includes system codes and command procedures.

Preparation for the VAX11/780 was begun. This included some preliminary code development for CAMAC support. Several members of support staff were trained in various areas of VAX11 system operations and programming.

Medium Energy Test Facility, High Power Test Facility, and Negative Ion Test Facility data handling support

C. R. Stewart, J. E. Francis, Jr.

The Medium Energy Test Facility was upgraded to the faster PDP11/34 processor, and its storage capability was increased to 20 million characters of data. This allows the experimental staff to maintain data on a substantial

number of shots at the data acquisition processor before transmission to the DECsystem10.

The High Power Test Facility data storage was increased to 28 million characters. The processor speed was significantly increased by by the addition of cache memory.

The Negative Ion Test Facility PDP11 was made operational with the software system developed for the other beam test facilities.

Various improvements to the support software for the test stands were installed to improve the experimentalists' access to machine parameters.

REFERENCES

1. D. A. Spong, *Review of Recent Coupled Ring-Core Stability Theory*, ORNL/TM-8021, Oak Ridge, Tennessee (1981).
2. N. A. Uckan and G. R. Haste, in *EBT Stability Theory. Proceedings of the Workshop*, CONF-810512, Oak Ridge National Laboratory, Oak Ridge, Tennessee (1981), p. 63.
3. D. A. Spong, J. W. Van Dam, H. L. Berk, and M. N. Rosenbluth, in *EBT Stability Theory: Proceedings of the Workshop*, CONF-810512, Oak Ridge National Laboratory, Oak Ridge, Tennessee (1981), p. 115.
4. J. W. Van Dam, H. L. Berk, M. N. Rosenbluth, and D. A. Spong, in *EBT Stability Theory: Proceedings of the Workshop*, CONF-810512, Oak Ridge National Laboratory, Oak Ridge, Tennessee (1981), p. 97.
5. J. W. Van Dam, H. L. Berk, M. N. Rosenbluth, and D. A. Spong, *Eigenmode Stability Analysis for a Bumpy Torus*, IFSR 34 (DOE/ET/53088-34), Institute for Fusion Studies, Austin, Texas (1981).
6. K. T. Tsang and C. Z. Cheng, in *EBT Stability Theory: Proceedings of the Workshop*, CONF-810512, Oak Ridge National Laboratory, Oak Ridge, Tennessee (1981), p. 141.
7. C. Z. Cheng and K. T. Tsang, in *EBT Stability Theory: Proceedings of the Workshop*, CONF-810512, Oak Ridge National Laboratory, Oak Ridge, Tennessee (1981), p. 161.
8. D. A. Spong, H. L. Berk, J. W. Van Dam, and M. N. Rosenbluth, in *Hot Electron Ring Physics: Proceedings of the Second Workshop*, CONF-811203, Oak Ridge National Laboratory, Oak Ridge, Tennessee (in press).
9. J. W. Van Dam, H. L. Berk, M. N. Rosenbluth, and D. A. Spong, in *Hot Electron Ring Physics: Proceedings of the Second Workshop*, CONF-811203, Oak Ridge National Laboratory, Oak Ridge, Tennessee (in press).
10. H. L. Berk, J. W. Van Dam, M. N. Rosenbluth, and D. A. Spong, *Curvature Driven Instabilities in a Hot Electron Plasma: Radial Analysis*, IFSR 50 (DOE/ET/53088-50), Institute for Fusion Studies, Austin, Texas (1981).
11. A. M. El-Nadi, "On the Stability of Flute Modes in the ELMO Bumpy Torus," submitted to Physics of Fluids.
12. N. A. Uckan, Nucl. Fusion 21, 1489 (1981).
13. A. M. El-Nadi and K. T. Tsang, "The Radial EBT Stability Problem," paper 1B3 presented at the 1981 Sherwood Meeting on Theoretical Aspects of Controlled Thermonuclear Research, Austin, Texas, April 7-10, 1981.
14. J. W. Van Dam, H. L. Berk, M. N. Rosenbluth, and D. A. Spong, "Radial Eigenmode Stability for Bumpiless EBT," paper 3B33 presented at 1981 Sherwood Meeting on Theoretical Aspects of Controlled Thermonuclear Research, Austin, Texas, April 7-10, 1981.
15. K. T. Tsang and C. Z. Cheng, "Coupling of Hot Electron Interchange and Ion Bernstein Modes in EBT," paper 3B24 presented at the 1981 Sherwood Meeting on Theoretical Aspects of Controlled Thermonuclear Research, Austin, Texas, April 7-10, 1981.
16. D. A. Spong et al., Bull. Am. Phys. Soc. 26, 995 (1981).

17. A. M. El-Nadi, Bull. Am. Phys. Soc. 26, 995 (1981).
18. H. L. Berk, M. N. Rosenbluth, J. W. Van Dam, and D. A. Spong, Bull. Am. Phys. Soc. 26, 995 (1981).
19. J. S. Tolliver, E. F. Jaeger, and C. L. Hedrick, "A Kinetic Model for Neoclassical Transport in EBT with Enhanced Ion Tail," to be published in Nuclear Fusion.
20. E. F. Jaeger, L. L. Lao, L. W. Owen, and C. L. Hedrick, "EBT Transport in 2-D Mirror Geometry with Finite Electron Annulus Pressure," submitted to Physics of Fluids [see also ORNL/TM-7558 (1980)].
21. E. F. Jaeger, L. L. Lao, L. W. Owen, and C. L. Hedrick, "ELMO Bumpy Torus Transport with Rigid Ring in Bumpy Cylinder Geometry," submitted to Physics of Fluids.
22. N. A. Uckan and R. F. Post, Nucl. Fusion 21, 1493 (1981).
23. C. L. Hedrick, in *Workshop on Ambipolar Potential Formation and Control in Bumpy Tori and Mirrors*, CONF-810511, Oak Ridge National Laboratory, Oak Ridge, Tennessee (1981), p. 19.
24. J. S. Tolliver, E. F. Jaeger, and C. L. Hedrick, in *Workshop on Ambipolar Potential Formation and Control in Bumpy Tori and Mirrors*, CONF-810511, Oak Ridge National Laboratory, Oak Ridge, Tennessee (1981), p. 267.
25. L. W. Owen, in *Workshop on Ambipolar Potential Formation and Control in Bumpy Tori and Mirrors*, CONF-810511, Oak Ridge National Laboratory, Oak Ridge, Tennessee (1981), p. 277.
26. E. F. Jaeger, R. K. Richards, and C. L. Hedrick, in *Workshop on Ambipolar Potential Formation and Control in Bumpy Tori and Mirrors*, CONF-810511, Oak Ridge National Laboratory, Oak Ridge, Tennessee (1981), p. 183.
27. R. K. Richards and E. F. Jaeger, in *Workshop on Ambipolar Potential Formation and Control in Bumpy Tori and Mirrors*, CONF-810511, Oak Ridge National Laboratory, Oak Ridge, Tennessee (1981), p. 167.
28. J. D. Callen, in *Workshop on Ambipolar Potential Formation and Control in Bumpy Tori and Mirrors*, CONF-810511, Oak Ridge National Laboratory, Oak Ridge, Tennessee (1981), p. 203.
29. E. F. Jaeger, R. K. Richards, and C. L. Hedrick, "EBT Transport and Ambipolar Potential Formation with Rapid Loss of High Energy Impurity Ions," paper 1B42 presented at the 1981 Sherwood Meeting on Theoretical Aspects of Controlled Thermonuclear Reserach, Austin, Texas, April 7-10, 1981.
30. J. S. Tolliver, E. F. Jaeger, and C. L. Hedrick, Bull. Am. Phys. Soc. 26, 994 (1981).
31. E. F. Jaeger and C. L. Hedrick, Bull. Am. Phys. Soc. 26, 995 (1981).
32. L. W. Owen and C. L. Hedrick, in *Proceedings of the U.S.-Japan Workshop on 3-D MHD Studies for Toroidal Devices*, CONF-8110101, Oak Ridge National Laboratory, Oak Ridge, Tennessee (1981), p. 197.
33. L. W. Owen, L. E. Deleanu, and C. L. Hedrick, in *Hot Electron Ring Physics: Proceedings of the Second Workshop*, CONF-811203, Oak Ridge National Laboratory, Oak Ridge, Tennessee (in press).
34. N. A. Uckan, in *Hot Electron Ring Physics: Proceedings of the Second Workshop*, CONF-811203, Oak Ridge National Laboratory, Oak Ridge, Tennessee (in press).
35. N. A. Uckan, Bull. Am. Phys. Soc. 26, 997 (1981).
36. D. B. Batchelor, Nucl. Fusion 21, 1615 (1981).
37. D. B. Batchelor and R. C. Goldfinger, in *Proceedings of Second Joint Grenoble-Varenna International Symposium*, EUR-7424EN (1981), Vol. I, p. 207.

38. D. B. Batchelor, R. C. Goldfinger, and H. Weitzner, in *Hot Electron Ring Physics: Proceedings of the Second Workshop*, CONF-811203, Oak Ridge National Laboratory, Oak Ridge, Tennessee (in press).

39. R. C. Goldfinger, A. H. Kritz, and D. B. Batchelor, Bull. Am. Phys. Soc. 26, 1034 (1981).

40. H. Weitzner and D. B. Batchelor, Bull. Am. Phys. Soc. 26, 930 (1981).

41. D. B. Batchelor, R. C. Goldfinger, and H. Weitzner, Bull. Am. Phys. Soc. 26, 995 (1981).

42. A. H. Kritz, H. Hsuan, R. C. Goldfinger, and D. B. Batchelor, Bull. Am. Phys. Soc. 26, 1035 (1981).

43. D. B. Batchelor, R. C. Goldfinger, and H. Weitzner, in *Proc. Fourth Topical Conference on Radio Frequency Plasma Heating* (1981), p. D13.

44. L. W. Owen and N. A. Uckan, J. Fusion Energy 1, 341 (1981).

45. N. A. Uckan, D. A. Spong, and D. B. Nelson, "Beta Limits in EBT and Their Implication for a Reactor," paper presented at the Symposium on Physics Problems of Fusion Reactors, Trieste, Italy, June 2-9, 1981 [see also ORNL/TM-7857 (1981)].

46. N. A. Uckan and EBT Theory Group, "Physics Issues of an EBT Reactor," paper presented at the Symposium on Physics Problems of Fusion Reactors, Trieste, Italy, June 2-9, 1981.

47. J. R. McNally, Jr., in *Workshop on Ambipolar Potential Formation and Control in Bumpy Tori and Mirrors*, CONF-810511, Oak Ridge National Laboratory, Oak Ridge, Tennessee (1981), p. 311.

48. N. A. Uckan et al., paper presented at the Ninth Symposium on Engineering Problems of Fusion Research, Chicago, Illinois, October 26-27, 1981.

49. T. Uckan and N. A. Uckan, in *Hot Electron Ring Physics: Proceedings of the Second Workshop*, CONF-811203, Oak Ridge National Laboratory, Oak Ridge, Tennessee (in press).

50. N. A. Uckan, R. G. Spencer, and T. Uckan, *Synchrotron Radiation from the Hot Electron Rings in EBT*, ORNL/TM-7687, Oak Ridge, Tennessee (1981).

51. N. A. Uckan et al., *Physics of Hot Electron Rings in EBT: Theory and Experiment*, ORNL/TM-7585, Oak Ridge, Tennessee (1981).

52. N. A. Uckan and D. A. Spong, paper 2B1 presented at 1981 Sherwood Meeting on Theoretical Aspects of Controlled Thermonuclear Research, Austin, Texas, April 7-10, 1981.

53. M. R. Gordinier and N. A. Uckan, Bull. Am. Phys. Soc. 26, 997 (1981).

54. L. W. Owen and N. A. Uckan, *Optimization of EBT Reactor Magnetics*, ORNL/TM-7729, Oak Ridge, Tennessee (1981).

55. N. A. Uckan, "Status of the ELMO Bumpy Torus Research," paper presented at the Tenth European Conference on Controlled Fusion and Plasma Physics, Moscow, U.S.S.R., September 14-19, 1981 (proceedings to be published).

56. C. L. Hedrick, "The Status of EBT Physics," paper 3A2-3 presented at the 1981 IEEE International Conference on Plasma Science, Santa Fe, New Mexico, May 18-20, 1981.

57. L. A. Charlton et al., Bull. Am. Phys. Soc. 26, 879 (1981).

58. J. K. Munro, Jr., et al., Bull. Am. Phys. Soc. 25, 976 (1980).

59. W. A. Cooper, *Tensor Pressure Tokamak Equilibrium and Stability*, ORNL/TM-7120, Oak Ridge, Tennessee (1981).

60. J. T. Hogan, "Periodic Large-Amplitude MHD Activity in Beam-Heated Tokamaks," paper presented at 1981 Sherwood Meeting on Theoretical Aspects of Controlled Thermonuclear Research, Austin, Texas, April 7-10, 1981.

61. V. V. Parail and G. V. Pereversev, Fiz. Plazmy 6, 27, 1980.

62. B. A. Carreras, M. N. Rosenbluth, and H. R. Hicks, Phys. Rev. Lett. 46, 1131 (1981).

63. V. E. Lynch, B. A. Carreras, H. R. Hicks, J. A. Holmes, and L. Garcia, Commun. Comput. Phys. 24, 465 (1981).

64. J. A. Holmes, B. A. Carreras, H. R. Hicks, V. E. Lynch, and K. E. Rothe, *Finite Beta Effects on the Nonlinear Evolution of the m=1;n=1 Mode in Tokamaks*, ORNL/TM-8063, Oak Ridge, Tennessee (1982).

65. B. A. Carreras, J. D. Callen, P. W. Gaffney, and H. R. Hicks, *Rippling Modes in the Edge of a Tokamak Plasma*, ORNL/TM-7989, Oak Ridge, Tennessee (1981).

66. H. R. Hicks, B. A. Carreras, J. A. Holmes, and V. E. Lynch, *Nonlinear Analysis of Disruptions in the JIPP T-II Tokamak*, ORNL/TM-7733, Oak Ridge, Tennessee (1981).

67. H. R. Hicks, B. Carreras, L. Garcia, J. A. Holmes, and V. E. Lynch, in *Proceedings of the U.S.-Japan Theory Workshop on 3-D MHD Studies for Toroidal Devices*, CONF-8110101, Oak Ridge National Laboratory, Oak Ridge, Tennessee (1982), p. 59.

68. J. L. Johnson et al., Phys. Fluids 1, 281 (1958).

69. J. A. Holmes, B. A. Carreras, L. A. Charlton, H. R. Hicks, and V. E. Lynch, in *Proceedings of the U.S.-Japan Theory Workshop on 3-D MHD Studies for Toroidal Devices*, CONF-8110101, Oak Ridge National Laboratory, Oak Ridge, Tennessee (1982), p. 156.

70. H. K. Meier, "Fast Moment Equation Method for Solving the Grad-Shafranov Equation," paper presented at 1981 Sherwood Meeting on Theoretical Aspects of Controlled Thermonuclear Research, Austin, Texas, April 7-10, 1981.

71. L. L. Lao, S. P. Hirshman, and R. M. Wieland, Phys. Fluids 24, 1431 (1981).

72. K. T. Tsang, Phys. Fluids 24, 11 (1981).

73. W. A. Cooper, G. Bateman, D. B. Nelson, and T. Kammash, Plasma Phys. 23, 105 (1981).

74. K. T. Tsang and D. J. Sigmar, Nucl. Fusion 21, 1227 (1981).

75. W. A. Cooper and K. T. Tsang, Nucl. Fusion 21, 1477 (1981).

76. W. A. Cooper, *Safety Factor Profile Optimization of High n Ideal Ballooning Mode Stability of Tokamaks*, ORNL/TM-7807, Oak Ridge, Tennessee (1981).

77. W. A. Cooper, "Diamagnetic Drift Frequency Effects on Tokamak Ballooning Stability," to be published in Plasma Physics.

78. C. O. Beasley, K. Molvig, and W. I. van Rij, *Universal Mode with Diffusive Electrons: Linear Stability and Nonlinear Saturation*, ORNL/TM-8132, Oak Ridge, Tennessee (1982).

79. W. I. van Rij and C. O. Beasley, Jr., *TEDIT, a Computer Code for Studying the Time Evolution of Drift Instabilities in a Torus*, ORNL/TM-8234, Oak Ridge, Tennessee (1982).

80. C. Beasley, K. Molvig, and W. I. van Rij, Bull. Am. Phys. Soc. 26, 1010 (1981).

81. S. P. Hirshman and P. H. Diamond, "Self-Consistent Spectrum of Electrostatic Drift Wave Fluctuations due to Electron Phase Space Correlations in a Sheared Magnetic Field," to be published in Physics of Fluids.

82. S. P. Hirshman and J. C. Whitson, "Spectral Analysis of Noisy Nonlinear Maps," to be published in Physics of Fluids.

83. K. T. Tsang, D. J. Sigmar, and J. C. Whitson, Phys. Fluids 24, 1508 (1981).

84. D. J. Sigmar, K. T. Tsang, and J. C. Whitson, Bull. Am. Phys. Soc. 26, 888 (1981).

85. S. P. Hirshman and D. J. Sigmar, Nucl. Fusion 21, 1079 (1981).

86. S. P. Hirshman and K. Molvig, Nucl. Fusion Lett. 21, 1480 (1981).

87. H. K. Meier, S. P. Hirshman, D. J. Sigmar, and L. L. Lao, *Plateau Diffusion Coefficient for Arbitrary Flux Surface Geometry*, ORNL/TM-7584, Oak Ridge, Tennessee (1981).

88. J. T. Hogan, Nucl. Fusion 21, 365 (1981).

89. D. B. Nelson and L. A. Charlton, "Neoclassical Resistive q(ψ)-Conserving-Tokamak Equilibria," paper presented at the 1981 Sherwood Meeting on Theoretical Aspects of Controlled Thermonuclear Research, Austin, Texas, April 7-10, 1981.

90. R. A. Dory, L. A. Charlton, D. B. Nelson, and D. K. Lee, Bull. Am. Phys. Soc. 25, 864 (1980); L. A. Charlton, R. A. Dory, and D. K. Lee, "Resistive Flux-Conserving-Tokamak Equilibria," submitted to Nuclear Fusion.

91. S. P. Hirshman, R. J. Hawryluk, and B. Birge, Nucl. Fusion 17, 611 (1977).

92. J. F. Clarke, Nucl. Fusion 20, 563 (1980).

93. W. A. Houlberg, Oak Ridge National Laboratory, private communication (1981).

94. H. C. Howe and A. J. Wootton, "Numerical Simulations of the Bundle Divertor," paper presented at the IAEA Technical Committee Meeting on Divertors and Impurity Control in Tokamaks, Garching, Federal Republic of Germany, July 6-9, 1981.

95. L. M. Hively et al., "Constrained Ripple Optimization of Tokamak Bundle Divertor," to be published in Nuclear Technology/Fusion.

96. L. M. Hively, G. H. Miley, and J. A. Rome, Nucl. Fusion 21, 1431 (1981).

97. J. A. Rome, J. F. Lyon, and R. H. Fowler, *Using a Constants-of-Motion Space to Clarify Measurements Involving Energetic Ion Orbits in Tokamaks*, ORNL/TM-7913, Oak Ridge, Tennessee (1981).

98. C. Ruchti, *FLT: A Field Line Tracing Code for Bundle Divertor Design*, ORNL/TM-7555, Oak Ridge, Tennessee (1981).

99. W. A. Houlberg, S. E. Attenberger, and L. L. Lao, "Developments in Tokamak Transport Modeling," paper presented at the ANS/ENS International Topical Meeting on Advances in Mathematical Methods for Nuclear Engineering Problems, Munich, Federal Republic of Germany, April 27-29, 1981.

100. L. A. Charlton, R. A. Dory, D. J. Sigmar, and D. W. Swain, "Transport Study of ISX-B Flux-Conserving Tokamak Heating Scenarios," paper presented at the 1981 Sherwood Meeting on Theoretical Aspects of Controlled Thermonuclear Research, Austin, Texas, April 7-10, 1981.

101. D. W. Swain et al., Bull. Am. Phys. Soc. 25, 875 (1980).

102. D. B. Nelson and H. Grad, *Heating and Transport in Tokamak Arbitrary Shape and Beta*, ORNL/TM-6094, Oak Ridge, Tennessee (1979).

103. L. A. Charlton, D. B. Nelson, and R. A. Dory, Phys. Rev. Lett. 45, 24 (1980).

104. J. K. Munro, J. Hogan, and G. H. Neilson, Bull. Am. Phys. Soc. 26, 879 (1981).

105. J. K. Munro, Jr., J. Hogan, H. Howe, and D. Arnurius, *A User's Manual for the Oak Ridge Tokamak Transport Code*, ORNL/TM-5262, Oak Ridge, Tennessee (1977).

106. J. Hogan, Nucl. Fusion 19, 753 (1979).

107. J. T. Hogan, "Rotation and Island Effects in Tokamaks with High-Power Neutral Beam Heating," paper presented at the Tenth European Conference on Controlled Fusion and Plasma Physics, Moscow, U.S.S.R., September 14-19, 1981.

108. G. G. Kelley and J. T. Hogan, Bull. Am. Phys. Soc. 26, 881 (1981).

109. R. H. Fowler, J. A. Holmes, and J. A. Rome, *NFREYA — A Monte Carlo Beam Deposition Code for Noncircular Tokamak Plasmas*, ORNL/TM-6845, Oak Ridge, Tennessee (1979).

110. D. J. Sigmar and H. C. Howe, "Transport Modeling of Impurity Control by Direct

Momentum and Inertial Effects," paper presented at the 1981 Sherwood Meeting on Theoretical Aspects of Controlled Thermonuclear Research, Austin, Texas, April 7-10, 1981.

111. W. M. Stacey and D. J. Sigmar, Nucl. Fusion 19, 1665 (1979).

112. K. H. Burrell, T. Ohkawa, and S. K. Wong, Phys. Rev. Lett. 47, 511 (1981).

113. J. T. Hogan, "Effects of Low Energy Electron Capture Collision ($H_0 + C^{n+}$) on the Particle and Energy Balance of Tokamak Plasmas," paper presented at the Twelfth International Conference on the Physics of Electronic and Atomic Collisions, Gatlinburg, Tennessee, July 15-21, 1981.

114. R. C. Isler et al., Phys. Rev. Lett. 47, 649 (1981).

115. E. C. Crume, Bull. Am. Phys. Soc. 26, 867 (1981).

116. R. J. Hawryluk, S. Suckewer, and S. P. Hirshman, Nucl. Fusion 19, 607 (1979).

117. Y-K. M. Peng et al., *Plasma Assessments for the Fusion Engineering Device (FED)*, ORNL/TM-7901, Oak Ridge, Tennessee (1981).

118. W. A. Houlberg and S. E. Attenberger, "Plasma Engineering Analyses of Tokamak Reactor Operating Space," paper presented at the Ninth Symposium on Engineering Problems of Fusion Research, Chicago, Illinois, October 26-29, 1981.

119. D. J. Sigmar, *Approach to Ignition of Tokamak Reactors*, ORNL/TM-7552, Oak Ridge, Tennessee (1981).

120. W. A. Houlberg, *Proceedings of INTOR Meeting, 1981*, INTOR/PHY/81-1, IAEA, Vienna, Austria (1981).

121. S. K. Borowski, W. A. Houlberg, Y-K. M. Peng, and T. Kammash, Bull. Am. Phys. Soc. 26, 963 (1981).

122. L. M. Hively, W. A. Houlberg, and S. E. Attenberger, "Optimal Neutral-Beam-Heating Scenario for FED," paper presented at the Ninth Symposium on Engineering Problems of Fusion Research, Chicago, Illinois, October 26-29, 1981.

123. H. C. Howe, *Physics Considerations for the FED Limiter*, ORNL/TM-7803, Oak Ridge, Tennessee (1981).

124. S. E. Attenberger, W. A. Houlberg, and S. L. Milora, "Numerical Simulation of Fueling in Tokamaks," to be published in the Journal of the American Vacuum Society.

125. R. H. Fowler and J. A. Rome, *The Effects of Toroidal Field Ripple on Injected Tokamaks in the FED Device*, ORNL/TM-7774, Oak Ridge, Tennessee (1981).

126. S. E. Attenberger, J. A. Holmes, W. A. Houlberg, and S. D. Scott, "Toroidal Field Ripple Conduction Losses in the FED Tokamak," paper presented at the 1981 IEEE International Conference on Plasma Science, Santa Fe, New Mexico, May 18-20, 1981.

127. J. R. McNally, Jr., Nucl. Technol./Fusion 2, 9 (1982).

128. Y-K. M. Peng, P. H. Rutherford, and J. F. Lyon, "Plasma Physics Assessments for the Fusion Engineering Device (FED)," paper presented at the Ninth Symposium on Engineering Problems of Fusion Research, Chicago, Illinois, October 26-27, 1981.

129. *Stellarators: Status and Future Directions*, IPP-2/254, Max Planck Institute for Plasma Physics, Garching bei München, Federal Republic of Germany (1981) [also available as DE81026572, U.S. Department of Energy Technical Information Center, Oak Ridge, Tennessee (1981)].

130. A. H. Boozer, Phys. Fluids 23, 904 (1980).

131. R. Chodura and A. Schlüter, J. Comput. Phys. 44, 68 (1981).

132. J. L. Johnson, C. R. Oberman, R. M. Kulsrud, and E. A. Frieman, Phys. Fluids 1, 281 (1958).

133. H. R. Strauss, Plasma Phys. 22, 733 (1980).

5. PLASMA–MATERIALS INTERACTIONS

R. E. Clausing[1]
R. J. Colchin
T. B. Cook[2]
E. Dullni[3]
L. C. Emerson[1]
B. Emmoth[4]
L. Heatherly[1]
H. C. Howe
R. C. Isler
P. W. King
R. A. Langley
K. O. Legg[5]
P. Mioduszewski
L. E. Murray
R. K. Richards
J. B. Roberto[6]
J. E. Simpkins
E. W. Thomas[5]
J. B. Whitley[6]
S. P. Withrow[7]
C. E. Young[7]
R. Young[5]
R. A. Zuhr[2]

1. Metals and Ceramics Division.
2. Solid State Division.
3. Ruhr-Universität Bochum and Kernforschungsanlage Jülich, Federal Republic of Germany.
4. Institute of Physics, Stockholm, Sweden.
5. Georgia Institute of Technology, Atlanta, Georgia.
6. Sandia National Laboratories, Albuquerque, New Mexico.
7. Argonne National Laboratory, Argonne, Illinois.

5. PLASMA-MATERIALS INTERACTIONS

ABSTRACT. The Plasma-Materials Interactions Program addresses issues relating to plasma edge phenomena in fusion devices and the interaction of the plasma with exposed surfaces. These issues affect impurity control, fuel management, particle handling, and materials selection in present devices and future reactors. The program characterizes hydrogen and impurity fluxes in the plasma edge, identifies mechanisms of hydrogen recycling and erosion, and contributes to the development of new materials and techniques for particle handling. The research focuses on the Impurity Study Experiment (ISX-B) and ELMO Bumpy Torus-Scale (EBT-S) fusion devices at ORNL and includes the participation of the Fusion Energy, Metals and Ceramics, and Solid State divisions.

During 1981, the program emphasized edge flux measurements, hydrogen recycling studies, and advanced limiter experiments. Surface probes were used to measure hydrogen and impurity fluxes to the walls of ISX-B and EBT-S and during programmed gas puffing in ISX-B. Laser-induced fluorescence (LIF) measurements identified wall sputtering as the central cavity release mechanism for aluminum in EBT-S. Minority hydrogen species recycling experiments demonstrated fast (≤20-ms), near-unity (≥0.95) recycling for nongettered, ohmic discharges in ISX-B and suggested a thermal recycling process. Plasma-limiter interactions were studied photographically during beam-heated discharges in ISX-B. New initiatives included participation in pumped limiter experiments on ISX-B and preparations for collaborative edge physics studies on the TEXTOR tokamak at Jülich.

5.1 MEASUREMENT OF THE DENSITY AND VELOCITY DISTRIBUTIONS OF SPUTTERED ALUMINUM ATOMS IN EBT-S BY LASER-INDUCED FLUORESCENCE

E. Dullni, J. B. Roberto, R. J. Colchin

The density and velocity distributions of neutral aluminum atoms have been measured in the vicinity of the outer wall of the EBT-S fusion device by laser-induced fluorescence (LIF). EBT-S is a steady-state plasma experiment consisting of 24 mirror sections bent into a torus. Macroscopic erosion rates are observed where magnetic field lines intercept the aluminum vacuum vessel walls. The mechanism of this erosion has been the subject of a great deal of speculation and is an important consideration in the design of the next-generation EBT Proof-of-Principle (EBT-P) device. LIF[1] provides direct information on the erosion process through measurements of the flux and velocity distribution of the eroded atoms.

The experimental setup is shown in Fig. 5.1. A flashlamp-pumped, frequency-doubled dye laser was tuned to the resonance transition of aluminum at 308.2 nm. The LIF was detected using a photomultiplier and lens system which optically intercepted the laser beam 5 cm in front of a cavity wall in EBT-S. An aluminum plate partially covered the access port at the wall position to simulate a continuous wall. Wavelength scanning of the dye laser at a narrow linewidth (~11 mA) allowed measurements of the Doppler-broadened profile of the aluminum line with a velocity resolution of ~10^4 cm/s (~0.1 eV). Plasma parameters for these measurements were: 100-kW microwave power at 28 GHz, B(0) = 1.4 T, $n_e(0) = 1.0 \times 10^{12}$ cm^{-3}, $T_e(0)$ = 400 eV, and $T_i(0)$ = 20-40 eV.

The Doppler-broadened absorption profile for aluminum is shown in Fig. 5.2. The integral of this profile corresponds to a neutral aluminum density of 6.5×10^7 atoms/cm^3. The maximum in the distribution is shifted to the left, indicating atoms moving away from the wall. The small peak on the right side of the distribution corresponds to atoms originating at the mirror throats, which would have an opposite velocity component at the detection volume. The mean energy of the aluminum atoms released from the wall is 1.6 eV with a Doppler width of 2.5 eV. These energies are typical of sputtering distributions and are much higher than the energies expected for other

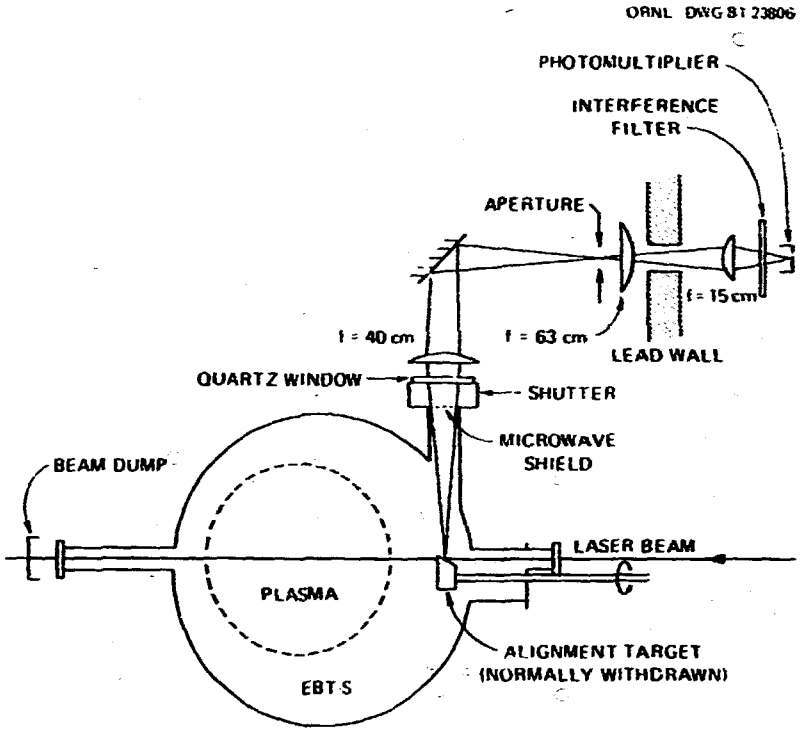

Fig. 5.1. Experimental setup for LIF measurements in EBT-S.

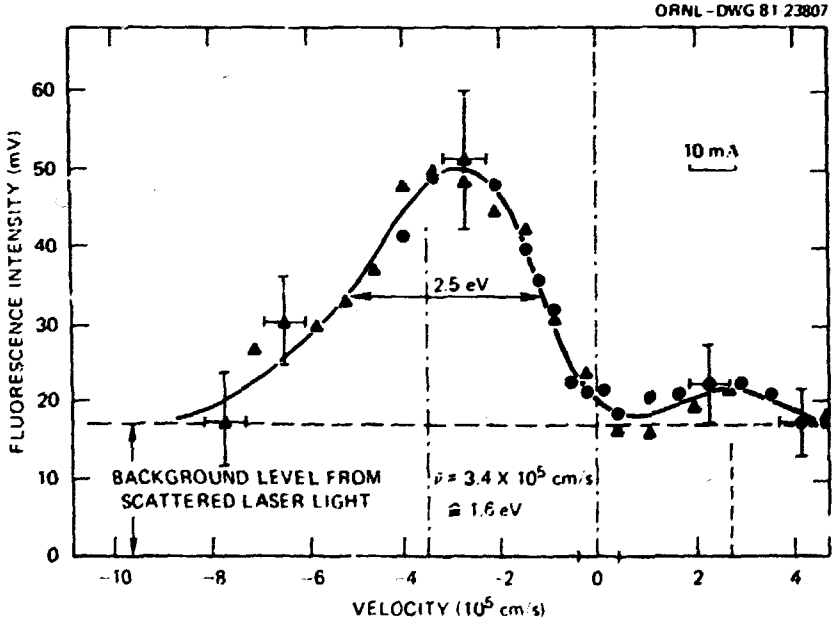

Fig. 5.2. Velocity distribution for neutral aluminum perpendicular to and 5 cm from an outer cavity wall in EBT-S. Atoms moving away from the wall show a negative velocity shift.

release mechanisms such as arcing or evaporation. Measurements made with different plasma parameters and made along the laser beam at different distances from the wall have been performed and are currently being evaluated.

5.2 CONTINUOUS WAVE LASER-INDUCED FLUORESCENCE MEASUREMENTS IN ISX-B

T. B. Cook, P. W. King, C. E. Young, W. R. Husinsky, J. B. Roberto*

The method of LIF is a powerful diagnostic for detection of trace species in hostile environments and has been demonstrated in studying impurity metal atoms in tokamaks.[2] The transport of such impurities into the tokamak plasma is a serious concern for fusion reactors, since as little as 0.1% contamination by heavy metals can prevent plasma ignition.

The application of LIF to plasma impurity studies has primarily involved pulsed laser systems.[3] There are, however, two disadvantages to such systems. First, it is difficult to operate a pulsed dye laser at bandwidths sufficiently narrow to allow estimation of thermal Doppler widths. This is significant because the relative importance of sputtering versus thermal evaporation has not yet been fully characterized. Second, pulsed laser systems provide information at only a few (1-10) submicrosecond intervals during the tokamak discharge. It is thus a time-consuming process to map the impurity evolution during a 200- to 300-ms shot. To better address these two problems of energy spectrum and temporal development, we have undertaken LIF experiments on ISX-B using a continuous wave (cw) dye laser.

The laser system is a tunable, actively stabilized, ring dye laser pumped by an argon ion laser. It produces single-frequency radiation with a linewidth of under 1 MHz and can therefore be tuned inside a Doppler-broadened transition even for low temperature thermal distributions. Output power is sufficient to saturate the relevant absorption transitions over an interaction volume of $\sim 1\ cm^3$.

The first studies have been performed on chromium neutrals in the vicinity of a chromium probe in the plasma edge of ISX-B. The dye laser is operated on one of the components of the atomic resonance line at ~425 nm (producing a power output of 50-150 mW). As indicated in Fig. 5.3, the laser is tuned to the absorption using a variety of devices, including a small grating spectrometer for rough tuning and a hollow cathode lamp (utilizing the optogalvanic effect) for fine tuning. Final adjustment, to allow for Zeeman shifts in the ~1-T toroidal field, is accomplished using a pair of scanning Fabry-Perot etalons. The laser beam is acousto-optically chopped (allowing high order diffraction spots to be used for the various monitoring functions) and injected into the tokamak vessel, which is located ~8 m from the laser table. Fluorescence from atoms illuminated by the laser just outside the plasma edge is collected, spectrally filtered using a double spectrometer with holographic gratings, and detected with a photomultiplier tube. A computer-controlled data acquisition system operates a gated counter, stores the data for later analysis, and graphically displays the results on a terminal in the laser enclosure.

Preliminary analysis of chromium results indicates a very weak signal due to chromium, but uncertainties in the measurements are large, principally because of extremely high count rates from plasma light scattered into the collection cone of the detector. Further application of the cw LIF technique in ISX-B will require better rejection of plasma light than has been achieved in these initial experiments.

*Technical University of Vienna, Vienna, Austria.

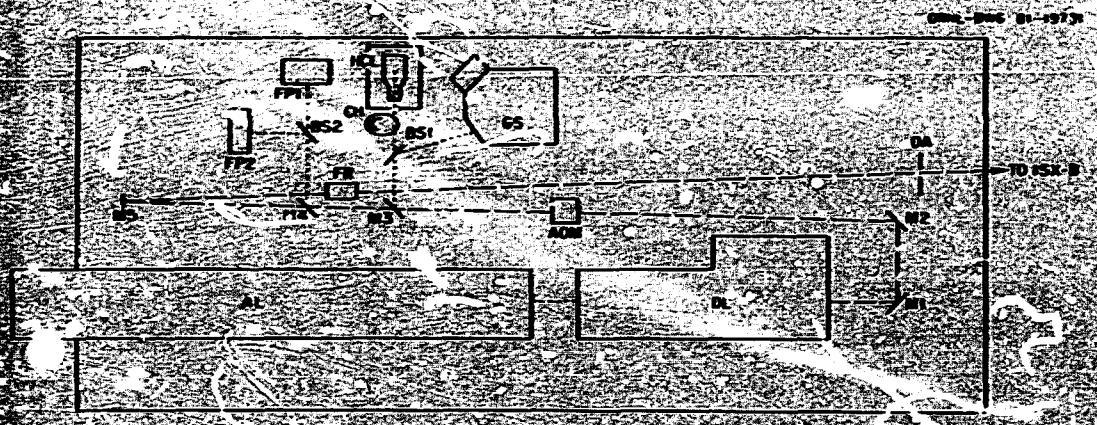

Fig. 5.3. Argon ion laser (AL) pumps dye laser (DL). The output beam is modulated by the acousto-optic modulator (AOM), its polarization rotated using a Faraday rotator (FR), passes through an output aperture (DA), and is transported to the tokamak. Mirrors (M3 and M4) pick off high order diffraction spots. A fraction of the beam from M3 is split off by using a beam splitter (BS1) and enters a mechanical spectrometer (GS) for rough tuning. The remainder of the M3 beam is modulated by a low speed mechanical chopper (FP1) and impinges on a hollow cathode lamp (HCL) for fine tuning to the atomic absorption. The M4 beam is divided by a beam splitter and analyzed by two Fabry-Perot scanning etalons to check for Zeeman tuning and for mode hops of the dye laser.

5.3 HYDROGEN RECYCLING AND IMPURITIES DURING ISOTOPIC EXCHANGE IN ISX-B*

J. B. Roberto, R. C. Isler, S. Kasai, L. E. Murray, J. E. Simpkins, S. P. Withrow, R. A. Zuhr*

The interaction of plasma particles with recycled surfaces in tokamaks contributes significantly to fueling and impurity introduction in existing devices. Hydrogen-deuterium (H-D) isotopic exchange experiments, which involve monitoring the plasma composition after switching to one working gas following many discharges in the other, allow direct observation of surface contributions to the plasma isotopic composition and isotope effects in impurity introduction. We report here measurements of working gas composition and edge impurity levels during H-D changeover experiments in the ISX-B tokamak. The results are interpreted in terms of recycling and impurity introduction mechanisms in ISX-B.

Plasma operation was shifted from deuterium to hydrogen (D → H) and from hydrogen to deuterium (H → D) by changing the fill and puffing gases for a sufficient number of discharges to obtain complete (>98%) changeover for each isotope. H/D ratios were monitored during the discharge from relative H_β and D_β spectral intensities and after each discharge by residual gas analysis (RGA) and nuclear reaction analysis (NRA) of silicon surface probes which were exposed in the plasma edge. Relative oxygen and iron impurity levels in the edge were determined from O VI and Fe IX spectral intensities. Plasma conditions for the nongettered, ohmic discharges were B_T = 1.3 T, I_p = 135 kA, $T_e(0)$ = 540 eV, and $n_e(0)$ = 6-7 x 10^{13} cm^{-3} with a current flat top of ~150 ms. ISX-B has type 304 stainless steel walls.

The isotopic changeover in the plasma edge as determined from optical measurements is shown in Fig. 5.4. Plotted in the figure is the fraction of plasma composition made up by the previous isotope as a function of the number of discharges in the new isotope. Data

*Japan Atomic Energy Research Institute, Tokai, Japan.

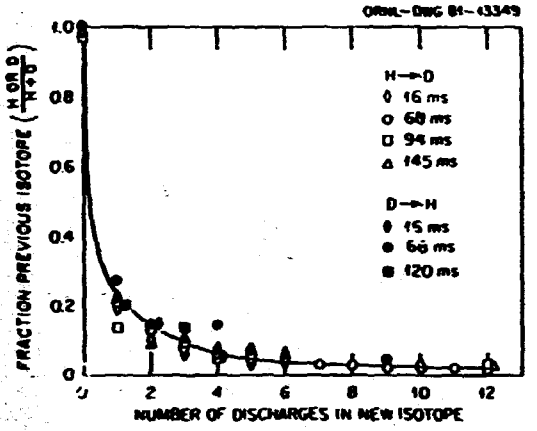

Fig. 5.4 Fractional contributions of the previous isotope to the plasma composition as a function of number of discharges in the new isotope. Data are from relative H_β and D_β spectral intensities and are shown for various times during the discharge for both H → D and D → H changeovers.

for H → D and D → H changeovers are shown at times varying from 16 to 145 ms into the discharge. The results indicate that the isotopic exchange in the plasma is ~80% complete after the first 15 ms of the first discharge in the new isotope, but requires ~10 discharges to reach 98% completion. There is no evidence of a trend in the isotopic composition as a function of time during the discharge. The RGA and surface probe results are consistent with the optical data.

The changeover results indicate that plasma isotopic composition for these experimental conditions in ISX-B is determined primarily by the fill gas, with ~20% of the plasma particles originating from exposed surfaces. This surface contribution appears within the first 20 ms of the discharge, after which the plasma composition remains approximately constant. These results suggest that recycling in ISX-B occurs without significant isotopic mixing after the first 20 ms of the discharge. This requires the rapid establishment of an equilibrium between the plasma composition and the interacting surfaces. Isotopic replacement in the walls does not contribute to the recycling, since this process would be continuous throughout the discharge. The isotopic replacement does occur in ~10 discharges by diffusion between discharges and subsequent release.

Iron levels in the plasma edge increase by a factor of ~3 for deuterium operation compared with hydrogen operation. This result is consistent with the expected D/H sputtering ratio for a Maxwellian distribution of hydrogen atoms on stainless steel near 100 eV. This suggests that charge exchange neutral sputtering of the walls may play a dominant role in the heavy impurity introduction mechanism in ISX-B. The importance of the wall as a heavy impurity source is also indicated by the low titanium levels[5] in ISX-B despite operation with a TiC outer limiter. The oxygen levels in the edge are the same for deuterium and hydrogen operation, consistent with a thermal release mechanism for light impurities.

Overall, the results demonstrate low hydrogen inventory and rapid isotopic changeover for tokamak operation with stainless steel walls. The surface-released contribution is ~20% of the plasma composition and appears within the first 20 ms of the discharge. This is associated with wall desorption and fast release processes at the limiter. Ion-induced effects do not contribute to recycling during the steady-state portion of the discharge. The results are consistent with a thermal mechanism for recycling and oxygen release and with hydrogen sputtering of the walls for heavy impurity introduction.

5.4 MINORITY HYDROGEN ISOTOPE RECYCLING IN ISX-B[7]

J. B. Roberto, H. C. Howe, R. C. Isler, L. E. Murray

The recycling of hydrogen from exposed surfaces controls plasma fueling in present tokamaks and will play a significant role in determining the wall tritium inventory in deuterium-tritium (D-T) devices. Recent H/D isotopic exchange experiments[7] for nongettered, ohmic discharges in the ISX-B tokamak suggest a fast recycling process with no significant

isotopic mixing after the first 20 ms of the discharge. This result is consistent with a hydrogen recycling mechanism for the wall that is not controlled by ion-induced effects. In the present experiment, H/D ratios were monitored in ISX-B plasmas for D_2 discharges during which a short pulse of H_2 was introduced as a minority isotope. The results confirm the previous observations and are consistent with near-unity recycling controlled by a thermally activated process.

In the experiment, a short burst of H_2 was puffed into an established ohmically heated D_2 plasma at 80 ms into the discharge. H/D ratios were determined throughout the discharge from relative H_β/D_β spectral intensities using a high resolution spectrometer equipped with an oscillating mirror for repetitively scanning a 10-Å region around 4861 Å. The spectrometer viewed the plasma along a major radius ~90° toroidally from the limiter and ~180° toroidally from the H_2 injection port. The narrow hydrogen Balmer lines in tokamaks are attributed to excited atoms formed during and following the dissociation of molecular hydrogen in the plasma edge and probably reflect molecular fluxes from the wall. Plasma conditions for this experiment were $n_e(0) = 6 \times 10^{13}$ cm^{-3}, $T_e(0) = 720$ eV, $B_T = 1.3$ T, and $I_p = 170$ kA with a current plateau from 80 to 180 ms. ISX-B had nongettered type 304 stainless steel walls at the time of this experiment and was equipped with a TiC outer and a stainless steel inner limiter.

Relative H_2/D_2 signals for several D_2 discharges with H_2 input are shown in Fig. 5.5. The H_2 signal rises rapidly during the puff to one-sixth of the D_2 signal, consistent with the ratio of overall H_2/D_2 gas input (0.15), and remains essentially constant during the remainder of the discharge. The hydrogen charge exchange neutral flux (measured radially outward at a location well away from both the limiter and the H_2 injection port) shows a comparable rapid increase during the H_2 puff with a plateau from 90 to 170 ms.[7] These

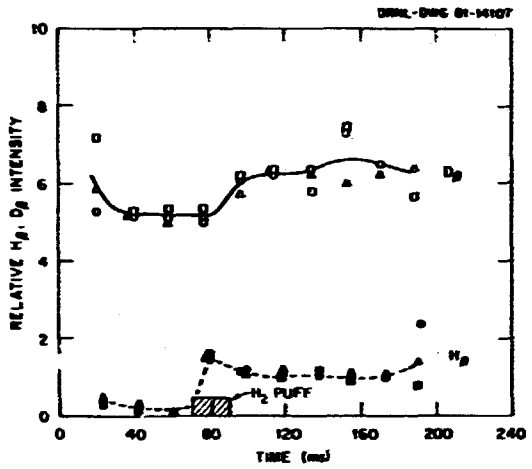

Fig. 5.5. Relative H_β and D_β spectral intensities for three successive D_2 discharges in ISX-B with a short puff of H_2 at 80 ms. The apparent time shift in the relative H_β and D_β increases during the puff probably reflects the time difference in H_β and D_β sampling.

results suggest recycle times of ≤20 ms and coefficients of ≥0.95 for the minority isotope from a time almost immediately following the H_2 puff until the end of the discharge. The H_β signal at the beginning of the discharge is approximately one-fifth of the steady-state value following the puff, consistent with the previous observation[8] that ~20% of the initial plasma composition for nongettered, ohmic ISX-B discharges is released from exposed surfaces.

For the case of recycling dominated by thermally activated processes, the hydrogen outflux for isotope i from the wall can be written as

$$\phi_i = k_r C_i (C_i + C_j) , \qquad (5.1)$$

where k_r is the recombination rate constant and $C_{i,j}$ is the near-surface hydrogen concentration for isotope i,j. This equation governs the formation of molecular hydrogen at the surface, which readily desorbs at room temperature.

Thermally activated recycling has been observed in plasma simulator experiments with stainless steel walls.[10,11] Equation (5.1) implies that the minority isotope release will be dominated by recombination with the majority isotope, forming the HD molecule in our case. This requires essentially the same recycling behavior for the minority and majority species and an increase in the majority isotope outflux approximately equal to the minority isotope release. This is consistent with Fig. 5.5, where the D_β signal increases after the H_2 puff by an amount comparable to the H_β increase.

The present results are not easily explained by recycling mechanisms based solely on ion-induced effects such as particle reflection or isotopic replacement in the walls. Reflection coefficients of ≤0.8 are expected for wall neutrals in ISX-B, and wall neutral fluxes are too low for significant replacement in the bulk to occur during a discharge. Neither mechanism explains the simultaneous rise in the H_β and D_β signals. On the other hand, a thermally activated process based on diffusion and surface recombination is consistent with the observed recycling behavior, although the recycling time is somewhat faster than theoretically expected[10,11] for ISX-B operating conditions. Overall, the present results demonstrate fast (≤20 ms), near-unity (>0.95) minority species recycling in a nongettered, stainless steel tokamak.

5.5 RECYCLING STUDIES IN ISX-B BY HYDROGEN ALPHA EMISSION

B. Emmoth, R. Young, E. W. Thomas, T. B. Cook

The recycling of gas atoms from the limiter and walls in a tokamak is as important as magnetic confinement in determining plasma density. In the current generation of fusion energy devices, most of the gas fueling is by recycling with only a small fraction of the plasma particles supplied by active gas puffing.

A useful diagnostic for studying recycling is the monitoring of H_α emission from the plasma edge. This radiation, generated by the excitation of neutral hydrogen as it moves into the plasma, has been shown to be a useful indicator of hydrogen flux into the plasma. The H_α detectors for the present experiment consist of a collimating lens, an interference filter to isolate the hydrogen line, and a photodiode as the receiver. Four such detectors have recently been installed on the ISX-B tokamak, each viewing a 2.5-cm-diam cylinder on a chord through the plasma and intercepting the relevant plasma edge region twice — once on the near side of the plasma and once on the far side.

Although the work is at an early stage, several preliminary observations have been made. We find that there are pronounced toroidal and poloidal variations in H_α emission, with the limiters and the gas puff being strong sources. For ohmic discharges, the detector viewing the gas puff region follows the flow of gas into the vessel; simultaneously, a detector viewing a region far from the gas puff or limiters shows a smooth increase in signal. For neutral beam injection, the H_α signal from the gas puff region increases steadily even with constant puffing, suggesting beam-induced desorption from the hardened energy spectrum of neutrals striking the wall. Several H_α experiments are planned for the near future to investigate particular issues in the recycling problem.

5.6 EFFECTS OF NEUTRAL BEAM INJECTION AND GAS PUFFING ON DEUTERIUM AND IMPURITY LEVELS IN THE SCRAPEOFF LAYER OF ISX-B[12]

R. A. Zuhr, J. R. Roberto, S. P. Withrow

Silicon deposition probes have been exposed to a variety of operating conditions in the plasma edge of ISX-B to investigate the effects of neutral beam injection and gas puffing on edge characteristics. The exposures were made using a bellows-sealed sample insertion system that allowed the samples to be positioned at any radius between the limiter and the outer wall. An electrically driven rotating shaft permitted multiple or time-resolved (15-ms)

sampling. All measurements were made in the horizontal midplane of the tokamak at a toroidal position 120° from the limiters in the positive ion current direction. For these experiments, ISX-B was operated with an inner bar limiter of stainless steel and an outer mushroom-shaped limiter of TiC-coated graphite.

Exposures were made for both ohmically heated and neutral-beam-injected (NBI) discharges and for discharges in which the fill gas puffing was programmed to determine its effect on the plasma edge. After exposure, the samples were transferred to the Solid State Division's 2.5-MeV Van de Graaff accelerator, where they were analyzed for impurity deposits using 2-MeV ^{4}He backscattering and for retained deuterium using the D(^{3}He,p)^{4}He nuclear reaction.

The temporal behavior of the principal impurities collected 2.5 cm behind the limiter during 1.1-MW NBI discharges in ISX-B indicates that oxygen is the most abundant impurity, with deposition more than an order of magnitude greater than that of the most common metallic element, iron. Chromium and nickel are present in approximately the same ratio to iron as they are in type 304 stainless steel, the wall material in ISX-B. The amount of titanium on the probe is an order of magnitude less than iron. A sharp increase in all impurity levels occurs at the onset of neutral beam injection. A similar increase is observed in the measured deuterium flux at the time of injection. These increases in edge fluxes vary from a factor of 2-3 for deuterium and oxygen to a factor of ~7 for metallic elements. A correlation is found between high metallic impurity fluxes and high levels of magnetohydrodynamic (MHD) activity in the plasma. Such a correlation has been observed in all previous time-resolved probe data from ISX.[13]

To clarify the effects of gas puffing on both impurity and plasma fluxes in the scrapeoff layer, an experiment was carried out in which a gas puff of ~0.3 torr·liter of deuterium gas was injected at 120 ms into a conventional ohmically heated deuterium plasma. This was in addition to the "normal" puff at ~40 ms as shown in Fig. 5.6. In this figure silicon surface damage, which is indicative of incident deuterium flux and energy,[14] is plotted as a function of time during the discharge. Comparisons are made with MHD level, density, and gas puffing rate for these discharges. A significant decrease in damage occurs with each gas puff. In this experiment, we primarily collect ions traveling parallel to the toroidal magnetic field, and the factor of 2 reduction in damage during puffing implies that the ion density has decreased by 2, that the average ion energy has decreased by $\sqrt{2}$, or that a combination of these effects has taken place. In all cases, it is clear that the deuterium flux in the edge has been "cooled" by the gas puffing.

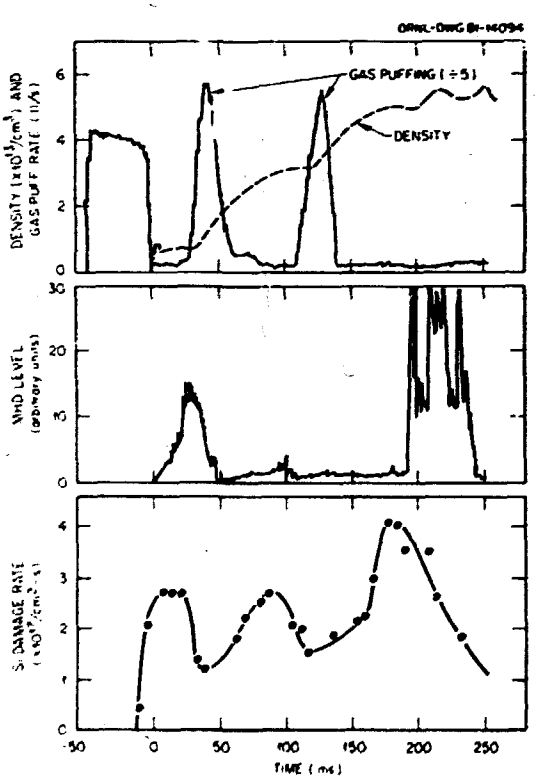

Fig. 5.6. Comparison of single-crystal silicon damage rate (indicative of deuterium flux and energy) with MHD activity, plasma density, and gas puff rate for ohmic deuterium discharges in ISX-B with 0.3-torr·liter gas puffing at 40 and 120 ms.

The effect of deuterium puffing on edge impurities is far less dramatic. Oxygen is unaffected, while iron shows only a small decrease at the time of the second puff. The lack of effect on oxygen is in agreement with the RBI results, while the minimal effect on iron is probably due to the stable, low MHD operation during this part of the discharge. Note that the slight peaking in iron flux just before 100 ms is also a time of incipient MHD activity. Both effects are eliminated during the second deuterium puff. It would appear that gas puffing can minimize edge metallic impurity levels only to the extent that it can maintain a stable, low MHD plasma.

The impurities found in the plasma edge of ISX-B were oxygen from the wall and residual gases, stainless steel (Fe, Cr, and Ni) from the vacuum vessel, and titanium from the TiC limiter. The relative amounts of iron and titanium indicate that the wall, and not the limiter, is the principal source of metallic impurities. Impurity levels in the edge were found to correlate well with both MHD activity and instabilities in plasma position, reaching levels 2 to 5 times higher during breakdown and the disruptive end of a discharge than during the steady-state portion. Finally, it was observed that gas puffing can effectively cool the plasma edge and, by minimizing instabilities, lower the level of impurities.

5.7 DEPOSITION PROBE MEASUREMENTS OF IMPURITY AND PLASMA FLUXES NEAR THE WALL IN ISX-B[15]

R. A. Zuhr, J. B. Roberto, J. P. Withrow

Deposition probe techniques have been used previously to study the fluxes of impurities and plasma particles incident on limiter-like probes in the scrapeoff layer of the ISX-B tokamak.[16] In the present work, surface probes were used to measure impurity and plasma fluxes perpendicular to the toroidal field, both at and beyond the radius of the vacuum vessel wall. A comparison of material collected on these wall position samples with the earlier measurements of fluxes parallel to the toroidal field shows that the wall fluxes are far lower for both impurities and plasma particles. In addition, at a location away from the limiters the wall is shown to be a source, rather than a sink, of metallic impurities.

The ISX-B vacuum vessel is constructed of type 304 stainless steel and was not gettered for these experiments. Operating conditions for the wall position exposures were B_T = 1.3 T, I_p = 170 kA, and $\bar{n}_e = 5 \times 10^{13}$ cm^{-3}, while for the limiter-like measurements they were B_T = 1.5 T, I_p = 120 kA, and $\bar{n}_e = 2 \times 10^{13}$ cm^{-3}. An outer mushroom limiter of TiC-coated graphite and an inner stainless steel bar limiter were in use during all the exposures reported.

Table 5.1 compares iron and deuterium deposition for exposures at the wall, behind the wall, and at limiter-like probes to typical ohmic discharges in ISX-B. Retained deuterium levels at the wall are an order of magnitude lower, while the iron is 3000 times lower. The neutral metallic impurity flux at the wall is clearly much smaller than the ionized metallic flux circulating along magnetic field lines in the plasma edge. The values given for iron at the wall locations are upper limits taken from the samples with the greatest accumulation. Many of the samples show no detectable iron. This variation in retained iron suggests that most of the iron may be deposited during disruptive behavior and that the steady-state flux to the walls is lower than indicated.

The quantity of retained deuterium as a function of exposure for the different probe locations is shown in Fig. 5.7. The upper curve, which shows the amount of retained deuterium on samples exposed perpendicular to the toroidal field at a radius 2 cm outside the limiter, has been fitted to trapping versus fluence curves.[17] If an isotropic Maxwellian energy distribution is assumed, this fit results in estimates of fluence and energy of $\sim 4 \times 10^{17}$ cm^{-2}/discharge at $\sim$20 eV. The shape of the experimental curves (Fig. 5.7) for the wall position samples indicates that the energy distribution of the particles striking the walls is neither monoenergetic nor a simple

Table 5.1. Retained deuterium and iron levels for samples oriented to collect radial fluxes near the wall and circulating ion fluxes 2 cm outside the limiter radius

	Deposition rate (cm^{-2}/discharge)		
	At wall	Behind wall (7 cm)	Limiter (2 cm)
Deuterium	1.9×10^{15}	9.4×10^{14}	1.6×10^{16}
Iron	$<3 \times 10^{11}$	$<2 \times 10^{11}$	1×10^{15}

Maxwellian. The data would be consistent with a bimodal distribution having a low energy component (~30 eV) that saturates at ~5×10^{15} cm^{-2} and a high energy tail that remains unsaturated at 18 discharges. It is clear from charge exchange neutral data[18] that such a high energy tail exists, but there are no other diagnostics that are capable of corroborating the low energy flux. The linear portion of the data can still be used to estimate the incident fluence. Results for the cases at the wall and behind the wall are approximately 5×10^{15} and 3×10^{15} cm^{-2}/discharge, respectively. The difference in these two values is explained completely by the change in exposure geometry.

It has been recently suggested that the primary source of metallic impurities in the plasma is charge exchange neutral sputtering of the wall.[19] If we use our estimated deuterium flux to the wall and assume a sputtering coefficient of 1×10^{-3} (D_i on silicon at ~60 eV), the iron sputtered from the walls is 1×10^{16}/discharge. (This figure would correspond to an erosion rate of 0.02 mm/year in a tokamak operating at a 10% duty cycle.) The iron deposited on the limiter-like probe 2 cm behind the plasma edge, when integrated over the area where such flux is present, is equivalent to 5×10^{17}/discharge. Considering the uncertainties involved in the above estimates, this is in reasonable agreement with the estimated total iron input. If a substantial fraction of the iron were being redeposited on the wall uniformly around the torus, it would have been detected by our wall position probes. Thus, our data are consistent with a model in which most of the metallic impurities are introduced by charge exchange neutral sputtering of the wall and are removed by impact with primary and secondary limiters.

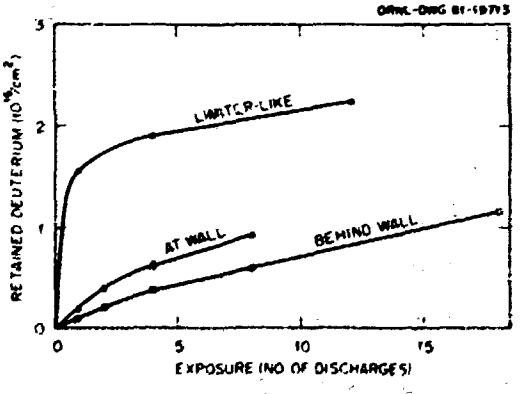

Fig. 5.7. Deuterium retained in Si probes vs exposure for ohmic discharges in ISX-B. Circles indicate data from a "limiter-like" probe (2 cm outside the limiter radius); triangles, data from a probe at the wall; squares, data from a probe 7 cm behind the wall.

In summary, we have shown that metallic impurity fluxes to the wall are far lower (× 3000) than those to limiter-like probes located 2 cm outside the limiter radius. Deuterium fluxes are also lower (× 10) at the wall position and are in reasonable agreement with single crystal silicon damage data. Finally, both wall and limiter position data are consistent with an impurity introduction model in which charge exchange neutral sputtering of the wall is the dominant introduction mechanism.

5.8 NEUTRAL ATOM IMAGING IN EBT USING A PINHOLE CAMERA

R. A. Zuhr, R. K. Richards

Initial exposures have been made using a pinhole camera to image the neutral atom distribution coming from the plasma in a sector of the EBT-S fusion device. EBT-S is a microwave-heated, steady-state plasma experiment consisting of a series of magnetic mirrors arranged end to end in a toroidal configuration. The angular distribution of neutral impurities and hydrogen isotopes gives information on impurity sources and mechanisms, particle transport, and charge exchange processes.

The camera consisted of a 0.76-mm pinhole located 7.5 cm outside the plasma-wall interface on the centerline of the cavity. Carbon and silicon deposition samples were placed 12.7 cm behind the pinhole to collect neutral plasma and impurity atoms. After exposure, the samples were removed and analyzed using Rutherford ion backscattering (RBS) for impurity detection and NRA with the $D(^3He,p)^4He$ reaction for deuterium detection.

Initial impurity results show the presence of carbon, oxygen, and silicon. It is surprising that silicon, which is present in EBT-S in very small quantities, is observed, while aluminum, from which the vacuum vessel is constructed, is not. The most likely source of the silicon appears to be silicon-greased O-ring seals. These seals can be heated to the point of failure by the microwave radiation if they are not perfectly shielded. The absence of aluminum, which is known to be transported in substantial quantities in EBT-S, can be explained if it is present in ionized form, since the camera is sensitive only to neutral particles.

Geometric data have been taken in a horizontal plane that cuts through the centerline of the torus. Such data represent the neutral density, integrated along chords through the plasma, as a function of position in the cavity. The geometry is such that observations can be made from the narrow region, or throat, where the coils are located on one end of the cavity to the same location on the other end. It has been proposed that these narrow throats would be regions of high neutral density because of the charge exchange that takes place at such surfaces. This idea is supported by our initial results, which show increased neutral deposition (~50%) of both deuterium and impurities from each of the throat regions.

A more thorough analysis of the data will require modeling of electron and ion densities and temperatures so that the integrated effects of neutralization and ionization along the chords can be calculated. For the present, the initial results show promise for using deposition probe techniques to take "pictures" of neutral distributions in the EBT-S plasma.

5.9 EROSION AND DEPOSITION OF ALUMINUM IN EBT-S

R. E. Clausing, L. Heatherly, L. C. Emerson

The erosion of aluminum from the walls of EBT-S constitutes the major source of medium Z impurities in this device. EBT devices are unique among today's large fusion experiments in that they typically operate in a steady state with energetic hydrogen plasmas for hours at a time. Erosion and deposition of aluminum are evident even to casual visual examination, and aluminum deposits cover exposed windows in a few hours during some types of operation. Recent experiments using LIF^{20} have measured the density and velocities of neutral aluminum atoms near the wall in EBT-S and are consistent with the release of aluminum from the walls by hydrogen ion sputtering. The present study provides a direct measure of the rate of aluminum transport both to and from surfaces exposed in a similar location along the midplane outside the wall.

The samples included both aluminum and stainless steel surfaces and were exposed for 1-min intervals to limit the temperature rise during exposure to 100°C or less. Auger electron spectroscopy was used to determine

the aluminum concentration on the surface of the stainless steel, and the aluminum sample served to monitor the role of contaminants. Figure 5.8 shows the aluminum concentration on the stainless steel surface as a function of exposure time. Analysis of these data provides deposition rates from the initial rate of change of concentration and erosion rates from the saturation levels.

The aluminum surface concentration (n_{Al}) can be described as a function of time t by

$$n_{Al} = n_{Al}^{s}[1 - \exp(-\phi_H \sigma t)] ,$$

where n_{Al}^{s} is the saturated or steady-state value of n_{Al}, ϕ_H is the flux of hydrogen that sputters the sample, and σ is the sputtering cross section. This equation is valid for coverages of less than a monolayer for which the removal rate eventually equals the deposition rate. The aluminum surface concentration saturates at

$$n_{Al}^{s} = \frac{\phi_{Al}^{d}}{\phi_H \sigma} ,$$

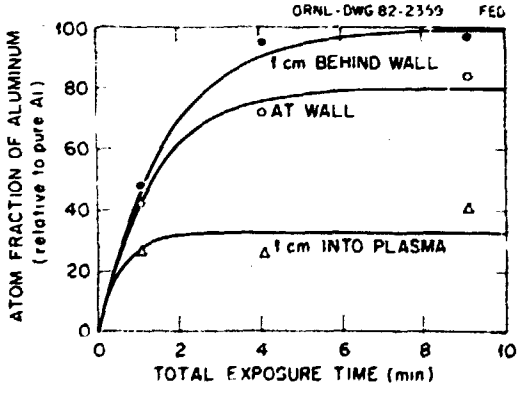

Fig. 5.8. Aluminum surface concentrations as a function of time.

where ϕ_{Al}^{d} is the deposited aluminum flux. The deposition rate can be obtained from the initial slope of the data, where

$$\phi_{Al}^{d} = \frac{dn_{Al}}{dt} .$$

The erosion rate for bulk aluminum is

$$\phi_{Al}^{e} = \phi_H \sigma n_{Al}^{o} = \phi_{Al}^{d} \frac{n_{Al}^{o}}{n_{Al}^{s}} ,$$

where n_{Al}^{o} is the aluminum surface concentration for bulk aluminum.

Table 5.2 gives the deposition and removal rates at the wall, 1 cm in front of the wall, and 1 cm behind the wall radius in the center of a 10-cm-diam port. The removal rates at the wall position are in good agreement with the data in Ref. 20 and are consistent with the hypothesis that sputtering is responsible for the erosion of aluminum in EBT-S. On the basis of these data, we should expect net erosion at the center midplane outer cavity wall of EBT-S at a rate of 10^{13} atoms/cm^2·s or ~0.01 monolayers/s (10 μm/y for a 10% duty cycle). This erosion rate is ~4 times lower than would be expected without redeposition.

5.10 OBSERVATION OF PLASMA-LIMITER INTERACTIONS IN ISX-B

R. E. Clausing, L. C. Emerson, L. Heatherly

Titanium-carbide-coated POCO graphite[21] has provided the best performance of all limiter materials tested thus far in ISX-B.[22] Even this material, however, is damaged by the severe heating and arcing which occurs during beam-heated plasma pulses and during plasma disruptions. In order to document damage to the limiter and to correlate the damage with plasma behavior, both still and motion pictures

Table 5.2. Erosion and deposition rates for aluminum at the equatorial position on the center of the outside wall of a rf cavity in EBT during exposure to a 100-kW hydrogen plasma with a pressure of 7.5×10^{-6} torr of hydrogen

Probe position (cm)	Deposition rate (atoms·cm^{-2}·s^{-1})	Erosion rate (atoms·cm^{-2}·s^{-1})	Erosion rate / Deposition rate
-1 (in port)	$\sim 3 \times 10^{13}$	3×10^{13}	<1
0 (at wall)	$\sim 3 \times 10^{13}$	4×10^{13}	1.3
+1 (in plasma)	$\sim 3 \times 10^{13}$	1×10^{14}	1.8

were taken of the limiter between and during plasma discharges in ISX-B. The photographic apparatus is shown schematically in Fig. 5.9.

Still pictures taken between each shot during the initial operation and conditioning of a new TiC-coated outer limiter in ISX-B show that limiter damage is minimal during ohmic operation but that damage occurs rapidly during the first NBI discharges.[22] This damage consists of the removal of the coating in the central "hot" region of the limiter and the formation of small microscopic melt craters, crevices, melted protrusions, and arcing patterns over nearly the entire limiter surface. Most of the coating removal and other damage occurred early in the life of the limiter and apparently did not adversely affect subsequent plasma operations.

There is considerable evidence for both thermal effects and unipolar arcing, and both can be associated with damage to the limiter. Figure 5.10 shows several frames from plasma shot 37099. Unipolar arc tracks are seen in Fig. 5.10(a), and an eruption of particles begins in Fig. 5.10(b). Comparison with the plasma current for this shot shows that this eruption occurred immediately preceding a current disruption. Additional observations are reported in Ref. 23.

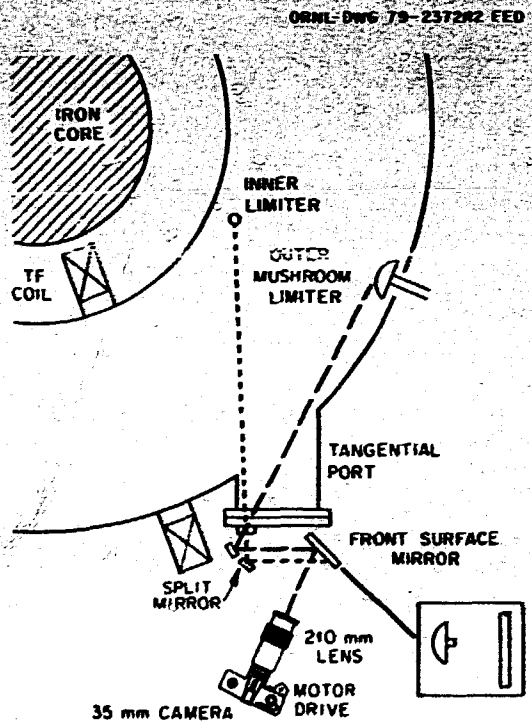

Fig. 5.9. Diagram of mirror system that gives a split field showing both inner and outer limiters of ISX-B. Both high speed motion pictures and still images were made with this apparatus.

Fig. 5.10. Plasma-limiter interaction sequence during shot 37099. This sequence shows the outer limiter at the beginning of a disruption at 162 ms. Unipolar arc tracks are shown by the arrows in frame (a). An eruption of particles is shown in frames (b)-(d). The four frames were made in sequence at 0.00033-s intervals. Particle velocities are >100 m/s.

REFERENCES

1. E. Hintz, J. Nucl. Mater. 93&94, 86 (1980).
2. H.-B. Schweer et al., J. Nucl. Mater. 93&94, 357 (1980).
3. A cw LIF measurement of zirconium impurities in the APEX tokamak has recently been reported by C. E. Young et al. (results to be published).
4. Summary of paper to be published in the Journal of Nuclear Materials.
5. R. A. Zuhr, J. B. Roberto, and S. P. Withrow, "Effects of Neutral Beam Injection and Gas Puffing on Deuterium and Impurity Levels in the Scrapeoff Layer of ISX-B," Sect. 5.6 of this report.
6. J. B. Roberto, R. C. Isler, H. C. Howe, and L. E. Murrary, "Minority Hydrogen Isotope Recycling in ISX-B," Sect. 5.4 of this report.
7. Summary of paper to be published in the Journal of Vacuum Science and Technology.
8. J. B. Roberto, R. C. Isler, S. Kasai, L. E. Murray, J. E. Simpkins, S. P. Withrow, and R. A. Zuhr, "Hydrogen Recycling and Impurities During Isotopic Exchange in ISX-B," Sect. 5.3 of this report.
9. S. D. Scott (ORNL), private communication.
10. F. Waelbroeck, J. Winter, and P. Wienhold, in *Proc. 2nd Topical Meeting on Fusion Reactor Materials*, to be published.
11. R. E. Clausing, L. C. Emerson, and L. Heatherly, J. Nucl. Mater. 76&77, 267 (1978).
12. Summary of paper to be published in the Journal of Nuclear Materials.
13. R. A. Zuhr et al., J. Nucl. Mater. 85&86, 979 (1979).
14. S. P. Withrow et al., J. Nucl. Mater. 98, 231 (1981).
15. Summary of paper to be published in the Journal of Vacuum Science and Technology.
16. R. A. Zuhr, S. P. Withrow, and J. B. Roberto, J. Nucl. Mater. 93&94, 127 (1980).

17. W. R. Wampler, private communication.
18. S. D. Scott (ORNL), private communication.
19. R. C. Isler et al., Phys. Rev. Lett. 47, 333 (1981).
20. E. Dullni, J. B. Roberto, and R. J. Colchin, "Measurement of the Density and Velocity Distributions of Sputtered Aluminum Ions in EBT-S by Laser-Induced Fluorescence," Sect. 5.1 of this report.
21. M. J. Davis, J. Nucl. Mater. 85&86, 1063-1072 (1979).
22. L. C. Emerson et al., to be published in the Journal of Nuclear Materials.
23. R. E. Clausing, L. C. Emerson, and L. Heatherly, to be published in the Journal of Nuclear Materials.

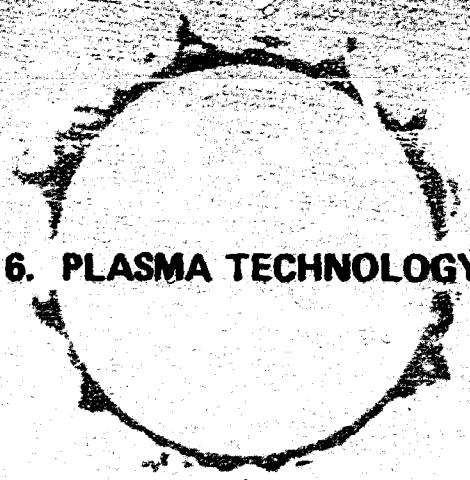

6. PLASMA TECHNOLOGY

H. H. Haselton, Section Head

R. G. Alsmiller, Jr.[1]
M. B. Baer[2]
F. W. Baity[3]
G. C. Barber
S. C. Bates[4]
W. R. Becraft[5]
C. W. Blue
A. Y. Broverman[2]
E. H. Bryant[2]
S. K. Combs[6]
C. Cornils[7]
C. D. Croessman[8]
W. K. Dagenhart
P. H. Edmonds[3]
O. C. Eldridge[3]
A. C. England[3]
R. R. Feezell[9]
P. W. Fisher[10]
S. C. Forrester
C. A. Foster
W. L. Gardner
P. Gelpi[11]
T. J. Huxford[2]
R. L. Johnson[2]
P. K. Kortman[12]
R. A. Lillie[1]
C. M. Loring[13]
R. V. Lunsford[2]
E. F. Marguerat[2]
J. C. Martin
D. H. McCollough[14]
R. W. McGaffey[14]
M. M. Menon
P. Meszaros[14]
S. L. Milora
J. A. Moeller[11]
N. S. Ponte
G. D. Ragan[15]
P. M. Ryan
R. T. Santoro[1]
D. E. Schechter
G. L. Schmidt[16]
D. D. Schuresko
F. Sluss
D. O. Sparks
W. L. Stirling
D. P. Stotler[17]
D. H. Thompson[2]
P. B. Thompson[2]
C. C. Tsai
J. Tucker[18]
J. E. Warwick[2]
J. W. Watson[10]
P. D. Weber[19]
D. J. Webster[2]
J. H. Whealton
J. A. White[2]
J. W. Wooten[14]
R. E. Wright
R. B. Wysor[2]

1. Engineering Physics Division.
2. UCC-ND Engineering.
3. EBT Experimental Section.
4. Tokamak Experimental Section.
5. General Electric Company, Schenectady, New York.
6. Engineering Technology Division.
7. Consultant, the University of Tennessee, Knoxville, Tennessee.
8. University of Missouri at Rolla, Rolla, Missouri.
9. Sigma Electronics Company, Oak Ridge, Tennessee.
10. Chemical Technology Division.
11. Grumman Aerospace Corporation, Bethpage, New York.
12. Science Applications, Inc., Bethesda, Maryland.
13. EBT-P Project.
14. UCC-ND Computer Sciences.
15. Student, the University of Tennessee, Knoxville, Tennessee.
16. Princeton Plasma Physics Laboratory, Princeton, New Jersey.
17. Student, William Marsh Rice University, Houston, Texas.
18. University of Michigan, Ann Arbor, Michigan.
19. Student, University of Michigan, Ann Arbor, Michigan.

6. PLASMA TECHNOLOGY

ABSTRACT. Advanced positive ion sources are being developed to meet the multisecond, multimegawatt neutral beam heating requirements of several near-term and future confinement experiments. Indirectly heated LaMo cathodes that can emit 5-6 A·cm^{-2} for several seconds have been developed and used in a 120-V, 1200-A, 35-s plasma generator. An ion source is being developed that incorporates the indirectly heated LaMo cathodes; it is expected to produce a 40-A, 80-keV, D^+ beam, a preprototype for the high energy pump beam to be used on the Mirror Fusion Test Facility upgrade (MFTF-B). The properties of triode and tetrode ion accelerators and the heat loading of accelerator and plasma generator components have been investigated experimentally. The design of ion accelerator electrodes is being studied theoretically, using a double plasma model, with the aim of reducing electrode loading. Direct energy recovery in injector systems is being studied theoretically and experimentally.

A Calutron-based negative ion generator has produced a 50-mA·cm^{-2}, 20-keV beam lasting for 5 s. Direct area scaling of beam characteristics was demonstrated and used in designing a 200-keV, 10-A, negative ion source neutral injection system.

The Medium Energy Test Facility (METF) west beam line was equipped with a rectangular neutralizer cell in order to test theoretical predictions of ion collection efficiency as a function of current density and retarding electric field orientation. The east end of METF is being upgraded for testing the long pulse, positive ion sources that are being developed for MFTF-B. The upgraded facility will have short and long pulse calorimeters, beam line power flow diagnostics, and an electrical system suitable for production of 80-keV, 60-A beams lasting for 30 s. The electrical system at the High Power Test Facility (HPTF) has been upgraded for high voltage (≤150-keV), long pulse (≤20-s) operation at currents up to 50 A.

Plasma Technology Section (PTS) personnel have assumed the responsibility for neutral beam injector operations on the Impurity Study Experiment (ISX-B). This task includes the installation of a third ISX-B beam line (counterinjection) to provide balanced neutral injection for high beta studies.

Advanced versions of mechanical and pneumatic solid fuel injection systems designed for reactor-scale fueling throughput requirements are being developed. A 4-pellet pneumatic injector, based on the ORNL single-pellet injector concept, was fabricated, tested, and delivered to the Princeton Plasma Physics Laboratory (PPPL) for installation on the Poloidal Divertor Experiment (PDX). Improved 4-pellet pneumatic injectors are being constructed at the Massachusetts Institute of Technology (MIT) and at ORNL for use on Alcator-C and ISX-B.

A radio frequency (rf) technology program was initiated during FY 1981 to define the rf technology developments and facilities required to support existing and future confinement experiments.

The Third International Neutral Beam Workshop was hosted by ORNL. The workshop was held in Gatlinburg, Tennessee, October 19-23, 1981.

6.1 NEUTRAL BEAM INJECTOR DEVELOPMENT

6.1.1 Positive Ion, Long Pulse Sources

All of the neutral beam injection (NBI) experiments to date have been performed using positive-ion-based systems with a short pulse duration (<0.5 s).[1] The most recent injection system developed at ORNL is the PDX injection system,[2] which has delivered about 2 MW of neutrals per source to the PDX plasma, subtending an angle of 5×10^{-3} sr with respect to the ion source. The ion source was operated at a current of up to 100 A (H^+) at 50 keV for pulse lengths up to 500 ms. Several upcoming confinement experiments require beam pulses lasting for several seconds. Pulse durations

of 30 s at beam energies of 80 keV are required to establish the thermal barrier in the MFTF-B experiment that is vital to the success of the mirror fusion program. Multisecond neutral injection, based on the neutralization of positive ion beams, is also being planned for the Tokamak Fusion Test Reactor (TFTR), Doublet III, the Advanced Toroidal Facility (ATF), and the Fusion Engineering Device (FED). The Advanced Positive Ion Source (APIS) Program at ORNL is geared to the development of suitable long pulse, multimegawatt NBI systems.

The research and development (R&D) activity in the APIS Program during 1981 can be divided into two categories: development of long pulse plasma generators and development of accelerators. In the first category, a long pulse plasma generator that illuminates an 18- by 48-cm extraction surface with sufficient plasma uniformity and density to provide an extraction current density of up to 0.25 $A \cdot cm^{-2}$ (D^+) was developed. Crucial to the success of this plasma generator was the development of a long pulse cathode. Several types of indirectly heated cathodes were considered.[3,4] The configuration shown in Fig. 6.1, which has a paraboloid emitting shell enclosing graphite heaters, was found to be the most promising. The emitting surface is made of molybdenum, coated with a mixture of 97.5% Mo, 2.0% $LaMo_3$, and 0.5% Pt by weight. Such cathodes were operated at emission levels of 12 $A \cdot cm^{-2}$ for subsecond pulse lengths and at 5-6 $A \cdot cm^{-2}$ for multisecond pulse lengths. Two such cathodes were used in parallel to obtain 120-V, 1200-A arc discharges with 35-s pulse durations (Fig. 6.2). The mouth of the electron feed assembly was found to be the most critical generator component as regards heat loading; its design was optimized to withstand the high heat flux (~2 $kW \cdot cm^{-2}$). Experience gained from operating this plasma generator was incorporated in the design of the experimental MFTF-B ion source, which is described in Sect. 6.2.

The accelerator development work during this report period consisted of characterizing

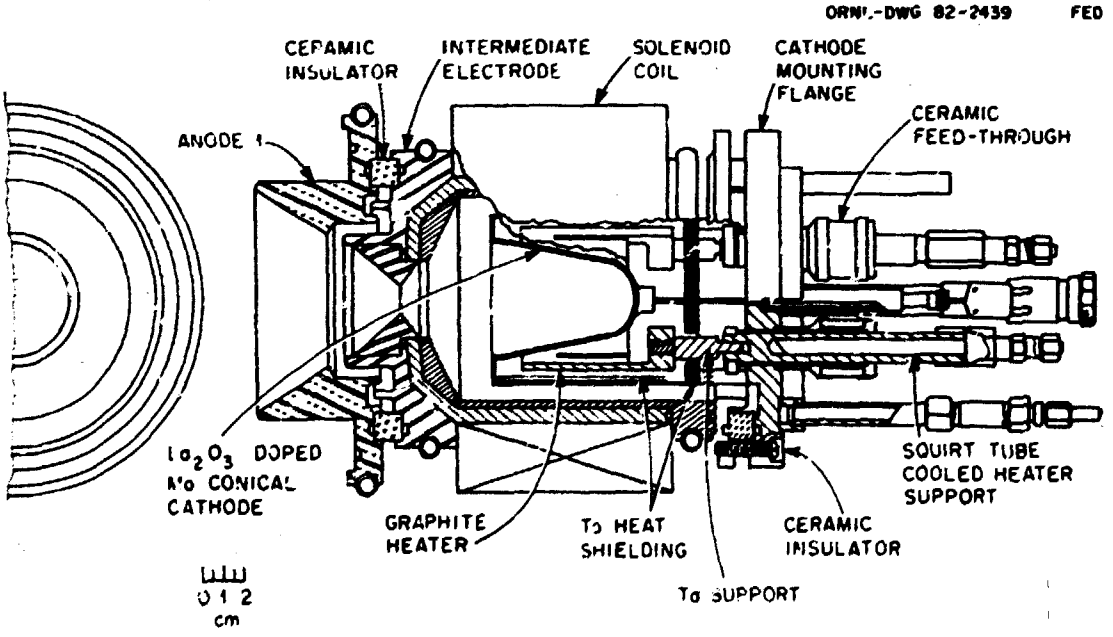

Fig. 6.1. Catnode and electron feed assembly.

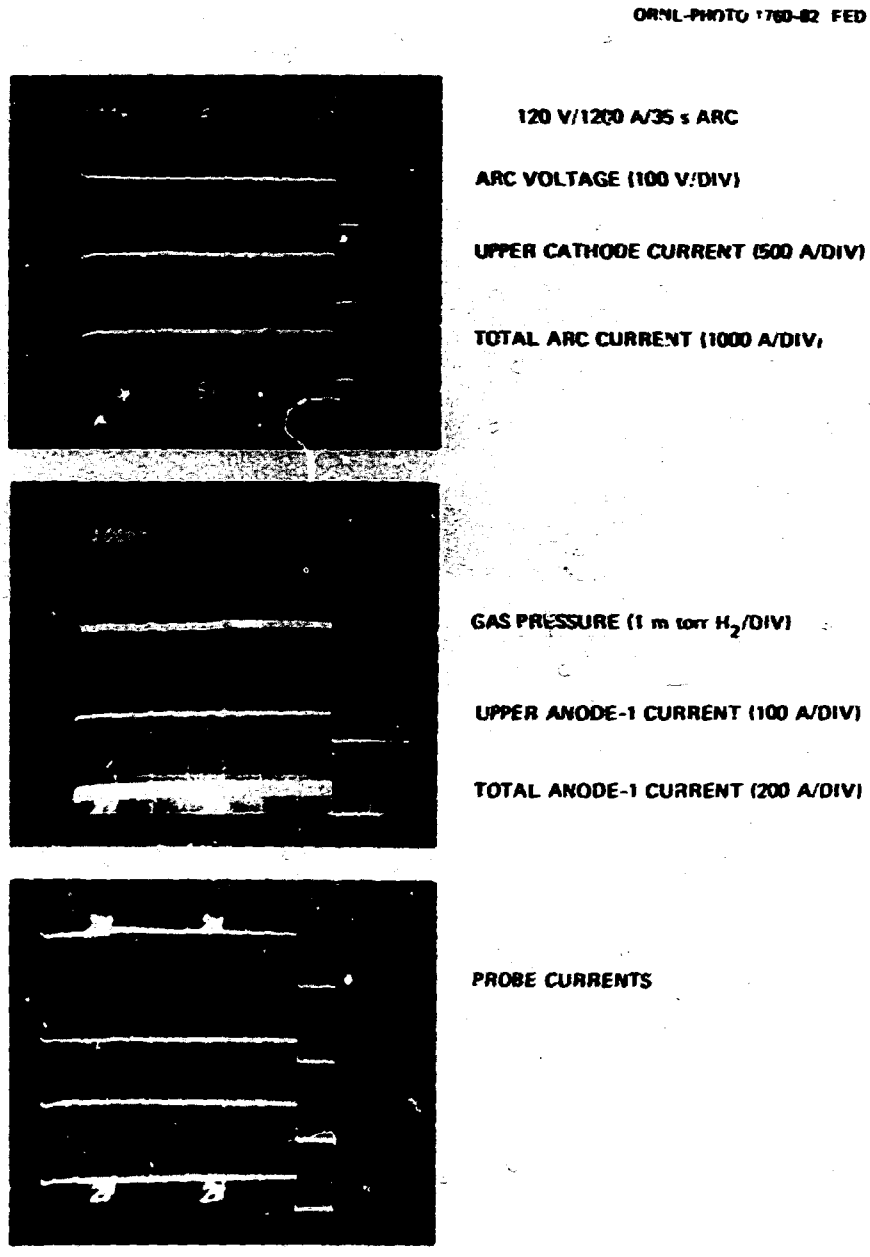

Fig. 6.2. Waveforms for a 120-V, 1200-A, 35-s arc discharge.

triode and tetrode accelerators and comparing their performances. The experiments were performed using the scaled APIS (10 by 25 cm) and employing notched apertures developed for PDX injectors.[5] The experiments revealed that triodes can be operated at energies of 80 keV without sacrificing the current density. For the electrode geometry considered, the primary advantage of tetrodes over triodes in the neighborhood of 80 keV was the improvement in beam optics.

A second characteristic of the tetrode is the dependence of its ion optics on the ratio between the electric field in the first gap and

that in the second gap. For the particular electrode geometry that was investigated, a higher ratio (second gap field to first gap field) resulted in lower beam divergence and lower optimum perveance, as shown in Fig. 6.3. Redistributing the two gaps while keeping the total accelerating gap constant did not result in any appreciable change in either the current density or the beam power transmission if the field ratio was kept constant.[6]

Heat loading on the accelerator and plasma generator components due to beam extraction was investigated in detail. The dominant mechanisms involved were identified.[7]

Energy dissipation during the high voltage breakdown of the accelerator grids was measured experimentally.[8] The experiments revealed not only the magnitudes of energy dissipated during typical breakdowns, but also the distribution of this energy among the accelerator grids.

6.1.2 Direct Energy Recovery

After repair of the water line freeze-up damage that terminated last year's experiment, modifications were made to the close-coupled energy recovery experiment.[9] Ground surfaces were isolated to allow electrical measurement of the net current striking them, small loop antennas were added to observe the rf noise spectrum, and the power supplies were connected in a new arrangement.[10]

In the previous power supply configuration (Fig. 6.4), the small (5-kV, 15-A) boost supply provided the extraction current, which limited the beam current and caused the boost potential to sag. The new configuration (Fig. 6.5), in which the boost supply biases the accel supply above ground, has the following advantages.

(1) Because the boost supply provided only the net recovery current, the boost potential remained more stable.
(2) Because the extraction current was provided by the larger (40-kV, 60-A) accel supply, operation at higher beam currents was possible.
(3) Changes in the boost potential did not affect the accel gap voltage, and hence the beam optics remained constant.
(4) The net recovered current could be measured directly as the boost supply current, rather than calculated as a sum and difference of three separately measured currents.

The following significant experimental observations were made.

(1) Net energy recovery was possible only over a limited range of magnetic field strengths.
(2) Electron collection efficiency was a weak function of collector bias potential with respect to the neutralizer.
(3) Recovery efficiency decreased as gas pressure increased in the recovery region.
(4) Recovery efficiency decreased as current density increased, as previously predicted.[11]
(5) Ion collection on ground surfaces had not saturated for a boost potential that was 12.5% of the beam energy.
(6) The rf noise spectrum extended from around 100 MHz to above 1.5 GHz. Most of the energy is in the 200- to 500-MHz range and increases with increasing beam current or decreasing magnetic field strength.

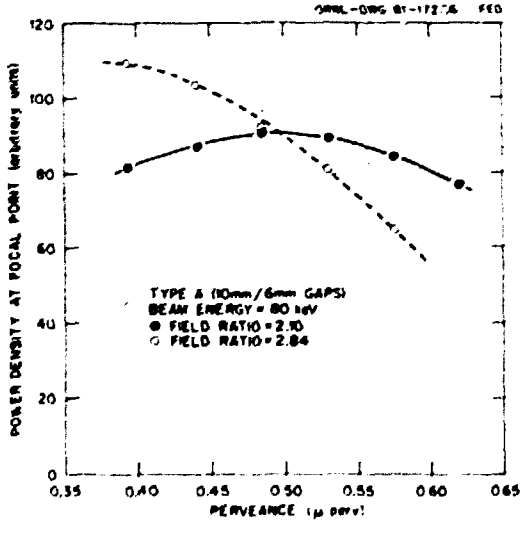

Fig. 6.3. The effect of field ratio on beam optics.

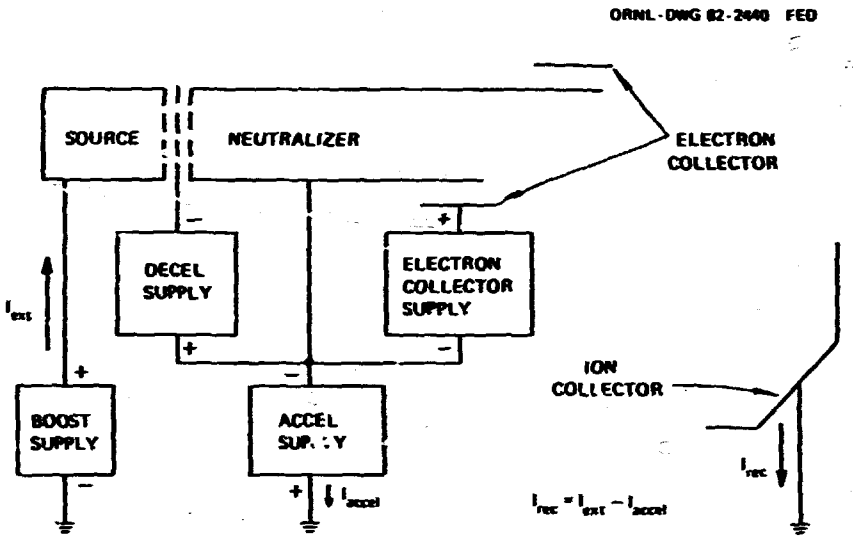

Fig. 6.4. Previous power supply configuration.

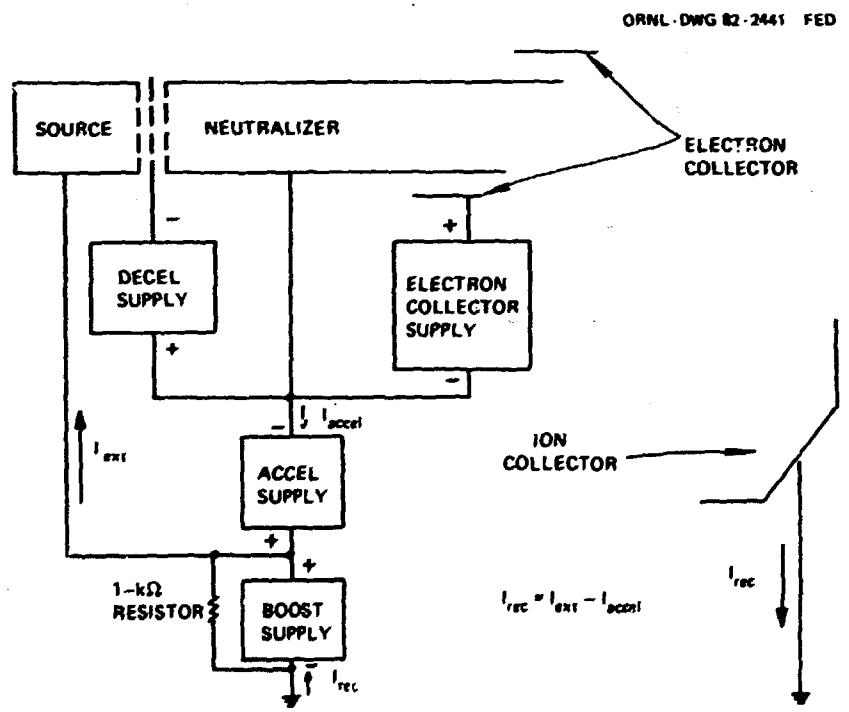

Fig. 6.5. Present power supply configuration.

A new rectangular neutralizer assembly (with a 10- by 25-cm cross section) was designed and fabricated. In conjunction with this effort, the bending magnet in the MFTF west beam line was reoriented so that its long pole face axis is perpendicular to the beam. This will test the two-dimensional (2-D), infinite slot, single Vlasov computer calculation, which predicts that a geometry in which the retarding electric field is predominantly colinear with the ion trajectories will have an ion collection efficiency that is virtually independent of current density.[12]

6.1.3 Negative Ion Sources

An extensively modified Calutron positive ion source is being used to generate negative ion beams through surface ionization transverse extraction (SITEX).[13] It has produced a 250-mA beam (50 mA·cm^{-2}) at 20 keV for 5 s, with a beam divergence of θ (= 1/e) = (2 ± 1)°.[14] Direct area scaling of extracted current has been demonstrated as shown in Fig. 6.6. For the 250-mA beam, the extracted I_e/I_{H^-} ratio has been reduced to 0.2, with >99% of I_e collected by the electron recovery system[15] at <10% of V_{accel}. A conceptual beam line design study was completed for a 200-keV, 10-A, dc SITEX negative-ion-based system.[15] This beam line, shown in Fig. 6.7, would deliver 1 MW of monoenergetic neutrals from a system the size of the PDX/ISX-B beam lines with θ < 0.4° and virtually no impurities.

6.1.4 Theoretical Ion Optics

The 2-D ion optics code[16-20] as previously verified[5,21-30] was used to study accelerator designs for MFTF injectors,[31,32] improved PDX injectors,[33] and negative ion accelerators. A double plasma model is being used for electrode design to reduce electrode loading.[34,35] A program to study the species mix in ion sources in one dimension was established.[36] Theoretical studies of direct recovery[37-41] were

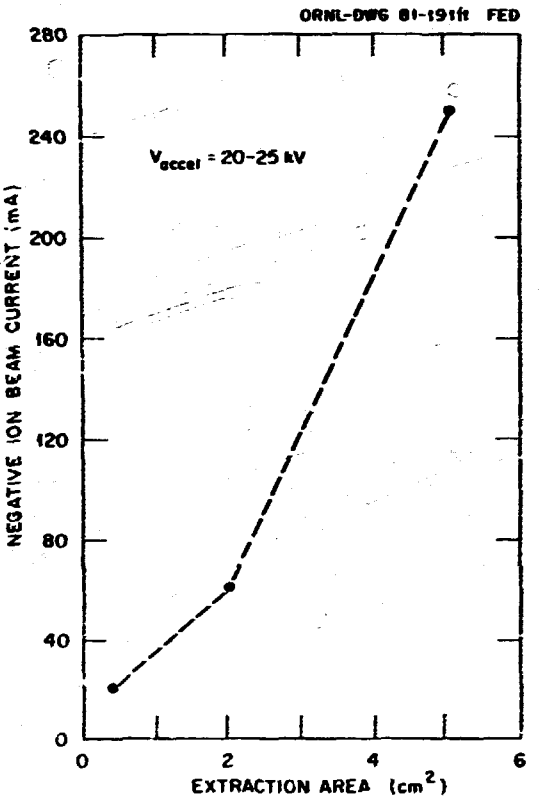

Fig. 6.6. SITEX extracted beam current I_{H^-} vs extraction area.

extended to three dimensions;[42] in addition, a panacean neutralizer magnet interface was suggested.[39]

6.1.5 Neutral Beam Diagnostics Development

The parallel-plate energy analyzer[43] was used to measure the atomic hydrogen fraction of a 30-cm ion source. Comparisons were also made with traditional magnetic momentum analysis, using the ion deflection magnet.

At an ion beam current density of 0.13 A·cm^{-2}, the source atomic fraction of the beam, composed of both ions and neutrals, was measured to be 82% at the center of the beam, where the full energy proton fraction is always maximum. At a current density of 0.10 A·cm^{-2}, the parallel-plate analyzer yielded a 79% source atomic

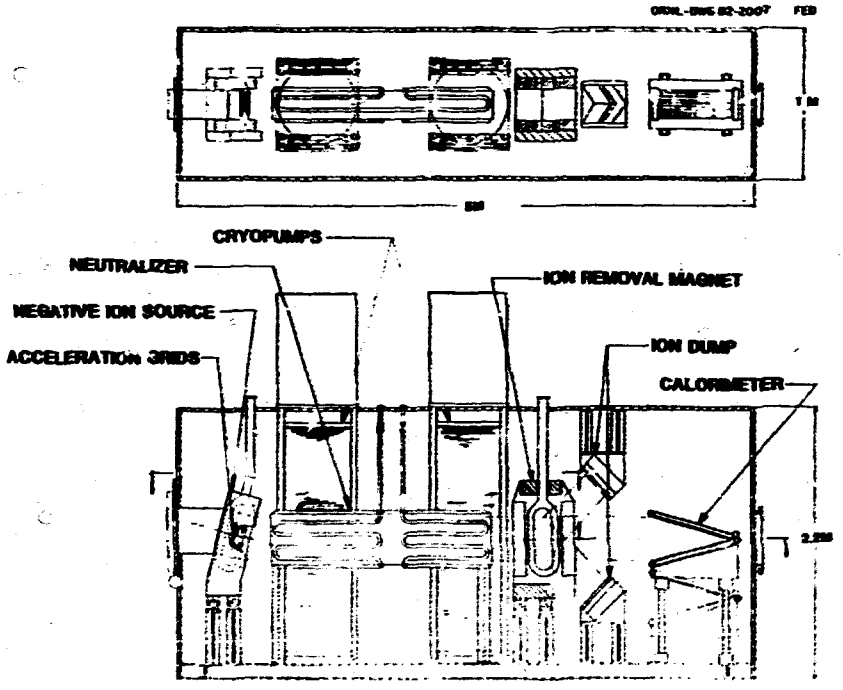

Fig. 6.7. Conceptual design for a 200-keV, 10-A, dc SITEX-based neutral beam line.

fraction when applied to the total beam (ions and neutrals), but only a 68% fraction when the beam was composed of neutrals only. This may be indicative of a nonequilibrium line density. Momentum analysis of the same beam, which spatially averages over the whole beam, gave a 73% fraction.

The source atomic fraction estimated from analyzing the total beam is always 5-10% higher than that obtained from neutrals only. The source atomic fraction estimated when a pre-acceleration potential is applied to the plasma grid is about 3% higher than that obtained from conventional operation.

6.1.6 METF Upgrade

The METF is a double-ended neutral beam test stand. The east end of it was used in developing the PDX injectors and, more recently, in testing the long pulse plasma generators. The west end is being used for energy recovery experiments. Both beam lines were originally designed for short pulse operation (≤500 ms).

The east end of METF is being modified to make it suitable for testing the 30-s MFTF-B experimental ion sources now under development. The upgraded beam line will accept the 13- by 43-cm ion source. The 150-cm-long neutralizer will have a 17- by 47-cm cross section. The beam line will be equipped with both a short pulse (0.1-s) and a long pulse (30-s) calorimeter. The calorimeters will be V-shaped to reduce the power density normal to the target. The short pulse calorimeter is designed to dissipate up to 30 kW·cm^{-2} normal to the beam. The long pulse calorimeter will be made of swirl tubes kept at an inclination of 5:1 with respect to the beam to increase its power handling capacity. The beam line will also be equipped with diagnostics for measuring the power flow along the beam line and the atomic species content of the beam. The main limitation of the beam line will be its inability to

separate the ion beam fraction after neutralization for long pulse durations.

In addition to the mechanical upgrades described above, several changes have been made in the electrical system to allow 30-s (long pulse) operation at voltages up to 80 keV and currents up to 60 A. A set of filament supplies has been installed, suitable for indirectly heated cathodes, each capable of providing up to 1000 A dc at 13 V. The electrical cables feeding the ion source have been upgraded for long pulse operation. In order to increase the voltage capability from the previous 50-kV to the new 80-kV level, the high voltage modulator has been rebuilt, enclosing the switch tubes in pressurized SF_6 medium. Provisions have been made in modulator design for substitution of a new switch tube type at a later stage with minimum downtime. A crowbar unit has been incorporated to protect the ion source in the event of a modulator system malfunction. A gravity-operated mechanical switch has been substituted for the solenoid-operated grounding switch to improve reliability and personnel safety.

6.1.7 HPTF Improvements

The High Power Test Facility (HPTF) is used for the development of high energy ion sources (up to 150 keV). At present, it is primarily used for the development of a scaled APIS (10 by 25 cm) with currents up to 25 A and voltages up to 150 kV.

During 1981, the HPTF electrical system was modified to increase its pulse length capability. The low voltage cables that had been insulated in PVC pipe and operated at high voltages were replaced with high voltage coaxial cables rated for 200-keV operation; previously, reliable operation was limited to <100 kV. To provide more room on the source table for larger (13-V, 1000-A) filament supplies, the arc rectifier section was rebuilt on a floating deck and installed in the power supply vault. The dc output of this rectifier is now brought to the source cage through coaxial cables rated for 200-kV operation. To overcome the limitation on pulse length imposed by the gradient grid resistor divider network, a new assembly with forced air cooling was fabricated and installed in the power supply vault. Personnel safety was improved by replacing the grounding switches inside the power supply tanks with gravity-operated switches outside the tanks. The leads from the source table to the ion source were replaced with copper bus bars. The electrical system on HPTF is now capable of high voltage (≤150-kV), long pulse (≤20-s) operation at currents up to 50 A.

Plans are to install a new neutralizer with a 15- by 45-cm cross section that will enable the HPTF to handle ion source operation of the full-size (13- by 43-cm) APIS at voltages up to 150 keV and currents up to 50 A. Pulse lengths will be limited by power density considerations on the neutralizer, beam stops, and beam-defining apertures. The beam bending magnet in its present configuration cannot handle the large beam; therefore, near-term operation of the full-size source will not include ion removal.

6.2 NEUTRAL BEAM APPLICATIONS AND OPERATIONS

6.2.1 MFTF-B Ion Sources

During the second half of 1981 the APIS Program was reoriented to meet the NBI requirements of the MFTF-B device. A variety of neutral injectors will be needed for MFTF-B, but the most severe requirement is for the high energy pump beam, where 25 A of 80-keV D^0 must be deposited in the plasma for pulse durations of 30 s. The beam optics requirement for this application is very severe because the plasma is located about 15 m downstream from the source and the beam must be transmitted through a restrictive aperture 13 m from the source that subtends only ±0.4° with respect to the exit grid. Additionally, the injected power should be tunable in a wide range (3:1), maintaining the beam energy at a constant 80 keV.

To meet these needs, an ion source is being developed that is expected to provide about 40 A of D^+ beam at 80 keV with low divergence (~0.25° rms) for pulse lengths of 30 s (see Fig. 6.8). The design of the plasma generator for this source is based on the generic plasma generator work described in Sect. 6.1.1; it employs LaMo cathodes of the type shown in Fig. 6.1. Two types of anode chambers are being fabricated: one with the permanent magnets located inside an aluminum vacuum chamber and the other with the magnets conventionally located outside the chamber. Two sets of accelerator structures, one of molybdenum and the other of copper, are also being fabricated. Both of these accelerators will use large shaped apertures (8 mm ID and 10 mm OD) for improved beam optics and high grid transparency. The molybdenum grids are being built by industry (United Technologies Research Center), while the copper grids are being made internally. Both types of grids will use advanced fabrication techniques to maximize the cooling efficiency without sacrificing the grid transparency. The molybdenum grids will be made by brazing two molybdenum sheets with a wavy pattern of cooling channels etched into one sheet. For the copper grids, the wavy cooling channels will be machined into a precut copper plate and the grid will be completed by an electroforming operation. Both types of sources are expected to be completed during the first half of 1982.

6.2.2 ISX-B Neutral Beam Injection

Operations

A cooperative effort between PTS staff and the ISX-B group of the Tokamak Experimental Section has been initiated. To its previous development and technology activities, PTS has added all aspects of NBI operations on ISX-B. This arrangement is expected to have favorable synergistic effects on both groups; PTS personnel will gain first-hand experience in actual day-to-day demands on injection systems, and the ISX-B group will gain immediately available, in-house NBI expertise.

Third beam line

In addition to handling all NBI operations on ISX-B, PTS staff will be adding a third beam line to the device. The location of this system is shown in Fig. 6.9. It will provide balanced counterinjection for high beta studies. The system is an upgraded Princeton Large Torus (PLT) system from PPPL that will receive the additions and changes needed to bring its capabilities to the level of the present systems.

6.3 PELLET FUELING

6.3.1 Advanced Injector Development

The emphasis of the pellet injector development program in 1981 was on construction of the advanced mechanical injector (AMI) and the advanced pneumatic injector (API) facilities. Both injectors are repetitive devices intended to demonstrate steady-state fueling systems in the reactor-relevant parameter ranges of 1000-m/s pellet velocity, variable pellet size up to 2 mm, and feed rates of 10-40 pellets per second.

The AMI facility was completed, and initial tests demonstrated the functionality of the various subsystems (the solid deuterium extruder, the composite arbor accelerator, and the synchronized pellet feed system). The AMI is illustrated in Fig. 6.10. A continuous solid deuterium extrusion process produces a filament 1.2 mm in diameter. Pellets are formed and launched into the inlet section of the the "snowshoe"-type arbor by a synchronized chopper wheel interposed between the extrusion die outlet and the rotational plane of the high speed arbor. The arbor operates at 160 Hz to achieve the 500-m/s tip speed required, but the chopper wheel turns at a reduced speed (factor of 4, 8, etc.) to obtain pellet feed rates of 40 pellets per second and lower. Jitter is eliminated by a phase-locked motor control system. The AMI is scheduled to operate early in 1982.

The API is a facility to test the applicability of the pneumatic acceleration technique in steady-state operation. This apparatus (Fig. 6.11) will combine the high speed

ORNL-DWG 82-2121 FED

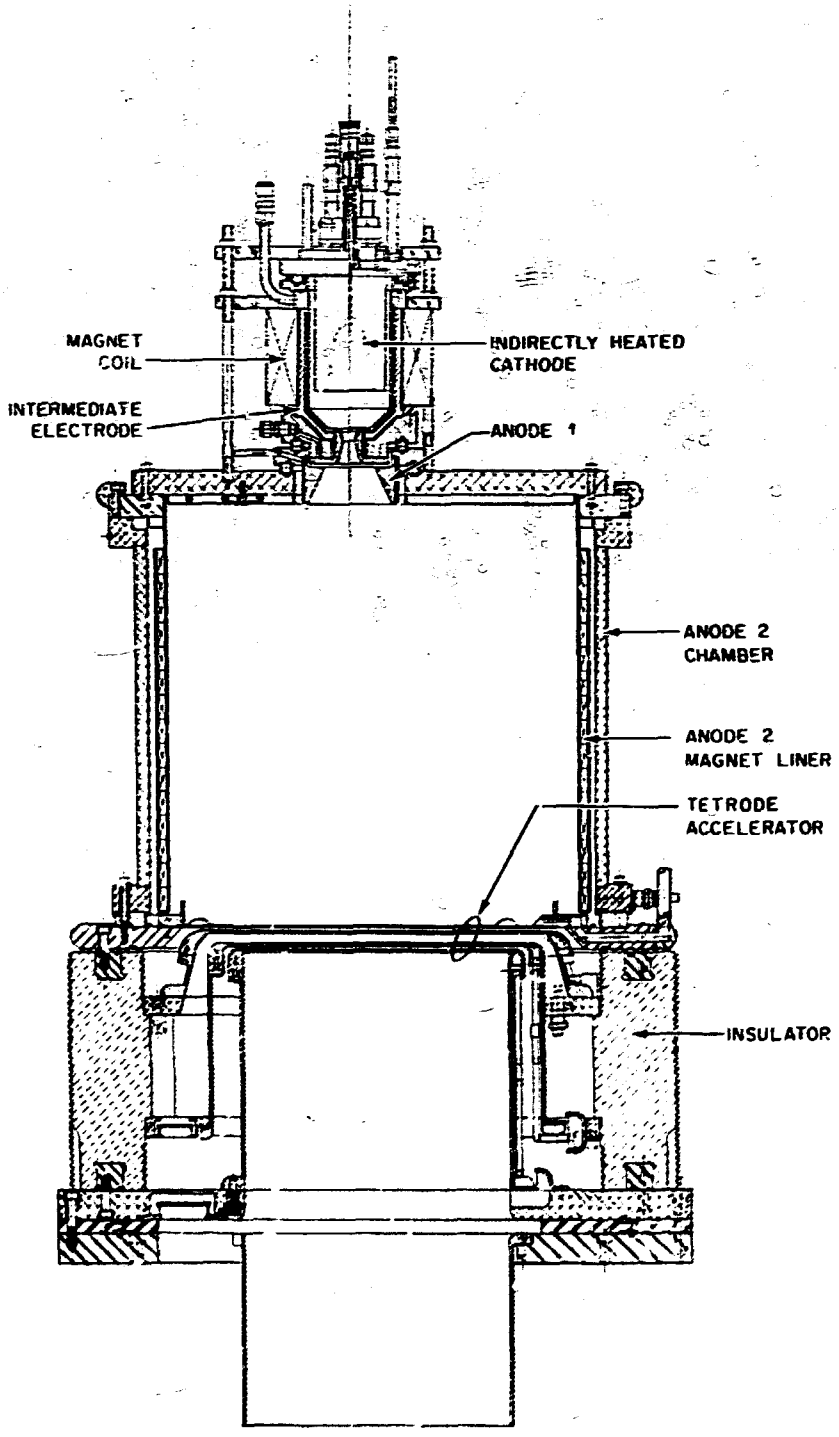

Fig. 6.8. THE MFTF-B experimental ion source. The extraction pattern is 13 × 43 cm; the left side corresponds to the short dimension and the right side to the long dimension.

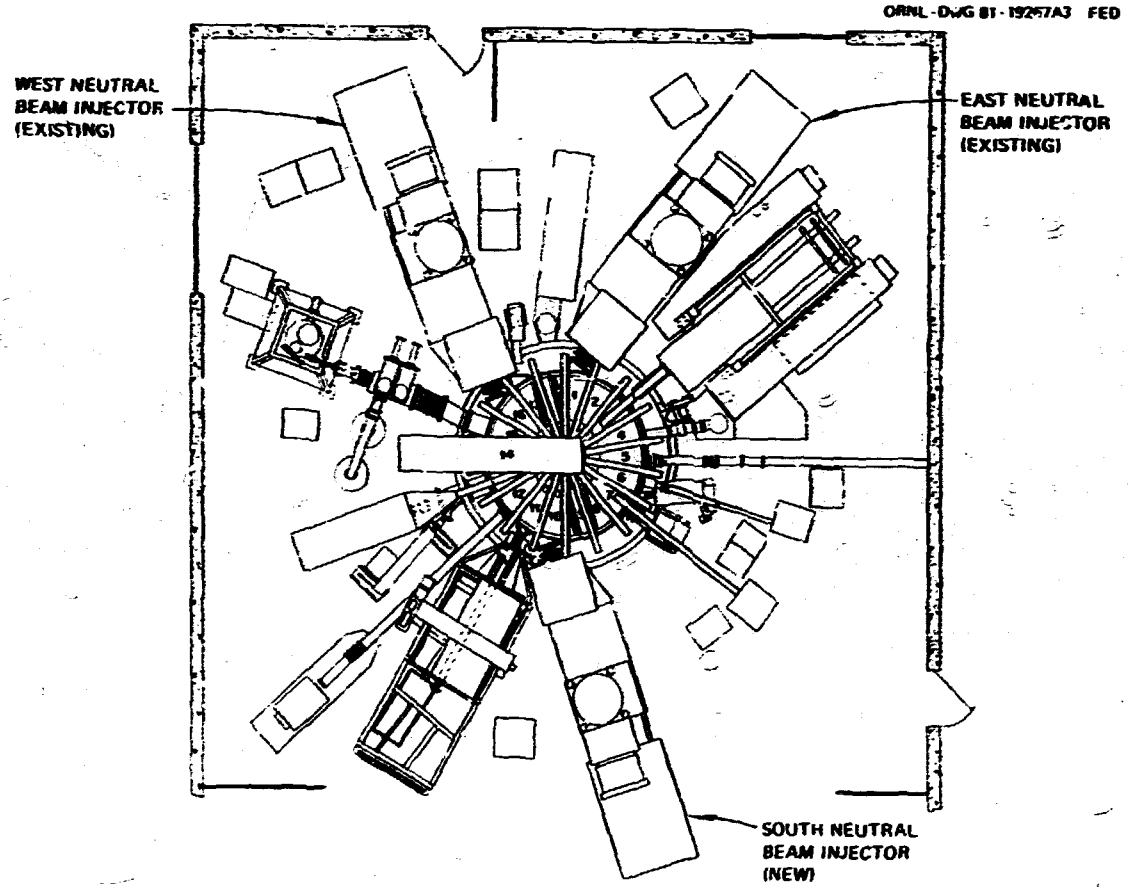

Fig. 6.9. ISX-B neutral beam lines.

extruder technology of the AMI project with the pneumatic acceleration technology developed at ORNL to demonstrate acceleration of 2-mm-diam hydrogen and deuterium pellets to 2 km/s at a repetition rate of 10 pellets per second. The API is scheduled for initial tests in the first quarter of 1982.

6.3.2 Confinement Systems Applications

During the past year a prototype 4-pellet pneumatic injector, based on the working principle of the ORNL single-pellet design, was successfully tested. The device shown in Fig. 6.12 is capable of delivering four 1-mm-diam pellets with programmable timing intervals extending to at least 16 ms (±0.5 ms) between pellets. The injector was delivered to PPPL and installed on the PuX device, where it will be used during 1982 in a joint ORNL/PPPL study of quasi-steady-state pellet fueling and transport in a "low" particle recycle regime.

An improved pellet injector design (see Fig. 6.13) was issued for construction at MIT. The system will be used on Alcator-C in 1982 to study the effects of central fueling (centrally peaked plasma density profiles) on confinement. At ORNL, construction of a third 4-pellet injector system for use in the ISX-B high beta studies was started.

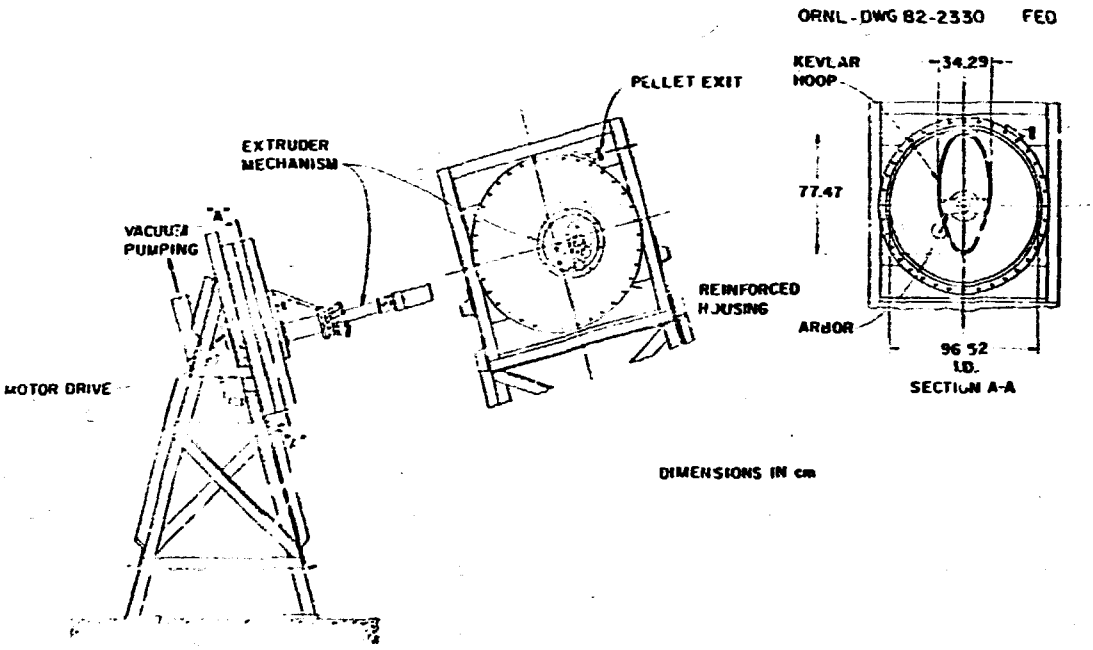

Fig. 6.10. Advanced mechanical pellet injector.

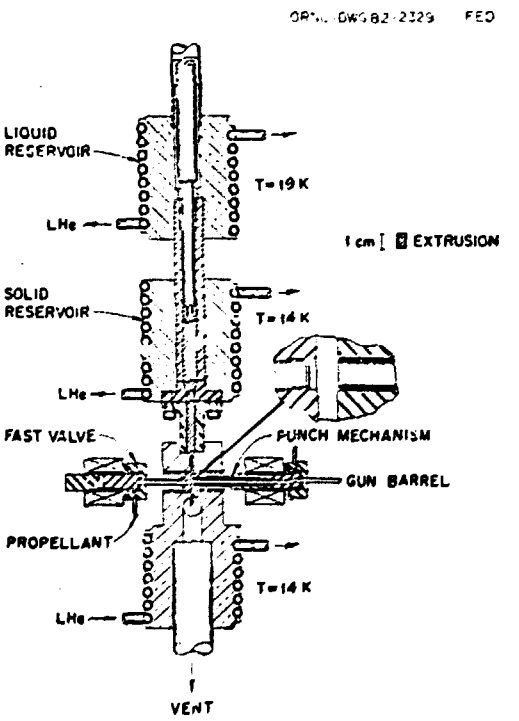

Fig. 6.11. Advanced pneumatic pellet injector extruder and punch mechanism.

6.4 RF HEATING

The growing interest in the use of rf energy for magnetic confinement fusion devices has been supported by expanded experimentation, which has provided increasing indications of the potential of this heating method. Studies of future machines and the testing plans for devices under construction are including more important roles for rf systems. The major potential use of rf energy for plasma heating has been joined by the possibility of using rf energy for current drive in tokamaks and for potential well maintenance in mirrors. Recently, it has been speculated that rf heating could be useful in impurity control and disruption control. This increase in expected rf use requires a technology development program to keep pace with the physics experiments and the schedule of design selections for the next generation of devices. The aim of the rf technology program, initiated in October 1981, is to define and carry out the

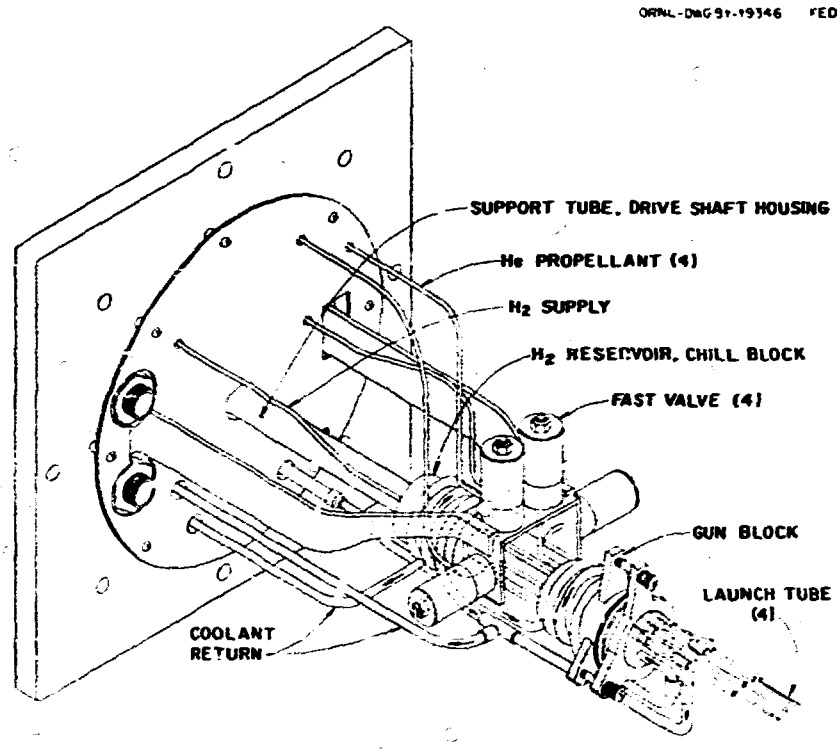

Fig. 6.12. The 4-shot pellet injector used on PDX.

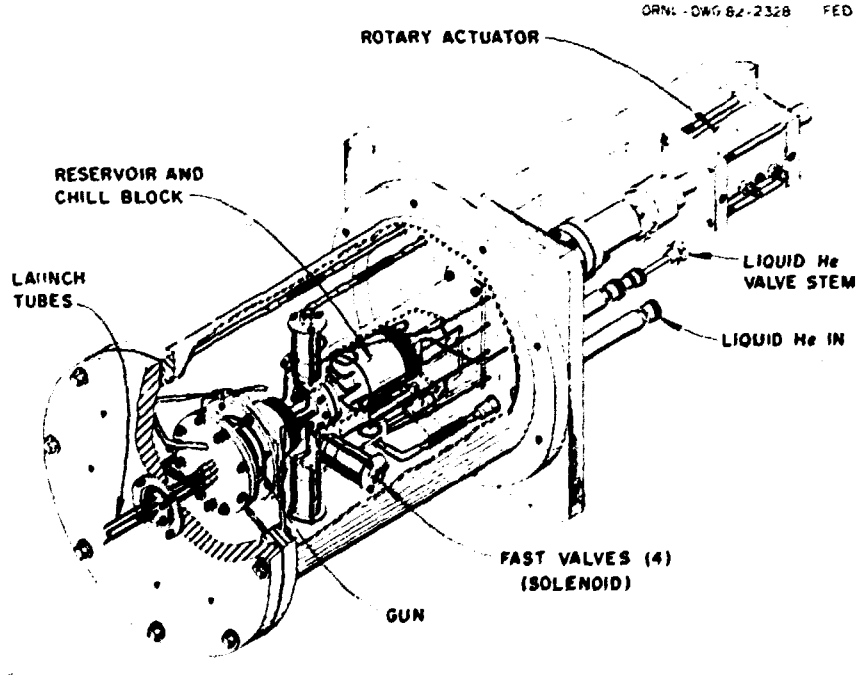

Fig. 6.13. Upgraded version of the 4-shot pellet injector.

specific time-phased developments and facilities necessary to support the present and future devices.

The planning part of the ORNL activities includes representation from all major U.S. rf groups (Fig. 6.14). The focus for long-range planning is the Fusion Demonstration Project (FDP), taking into consideration that the tokamak, mirror, or ELMO Bumpy Torus (EBT) concept may be chosen for a FDP. The nearer-term planning is being guided by a rollback of needs for the Fusion Engineering Device (FED), assuming a Title I design effort starting in 1986 and, again, the possibility that any one or all three confinement concepts will be considered. The resulting plan will concentrate on the next five years (FY 1983–FY 1987). The frequency regimes to be considered for development needs include ion cyclotron resonance heating (ICRH), lower hybrid heating (LHH), and electron cyclotron resonance heating (ECRH), although it is recognized that source development for ECRH frequency ranges is under way in another ORNL-managed program. The dedicated test facilities necessary to support rf development are being determined for construction starting in FY 1983. The Plasma Technology Section will support FED confinement experiments by developing and providing the complete rf system, including the wave energy launching structure.

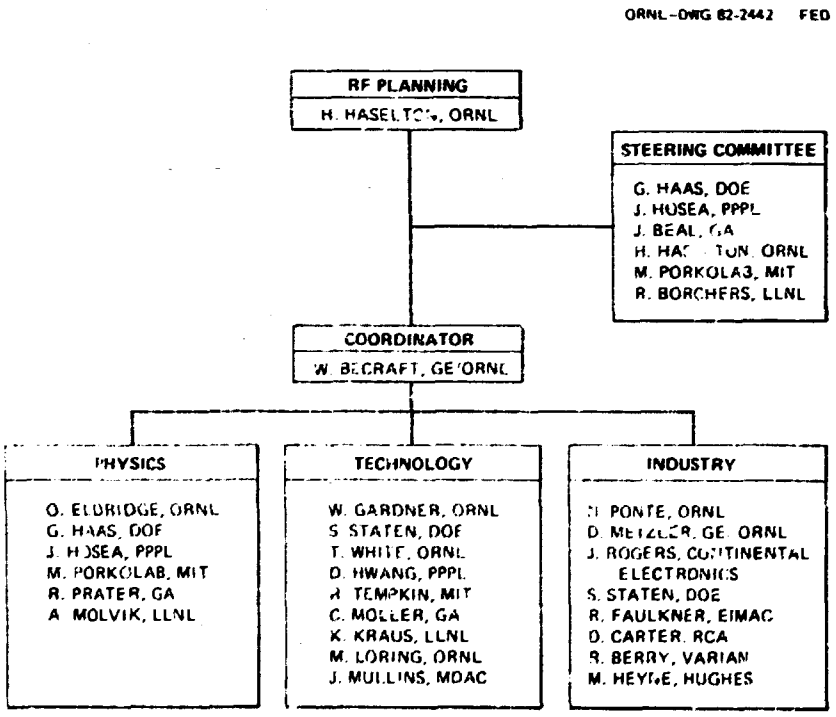

Fig. 6.14. ORNL rf technology planning program. DOE: Department of Energy; GA: General Atomic Company; GE: General Electric Company; LLNL: Lawrence Livermore National Laboratory; MDAC: McDonnell Douglas Astronautics Company.

REFERENCES

1. M. M. Menon, Proc. IEEE 69, 1012-29 (1981).
2. W. L. Gardner et al., "Properties of an Intense 50-kV Neutral Beam Injection System," to be published in the Review of Scientific Instruments.
3. D. E. Schechter and C. C. Tsai, paper presented at the Ninth Symposium on Engineering Problems of Fusion Research, Chicago, Illinois, October 26-29, 1981 (proceedings to be published).
4. C. C. Tsai, M. M. Menon et al., "A Long Pulse Ion Source for Neutral Beam Applications," to be published in the Review of Scientific Instruments.
5. W. L. Gardner, J. H. Whealton et al., Rev. Sci. Instrum. 52, 1625-28 (1981).
6. M. M. Menon, C. C. Tsai et al., Bull. Am. Phys. Soc. 26, 1017 (1981).
7. M. M. Menon, C. C. Tsai et al., "Heat Loading on Source Components During Multimegawatt Ion Beam Extraction" (unpublished, 1982).
8. M. M. Menon and N. S. Ponte, paper presented at the Ninth Symposium on Engineering Problems of Fusion Research, Chicago, Illinois, October 26-29, 1981 (proceedings to be published).
9. W. L. Stirling et al., IEEE Trans. Nucl. Sci. NS-28(2), 1319 (1981).
10. P. M. Ryan et al., Bull. Am. Phys. Soc. 26, 1017 (1981).
11. J. H. Whealton et al., Bull. Am. Phys. Soc. 25, 983 (1980).
12. J. W. Wooten and J. H. Whealton, Bull. Am. Phys. Soc. 26, 941 (1981).
13. W. K. Dagenhart, W. L. Stirling, and J. Kim, *Negative Ion Beam Generation with the ORNL SITEX Source*, ORNL/TM-7895, Oak Ridge, Tennessee (in press).
14. W. K. Dagenhart, W. L. Gardner, G. G. Kelley, W. L. Stirling, and J. H. Whealton, "SITEX Negative Ion Source Scaling Studies to Produce 200-keV, 10-A, Long Pulse D⁻ Beams," paper presented at the Third International Neutral Beam Workshop, Gatlinburg, Tennessee, October 19-23, 1981 (proceedings to be published).
15. W. L. Gardner, W. K. Dagenhart, G. G. Kelley, W. L. Stirling, and J. H. Whealton, "Design Concept for a 200 keV, 10 A, Negative Ion Based Neutral Beam System," paper presented at the Third International Neutral Beam Workshop, Gatlinburg, Tennessee, October 19-23, 1981 (proceedings to be published).
16. J. H. Whealton, E. F. Jaeger, and J. C. Whitson, J. Comput. Phys. 27, 333 (1978).
17. J. C. Whitson, J. Smith, and J. H. Whealton, J. Comput. Phys. 28, 408 (1978).
18. J. H. Whealton, J. Comput. Phys. 40, 491 (1981).
19. J. H. Whealton, Nucl. Instrum. Methods 189, 55 (1981).
20. J. H. Whealton, IEEE Trans. Nucl. Sci. NS-28, 1358 (1981).
21. J. H. Whealton, E. F. Jaeger, and J. C. Whitson, Rev. Sci. Instrum. 48, 829 (1977).
22. L. R. Grisham, C. C. Tsai, J. H. Whealton, and W. L. Stirling, Rev. Sci. Instrum. 48, 1037 (1977).
23. J. Kim, J. H. Whealton, and G. Schilling, J. Appl. Phys. 49, 517 (1978).
24. J. H. Whealton and C. C. Tsai, Rev. Sci. Instrum. 49, 495 (1978).
25. J. H. Whealton, L. R. Grisham, C. C. Tsai, and W. L. Stirling, J. Appl. Phys. 49, 3091 (1978).
26. J. H. Whealton, C. C. Tsai, W. K. Dagenhart, W. L. Gardner, and H. H. Haselton, Appl. Phys. Lett. 33, 278 (1978).
27. J. H. Whealton and J. C. Whitson, J. Appl. Phys. 50, 3964 (1979).
28. J. H. Whealton, R. W. McGaffey, and E. F. Jaeger, Appl. Phys. Lett. 36, 91 (1980).
29. J. H. Whealton and J. C. Whitson, Part. Accel. 10, 235 (1980).
30. C. N. Meixner, M. M. Menon, C. C. Tsai, and J. H. Whealton, J. Appl. Phys. 52, 1167 (1981).

31. J. H. Whealton. Bull. Am. Phys. Soc. 26, 1017 (1981).
32. J. H. Whealton, *Primary Ion Tetrode Optics for High Transparency Multibeamlet Neutral Injectors*, ORNL/TM-7870, Oak Ridge, Tennessee (1981).
33. J. H. Whealton, Bull. Am. Phys. Soc. 26, 940 (1981).
34. J. H. Whealton, R. W. McGaffey, and J. W. Wooten, Bull. Am. Phys. Soc. 26, 940 (1981).
35. J. H. Whealton and R. W. McGaffey, "Double Bifurcation Optimization for Reduction of Secondaries from Neutralizer Plasma Ions," paper presented at the IEEE 1981 International Conference on Plasma Science, Santa Fe, New Mexico, May 18-20, 1981.
36. D. P. Stotler, J. H. Whealton, and J. W. Wooten. Bull. Am. Phys. Soc. 26, 1017 (1981).
37. J. H. Whealton, J. W. Wooten, R. W. McGaffey, and W. L. Stirling, Bull. Am. Phys. Soc. 25, 983 (1980).
38 J. H. Whealton, G. G. Kelley, O. B. Morgan, and G. Schilling, Nucl. Instrum. Methods 154, 441 (1978).
39. J. H. Whealton, R. W. McGaffey, and J. W. Wooten, Bull. Am. Phys. Soc. 25, 919 (1980).
40. J. H. Whealton, J. W. Wooten, and R. W. McGaffey, *Magnetic Blocking Direct Recovery Efficiency*, ORNL/TM-7849, Oak Ridge, Tennessee (1981).
41. J. W. Wooten and J. H. Whealton, Bull. Am. Phys. Soc. 26, 941 (1981).
42. J. W. Wooten, J. H. Whealton and D. H. McCollough, Bull. Am. Phys. Soc. 26, 1017 (1981).
43. C. F. Barnett and J. A. Ray, *Beam Species Analyzer for Intense Neutral Beams*, ORNL/TM-7656, Oak Ridge, Tennessee (1981).

7. SUPERCONDUCTING MAGNET DEVELOPMENT

P. N. Haubenreich, Large Coil Program Manager

M. S. Lubell, Magnetics and Superconductivity Section Head

J. K. Ballou
T. V. Baudry[1]
R. D. Benson[2]
R. E. Bohanan
C. Bridgman[3]
R. L. Brown
L. Dresner
B. C. Duggins[4]
J. F. Ellis
W. A. Fietz
C. M. Fitzpatrick
W. M. Fletcher[4]
J. S. Goddard[4]
W. H. Gray
E. L. Halstead[3]
D. R. Hatfield[3]
W. Herz[5]
C. G. Hudson[6]
R. O. Hussung[3]
H. K. Katheder[5]
W. J. Kenney
R. K. Kibbe
P. S. Litherland[3]
J. W. Lue
J. N. Luton, Jr.
J. R. May
T. J. McManamy[3]
H. E. Miller[6]
J. R. Miller
J. F. Monday
J. L. Murphy[4]
B. E. Nelson[3]
M. F. Nishi[7]
C. C. Queen[2]
J. P. Rudd
T. L. Ryan[3]
S. W. Schwenterly
S. S. Shen
R. E. Stamps[3]
W. C. T. Stoddart[1]
D. J. Taylor[2]
P. B. Thompson[2]
P. L. Walstrom
R. J. Wood[4]
W. L. Wright[2]
J. A. Zichy[8]

---

1. UCC-ND Engineering.
2. UCC-ND Engineering, Fusion Projects Engineering Department.
3. UCC-ND Engineering, Research Engineering Department.
4. UCC-ND Engineering, Fusion Energy Electrical and Instrument Engineering Department.
5. Assignee from Kernforschungszentrum Karlsruhe, Federal Republic of Germany.
6. UCC-ND Engineering, ORNL (Y-12) Project Engineering Department.
7. Assignee from Japan Atomic Energy Research Institute, Tokai, Japan.
8. Assignee from Swiss Institute for Nuclear Studies, Villigen, Switzerland.

7. SUPERCONDUCTING MAGNET DEVELOPMENT

ABSTRACT. The Large Coil Program (LCP) continued to manage the design and manufacture by U.S. firms of three superconducting magnet coils that will be tested and evaluated in the Large Coil Test Facility (LCTF) now under construction at ORNL. During 1981, General Dynamics-Convair Division (GD) completed two-thirds of the conductor for its coil and began winding. General Electric (GE) finished winding its coil and began fitting the coil case. Conductor production and coil plate machining for the Westinghouse Electric Corporation (Westinghouse) coil progressed, and Westinghouse installed two winding lines. The international Large Coil Task (LCT) also proceeded during 1981. The Japanese coil was completed and preliminary tests were performed in Japan. In the Euratom coil project, Siemens began winding conductor while Krupp began fabrication of the coil case. Brown-Boveri began work on the case for the Swiss coil while final development work was completed on its conductor. Technical problems delayed all six projects.

Construction of the LCTF proceeded with major procurements of cryogenic equipment and power supplies and installation of a liquid-nitrogen-cooled cold wall, piping, electrical buswork, and platforms. Project cost and completion milestones did not require change.

Work by the Magnetics and Superconductivity (M&S) Section included notable progress in four areas: research and development (R&D) activities in support of the LCP, two 12-T coil projects, advanced conductor development, and development of toroidal field (TF) coils for the ELMO Bumpy Torus Proof-of-Principle (EBT-P) Project. A 12-T facility magnet, the Coil Winding Test Experiment (CWTX), was successfully placed in service.

7.1 INTRODUCTION

P. N. Haubenreich, M. S. Lubell

The ORNL Fusion Energy Division continues to play a leading role in the development of superconducting magnets for toroidal fusion reactors. The greatest effort in 1981 was in the LCP, which entails designing, building, and testing several different 8-T TF coils about one-third to one-half the size of those for the tokamak Fusion Engineering Device (FED). ORNL is guiding and monitoring GD, GE, and Westinghouse in the design and manufacture of one coil each. In addition, through an International Energy Agency (IEA) agreement, Euratom, Japan, and Switzerland are building one coil each to LCP specifications for testing in the LCTF along with the U.S. coils. Supporting R&D for the LCP is carried out in the M&S Section.

The R&D activities in support of the LCP include work on instrumentation and diagnostics, conductor verification tests, and coil winding technology. The M&S Section also supplies structural analysis in support of the LCTF test stand design and technical support necessary to monitor the coil contracts.

In addition to supporting the LCP, the M&S Section has a major role in the U.S. 12-T Coil Program, initiated in 1978 to supplement the goals of the LCP. In this program, ORNL is directing two projects involving major industrial subcontractors in the design and development of large conductors suitable for tokamak TF coils to be operated at fields to 12 T. To carry out measurements on these conductors, an insert was procured for the CWTX magnet facility that permits test fields to 12 T in a 22-cm-bore split solenoid.

ORNL continues to advance magnet technology in areas specific to fusion applications by developing better analysis techniques, generating basic design information, and evaluating small quantities of experimental conductor embodying advanced concepts. In 1981, the advanced conductor development program continued to concentrate on developing multifilamentary (MF) Nb_3Sn, understanding force-cooled magnets, and gaining more perspective on ac losses, all closely tied to the LCP and 12-T Coil Program activities. The concept of velocity-enhanced stability for an internally

cooled superconductor (ICS) was tested in a small NbTi magnet and found to work extremely well. High stability margin at high current density and high field without helium flow was demonstrated. The cable-in-conduit ICS concept is most appropriate for an extended field FED TF coil.

The principal magnet technology project of the M&S Section was the design, fabrication, and successful testing to full design values of two development magnets for the EBT-P Project.

7.2 LARGE COIL PROGRAM

7.2.1 Program Management

P. H. Haubenreich

Collaboration in the LCT progressed satisfactorily. Representatives of all three participants were at the LCTF site for extended assignments. Semiannual meetings of project officers were held at Kernforschungszentrum Karlsruhe (KfK) and at ORNL. The major issue was provision of signal conditioning channels for coil diagnostics. The other participants wanted more channels than the U.S. proposed to provide in the LCTF under the stringent constraints imposed by the budget. By the end of 1981, acceptable compromises appeared near.

Agreement was reached on the outline of the LCT test program. Target dates remained the same: tests of bath-cooled coils at the end of 1982 and tests of a full array beginning early in 1984. At year's end, however, the task schedule was in jeopardy because of problems in coil manufacturing (described in Sect. 6.2.3).

A great deal of management attention was required by the coil subcontracts, which are administered by UCC-ND Purchasing and managed by Fusion Energy Division. Continual review, evaluation, and advice from technical experts were provided in the areas of magnet technology, engineering, metallurgy, and quality assurance. Limited funds and rising costs due to technical problems required the development of funding allocations most conducive to the achievement of overall program objectives. Staff at GD were required to proceed at a reduced level of effort from March through September. Westinghouse was also substantially restricted in its preparations for manufacturing. Several reviews at the highest levels of fusion program management led to strategies and agreements to achieve reasonably satisfactory progress despite the circumstances.

The LCTF construction project plans were altered by rearrangement of schedules (notably for the torque rings) to make the best use of funds provided in three categories: capital construction, capital equipment, and operating expense. New management procedures that are being applied to large projects in Oak Ridge for the first time were instituted on the LCTF construction by UCC-ND and DOE-ORO.

7.2.2 Large Coil Test Facility

Large strides were made on the LCTF project in 1981. At year's end, engineering design was 91% complete, procurement was 57% complete, and construction was 37% complete. A union strike during the summer eliminated schedule contingencies, but major milestones still appeared attainable. A complete estimate, finished in December 1981, indicated a total cost of $36,850,000 (the same as the previous estimate made in 1980).

Major procurement in 1981 included helium refrigerator modifications, cryogenic piping, and power supplies. Principal construction activities included fabrication of sections of the liquid-nitrogen-cooled cold wall and construction of the piping in the vacuum tank, the platforms around the tank, the electrical buswork, and the control room. Outlay for engineering, procurement, and construction during FY 1981 amounted to $7.4 million.

7.2.3 U.S. Test Coils

R. K. Kibbe

GD coil

Production of 2.0 km of 8-T grade conductor was completed after problems of cold welding,

soldering, and inspection were overcome. After practice winding with dummy conductor, actual conductor winding on the coil bobbin began in August. Three (of fourteen) layers were wound before the operation was halted by the discovery of shorts through sensor leads. Plans were made to unwind and correct the problems (see Sect. 7.2.5). Meanwhile, 1.8 km of 6-T grade conductor was produced during lulls in coil winding operations.

GE coil

The winding operation at GE, which began in November 1980, was completed in December 1981, with 7.3 km of conductor in 12 spiral pies on the coil bobbin. All parts of the heavy stainless steel coil case were delivered by Chicago Bridge and Iron Nuclear to the Schenectady plant. At year's end, insulation was being fitted in preparation for assembly of the case around the winding.

Installation of conductor splices (two in each pie), test heaters, and sensors proved unexpectedly time-consuming. Substantial improvements in winding time were achieved, with the time for winding alone (not including heaters and sensors) decreasing from 12 weeks to 2 weeks per pie.

Westinghouse coil

After considerable planning and high level reviews, Westinghouse began implementing plans to install two parallel winding lines, with a coil completion target date of June 1983. The first line was completed in October, and the second line (privately funded by Westinghouse) was scheduled to be completed by February 1982.

A specification was completed for the JBK-75 stainless steel conductor sheath material. The total quantity (9090 kg) of this special material was delivered in strip form to ORNL by Carpenter Technology Corporation in August 1981 for ultrasonic inspection before being forwarded to Airco. By December 1981, ORNL had performed ultrasonic inspection on about 30% of the material with no rejectable flaws detected.

Aluminum plate machining was initiated with a fixed price subcontract to Erie Press Systems. The first three plates were delivered to Westinghouse, and trial winding activities started in October 1981.

Airco began producing the conductor for the Westinghouse coil. Wire production proceeded smoothly, and the first of four batches of wire passed all quality control (QC) tests in June 1981 with only minor nonconformances. Development of the sheathing process continued, with ORNL welding specialists becoming heavily involved in a consulting capacity. This was highlighted in October 1981 by the successful production of eight trial winding conductor lengths, which were identical to production lengths except for the use of a copper conductor in lieu of the superconductor. The problem of effective on-line QC inspection of the continuous-weld sheathing process was resolved; the ORNL Metals and Ceramics Division successfully adapted to this application some advanced multifrequency eddy current inspection concepts developed in breeder reactor programs.

7.2.4 Other Test Coils

Japanese coil

Hitachi completed the winding of 20 double spirals of conductor, with 14 internal splices and a full complement of diagnostic sensors. While these were being wound on forms, the coil case parts were fabricated. By using this manufacturing strategy, two winding lines, and three-shift operations, Hitachi was able to deliver the completed coil just under 12 months from the start of coil winding. The coil was installed in the Japan Atomic Energy Research Institute (JAERI) facility at Tokai for testing before shipment to the LCTF. During cooldowns in November and December, unacceptably large leakages of helium developed. These were located in sensor lead feedthroughs in the coil case. Staff at JAERI and Hitachi agreed that design revisions would be necessary.

Euratom coil

Conductor production was initiated and over half of the conductor was completed. The detailed design of the coil was completed and winding (on a removable form) was begun in October by Siemens. Meanwhile, Krupp proceeded with coil case fabrication. Installation of equipment began at TOSKA, the facility at KfK that will be used to cool down and test the Euratom coil before shipment to the LCTF.

Swiss coil

Brown-Boveri finished the detailed design of the Swiss coil and prepared a final design report. All production steps for the conductor were developed and verified, and cutting and welding of coil case parts was initiated.

7.2.5 LCP Research and Development

R. L. Brown, L. Dresner, J. F. Ellis, W. A. Fietz, W. H. Gray, M. S. Lubell, J. W. Lue, J. R. Miller, S. W. Schwenterly, S. S. Shen, P. L. Walstrom

Conductor experiments

Guidelines for use of damaged conductors in LCP. Guidelines were issued to GE covering the use of conductor with one missing or broken strand. Such conductor may be used if the break is located in an area where the magnetic field is low enough that the remaining 15 strands have the same current capacity as 16 strands at the peak field for that conductor grade. ORNL must be notified when damaged conductor is used, but if the guideline condition is met, winding should not be delayed for ORNL approval. Full documentation is required.

Splice development for GE. An apparatus was constructed to measure the mechanical properties of full-size GE joints. It can apply forces greater than 5000 lb at room temperature, at liquid nitrogen temperature, and at helium temperature with approximately 1% accuracy. The force is generated using a manual hydraulic piston, and the elongation is measured using two moving coil differential transformer (MCDT) extensometers developed for LCP coils. This equipment was used to test the concept of a soldered lap joint proposed by ORNL. The joint is made by overlapping several inches of copper core and soldering, thus replacing the superconducting strands over the lapped cores.

Tests of three different solders, 60 Sn-40 Pb, 97.5 Pb-2.5 Ag, and 97.5 Pb-1.5 Ag-1.0 Sn, showed that any of these solders can produce a joint that is stronger than the copper core itself. The core joint specimens were tested well beyond the yield of the cores, measuring the applied load and extension of the entire joint. None of the joints failed during the test. Two versions of the GE LCP joints were tested electrically and mechanically. One was the LCP standard machined block type; the other was a simplified soldered version proposed by ORNL. Both joints had a resistance of less than 10^{-9} Ω at 7500 A and 5.5 T. Both were subjected to 10 cycles of loading at 4.2 K up to 6000 lb, were loaded once to 9000 lb, and appeared to withstand the mechanical load without appreciable yielding.

The new grading joint design for the GE LCP coil, developed by ORNL, was qualified by GE, and one production joint has been wound into the coil.

Quench pressure waves from internally cooled magnets. A primary concern identified during 1981 was that a quenching ICS magnet in LCTF might cause a shock wave to propagate through refrigeration lines to one of the turboexpanders, where it would cause damage. An experiment to simulate the formation and propagation of such a pressure wave from the ends of a quenching ICS coil was performed. The apparatus used was that previously constructed for examining maximum quench pressures, with tubes added at each end to simulate refrigeration lines. On one end the tube was baffled in an attempt to explore the effectiveness of the baffling in suppressing a shock wave. However, no shock waves were formed. During a simulated quench, the pressure on the "refrigeration lines" rose smoothly to a maximum over a period of seconds.

The helium was not "blasted" out; rather, it "oozed" out. If the simulation is good, there should be no serious problem for the LCTF refrigerator. However, the experiment must be closely examined to evaluate its appropriateness.

Internally cooled solenoid. The 11-cm-bore, force-cooled solenoid (NbTi cable-in-conduit) was tested. A field of 8 T at the windings was attained on the first ramp without training. Current at this level was 4800 A; stored energy was 267 kJ. Current density in the cable space was 11.3 kA/cm^2, but because a round conduit was used and no special effort was expended to achieve a high packing factor, the overall current density was only 6.3 kA/cm^2. Stability tests at 7 T were cursory but suggest a stability margin around 30-40 mJ per cubic centimeter of conductor. A 1-m length of conductor in the high field region recovered when driven fully into the normal state. More testing will be done later. The coil was successfully dumped more than a dozen times from fields in the 7- to 8-T range. Dump voltages were 400-500 V. All testing was carried out at quite low flow rates (~0.1 g/s), as leaks in the pump loop forced us to use the backup blowdown system.

Facilities

Test of cryogenic helium pump. A developmental helium pump manufactured by Gardner Cryogenics has been tested. This type of pump is suitable for use in force-flowing supercritical helium through ICS magnets. Despite flaws in the demountable connections, the piston pump itself has performed satisfactorily. It has pumped supercritical helium at up to 7.5 atm with a pump head up to 2.8 atm. The maximum mass flow rate obtained was 16 g/s. Though this is 20% below the design goal, we are well pleased with this result.

Helium liquefier. A Koch Process Systems (CTI) 1430 helium refrigerator/liquefier is being installed in the magnet laboratory to supply helium for various magnet development experiments. The cold box and compressor units have been set in place, and all electrical wiring has been completed. Fabrication of the gaseous helium and cooling water piping has been delayed because further engineering was required to reduce the high estimated costs of the system as originally designed. However, installation should be completed in 1982.

The 100-liter liquid helium storage dewar was received from Cryofab, Inc. The completed system is quite versatile, can be hooked up to various experiments, and will be capable of closed cycle cooling in both pool-boiling and forced-flow modes. It will be capable of producing either 40 liter/h of liquid helium or 100 W of refrigeration at 4.6 k, as well as any combination in between.

Analytical work

LCTF partial toroidal test conditions. We calculated the test fields that can be reached in LCTF with less than six coils, using the presently available estimates of facility load capability but assuming that all coils are equal and neglecting the pulse field load without exceeding the coil design currents. A single coil reaches 6 T, a nonadjacent pair reaches 6.2 T, an adjacent pair reaches 6.4 T, the center coil of a triplet reaches 6.7 T, and five coils reach 7.2, 7.7, and 7.9 T, depending on their positions in the array. Out-of-plane loads are significant, and the peak fields do not occur on the torus equatorial plane.

LCTF computer analysis. Because of increasing security restrictions at K-25, the LCTF structural analysis has been moved to the X-10 computers. ORNL's NASTRAN lease agreement was modified to permit use of the X-10 IBM CPUs. The executable module was successfully installed, and movement of the LCTF analysis is under way. The new NASTRAN plotting program was also installed on the X-10 computers. Several on-line procedures to simplify access to all this software were written and made available.

LCTF structural analysis. The LCTF two-coil analysis model has been substructured, and one load case (one coil at 100% current) was

successfully compared to the original unsubstructured analysis. The model can now be upgraded to include three coils, which would not have been feasible with the unstructured model.

Effects of shorts in LCP coils. Circuit analysis of the mechanical and thermal effects of shorts in a typical LCP coil has been updated. The results indicate that only turn-to-turn short circuits with contact resistance less than 10^{-4} Ω may result in excessive mechanical stress and heating during a LCTF discharge. Techniques to detect such shorts and a protection scheme for a shorted LCP coil were being considered at the end of this report period.

Eddy current effects in LCTF pulsed coil system. The effect of the LCTF pulsed coil system on the coil cases and support system has been estimated. The results indicate that the energy dissipations due to eddy currents in these structures are negligible. It is also found that the effect of these current flows on the pulsed field distribution at the LCP test coils is insignificant.

Pumping requirements for ICS. An estimate has been made for ICS cable-in-conduit conductors that may require a forced flow of supercritical helium to ensure upper stability margins and therefore recovery from very large perturbations. Apparently, it is better to design for high current from small-diameter strands than to use high velocity helium to stabilize large-diameter strands.

Stability-optimized cable-in-conduit superconductors. Over the last year a large body of data has been accumulated on the stability of cable-in-conduit conductors. A new calculation, using procedures previously reported, has been made on stability-optimized conductors. The earlier solution is no longer valid. The present results favor a conductor fraction of 60% (i.e., a helium void of 40%) and provide guidance on the stability margin as the copper-to-superconductor ratio is varied in the conductor fraction.

Cryogenic experiments

K-seal pressure tests for LCP. The second Teflon-coated K-seal was tested, completing the test program of four seals (two lead-coated, two Teflon-coated). This seal performed even more poorly than the first Teflon sample — it would not even seal at room temperature. Both lead-coated seals survived pressure cycles at 15 atm with two complete cooldowns each, and these lead seals are recommended for use in LCP. As a final test, one of the lead seals was reinstalled, to check its reuse capabilities. Initially, it would not seal at room temperature. However, with a thin coating of Apiezon N vacuum grease, the used seal performed as well as the new one at all temperatures.

Heat transfer tests. A heat transfer test was performed on samples of GE LCP 8-T conductor. The test bundle, which was a stack of twelve 1-ft lengths of LCP production conductor, was made up with LCP turn-to-turn and pancake-to-pancake insulation to simulate as closely as possible the channels, etc., of the GE LCP magnet. GE modified three of the conductor lengths by pulling the superconductor out of the subelements before delivery. We soldered heater cable (a Nichrome wire insulated with MgO and enclosed in a stainless steel sheath) into the grooves where the superconductor had been. The conductor lengths were instrumented with a total of 36 gold-iron versus copper thermocouples and assembled with insulation in a clamping fixture. The entire fixture was placed in a swivel mechanism that allowed variation of angle while the sample bundle was in the helium bath. An automated data acquisition and control system (part of the LCP data acquisition system) was used to program the power supply in a staircase fashion and to record the data. (Incidentally, the test proved to be a very useful test of the data acquisition software and hardware and uncovered some problems with some of the display software.) Preliminary results indicate that the GE LCP magnet will be barely cryostable. The data will be compared

with the coil performance data. If a correlation can be established, the bundle test could be a valuable and relatively inexpensive design evaluation tool. Limitations of steady-state data in predicting steady-state performance are, however, known to exist, and dynamic testing methods may be needed to model the actual normal zone recovery behavior of a cryostable coil.

Inverted operation of vapor-cooled leads. Loss rates and inertial properties of American Magnetics 28-in., nominal 2000-A, vapor-cooled leads have been measured in both normal and upside-down positions. Standby losses in the upside-down position were 80% higher than in the normal position, whereas at 2000 A, losses were approximately equal for the two positions. To test the inertial character of the leads, the flow through the leads was interrupted. The voltage drop per lead and the temperature of the hot spot rose linearly: 63 mV and 70 K, respectively, in 30 s.

LCTF superconducting bus heat transfer. Although previous calculations indicate that the insulated, massive, copper-stabilized superconducting buses connecting the coils with the lead dewars in LCTF will be cryostable at the design current, there is considerable uncertainty in the thermal conductivity data and the possibility of contact resistance, etc. A mockup section of bus was insulated as it would be in LCTF, instrumented with a heater and thermocouples, and subjected to thermal shock cycling in liquid nitrogen. Then its power versus temperature curve was measured in liquid helium. The heat transfer data show that the bus will be unconditionally stable at the design current.

Instrumentation and diagnostics

GE strain gages. A series of thermal cycling verification tests of GE-installed strain gages was performed for the LCP. These gages were installed using a different cement and curing cycle than used in previous installations. Another set of test gages of the same type was prepared at ORNL by a technician. The two sets exhibited similar behavior during cycling to liquid nitrogen temperature, and the sample and procedure were therefore judged acceptable.

Carbon temperature sensors. A set of five thin film carbon sensors (identical to that installed by GD) was installed by GE as part of its verification test program. The gages were tested at ORNL by cycling five times to liquid helium temperature. The sensors were judged to be adequately stable, and the installation procedure was approved for LCP use.

Signal conditioning. Each channel in both the "isolated" and the "nonisolated" strain gage instrumentation includes a 3-kHz carrier-amplifier-demodulator module. Another carrier-amplifier module (less expensive than the one originally tested) was evaluated for compatibility with both systems and was found to be adequate for use with the nonisolated system. Use of the Validyne Corporation Model CD-19 in the nonisolated system will result in a total cost savings of about $8540. The Validyne CD-90 modules will still be used in the isolated system. Both modules use the same main frame type, which provides a degree of standardization between the two systems (i.e., conduit in plate structure). The nonisolated system will be tested at ORNL. A test plan has been formulated, and Westinghouse has submitted a preliminary design for the test piece. The objective is to establish the safe proof voltage that can be applied to the finished coil under ambient conditions, which will give confidence that the coil will have adequate low temperature breakdown strength.

GE LCP instrumentation. A M&S staff member visited GE on March 26, 1981, to observe voltage breakdown tests on a GE coil conductor heater and to suggest and help perform quick quality checks on the heater and its installation. The heaters for the GE coil conductors are made of a thin strip of Inconel sandwiched between two thin layers of Kapton. This ribbon is cemented to the conductor elements with epoxy. The present installation is not

acceptable; the major difficulty appears to be in the quality of the purchased heater strips. Microscopic examination of samples of the strip material reveals delamination (which is either caused or worsened by poor bonding), internal buckling of the Inconel, internal voids, and edges where the insulation has been trimmed too close to the element. This problem is now under intensive study. Considerable effort will be required to arrive at a timely and cost effective solution.

GE LCP turn heater verification testing. High voltage breakdown tests were completed on a 51-cm sample of GE LCP conductor with strip heaters (0.08-mm-thick by 2.08-mm-wide Inconel 600, with 0.05-mm-thick Kapton insulation) installed by GE on each of the 16 subelements, just as in the actual coil. The sample was wired to provide several separate circuits that could be individually selected, thus allowing the generation of a maximum amount of information. The test was arranged to provide simultaneous full voltage and current, in order to avoid errors resulting from the greater insulating capability of unheated liquid helium. Up to 1500 V and 4 A per strip were applied, with rectangular voltage pulses ranging from 10 to 150 ms. Generally, the sample failed with a nondestructive surface flashover at 1500 V and 60-70 ms. This exceeds the predicted requirements (as recently amended by GE) of 780 V for 16 ms. However, another test performed on the same 51-cm sample with all 16 taps energized indicates that a pulse length of about 35 ms will actually be required. This is still well within the capabilities of the heaters, provided that the quality in the actual coil installation is comparable to that in the sample. A third GE LCP turn heater sample was tested for heat transfer capabilities. Heater strips without deliberate flaws were mounted on a 60-cm section of 6-T grade conductor. In contrast to the arrangement for the sample 1 heat transfer tests, interpancake insulation was installed along the sides of the conductor pack, which again consisted of a sample section sandwiched between two dump conductor sections. The cooling grooves in the interpancake insulation were oriented at 45° from vertical. Rectangular voltage pulses of 200-500 V were applied for 10-50 ms. At a given power level, the resulting peak conductor temperatures were 0.5-1.0 K higher than those for sample 1. The addition of the interpancake insulation thus appears to allow slightly greater heating of the conductor due to the restriction of coolant flow into the conductor pack.

GD LCP heater verification tests. Due to a potentially insufficient mechanical strength for the originally planned heaters potted in Wood's metal, GD proposed that the heaters be wrapped with copper foil and soldered into the conductor groove with 60 Nb-40 Sn solder. We asked GD to submit a 30-cm sample for further verification tests of this new concept. The sample was instrumented with two differential thermocouples and tested in a 4.2 K helium bath. A 4-channel Biomation waveform recorder measured the transient heater voltage, current, and the thermocouple output. In all cases, the heater consisted of two Kapton-insulated Nichrome wires laid in the conductor groove and secured with solder.

The sample showed no appreciable heating until over 500 mJ/cm³ of energy was applied (five times the amount required in the original test) and exhibited a very long time lag between application of the heater pulse and the resulting conductor temperature rise. This installation was judged unacceptable.

GD then produced two more samples, one with copper electroplated over the Kapton and potted with 60 Nb-40 Pb solder and the other (a control) with Wood's metal potted over the bare Kapton. Both samples performed better than the first but were still much worse than the original verification test sample. GD then sectioned another sample and found that the heater wire had 3.5 layers of wrapped Kapton insulation instead of the 1.5 layers specified. The much higher thermal resistance of the thick insulation accounts for the poor performance.

Next, GD procured a quantity of heater wire with 2-mil-thick molded Kapton insulation. However, the electroplating process resulted in low dielectric breakdown strength, because the plated copper was entering pinholes in the Kapton layer.

GD then suggested putting the Kapton-enameled wire heaters inside tubular braided metal shields, with the idea that the braid would "wick" the solder in tightly around the heater wires. Two more samples were fabricated, one with a single braid enclosing both heater wires and one with a braid around each wire. Both samples performed as well as or better than the original verification test sample, although the single-braid sample was slightly more efficient than the other. GD later sectioned both samples and found voids in the dual-braid sample. However, the dual-braid version is easier to install, and GD is currently installing this type of heater in the coil.

Two additional samples of conductor with heaters from GD were tested by immersing them in liquid helium, pulsing them with current, and recording their temperature response. One, a ribbon-type conductor, had a response about the same as the Kapton enamel-insulated heaters now installed in the first layer of the coil. However, its electrical reliability is not established. The second heater was a Kapton film-wrapped wire. Its heating efficiency was found to be lower than that of the Kapton enamel wires. These data, along with electrical test data for the first layer, were used to decide whether to use Kapton-wrapped heaters in subsequent layers or to continue using the enameled wire, 50% of which had to be rejected due to pinhole defects. Because tests at ORNL showed that the wrapped Kapton-insulated wire in a solder-impregnated braid gave considerably poorer performance than the Kapton enamel-insulated wire, GD decided to continue using the enameled wire heaters enclosed in braid, which were used in layer 1.

The ORNL verification testing, carried out under the LCP/R&D activities (RDAC) program, was essential in helping GD to resolve a serious eleventh-hour production problem. Of equal importance is the fact that the potentially poor heater response was initially identified by a LCP/RDAC staff member who carefully reviewed GD's monthly technical progress report. (GD had not previously communicated with UCC-ND regarding the proposed change from the Wood's metal potted heater to the soldered design.) This is another example of how attention to detail and the ability of LCP/RDAC staff to respond rapidly have been of significant benefit to the program.

Field sensitivity of voltage-to-pressure (E/P) transducers. Because of the method used in their operation and construction, E/P transducers, which convert a current signal to a pressure level, can be expected to be sensitive to ambient magnetic fields. These transducers are used in several critical components of LCTF, including the auxiliary cold box. Japanese tests on an E/P transducer (type unspecified) showed it to be field-sensitive – an error of 10% was observed at an applied field of 50 G. We tested a Moore Model 77-16 E/P transducer to a field of 1000 G without observing a measurable effect on its output pressure. We attribute this unexpected lack of field sensitivity to the transducer's massive cast steel housing, which apparently acts as a magnetic shield.

Troubleshooting the GD and GE LCT coils. In November, ORNL was informed that a voltage tap lead wire in the partially wound GD coil was open and that two of the lead wires in a temperature sensor lead cable were shorted. At that time, GD was not aware of any short of a sensor to the windings. The possibility that an event that could pinch a lead cable sufficiently to short out wires internally could also have shorted the shield to a conductor caused enough concern that the M&S Section devised a test to detect shorts in lead wires. The ohmmeter tests being performed by GD were not sensitive enough to distinguish between the deliberate electrical

connection of the sensor to the conductor on which it was installed and any additional connection caused by a short to another turn. The M&S Section test consisted of running a 5- to 10-A current through the windings and reading out the voltage at the end of every sensor wire and sheath in contact with the windings, including voltage taps, strain gages, and temperature sensors, with a scanning data logger. The data were then plotted against the calculated voltage. Shorted leads appeared as points deviating from the curve. If a sufficient number of turns was shorted, a change in slope was observed.

A M&S Section staff member traveled to San Diego in November to assist in performing the test on the coil. Three shorted sensors were found in the heavily instrumented first layer. Two of the shorts occurred in temperature sensors; one of these was in the cable with the two internally shorted leads. The third short did not show up as an out-of-sequence voltage reading because the shorted lead wire had been severed, but its presence was deduced by the change in slope of layer 1; the data showed that a short between the beginning of layer 1 and the end of layer 2 must be present. (This short should have been detected by GD's layer short detection technique, which was based on an ac method; it is not known why GD's tests did not detect this short.)

While the voltage data were being analyzed, GD personnel performed other tests, including an infrared imaging test and further voltage measurements with probes inserted through grooves in the insulation to confirm the presence of the shorts and pinpoint them more exactly. After the presence of the shorts was confirmed, options for corrective action were identified and evaluated by a team at GD and by the M&S Section and UCC-ND Engineering staff. M&S personnel performed tests to determine the feasibility of burning out the shorts, made calculations to estimate consequences of discharge of the coil with the shorts, and evaluated various options, including use of lower grade material and reuse of the conductor. At the same time, GD performed various tests to evaluate the feasibility of unwinding the coil and reusing the conductor.

By the end of December, GD and ORNL personnel, in conjunction with the LCP Advisory Committee, agreed that the best course of action was to unwind the conductor and to attempt to salvage it. Deformation of the copper stabilizer by bending turned out to be less of a problem than initially thought, and it appears likely that the conductor can be rewound on the coil.

A M&S Section member again traveled to GD to witness the unwinding of layer 2 and to assist in the diagnosis of the shorts. When the shorts became visible, their locations agreed well with the predictions based on the tests. The layer-to-layer short was caused by a voltage tap at the end of layer 1 (this tap was required for coil protection as well as for diagnostic data) that was pinched by the last turn in layer 2. It was concluded that two of the shorts could be ascribed to faulty workmanship, while the third (a shorted shield of a temperature sensor lead cable) was caused by a last-minute design change, which proved to be deficient in that it failed to account for shifting of the layer insulation.

The unwinding of layers 2 and 3 also revealed serious problems of a nonelectrical nature. Severe damage to the conductor and to the turn-to-turn insulation had been done by levering and wedging operations. In addition, shifting of the layer insulation during winding caused some portions of the end turns to be unsupported on one side for lengths of up to 1 ft in a few places. It is not known whether these defects would have led to coil failure.

The M&S Section is actively involved in evaluating GD's proposals for redesign of the instrumentation, improvement of winding procedures, and plans for more stringent QC inspection to prevent any more defects from occurring.

The experience with GD caused concern that shorts might also be present in the GE LCP coil. A M&S staff member traveled to GE's winding facility in Schenectady to perform the shorted lead test on their coil before the

windings were closed up inside the case. The test uncovered two shorts in one of the sensor cables, one intermittent and one continuous. The present approach is to attempt to repair the short without unwinding the coil or portions thereof. The shorted lead test will be performed periodically to determine whether there are more shorts in any other sensor leads. M&S personnel are working closely with GE personnel to evaluate the options. At present, the preferred option is to cut the leads between the short and the sensor after the pancakes are separated by wedges.

7.3 ADVANCED CONDUCTOR DEVELOPMENT

L. Dresner, W. A. Fietz, M. S. Lubell, J. W. Lue, J. R. Miller, S. S. Shen

7.3.1 12-T Insert for CWTX

Our facility magnet, the 8-T, 38-cm-bore CWTX, was tested with a Nb_3Sn tape insert to produce a 12-T working field in a 22-cm bore (maximum field on conductor is 13.5 T). The insert was principally designed and fabricated by Intermagnetics General Corporation (IGC). Parameters of CWTX and the tape insert are listed in Table 7.1.

The test was completely successful in that the insert reached full operating current on the first attempt without any training or a quench. The system was tested above the rated field to ~12.8 T in the bore (>13.5 T at the winding) and was then quenched. The protection system successfully prevented any damage, even though the quench resulted from an inadvertent overcurrent in the CWTX background coil (2400 A versus 2150 A rated). This was 25% over the rated stored energy (~7.5 MJ). About 75-80% of the total stored energy was extracted by the dump resistor. The system was reenergized to full rated field to make certain that no damage had occurred.

Table 7.1. Parameters of CWTX and Nb_3Sn tape insert

	Insert	CWTX
B_0	12 T	8 T
B_{max}	13.5 T	8.8 T
Material	Nb_3Sn	NbTi
Bore	220 mm	380 mm
Radial access	66 mm	66 mm
j	8900 A/cm²	5100 A/cm²
E_s	0.5 MJ	6.0 MJ

Upon completion of the facility proof test, a MF Nb_3Sn conductor sample, made for the High Field Test Facility (HFTF) at Lawrence Livermore National Laboratory (LLNL), was evaluated through measurements of the short sample critical current up to 7500 A between 10 and 12.5 T. Our results were in agreement with data taken at the Francis Bitter National Magnet Laboratory.

Installation of a CTI 1430 refrigerator to operate the facility was begun. When the installation is finished (only the electrical wiring is complete), the system will operate in a closed cycle on the magnet itself to allow economical use of the facility and sample insertion and removal.

The CWTX is the largest high field split solenoid constructed to date. It surpasses the achievement boundary of magnetic field versus bore for all other MF Nb_3Sn and MF V_3Ga coils.

7.3.2 Specific Heat Measurements

A cryostat for measuring heat capacity in the ranges of 2.5-70 K and 0-8 T was fabricated. Specific heat measurements on a Nb-46 Ti sample at 0, 4, and 7 T were completed by an Oak Ridge Associated Universities (ORAU) student. The data are available for use in conductor stability calculations. The fit to an analytic expression derived from simple theory is reasonable.

7.3.3 Heated Length Dependence of the Stability of Internally Cooled Superconductors

An experimental study of the heated length dependence of the stability of ICS has been

completed. The results indicate that the limiting current (below which there is only an upper high stability margin) scales with heated length and pulse duration as $I_{lim} \propto l^{-2/5} t^{-1/5}$. This is in contrast to the 2/5 and -1/5 powers originally derived from a semi-quantitative theory by L. Dresner. Dresner's original theory used a Dittus-Boelter correlation for the heat transfer coefficient produced by the heating-induced flow. After the onset of heating, the induced flow changes rapidly with time, and it is possible that the heat transfer coefficient has a different correlation to flow velocity than it does in steady state. If we assume $h \propto v^a$, the present results indicate that $a = 4/15$ instead of the Dittus-Boelter value of 4/5.

This result implies that an ICS is more stable against a short pulse applied over a long length of conductor than the inverse situation. This is contrary to the accepted belief for the pool-cooled superconducting magnets, in which minimum propagation length and sudden heat input by conductor slippage or flux jumps are the usual concerns. Perhaps long, narrow cooling channels that can induce high transient flow are a possible cure for this problem.

7.3.4 Design, Construction, and Test of a NbTi ICS Coil

We have designed and constructed a 113-mm-bore ICS solenoid using a cable-in-conduit conductor with NbTi composite and copper strands as a focus for practical conductor fabrication techniques and coil winding methods using such conductors. The finished coil provides the opportunity for global tests of the performance of this type of conductor in a real coil that produces a high field (~8 T) and uses a long (340-m) section of conductor. The conductor cable is a concentric layer type containing 19 triplex strands made from 0.7-mm-diam wire. The superconducting strands are contained entirely within the outer layer of the cable and thus are fully transposed. The cable is jacketed with stainless steel tubing; the overall conductor diameter is 8.6 mm. Induction heaters, voltage taps, pressure taps, and temperature sensors are installed in the windings to aid in stability measurements. Flow to the coil is provided by a piston pump capable of providing 20 g·s^{-1}. The coil reached a maximum field of 8 T without quenching, a level corresponding approximately to the short sample critical current. In subsequent tests the coil was demonstrated to have appreciable stability at the 7-T level, and stability phenomena previously observed only in small-scale tests were verified in the operation of a real coil of useful size.

7.4 12-T COIL DEVELOPMENT PROGRAM

L. Dresner, W. A. Fietz, M. O. Hoenig, C. E. Oberly

Because of budget constraints, progress in the 12-T program has been limited to conductor design and procurement. It is summarized as follows.

7.4.1 GE Model Coil Program

The engineering specification for a 12-T cable composite superconductor was prepared by GE to ensure that conductor acquired by ORNL would be suitable for use in its model coil. A contract with Airco to produce this conductor, using in part material already belonging to the government, was initiated. However, due to a shortage of funds, the contract approval cycle was halted.

7.4.2 IGC Material Development Program

IGC has been awarded a contract to manufacture a short length of 20-kA, 12-T, Nb$_3$Sn superconductor cable of the type proposed in the GE/IGC model coil design. The superconductor will be manufactured by the external bronze process, using CuNb MF composite previously purchased by ORNL, and will be tested in the 12-T CWTX magnet. Because the length

of conductor required for this test is relatively small, the cable concept can be tested even though the problem of long-length plating has not been solved. IGC will also supply ORNL with extra diffusion-protected copper stabilizer, with which ORNL can manufacture additional cables using previously purchased Nb_3Sn/bronze wires.

Over 50 ft of dummy cable was successfully produced. The objectives of establishing tooling and operating procedures for fabrication of such conductor were thus accomplished.

7.4.3 Additional 12-T Conductors

We have cooperated in research efforts with outside institutions to explore the possibilities of producing 12-T cable conductors with other techniques. Teledyne Wah Chang has produced and delivered a full-size, 12-T conductor using a modified jellyroll method. This cable is identical to that proposed by GE for the model coil and will be tested in our 12-T facility.

7.4.4 Measurements of Premature Nb_3Sn Formation in Unreacted MF Composites

Magnetization measurements were carried out on unreacted Nb_3Sn composites from Airco similar to those used in the HFTF conductors. Results indicated that 15% (by volume) of the niobium filaments have been reacted into Nb_3Sn before the final heat treatment process. Presumably, either the extrusion process or the drawing anneals raise the conductor to a high enough temperature for the formation of Nb_3Sn. On the other hand, a specifically prepared sample (with a lower lead content and a poisoning element to reduce thermal diffusion) showed negligible amounts of Nb_3Sn. The possibility of avoiding the formation of premature Nb_3Sn in a commercial production process (now that it is known to be possible in a lab sample) is currently being investigated.

7.4.5 Extended Operation of a FED Magnet

A study was made of the feasibility of designing a NbTi ICS magnet for FED that would operate at 8 T and 4.2 K and that could later be extended to 10-T operation by simply lowering the temperature. Based on a sound experimental database, it can be shown that a reduced temperature of 3 K is sufficient to reach the extended operation of 10 T while maintaining the stability margin of 200 mJ/cm^3. These calculations are based on well-verified formulas for temperature, field variation of critical temperature, critical current, current sharing temperature, and liquid helium properties. The one formula not previously well verified concerns the limiting current, below which the stability margin increases by almost an order of magnitude to a value that can be calculated from known helium parameters. In a small, internally cooled magnet made of NbTi cable-in-conduit conductor, experiments at 8 and 7 T were carried out above the limiting current and on the lower stability level. For these particular parameters, theory predicts that lowering the operating current until the maximum field is only 5.5 T will allow one to reach the upper stability margin levels. The experiment was performed, and lowering the field to 5.8 T produced the upper stability margin. This confirmation of the theory for calculating limiting current provides confidence that our ideas concerning an 8-T FED magnet extendable to 10 T are sound and should be seriously considered. The ICS concept provides the least expensive and most reliable means of all the options available for a FED design.

7.5 MAGNET TECHNOLOGY

J. K. Ballou, R. L. Brown, W. H. Gray, M. S. Lubell, J. W. Luc, J. R. Miller, S. S. Shen

The EBT-P magnet development program began in May 1979 and used the time between the start of the EBT-P program and the selection of the

industrial participant to perform some of the magnet development work. Briefly stated, the basic plan was for ORNL to design, build, and test two full-size development magnets and to transfer the technical information obtained during the development work to the industrial manufacturer in charge of magnet construction. The magnet manufacturer would then wind a prototype magnet, with basically the same design parameters, which would be tested in a three-magnet array simulating the magnetic conditions of EBT-P.

The EBT-P magnet design parameters were agreed upon during Phase I of the EBT-P project by ORNL Fusion Energy Division staff members, DOE-ORO staff members, and the four competing industrial teams during a series of meetings in the fall of 1979. Naturally, the chosen parameters were the result of a series of compromises among several factors; the most significant were (1) EBT physics constraints, (2) EBT-P performance goals, (3) acceptable risk levels, and (4) projections of available funding.

To date, ORNL has fabricated and tested the two development coils. These coils met the design criteria of field (7.4 T on the conductor at 10 kA/cm^2) and withstood simulated x-ray heating as required. Further information on the design, construction, and testing of the coils may be found in Refs. 1-3.

REFERENCES

1. J. K. Ballou, T. J. McManamy, R. L. Brown, W. H. Gray, and M. S. Lubell, in *Proc. 9th Symp. on Engineering Problems of Fusion Research, Chicago, 1981* (IEEE, New York, 1982), pp. 543-46.
2. W. H. Gray, T. J. McManamy, J. K. Ballou, and R. L. Brown, in *Proc. 9th Symp. on Engineering Problems of Fusion Research, Chicago, 1981* (IEEE, New York, 1982), pp. 316-19.
3. J. R. Miller, J. W. Lue, and S. S. Shen, in *Proc. 9th Symp. on Engineering Problems of Fusion Research, Chicago, 1981* (IEEE, New York, 1982), pp. 2012-15.

8. ADVANCED SYSTEM STUDIES

FUSION ENGINEERING DESIGN CENTER

D. Steiner, Program Manager (to November 15, 1981)
T. E. Shannon,[1] Program Manager (after November 15, 1981)
C. A. Flanagan,[1] Deputy Program Manager

Plasma System
Y-K. M. Peng
S. E. Attenberger[2]
S. K. Borowski[3]
L. M. Hively[4]
J. A. Holmes[2]
K. E. Rothe[2]
D. J. Strickler[3]

Nuclear Systems
P. H. Sager[4]
B. A. Cramer[2]
J. P. Davisson[2]
G. M. Fuller
J. R. Haines[2]
J. Kirchner[2]

Electrical Systems
J. M. Murray[4]
C. E. Gorker[5]
D. H. Metzler[5]
W. D. Nelson[5]

Magnetic Systems
R. W. Derby[2]
R. J. Hooper[6]
B. L. Hunter[6]
S. S. Kalsi[5]
V. C. Srivastava[5]

Systems Engineering
T. E. Shannon[1]
R. J. Barrett[10]
T. G. Brown[11]
S. K. Ghose[12]
R. L. Reid[2]
W. T. Reiersen[11]
G. E. Smith[11]
F. T. Spampinato[11]
S. L. Thompson[12]
K. F. Wu[1]

FED Physics Group
P. H. Rutherford[9]
J. F. Lyon

ENVIRONMENTAL ASSESSMENT PROGRAM

J. B. Cannon,[13] Program Manager

R. B. Braid[15]
W. Davis, Jr.[16]
C. E. Easterly[15]
H. E. Goeller[14]
G. S. Hill[15]
J. F. McBrayer[15]
F. W. Wiffen[18]
J. R. McNally, Jr.
R. T. Santoro[17]
J. S. Watson[16]
D. J. Wilkes[13]

---

1. UCC-ND Engineering.
2. Westinghouse Electric Corporation, Pittsburgh, Pennsylvania.
3. UCC-ND Computer Sciences.
4. University of Michigan, Ann Arbor, Michigan.
5. General Electric Company, Schenectady, New York.
6. General Atomic Company, San Diego, California.
7. McDonnell Douglas Astronautics Company, St. Louis, Missouri.
8. Princeton Plasma Physics Laboratory, Princeton, New Jersey.
9. Massachusetts Institute of Technology, Cambridge, Massachusetts.
10. Burns & Roe, Inc., Oradell, New Jersey.
11. Grumman Aerospace Corporation, Bethpage, New York.
12. Bechtel National, Inc., San Francisco, California.
13. Energy Division.
14. Chemical Technology Division.
15. Health and Safety Research Division.
16. Environmental Sciences Division.
17. Engineering Physics Division.
18. Metals and Ceramics Division.

8. ADVANCED SYSTEM STUDIES

ABSTRACT. The Magnetic Fusion Energy Engineering Act of 1980 calls for the operation of a Fusion Engineering Device (FED) in the 1990s. It is the intent of the Act that the FED, in combination with other test facilities, will establish the engineering feasibility of magnetic fusion.

Advanced system studies at ORNL include work supporting the design of the FED and the International Tokamak Reactor (INTOR) study and development of a Generic Environmental Impact Statement (GEIS) for fusion, as required by the National Environmental Policy Act of 1969 (NEPA).

During 1981, the Fusion Engineering Design Center (FEDC) developed a baseline design for the FED that provides a basis from which a full conceptual design effort can proceed. The Fusion Environmental Assessment Program made significant progress in developing a technical basis document for the GEIS. These efforts are described in detail.

8.1 FUSION ENGINEERING DESIGN CENTER

8.1.1 Introduction

The FEDC was established in 1978 by the Department of Energy (DOE) as a centralized laboratory/industry design team hosted by ORNL and responsible for developing the design of the fusion device to follow the Tokamak Fusion Test Reactor (TFTR). This year, the Design Center concentrated on two major activities: developing the concept and associated design for a FED and performing the engineering design in support of the U.S. INTOR activity. The FED design is briefly summarized here; the Design Center activities in support of INTOR are described in Ref. 1.

The FED baseline design developed in 1981,[2] although not optimized, represents a reasonable device with feasible concepts for all major systems and components. A comprehensive discussion of the FED design, the supporting analyses, and the options considered are found in Ref. 3.

In addition to developing a design for the major FED systems and subsystems, the year's efforts included performing the supporting plasma engineering design analysis, developing a projected device cost and associated construction schedule, and developing a description of facilities to house and support the device. Many of the design decisions have been based on numerous system and trade studies. Other considerations that have been instrumental in shaping the general features of the FED device include:

- availability of needed technologies,
- remote maintenance requirements,
- system reliability requirements,
- impact of machine test program on access and operation,
- need for flexibility to accommodate uncertainties in plasma performance and potential improvements in both physics and technology, and
- overall capital cost.

The development of the FED baseline design was an evolutionary process. Initially, the Technical Management Board (TMB) established a set of working parameters and design guidelines and specified that the FED should incorporate toroidal field (TF) coils designed to operate at a nominal maximum field of 8 T at the conductor but capable of limited operation at 10 T. The 10-T capability is viewed as a desirable perturbation to the basic device but does not drive the design; only about 10% of the total machine operation is at the 10-T level. The 10-T capability allows for limited operation with enhanced plasma performance and provides for additional engineering scaling tests, if needed.

8.1.2 Machine Configuration

Elevation and plan views of the FED baseline configuration are shown in Figs. 8.1 and 8.2, respectively. Figure 8.3 is a perspective view of the device. Table 8.1 lists key parameters of the baseline for both 8-T and 10-T operating modes.

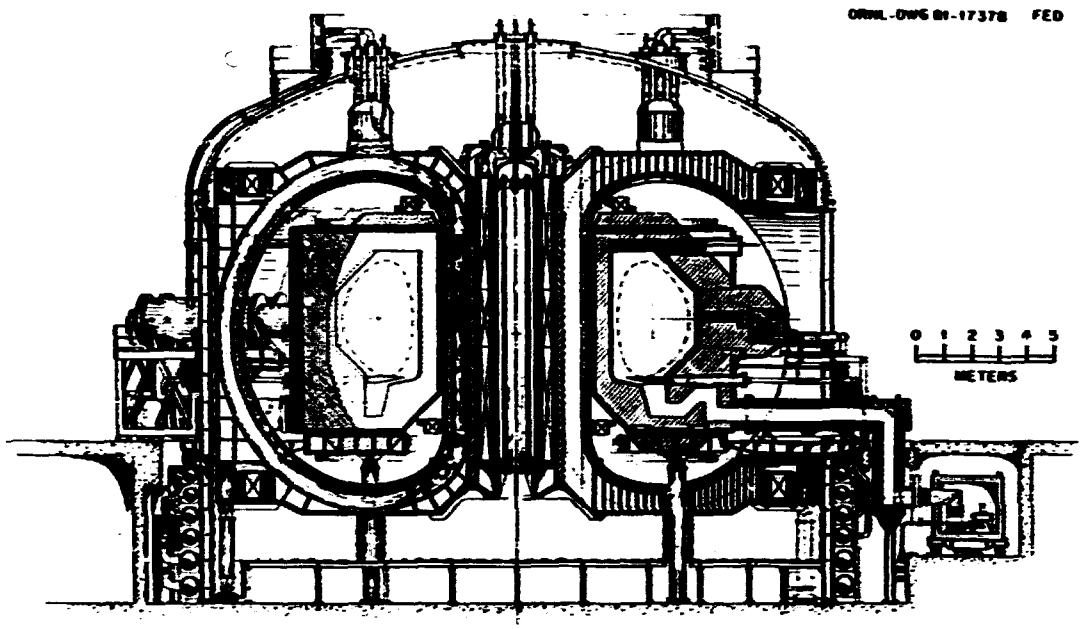

Fig. 8.1. FED baseline configuration, elevation view.

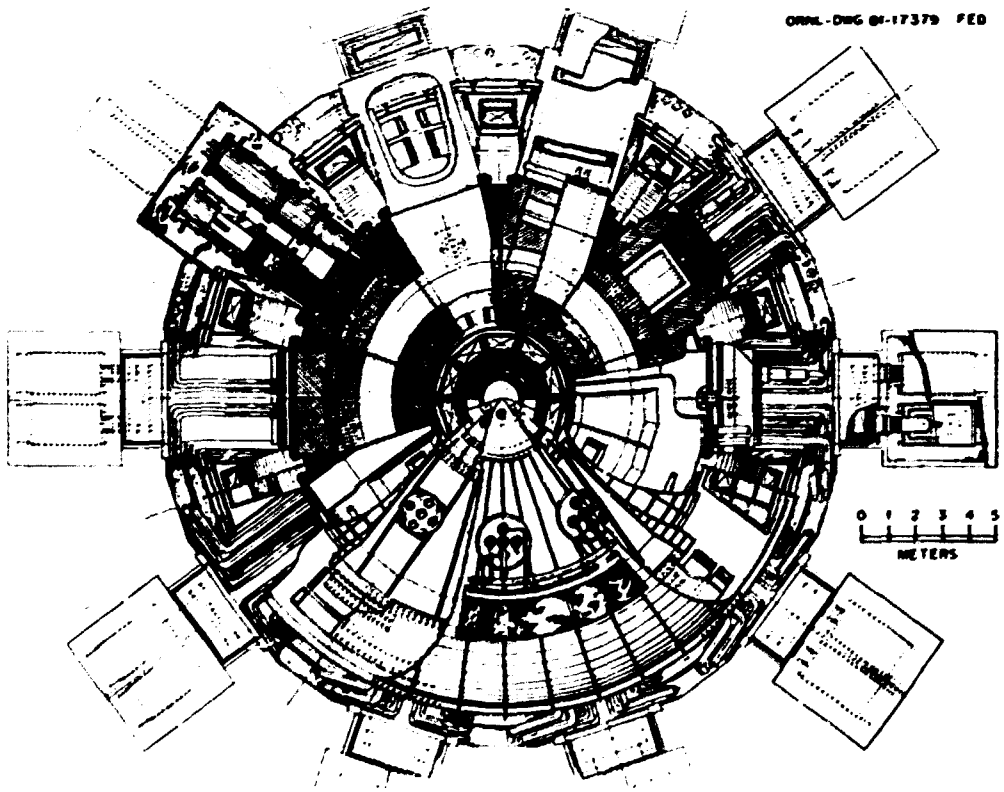

Fig. 8.2. FED baseline configuration, plan view.

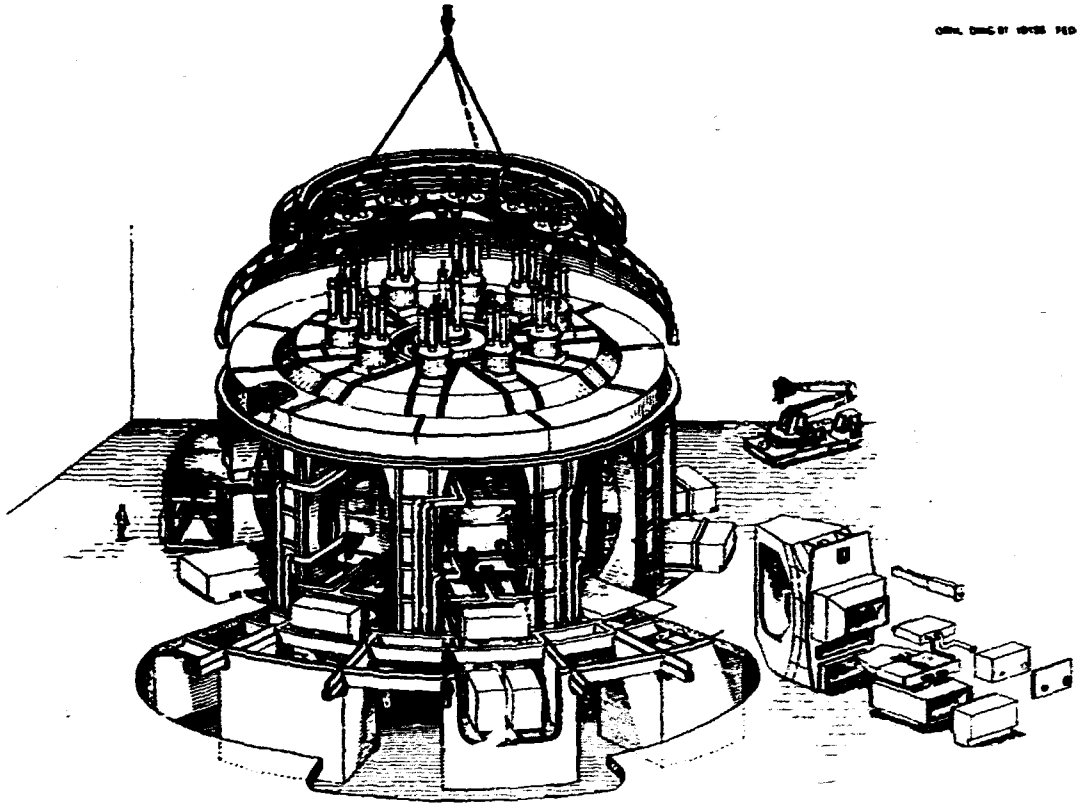

Fig. 8.3. FED baseline configuration, diametric view.

Maintenance was a significant consideration in developing the FED configuration. Other key elements are discussed below.

Modularity has been a design goal for all components expected to require replacement or frequent maintenance (e.g., the pumped limiter blade).

Good access has been a central design consideration of the overall configuration and has strongly influenced the design of the TF coils (size and number) and of the torus.

For all device components external to the shield, hands on access appears to be a practical necessity for many operations and was adopted as a design requirement. Hands-on maintenance is possible approximately one day after shutdown. Providing this capability has strongly influenced the design of the outboard shield.

Two component lifetime categories were established: long-lifetime components are expected to operate for the lifetime of the device without replacement (e.g., the TF coils), and short-lifetime components are expected to require relatively frequent replacement (e.g., the pumped limiter blade). This designation has been important in developing the FED maintenance needs, including maintenance equipment.

Access was the dominant consideration in the selection of a 10-coil arrangement for the TF coil system. These coils react against a central bucking cylinder and have a 7.4- by 10.9-m bore. Together they produce a 3.6-T field on axis when operating at 8 T and a 4.6-T field on axis when operating at 10 T. It is possible to insert or withdraw a torus sector solely by radial motion between the outer legs of the TF coils.

Table 8.1. Key parameters for the FED baseline

	8 T	Common value	10 T
Major radius		5.0 m	
Plasma radius		1.3 m	
Plasma elongation		1.6	
Fusion power	180 MW		450 MW
Neutron wall loading	0.4 MW/m^2		1.0 MW/m^2
Heating power			
Initial		50 MW	
Burn	36 MW		0
Amplification factor, Q	5		Ignited
Burn time	≥100 s		~50 s
Duty factor[a]	0.65		0.5
Average D-T density	0.8×10^{20} m^{-3}		1.2×10^{20} m^{-3}
Average total beta		5.2%	
Plasma current	5.4 MA		6.5 MA
TF coil clear bore, width × height		7.4 × 10.9 m	
Field on axis	3.6 T		4.6 T
Number of full field pulses	2.5×10^5		2.5×10^4
Availability[b]	10-20%		10-20%

[a]Defined as ratio of burn time to cycle time.

[b]Defined as ratio of operating time to operating time plus down time.

8.1.3 Magnetic Systems

The magnetic systems comprise the superconducting TF coils; the poloidal field (PF) coils, including the superconducting ohmic heating (OH) solenoid, the superconducting equilibrium field (EF) coils outside the TF coil bore, and the normal copper coils inside the TF coil bore; and the cryostat.

TF coils

A conductor capable of operating at ≤10 T is required for the FED baseline. Three candidate coil technology approaches can achieve the required 10-T field: pool-boiled superfluid-cooled NbTi at 1.8 K, forced-flow subcooled NbTi at 3 K, and a Nb_3Sn/NbTi combination cooled to 4.2 K. There is no clear technical basis for a preferred option at this time. To illustrate design considerations, the forced-flow subcooled NbTi (3 K) option was selected as the FED baseline.

An overall winding current density of 2200 A/cm^2 has been used in assessing 10-T operation at 3 K. The coils are pancake-wound with a total of 444 turns and use NbTi strands in a steel conduit cooled by supercritical forced-flow helium. The overturning moments are reacted by an intercoil support structure at the top and bottom of the TF coils. The dead weight of the TF coils is supported by a series of outboard pedestal supports that can also withstand a 1-g-seismic load.

PF coils

The PF coil system consists of one OH solenoid of superconducting NbTi, two normal copper EF coils located inside the TF bore toward the inboard side of the plasma, two superconducting (NbTi) EF coils located outside the TF bore on the outboard side of the plasma, and four control coils, which are relatively small trim coils of normal copper located inside the TF coil bore.

The design of the superconducting OH and EF coils is scaled from the Los Alamos National Laboratory (LANL) design for the 20-MJ Pulsed Coil Program. The design of the normal copper EF coils is dominated by the requirement for demountable mechanical joints to facilitate assembly and coil replacement. These coils are structurally supported from the torus spool structure.

Cryostat

A common vacuum cryostat contains all of the superconducting coils. The cryostat has separate enclosures for each of the outboard legs of the TF coils. This approach maintains the good access between the TF coils and requires no penetration of the cryostat boundary for torus access. It also separates the warm and cold components of the FED configuration.

8.1.4 Nuclear Systems

The nuclear systems include the torus (spool assembly, shield sectors, and support), the first wall (outboard panels and inboard armor), and the mechanical pumped limiter.

Torus

The assembled torus constitutes the plasma vacuum chamber. It is made up of ten sectors inserted into a spool structure. Each sector is inserted into the spool solely by radial motion (see Figs. 8.4 and 8.5). The spool structure provides high vacuum integrity and high electrical resistance. The shield sectors attenuate nuclear radiation, convert neutron kinetic energy into heat, provide for the removal of this heat, and support the first wall and limiter components. The spool is constructed of Inconel, selected because of its high electrical resistance, and the shield sectors are constructed of Nitronic 33, selected because it is highly corrosion-resistant, exhibits low levels of long-life radionuclides, and is commercially available. The shield is cooled with pressurized water and is 60 cm thick on the inboard side and 120 cm thick on the top, outboard, and bottom sides. It limits radiation damage at the TF coil insulation to $<10^9$ rad and allows hands-on maintenance by limiting the activation level outside the shield to <2.5 mrem/h about one day after shutdown.

First wall

The FED first wall system consists of actively cooled stainless steel panels on the outboard wall and passively cooled graphite armor tiles on the inboard and top walls. This design can accommodate the nominal startup and burn heat loads and the anticipated disruption energy without replacement for the design life of the device (10 years).

The outboard first wall panels are of type 316 stainless steel. There are six panels on each torus sector so that each panel is about 2 m on a side and 7 cm thick. The vertical facet also serves as a startup limiter.

The armor tiles are attached to the torus chamber with graphite bolts. Each tile is 5 cm thick and 15 cm on a side. About 6300 tiles are required in the device. The tiles are coated with titanium carbide to limit chemical erosion. Depending on the assumed plasma edge condition (which is highly uncertain at present), the predicted erosion of the armor tiles varies from ~0.3 cm/y to 7.0 cm/y. The resulting tile lifetime is between ~4 years and ~2 months.

Mechanical pumped limiter

The FED baseline has a mechanical pumped limiter for particle and impurity control. The limiter is located at the bottom of the vacuum chamber and is continuous in the toroidal direction. It establishes the plasma edge, pumps helium ash and hydrogen particles, and helps protect first wall components from large particle and energy fluxes. The limiter is divided into ten removable segments, one in each torus sector of the device, and each limiter segment can be removed without moving the shield sector. The segments consist of a reusable core structure, consisting of an

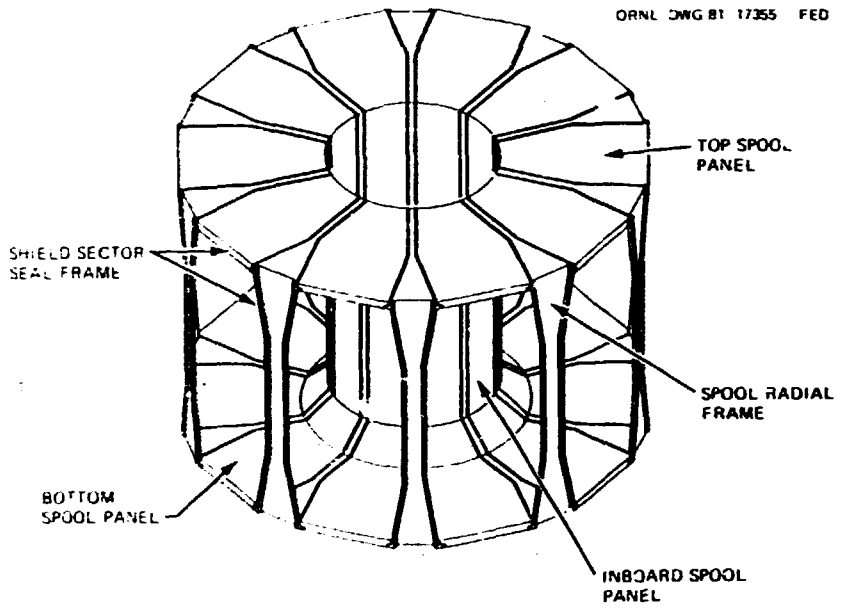

Fig. 8.4. Torus support spool.

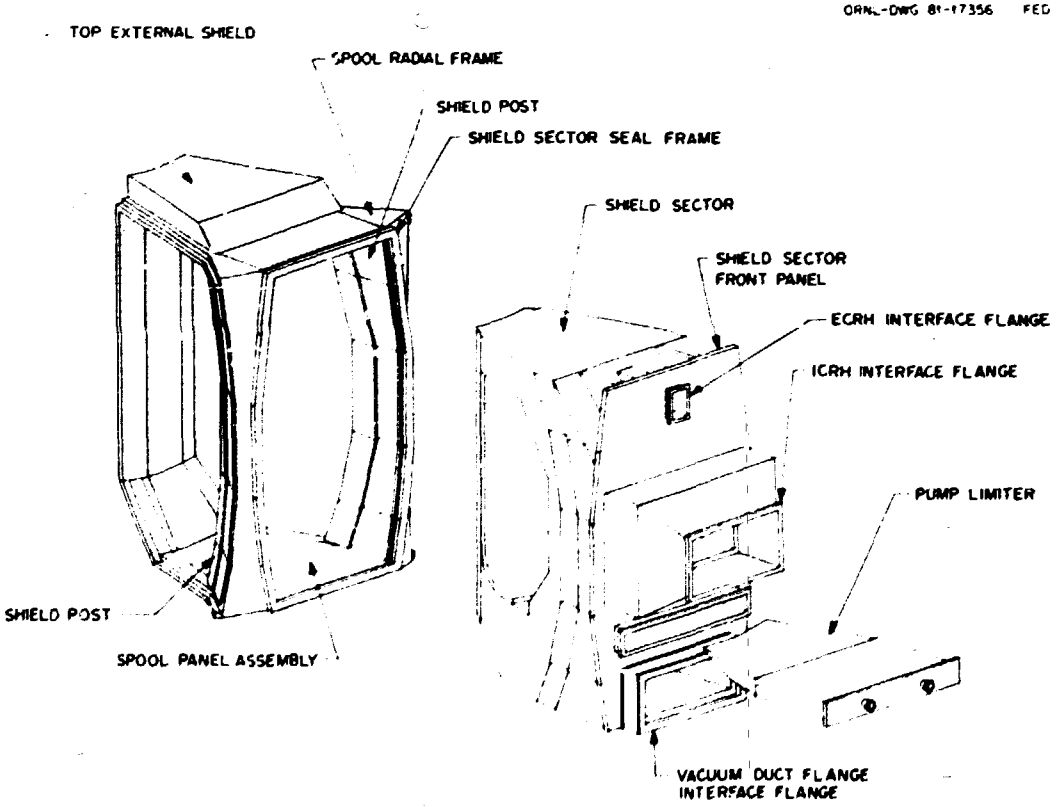

Fig. 8.5. Torus sector assembly.

internally stiffened Nitronic 33 box, and a replaceable protective surface, consisting of surface armor tiles attached to substrate copper. The segments are water-cooled and are electrically connected with metal bellows and copper bus plates along one edge of each segment. Analysis indicates that the limiter will provide the desired particle pumping (at least 5% of the total ion flux leaving the plasma). The alternative to the pumped limiter is a single null poloidal divertor for particle and impurity control.

8.1.5 Plasma Heating Systems

Systems for plasma initiation and startup and for plasma bulk heating make up the FED plasma heating systems. A radio frequency (rf) system is used for initial heating of the plasma. This consists of ∿1 MW of electron cyclotron resonance heating (ECRH) [90 GHz (8 T) and 113 GHz (10 T)] launched through waveguides on the high field side of the plasma using the extraordinary mode of wave propagation. The bulk heating is based on ion cyclotron resonance heating (ICRH). Second harmonic deuterium species used for majority heating is the baseline approach for bulk heating and heating during burn (8 T). The equencies required are ∿54 MHz (8 T) and ∿68 MHz (10 T). A total of 50 MW is provided for the bulk heating phase. The alternative to ICRH for bulk heating is 150-keV, positive-ion-based neutral beams.

8.1.6 Reactor Support Systems

Reactor support systems are required for tritium; fueling; diagnostics, information, and control; power handling and conversion; electrical energy storage; vacuum pumping; and cryogenics. Remote maintenance equipment must also be provided to support reactor operations.

Tritium systems

The tritium systems must provide fuel for the device, safely handle the tritium inventory, and serve as an integrated test of tritium handling technology. The system comprises primary systems to handle the primary fuel cycle requirements (fuel cleanup, isotope separation, tritium analysis) and secondary systems to provide for safe operation of all systems involving deuterium and tritium (waste treatment, glovebox detritiation, tritiated water recovery). The tritium system will have a tritium inventory of ∿ 825 kg for continuous 8-T operation or 1.470 kg for continuous 10-T operation. In addition, a building detritiation system provides for tritium handling and containment in the reactor building, the hot cell facility, and the tritium processing building. A data acquisition system is employed to monitor all of these systems.

Fueling systems

The FED fueling systems consist of gas puffers and pellet injectors. Two independent gas puffing systems (one for redundancy) will provide fuel gas (deuterium, tritium, or a mixed species) to each of ten inlet ports. Gas puffing is used to backfill the torus before startup and continues until a 1-keV plasma is established. Frozen deuterium and tritium pellets are then injected to control the plasma density. Two pellet injectors are located on one torus sector. Each can inject up to twenty 4-mm pellets per second at a velocity of 2 km/s. Either pneumatic or centrifugal pellet injectors can be used.

Diagnostics, information, and control systems

The diagnostics system must provide instrumentation for developing physics understanding, for verification and optimization of machine performance, for control, for safe and reliable operation, and for component and reactor-relevant testing. The diagnostics will dominate two torus sectors, and additional diagnostics will be present on all torus sectors. Many of the instruments will have to be replaced once deuterium-tritium (D-T) operations commence because of the radiation environment.

The information and control system for FED consists of the hardware and software to perform

all programmable processes for the entire FED complex. These include control, monitoring, data acquisition and processing, analyses, display, and archiving. The system includes a control center, local and remote controls, and timing, communications, and safety systems. The FED system is an extrapolation of systems under development in similarly complex facilities.

Power handling and conversion systems

The electrical power handling and conversion systems include the ac power system and the TF and PF coil power conversion systems. The ac power system provides both pulsed and steady-state power for the FED loads. The required maximum ac power system capacity is 350 MVA for pulsed power loads. The TF coil power conversion system can charge the TF coils (in about 4 h with two 50-V power supplies) and discharge them through dump resistors (in about 2 h). During a quench, the stored energy (~23 GJ for 10-T operation) is dissipated through external dump resistors with a time constant of ~40 s; the maximum TF coil temperature is limited to <200 K. The PF coil power convertors are used to take ac power from the motor-generator (MG) flywheel units (or utility line) and convert it to the pulsed dc power needed for the PF coils during each operating cycle. The system also provides protection for the PF coil in case a quench occurs.

Electrical energy storage system

Energy storage is required for the PF coils and for the rf system; a total of ~6 GJ of energy is required during startup with a peak MVA load of ~1850 MVA. These requirements are met in FED with two MG flywheel units. Each is a wound-rotor induction motor with 15,000 HP, providing variable frequency, 13.8-kV pulsed power. These units are safe, reliable, economical, and easy to control. Voltage can be regulated to within ±1% with conventional controls.

Vacuum pumping system

Twenty large turbomolecular pumps, one at each end of the ten vacuum ducts, are used as the vacuum pumping system for FED. They are backed by 20 scroll pumps. This system is used to pump down the torus initially and between burns and to remove the gas load from the pumped limiter during the burn. The initial base pressure is 10^{-7} torr, and the pumpdown pressure between burns is 10^{-5} torr, with a 30-s evacuation time between burns. The high vacuum turbomolecular pumps have a pump speed of 5.0 $m^3 \cdot s^{-1}$. The scroll pumps are used to back the turbomolecular pumps and for rough pumping of the plasma chamber. These are sealed pumps that have no heavy lubricant in contact with the pumped gas. A first-stage pump backs each turbomolecular pump and pumps at 33 liter/s, exhausting at a pressure of 25 torr. The exhaust of all 20 first-stage pumps is combined and fed to a single small second-stage pump that operates at ~2 liter/s and exhausts at about atmospheric pressure. This system satisfies all of the FED vacuum pumping requirements.

Cryogenic system

The cryogenic system for FED provides an entropy generation rate several times larger than that of any existing or planned cryogenic refrigeration system in the world. The system must perform 63 MW of work on helium at room temperature and must produce and transfer cryogens at a sufficient rate to sustain normal operations of the superconducting magnet systems of FED, the only cryogenic systems in the baseline design. The system consists of forced-flow, closed coolant loops for the TF coils and coil cases, with a separate loop for the PF coils.

Remote maintenance equipment

An extensive list of remote maintenance equipment required for FED has been developed.

It includes both general-purpose equipment, such as manipulators and cranes, and special-purpose equipment for specific applications.

8.1.7 Facilities

A complete facility design for FED has been developed, including the reactor building, the hot cell facilities, the necessary additional support buildings, and a site layout.

The reactor building is a rectangular building, approximately 60 × 50 × 40 m, with a small (3- to 5-psi) overpressure capability. The walls and roof are 2 m thick to provide for adequate shielding. The building has been designed to mitigate and reduce the consequences of postulated accident conditions. The hot cell facilities support the maintenance and operation of the reactor building and those other facilities involving radioactive operations. Controlled ventilation construction is used for the hot cell facilities, which are ~80 × 50 × 30 m. The walls and roof are made of concrete up to 2 m thick. The additional facilities required for the total FED complex have been identified and a site layout developed.

8.1.8 Cost and Construction Schedule Projections

Cost and construction schedules have been projected for the FED capital project to provide an early appreciation of the project scope. The cost projections were obtained using system and component unit costs and cost algorithms. Numerous other organizations knowledgeable in fusion were consulted and performed independent partial or complete assessments of FED costs, which were then compared with the FEDC cost projections (results were within ±20% on total cost). Table 8.2 gives the cost estimate and assumptions.

An estimate of the FED construction schedule was made and is summarized in Fig. 8.6. The schedule is success-oriented and assumes many parallel operations; availability of labor, equipment, and funding when needed; and delivery of device components from fabricators on time. The entire schedule, from the beginning of preliminary design through the end of preoperational testing, is estimated to take seven years and eight months (92 months).

Table 8.2. FED cost projection summary (in millions of dollars)

Direct costs	
Magnet system	312
Torus	162
Cooling systems	38
Tritium and fuel handling	54
RF systems	89
Electrical systems	99
Vacuum pumping system	24
Instrumentation and control	67
Remote maintenance equipment	60
Facilities	139
Total direct cost	1044
Indirect costs	
Engineering and management (45%)	470
Installation (15%)	157
Total indirect cost	627
Contingency (30%)	501
Total cost	2172

Assumptions

All costs are based on constant 1981 dollars; no escalation is included.

Direct capital costs include all costs associated with component procurement and fabrication including shipping to the construction site.

The indirect capital costs include engineering design and project management as well as all equipment installation and assembly at the construction site.

This estimate is only for the FED construction project and does not include any funds for operations, maintenance, spare parts, fuel, associated research and development, transmission lines, or decomissioning.

8.1.9 Concluding Remarks

This baseline design represents a workable tokamak design concept that satisfies the FED objectives. Physics analyses indicate that the device can achieve the required plasma

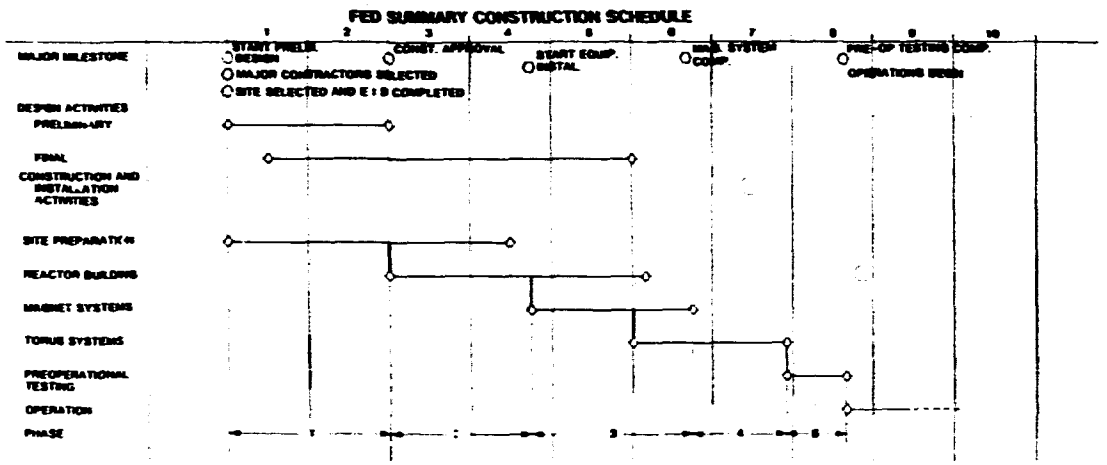

Fig. 8.6. FED summary construction schedule.

performance goals under a range of reasonable assumptions and eventualities." A feasible approach has been developed for all of the major device systems and components. A machine configuration has been developed that incorporates the important needs of maintenance and access. Reactor support systems, facilities, and a site layout have also been developed. This baseline design provides the basis upon which a full conceptual design effort can be initiated.

8.2 FUSION ENVIRONMENTAL ASSESSMENT PROGRAM

The Fusion Environmental Assessment Program was established in 1979 to provide technical assistance to the DOE Office of Fusion Energy in coordination and preparation of NEPA compliance documents. The program is administratively part of the Environmental Impact Section of the ORNL Energy Division, but it draws on the technical backgrounds of staff from the Chemical Technology, Engineering Physics, Environmental Sciences, Fusion Energy, Health and Safety Research, Information, and Metals and Ceramics divisions as well.

The current focus of the program is the development of a GEIS, which is required by NEPA regulations as the national magnetic fusion energy program advances from basic and applied research to engineering development. In 1981, the environmental assessment work centered on the development of a technical basis document for the GEIS, to demonstrate that the technology of fusion is advanced enough that a meaningful GEIS can be prepared. The following issues were addressed: radioactive inventories, plant effluents, occupational health and safety, reactor safety, radioactive waste management, and availability of basic constituent materials. Based on favorable reviews of the resulting >1000-page draft report, DOE made a decision to proceed with the development of a GEIS. Efforts were initiated to upgrade the draft report for use as a major reference for the GEIS.

REFERENCES

1. W. M. Stacey, M. A. Abdou, J. A. Schmidt, and T. E. Shannon, *The U.S. Contribution to the International Tokamak Reactor Phase I Workshop – Conceptual Design*, USA INTOR/81-1, Atlanta, Georgia (June 1981).
2. *The Fusion Engineering Device, Vol. II, Design Description*, DOE/TIC-11600, Technical Information Center, Oak Ridge, Tennessee (October 1981).
3. Fusion Engineering Design Center staff (C. A. Flanagan, D. Steiner, and G. E. Smith, eds.), *Fusion Engineering Device Design Description*, ORNL/TM-7948, Oak Ridge, Tennessee (1981).
4. *The Fusion Engineering Device, Vol. I, Mission and Program Summary*, DOE/TIC-11600, Technical Information Center, Oak Ridge, Tennessee (October 1981).

9. RADIATION MATERIALS TESTING

E. J. Allen[1]
C. J. Altstetter[2]
J. Bentley[3]
E. E. Bloom[3]
A. D. Brailsford[4]
O. K. Braski[3]
R. W. Carpenter[5]
R. L. Childs[6]
O. K. Chopra[7]
F. W. Clinard, Jr.[8]
W. A. Coghlan[9]
R. R. Coltman, Jr.[3]
J. H. DeVan[3]
D. L. Douglass[10]
H. Farrar IV[11]
K. Farrell[3]
T. A. Gabriel[12]
R. E. Gold[13]
M. L. Grossbeck[3]
W. R. Hayns[14]
A. Hishinuma[15]
J. J. Holmes[16]
J. A. Horak[17]
J. R. Horton[18]
L. L. Horton[3]
H. R. Inle[19]
W. A. Jesser[20]
Y. Katano[21]
J. R. Keiser[3]
H. T. Kerr[3]
K. Kitajima[22]
C. E. Klabunde[3]
R. L. Klueh[3]
C. F. Knights[23]
C. C. Koch[5]
H. R. Konvicka[24]
E. Kuramoto[25]
E. H. Lee[3]
M. B. Lewis[3]
R. A. Lillie[26]
C. T. Liu[3]
K. C. Liu[3]
L. K. Mansur[3]
Y. A. Marcmi[27]
P. J. Mazia[28]
S. Nasu[29]
J. O. Navratil[30]
P. C. Nordine[31]
G. R. Odette[32]
S. W. Ohr[3]
N. H. Packan[3]
P. F. Tortorelli[3]
K. Tsukuda[33]
H. D. Upton[3]
J. M. Vitek[3]
D. P. Whittle[34]
S. W. Wiffen[3]
J. M. Williams[3]
W. G. Wolfer[35]
J. W. Woods[3]
R. W. Yonco[7]
N. Yoshida[36]

1. Engineering Technology Division.
2. University of Illinois, Urbana, Illinois.
3. Metals and Ceramics Division.
4. Ford Motor Company, Dearborn, Michigan.
5. Center for Solid State Studies, Arizona State University, Tempe, Arizona.
6. UCC-ND Computer Sciences.
7. Argonne National Laboratory, Argonne, Illinois.
8. University of California, Los Alamos National Laboratory, Los Alamos, New Mexico.
9. Solid State Division.
10. University of California, Los Angeles, California.
11. Rockwell International, Canoga Park, California.
12. Engineering Physics Division.
13. Westinghouse Electric Corporation, Madison, Pennsylvania (formerly at Pittsburgh).
14. Safety and Reliability Directorate, Warrington, United Kingdom (formerly on assignment to Metals and Ceramics Division from Atomic Energy Research Establishment, Harwell, United Kingdom).
15. Japan Atomic Energy Research Institute, Tokai, Japan (former guest of Metals and Ceramics Division on assignment from JAERI).
16. Hanford Engineering Development Laboratory, Richland, Washington.
17. Kernforschungsanlage Jülich, Jülich, Federal Republic of Germany.
18. University of Virginia, Charlottesville, Virginia.
19. Japan Atomic Energy Research Institute, Tokai, Japan.
20. Research Institute for Applied Mechanics, Kyushu University, Kasuga, Fukuoka 812, Japan.
21. Atomic Energy Research Establishment, Harwell, United Kingdom.
22. Osterreichische Studiengesellschaft für Atomenergie, Vienna, Austria.
23. Tokai Research Establishment, Tokai, Japan.
24. International Atomic Energy Agency, Vienna, Austria.
25. Yale University, New Haven, Connecticut.
26. University of California, Santa Barbara, California.
27. University of Pittsburgh, Pittsburgh, Pennsylvania.
28. Ohio State University, Columbus, Ohio.
29. Now at IBM, Yorktown Heights, New York (formerly with Metals and Ceramics Division).
30. U.S. Department of Energy, Washington, D.C.
31. General Atomic Company, San Diego, California.
32. Centre d'Etudes Nucléaires de Saclay, Gif-sur-Yvette, France.
33. Now at Rockwell International, Golden, Colorado (formerly with Metals and Ceramics Division).
34. Westinghouse Research and Development Center, Pittsburgh, Pennsylvania.
35. INTEC, Inc., San Diego, California (formerly with General Atomic Company).
36. University of California, Lawrence Berkeley Laboratory, Berkeley, California.
37. Now at University of Wisconsin, Madison, Wisconsin (formerly with Metals and Ceramics Division).

9. RADIATION MATERIALS TESTING

ABSTRACT. The objective of the Fusion Materials Program at ORNL is to develop materials for service in high fluence regions of near-term reactors, such as the Fusion Engineering Device (FED), and long-term commercial fusion reactors. The 14-MeV neutrons produced in these reactors result in unique irradiation damage because of the high defect generation rate and the simultaneous production of high concentrations of helium and hydrogen. Although no fusion test reactor exists, the effects of combined displacement damage plus helium can be studied in mixed-spectrum fission reactors for alloys containing nickel (e.g., the austenitic stainless steels). Extensive test programs are under way on the prime candidate alloy (PCA), austenitic stainless steel, and ferritic steels for use in FED. Results on swelling and on changes in mechanical properties are carefully evaluated and then made available to the design community via the *Materials Handbook for Fusion Energy Systems*. Long-range-ordered (LRO) alloys and vanadium alloys are being investigated for the longer term.

Since the mechanical properties of alloys are related to their microstructure, studies are continuing on the evolution of microstructure during irradiation. Through an understanding of the basic phenomena occurring during irradiation and of the relationships between microstructure and properties, alloys can be tailored to minimize radiation-induced swelling and to improve mechanical properties in fusion reactor service.

A small but important study involves the irradiation of superconducting magnet materials at 4 K. The behavior of copper during irradiation and periodic anneals has been measured and compared with the lifetime of candidate insulator materials.

9.1 ALLOY DEVELOPMENT FOR IRRADIATION PERFORMANCE

M. L. Grossbeck, E. E. Bloom

The following abstracts and summaries describe alloy development activities in the area of irradiation performance during 1981.

9.1.1 *Abstract of* Radiation Effects in Materials for Fusion Reactors[1]

J. L. Scott, M. L. Grossbeck, P. J. Maziasz

The 14-MeV neutrons produced in a fusion reactor result in different irradiation damage than the equivalent fluence in a fast breeder reactor, not only because of the higher defect generation rate, but also because of the production of significant concentrations of helium and hydrogen. Although no fusion test reactor exists, the effects of combined displacement damage plus helium can be studied in mixed-spectrum fission reactors for alloys containing nickel (e.g., austenitic stainless steels). The presence of helium appears to modify vacancy and interstitial recombination such that microstructural development in alloys differs between the fusion and fission reactor environments.

Since mechanical properties of alloys are related to the microstructure, the simultaneous production of helium and displacement damage has an impact on key design properties such as tensile, fatigue, creep, and crack growth. Through an understanding of the basic phenomena occurring during irradiation and the relationships between microstructure and properties, alloys can be tailored to minimize radiation-induced swelling and improve mechanical properties in fusion reactor service.

9.1.2 *Summary of* Progress in the Development of the Blanket Structural Material for Fusion Reactors[2]

J. L. Scott, E. E. Bloom, R. E. Gold, M. L. Grossbeck, J. J. Holmes, P. J. Maziasz, T. C. Reuther, Jr., C. M. Rosenmasser, F. W. Wiffen

The Alloy Development for Irradiation Performance (ADIP) Program has become more focused since the last Fusion Reactor Technology Conference two years ago. Since austenitic stainless steels and ferritic steels are candidate structural materials for the near-term Engineering Test Facility (ETF) and International Tokamak Reactor (INTOR) and

austenitic stainless steel is also the preferred structural material for the steady-state commercial fusion reactor STARFIRE, a vigorous experimental program is under way to identify the best alloy from each of these alloy classes and to provide the engineering database in a timely manner. In addition, the comprehensive program that includes high strength Fe-Ni-Cr alloys, reactive and refractory metals, and advanced concepts continues in an orderly fashion.

9.1.3 Summary of Fusion Reactor Materials: M325/01028[3]

J. L. Scott

The problems involved with materials used in fusion reactors rival those of plasma physics with regard to difficulty. The structural first wall experiences high neutron fluences, high temperatures, and large cyclic thermal stresses. The 2.2-pJ neutrons from fusion reactors produce high concentrations of helium and hydrogen as well as conventional displacement damage, so a loss of ductility as well as swelling occurs in structural materials. Refractory metals, iron- and nickel-base alloys, aluminum alloys, and SiC have been proposed as structural materials. Since superconducting magnets are required in magnetic fusion devices, the range of materials problems integral with this technology must be solved. Specialty materials are required for limiters that intercept the plasma before it strikes the walls, electrical insulation, tritium breeding, neutron moderators, and shielding.

9.1.4 Abstract of Materials Technology for Fusion: Current Status and Future Requirements[4]

R. W. Conn, E. E. Bloom, R. W. Conrad, Jr., D. L. Smith, R. D. Stambaugh, W. G. Wolfer

An overview is presented of the general status of materials research and development activities related to the needs of controlled thermonuclear fusion reactors. Emphasis is placed on materials research and applications pertinent to magnetic confinement reactor concepts vis-à-vis inertial confinement reactor requirements; this reflects the greater maturity of the magnetic confinement technology programs. The research efforts associated with materials development for first wall applications are given special attention; in addition, the research and general status of programs aimed at non-first-wall or nonstructural fusion reactor materials requirements are also reviewed.

9.1.5 Abstract of Swelling, Creep, and Mechanical Properties of First Wall and Structural Alloys[5]

J. L. Straalsund, E. E. Bloom

One of the most interesting materials science challenges of this decade is the development of the magnetic fusion first wall structural materials required to achieve the objectives of the Magnetic Fusion Energy Engineering Act of 1980. The design features of demonstration and early commercial power plants are not yet sufficiently fixed to provide a precise description of the environment that these materials must withstand. It is probable, however, that economic power production will require first wall operation at temperatures ranging from 300 to 550°C and a service lifetime of 10 to 20 megawatt-y/m^2, amounting to neutron damage levels of 100 to 200 atomic displacements per atom (dpa). In addition, the high energy neutrons will generate significant amounts of transmutation products, such as 2000 to 4000 ppm of helium and more than twice as much hydrogen in a long-life stainless steel wall.

Materials development activities in support of fission reactors cover much of this application range, and it is possible from this experience to infer which materials properties are important to first wall life and performance. Depending on reactor design, postirradiation ductility and strength, thermal creep strength

and ductility as perturbed by the neutron flux, irradiation-induced creep and swelling, or fracture toughness behavior could be life-limiting. Reactor concepts which employ cyclic power generation introduce fatigue crack initiation and growth as additional potentially life-limiting properties.

The evolving nature of the fusion plant design concepts dictates that the alloy development program be broadly based, allowing for a wide range of attainable properties and trade-offs. This is achieved by studying a variety of material classes. For example, ferritic materials, as a class, have relatively low thermal expansion coefficients and are therefore inherently more resistant to fatigue crack growth in response to cycling thermal gradients. The ferritic alloys, however, generally lack the high temperature strength characteristic of nickel-base or refractory alloys, which in turn lack the ductility of the austenitic stainless steels. The relative merit of each alloy class will depend on the design criteria of the given reactor. The following classes of alloys are thus included in the fusion alloy development program:

- austenitic stainless steels,
- ferritic stainless steels,
- reactive/refractory alloys,
- nickel-base alloys, and
- innovative materials.

Examples of innovative materials are LRO alloys and rapidly solidified alloys.

The fusion neutron energy spectrum produces a variety of transmutation products which are usually difficult and sometimes impossible to reproduce in fission reactors. Nevertheless, much has been learned from fission reactor experiments conducted in support of fission reactor as well as fusion reactor development programs. This overview paper will summarize the general properties and expected responses to irradiation of each of the general classes of alloys and assess their relative strengths and weaknesses. This assessment will be used to identify the key issues for each alloy class.

9.1.6 *Abstract of* High Temperature Fatigue Life of Type 316 Stainless Steel Containing Irradiation-Induced Helium[6]

M. L. Grossbeck, K. C. Liu

Since a tokamak fusion reactor is most likely to operate in a cyclic mode, fatigue arising from thermal stresses in the first wall and blanket is of concern. As well as the effects of cyclic stresses, the effects of irradiation must be considered. In addition to atom displacements, the 14-MeV neutrons arising from deuterium-tritium (D-T) fusion result in (n,α) reactions in the elements used in most structural alloys. The resulting helium is highly insoluble in metals and is known to reduce tensile ductility through migration to grain boundaries where it causes intergranular failure. The extent to which neutron irradiation and simultaneous helium formation influence mechanical properties must be known prior to design of a fusion reactor.

Austenitic stainless steels, and in particular 20% cold-worked type 316 stainless steel (20% CW 316), are candidate materials for fusion reactor first wall and blanket structural applications. Therefore, 20% CW 316 was selected as the alloy to scope the extent of the problem of degradation of fatigue properties in a radiation environment forming helium.

In order to achieve simultaneous displacement damage and helium production, a mixed-spectrum fission reactor, the High Flux Isotope Reactor (HFIR), was used. This reactor has an intense flux of fast neutrons, $\phi > 10^{19}$ n/m^2·s (E > 0.1 MeV) as well as a nearly equal thermal flux. The fast neutrons produce displacement damage not fundamentally different from that produced by 14-MeV neutrons. The thermal neutrons produce helium through the following reactions:

$$^{58}Ni + n_{th} \rightarrow {}^{59}Ni ,$$

$$^{59}Ni + n_{th} \rightarrow {}^{56}Fe + {}^{4}He .$$

A miniature hourglass-shaped fatigue specimen was designed specifically for this series of

experiments. Specimens were irradiated at 550°C in a manner similar to that used in a study conducted at 430°C. The elevated temperature was achieved by insulating the specimens with a helium gas gap to restrict outward heat conduction. Passive temperature monitors were included for postirradiation analysis. Specimens were irradiated to a fast fluence of 0.7-1.9 × 10^{26} n/m^2 (E > 0.1 MeV), resulting in 6-15 dpa and 200-900 appm He.

Following irradiation, the specimens were tested on a servohydraulic fatigue testing system equipped with a high vacuum chamber and installed in a radiation-shielded hot cell. Testing was conducted at the irradiation temperature, 550°C, at pressures below 10^{-4} Pa. A fully reversed ramp function was employed, using a strain rate of 4 × 10^{-3} s^{-1} for all low cycle testing. High cycle testing was conducted at a strain rate higher by a factor of 10 in load control after stabilized elastic cycling was established.

Preliminary results have shown little effect of neutron irradiation and helium at 550°C for damage levels up to 9 dpa and helium contents of 450 appm. This compares with a factor of 3-10 reduction in fatigue life for similar specimens irradiated and tested at 430°C. However, there appears to be a change in the endurance limit, which requires further study.

The absence of an effect of irradiation is likely to reflect the fracture mechanism rather than the bulk properties of the material. At the fluence investigated in the preliminary tests, the strength is somewhat lower after irradiation at 550°C, but the ductility is not markedly different. At 430°C neither strength nor tensile ductility is markedly different upon irradiation to 9 dpa. However, fatigue life is significantly lower at 430°C. Preliminary investigations seem to indicate a shear failure in the fatigue tests at 550°C. This is to be compared to a cleavage-like fracture at 430°C. Further investigation will be conducted to elucidate the fracture mechanisms in 20% CW 316 in fatigue failure, which appear to be the critical factors in fatigue life of irradiated material.

9.1.7 *Abstract of* Tensile Properties of a Titanium-Modified Type 316 Stainless Steel Irradiated in a Mixed-Spectrum Fission Reactor[7]

M. L. Grossbeck, P. J. Maziasz

Austenitic stainless steels have demonstrated radiation and corrosion resistance sufficient for service in nuclear reactors. The similarity of the fusion reactor to fission reactors is in itself reason for consideration of these materials for fusion reactor first wall and blanket structures. The most important feature making fusion reactor service unique is the formation of helium through (n,α) reactions in most common structural metals produced by the 14-MeV neutrons resulting from D-T fusion. Previous work has shown that small additions of titanium to stainless steels produce titanium carbide, which serves as an effective sink for helium and results in a stable and innocuous distribution of helium in the lattice. Since preliminary work has shown that the titanium-rich MC can retard migration of helium to grain boundaries, titanium-modified stainless steels are expected to demonstrate superior mechanical properties at high temperatures. Titanium addition is therefore an important technique for developing alloys for high temperature fusion reactor service.

In order to evaluate these alloys, they must be irradiated under conditions which form helium in the alloy simultaneously with atom displacement damage. Irradiation is conducted in a mixed-spectrum reactor, the HFIR. Helium is produced by thermal neutrons through a two-step absorption reaction beginning with ^{58}Ni. Miniature specimens of AISI type 316 stainless steel with 0.23% Ti (316 + Ti) and standard AISI type 316 stainless steel (316) in both annealed and 20% CW conditions were irradiated in the HFIR at temperatures in the approximate range of 55-600°C with specimens at elevated temperatures in a helium atmosphere. The specimens were irradiated in a reactor position providing a peak thermal flux of 2.5 × 10^{19} n/m^2·s and a peak fast flux of 1.3 × 10^{19}

n/m^2-s (E > 0.1 MeV). Fast fluences of 0.63-2.1 x 10^{26} n/m^2 were attained, resulting in 5-17 dpa and 200-1000 appm He.

Specimens had a gage section of 2.03 mm in diameter and were 18.3 mm long. Tensile testing was conducted in ar air atmosphere in an Instron machine at a strain rate of 4.6 x 10^{-5} s^{-1}. Test temperatures close to the calculated irradiation temperatures were selected with emphasis on 350, 450, and 575°C. After tensile testing, reduction of area (RA) measurements were made using low magnification fractography in a scanning electron microscope.

The results of the tensile tests are to be compared with those previously reported on AISI type 316 stainless steel. In the annealed condition, (316 + Ti) has nearly the same yield strength as 316 but has higher ductility at 450 and 575°C. For the 20%-CW condition, two general observations may be made. The first is that (316 + Ti) is stronger than 316 and is less ductile (as measured by total tensile elongation) at 450 and 575°C. At 350°C, 316 is more ductile until a fluence of about 1.2 x 10^{26} n/m^2 (E > 0.1 MeV), beyond which (316 + Ti) becomes more ductile. At 575°C there is indication of a crossover in total elongation beyond 2.1 x 10^{26} n/m^2 (E > 0.1 MeV), the highest fluence examined. The second general observation is that (316 + Ti) is affected little by irradiation within the fluence range investigated. This is most evident in yield strength at 350°C, where the 0.2% yield strength is nearly constant at 800 MPa, and in total elongation (ϵ_T) at 450°C, where ϵ_T is nearly constant at 7.5%.

The RA measurement of irradiated 20% CW (316 + Ti) exhibits values from 68 to 55% as fluence increases from 0 to 2 x 10^{26} n/m^2 at 350°C. At 450°C the decrease is more rapid, with RA running from 65 to 40% over the same range of fluence. At 575°C RA decreases from 65 to 12% as fluence increases from 0 to 1.2 x 10^{26} n/m^2, beyond which RA remains constant to 2 x 10^{26} n/m^2, the limit of investigation. In all regions except the apparent region of saturation at 575°C, the specimens failed by ductile dimple rupture. In the plateau region at 575°C, the fracture was primarily intergranular with small regions of plastic deformation providing the 12% RA. This behavior contrasts with that of 316 at 450°C, where 316 fails by an intragranular cleavage-like mechanism in which the crack appears to follow preexisting slip bands which result from the preirradiation cold work and which are heavily decorated with η (M_6C) phase precipitation. Although the tensile elongation of 316 is greater than that of (316 + Ti), the RA of 316 is lower than that of (316 + Ti). This result, combined with the change in fracture mechanism, is believed to be an early indication of a significant reduction in ductility of 316 at higher fluence levels.

Examination of the temperature dependence of yield strength and correlation with microstructure is of interest. Both 316 and (316 + Ti) have 0.2% yield strengths above 900 MPa from 35 to 300°C. In this range, hardening is achieved by the complex interactions of dislocation loops and networks and the distribution of helium. In the range of 300-600°C the small dislocation loops are replaced by a less localized dislocation structure, and precipitation of solid solution strengthening elements occurs with a resulting decline in strength. The yield strength of (316 + Ti) decreases significantly more slowly than that of 316 in this temperature range. Beyond approximately 450°C, titanium-rich MC is precipitating in a very fine dispersion, causing effective dislocation pinning in this alloy, and therefore is responsible for the lower rate of strength loss. The fracture mode in 20% CW (316 + Ti) remains ductile rupture over the temperature range of 35-450°C following irradiation. Intergranular fracture is observed at 575°C, which is consistent with the emergence of grain boundary cavitation.

The resistance of titanium-modified austenitic stainless steels to high temperature irradiation and helium has led to the selection of this class of alloys as a prime candidate material in the ADIP Program. These alloys will be

considered for use as first wall and blanket materials for machines beyond the FED.

9.1.5 [illegible] of The Influence of Neutron Irradiation at 55°C on the Properties of Austenitic Stainless Steels[6]

E. H. Lippincott, T. C. Reuthe

Types 316 and 316 + 0.23% Ti stainless steels and 16-8-2 weldment were irradiated in HFIR at 55°C to fluences up to 1.35×10^{26} n/m^2 (>0.1 MeV), which produced up to 10.5 dpa and 520 appm He. Examination showed no swelling, no cavities, no precipitates, but a high concentration of dislocations. Tensile tests showed large increases in the 35°C strength properties, with the weldments the weakest of the materials. The ductility of all materials was reduced by the irradiation, the uniform elongation to only 0.4% in the cold-worked material. Tests at temperatures above the irradiation temperature showed an approach to unirradiated properties as the temperature was increased from 200 to 600°C. Helium embrittlement at 700°C severely reduced the total elongation.

9.1.9 [illegible] of Precipitation and Cavity Formation in Austenitic Stainless Steels during Irradiation[7]

E. A. Loss, A. F. Rowcliffe, E. H. Lee

Austenitic stainless steels are currently the most widely considered materials for structural applications in both fast breeder reactors and fusion energy devices. During exposure to high energy radiation at high temperatures, these materials undergo significant changes in physical and mechanical properties due to the combined effects of displacement damage and helium generation. In particular, the phenomenon of cavity swelling can lead to significant dimensional changes in vital components. Extensive phase changes occur simultaneously with cavity swelling. It is now realized that both the magnitude and the temperature dependence of swelling in these materials are strongly dependent upon the nature and extent of the phase changes which occur during irradiation. A universal feature of the microstructure of irradiated stainless steels is the physical association of cavities with precipitate particles. This is an important topic for investigation, since in many instances a major fraction of the total swelling is associated with cavity-precipitate pairs.

In stainless steels of the AISI 316 class modified with titanium, five major phases, namely γ', η, G, Laves, and MC, develop during neutron irradiation at temperatures in the range 400-650°C. These phases vary widely in their physical characteristics such as crystal structure, morphology, size, and composition. They also exhibit significant differences in behavior in terms of their interaction with dislocations, point defects, and gas atoms. During neutron irradiation in the Experimental Breeder Reactor (EBR-II), it is found that the finely dispersed coherent or partially coherent γ' and MC phases pin the dislocation structure, whereas the G, η, and Laves phases, which generally develop on a much coarser scale, are ineffective in this regard. We have discussed previously the many possible mechanisms by which both types of precipitates may affect cavity swelling, and these are summarized for perspective in the present paper. Of main interest in the present paper is the fact that the interfaces among the G, η, and Laves phases and the matrix provide the sites at which the development of large cavities occurs. The microstructural observations made on EBR-II-irradiated alloys suggest that these sites are efficient traps for helium and that there is a correlation between the growth of the cavities and the growth of the precipitate particles, with large cavities associated with large particles.

Certain aspects of the particle-cavity phenomenon have been investigated using the ORNL dual ion beam Van de Graaff facility. Disks 3 mm in diam of a titanium-modified

stainless steel were solution annealed at 1100°C and then irradiated at the peak swelling temperature, 675°C, with 4-MeV nickel ions at a damage rate of $\sim 10^{-3}$ dpa/s. Under these conditions, precipitation behavior is overwhelmingly dominated by the formation of a nickel- and silicon-rich G phase. The following types of irradiation at 675°C were carried out: (1) irradiation with nickel ions only, (2) simultaneous injection of helium and nickel ions, (3) injection of helium followed by irradiation with nickel ions, (4) irradiation with nickel ions followed by injection of helium, and (5) irradiation with nickel ions, followed by injection of helium, followed by further irradiation with nickel ions. Preinjected helium levels varied between 30 and 1400 appm. In dual beam irradiation experiments the rates of helium injection investigated were 0.4 and 4.0 appm/dpa. When nickel ion irradiations were carried out without the addition of helium, cavities did not develop in spite of the growth of a coarse dispersion of G phase. However, cavities developed readily both within the matrix and at the particle-matrix interface when helium was injected either before or during ion irradiation. With increasing levels of helium injection, the number density of both G particles and cavities increased. When helium was injected after G phase particles had been formed during a prior nickel ion irradiation, helium bubbles developed at dislocation sites and at particle matrix interfaces. These bubbles developed into cavities during further nickel ion irradiation. The cavities attached to precipitate particles grew more rapidly than those nucleated on dislocations.

To understand the physical basis for the fact that the cavities associated with precipitate particles generally are larger than cavities in the matrix, a theoretical model has been developed. It is based on the hypothesis that the precipitate matrix interface assists in the collection of point defects, which are channeled to the attached cavity. The analysis predicts that a cavity attached to a precipitate particle will grow to several times the size of a cavity in the matrix. Cavity size observations obtained from the experiments described above are interpreted in light of the theoretical analysis.

9.1.10 *Summary of* Tensile Properties of Ferritic Steels After Low Temperature HFIR Irradiation[10]

R. L. Klueh, J. M. Vitek

Tensile specimens from small heats of ferritic (martensitic) steels based on 12 Cr-1 MoVW, 9 Cr-1 MoVNb, and the low alloy ferritic 2¼ Cr-1 Mo steel have been irradiated at coolant temperature in HFIR to displacement damage levels of up to 9.3 dpa and helium contents of 10-82 appm. The base compositions and similar alloys to which nickel had been added for helium production are included in the irradiations.

During the present reporting period, irradiated specimens from a heat of 9 Cr-1 MoVNb and two heats of 9 Cr-1 MoVNb with 2% Ni were tensile tested at room temperature and 300°C. Yield strength and ultimate tensile strength of the irradiated samples displayed considerable hardening over the unirradiated condition. The increased strength was accompanied by a decreased ductility. Indications are that the hardening resulted only from the displacement damage and was not affected by the transmutation helium formed during irradiation. These results are similar to those for the 12 Cr-1 MoVW-base alloys, which were previously reported.

9.1.11 *Abstract of* Swelling, Microstructural Development, and Helium Effects in Type 316 Stainless Steel Irradiated in HFIR and EBR-II[11]

P. J. Maziasz, M. L. Grossbeck

Several key performance parameters for candidate first wall materials for tokamak magnetic fusion energy (MFE) devices are thermal properties, coolant compatibility, mechanical properties, and radiation damage

resistance. Several measures of radiation damage are dimensional change (either densification or, more likely, swelling) and mechanical properties changes (usually embrittlement). These changes often determine the useful wall lifetime of the material, which is a critical design parameter. There are significant design and operational reliability benefits to first wall materials being able to withstand higher neutron wall loadings and higher upper temperature limits (within the range of 400 to about 700°C).

Austenitic stainless steels are leading first wall candidates, and 20% CW type 316 is the reference material for this alloy class. Titanium-modified austenitic stainless steels generally exhibit better mechanical properties and swelling resistance in a variety of reactor environments, apparently due to the mechanism of MC interfacial helium trapping, and thus are the preferred alloys in this class. Many aspects of radiation damage limits on wall lifetime are directly or indirectly related to the microstructural development. Since no actual fusion reactors currently exist, investigations are conducted in a variety of irradiation environments to determine both properties and mechanisms and how they relate to a fusion environment. Irradiation in the HFIR is particularly useful for investigating microstructural evolution and mechanical properties changes during irradiation because helium and displacement damage are cogenerated in significant amounts continuously. The He/dpa ratio during the first 1-3 dpa in HFIR is close to that anticipated for a first wall (12-15 appm/dpa). This work investigates and compares the swelling and microstructural development in 20% CW type 316 and 316 + 0.23% Ti (316 + Ti) after HFIR irradiation at 55-670°C to fluences producing 7.7-16 dpa and 380-1080 appm He. The purpose is to determine the mechanisms involved in microstructural development, particularly those related to the role of helium, and to eventually correlate microstructure and mechanical properties. It is hoped that these will reveal principles for properties improvement to apply in the ADIP Program for MFE.

Both CW 316 and CW (316 + Ti) show considerable microstructural changes at all temperatures compared to the as-cold-worked microstructures present prior to irradiation. The network dislocation structure recovers at all temperatures from 55°C up to 570°C in both alloys. Frank faulted loops are observed in both alloys at 55-375°C, but no loops are found at 475°C and above. The loop microstructure is considerably refined in CW (316 + Ti) compared to CW 316. At 375°C, both alloys show a sharp recovery of the dislocation structure as the fluence increases from 8.5 to 13 dpa. The total dislocation density peaks at ~1-2 x 10^{15} n/m^3 in CW 316 at 375°C and 8.5 dpa and then drops an order of magnitude at 13 dpa, due both to complete disappearance of the loops and to considerable relaxation of the network. In CW 316 at 475°C and above, the dislocation density apparently saturates with increased temperature or fluence at ~6-8 x 10^{13} n/m^3. In CW (316 + Ti), the dislocation density is roughly an order of magnitude higher at all temperatures and fluences compared to CW 316.

Both alloys show considerable intragranular cavity development at 285°C and above and grain boundary cavitation at about 565°C and above. The magnitude of cavity volume fraction (CVF) swelling is small but easily measurable using transmission electron microscopy (TEM) in both alloys from 7.7 to 16 dpa, being less than 0.1% in most cases with the maximum of 0.5% (at 285°C). Both CW 316 and CW (316 + Ti) appear to show maximum swelling at 285°C or below with a definite minimum in the swelling curves at 450-550°C for these low fluences.

This same temperature dependence persists for CW 316 irradiated to 40-60 dpa in HFIR. The CVF swelling for CW 316 shows considerable fluence dependence at 375 and 475°C between 8 and 16 dpa, with an initial increase, then a slight decrease for several different microstructural reasons before finally increasing monotonically with fluence. At 565°C, the swelling increases monotonically at all fluences. Cavity behavior, at least at the lower temperatures in CW 316, appears strongly coupled to the dislocation and precipitation behavior. In

most cases, the amount of swelling is less for CW (316 + Ti) than for CW 316. Titanium carbide (MC) formation directly affects cavity development through the mechanism of MC interfacial helium trapping and directly affects the network dislocation density through dislocation pinning. The cavities in both alloys seem to be voidlike at 285°C but have every indication of being bubble-like at 375°C and above, based on calculations of the equilibrium amount of helium in the cavities using the most current high density equations of state for the gas.

There is considerable precipitation in CW 316 at 375°C and above and in CW (316 + Ti) at 285°C and above. CW 316 develops γ' (Ni_3Si type) after 8.5 dpa at 375°C, which apparently dissolves and is replaced by η (M_6C type) phase after 13 dpa. The η and Laves (Fe_2Mo type) phases are observed at 475°C in CW 316; τ ($M_{23}C_6$ type) and Laves are found at 565°C and σ and χ are included at higher temperatures. MC is the dominant intragranular phase in CW (316 + Ti). Laves and η are reduced and τ and γ' are eliminated compared to CW 316.

The development of the various microstructural components indicates a strong interaction between helium and vacancies that interferes with bulk recombination and contributes to enhanced solute segregation, precipitation, and dislocation development. MC formation is beneficial in controlling cavity formation to reduce swelling, in reducing uncontrolled phase instability, and in giving more stable microstructural dependence for CW (316 + Ti) compared to CW 316.

9.1.12 *Abstract of* Preirradiation Microstructural Development Designed to Minimize Properties Degradation during Irradiation in Austenitic Alloys[12]

P. J. Maziasz, T. K. Roche

The effort of the ADIP Program for MFE is divided into several parallel paths for different classes of alloys, each identifying, investigating, and developing a PCA in that particular class. Austenitic stainless steels are leading candidates for early MFE devices and strong candidates in most of the larger reactor design studies for future machines. The reference material for the austenitic stainless steels is 20% CW type 316 (18 Cr-13 Ni-2 Mo-2 Mn-0.05 C-0.4 Si-bal Fe), and the PCA is a 14 Cr-16 Ni-0.25 Ti modification of the type 316 alloy. Several distinct advantages of the austenitic alloy are the wealth of irradiation data from a variety of sources including the Fast Breeder Reactor (FBR) program, compatibility with coolants, fracture toughness, ease of fabricability and welding, and reasonable materials costs. Disadvantages of these alloys include the low thermal conductivity and the long-lived, high level of induced residual radioactivity. A key parameter for material performance is wall lifetime; embrittlement and swelling are important forms of radiation damage that affect this parameter. In addition, these radiation damage responses determine the acceptable neutron wall loading and maximum temperature limit of operation. Swelling and many of the mechanical properties changes are directly related to the microstructure developed during irradiation. The basic philosophy behind alloy development in ADIP is that through control of the initial microstructure, subsequent microstructural evolution and properties changes during irradiation can be controlled. In this respect, titanium-modified alloys are generally superior to unmodified austenitics.

The basic microstructural difference between the titanium-modified and ordinary austenitic stainless steels is the formation of the titanium MC carbide in the former. MC formation can reduce or prevent formation of precipitate phases like τ ($M_{23}C_6$), η (M_6C), and Laves (Fe_2Mo) that can seriously degrade properties at temperatures where precipitation in these alloys is important, during aging ($0.5T_m$ and above) or irradiation ($0.3T_m$ and above). Fine MC can contribute to strengthening, but the most important benefit of MC formation for fusion application is the powerful mechanism of MC interfacial helium trapping. This

behavior is unique to MC relative to the other phases formed in steel.

The results of Phase I of the Path A (austenitic alloys) PCA development effort — design and fabrication of preirradiation microstructure — are presented in this paper. Microstructural design was conducted using principles for reducing swelling and helium embrittlement obtained from irradiations performed in the HFIR and other irradiation environments. Two general principles for improving properties are: either keep helium away from the grain boundaries or trap it with precipitates in the grain boundary, and reduce swelling by refining the cavity dispersion. These can be accomplished by increased dislocation density and particularly through MC helium trapping. To this end, various preirradiation microstructures were designed that included various dispersions of grain boundary and matrix carbides (primarily MC) combined with various matrix dislocation densities. In addition, grain size was varied independently of microstructural manipulation.

PCA stock (plate and bar) as received from the vendor was inhomogeneous with macroscopic stringers of MC carbides and a duplex grain structure, a common problem for titanium-modified alloys. An investigation was conducted both to rehomogenize the alloy and to determine how to preserve the homogeneity during subsequent fabrication. Homogenization for 24 h at 1275°C in either a static vacuum or high purity argon produced excellent results, and homogeneity was preserved by subsequent homogenization for 1 h at 1200°C at regular intervals during the fabrication.

The homogenized PCA material was examined after short thermal aging in the 0, 10, and 25% CW conditions at temperatures of 600-1000°C for times ranging from 5 min. to 166 h. The time-temperature-precipitation (TTP) behavior, the various microstructures available in this type of alloy, and the thermal-mechanical treatments required to produce them were thus established. Intragranular MC normally forms in type (316 + Ti) and prevents intragranular formation of other carbides like τ and η phase and reduces Laves phase formation compared to ordinary type 316. Even though MC forms intragranularly in (316 + Ti), it does not form at the grain boundaries, and therefore the grain boundary precipitation of (316 + Ti) consists of τ and η carbides, as in 316. This is important because τ and η play only a passive role in preventing large grain boundary cavities, rather than displaying active interfacial helium gettering, as MC does. The 14 Cr-16 Ni PCA is far superior to (316 + Ti) because MC is the stable grain boundary carbide, to the exclusion of τ and η. Laves phase formation is also reduced in the PCA compared to type (316 + Ti). Through proper combinations of cold working and heat treatment, the grain boundary and matrix MC carbide size and distribution, as well as the matrix dislocation density, were independently varied. Furthermore, a rapid heating rate in properly homogenized material allowed the grain size to be refined without seriously perturbing the various microstructural manipulations defined above. Seven preirradiation microstructures were produced. Three of these are simple solution-annealed, 10 or 20% CW material. Four of them are complex, innovative microstructures with either fine (2-5 nm) or coarse (20-80 nm) MC particle dispersions at the grain boundary or in the matrix together with either solution-annealed or CW dislocation densities. These are currently being evaluated in both irradiated and unirradiated conditions to determine the effects of these microstructural manipulations on properties.

9.1.13 *Abstract of* The Effect of Precipitate-Matrix Interface Defect Sinks on the Growth of Voids in the Matrix[13]

A. D. Brailsford, L. K. Mansur

The trapping of point defects at localized sites on a precipitate-matrix interface is an important process tending to inhibit the void swelling of irradiated materials. Under irradiation, such traps attain a steady-state occupation probability as a result of the competition between defect trapping and thermal reemission or on-site recombination with the

corresponding antidefect. The sink strengths for both the defect and antidefect are here derived for a dispersion of arbitrarily shaped precipitates. These strengths can be expressed as a product of two factors, an "ideal" sink strength and a capture efficiency. The first of these contains details of the precipitate geometry (and volume concentration). It is shown to be related to the electrical capacitance of a metal electrode of the same shape. The capture efficiency, on the other hand, depends upon both the energetics of the trapping process and the nature of other point defect sinks in the system. Such a property is in general agreement with the results of earlier work. However, a new feature is also considered here — namely, the variation of the capture efficiency of precipitate-associated traps in the proximity of a free surface. Quantitative examples of the above factors will be given and their experimental ramifications discussed.

9.1.14 *Abstract of* Characteristics of Irradiation Creep: The First Wall of a Fusion Reactor[14]

W. A. Coghlan, L. K. Mansur

The importance of irradiation creep has been apparent to designers of fission reactors for several years, and as a result there has been a variety of research in this area. Creep rates under real or simulated reactor conditions have been measured along with the dependence of these rates on material and reactor parameters.

Creep behavior is now accounted for in the design of reactors to minimize the detrimental effects produced by creep of the structural parts of the core. Finally, to understand the physical basis of irradiation creep several theoretical models have been developed and tested.

As might be expected, most of the investigations of irradiation creep in fission reactor environments were conducted in support of specific designs. Therefore, most measurements have been made on zirconium alloys and various types of stainless steel with a few experiments on other materials. In addition to this limited selection of materials, the irradiation conditions have generally been limited to the operating temperatures and radiation conditions of the test reactors.

An obvious but basic problem in choosing a material for the first wall of a fusion reactor is that there are no fusion reactors in which to test materials. This problem is important because there are some special characteristics of the fusion irradiation environment that are common to most fusion devices. In all planned fusion devices the dominant nuclear reaction is a reaction between deuterium and tritium which produces 3.5-MeV alpha particles and 14-MeV neutrons. The alpha particles are stopped very quickly in most materials, but the neutrons have a long range and will cause atomic displacement damage throughout the first wall as well as other reactor components. These high energy neutrons will produce many more free defects per collision (composed of subcascades) than those found in fission reactors and will also produce much more helium by (n,α) transmutation reactions. In addition to these special characteristics, almost all the fusion reactor designs involve cyclic operation with burn times from a fraction of a second to several thousand seconds. The resulting cyclic temperature condition, cyclic radiation field, and cyclic stress combine with irradiation creep to produce compressive stresses on parts of the first wall. Finally, in many designs, the first wall temperature is below the temperatures where irradiation creep measurements are available. The effect of these special conditions on irradiation creep is not known and in most cases there is little experimental information available to predict the response.

In this paper we have applied the existing theory of irradiation creep and studied the available data to anticipate the characteristics of irradiation creep in fusion reactor first walls. The effort is concentrated on the special conditions that characterize the fusion irradiation damage environment discussed above. For example, we have tried to identify the role that increased helium production plays in

promoting or limiting irradiation creep by comparing experiments done in different fission reactors where helium production is very different. Several important areas exist where very little experimental information is available. For example, the average damage cascade in all fission reactors is nearly the same, so the effect of increased defect production per neutron collision in fusion reactors cannot be determined. Therefore, we found it useful to evaluate the several published creep mechanisms to determine theoretically if the special conditions would lead to a difference in creep behavior. From this evaluation, two areas have been identified as important. The increased helium production is likely to result in increased void nucleation. The additional voids will change the character of the sinks in the system and will decrease the creep rate versus swelling rate ratio. For the case of stress-induced preferred absorption (SIPA) creep we found a decrease of a factor of ~5 in this ratio for only an order of magnitude increase in the void density. The second important difference results from a new analysis of climb based on the discontinuous defect production from cascades. Creep from this mechanism is greatly enhanced in the fusion environment. From this analysis, we have suggested several possible experiments, which could be carried out using existing facilities, that would answer some of the important questions.

9.1.15 *Abstract of* Applications of the Theory of Cavity Growth to Dual Ion Swelling Experiments[15]

M. R. Hayns, L. K. Mansur

The rate theory of cavity growth is applied to study the effects of helium gas on cavity swelling. The variation of swelling with temperature is emphasized. (1) Expressions are derived showing that the primary effect of the helium is in pressurizing cavities and that a secondary effect is in altering the microstructural sink strengths. (2) Recent experimental data on swelling of a pure stainless-steel-type alloy under dual nickel and helium ion bombardment are interpreted. Helium-free, helium-coimplanted, and helium-preimplanted swelling results can be explained by the theory. It is necessary to account for the partitioning of the helium to dislocations as well as to cavities in order to explain the experimental results for helium coimplantation. (3) Model studies for physically reasonable parameters reveal the importance of the He/dpa ratio.

9.1.16 *Abstract of* TEM Observations of Crack Propagation in Metals Containing Helium Bubbles[16]

J. A. Horton, S. M. Ohr, W. A. Jesser

The understanding of the effects of helium on physical and mechanical properties is important in the development and qualification of alloys for the first wall of a fusion reactor. The helium produced by neutron irradiation is known to affect the microstructural response, and through this to affect swelling, deformation, and fracture mode. In particular, very little is known of the interaction of deformation dislocations and propagating matrix cracks with preexisting helium bubbles. In order to study these aspects of helium effects, experiments were designed to observe the deformation and transgranular crack propagation in type 316 stainless steel which contained small helium bubbles.

The type 316 stainless steel specimens were annealed for 2.5 h at 1050°C and then electropolished to perforation. These specimens were bombarded in a flux of 12×10^{18} ions/m^2·s of 80-keV helium ions, to fluences up to 5×10^{21} ions/m^2. No additional specimen heating was provided. The maximum fluence irradiation produced small helium bubbles which ranged in diameter from 2 to 12 nm. The bubble density

of 2×10^{22} bubbles/m^3 gave a calculated swelling of 0.2% and an average interbubble spacing of 37 nm.

Irradiated specimens were strained at room temperature in a Philips EM400T transmission electron microscope. Transgranular cracks were produced and propagated through bubble-containing regions of the specimen matrix. Sequential micrographs were made of crack opening displacements of 10 nm per step. Bubbles intersected by a propagating crack undergo an elongation normal to the crack and an increase in bubble volume. An interbubble fracture follows, resulting in fracture surface dimples. One such dimple was studied and was approximately 6 nm in diameter and 12 nm long but originated as a 3-nm-diam bubble. The volume increased by a factor of 20, assuming a circular cross section. Some bubbles near the fracture surface tended to elongate normal to the crack with little volume change. The amount of bubble elongation suggests local strains of at least 4. Bubbles observed as close as 12 nm from the final fracture surface appeared unaffected by the fracture process.

In order to further investigate the bubble elongation without enlargement process, one area was examined in detail. The band of elongated bubbles was in front of and in line with the propagating crack, lay in a [211] direction, and exhibited a twin relationship to the regions without elongated bubbles. The direction of elongation was not perpendicular to the crack. The average shear strain of 3.0 (shear angle 72°) requires the passage of two complete dislocations and one twinning dislocation per atomic plane. Apparently the passage of many dislocations sheared the bubbles without a resulting enlargement.

The observed fracture surface dimples are approximately twice the original bubble diameter and have the same planar density. Observations by others of fracture surface dimple and original bubble sizes and densities have been limited to TEM specimens prepared close to the fracture surface. These observations showed a greater dimple density than bubble density. A large fracture surface in the electron transparent region which formed during a 600°C helium irradiation at the University of Virginia facility was examined with concurrent scanning TEM images and secondary electron detector images. These micrographs showed fracture surface dimples up to 400 nm in diameter. The smallest fracture surface dimples were 20 to 40 nm in diameter with a fracture surface density of 3.5×10^{12} m^{-2}. The helium bubbles below the surface ranged from 20 to 40 nm in diameter with an equivalent planar density of 1×10^{15} m^{-2}. There appears to be no size or density relationship between the helium bubbles and the fracture surface dimples.

In summary, localized flow in front of the crack leads to a bubble elongation normal to the crack propagation direction. In addition to the elongation, those bubbles actually in the crack path enlarge by a factor of up to 20 and so become fracture surface dimples. No correlation was found between these dimples and the large dimples normally observed by scanning electron microscopy (SEM). The localized flow leaves bubbles 12 nm from the fracture surface undeformed. Further straining experiments are planned on specimens irradiated to produce larger and fewer helium bubbles. The observations reported here help explain the interaction of plastic deformation and crack propagation with helium bubbles.

9.1.17 *Abstract of* The Microstructure of "Triple Beam" Ion-Irradiated Fe and Fe-Cr Alloys[17]

L. L. Horton, J. Bentley, W. A. Jesser

The potential of ferritic steels as a first wall material for proposed fusion reactors is currently being evaluated. Detailed analyses of the defect structures which result from fusion environment irradiation will be an

important aspect of this evaluation. Examination by TEM of specimens bombarded simultaneously with a "triple beam" of energetic helium, hydrogen, and heavy ions should provide data helpful in understanding material response under first wall irradiation conditions. Unfortunately, TEM of ferritic steels is complicated by both the ferromagnetic nature of the material and the complexity of the unirradiated microstructure. In this investigation, the development of defect structures in "triple beam" irradiated iron and iron-chromium alloys, which form the basis of the more complex steels, has been studied in order to provide a foundation for an eventual analysis of radiation damage in these steels.

Disk specimens 3 mm in diameter of high purity Fe, Fe-5 Cr, and Fe-10 Cr were bombarded with a triple beam of He^+, D_2^+, and 4-MeV Fe^{+2} ions in the dual Van de Graaff accelerator system at ORNL. The energy of the He^+ and D_2^+ beam was ramped sinusoidally at 2.5×10^{-2} Hz between 0.2 and 0.4 MeV. The specimens were irradiated to 10 dpa with 100 appm He and 410 appm D. These are the He/dpa and H/dpa ratios expected for ferritic steels in a fusion reactor first wall. The irradiation temperatures were 725, 775, 800, 850, 900, and 950 K. In this type of irradiation, the damaged region is within ≈3 μm of the irradiated surface. The first step in preparing these specimens for TEM was the controlled removal or "sectioning" of the damaged region to ≈0.9 μm from the irradiated surface, followed by "back-thinning." The sectioning depth was based on TEM examinations of the damage depth profile for iron irradiated at 850 K. Sectioning and back-thinning were performed using established electropolishing techniques. Since the chromium content of many of the commercial ferritic steels under consideration is ≈10%, emphasis has been placed on the quantitative analyses of the defect structures in Fe-10 Cr alloys. These results are described below.

Some quantitative data for the dislocation component of the microstructure are shown in Table 9.1. At irradiation temperatures, T_{irr}, of 725, 775, and 800 K the dislocations were mainly in the form of a fairly homogeneous distribution of loops. For these three lowest irradiation temperatures, the average loop diameter, d_L, increased and loop concentrations, C_L, decreased with increasing temperature as seen in Table 9.1. At 800 K, many of the loops intersect the foil surfaces without gliding out. This indicates pinning, possibly by Cottrell atmospheres since no precipitates were observed in association with the dislocations. The dislocation loops were analyzed and found to be interstitial type with predominantly a[100] Burgers vectors. However, some a/2[111] Burgers vectors were also found. At 850 K a coarse distribution of network dislocation segments was observed.

Table 9.1. Quantitative data for dislocation microstructure of Fe-10 Cr

T_{irr} (K)	d_L (nm)	C_L (m^{-3})	ρ_d (m^{-2})
725	18	6×10^{21}	4×10^{14}
775	24	3×10^{21}	2×10^{14}
800	60	3×10^{20}	1×10^{14}
850			1×10^{14}
900			2×10^{12}
950			2×10^{12}

At 900 and 950 K the dislocation structure appeared to be little changed from that existing in the unirradiated specimens. Dislocation densities, ρ_d, are also shown in Table 9.1. The results indicate a general coarsening with increasing temperature. At the two highest temperatures, a two orders of magnitude drop in the dislocation density is observed.

Cavities have been observed only at 850 and 900 K. At 850 K there was a low concentration (2.6×10^{19} m^{-3}) of cavities with an average diameter of ≈23 nm. The measured cavity volume fraction was 0.02%. At 900 K the cavity concentration was a factor of 3 lower than that at 850 K. The average cavity diameter was 4 nm, yielding a cavity volume fraction of <0.0001%.

The usual effect of a factor of 6 decrease in the cavity diameter at 900 K as compared to 850 K is possibly due to the much lower dislocation density at 900 K. At 850 K the dislocations provide a biased sink for the interstitials, allowing the cavities to grow and become more voidlike in character (bias-driven growth). At 900 K many fewer biased sinks for the interstitials are present, thereby reducing the number of vacancies available for growth of the cavities which are constrained to grow as bubbles (gas-driven growth). Cavities were also observed on grain boundaries and at the intersection of grain boundaries and $M_{23}C_6$ precipitates.

A quantitative comparison of the damage microstructures observed in iron and in Fe-10 Cr at 850 K is shown in Table 9.2. The iron had an order of magnitude more swelling than the Fe-10 Cr. Although the cavities have larger diameters, d_C, in the Fe-10 Cr, the concentration, C_C, is two orders of magnitude lower. The dislocation density of the Fe-10 Cr is twice that of the iron. These results indicate that the presence of chromium inhibits cavity nucleation and so reduces the cavity volume fraction.

Qualitatively, the damage structures in the Fe-5 Cr are similar to those in the Fe-10 Cr specimens. A more complete characterization of the damage structures in iron and Fe-5 Cr is in progress.

Extensions of this investigation are planned to include a study of the dose dependence of the damage for Fe-10 Cr. When data from these "triple beam" irradiations are complete, a quantitative comparison to currently available neutron irradiation damage results will be made. In conclusion, these results will help to provide a firm foundation for future analyses of radiation damage in ferritic steels.

Table 9.2. Comparison of damage microstructures of Fe and Fe-10 Cr at 850 K

	Swelling (%)	C_C (m^{-3})	d_C (nm)	ρd (m^{-2})
Fe	0.22	2×10^{21}	13	5×10^{13}
Fe-10 Cr	0.02	2×10^{19}	23	1×10^{14}

9.1.18 *Abstract of* The Depth Distribution of Displacement Damage in α-Iron under "Triple Beam" Ion Irradiation[18]

L. L. Horton, J. Bentley, W. A. Jesser

Ferritic steels are currently being considered as possible first wall materials for proposed fusion reactors. The defect structures which result from fusion environment irradiation of ferritic steels are of interest. Examination by TEM of specimens of ferritic steels bombarded simultaneously with a "triple beam" of energetic helium, hydrogen, and heavy ions should provide data helpful in understanding their response under first wall conditions. In this type of irradiation, the damaged region of the specimen is usually within a few micrometers of the irradiated surface. The usual method for preparing these specimens for TEM examination involves the controlled removal or "sectioning" of the damaged region to some predetermined depth from the irradiated surface, followed by electropolishing from the unirradiated surface ("back-thinning") to perforation. The sectioning depth is important as characteristics of the defect structures vary significantly with distance from the irradiated surface. The sectioning depth can best be selected by experimentally determining the depth distribution of the defect structures. In this investigation, the depth dependence of the damage in irradiated α-iron was determined to guide microstructural examination. The results are expected to be applicable to ferritic steels.

Disk specimens 3 mm in diameter of high purity iron were bombarded with a triple beam of He^+, D_2^+, and 4-MeV Fe^{+2} ions in the dual Van de Graaff accelerator system at ORNL. The energy of the He^+ and D_2^+ beam was ramped sinusoidally at 2.5×10^{-2} Hz between 0.2 and 0.4 MeV. The specimens were irradiated at

850 K to ~10 dpa with ~100 appm He and ~410 appm D. The irradiated specimens were electroplated at 370-372 K in a ferrous chloride plating bath with an iron anode until ≅4 mm of iron had plated on the specimen. Slices with a thickness of ≅0.3 mm were cut normal to the original specimen surface. Disk specimens 3 mm in diameter were electrodischarge machined from these slices. With careful electropolishing, it was possible to thin to the interface between the electroplated iron and the original irradiated surface. Damage distribution was observed at 120 keV in a JEM 120C transmission electron microscope equipped with a special objective lens polepiece (AMG) for the observation of ferromagnetic materials. The swelling and dislocation density profile results do not correspond to the deposited energy depth profiles calculated by the E-DEP-1 computer code. Based on TEM examinations of nickel bombarded with 4-MeV Ni^{+2} ions, it has been suggested by others that the electronic stopping parameter used by the E-DEP code is about 22% too large. The current results support this conclusion. The dislocation loops were analyzed and found to be interstitial loops with Burgers vectors of a<100> and a/2<111>. Of special interest is the band of dislocation loops at ≅2.8 μm from the irradiated surface, about a factor of 3 deeper than the projected range of 4-MeV Fe ions in iron. Possible explanations for this phenomenon and the selection of a sectioning depth, based on the damage profiles, will be discussed. These results will be compared to previous results for the depth dependence of damage in triple beam (4-MeV Ni^{+2}) irradiated nickel.

An important practical result of this investigation has been to provide an experimental base for the selection of sectioning depths for damage studies of ferritic steels utilizing the "triple beam" bombardment technique.

9.1.19 *Abstract of* Chromium-Molybdenum Steels for Fusion Reactor Applications[19]

R. L. Klueh

Because ferritic steels have been found to have excellent resistance to swelling when irradiated in a fast breeder reactor, Cr-Mo steels have recently become of interest for nuclear applications, both as cladding and duct material for fast breeder reactors and as a first wall and blanket structural material for fusion reactors. In this paper we will assess the Cr-Mo steels for fusion reactor applications. Possible approaches on how Cr-Mo steels may be further developed for this application will be proposed.

Generally, the Cr-Mo steels can be divided into two categories: unmodified, basically Cr-Mo-C steels and Cr-Mo-C steels modified by the addition of carbide-forming elements — in addition to chromium and molybdenum. Extensive research and development efforts have been conducted on the unmodified steels, especially 2¼ Cr-1 Mo and 12 Cr-Mo steels. Considerable work has also been done on 12 Cr-Mo steels modified with additions of vanadium, niobium, titanium, and tungsten. In recent years much of the research effort on this type of alloy has been directed at developing modified Cr-Mo steels with less than 12% Cr (≥9%) for applications where the "stainless" properties imparted by chromium additions of at least 12% are not needed.

We will examine the unmodified and modified steels in terms of hardenability, precipitation processes (stability at elevated temperatures), strength, and toughness. Where possible, we will discuss the effects of irradiation on these properties. Such a study leads to the types of trade-offs that may be necessary when choosing between the well-researched unmodified 2¼ Cr-1 Mo steel and a high chromium modified steel.

9.1.20 *Abstract of* Effect of Low Temperature Irradiation with (n,α) Helium Production on Tensile Properties of 12 Cr-1 MoVW-Type Steels[20]

R. L. Klueh, J. M. Vitek, M. L. Grossbeck

The irradiation-resistant properties of ferritic (martensitic) steels, such as those based on 12 Cr-1 Mo, have led to these alloys being considered for use as fusion reactor blanket structural components. Because an adequate source of D-T fusion neutrons is not

available, an alternative method for simulating 14-MeV (2.2-pJ) neutron irradiation must be used. For austenitic stainless steels, sufficient nickel is present in the alloy that irradiation in some mixed-spectrum fission reactors produces the required (n,α) helium by thermal neutron captures. However, the commercial ferritic steel based on 12 Cr-1 Mo generally contains less than 0.5% Ni, which is not adequate for this helium simulation. If these alloys contained approximately 2% Ni, they could be irradiated in the HFIR to obtain approximately the same (n,α) helium production rate as the original alloys would develop during fusion reactor service for a neutronic wall loading near 3 MW/m^2. The rate of displacement damage production under these conditions is also appropriate for this wall loading.

Small heats of ferritic (martensitic) steels based on 12 Cr-1 Mo with approximately 0.2% C, 0.3% V, 0.5% W, 0.4% Ni, 0.5% Mn, and 0.02% Nb (the composition was based on the commercial Sandvik alloy HT9) were prepared with 0, 1, and 2% Ni added to the base composition. An additional heat was made with 2% Ni, in which the content of the ferrite-forming elements was adjusted to restore the net chromium equivalent to a value near that of the unmodified alloy. During irradiation in HFIR, transmutation of the ^{58}Ni in these alloys will give helium concentrations approximating those produced in such steels in fusion reactor service.

Tensile specimens from the four experimental heats plus specimens from the commercial Sandvik heat (this heat has been irradiated and tested in the U.S. Breeder Reactor Clad/Duct Alloy Development Program) were irradiated at 50°C in HFIR to 1.3×10^{22} n/cm^2, resultin in displacement damage levels of up to 10 dpa and helium levels of up to 90 appm (depending on the nickel content of the alloy and the location in the irradiation capsule). Prior to irradiation, the steel specimens were normalized and tempered. The normaliz'ng heat treatment consisted of heating the specimens for 0.5 h at 1050°C in a flowing helium atmosphere, after which they were removed from the furnace and cooled in the flowing helium. The steels with 0 and 1% Ni were tempered 2.5 h at 780°C; the 2% Ni alloy and 2% Ni alloy with adjusted chromium equivalent were tempered at 700°C for 5 h and 8 h, respectively.

Immersion density measurements were made on all irradiated specimens. Specimens were tensile tested at room temperature and 300°C at a strain rate of 4.2×10^{-5} s^{-1}. There was no indication of a change in density of the specimens that could be attributed to the irradiation. Significant changes due to irradiation were observed in the tensile properties.

When the tensile properties of the commercial heat of HT9 were compared with the experimental heat that was melted and used as the base composition for the nickel-doped alloys, no difference was observed. For all but the unirradiated ultimate tensile strengths at room temperature, the difference in yield strength and ultimate tensile strength for the two heats was less than 1% (at room temperature the ultimate tensile strength of the experimental heat was approximately 5.5% greater than that of the commercial heat).

For all of the alloys tested, irradiation caused a significant increase in the yield strength and ultimate tensile strength at room temperature and 300°C. The increase in strength was accompanied by a decrease in ductility (lower uniform and total elongation). The decrease in ductility was greatest at room temperature: uniform elongation decreased from 4-8% to 0.3-0.6%; total elongation decreased from 8-11% to 2-3%. At 300°C the ductility changes were significantly less.

The low concentrations of (n,α) helium (up to 90 appm) generated during the present irradiation were concluded to have no effect on the tensile properties. Because of the different starting strengths, this conclusion was reached by comparing the relative effect of irradiation on the various alloys. The ratios of irradiated to unirradiated properties (strength and ductility) were determined and found to remain relatively unchanged with increasing nickel concentration. Thus, the hardening effect was attributed to the displacement damage.

The results of these preliminary tests indicate that the 12 Cr-1 Mo type martensitic steels offer potential for fusion reactor first wall structures.

9.1.21 *Summary of* Tensile Properties of Ferritic Steels After Low Temperature HFIR Irradiation[21]

R. L. Klueh, J. M. Vitek

Tensile specimens from small heats of ferritic (martensitic) steels based on 12 Cr-1 MoVW, 9 Cr-1 MoVNb, and the low alloy ferritic 2¼ Cr-1 Mo steel have been irradiated in HFIR to displacement damage levels of up to 9.3 dpa and helium contents of 10-82 appm. The 12 Cr-1 MoVW-base and 9 Cr-1 MoVNb-base compositions were irradiated along with similar alloys to which nickel had been added for helium production.

During the present reporting period, irradiated specimens of 2¼ Cr-1 Mo steel in the normalized and tempered and the isothermally annealed conditions were tensile tested at room temperature and 300°C. The yield strength and ultimate tensile strength of the irradiated samples displayed considerable hardening over the unirradiated condition. The increased strength was accompanied by decreased ductility. The strength and ductility values of the normalized and tempered 2¼ Cr-1 Mo steel compared favorably with the results on the 12 Cr-1 MoVW and 9 Cr-1 MoVNb steels. In the isothermally annealed condition, 2¼ Cr-1 Mo steel is considerably weaker than the normalized and tempered steel. However, after irradiation the isothermally annealed steel retains considerably more ductility than the other alloys did for tests at 300°C.

9.1.22 *Abstract of* Theoretical Relationships Between Creep and Swelling Rates by Point Defect Absorption During Irradiation[22]

L. K. Mansur, W. A. Coghlan

Irradiation creep and swelling are each made possible by the absorption at sinks of point defects produced by irradiation. Asymmetric partitioning of vacancies and interstitials among cavities, dislocations, and other sinks leads to swelling. The primary mechanisms of irradiation creep also each require a type of asymmetric partitioning. In dislocation climb creep caused by SIPA, more interstitials are absorbed at dislocations favorably oriented with the stress and more vacancies are absorbed at unfavorably oriented dislocations. Creep by dislocation glide enabled by climb may also take place. Net long-term climb arises from SIPA, leading to the mechanism of preferred absorption glide (PAG), as we have described recently. Net climb also arises from swelling, in which case we denote the mechanism as swelling-driven glide creep. Irradiation creep by climb-enabled glide may also occur by dislocation climb excursions caused by cascade-induced point defect concentration fluctuations even in the absence of net long-term climb. Our recent development of the theory of cascade-induced creep is included in the present discussion.

The mathematical relations by which swelling and each mechanism of irradiation creep depend on point defect properties and on microstructure are given. The ratio of the creep rate by each mechanism to the swelling rate is derived. These expressions relate the creep rate to the swelling rate through microstructural and point defect properties. It is found for typical ranges of parameters that the ratio of creep rate to swelling rate may vary by orders of magnitude. These results are important in applications where the ratio of creep rate to swelling rate and its variation with microstructure and temperature affect materials design and performance. The relevance of present results to microstructures observed in irradiation experiments is emphasized.

9.1.23 *Abstract of* Irradiation Creep by Cascade-Induced Point Defect Fluctuations[23]

L. K. Mansur, W. A. Coghlan, T. C. Reiley, W. G. Wolfer

A mechanism of irradiation creep caused by cascade-induced point defect fluctuations is described. The underlying principles and theoretical methods necessary to evaluate the

creep rate are developed. Creep takes place by the glide of dislocation segments, which are released from pinning obstacles by the local climb enabled by cascade-induced point defect fluctuations. This process is denoted statistical absorption glide creep (SAG creep). It operates independently of SIPA creep and of other mechanisms of climb-enabled glide creep and occurs whether or not other mechanisms are active. These include swelling-driven climb-glide creep and PAG creep.

To evaluate cascade-induced creep, it is necessary to develop methods with greater capability than the widely used quasi-chemical rate theory. To emphasize this point, a hypothetical system where the only sinks are dislocations and where stress-induced preferred point defect absorption does not take place is considered. For this case, it is shown that rate theory predicts a zero creep rate in principle, while the theory we employ, which accounts for spatial and temporal inhomogeneities caused by point defect production in cascades, predicts a finite creep rate in principle. This result makes it clear that the present developments are of the essence in understanding cascade-induced creep and are not merely a refinement of the rate theory.

After establishing that the dislocation climb excursions caused by cascade-induced point defect fluctuations lead to creep in principle, the magnitude of the creep rate is next estimated. The creep rate depends on the height and frequency of these climb excursions. Three methods are developed to estimate the climb frequency versus climb height spectrum. A method based on the cascade diffusion theory of Mansur, Coghlan, and Brailsford is developed. An important refinement in this method is then introduced to account for the randomness of point defect absorption from a given cascade. A direct geometric method is also developed for estimating the climb frequency versus climb height spectrum at a random pinning point, giving an independent approach to the problem. This method gives a lower bound to the expected climb height at a pinning point. It is found that climb heights of many atomic distances are possible. For typical fusion reactor cascades and dislocation densities, such climb heights are produced predominantly by cascades occurring within tenths of a point defect diffusion length of the dislocation (diffusion length = sink strength$^{-1/2} \leq 10^2$ nm for reasonable sink strengths). Climb excursions on the order of one atomic distance are found to be quite frequent and also to be produced by more distant cascades.

Climb excursions are assumed to lead to creep only when they cause the unpinning of the dislocation segment. The climb frequency versus climb height spectrum is incorporated into a creep model where creep rate is proportional to the effective dislocation glide velocity. Glide between pinning points is taken to be rapid so that the time necessary to unpin the segment determines the effective glide velocity. The effective glide velocity is estimated from the climb frequency versus climb height spectrum, the fraction of climb excursions of a given height that lead to dislocation unpinning events, and the associated glide distance. The fraction leading to unpinning is obtained by assuming that in a large ensemble of pinned dislocations there will be a distribution of dislocation distances from the unpinning position ranging from one atomic distance to half the obstacle height. Thus, cascade-induced climb excursions cause unpinning from a fraction of the obstacles in the ensemble. It is concluded that creep rates of technological significance are produced by this mechanism.

9.1.24 *Abstract of* Physical Metallurgy and Structural Applications of Ductile Ordered Alloys $(Ni,Co,Fe)_3V$[24]

C. T. Liu

Metallurgical and mechanical properties of LRO alloys based on the quasi-ternary system Ni_3V-Co_3V-Fe_3V will be reviewed comprehensively. The ordered crystal structure in the $(Ni,Co,Fe)_3V$ alloys, which is characterized by stacking of closely packed ordered layers, can be altered

systematically by control of electron density (e/a) in the alloys. As e/a decreases, the stacking character changes from purely hexagonal, through different ordered mixtures of hexagonal and cubic layers, to purely cubic. Partial replacement of cobalt and nickel with iron lowers the e/a in the alloys and stabilizes the ordered structure with a cubic stacking character ($L1_2$-type). The alloys with multilayered hexagonal ordered structure exhibit brittle fracture with very little ductility, while those with the cubic ordered structure are ductile with tensile elongation exceeding 40% at room temperature. This is a major breakthrough in the design of ductile ordered alloys for structural applications.

Mechanical behavior of these ductile LRO alloys will be reviewed with emphasis on deformation at elevated temperatures. The yield strength of the LRO alloys, instead of decreasing as with conventional alloys, increases with temperature and reaches a maximum around T_c, the critical ordering temperature. The T_c of the alloys varies from 650 to 950°C, depending on the iron concentration. The room temperature yield stress is independent of quench temperature except in the vicinity of T_c. Calculation of the stress increment suggests that the anomalous temperature dependence of yielding in the LRO alloys is caused by a thermally activated process rather than a disordering process.

The LRO alloys exhibit excellent creep resistance; their creep rate is lower than that of commercial fabricable superalloys by several orders of magnitude. The creep behavior of the alloys will be characterized by use of the rate equation $\dot{\varepsilon} = A\sigma^n \exp(-Q/RT)/T\mu^{n-1}$. All the alloys exhibit a sharp drop in creep rate ($\dot{\varepsilon}$) around T_c as a result of formation of long-range order. The activation energy for creep, Q, and the stress exponent, n, in ordered and disordered states will be discussed and compared with the predictions from the creep models operating in ordered alloys.

Other metallurgical and mechanical properties of the LRO alloys which will be discussed include microstructural stability, hydrogen embrittlement, fatigue, air oxidation, and steam and liquid metal corrosion. The review will emphasize correlation of these properties with fundamental metallurgical variables in these alloys. We will also evaluate the potential of developing the LRO alloys as a new class of structural materials for high temperature applications. We expect that these ductile LRO alloys will contribute significantly in the years ahead to more efficient and reliable energy conversion systems.

9.1.25 *Abstract of* Development of Iron-Base Long-Range-Ordered Alloys for Fusion Reactor First Wall and Blanket Applications[25]

C. T. Liu

The structural material used for construction of the first wall in fusion reactor systems requires good high temperature mechanical properties, resistance to radiation-induced swelling and embrittlement, and good compatibility with low pressure hydrogen, liquid lithium, and coolants. To meet these requirements, a wide variety of alloys based on Fe, Ni, V, Mo, and Nb are being studied as possible candidate materials. LRO alloys are a unique class of materials with an atomic arrangement distinctly different from conventional or disordered alloys. The solute atoms in LRO alloys arrange themselves periodically and form an ordered crystal structure. The LRO alloys offer potential advantages over the conventional or disordered alloys for high temperature applications. This is because kinetic processes involving solid-state diffusion, such as creep or migration of point defects, are reduced in the ordered lattice. Also, the unique dislocation dynamics of ordered lattices provides the LRO alloys with excellent high temperature strength and fatigue resistance. The main disadvantage limiting the use of LRO alloys is their tendency to be brittle in the ordered state. However, our work on the ordered alloy system $(Fe,Co,Ni)_3V$ has overcome this limitation. The alloys with controlled ordered

structure are ductile with tensile elongation exceeding 35% at room temperature. In this paper, we report our development of ductile iron-base LRO alloys for fusion reactor first wall and blanket applications.

The LRO alloys are prepared based on the alloy system $(Fe,Ni)_3V$, containing 30-40% Ni and 22-23% V (by weight). The base alloys are also modified with less than 1% Ti for further improvement in metallurgical and mechanical properties. The alloys can be easily fabricated and welded by conventional techniques. We found that the phase relation in the LRO alloys depends strongly on the nickel concentration. The σ phase is observed in the alloys with lower nickel concentration at temperatures above the critical ordering temperature (T_c). The formation of σ phase in the alloys is not desirable, because, in some cases, the retention of the σ phase below T_c lowers the ductility and weakens atomic order in the alloys. The σ phase region can be completely eliminated by increasing nickel content to ≥40%. This observation is in agreement with the prediction from the PHACOMP procedure, which is commonly used to predict the stability of σ phase in superalloys.

Tensile properties of the base and titanium-modified LRO alloys were determined at room and elevated temperatures. The results obtained from the base alloy LRO-20 (Fe-40 Ni-23 V) and the titanium-modified alloy LRO-37 (Fe-40 Ni-22 V-0.4 Ti) indicate that the yield strength of the LRO alloys increases with test temperature and reaches a maximum in the vicinity of T_c. As a result the ordered alloys are much stronger than conventional alloys such as type 316 stainless steel. The ductility of the base alloy decreases with temperature and reaches a minimum of 14.5% near T_c. In comparison, the ductility of the titanium-modified alloy is much less dependent on temperature and shows only a moderate drop near T_c. Thus, alloying with titanium additions improves the ductility of the iron-base alloys at elevated temperatures.

The LRO alloys show excellent creep resistance and structural stability. Long-term aging at 500°C does not cause any significant change in the tensile properties of the LRO alloys at room and elevated temperatures. Creep properties of the LRO alloys were determined as a function of stress at 650°C. The creep rate of the LRO alloys is lower than that of the annealed type 316 stainless steel by more than 3 orders of magnitude.

Detailed characterization of irradiation and swelling behavior, lithium corrosion, and fatigue properties has been carried out at ORNL and Rensselaer Polytechnic Institute (RPI). The study to date has demonstrated the promising metallurgical and mechanical properties of the LRO alloys for fusion reactor first wall and blanket applications.

9.1.26 *Abstract of* Rapidly Solidified Long-Range-Ordered Alloys[26]

E. H. Lee, C. C. Koch, C. T. Liu

The influence of rapid solidification processing on the microstructure of LRO alloys in the $(Fe,Co,Ni)_3V$ system has been studied by TEM. The main microstructural feature of the as-quenched alloys was a fine cell structure (~300 nm in diameter) decorated with carbide particles. This structure was maintained after annealing treatments which develop the ordered crystal structure. Other features of the microstructures both before and after annealing are presented and discussed.

9.1.27 *Summary of* The Effect of Neutron Irradiation on the Tensile Properties of Long-Range-Ordered Alloys[27]

D. N. Braski

Postirradiation tensile tests were conducted on specimens of two different LRO alloys that had been irradiated in the Oak Ridge Research Reactor (ORR) at temperatures of 250, 350, and 550°C, to a fluence producing 3.8 dpa and 19-29 appm He. The irradiation increased the yield strength or "hardened" the material, while the ultimate strength was decreased at all temperatures except 350°C. The ductility also decreased at all test temperatures, as evidenced by the reduction in uniform elongation and the appearance of areas of intergranular fracture in SEM fractographs. The reason for

the relatively high ductility of the specimens that were irradiated and tested at 350°C compared to those at either 250 or 550°C is not clear.

9.1.28 *Abstract of* The Microstructure of Ordered $(Co_{0.78}Fe_{0.22})_3V$ Alloy[28]

D. N. Braski, R. W. Carpenter, J. Bentley

The $(Co_{0.78}Fe_{0.22})_3V$ alloy belongs to a class of LRO alloys that is being developed for elevated temperature applications. The microstructure after quenching and after subsequent aging at temperatures between 700 and 800°C has been characterized by analytical electron microscopy. Short-range-order (SRO) and small VC matrix precipitate particles were observed in the as-quenched material. At 700°C VC precipitated discontinuously in grain boundaries and on extrinsic stacking faults. Aging at 800°C precipitated VC in grain boundaries and on extrinsic stacking faults and produced intrinsic stacking faults that were precipitate-free. Ordered domains grew upon aging at rates proportional to $t^{1/2}$; the activation energy for growth was 222 ± 20 kJ/mol. Thermal antiphase boundaries (APBs) had isotropic energies and (a/2)<110> displacement vectors. Intrinsic and extrinsic stacking faults also serve as APBs, with displacement vectors of (a/6)<112> and (a/3)<111>, respectively. Intrinsic faults had relatively high APB energies and interacted strongly with thermal APBs, while the reverse was true for extrinsic faults. Extrinsic stacking faults nucleated at VC particles in the matrix by punching out (a/2)[011] dislocations, which dissociated into Frank and Shockley dislocations. The Frank partial climbed away from the particle, and growth proceeded via the Silcock-Tunstall mechanism of alternate precipitation and climb of the Frank partial. Intrinsic stacking faults were also nucleated at VC particles, but the perfect dislocation around the particle dissociated into two Shockley partials: (a/2)[101] → (a/6)[112] + (a/6)[211]. Then the intrinsic fault grew by glide of the outer Shockley partial.

9.1.29 *Abstract of* The Microstructure and Mechanical Properties of $(Co,Fe,Ni)_3V$ Long-Range-Ordered Alloys[29]

D. N. Braski

A number of $(Co,Fe,Ni)_3V$ LRO alloys are being developed at ORNL for potential use at elevated temperatures. The alloys have yield strength values that increase rather than decrease with increasing temperature, show a high work-hardening rate, and have good fatigue properties. In addition, they have shown good resistance to radiation-induced swelling. The LRO alloys have a stable $L1_2$ ordered structure below their critical ordering temperatures, which vary from 700 to 1000°C depending on the alloy composition. In general, the alloys have low stacking fault energies and form stacking faults quite readily upon aging or with deformation. They contain VC particles which precipitate on grain boundaries, dislocations, and stacking faults. Both neutron and ion irradiation produced interstitial dislocation loops (Frank) which were also APBs. The introduction of APBs effectively reduced the size of the ordered domains. After a 4-MeV nickel ion irradiation (70 dpa) with simultaneous helium injection the LRO alloys had considerably less swelling than a type 316 stainless steel (20% CW) alloy irradiated under the same conditions.

9.1.30 *Abstract of* The Resistance of $(Fe,Ni)_3V$ Long-Range-Ordered Alloys to Neutron and Ion Irradiation[30]

D. N. Braski

A class of LRO alloys in the $(Fe,Ni,Co)_3V$ system is being developed at ORNL for possible use in future fusion reactors as well as other high temperature applications. These alloys exhibit high work-hardening rates, low creep rates, good resistance to fatigue, and excellent strength and ductility from room temperature to just below the critical ordering temperature, T_c (~670-950°C depending on the alloy). A unique property of the LRO alloys is their

increase in yield strength with increasing test temperature. Initial ion bombardment experiments on a $(Co,Fe)_3V$ alloy indicated that the LRO alloys were resistant to cavity swelling. This paper describes the effect of irradiation on the microstructure and other selected properties of several $(Fe,Ni)_3V$ LRO alloys which are being developed for first wall application. Three different types of bombarding particles have been employed for the irradiations: (1) 4-MeV nickel ions, (2) neutrons (ORR), and (3) 60-MeV alpha particles. The first two irradiations were used to evaluate the response of microstructure and/or mechanical properties to irradiation, while the third was an irradiation creep experiment.

The microstructures of a number of $(Fe,Ni)_3V$ LRO alloys have been characterized before and after ion bombardment which was designed to simulate fusion reactor exposure. Displacement damage was produced by 4-MeV ions; helium and deuterium ions were simultaneously injected at levels of 8 and 28 appm/dpa. Irradiation temperatures ranged from 525 to 680°C. The first alloy to be investigated was LRO-16, with a composition of 46% Fe, 31% Ni, and 23% V (by weight). Sigma phase formed in LRO-16 upon quenching from the solution-annealing temperatures of 1100 to 1200°C. Sigma phase formation was eliminated in a second alloy, LRO-20, by changing the iron and nickel concentrations to 37 and 40%, respectively. Small amounts of titanium (~0.4%) were added to both LRO-16 and -20 alloys to investigate their effect on radiation resistance. The unirradiated alloys contained VC particles in the matrix and at the grain boundaries. Those alloys with titanium additions also contained small amounts of a titanium-rich phase. After irradiation to 70 dpa, faulted interstitial loops, dislocations, and cavities were observed in all of the alloys. The dislocation density decreased with increasing irradiation temperatures, while the volume fraction of cavities, or swelling, increased with temperature. All of the LRO alloys irradiated below the critical ordering temperature of ~670°C maintained the ordered structure and demonstrated good resistance to swelling. The values of swelling were always less than 1%, about half the value measured for 20% CW type 316 stainless steel irradiated under identical conditions. The titanium addition reduced swelling for LRO-16 composition but had little effect on LRO-20. A redistribution of VC occurred during the irradiation.

Small tensile specimens of LRO-16 were irradiated in the ORR to 7 dpa at temperatures of 250, 350, and 550°C. Postirradiation tensile tests at the irradiation temperature showed that the yield strength increased while the ultimate strength decreased. Uniform elongation of ~15% was measured in specimens irradiated at 350°C, with lower uniform elongation (<4%) observed in specimens irradiated at 550°C. Uniform elongation of unirradiated material was ~28% at these temperatures. SEM fractography is in progress.

Irradiation creep under light ion bombardment was measured in one of the titanium-modified alloys. The specimen was loaded to a stress of 200 MPa and bombarded with 60-MeV alpha particles at 440 and 540°C. Bombardment at a damage rate of $\sim 2 \times 10^{-6}$ dpa/s was continued to a total damage level of ~0.2 dpa. The measured irradiation creep rates were nearly the same as those for 20% CW type 316 stainless steel tested under similar conditions.

These preliminary results are encouraging and warrant more extensive study of the potential of the LRO alloy classes. In addition to the attractive mechanical properties of the $(Fe,Ni)_3V$ alloys, they also appear to be resistant to radiation damage under conditions that partially simulate fusion reactor service.

9.1.31 *Summary of* Effect of Preinjected Helium on Swelling and Microstructure of Neutron-Irradiated Stressed Type 316 Stainless Steel[31]

A. Hishinuma, J. M. Vitek, J. A. Horak

In this period, examination was performed on pressurized tubes of 22% CW type 316 stainless

steel after irradiation at 525°C. The hoop stress was 31.7 MPa and the fluence was 5×10^{26} n/m^2 (>0.1 MeV) producing 23 dpa. Helium was preinjected into the center portion of the tube specimen to levels of 20 and 60 appm.

Diameter measurements, which include both swelling and creep effects, show that a 20-appm-He preinjected region expanded about 30% less than the uninjected regions. For a sample with 60 appm He, a 60% lower expansion was found.

The microstructure of a 60-appm-He preinjected region shows a bimodal cavity distribution. An inhomogeneous distribution of voids less than 50 nm in diameter is accompanied by a homogeneous population of tiny cavities, with a concentration near 10^{21} m^{-3}. In the uninjected region, a single distribution of cavities was observed with a number density of about 1×10^{20} m^{-3} and an average diameter of about 100 nm. Precipitates were observed in both regions. Almost all were η phase, with a number density of about 5×10^{19} m^{-3}.

9.1.32 *Abstract of* Swelling and Nickel Segregation Around Voids in Electron-Irradiated Fe-Cr-Ni Alloys[32]

A. Hishinuma, Y. Kazano, K. Shiraishi

The swelling dependence on nickel content in Fe-Cr-Ni ternary alloys irradiated by both ions and neutrons is well known, but the mechanism has not been fully understood. It is shown that the swelling in Fe-Cr-Ni alloys is related closely to the formation of void embryos with strain field contrast due to the segregation of solute atoms. In the present work we show experimentally the nickel dependence of the segregation and discuss effects of the segregation on the stabilization of the void embryos and, also, the nickel concentration dependence of the swelling.

Specimens used in this work were commercial austenitic alloys containing 12, 35, and 50 wt % nickel (type 316 stainless steel, Incoloy 800, Hastelloy-X) and high purity Fe-Cr-Ni alloys (HP12Ni, HP35Ni, HP50Ni) in which nickel contents correspond to the commercial alloys. These alloys were solution annealed and irradiated with 1-MeV electrons using a high voltage electron microscope (HVEM) in the temperature range of 350-600°C to a maximum dose of 30 dpa.

The void swelling of both commercial and high purity alloys decreases with increasing nickel content in the alloys. The swelling peak temperature in type 316 stainless steel irradiated to 30 dpa is about 570°C, and the swelling is about 14%. On the other hand, the swelling in Hastelloy-X is below 2% in the temperature range examined and the magnitude decreases with increasing irradiation temperature. The swelling in Hastelloy-X compared to that of type 316 stainless steel is very small at irradiation temperatures above 500°C. Similar results were observed in high purity alloys of HP12Ni and HP50Ni. A swelling peak of about 6% was observed in HP12Ni alloy irradiated at 600°C to a dose of 30 dpa, and the swelling decreased with decreasing irradiation temperature. No swelling was observed in the HP50Ni alloy irradiated at temperatures above 500°C. Peak swelling smaller than 1% was observed at 450°C in this alloy.

Comparing results at 550°C irradiation temperature, the void number density in Hastelloy-X was very small compared to that of type 316 stainless steel, but there was no large difference in the diameter of voids produced in type 316 stainless steel and Hastelloy-X. Similar results were also observed in high purity alloys; a large number of voids of about 1×10^{15} cm^{-3} and 2×10^{14} cm^{-3} were observed in HP12Ni alloys irradiated at 500 and 550°C respectively, but no voids were observed in HP50Ni alloy irradiated above 500°C. The results show that the nickel dependence of swelling corresponds not to average void diameter, but to void number density. In other words, the low swelling of nickel-base alloys at high irradiation temperatures above 500°C is caused by the small void number density produced.

A great number of void embryos with strain field contrast and a small number of dislocation loops were seen in HP12Ni alloy irradiated at 500°C in the initial stage of irradiation. In contrast with this, many dislocation loops and lines were observed in HP35Ni and HP50Ni alloys with very few void embryos of the type observed in HP12Ni alloy. Similarly, void embryos with strain field contrast were seen in type 316 stainless steel, but not in Incoloy 800 and Hastelloy-X. The void embryos in iron-base alloys nucleate in the initial stage of irradiation and grow to voids during subsequent irradiation, without an observed incubation period. These void embryos are very stable under irradiation and can grow with the help of dislocations, which are strongly biased sinks for interstitials. On the other hand, the voids in nickel-base alloys were observed after a long incubation period only when a high dislocation density was produced; the incubation dose of Hastelloy-X irradiated at 550°C was about 10 dpa. X-ray analysis results obtained with energy-dispersive spectroscopy (EDS) show that the strain field contrast around void embryos was caused by the segregation of nickel and the depletion of chromium.

The segregation of nickel around the voids gives rise to a shell of different properties than that of the matrix. These differences include the known smaller lattice parameter and shear modulus in the shell and possible differences in the diffusivities and relaxation volumes of vacancies and interstitials in the shell as compared to the matrix. It is hypothesized that these combined differences between the shell and the matrix give rise to an energy barrier that the point defects must overcome to be incorporated into the void. The net effect is that the energy barrier is larger for interstitials than for vacancies, so that the bare void, which has a preference for interstitials, when surrounded by a shell takes on a preference for vacancies.

From these results, the small swelling in nickel-base alloys compared to that in iron-base alloys is attributable to the small void number density. The void number density depends on the stability of void embryos under irradiation. The stability is caused by nickel segregation, which easily occurs in iron-base alloys and becomes increasingly difficult with increasing nickel content in Fe-Cr-Ni alloys.

9.1.33 *Abstract of* High Temperature Fatigue Behavior of Unirradiated V-15 Cr-5 Ti Tested in Vacuum[33]

K. C. Liu

For some fusion reactors which operate in a pulse mode, cyclic fatigue and crack growth may limit the service life of the first wall component. Refractory metal alloys would reduce these limitations, because of high temperature strength, good thermal conductivity, compatibility with liquid metal coolants, and apparent resistance to radiation damage. The thermal stress resistance, which is a function of thermal conductivity, thermal expansion coefficient, Poisson's ratio, modulus of elasticity, and yield strength, is generally several times better than stainless steel. This would allow higher operating temperature and therefore take advantage of increased thermal conversion efficiency or higher wall loading. Offsetting these advantages are high costs, lack of production capacity, environmental effects, and a limited database.

Candidate refractory metal alloys for fusion first wall application include V-15 Cr-5 Ti. This paper reports limited results of in-vacuum fatigue tests on this alloy at room temperature, 550°C, and 650°C. Miniature hourglass specimens with a gage diameter of 3.18 mm were used. The material was annealed 1 h in vacuum at 1200°C before machining, to produce an average grain size of ASTM No. 7. The specimens were stress relieved for 0.5 h at 1200°C after machining.

Tests were performed on a servocontrolled hydraulic testing system equipped with a vacuum chamber capable of pressures below 10^{-5} Pa. Specimens were heated by an induction heater,

maintaining temperatures within ±2°C of the test temperature during the test. A diametral extensometer was used, but axial strain calculated via a strain computer was used for machine control. A fully reversed triangular wave function beginning with compression was employed at a strain rate of 4×10^{-3} s^{-1} for all low cycle tests. High cycle testing was conducted initially in strain control but switched to load control after stable, essentially elastic cycling was established.

Results were obtained by in-vacuum fatigue tests on V-15 Cr-5 Ti at room temperature, 550°C, and 650°C. The data indicate that a power law relation between the total strain range and cycles to failure is appropriate.

A room temperature test conducted at a strain range of 0.6% was discontinued after 2×10^5 cycles; apparently this strain range was below the endurance limit at this temperature. All tests at room temperature demonstrated monotonic cyclic hardening as the number of cycles increased, whereas at 650°C some stress range stability was noted after initial hardening occurred.

The vanadium alloy data were compared to recently obtained vacuum fatigue data on 20% CW type 316 stainless steel tested at 430°C. The vanadium alloy data fell within the scatter band of stainless steel data in the low cycle range (life below 5×10^4). However, at strain ranges below 0.3% the vanadium alloy exhibited superior fatigue behavior in comparison to the stainless steel, which in earlier tests showed an apparent endurance limit at 0.35% strain. The endurance limit strain range for V-15 Cr-5 Ti tested at 650°C appears to be about a factor of 2 greater than this value.

Investigations at high temperature in the range below 0.9% strain are continuing. On the basis of existing data and the extrapolation, it appears that this alloy has potential value for fusion reactor applications. However, no conclusion can be made until more high temperature data become available for further evaluation.

9.1.34 *Abstract of* High Temperature Corrosion in Energy Systems[34]

R. A. Rapp, J. E. DeVan, D. L. Douglass, P. C. Gordine, F. S. Pettit, D. P. Whittle

At high temperatures, particularly in response to the unique environments associated with the conversion or combustion of fossil fuels, further fundamental studies of alloy reactions with mixed gaseous oxidants are required. Thermodynamic, phase equilibria, and diffusion data are lacking in part, and isotope and tracer studies have not been forthcoming. Corrosive thin films of salts and slags on the hardware of gas turbines, heat exchangers, fuel cells, and batteries cause an accelerated "hot corrosion." Thin film electrochemical studies for simple salts and alloys, and supporting thermodynamic studies (solubilities of solids and gases in salts), are required to understand the corrosion mechanism. The effects of several trace gaseous impurities (particularly chlorine), both on the growth and damaging of protective oxide scales and on the degradation of alloy mechanical properties, should be studied. High resolution, in situ SEM studies could prove fruitful in clarifying uncertain scale growth mechanisms.

New protective coating compositions must be found for specific corrosive environments, and more reliable but less expensive coating methods are required. Factors critical to the adhesion of oxide scales (e.g., -Al_2O_3 and Cr_2O_3) on alloys and the effects of trace alloying elements or dispersed second phases on scale adherence deserve further attention. The effect on gas alloy attack of solid deposits, either reactive or relatively inert, should be examined. Electrochemical studies should be made of alloy corrosion in deep salt melts or slags, where the gaseous environment is remote from the alloy surface. The role of grain boundaries in corrosion product scales as short-circuit transport paths for the outward diffusion of metal and the inward ingress of oxygen, sulfur, and carbon needs to be clarified. Erosion-corrosion interactions should be

studied, with attempts to define the types of coatings that are most resistant to such conditions. Particularly in solar applications, the role of thermal cycling and cyclic stressing on high temperature scaling (corrosion fatigue) needs to be studied. New methods for the monitoring of the concentrations of corrosive components, particularly sulfur and chlorine, in gaseous and fused salt environments require development. The influences of temperature gradients and heat fluxes on material compatibility, redistribution of chemical components, and properties of corrosion product layers need further study. High temperature corrosion-resistant alloys excluding the strategic metals chromium and cobalt need to be developed.

9.1.35 *Abstract of* The Sputtering Yield of Polycrystalline Materials[35]

P. P. Tortorelli, C. J. Altstetter

Measurements were made of the sputtering yield of polycrystalline niobium due to 15-keV argon ion bombardment. The cyrstallographic orientations of individual grains were carefully surveyed using selected area electron channeling patterns. It was demonstrated that the average yield behavior could be calculated from theory, provided allowance was made for ion channeling. The method for calculating yields can be applied to any combination of ion-polycrystalline target material provided the distribution of grain orientations (texture) is known.

9.1.36 *Abstract of* Corrosion and Compatibility Considerations of Liquid Metals for Fusion Reactor Applications[36]

P. P. Tortorelli, O. K. Chopra

Liquid metals have several potential applications in proposed fusion energy systems. Alkali metals, such as sodium and lithium, are efficient heat transfer media because of their excellent thermal transport properties, that is, their high thermal conductivity and heat capacity and the temperature range over which they are liquid. The tritium breeding properties of lithium make it especially attractive for applications in fusion reactors operating on the D-T cycle, while liquid lithium alloys, namely, Pb-Li eutectic and Li-Bi-Pb, provide tritium breeding as well as neutron multiplication. Finally, liquid metals such as lead or bismuth can be used for neutron multiplication in conjunction with solid tritium breeders.

The potential uses of liquid metals and alloys as a coolant and/or tritium breeding fluid, or as a neutron multiplier, require an evaluation of their compatibility with the containment material under conditions of interest for fusion reactors. The containment material must maintain its structural integrity under conditions of large temperature gradients, severe thermal cycling, and intense irradiation. In liquid metal heat transport systems, dissolution of the structural material results in mass transfer and deposition of corrosion products in the cold regions of the loop with consequent heat exchanger fouling, flow restrictions, and other related problems. The compositional and microstructural changes due to selective dissolution and intergranular corrosion can lead to degradation of the material.

This paper reviews the current understanding of the corrosion, chemistry, and environmental effects on materials behavior associated with the use of liquid metals in fusion reactors and is primarily concerned with chemical compatibility and the influence of fusion-related liquid metals and alloys on the mechanical properties of structural materials. The mechanisms and kinetics of the corrosion processes in liquid systems are examined and their influence on material degradation is discussed. Compatibility concerns arising from use of lead or bismuth are reviewed relative to fusion applications. A brief overview of other possible problems related to the use of liquid metals in fusion reactors, such as the compatibility of a lithium or lithium alloy breeding fluid with water or other coolants, is also presented.

9.1.37 *Abstract of* Effect of Nickel Concentration on the Mass Transfer of Fe-Ni-Cr Alloys in Lithium[37]

P. F. Tortorelli, J. H. DeVan

Because of its excellent heat transfer properties and its ability to generate tritium through interactions with fusion-produced neutrons, molten lithium has been considered as a coolant and/or tritium breeding fluid in fusion reactors. It is therefore important to characterize the corrosion resistance of potential containment materials to circulating lithium. Of concern is the loss of structural integrity by lithium dissolution and the possible restriction of flow by mass transfer deposits. To this end, thermal convection loops were used to study the corrosion and mass transfer of selected Fe-Ni-Cr alloys in slowly moving lithium (~20 mm/s). Data were obtained for three alloys with different Fe-Ni-Cr ratios: type 316 stainless steel and two fusion developmental alloys composed of 64 Fe-25 Ni-10 Cr-1 Mo (wt %) and 56 Fe-30 Ni-12 Cr-3 Mo (wt %). Coupons of all three alloys were exposed to lithium flowing between 500°C and approximately 325°C. The type 316 stainless steel specimens were enclosed in a loop fabricated of type 316 stainless steel, while the specimens of the other two alloys were inserted side by side into an alloy 800 [46 Fe-32 Ni-21 Cr (wt %)] loop. Both loops operated for approximately 3000 h. Comparison of the weight losses of the coupons in the dissolution zones of these loops indicated that the corrosion rates were directly proportional to the nickel concentration of the respective alloys. For example, the weight loss rate at 500°C of type 316 stainless steel (12% Ni) was 3.8 mg/m^2·h, and that of the 25% and 30% nickel alloys was 7.9 and 11.6 mg/m^2·h, respectively. Metallographic examinations of selected loop coupons showed that the type and extent of attack on the two higher nickel alloys were similar to those on type 316 stainless steel despite their higher dissolution rates. All three alloys exhibited porous near-surface layers that were between 15 and 20 μm in depth. The layers were produced by the selective removal of chromium and nickel with concomitant enrichment of iron. It appeared that the enhanced weight loss of the 30% nickel alloy, relative to the 25% nickel material, could be correlated with a higher volume fraction of porosity, thereby suggesting that the higher the starting nickel content of the alloy, the greater the volume of nickel removed from the alloy by the lithium.

The average near-surface concentrations of the major elements of the coupons in the alloy 800 loop were determined by x-ray fluorescence. These results showed that the degree of nickel and chromium depletion increased with increasing temperature in the loop's hot leg with an average surface layer concentration of about 3% nickel at 500°C for both alloys.

The observed corrosion effects are related to the respective tendencies for chromium, nickel, and iron to dissolve and deposit in the presence of a thermal gradient in a molten lithium system. The results from this study indicate that the corrosion rates in lithium of Fe-Cr-Ni alloys containing >25% nickel are significant at 500°C. However, any benefits of improved corrosion resistance gotten from reducing the nickel concentration of an alloy must be compared with effects on other important material properties, such as strength or resistance to neutron radiation damage.

9.1.38 *Abstract of* Corrosion of Type 316 Stainless Steel in Molten LiF-LiCl-LiBr[38]

P. F. Tortorelli, J. H. DeVan, J. R. Keiser

A LiF-LiCl-LiBr salt has been proposed as a solvent for extracting tritium from a lithium blanket. The salt is directly contacted with a side stream of lithium, separated, and processed to remove the extracted tritium. Consequently, the corrosion of type 316 stainless steel by flowing (about 15-mm/s) LiF-LiCl-LiBr was studied to determine whether compatibility with the structural material

would be limiting in such a system. The studies were conducted in a thermal convection loop designed to allow specimens of the steel to be cycled in and out of both heated and cooled legs without severely disrupting the flow of the salt. Loop operation was terminated after more than 8000 h of coupon exposure to LiF-LiCl-LiBr flowing between 540 and 470°C. The corrosion rate up to about 2700 h was low: 1.6 mg/m^2-h (~2 μm/y). At that time 0.8 g of lithium metal was added to 6.5 kg of salt in the loop to simulate processing conditions, and the weight loss increased dramatically during the next few hundred hours. This can probably be attributed to free lithium in the loop acting as a mass transport vehicle rather than to an effect of lithium on the corrosion behavior of the salt. The effect was temporary, however, and after an additional 1500 h the corrosion rate decreased to 0.4 mg/m^2-h (~0.5 μm/y).

Details of the change in weight loss behavior were correlated with changes in the salt chemistry using controlled potential voltametry. Microstructural changes of the near-surface regions of exposed coupons were characterized by optical metallography and electron microprobe analysis.

The results from this study indicate that type 316 stainless steel has a low corrosion rate (<2 μm/y) in slowly flowing LiF-LiCl-LiBr. The effect of free lithium in the salt is to increase the dissolution rate so that it is nearer to that of type 316 stainless steel exposed to flowing lithium. At the proposed operating temperature (≤500°C), however, it appears that type 316 stainless steel has acceptable compatibility with the tritium processing salt LiF-LiCl-LiBr.

9.1.39 *Abstract of* Corrosion Inhibition in Systems of Lithium with Nickel-Bearing Alloys[39]

P. F. Tortorelli, J. H. DeVan, J. E. Selle, H. D. Upton

Molten lithium, which is being considered for use as a tritium breeding fluid and/or coolant in fusion reactors, could dissolve enough of the first wall that loss of structural integrity and flow restrictions by mass transfer deposits could become serious problems during the reactor lifetime. Nickel-base alloy 600 corroded much more rapidly in lithium than type 316 stainless steel. Adding about 5% aluminum to the lithium before testing dramatically reduced the corrosion. The aluminum in the lithium reacted with the nickel in the alloys to form a surface intermetallic layer that was significantly more corrosion-resistant than the original material. Such a procedure decreased the maximum corrosion rate of type 316 stainless steel at 600°C in flowing lithium by a factor of 5 and also inhibited the dissolution of alloy 600 in static lithium between 500 and 700°C. Tests with type 316 stainless steel in static lithium defined the dependence of the aluminum reaction on time and temperature. In addition, silicon and possibly manganese could be used as corrosion-reducing additives. This method of corrosion inhibition is particularly attractive because of its ease of implementation since the reaction layers can be produced in situ.

9.1.40 *Abstract of* Compatibility of Fe-Cr-Mo Alloys with Static Lithium[40]

P. F. Tortorelli, J. H. DeVan, R. M. Yonco

The interactions between Fe-Cr-Mo alloys (2¼ Cr-1 Mo steel and Sandvik HT9) and static lithium were studied by means of weight changes, tensile properties, carbon concentrations in the lithium, and optical metallography. The principal result of such exposures was decarburization of 2¼ Cr-1 Mo steel by the lithium, particularly at the highest exposure temperature (600°C). A higher chromium content (11.3%) steel, HT9, did not decarburize under similar 500°C exposure conditions. In addition to chromium content of the steel, carbon transfer was found to depend on the exposure temperature and the steel's initial heat treatment (that is, the relative stability of the carbides in the steel). Exposure of

2¼ Cr-1 Mo steel to Li-5 Al resulted in a loss of the steel's tensile ductility.

9.1.41 *Abstract of* Chemical Aspects of Controlled Nuclear Fusion[4,1]

J. E. DeVan, E. R. Ihle, C. F. Knight, E. R. Kowalska, V. A. Maroni, S. Nasu, J. D. Sovereil, E. Roth

The current status of fusion chemistry was reviewed and priorities were identified for future work related to chemical aspects of fusion technology. The highest priority will be given to work in support of the International Tokamak Reactor (INTOR) program. This work should include ceramic breeder development, the technology of coolants for the breeder, and chemical aspects of plasma-first wall interactions and hydrogen-materials interactions. Priorities for longer-term objectives were also considered.

9.1.42 *Abstract of* Damage Structure in Nimonic PE16 Alloy Ion Bombarded to High Doses and Gas Levels[4,2]

K. Farrell, N. H. Packan

The Nimonic PE16 alloy in solution-treated and aged condition was bombarded simultaneously with nickel ions and alpha and deuteron beams at 625°C to doses of 80-313 dpa at He/dpa = 10 and D/dpa = 25. Microstructural changes consisted of the introduction of dislocations and of cavities and the redistribution of γ' precipitates to these defects. Cavitational swelling remained below 1%. Cavities were represented by several distinct size classes, the smaller ones believed to be gas bubbles and some larger ones associated with preferred growth of precipitates. Formation of bubbles at grain boundaries and large cavities at incoherent twins intensified the possibility of mechanical separation of interfaces under high gas irradiation conditions.

9.1.43 *Abstract of* Tensile Properties and Microstructure of Helium-Injected and Reactor-Irradiated V-20 Ti[4,3]

M. P. Tanaka, E. E. Bloom, J. A. Horak

Among the refractory metals, the alloy vanadium-20% titanium (V-20 Ti) is one of the potential candidate materials for fusion reactor structural components. This alloy is highly resistant to neutron damage, maintains good mechanical strength at temperatures to about 700°C, and is compatible with lithium. Major questions relating to the use of this alloy as a fusion reactor structural material include the effect of helium, transmuted by an intense high energy neutron flux, on the ductility and the swelling.

Sheet specimens of V-20 Ti were injected with alpha particles at the Oak Ridge Isochronous Cyclotron (ORIC) to helium contents of 90 and 200 appm. After the injection, the tensile specimens were irradiated in row 7 of EBR-II to a fluence of about 3×10^{26} n/m^2 (>0.1 MeV), corresponding to about 17 dpa, at temperatures of about 400, 575, and 700°C, either in static sodium or in helium. After neutron irradiation, the microstructures were characterized by TEM; tensile tests were conducted at the respective irradiation temperatures and fracture surfaces were examined by SEM.

The following observations have been made.

(1) Above 600°C the ductility was reduced by helium; the reduction becomes larger with increasing helium content.

(2) A further reduction in high temperature ductility occurred following neutron irradiation; above about 600°C, the fracture mode becomes intergranular. The degree of embrittlement and intergranular fracture again depended on the amount of injected helium.

(3) Cavity formation was observed in pre-injected and irradiated specimens. No cavities were observed in uninjected control specimens except for the specimen which was irradiated at 400°C.
(4) The size and number density of cavities depended on the amount of injected helium.

The results show a clear effect of helium on the evolution of the damage microstructure, the temperature dependence of swelling, and the high temperature ductility and fracture mode of the V-20 Ti alloy. Transmutation-produced helium can be expected to play a major role in the irradiation behavior of this and similar alloys in the fusion environment.

9.1.44 *Summary of* Effect of Heat Treatment Variations on 9 Cr-1 MoVNb and 12 Cr-1 MoVW Ferritic Steels[44]

J. M. Vitek, R. L. Klueh

The effects of variations in the heat treatment of 9 Cr-1 MoVNb and 12 Cr-1 MoVW have been evaluated. Dissolution of carbides during austenitization was found to be somewhat faster in 9 Cr-1 MoVNb than in 12 Cr-1 MoVW. The effect of cooling rate after austenitization was strongly dependent on the austenitization time and temperature. The 9 Cr-1 MoVNb alloy structure was found to be more sensitive to cooling rate than the structure of 12 Cr-1 MoVW. Under some circumstances, furnace cooling of 9 Cr-1 MoVNb after austenitizing resulted in a ferrite plus carbide structure rather than a martensite lath structure, and in addition the carbide was not the same as that formed during tempering. The precipitation reactions in both alloys are essentially complete after tempering 1 h at 650°C. In 12 Cr-1 MoVW the principal carbides are chromium-iron-rich $M_{23}C_6$ and vanadium-rich MC, whereas those in 9 Cr-1 MoVNb were chromium-iron-rich $M_{23}C_6$ and niobium-vanadium-rich MC.

9.2 IRRADIATION EXPERIMENTS

9.2.1 *Abstract of* Radiation Facilities for Fusion Reactor First Wall and Blanket Structural Materials Development[45]

R. L. Klueh, E. E. Bloom

Present and future irradiation facilities for the study of fusion reactor irradiation damage are reviewed. Present studies are centered on irradiation in accelerator-based neutron sources, fast- and mixed-spectrum fission reactors, and ion accelerators. The accelerator-based neutron sources are used to demonstrate damage equivalence between high energy neutrons and fission reactor neutrons. Once equivalence is demonstrated, the large volume of test space available in fission reactors can be used to study displacement damage and, in some instances, the effects of high helium concentrations on properties. Ion bombardment can be used to study the mechanisms of damage evolution and the interaction of displacement damage and helium. These techniques are reviewed, and typical results obtained from such studies are examined. Finally, future techniques and facilities for developing damage levels that more closely approach those expected in an operating fusion reactor are discussed.

9.2.2 *Abstract of* Neutronics Calculations for the Conceptual Design of an In-Reactor Solid Breeder Experiment, Trio-01[46]

R. L. Childs, T. A. Gabriel, R. A. Lillie

Neutronics calculations have been performed to obtain tritium production and heat generation rates for the irradiation of solid tritium breeding materials in the ORR. Two breeder materials, Li_2O and $LiAlO_2$, were considered. Burnup calculations were performed to estimate the amount of ^6Li present as a function of time.

9.2.3 *Abstract of* Spectral Tailoring for Fusion Radiation Damage Studies: Where Do We Stand?[47]

T. A. Gabriel, R. A. Lillie, K. Thoms, R. L. Childs

The radiation damage of the first wall of a D-T fired fusion reactor is one of the quantities limiting the feasibility of these machines. The damage parameters of interest in this paper are the dpa and helium production (appm) levels. For a type 316 stainless steel first wall and a 14-MeV neutron wall loading of 1 MW/m^2, the anticipated annual levels for these parameters are 10 and 140, respectively, for a typical fusion device. Since there currently exist no experimental data that represent these damage levels, the purpose of this work is to present a method that is being used to yield in real time the necessary damage information.

Fourteen-MeV neutron generators can yield the correct He/dpa ratio, but the time frame to obtain the high dpa and gas production levels precludes total reliance on data obtained in this fashion. Also, the amount of irradiated material tends to be quite limited. Fast reactors can yield in short times high dpa levels for large samples, but only low helium production levels via direct fast neutron interactions. Thermal reactors can also yield high dpa levels in large samples and, if the alloy under consideration contains nickel, high gas levels via the thermal neutron reactions

$$Ni^{58} + n_{th} \rightarrow Ni^{59} ; \quad Ni^{59} + n_{th} \rightarrow Fe^{56} + \alpha$$

are obtainable. Therefore, if some control over the thermal and fast flux can be accomplished, thermal reactors may be used to irradiate nickel-bearing alloys to obtain within a reasonable time frame the desired dpa and helium production levels.

The ORR is currently being used to irradiate an experiment (MFE-4A) containing type 316 stainless steel (and PCA). The anticipated dpa and helium production levels are expected to closely resemble fusion reactor levels. As of August 26, 1980, 1.1-dpa and 3.3-appm-He levels were reached.

During the initial phase of irradiation, increased thermal fluxes and decreased fast fluxes are required to initiate the two-step alpha production reactions and to reduce the dpa rate, respectively. These spectral changes are being accomplished by using an ORR core piece around the experiment which is 63% water and 37% aluminum. During later irradiations, the core piece will be 100% aluminum so that the two-step alpha production rate can be reduced and the dpa rate increased. Eventually, larger reductions of the thermal flux (up to 85% of normal) and increases in the fast flux will be necessary. These changes will be accomplished by surrounding the samples with various thicknesses of hafnium, which has a large thermal neutron capture cross section, and by increasing the average fuel loading around the experiment.

By March 31, 1982, the samples will have reached the 10-dpa and 140-appm He levels and some samples will be removed for analysis. The remaining samples plus some additional samples will be returned to the reactor for more irradiation. It is currently hoped to irradiate the samples to at least the 50-dpa and 700-appm-He levels.

9.2.4 *Abstract of* Simulation Irradiation Studies on Iron[48]

E. Kuramoto, N. Yoshida, N. Tsukuda, K. Kitajima, N. H. Packan, M. B. Lewis, L. K. Mansur

Four-MeV nickel ion irradiation was performed for pure iron up to 50 dpa between 350°C and 500°C with and without simultaneous helium ion injection to simulate and understand the fundamental irradiation behaviors of ferritic stainless steels in fusion environment. Results were compared with those from electron- (HVEM), neutron-, and proton-irradiated pure

iron specimens. Voids were observed in nickel-ion-irradiated iron at 450°C and 500°C for both single and dual beam irradiation, but no voids were observed at 350°C and 400°C. A number of small vacancy type dislocation loops were observed at 350°C and 400°C especially along dislocation lines. It is considered that these small loops are tightly connected to cascade formation and contribute to suppress void formation at low temperatures.

9.2.5 *Abstract of* Effects of Pulsed Dual Ion Irradiation on Microstructural Development[49]

H. H. Packan

The effect of pulsed irradiation on the development of microstructure during nickel ion bombardment has been investigated in a simple austenitic alloy similar to type 316 stainless steel. Bombardment conditions were 10 dpa, 940 K, pulsing with equal on/off times of either 0.5 or 60 s, and the addition of 20 appm He/dpa to some specimens either by room temperature preimplantation or by dual beam coimplantation. Particular care was taken to minimize thermal pulses from beam heating (to <2°C). The results show that pulsing has a subtle influence, and the effects on specific cavity parameters are complex. Pulsing produced a small increase in swelling in the helium-free case, but a slight decrease for helium-implanted specimens, and it seems to have counteracted the usual stimulative effects of helium on cavity nucleation. An assessment is made of the often conflicting observations in the literature; there is a need for further, well-controlled experiments.

9.2.6 *Abstract of* The Production Rate of Helium During Irradiation of Nickel in Thermal-Spectrum Fission Reactors[50]

F. W. Wiffen, E. J. Allen, H. Farrar IV, E. E. Bloom, T. A. Gabriel, H. T. Kerr, P. G. Perey

For alloys with nickel as a major component, irradiation in mixed-spectrum fission reactors produces a range of displacement damage and helium levels that can overlap a large part of the range calculated for fusion reactor service conditions. Irradiations in the HFIR have produced a data set adequate to define equations that give the total helium production. The data are for total neutron fluences of 0.09 to 3.09×10^{27} n/m^2, yielding helium contents of 34 to 6108 appm. The primary source of helium is the reaction sequence with thermal neutrons:

$$^{58}Ni(n,\gamma)^{59}Ni \; ; \qquad ^{59}Ni(n,\alpha)^{5}\,Fe \; .$$

Examination of the available cross sections for these reactions and for other reactions that compete for ^{58}Ni and ^{59}Ni showed that the data are best fit when the 2200-m/s cross section for the second reaction is 11.60 ± 1.08 barn. The resulting helium production equation is:

$$\frac{N(He)}{N(Ni\text{-}58)} = 0.12608 - 0.13272 \exp(-4.6\phi_t) + 0.00664 \exp(-92\phi_t) \; ,$$

where ϕ_t is the conventional 2200-m/s fluence of thermal neutrons, in units of neutrons per barn. This equation also gives a good fit to available experimental data from the literature.

9.2.7 *Summary of* Experiment HFIR-MFE-T3 for Low Temperature Irradiation of Miniaturized Charpy V-Notch Specimens of Nickel-Doped Ferritic Steels[51]

J. M. Vitek, J. W. Woods

The HFIR-MFE-T3 experimental capsule is described. This experiment consists of miniature Charpy V-notch specimens of 12 Cr-1 MoVW and 12 Cr-1 MoVW-2 Ni alloys. The different levels of nickel will result in different helium levels generated during irradiation and thus will allow for an evaluation of the effect of helium on impact properties. Irradiation of the capsule has started with projected fluence at midplane that will produce 10 dpa expected by January 1982.

9.2.8 Summary of Experiments HFIR-MFE-RB1, -RB2, and -RB3 for Low Temperature Irradiation of Path E Ferritic Steels[52]

J. M. Vitek, J. W. Woods

The HFIR-MFE-RB1, -RB2, and -RB3 experiments are planned for low temperature irradiation of a variety of specimen types of ferritic steels to approximately 10 and 20 dpa. The final specimen matrices for RB1 and RB2 are given, along with a preliminary matrix for RB3. Also given are details on the alloys included and their conditions. Assembly of the RB1 and RB2 capsules is presently underway. Irradiation of the RB1 capsule was planned to start in November 1981, and irradiation of RB2 is expected to begin about January 1982.

9.2.9 Abstract of Fission-Fusion Correlations for Swelling and Microstructure in Stainless Steels: Effect of the Helium to Displacement Per Atom Ratio[53]

D. R. Odette, P. J. VanDen, E. A. Goldstaal

The initial irradiated structural materials database for fusion applications will be developed in fission reactors. Hence, these data may need to be adjusted using physically based procedures to represent behavior in fusion environments, viz., fission-fusion correlations. Such correlations should reflect a sound mechanistic understanding and be verified in facilities which most closely simulate fusion conditions. In this paper we review the effects of only one of a number of potentially significant damage variables, the helium to dpa ratio, on microstructural evolution in austenitic stainless steels. Dual ion and helium preinjection data are analyzed to provide mechanistic guidance; these results appear to be qualitatively consistent with a more detailed comparison made between fast-spectrum (EBR-II) and mixed-spectrum (HFIR) neutron data for a single heat of 20% CW type 316 stainless steel. These two fission environments bound fusion He/dpa ratios. A model calibrated to the fission reactor data is used to extrapolate to fusion conditions. Both the theory and broad empirical observation suggest that He/dpa ratios have both a qualitative and quantitative influence on microstructural evolution and that the very high and low ratios found in HFIR and EBR-II may not result in behavior which brackets intermediate fusion conditions.

9.3 DAMAGE ANALYSIS AND DOSIMETRY: *ABSTRACT OF* THE REFLECTION OF LOW ENERGY HELIUM ATOMS FROM TUNGSTEN SURFACES[54]

M. T. Robinson

The interactions of low energy ions with solid surfaces play an important role in divertor design and performance as well as in other areas of fusion technology. Experimental information is very difficult to obtain because most backscattered particles are neutral. Consequently, considerable reliance has been placed on calculations to supply the needed information. A small amount of experimental information has recently become available on the interactions of ^3He and ^4He ions with monocrystalline tungsten targets at energies below 1.5 keV and, in some cases, below 100 eV. The availability of these data inspired the present computations

The trajectories of incident helium ions, slowing down in tungsten crystals, were constructed in the binary collision approximation (BCA) using the computer code MARLOWE (version 11.5). The atomic scattering was based on the Moliere potential with the Firsov screening length. Inelastic energy losses proportional to the particle velocity were based on the nonlocal LSS model. The incident particles were considered to be stopped when their kinetic energies fell below a value E_c, except for those particles colliding near the surface. These were followed below E_c until they either escaped the target or turned inward. Changing E_c from 5 eV to 2 eV produced insignificant changes in the results for incident kinetic energies greater than about 50 eV. Only below 30 eV were significant numbers of particles emitted with kinetic energies of $<E_c$. Results

below 100 eV are based on sets of 5000 incident particles uniformly distributed over the target surface; above 100 eV, 1000 particles were used. Several studies were made of the differences between ^{3}He and ^{4}He ions, but only a small isotope effect was found. Although the inelastic stopping cross section of ^{3}He is 12% greater than that of ^{4}He at the same energy, the slowing-down is controlled mainly by the elastic stopping cross section which is essentially the same for these isotopes. The smallness of the isotope effect is also in general agreement with the limited experimental data. In the remaining calculations, therefore, only ^{4}He ions were used.

Some of the low energy experiments were performed on field ion microscope specimens. These took the form of monocrystal fibers with <110> axes and hemispherical tips about 30 nm in radius. Thus, the ions were incident at a variety of angles, although always along <110> crystal directions. In addition, because of lateral spreading of the beam, an excess loss of particles through the lateral target surfaces could occur. Computations were performed at 100 eV and 300 eV for ions incident along <110> on a variety of different crystal faces. Using these calculations as a basis, a plausible description of the experiments can be given. The experimental statistics (typically, about 100 helium atoms were involved in each observation) and uncertainties about the behavior of atoms very close to the surface preclude a more satisfying conclusion.

Other calculations were performed for 10-eV to 100-eV ions normally incident on both <110> and polycrystalline tungsten. Even at 10 eV, only about 80% of the ions are reflected from the {110} surface, and this value changes only slightly below about 70 eV. This appears to be a result of subsurface channeling. Such behavior is not important in polycrystalline targets where total reflection occurs at about 5 eV. However, at energies as low as 10 to 20 eV, those incident particles which are not reflected are stopped so close to the target surface (<0.5 nm) that they are likely to desorb athermally. This effect, for which there is some experimental evidence, is not included in the MARLOWE model.

The energy spectrum of backscattered ^{4}He atoms at the lowest energies resembles a single scattering distribution, shifted to somewhat lower energies by inelastic effects. At energies near 100 eV, a more complicated structure appears in the spectrum of particles scattered from <110> targets, in which both quasi-single and plural scattering are evident. Quasi-single scattering does not occur from polycrystalline targets because of their more irregular surface structures. At all energies, the angular distributions are peaked significantly toward the surface normal, as compared with a cosine distribution, especially from the <110> surfaces. This is the result of the strong surface scattering of the low energy emergent particles. Such surface scattering is less important from polycrystals.

9.4 INSULATORS AND STABILIZERS FOR SUPERCONDUCTING MAGNETS

9.4.1 *Summary of* Magnet Materials Studies in the Solid State Division, ORNL[55]

R. R. Coltman, C. E. Klabunde

Insulators

(1) Mechanical, electrical, and several other property changes have been studied on several filled epoxies after gamma ray irradiation at 4.9 K to doses of 2×10^8, 2.4×10^9, and 1×10^{10} rad.

(2) Mechanical and electrical properties of unfilled and glass-filled polyimides have been studied after irradiation at 4.9 K to 1×10^{10} rad. (This work is now in progress.)

Stabilizers

Using the limited data available on the magnetoresistance of irradiated copper and aluminum, analyses have been made which predict total resistivities at various magnet locations in a tokamak. (Neutronics calculations are by Santoro et al.) Further experimentation is planned.

9.4.2 *Abstract of* Organic Insulators and the Copper Stabilizer for Fusion Reactor Magnets[56]

R. R. Coltman, Jr.

The materials which compose the large composite superconducting fusion reactor magnets are subjected to mechanical stress, neutron and gamma ray radiation with broad energy spectra, high magnetic fields, and thermal cycling from 4 to 300 K. Of the materials now considered for use in the magnets results show that the organic insulators and the copper stabilizer are the most sensitive to this environment. In response to the need for stabilizer data, magnetoresistivity changes were studied in eight variously prepared specimens of copper throughout five cycles of an alternate neutron irradiation (4.0 K) and annealing (14 h at 307 K) program. The results were combined with those on the radiation behavior of epoxy and polyimide organic insulators to provide a preliminary assessment of their comparative radiation resistance in a typical magnet location of the Experimental Power Reactor (EPR). It was found that insofar as the chosen conditions typify the mix of gamma ray and neutron dose rates in fusion reactor magnet locations, the radiation resistance of the stabilizer is at best equal to that of the epoxies and much less than that of the polyimides. The poor performance of the copper stabilizer suggests that additional shielding for magnet protection or serious magnet design changes are needed. Several needs for further organic insulator and stabilizer research are described.

9.4.3 *Abstract of* Rates of Defect Production by Fission Neutrons in Metals at 4.7 K[57]

R. R. Coltman, Jr., C. E. Klabunde, J. M. Williams

As part of an interlaboratory program, we have measured the resistivity damage rates at 4.7 K for the dilute alloys, V-300 ppm Zr, Nb-300 ppm Zr, and Mo-300 ppm Zr, irradiated by virtually unmoderated fission neutrons. In addition, aluminum, nickel, copper, and stainless steel have also been measured to provide a broader database for comparison with other experimental work using a variety of neutron spectra and with defect production theory. A broad view of the results shows that the ratio of experimentally to theoretically determined production rates (damage efficiencies) for various fast neutron spectra ranges from about 0.25 to 0.50. On the other hand, for a given element various neutron energy spectra peaked from 1 to 15 MeV give variations in damage efficiency values of only 7-30%.

9.4.4 *Abstract of* A Fission Neutron Source for the Study of Defect Production in Metals[58]

C. E. Klabunde, J. M. Williams, R. R. Coltman, Jr.

A fission neutron source for the study of defect production in metals at 4.7 K has been constructed for use in the ORNL Low Temperature Irradiation Facility (LTIF). The source is in the form of a highly enriched ^{235}U ribbon which generates 8 W of heat power and is operated in liquid helium in the sample chamber of the LTIF. It provides a fission neutron flux of 5.7×10^{15} n/m^2-s to adjacent 0.025-mm-thick ribbon-shaped specimens. A surrounding thin-walled superconducting solenoid provides magnetic fields up to 1.3 T to suppress superconductivity in specimens when needed for resistivity measurements.

9.4.5 *Abstract of* Mechanical Strength of Low-Temperature-Irradiated Polyimides: A Five- to Ten-fold Improvement in Dose Resistance over Epoxies[59]

C. F. Klabunde, R. R. Coltman, Jr.

A program is under way at ORNL to study the irradiation behavior of organic insulating material that may be used in the construction of large superconducting coils that provide magnetic containment for the plasma in a fusion reactor. The use of such materials

provides an economical method for producing not only electrical insulation, but also mechanical support needed in coil construction. Although many studies on the effects of radiation on organic insulators exist, there are very few studies on the most recently developed materials or on the simultaneous effects of radiation and low temperatures. Recent calculations by B. A. Engholm show that without additional protective shielding even the first test reactors such as the FED will produce lifetime doses at insulator locations that exceed the radiation tolerance of glass-fiber-filled epoxies in present use. For these reasons, new irradiations were carried out in the ORNL LTIF on pure and glass-filled polyimide materials. The superior radiation resistance of pure polyimides at room temperature has been known for some years.

Only recently, however, have bulk glass-filled polyimides become available. These materials have the strengths needed in magnet construction. After a gamma ray irradiation dose of 100 MGy (10^{10} rad) at 5 K, the losses in flexural and compressive strength measured at 78 K were less than 40%, and at 300 K slight increases were observed. These data, combined with measurements made after two other smaller doses, yield strength-versus-dose curves, which will be presented. Earlier studies for the same dose and irradiation conditions showed that there is virtually no degradation of electrical properties in polyimides. Overall, the glass-fiber-filled polyimide materials are 5 to 10 times more radiation-resistant than glass-fiber-filled epoxy materials. We can estimate by comparing the present results with Engholm's calculations that the use of glass-filled polyimide materials as magnet insulators in the FED can lead to designs for shields and magnet coils that are economically acceptable.

REFERENCES

1. J. L. Scott, M. L. Grossbeck, and P. J. Maziasz, "Radiation Effects in Materials for Fusion Reactors," invited paper presented at American Vacuum Society 28th National Symposium, Anaheim, California, November 3-6, 1981 (proceedings to be published).
2. J. L. Scott, E. E. Bloom, R. E. Gold, M. L. Grossbeck, J. J. Holmes, P. J. Maziasz, T. C. Reuther, Jr., S. M. Rosenwasser, and F. W. Wiffen, "Progress in the Development of the Blanket Structural Material for Fusion Reactors," in *The Technology of Controlled Nuclear Fusion, Proceedings of the Fourth Topical Meeting*, F. H. Tenney and C. C. Hopkins, eds., CONF-801011, Oak Ridge, Tennessee (July 1981), pp. 1661-72.
3. J. L. Scott, "Fusion Reactor Materials: M325/01088," invited chapter for *Encyclopedia of Materials Science and Engineering*, to be published by Pergamon Press Ltd., Oxford, England, in 1982.
4. R. E. Gold, E. E. Bloom, F. W. Clinard, Jr., D. L. Smith, R. D. Stevenson, and W. G. Wolfer, "Materials Technology for Fusion: Current Status and Future Requirements," Nucl. Technol./Fusion 1(2), 169-237 (1981).
5. J. L. Straalsund and E. E. Bloom, "Swelling, Creep, and Mechanical Properties of First Wall and Structural Alloys," invited paper presented at the Second Topical Meeting on Fusion Reactor Materials, Seattle, Washington, August 9-12, 1981 (proceedings in press).
6. M. L. Grossbeck and K. C. Liu, "High Temperature Fatigue Life of Type 316 Stainless Steel Containing Irradiation-Induced Helium," paper presented at the Second Topical Meeting on Fusion Reactor Materials, Seattle, Washington, August 9-12, 1981 (proceedings in press).
7. M. L. Grossbeck and P. J. Maziasz, "Tensile Properties of a Titanium-Modified Type 316 Stainless Steel Irradiated in a Mixed-Spectrum Fission Reactor," paper presented at the Second Topical Meeting on Fusion Reactor Materials, Seattle, Washington, August 9-12, 1981 (proceedings in press).

8. F. W. Wiffen and P. J. Maziasz, "The Influence of Neutron Irradiation at 55°C on the Properties of Austenitic Stainless Steels," paper presented at the Second Topical Meeting on Fusion Reactor Materials, Seattle, Washington, August 9-12, 1981 (proceedings in press).
9. E. H. Lee, A. F. Rowcliffe, and L. K. Mansur, "Precipitation and Cavity Formation in Austenitic Stainless Steels during Irradiation," paper presented at the Second Topical Meeting on Fusion Reactor Materials, Seattle, Washington, August 9-12, 1981 (proceedings in press).
10. R. L. Klueh and J. M. Vitek, "Tensile Properties of Ferritic Steels After Low-Temperature HFIR Irradiation," in *Alloy Development for Irradiation Performance Quarterly Progress Report for Period Ending March 31, 1981*, DOE/ER-0045/6, Oak Ridge, Tennessee (July 1981), pp. 139-47.
11. P. J. Maziasz and M. L. Grossbeck, "Swelling, Microstructural Development and Helium Effects in Type 316 Stainless Steel Irradiated in HFIR and EBR-II," paper presented at the Second Topical Meeting on Fusion Reactor Materials, Seattle, Washington, August 9-12, 1981 (proceedings in press).
12. P. J. Maziasz and T. K. Roche, "Preirradiation Microstructural Development Designed to Minimize Properties Degradation during Irradiation in Austenitic Alloys," paper presented at the Second Topical Meeting on Fusion Reactor Materials, Seattle, Washington, August 9-12, 1981 (proceedings in press).
13. A. D. Brailsford and L. K. Mansur, "The Effect of Precipitate-Matrix Interface Defect Sinks on the Growth of Voids in the Matrix," paper presented at the Second Topical Meeting on Fusion Reactor Materials, Seattle, Washington, August 9-12, 1981 (proceedings in press).
14. W. A. Coghlan and L. K. Mansur, "Characteristics of Irradiation Creep: The First Wall of a Fusion Reactor," paper presented at the Second Topical Meeting on Fusion Reactor Materials, Seattle, Washington, August 9-12, 1981 (proceedings in press).
15. M. R. Hayns and L. K. Mansur, "Applications of the Theory of Cavity Growth to Dual-Ion Swelling Experiments," in *Special Technical Publication 725*, American Society for Testing and Materials, Philadelphia, Pennsylvania, 1981, pp. 213-30.
16. J. A. Horton, S. M. Ohr, and W. A. Jesser, "TEM Observations of Crack Propagation in Metals Containing Helium Bubbles," paper presented at the Second Topical Meeting on Fusion Reactor Materials, Seattle, Washington, August 9-12, 1981 (proceedings in press).
17. L. L. Horton, J. Bentley, and W. A. Jesser, "The Microstructure of 'Triple-Beam' Ion Irradiated Fe and Fe-Cr Alloys," paper presented at the Second Topical Meeting on Fusion Reactor Materials, Seattle, Washington, August 9-12, 1981 (proceedings in press).
18. L. L. Horton, J. Bentley, and W. A. Jesser, "The Depth Distribution of Displacement Damage in α-Iron under 'Triple Beam' Ion Irradiation," paper presented at the Second Topical Meeting on Fusion Reactor Materials, Seattle, Washington, August 9-12, 1981 (proceedings in press).
19. R. L. Klueh, "Chromium-Molybdenum Steels for Fusion Reactor Applications," in *Trans. 6th Int. Conf. Structural Mechanics in Reactor Technology* (Elsevier North-Holland Inc., New York, 1981), p. M3/1 1-9.
20. R. L. Klueh, J. M. Vitek, and M. L. Grossbeck, "Effect of Low-Temperature Irradiation with (n,α) Helium Production on Tensile Properties of 12 Cr-1 MoVW-Type Steels," paper presented at the Second Topical Meeting on Fusion Reactor Materials, Seattle, Washington, August 9-12, 1981 (proceedings in press).

21. R. L. Klueh and J. M. Vitek, "Tensile Properties of Ferritic Steels After Low-Temperature HFIR Irradiation," in *Alloy Development for Irradiation Performance Semiannual Progress Report for Period Ending September 30, 1981*, DOE/ER-0045/7, Oak Ridge, Tennessee (1982), pp. 275-83.
22. L. K. Mansur and W. A. Coghlan, "Theoretical Relationships Between Creep and Swelling Rates by Point Defect Absorption During Irradiation," invited paper presented at Yamada Conference V on Point Defects and Defect Interactions in Metals, Kyoto, Japan, November 16-20, 1981 (proceedings in press).
23. L. K. Mansur, W. A. Coghlan, T. C. Reiley, and W. G. Wolfer, "Irradiation Creep by Cascade-Induced Point Defect Fluctuations," paper presented at the Second Topical Meeting on Fusion Reactor Materials, Seattle, Washington, August 9-12, 1981 (proceedings in press).
24. C. T. Liu, "Physical Metallurgy and Structural Applications of Ductile Ordered Alloys $(Ni,Co,Fe)_3V$," invited paper to be published in *International Metals Reviews* (1982).
25. C. T. Liu, "Development of Iron-Base Long-Range Ordered (LRO) Alloys for Fusion Reactor First Wall and Blanket Applications," paper presented at the Second Topical Meeting on Fusion Reactor Materials, Seattle, Washington, August 9-12, 1981 (proceedings in press).
26. E. H. Lee, C. C. Koch, and C. T. Liu, "Rapidly Solidified Long Range Ordered Alloys," paper presented at Symposium on Rapidly Solidified Amorphous and Crystalline Alloys, Boston, Massachusetts, November 17-19, 1981 (proceedings to be published).
27. D. N. Braski, "The Effect of Neutron Irradiation on the Tensile Properties of Long-Range-Ordered Alloys," in *Alloy Development for Irradiation Performance Quarterly Progress Report for Period Ending March 31, 1981*, DOE/ER-0045/6, Oak Ridge, Tennessee (1981), pp. 116-24.
28. D. N. Braski, R. W. Carpenter, and J. Bentley, *The Microstructure of Ordered $(Co_{0.78}Fe_{0.22})_3V$ Alloy*, ORNL/TM-7702, Oak Ridge, Tennessee (1981).
29. D. N. Braski, "The Microstructure and Mechanical Properties of $(Co,Fe,Ni)_3V$ Long-Range-Ordered Alloys," invited seminar at NASA Langley Research Center, Hampton, Virginia, June 19, 1981.
30. D. N. Braski, "The Resistance of $(Fe,Ni)_3V$ Long-Range-Ordered Alloys to Neutron and Ion Irradiation," paper presented at the Second Topical Meeting on Fusion Reactor Materials, Seattle, Washington, August 9-12, 1981 (proceedings in press).
31. A. Hishinuma, J. M. Vitek, and J. A. Horak, "Effect of Preinjected Helium on Swelling and Microstructure of Neutron Irradiated Stressed Type 316 Stainless Steel," in *Alloy Development for Irradiation Performance Semiannual Progress Report for Period Ending September 30, 1981*, DOE/ER-0045/7, Oak Ridge, Tennessee (1982), pp. 48-53.
32. A. Hishinuma, Y. Katano, and K. Shiraishi, "Swelling and Nickel Segregation Around Voids in Electron-Irradiated Fe-Cr-Ni Alloys," paper presented at the Second Topical Meeting on Fusion Reactor Materials, Seattle, Washington, August 9-12, 1981 (proceedings in press).
33. K. C. Liu, "High Temperature Fatigue Behavior of Unirradiated V-15% Cr-5% Ti Tested in Vacuum," paper presented at the Second Topical Meeting on Fusion Reactor Materials, Seattle, Washington, August 9-12, 1981 (proceedings in press).
34. R. A. Rapp, J. H. DeVan, D. L. Douglass, P. C. Nordine, F. S. Pettit, and D. P. Whittle, "High Temperature Corrosion in Energy Systems," Mater. Sci. Eng. 50(1), 1-17 (1981).

35. P. F. Tortorelli and C. J. Altstetter, "The Sputtering Yield of Polycrystalline Materials," in Radiat. Eff. 51, 241-8 (1980).

36. P. F. Tortorelli and O. K. Chopra, "Corrosion and Compatibility Considerations of Liquid Metals for Fusion Reactor Applications," invited paper presented at the Second Topical Meeting on Fusion Reactor Materials, Seattle, Washington, August 11, 1981 (proceedings in press).

37. P. F. Tortorelli and J. H. DeVan, "Effect of Nickel Concentration on the Mass Transfer of Fe-Ni-Cr Alloys in Lithium," paper presented at the Second Topical Meeting on Fusion Reactor Materials, Seattle, Washington, August 9-12, 1981 (proceedings in press).

38. P. F. Tortorelli, J. H. DeVan, and J. R. Keiser, "Corrosion of Type 316 Stainless Steel in Molten LiF-LiCl-LiBr," paper presented at the Second Topical Meeting on Fusion Reactor Materials, Seattle, Washington, August 9-12, 1981 (proceedings in press).

39. P. F. Tortorelli, J. H. DeVan, J. E. Selle, and H. D. Upton, "Corrosion Inhibition in Systems of Lithium with Nickel-Bearing Alloys," in *Proc. 8th Symp. on Engineering Problems of Fusion Research* (Institute of Electrical and Electronics Engineers, Inc., New York, 1979), pp. 1610-13.

40. P. F. Tortorelli, J. H. DeVan, and R. M. Yonco, "Compatibility of Fe-Cr-Mo Alloys with Static Lithium," in J. Mater. Energy Syst. 2, 5-15 (1981).

41. J. H. DeVan, H. R. Ihle, C. F. Knights, H. R. Konvicka, V. A. Maroni, S. Nasu, J. D. Navratil, and E. Roth, "Chemical Aspects of Controlled Nuclear Fusion," in At. Energy Rev. 18, 553-74 (1981).

42. K. Farrell and N. H. Packan, "Damage Structure in Nimonic PE16 Alloy Ion Bombarded to High Doses and Gas Levels," paper presented at the Second Topical Meeting on Fusion Reactor Materials, Seattle, Washington, August 9-12, 1981 (proceedings in press).

43. M. P. Tanaka, E. E. Bloom, and J. A. Horak, "Tensile Properties and Microstructure of Helium Injected and Reactor Irradiated V-20 Ti," paper presented at the Second Topical Meeting on Fusion Reactor Materials, Seattle, Washington, August 9-12, 1981 (proceedings in press).

44. J. M. Vitek and R. L. Klueh, "Effect of Heat Treatment Variations on 9 Cr-1 MoVNb and 12 Cr-1 MoVW Ferritic Steels," in *Alloy Development for Irradiation Performance Semiannual Progress Report For Period Ending September 30, 1981*, DOE/ER-0045/7, Oak Ridge, Tennessee (1982), pp. 263-74.

45. R. L. Klueh and E. E. Bloom, "Radiation Facilities for Fusion Reactor First Wall and Blanket Structural Materials Development," invited paper presented at Seminar on Radiation Behavior on Materials and Its Impact on Fusion Reactor Design, Paris, France, August 25-26, 1981; see also ORNL-5830 (December 1981).

46. R. L. Childs, T. A. Gabriel, and R. A. Lillie, "Neutronic Calculations for the Conceptual Design of an In-Reactor Solid Breeder Experiment, Trio-01," to be published in Nuclear Technology (preprinted as ORNL/TM-7758, March 1981).

47. T. A. Gabriel, R. A. Lillie, K. Thoms, and R. L. Childs, "Spectral Tailoring for Fusion Radiation Damage Studies: Where Do We Stand?", paper presented at the Second Topical Meeting on Fusion Reactor Materials, Seattle, Washington, August 9-12, 1981 (proceedings in press).

48. E. Kuramoto, N. Yoshida, N. Tsukuda, K. Kitajima, N. H. Packan, M. B. Lewis, and L. K. Mansur, "Simulation Irradiation Studies on Iron," paper presented at the Second Topical Meeting on Fusion Reactor Materials, Seattle, Washington, August 9-12, 1981 (proceedings in press).

49. N. H. Packan, "Effects of Pulsed Dual-Ion Irradiation on Microstructural Development," paper presented at the Second Topical Meeting on Fusion Reactor Materials, Seattle, Washington, August 9-12, 1981 (proceedings in press).

50. F. W. Wiffen, E. J. Allen, H. Farrar IV, E. E. Bloom, T. A. Gabriel, H. T. Kerr, and F. G. Perey, "The Production Rate of Helium During Irradiation of Nickel in Thermal Spectrum Fission Reactors," to be published in Journal of Nuclear Materials.

51. J. M. Vitek and J. W. Woods, "Experiment HFIR-MFE-T3 for Low-Temperature Irradiation of Miniaturized Charpy V-Notch Specimens of Nickel-Doped Ferritic Steels," in *Alloy Development for Irradiation Performance Semiannual Progress Report for Period Ending September 30, 1981*, DOE/ER-0045/7, Oak Ridge, Tennessee (1982), pp. 36-59.

52. J. M. Vitek and J. W. Woods, "Experiment HFIR-MFE-T3, -RB2, and -RB3 for Low-Temperature Irradiation of Path E Ferritic Steels," in *Alloy Development for Irradiation Performance Semiannual Progress Report for Period Ending September 30, 1981*, DOE/ER-0045/7, Oak Ridge, Tennessee (1982), pp. 30-35.

53. G. R. Odette, P. J. Maziasz, and J. A. Spitznagel, "Fission-Fusion Correlations for Swelling and Microstructure in Stainless Steels: Effect of the Helium to Displacement Per Atom Ratio," invited paper presented at the Second Topical Meeting on Fusion Reactor Materials, Seattle, Washington, August 9-12, 1981 (proceedings in press).

54. Mark T. Robinson, "The Reflection of Low Energy Helium Atoms from Tungsten Surfaces," paper presented at the Second Topical Meeting on Fusion Reactor Materials, Seattle, Washington, August 9-12, 1981 (proceedings in press).

55. R. Coltman and C. Klabunde, "Magnet Materials Studies in the Solid State Division, ORNL," in *Proceedings of the Meeting on Electrical Insulators for Fusion Magnets*, CONF-801237 (U.S. Department of Energy, November 1981), pp. 16.1-16.13.

56. R. R. Coltman, Jr., "Organic Insulators and the Copper Stabilizer for Fusion Reactor Magnets," invited paper presented at the International Conference on Neutron Irradiation Effects, Argonne National Laboratory, Argonne, Illinois, November 9-12, 1981 (to be published in Journal of Nuclear Materials).

57. R. R. Coltman, Jr., C. E. Klabunde, and J. M. Williams, "Rates of Defect Production by Fission Neutrons in Metals at 4.7 K," J. Nucl. Mater. 99, 284-93 (1981).

58. C. E. Klabunde, J. M. Williams, and R. R. Coltman, Jr., "A Fission-Neutron Source for the Study of Defect Production in Metals," J. Nucl. Mater. 99, 294-305 (1981).

59. C. E. Klabunde and R. R. Coltman, Jr., "Mechanical Strength of Low-Temperature-Irradiated Polyimides: A Five-to-Tenfold Improvement in Dose Resistance over Epoxies," paper presented at the Second Topical Meeting on Fusion Reactor Materials, Seattle, Washington, August 9-12, 1981 (proceedings in press).

10. NEUTRON TRANSPORT

R. G. Alsmiller, Jr.[1]

J. M. Barnes[2]
G. T. Chapman[1]
J. K. Dickens[1]
R. A. Lillie[1]
B. F. Maskewitz[1]
F. J. Muckenthaler[1]
E. M. Oblow[1]
R. W. Peelle[1]
R. W. Roussin[1]
R. T. Santoro[1]
J. S. Tang[2]
D. K. Trubey[1]

1. Engineering Physics Division.
2. UCC-ND Computer Sciences.

10. NEUTRON TRANSPORT

ABSTRACT. The neutron transport program includes both experimental and analytic phases. The experimental program is designed to provide (1) data necessary for verifying the analytic methods and (2) cross-section data used at ORNL and throughout the United States for fusion reactor neutronics design calculations. Experiments are being carried out to determine the neutron transport in typical fusion reactor shield materials and configurations and to determine the effects of penetrations in these shields. The analytic program supports the design of the integral experiments and compares calculated data with data obtained experimentally. Neutronics calculations were also carried out in support of the Engineering Test Facility (ETF) design. Finally, the Radiation Shielding Information Center (RSIC) has continued to supply a broad range of services to the fusion energy research community.

10.1 *ABSTRACT OF* CALCULATED NEUTRON AND GAMMA-RAY ENERGY SPECTRA FROM 14-MeV NEUTRONS STREAMING THROUGH AN IRON DUCT: COMPARISON WITH EXPERIMENT[1]

R. T. Santoro, R. G. Alsmiller, Jr., J. M. Barnes, G. T. Chapman, J. S. Tang

Integral experiments that measure the streaming of ~14-MeV neutrons through a 0.30-m-diam iron duct (length-to-diameter ratio ~3) imbedded in a concrete shield have been carried out at ORNL. Calculated and measured neutron and gamma-ray energy spectra are compared at 16 detector locations on and off the cylindrical axis of the duct. The measured spectra were obtained using an NE-213 liquid scintillator detector with pulse-shape discrimination to simultaneously resolve neutron and gamma-ray events. The calculated spectra were obtained using a computer code network that incorporates two radiation transport methods: discrete ordinates (with P_3 multigroup cross sections) and Monte Carlo (with continuous point cross sections). The two radiation transport methodologies are required to properly account for neutrons that single scatter from the duct to the detector. The calculated and measured outgoing neutron energy spectra above 850 keV agree within 5-50%, depending on detector location and neutron energy. The calculated and measured gamma-ray spectra above 750 keV are also in favorable agreement, ~5-50%, depending on detector location and gamma-ray energy.

10.2 *ABSTRACT OF* CALCULATION OF NEUTRON AND GAMMA-RAY SPECTRA FOR FUSION REACTOR SHIELD DESIGN: COMPARISON WITH EXPERIMENT II[2]

R. T. Santoro, R. G. Alsmiller, Jr., J. M. Barnes, G. T. Chapman

Measured and calculated neutron and gamma-ray energy spectra resulting from the transport of ~14-MeV neutrons through a 0.30-m-thick lithium hydride slab and through a 0.05-m-thick lead slab followed by 0.30 m of lithium hydride are compared. Also reported are comparisons of the measured and calculated neutron energy spectra behind a 0.80-m-thick assembly composed of type 304 stainless steel and borated polyethylene. The spatial dependence of the gamma-ray energy deposition rate, measured using thermoluminescent detectors, is compared with calculated data.

The calculated data obtained using two-dimensional (2-D) radiation transport methods and ENDF/B-IV cross-section data are in good agreement for all of the experimental configurations. Calculated integral neutron energy spectra agree with the measured data within ~5% to ~20%, depending on neutron energy for the lithium hydride and the lead plus lithium hydride assemblies. The gamma-ray spectra agree within 20% for these slabs. The measured and calculated neutron energy spectra behind the type 304 stainless steel plus borated polyethylene assembly agree within ~5%, except

at neutron energies below ~5 MeV, where background radiation influences the measured spectra. The gamma-ray energy deposition rates as a function of depth agree within a factor of 2 at all detector locations.

10.3 *ABSTRACT OF* CALCULATIONAL PROCEDURES FOR THE ANALYSIS OF INTEGRAL EXPERIMENTS FOR FUSION REACTOR DESIGN[3]

R. T. Santoro, J. M. Barnes, R. G. Alsmiller, Jr., E. M. Oblow

The calculational models, nuclear data, and radiation transport codes that are used in the analysis of integral measurements of the transport of ~14-MeV neutrons through laminated slabs of materials typical of those found in fusion reactor shields are described. The 2-D discrete ordinates calculations to optimize the experimental configuration for reducing the neutron and gamma-ray background levels and for obtaining an equivalent, reduced geometry of the calculational model to reduce computer core storage and running times are also presented. The equations and data to determine the energy-angle relations of neutrons produced in the reactions of 250-keV deuterons in a titanium-tritide target are given. The procedures used to collapse the 171n-36$_\gamma$ VITAMIN-C cross-section data library to a 53n-21$_\gamma$ broad group library are described. Finally, a description of the computer code network used to obtain neutron and gamma-ray energy spectra for comparison with measured data is included. The network incorporates several 2-D discrete ordinates codes to treat first collisions (GRTUNCL), multiple collisions (DOT), and last collisions (FALSTF) of the neutrons and gamma rays in the transport sequence from the neutron source to the detector.

10.4 *ABSTRACT OF* FLUNG: COUPLED 35-GROUP NEUTRON AND 21-GROUP GAMMA-RAY, P_3 CROSS SECTIONS FOR FUSION APPLICATIONS[4]

R. T. Santoro, R. W. Roussin, J. M. Barnes

A 35-neutron, 21-gamma-ray, P_3 cross-section library for 63 nuclides is described. The library, called FLUNG (Fusion Library for Unshielded Neutron-Gamma-Ray Transport), was derived from the VITAMIN-C general-purpose fine group library and is useful for the neutronic analysis of fusion reactors and other applications.

10.5 *ABSTRACT OF* DOSE RATES FROM THE INDUCED ACTIVITY IN THE ETF NEUTRAL BEAM INJECTOR[5]

R. T. Santoro, J. M. Barnes, R. A. Lillie, R. G. Alsmiller, Jr.

The dose equivalent rates outside the ETF neutral beam injector (NBI) shield from the induced radioactivity have been calculated for the reactor operating at 1140 MW for 1, 30, and 365 days. The dose rates at 1 day after shutdown are large even after 1 day of operation. Depending on the location and operating time, cooling times from 30 days to ~5 years are required before the dose rates are sufficiently low to allow routine maintenance work in the vicinity of the NBI shield.

10.6 *ABSTRACT OF* ISO-RESPONSE CONTOURS IN THE ETF NEUTRAL BEAM INJECTORS[6]

J. M. Barnes, R. T. Santoro, R. A. Lillie, R. G. Alsmiller, Jr.

Iso-response contours in the ETF neutral beam injector have been calculated for the neutron flux, nuclear heating in type 316 stainless steel and G10 insulation, biological dose rate, and the $^{58}Ni(n,p)^{58}Co$ and

$^{59}Co(n,\gamma)^{60}Co$ reactions. The spatial dependence of these responses in the injector, in the shielding that surrounds it, and in the injection duct is presented.

10.7 NEUTRONICS EXPERIMENTS AND ANALYSIS AT THE TFTR

J. K. Dickens, R. T. Santoro, K. O. Alsmiller, Jr., F. J. Muckenthaler, R. W. Peelle

The Tokamak Fusion Test Reactor (TFTR) will be the first operating tokamak fusion reactor that has substantial neutron flux; therefore, it seems reasonable that as much information as possible on neutronics design data and methods be obtained from this reactor. A program has been initiated to carry out neutronics experiments at the TFTR and to obtain comparisons between these experimental data and state-of-the-art neutronics calculations. The TFTR will operate on a deuterium-deuterium (D-D) cycle for some time before deuterium-tritium (D-T) operation will commence. During D-D operation a small fraction (~3%) of the neutrons will be produced by D-T reactions, and this will make it possible to obtain data during D-D operation on the high energy neutrons produced by D-T reactions.

The experimental program adopted for the purpose of obtaining neutron flux measurements during a TFTR pulse was initiated. The most difficult aspects of the experimental program are the design and fabrication of the fast scintillator detector system. The first design of the detector involves a shaped piece of NE-110 solid plastic mounted on a quartz light pipe connected to a photomultiplier tube. For this detector concept, a working electronic schematic was developed. The most important component requiring further development is the fast-timing amplifier. An existing state-of-the-art ORNL design was studied to determine whether its count rate could be extended to 5×10^6 counts/s. A new, faster amplification circuit was developed and when tested on the bench fulfills the times required to obtain this count rate. The filtering circuit was also developed using computer simulation methods. The breadboard package of filtering circuits and amplification circuits has been assembled, but the assembly has not been tested as a unit.

As part of the analysis program, the modeling of the TFTR and test cell building using the combinatorial geometry package of the MORSE[7] code was initiated. The reactor vessel, toroidal field coils, poloidal coils, and some of the support structure were represented. The components were modeled in sufficient detail to take proper account of their presence in radiation transport calculations without compromising computer code running times. The toroidal vacuum vessel was described using toroidal geometry descriptors that were added to the MORSE code.[8]

10.8 RADIATION SHIELDING INFORMATION CENTER

R. W. Roussin, B. F. Maskewitz, D. K. Trubey

The RSIC serves an international community by responding to inquiries about radiation transport problems. RSIC staff members provide guidance by drawing on a technical database that includes a computerized literature file, a collection of complex computer programs, and a substantial body of nuclear data libraries, pertinent to the solution of such problems.

Acquiring the needed computer-based technology base requires the collaboration of the neutronics community with RSIC staff members to collect, organize, process, evaluate, and package relevant technology developed in the community. This technology is disseminated

throughout the community with a mechanism for feedback of experience through usage, which results in an improved product. The resulting technology base provides an overall advancement of the state of the art. The following examples of this information cycle process are newly available and relevant to fusion neutronics. A processing code system (RSIC code package PSR-157/PUFF2[9]) for producing multigroup covariance files was contributed by ORNL. A sensitivity and uncertainty analysis system (CCC-405/SENSIT[10]), used in fusion neutronics studies, was provided by Los Alamos National Laboratory (LANL). Two multigroup cross-section data libraries, packaged as DLC-86/FLUNG[4] and DLC-87/HILO[11] and developed at ORNL for fusion and high energy neutronics, were added to the collection. Both of these were derived from the general-purpose fine group data library DLC-41/VITAMIN-C[12] developed at ORNL. Another data library (DLC-84/MENSLIB[13]), developed at LANL for high energy neutronics, was included. Contributions from the international community include PSR-160/ENBAL2,[14] a code package to generate multigroup neutron kerma factors, from the University of Birmingham, England; PSR-166/PREANG,[15] for calculating preequilibrium angular distributions for nuclear reactions, from the Netherlands Energy Research Foundation (ECN), Petten, the Netherlands; and CCC-410/THIDA,[16] a dose calculational system for a nuclear fusion facility, from the Japan Atomic Energy Research Institute, Tokai, Japan.

These examples represent a small portion of the total activity of the RSIC. Information processing (including evaluation and packaging) is a daily concern. In addition to a comprehensive literature database, RSIC-packaged products include 87 data packages (DLC), 413 neutronics and shielding code packages (CCC), and 167 data processing and other miscellaneous code packages (PSR).

REFERENCES

1. R. T. Santoro, R. G. Alsmiller, Jr., J. M. Barnes, G. T. Chapman, and J. S. Tang, *Calculated Neutron and Gamma Ray Energy Spectra From 14 MeV Neutrons Streaming Through an Iron Duct: Comparison with Experiment*, ORNL/TM-7878, Oak Ridge, Tennessee (1981).
2. R. T. Santoro, R. G. Alsmiller, Jr., J. M. Barnes, and G. T. Chapman, *Calculation of Neutron and Gamma-Ray Energy Spectra for Fusion Reactor Shield Design: Comparison with Experiment II*, ORNL/TM-7927, Oak Ridge, Tennessee (1981).
3. R. T. Santoro, J. M. Barnes, R. G. Alsmiller, Jr., and E. M. Oblow, *Calculational Procedures for the Analysis of Integral Experiments*, ORNL-5777, Oak Ridge, Tennessee (1981).
4. R. T. Santoro, R. W. Roussin, and J. M. Barnes, *FLUNG: Coupled 35-Group Neutron 21-Group Gamma Ray, P_3 Cross Sections*, ORNL/TM-7828, Oak Ridge Tennessee (1981).
5. R. T. Santoro, J. M. Barnes, R. A. Lillie, and R. G. Alsmiller, Jr., *Dose Rates From the Induced Activity in the ETF Neutral Beam Injector*, ORNL/TM-7999, Oak Ridge, Tennessee (1981).
6. J. M. Barnes, R. T. Santoro, R. A. Lillie, and R. G. Alsmiller, Jr., *Iso-Response Contours in the ETF Neutral Beam Injectors*, ORNL/TM-7783, Oak Ridge National Laboratory (1981).
7. M. B. Emmett, *The MORSE Monte Carlo Radiation Transport Code System*, ORNL-4972, Oak Ridge, Tennessee (1975).
8. M. Yamauchi, M. B. Emmett, R. T. Santoro, H. Iida, Y. Seki, and H. Narita, *Toroidal Geometry Subroutines for MORSE-CG*, ORNL/TM-8244 (in preparation).
9. J. D. Smith III, *Processing ENDF/B-V Uncertainty Data Into Multigroup Covariance Matrices*, ORNL/TM-7221, Oak Ridge, Tennessee (1980).

10. S. A. W. Gerstl, *SENSIT: A Cross Section and Design Sensitivity and Uncertainty Analysis Code*, LA-8498, Los Alamos National Laboratory, Los Alamos, New Mexico (1980).
11. R. G. Alsmiller, Jr., and J. Barish, *Neutron-Photon Multigroup Cross Sections for Neutron Energies <400 MeV*, ORNL/TM-7818, Oak Ridge, Tennesseee (1981).
12. R. W. Roussin, C. R. Weisbin, J. E. White, N. M. Greene, R. Q. Wright, and J. B. White, *VITAMIN-C: The CTR Processed Multigroup Cross Section Library for Neutronics Studies*, ORNL/RSIC-37, Oak Ridge, Tennessee (1980).
13. W. B. Wilson, *Nuclear Data Development and Shield Design for Neutrons Below 60 MeV*, LA-7159-T, Los Alamos National Laboratory, Los Alamos, New Mexico (1978).
14. N. P. Taylor, *ENBAL-2: A Programme to Generate Multigroup Neutron Kerma Factors*, Paper 81-02, University of Birmingham, Birmingham, England (1981).
15. J. M. Akkermans and H. Gruppelaar, *Calculation of the Preequilibrium Angular Distributions with the Exciton Model Code PREANG*, ECN-60, Netherlands Energy Research Foundation, Petten, the Netherlands (1979).
16. H. Iida, *THIDA: Dose Calculation System for a Nuclear Fusion Facility*, ORNL/tr-4713, Oak Ridge, Tennessee (1978) [JAERI-M 9319, Japan Atomic Energy Research Institute, Tokai, Ibaraki, Japan].

11. MANAGEMENT SERVICES

V. C. Kruzic, Section Head

S. K. Adkins
D. R. Alford
D. R. Baumgardner[1]
P. G. Beasley
B. J. Beem
W. C. Brock, Jr.
D. P. Brooks
J. L. Burke
E. L. Cagle[1]
C. H. Cox
M. W. Darnell[1]
K. M. Dobbs[1]
M. V. Dunn
R. S. Edwards
J. C. Ezell
D. A. Fisher
M. L. Fullard[1]
R. K. Gryder
J. R. Hickey[2]
D. M. Ivey
H. W. Jernigan
J. R. Jernigan*
R. P. Jernigan
B. L. Johnson[1]
C. H. Johnson[1]
D. Y. Johnson[1]
M. N. Johnson*
C. H. Jordan
J. B. Martin[1,*]
B. J. McDaniel[1]
J. H. McNeillie
J. C. Neeley[1]
L. A. Pollard*
P. L. Ray
E. M. Ruckart
W. K. Russell
R. C. Satterfield
S. R. Schwartz[1]
C. M. Sekula[1]
D. G. Sharp
L. A. Smith
S. E. Stockbridge[1]
B. L. Straine
C. S. Strickler[1,*]
C. K. Thomas
E. L. Watkin[1]
E. E. Webster[1]
E. R. Wells

*Part-time.

1. Information Division.
2. Finance and Materials Division.

11. MANAGEMENT SERVICES SECTION

ABSTRACT. The sole function of the Management Services Section is to support the programmatic research and development activities of the Fusion Energy Division. Areas of support are the following: general personnel administration; material and service procurements; subcontracting; national and international agreements coordination; nonprogrammatic engineering services for support systems and equipment; planning and coordination of general plant project and facility requirements; maintenance and machine shop work coordination; labor relations; telecommunications; financial management; automated management information systems; library services and resources; publication services, including editing, word processsing, graphics, photography, and reproduction; safety; emergency planning; and quality assurance. This support is provided through interpersonal relations with Fusion Energy Division programmatic personnel and through the coordination of support resources from a variety of disciplines outside the division.

11.1 OFFICE OF THE MANAGER FOR GENERAL ADMINISTRATION AND PROCUREMENT

The office of the manager is responsible for most of the general administrative functions of the Division.

11.1.1 Personnel Functions

During 1981, 73 prospective employees were interviewed for 26 positions. There were 20 acceptances out of 28 offers made. Three persons transferred into the Division from other UCC-ND divisions. Although 23 persons joined the Division during this report period, the net increase was only 3 because 20 persons retired, transferred out, or accepted positions with other organizations. Recruitment for nine positions was slowed because of delays in completion of the Large Coil Test Facility (LCTF).

Ten persons were employed through the ORNL summer program, and three persons worked in the Division under the Oak Ridge Associated Universities program. Guest assignments were processed for 70 scientific guests and subcontractor personnel.

11.1.2 Subcontracts

Industrial involvement through subcontracts in the Large Coil Program (LCP), the gyrotron development program, and the ELMO Bumpy Torus Proof-of-Principle (EBT-P) project was in excess of $15 million. This amount was very near (but did not exceed) the 1980 level because of uncertainty over funding for FY 1982 and some negotiating problems in the EBT-P project.

11.1.3 National and International Agreements

At the request of the Swiss delegation, the manager's office prepared administrative requirements that were added to the implementing agreements for the International Energy Agency (IEA) Large Coil Task (LCT). There was little activity in the exchange program with the U.S.S.R. The Japanese exchange involvement increased during the year.

The implementing agreement with Kernforschungszentrum Karlsrune (KfK) was changed to cover all fusion programs. Before this year, the only agreement with KfK for fusion work was the IEA agreement for the LCT.

Arrangements for other national laboratories and private firms to participate in the Fusion Engineering Design Center (FEDC) and the EBT-P project were continued.

11.1.4 Procurement

During 1981, the procurement group processed about 2000 purchase requisitions, representing a volume of over $10 million. Approximately 850 shipping requests were handled. A series

of information seminars was held for Division and Laboratory management to address the problems of procuring materials for fusion projects. Training sessions were held to help personnel assigned to the manager's office understand the finance and procurement interconnections in the Nuclear Division.

11.2 ENGINEERING SERVICES

The Engineering Services Group provides a coordinating service for all engineering work performed in the Division. This includes providing or directing the engineering for all nonprogrammatic work, coordinating maintenance and machine shop work, supervising the inventory and storage of materials, coordinating telecommunications, and overseeing all general plant project (GPP), general-purpose facility (GPF), line item, and general plant equipment (GPE) improvements. This group is also responsible for maintaining building facilities and planning future facilities. Some highlights of the 1981 activities follow.

- The renovation of the auditorium in Bldg. 9201-2 was completed.
- The new lunch room in Bldg. 9201-2 was completed.
- A stairway to the southeast roof of Bldg. 9201-2 was designed and installed.
- First-floor offices in Bldg. 9201-2 were renovated.
- The central stairway in Bldg. 3201-2 was upgraded.
- Design was started for a stock room lift, for third-floor office improvements, and for expansion of the computer facility in Bldg. 9201-2.
- Improvement of the west access and identification of the demineralized water piping were undertaken in Bldg. 9204-1.
- Work was started on a recall maintenance program for equipment and systems supporting Division activities.
- A walkway was installed in the basement of Bldg. 9204-1 to facilitate material storage.
- Contracting and construction of the FEDC building, which was built by a private contractor and leased for five years to ORNL, were coordinated.
- Staff were moved into the new FEDC building.
- A fence west of Bldg. 9204-1 was relocated and the drainage was improved.
- The fusion energy exhibits for the annual American Vacuum Society meeting were coordinated and presented.
- Work was started on exhibits for the 1982 World's Fair.
- Design was started on improved and more reliable electrical circuits for the pump house that supports research and development in Bldg. 9201-2.
- Renovation of the cooling tower that supports research and development in Bldg. 9201-2 was started.
- Shop fabrication at Y-12, X-10, K-25, and outside shops was coordinated. This work consisted of over 600 jobs and 40 personnel-years; approximately $2.5 million of work was coordinated, excluding LCTF and EBT-P fabrication.

11.3 FINANCE

The Finance Office is an integral part of the Management Services Section and provides financial management support for the Division's administrative, engineering, and research personnel in areas including budget preparation, cost scheduling, and variance analysis. This office also provides meaningful and appropriate accounting and cost control. Interaction with Division management is an essential part of administering the budget, accounting policies, and procedures.

As shown in Table 11.1 and Fig. 11.1, the funding trends for the Division and for the Fusion Program continue to exhibit growth. This trend creates a need for greater efficiency and improvement in specific areas of financial control. In this spirit, the Finance Office must be innovative in the development of financial techniques to meet the growing and changing financial needs of the Division.

Table 11.1 Fusion Program expense funding (in thousands of dollars)

Activity	FY 1979 actual cost	FY 1980 actual cost	FY 1981 actual cost	FY 1982 funding as of February 1982	FY 1983 budget submission	FY 1984 budget submission
Applied Plasma Physics						
Fusion Plasma Theory	$ 2,335	$ 2,269	$ 2,809	$ 2,984	$ 3,460	$ 3,280
Experimental Plasma Research	894	964	1,092	1,110	1,355	1,285
National MFE Computer Network	270	361	289	310	350	400
Total Applied Plasma Physics	$ 3,499	$ 3,585	$ 4,190	$ 4,404	$ 5,165	$ 5,565
Confinement Systems						
Toroidal Systems						
Research Operations	$ 7,481	$ 8,990	$ 9,875	$ 9,780	$10,600	$11,650
Major Device Fabrication	4,044	2,590	862	0	0	0
Magnetic Mirror Systems						
Research Operations	3,705	8,851	8,382	10,995	12,100	20,950
Total Confinement Systems	$15,230	$20,431	$19,119	$20,775	$22,700	$32,600
Development and Technology						
Magnetic Systems	$11,432	$10,276	$10,143	$11,100	$ 9,599	$ 7,746
Plasma Engineering	6,442	7,100	8,424	9,000	11,820	13,900
Fusion Reactor Materials	2,998	3,621	4,354	4,785	6,440	7,253
Fusion Systems Engineering	2,025	4,518	4,159	760	1,568	1,686
Environment and Safety	254	605	667	520	550	305
Fusion Energy Applications	0	12	0	0	0	0
Total Development and Technology	$23,151	$26,032	$27,747	$26,165	$29,977	$30,964
Center for Magnetic Fusion Engineering						
Design Effort	$ 0	$ 0	$ 0	$ 3,150	$ 4,020	$ 4,500
Program Direction						
Contractual Services and Supplies	$ 0	$ 0	$ 71	$ 0	$ 0	$ 0
TOTAL ORNL FUNDING	$41,880	$50,048	$51,076	$54,494	$61,842	$73,569

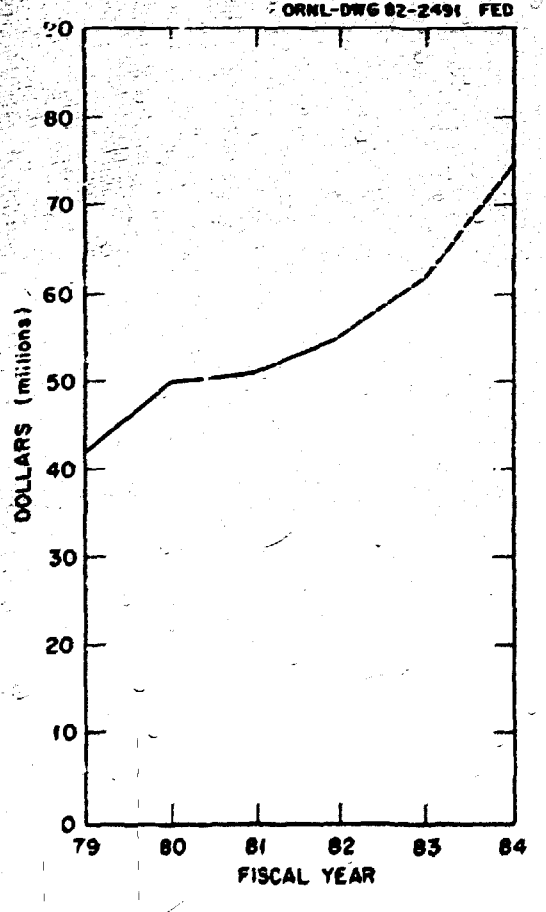

Fig. 11.1. Fusion Program funding history.

11.4 MANAGEMENT INFORMATION SYSTEM

The Division Management Information System (MIS) provides timely and relevant information on the schedules and costs of the Division's research activities. During 1981, the amount of information available has been extended through the addition of several databases that contain items of administrative importance.

The new databases include information on travel by Division staff members and on the status of Division work orders. The travel information makes it possible for a manager to determine who has traveled, what locations have been visited, and how much of a group's travel budget has been spent. The work order status database allows a manager to determine how much money has been spent during the current month, during the present fiscal year, and over the life of the project in question.

A new effort in 1981 was the study of the Division's word processing requirements and of the systems available to meet these needs. The study led to a recommendation that the Division install current technology systems for testing and evaluation but defer a full

implementation until it can be determined that the available equipment will meet the requirements.

A need for computer graphics was identified, and a plan was devised to provide additional tools for the Divison to use in preparing publication-quality computer output (see Sect. 11.6).

11.5 LIBRARY

The Fusion Energy Library, part of the ORNL Information Division's Library System, provides varied services, including reference service, interlibrary loans, document delivery, and computerized information retrieval service. During 1981, the Library added 116 books, 708 full-size reports, and 2119 microfiche reports to the collection. The library lent 884 books and 749 technical reports and conducted 103 off-area interlibrary loan transactions and over 1500 reference requests. Eight computerized information retrieval services are available in the library, providing access to over 150 databases. This service enables the library staff to provide comprehensive literature searches, updates on previous searches, or current references on a research topic.

In the coming year, improvements will include on-line circulation and an on-line catalog for books and reports. This will benefit Division staff by giving them immediate access to the entire ORNL Library System collection.

11.6 REPORTS OFFICE

The Division Reports Office provides a wide range of publications services, including editing, word processing, graphics preparation, photography, and reproduction. During 1981, over 600 publications were processed for the Division. This total includes 47 technical memoranda, 235 journal articles and conference papers, and 306 abstracts. The graphic arts group produced 2850 original drawings and over 150 posters, covers, signs, and special projects. The Xerox 9400 copier was used to produce about 2.5 million copies. In addition, as part of the ORNL Information Division's Technical Publications Department (TPD), the Reports Office processed a large quantity of work for other ORNL divisions under TPD's work leveling program.

In late 1981, the Reports Office began testing the IS/1 UNIX* Text Management System, which may provide the basis for a complete computerized word processing system. The UNIX system uses a generic coding scheme that simplifies the preparation of technical documents or other large reports that go through several cycles (e.g., drafting, editing, revision, proofing). Also, because initial input is not device-specific, several output devices may used with this sytem (e.g., the Versatec printer/plotter, the Diablo printer, and the phototypesetter).

The graphic arts group initiated a computer graphics program in 1981. The overall goal of this program is to enlarge and enhance the group's capability by providing a means of increasing efficiency and thus adding to the time available for other projects. The immediate objective of the computer graphics program is to increase productivity for cases in which plots or graphs can be readily digitized using MAPPER. Plans call for establishing a graphics coordinator to function as an intermediary between graphic arts and Division personnel and for procuring the computer hardware to generate publication-quality graphics.

11.7 SAFETY, EMERGENCY PLANNING, AND QUALITY ASSURANCE

11.7.1 Safety and Emergency Planning

The Division's safety program includes monthly safety inspections by individual sections; quarterly safety inspections by an

*Trademark of Bell Laboratories.

independent inspection committee comprising the Division safety officer, Y-12 safety representatives, and Y-12 Maintenance supervision; and monthly fire inspections performed by professional fire inspectors. Six safety training sessions are held each year; attendance at these sessions is mandatory for all Division personnel.

During 1981 the Division emergency training program continued. The cardiopulmonary resuscitation (CPR) and first aid classes conducted by the building emergency squad resulted in the certification of 62 employees in CPR and 27 in first aid. A new squad was formed in Bldg. 9204-1 for the LCTF, and plans were formulated for a squad in the FEDC building. Training continued for maximum response to building emergencies.

11.7.2 Quality Assurance

The Division's Quality Assurance (QA) Program continued to improve during 1981. The program was expanded to include implementation of QA requirements on all subcontracts for major external work for the Division, and the program continued to be effective in ensuring the fabrication and the purchase of reliable and cost-effective experimental equipment. A special power supply committee, chaired by the QA coordinator, continued its surveillance of the quality of purchased power supplies.

QA audits were conducted at vendors' sites during the year. The QA Assessment for the EBT-P Project was made final, and approval was given for the QA Plan.

The Division QA Manual was updated and reissued to bring it into compliance with ORNL and DOE requirements. A workshop on quality assurance in fusion, held at Lawrence Livermore National Laboratory, resulted in a comprehensive review and numerous recommendations for improving the QA programs at all fusion laboratories.

PUBLICATIONS AND PRESENTATIONS

BOOKS AND JOURNAL ARTICLES

J. K. Ballou, R. L. Brown, W. A. Fietz, J. W. Forseman, W. H. Gray, W. J. Kenney, and R. B. Wysor, "Design and Testing of a Dual 8-Tesla 300 mm/12-Tesla 220 mm Split Superconducting Solenoid for ORNL," IEEE Trans. Magn. MAG-17, 2278 (1981).

C. F. Barnett, "Atomic Collision Properties," Chapter 4 in *AIP 50th Anniversary Physics Vade Mecum* (American Institute of Physics, New York, 1981), p. 41.

S. D. Berry and C. Bottcher, "Time-Dependent Response of a Two-Level System with Degenerate Levels to Coherent Radiation," Chem. Phys. Lett. 81, 320 (1981).

L. Bighel and J. A. Cobble, "Electron Heating and Confinement Measurements in EBT Toroidal Core Plasma Using Thomson Scattering," Phys. Rev. Lett. 46, 430 (1981).

C. Bottcher, "Numerical Solution of the Peterkop-Rabik Temkin-Hahn Model of Electron-Impact Ionization," J. Phys. (London) B14, L349 (1981).

C. Bottcher, "Numerical Solution of the Time-Dependent Schrödinger Equation with Coulomb Interactions," Int. J. Quantum Chem. Symp. 15, 671 (1981).

C. Bottcher and C. Feuillade, "Coherent Pumping of Microwave Transitions Between Highly Excited States," Chem. Phys. 54, 227 (1981).

K. H. Burrell, S. K. Wong, C. H. Muller III, M. P. Hacker, H. E. Ketterer, R. C. Isler, and E. A. Lazarus, "Observation of Long Impurity Confinement Times in the ISX-B Tokamak," Nucl. Fusion 21, 1009 (1981).

B. A. Carreras, J. A. Holmes, H. R. Hicks, and V. E. Lynch, "Tearing Mode Stability of Tokamak Plasmas with Elliptical Cross Section," Nucl. Fusion 21, 511 (1981).

B. A. Carreras, H. R. Hicks, and D. K. Lee, "Effects of Toroidal Coupling on the Stability of Tearing Modes," Phys. Fluids 24, 66 (1981).

B. A. Carreras, M. N. Rosenbluth, and H. R. Hicks, "Nonlinear Destabilization of Tearing Modes," Phys. Rev. Lett. 46, 1131 (1981).

R. J. Colchin, "Status of the ELMO Bumpy Torus (EBT) Experiment," Bull. Am. Phys. Soc. 26, 845 (1981).

R. R. Coltman, Jr., C. E. Klabunde, and J. M. Williams, "Rates of Defect Production by Fission Neutrons in Metals at 4.7 K," J. Nucl. Mater. 99, 284 (1981).

W. A. Cooper, G. Bateman, D. B. Nelson, and T. Kammash, "Neutral Beam Effects on Tokamak Ballooning Mode Stability," Plasma Phys. 23, 105 (1981).

L. Dresner, "Parametric Study of the Stability Margin of Cable-in-Conduit Superconductors: Theory," IEEE Trans. Magn. MAG-17, 753 (1981).

C. E. Easterly, "Cancer Link to Magnetic Field Exposure: A Hypothesis," Am. J. Epidemiol. 114 (22), 169 (1981).

S. A. Elrod, J. R. Miller, J. W. Lue, and L. Dresner, "Metastable Superconductive Composites: Dependence of Stability on Copper-to-Superconductor Ratio," IEEE Trans. Magn. MAG-17, 1083 (1981).

R. A. Falk, G. H. Dunn, D. C. Griffin, C. Bottcher, D. C. Gregory, D. H. Crandall, and M. S. Pindzola, "Excitation-Autoionization Contributions to Electron Impact Ionization," Phys. Rev. Lett. 47, 494 (1981).

C. Feuillade and C. Bottcher, "Double Resonance and Relaxation in a Three-Level System," Chem. Phys. 62, 67 (1981).

C. Feuillade and C. Bottcher, "A Multipole Treatment of the Degenerate Maser Problem," Chem. Phys. Lett. 77, 195 (1981).

W. L. Gardner, J. H. Whealton, G. C. Barber, C. W. Blue, W. K. Dagenhart, H. H. Haselton, J. Kim, M. M. Menon, N. S. Ponte, P. M. Ryan, D. E. Schechter, W. L. Stirling, C. C. Tsai, and R. Wright, "Ion Optics Improvements to the PDX/ISX-B Type of Multiple Aperture Ion Source," Rev. Sci. Instrum. 52, 1625 (1981).

R. M. Gilgenbach, M. E. Read, K. E. Hackett, R. F. Lucey, V. L. Granatstein, A. C. England, C. M. Loring, J. B. Wilgen, R. C. Isler, Y-K. M. Peng, K. H. Burrell, O. C. Eldridge, M. P. Hacker, P. W. King, A. G. Kulchar, M. Murakami, and K. K. Richards, "Electron Cyclotron/Upper Hybrid Resonant Pre-Ionization in the ISX-B Tokamak," Nucl. Fusion 21, 315 (1981).

J. C. Glowienka, "EBT: An Alternate Concept to Tokamaks and Mirrors," J. Vac. Sci. Technol. 18, 1088 (1981).

R. E. Gold, E. E. Bloom, F. W. Clinard, Jr., D. L. Smith, R. D. Stevenson, and W. G. Wolfer, "Materials Technology for Fusion: Current Status and Future Requirements," Nucl. Technol./Fusion 1, 169 (1981).

D. C. Gregory, B. M. Johnson, and K. W. Jones, "Interaction of Multiply Charged Ions with Electrons and Photons," IEEE Trans. Nucl. Sci. NS-28, 1362 (1981).

J. Hall, P. Richard, T. J. Gray, C. D. Lin, K. Jones, B. Johnson, and D. Gregory, "Double K-Shell-to-K-Shell Electron Transfer in Ion-Atom Collisions," Phys. Rev. A 24, 2415 (1981).

M. R. Hayns and L. K. Mansur, "Applications of the Theory of Cavity Growth to Dual-Ion Swelling Experiments," in *Special Technical Publication 725* (American Society for Testing and Materials, Philadelphia, Pennsylvania, 1981), pp. 213-30.

S. P. Hirshman and K. Molvig, "Temperature Dependence of the Electron Thermal Conductivity Coefficient Inferred from Neutral Beam Injection," Nucl. Fusion 21, 1480 (1981).

S. P. Hirshman and D. J. Sigmar, "Neoclassical Transport of Impurities in a Tokamak Plasma," Nucl. Fusion 21, 1079 (1981).

L. M. Hively, G. H. Miley, and J. A. Rome, "Fast Ion Thermalization in Non-Circular Tokamaks with Large Banana Width Effects," Nucl. Fusion 21, 1431 (1981).

J. T. Hogan, "Neoclassical Current Effects in Neutral-Beam-Heated Tokamak Discharges," Nucl. Fusion 21, 365 (1981).

C. H. Holder, Jr., D. Gregory, and M. Fink, "Data Correlation Analysis Applied to Electron Diffraction," J. Chem. Phys. 75, 5318 (1981).

R. H. Hughes, T. A. Heumier, and P. M. Griffin, "Vacuum UV and Soft X-ray Optical Emissions from Electron Impact on Metals," Appl. Opt. 20, 1530 (1981).

W. R. Husinsky, "Impurity Studies in Fusion Devices Using Laser-Fluorescence Spectroscopy," J. Vac. Sci. Technol. 18, 1054 (1981).

D. P. Hutchinson, C. H. Ma, P. A. Staats, and K. L. Vander Sluis, "Simultaneous Measurement of Line Electron Density and Faraday Rotation in the ISX-B Tokamak," Nucl. Fusion 21, 1535 (1981).

R. C. Isler, "Radiation from High Temperature Tokamak Plasmas," Proc. Soc. Photo-Opt. Instrum. Eng. 279, 29 (1981).

R. C. Isler, S. Kasai, L. E. Murray, M. Saltmarsh, and M. Murakami, "Impurity Sources and Accumulation in Ohmically Heated ISX-B Discharges," Phys. Rev. Lett. 47, 333 (1981).

R. C. Isler, L. E. Murray, S. Kasai, D. E. Arnurius, S. C. Bates, E. C. Crume, J. L. Dunlap, P. H. Edmonds, E. A. Lazarus, M. Murakami, V. K. Paré, M. J. Saltmarsh, D. W. Swain, and C. E. Thomas, "Influence of Neutral Beam Injection on Impurity Transport in the ISX-B Tokamak," Phys. Rev. Lett. 47, 649 (1981).

R. C. Isler, L. E. Murray, S. Kasai, J. L. Dunlap, S. C. Bates, P. H. Edmonds, E. A. Lazarus, C. H. Ma, and M. Murakami, "Charge Exchange Excitation and Recombination of Oxygen in the ISX-B Tokamak," Phys. Rev. A 24, 2701 (1981).

B. M. Johnson, K. W. Jones, and D. C. Gregory, "Contributions to Fusion Research from Studies of Foil-Excited Heavy Ion Beams," IEEE Trans. Nucl. Sci. NS-28, 1350 (1981).

B. M. Johnson, D. C. Gregory, K. W. Jones, D. J. Pegg, P. M. Griffin, T. H. Kruse, J. L. Cecchi, and J. O. Ekberg, "Anomalies in the Beam-Foil Measurements for $\Delta n = 0$ Transitions in Highly Ionized Members of the Li, Na, and Cu Sequences," IEEE Trans. Nucl. Sci. NS-28, 1159 (1981).

B. M. Johnson, K. W. Jones, D. C. Gregory, T. H. Kruse, and E. Trabert, "Beam-Foil Lifetimes of n = 3 Levels of Fe XIII to Fe XVI: I. Experiment Using Position Sensitive Detections," Phys. Lett. 86A, 285 (1981).

C. E. Klabunde, J. M. Williams, and R. R. Coltman, Jr., "A Fission-Neutron Source for the Study of Defect Production in Metals," J. Nucl. Mater. 99, 294 (1981).

L. L. Lao, S. P. Hirshman, and R. M. Wieland, "Variational Moment Solutions to the Grad-Shafranov Equation," Phys. Fluids 24, 1431 (1981).

D. K. Lee and Y-K. M. Peng, "An Approach to Rapid Plasma Shape Diagnostics in Tokamaks," J. Plasma Phys. 25, 161 (1981).

J. W. Lue and J. R. Miller, "Parametric Study of the Stability Margins of Cable-in-Conduit Superconductors. II. Experiment," IEEE Trans. Magn. MAG-17, 757 (1981).

V. E. Lynch, B. A. Carreras, H. R. Hicks, J. A. Holmes, and L. Garcia, "Resistive MHD Studies of High β Tokamak Plasmas," Comput. Phys. Commun. 24, 465 (1981).

C. N. Meixner, M. M. Menon, C. C. Tsai, and J. H. Whealton, "Geometrical Effects on the Beamlet Optics of a Two-State Accelerator," J. Appl. Phys. 52, 1167 (1981).

M. M. Menon, "Neutral Beam Heating Applications and Development," Proc. IEEE 69, 1012 (1981).

J. R. Miller, J. W. Lue, R. L. Brown, and W. J. Kenney, "Design, Construction, and Test of a 115-mm Bore Solenoid with NbTi Cable-in-Conduit Superconducting Windings," IEEE Trans. Magn. MAG-17, 2250 (1981).

A. P. Navarro, V. K. Paré, and J. L. Dunlap, "Two-Dimensional Spatial Distribution of Volume Emission from Line Integral Data," Rev. Sci. Instrum. 52, 1634 (1981).

R. A. Phaneuf, "Electron Capture in Very Slow C^{3+} + H Collisions," Phys. Rev. A. 24, 1138 (1981).

R. A. Phaneuf, "Production of High-Q Ions by Laser Bombardment Method," IEEE Trans. Nucl. Sci. NS-28, 1182 (1981).

R. A. Phaneuf, D. H. Crandall, and F. W. Meyer, "Low-Energy Electron Capture by Multicharged Ions from Hydrogen," Phys. Scr. 23, 188 (1981).

R. A. Rapp, J. H. DeVan, D. L. Douglass, P. C. Nordine, F. W. Pettit, and D. P. Whittle, "High Temperature Corrosion in Energy Systems," Mater. Sci. Eng. 50, 1 (1981).

P. H. Sager, "ETF Reactor Design Status," J. Vac. Sci. Technol. 18, 1081 (1981).

R. T. Santoro, R. G. Alsmiller, Jr., J. M. Barnes, and G. T. Chapman, "Calculation of Neutron and Gamma Ray Energy Spectra for Fusion Reactor Shield Design: Comparison with Experiment," Nucl. Sci. Eng. 78, 259 (1981).

J. Sheffield, "Status of the Tokamak Program," Proc. IEEE 69, 885 (1981).

S. S. Shen and J. D. Verhoeven, "Magnetization of In Situ Multifilamentary Superconducting Nb_3Sn-Cu Composites," IEEE Trans. Magn. MAG-17, 248 (1981).

D. Steiner, W. R. Becraft, and P. H. Sager, "The Engineering Test Facility," Nucl. Eng. Des. 63, 189 (1981).

D. W. Swain, M. Murakami, S. C. Bates, C. E. Bush, J. L. Dunlap, P. H. Edmonds, D. P. Hutchinson, P. W. King, E. A. Lazarus, J. F. Lyon, C. H. Ma, J. T. Mihalczo, L. E. Murray, G. H. Neilson, V. K. Paré, M. J. Saltmarsh, S. D. Scott, C. E. Thomas, J. R. Wilgen, and R. M. Wieland, "High Beta Injection Experiments on the ISX-B Tokamak," Nucl. Fusion 21, 1409 (1981).

P. F. Tortorelli, J. H. DeVan, and R. M. Yonco, "Compatibility of Fe-Cr-Mo Alloys with Static Lithium," J. Mater. Energy Syst. 2, 5 (1981).

K. T. Tsang, "Finite Larmor Radius Stabilization of Ballooning Modes in Tokamaks," Phys. Fluids 24, 2017 (1981).

K. T. Tsang and D. J. Sigmar, "Stabilization of Ballooning Modes by Energetic Particles in Tokamaks," Nucl. Fusion 21, 1227 (1981).

K. T. Tsang, D. J. Sigmar, and J. C. Whitson, "Destabilization of Low Mode Number Alfvén Modes in a Tokamak by Energetic or Alpha Particles," Phys. Fluids 24, 1500 (1981).

N. A. Uckan, "Ambipolar Potential Formation and Control in Bumpy Tori and Mirrors," Nucl. Fusion 21, 1493 (1981).

N. A. Uckan, "EBT Stability Theory," Nucl. Fusion 21, 1489 (1981).

N. A. Uckan, "Overview of EBT Reactor Projections," Nucl. Eng. Des. 63, 271 (1981).

T. Uckan, "Design of a Hyperbolic Microwave Metallic Lens," Rev. Sci. Instrum. 52, 21 (1981).

T. Uckan, "Finite Temperature and Wall Effects on the Absorption of Electron Cyclotron Waves in an EBT Plasma," IEEE Trans. Plasma Sci. PS-9, 96 (1981).

J. H. Whealton, "Expeditious Vlasov Solver for Computation of Ion Extraction from a Plasma," J. Comput. Phys. 40, 491 (1981).

J. H. Whealton, "Improvement in Gas Efficiency of Negative Ion Sources," Nucl. Instrum. Methods 18, 25 (1981).

J. H. Whealton, "Ion Extraction and Optics Arithmetic," Nucl. Instrum. Methods 18, 55 (1981).

J. H. Whealton, "Ion Optics Arithmetic and Its Applications for the Positive Ion CTR Program," IEEE Trans. Nucl. Sci. NS-28, 1359 (1981).

J. H. Whealton, R. W. McGaffey, and W. L. Stirling, "Ion Beam Extraction from a Plasma with Aberration Reduction by Method of Mutual Exclusion," J. Appl. Phys. 52, 3787 (1981).

J. J. Wolland, M. S. Walker, B. A. Zeitlin, D. A. Pollock, and S. S. Shen, "Evaluation of a Cryostable Low-Loss Conductor for Pulse Field Applications," IEEE Trans. Magn. MAG-17, 482 (1981).

J. W. Wooten, J. H. Whealton, and D. H. McCollough, "Effect of Slot Ends on Ion Extraction Optics," J. Appl. Phys. 52, 6418 (1981).

J. W. Wooten, J. H. Whealton, D. H. McCollough, R. W. McGaffey, J. E. Akin, and L. J. Brooks, "Ion Extraction and Optics in 3D," J. Comput. Phys. 43, 347 (1981).

PAPERS PRESENTED AT MEETINGS AND CONFERENCES

International Tokamak Reactor Workshop in the Engineering and Project Areas, Vienna, Austria, January 19-23, 1981

T. G. Brown, G. M. Fuller, J. Kirchner, J. G. Murray, G. Bronner, S. L. Thomson, H. Vogel, S. S. Kalsi, R. Hooper, J. Alcorn, B. Montgomery, V. Srivastava, B. Hunter, L. Turner, G. Gorker, D. Metzler, L. Stewart, R Barrett, W. I. Reiersen, G. E. Smith, T. E. Shannon, and R. L. Reid, "Documents Prepared for the INTOR Session V Workshop in the Engineering and Project Areas"

W. A. Houlberg, "Ignition Studies"

U.S.-Japan Workshop on Divertors, Impurity Control, and Plasma-Wall Interactions, Princeton, New Jersey, February 2-5, 1981

P. Mioduszewski, "Pump Limiter Work at ORNL"

J. B. Roberto, "Plasma-Material Interaction Research on ISX"

Fourth Topical Conference on Radio Frequency Plasma Heating, Austin, Texas, February 9-10, 1981

D. B. Batchelor, R. C. Goldfinger, and H. Weitzner, "Cyclotron Absorption by the Relativistic Electron Rings in EBT"

A. C. England, "Antennas and Waveguides for Electron Cyclotron Heating of Plasmas"

Workshop on Plasma Position Control, Princeton, New Jersey, February 16-17, 1981

G. H. Neilson et al., "Position Measurement and Control in ISX-B"

APS Third Topical Conference on Atomic Processes in High Temperature Plasmas, Baton Rouge, Louisiana, February 25-27, 1981

J. T. Hogan, "Electron Capture (H_e + C^{n+}) Effects on Plasma Transport"

R. C. Isler, L. E. Murray, and S. Kasai, "Charge Exchange Excitation and Recombination of Oxygenn the ISX-B Tokamak"

J. B. Roberts, "Laser Fluorescence Spectroscopy in Tokamak-Produced Plasmas"

Seventh International Conference on Magnet Technology, Karlsruhe, Federal Republic of Germany, March 30-April 3, 1981

J. K. Ballou, R. L. Brown, W. A. Fietz, J. W. Forseman, W. H. Gray, W. J. Kenney, R. B. Wysor, W. D. Markiewicz, and R. G. Van Aletyne, "Design and Testing of a Dual 8-Tesla 330 mm/12-Tesla 222 mm Split Superconducting Solenoid for ORNL"

J. R. Miller, J. W. Lue, R. L. Brown, and W. J. Kenney, "Design, Construction, and Test of a 115-mm Bore Solenoid with NbTi Cable-in-Conduit Superconducting Windings"

First European Conference on Atomic Physics, Heidelberg, Federal Republic of Germany, April 1981

F. W. Meyer and H. C. Kim, "Electron Loss from Rydberg States of Atomic Hydrogen in Collisions with Multi-Charged Ions"

U.S.-Mexico Cooperative Joint Workshop on Atomic Physics, Galindo, Mexico, April 1981

C. F. Barnett, "Dissociation and Electron Capture Collisions of Diatomic and Triatomic Hydrogen Ions in H_2 and Xe"

Atomic Physics Contractors Workshop, Argonne, Illinois, April 1-2, 1981

R. A. Phaneuf and D. H. Crandall, "Collisions of Low-Energy Multicharged Ions"

Annual Meeting on Theoretical Aspects of Controlled Thermonuclear Research (Project Sherwood), Austin, Texas, April 7-10, 1981

C. O. Beasley, K. Molvig, W. I. van Rij, and J. C. Whitson, "Nonlinear Universal Modes with Diffusive Electrons"

L. A. Charlton, R. A. Dory, D. J. Sigmar, and D. W. Swain, "Transport Study of ISX-B Flux-Conserving Tokamak Heating Scenarios"

W. A. Cooper, "Safety Factor Profile Optimization of High n Ideal Ballooning Mode Stability of Tokamaks"

A. M. El-Nadi and K. T. Tsang, "The Radial LBT Stability Problem"

H. R. Hicks, B. A. Carreras, J. A. Holmes, and V. E. Lynch, "Tearing Modes in Stellarator-Tokamaks"

S. P. Hirshman, "Neoclassical Transport Theory of Impurities in Tokamaks"

J. T. Hogan, "Periodic Large-Amplitude MHD Activity in Beam-Heated Tokamaks"

J. A. Holmes, B. A. Carreras, H. R. Hicks, and K. E. Rothe, "Finite β Effects on the Nonlinear Evolution of the (m = 1;n = 1) Tearing Mode in Tokamaks"

W. A. Houlberg, "Plasma Operation Contours for the FED"

E. F. Jaeger, R. K. Richards, and C. L. Hedrick, "EBT Transport and Ambipolar Potential Formation with Rapid Loss of High Energy Impurity Ions"

H. K. Meier, "Fast Moment Equation Method for Solving the Grad-Shafranov Equation"

D. B. Nelson and L. A. Charlton, "Neoclassical Resistive $q(\psi)$-Conserving Tokamak Equilibria"

D. J. Sigmar and H. C. Howe, "Transport Modeling of Impurity Control by Direct Momentum and Inertial Effects"

D. J. Strickler, Y-K. M. Peng, and D. K. Lee, "Pressure Profile Effects on Ballooning Mode Stability"

K. T. Tsang and C. Z. Cheng, "Coupling of Hot Electron Interchange and Ion Bernstein Modes in EBT"

N. A. Uckan and G. A. Spong, "Role of Beta Limits on Reactor Q Value in EBT"

J. W. Van Dam, H. L. Berk, M. N. Rosenbluth, and D. A. Spong, "Radial Eigenmode Stability for 'Bumpiless' EBT"

ANS/ENS International Topical Meeting on Advances in Mathematical Methods for Nuclear Engineering Problems, Munich, Federal Republic of Germany, April 27-29, 1981

W. A. Houlberg, S. E. Attenberger, and L. L. Lao, "Developments in Tokamak Transport Modeling"

Workshop on Ambipolar Potential Formation and Control in Bumpy Tori and Mirrors, Oak Ridge, Tennessee, May 11-12, 1981

L. Dighel, G. Haste, and A. Komori, "Fluctuation Measurements in EBT-S"

C. L. Hedrick, "The Ambipolar Potential in EBT, a Theoretical Summary"

E. F. Jaeger, R. K. Richards, and C. L. Hedrick, "EBT Transport and Ambipolar Potential Formation with Rapid Loss of High Energy Impurity Ions"

J. R. McNally, "Prospects for EBT-R Potential Control"

L. W. Owen, "Effects of Fluctuating Electric Fields on Hydrogen and Impurity Ions in EBT"

R. K. Richards and E. F. Jaeger, "Aluminum Impurity Ions and the Ambipolar Potential in EBT"

J. S. Tolliver, E. F. Jaeger, and C. L. Hedrick, "A Kinetic Model for Ion Transport in EBT with Enhanced Ion Tail"

J. S. Tolliver, E. F. Jaeger, and C. L. Hedrick, "Power Requirements for Ion Tail Formation in EBT"

T. Uckan, R. J. Colchin, W. A. Davis, G. R. Haste, D. L. Hillis, and L. Solensten, "Ambipolar Potential and Its Effects on the Confinement Parameters of the EBT Plasma"

J. W. Van Dam, H. L. Berk, M. N. Rosenbluth, and D. A. Spong, "Radially Dependent Stability Theory for EBT"

Workshop on EBT Stability Theory, Oak Ridge, Tennessee, May 13-14, 1981

C. Z. Cheng and K. T. Tsang, "Analytical Theory of Interchange and Compressional Alfvén Instabilities in EBT"

D. A. Spong, "Numerical Solutions of the EBT Radial Eigenmode Problem"

D. A. Spong, "Review of Recent EBT Coupled Ring-Loss Stability Theory"

K. T. Tsang and C. Z. Cheng, "Stability of Hot Electron Plasma in the ELMO Bumpy Torus"

N. A. Uckan and G. R. Haste, "Brief Survey of Experimental Investigation of Instabilities in Microwave Heated Plasmas"

N. A. Uckan, D. A. Spong, and D. B. Nelson, "Effect of Beta Limits on Reactor Performance in EBT"

1981 IEEE International Conference on Plasma Science, Santa Fe, New Mexico, May 18-20, 1981

S. E. Attenberger, J. A. Holmes, W. A. Houlberg, and S. D. Scott, "Toroidal Field Ripple Conduction Losses in the FED Tokamak"

S. E. Attenberger and W. A. Houlberg, "Heating Power Contours for the FED Tokamak"

F. W. Baity, O. C. Eldridge, T. L. Owens, and J. H. Mullen, "Heating Experiments in the Ion Cyclotron Range of Frequencies on EBT-S"

R. L. Copeland and J. C. Glowienka, "Diagnostic Neutral Beam System for EBT"

W. A. Davis, F. W. Baity, L. Bighel, C. E. Bush, J. A. Cobble, R. J. Colchin, R. L. Copeland, H. O. Eason, J. C. Glowienka, G. R. Haste, D. L. Hillis, A. Komori, R. K. Richards, L. Solensten, T. Uckan, T. L. White, and J. B. Wilgen, "Bulk Plasma Properties of EBT-S"

W. K. Dagenhart and W. L. Stirling, "SITEX Plasma Generator Scaling Studies for Long Pulse H^-/D^- Beam Generation"

J. C. Glowienka, F. W. Baity, L. Bighel, C. E. Bush, J. A. Cobble, R. J. Colchin, R. L. Copeland, W. A. Davis, H. O. Eason, G. R. Haste, D. L. Hillis, A. Komori, R. K. Richards, L. Solensten, T. Uckan, T. L. White, and J. B. Wilgen, "Heating Studies in EBT-I/S"

C. L. Hedrick, "The Status of EBT Physics"

L. M. Hively and J. A. Rome, "Optimization of a Compact Bundle Divertor for FED"

P. L. Huddleston, R. J. Kashuba, and J. H. Mullen, "A Finite Difference Model for ICRH Waves in an EBT with Periodic Axial and Radial Gradients"

A. G. Kulchar, O. C. Eldridge, A. C. England, C. M. Loring, P. H. Edmonds, and M. Murakami, "Low Voltage Startup with RF Assist and Other Preionization Experiments on ISX-B at the Electron Cyclotron Frequency"

J. R. McNally, "Physics of Fusion Fuel Cycles"

M. M. Menon, "Neutral Beam Heating Applications and Development"

J. Sheffield, "Status of the Tokamak Program"

C. C. Tsai, G. C. Barber, C. W. Blue, W. K. Dagenhart, R. R. Feezell, W. L. Gardner, H. H. Haselton, J. A. Moeller, M. M. Menon, N. S. Ponte, P. M. Ryan, D. E. Schechter, W. L. Stirling, J. H. Whealton, and R. E. Wright, "Plasma Generator Development of a 30 s, 100 A Ion Source for Neutral Beam Applications"

J. H. Whealton and R. W. McGaffey, "Double Bifurcation Optimization for Reduction of Secondaries from Neutralizer Plasma Ions"

Digital Equipment Corporation Users Society Meeting, Miami, Florida, May 18-22, 1981

D. N. Clark and J. K. Ballou, "WHO: A TOPS-10 User Utility Associating Names to PPNs"

Fourth International Conference on Nuclei Far from Stability, Helsingor, Denmark, June 1981

J. H. Hamilton, R. B. Piercey, R. Soundrayayagam, A. V. Ramayya, C. F. Maguire, X. J. Sun, Z. Z. Zhao, J. Roth, L. Cleeman, J. Eberth, T. Heck, W. Neumann, M. Nolte, R. L. Robinson, H. J. Kim, S. Fraudendorf, J. Doring, L. Funke, G. Winter, J. C. Wells, J. Lin, A. C. Rester, and H. K. Carter, "Deformed Ground States and Double Backbending at High Spins in Light Kr Isotopes"

Symposium on Physics Problems of Fusion Reactors, Trieste, Italy, June 2-9, 1981

Y-K. M. Peng, P. H. Rutherford, and J. F. Lyon, "Plasma Physics Assessments for the Fusion Engineering Device (FED)"

N. A. Uckan, D. B. Batchelor, L. A. Berry, M. R. Gordinier, C. L. Hedrick, E. F. Jaeger, L. W. Owen, and D. A. Spong, "Physics Issues of an EBT Reactor"

N. A. Uckan and D. A. Spong, "Beta Limits in EBT and their Implications for a Reactor"

Japanese Cryogenic Engineering Conference, Sapporo, Japan, June 3-5, 1981

L. Dresner, "Stability and Protection of Cable-in-Conduit Superconductors"

PAFEC User's Conference, Knoxville, Tennessee, June 9, 1981

W. H. Gray and T. V. Baudry, "PAFMOV, a PAFEC-to-MOVIE.BYU Conversion"

W. H. Gray and T. V. Baudry, "PAFNAS, a PAFEC-to-COSMIC/NASTRAN Conversion"

W. H. Gray and T. V. Baudry, "Interfacing PAFEC Passive Graphics to the DISSPLA Software Package"

First Conference on Lasers and Electro-Optics, Washington, D.C., June 10-12, 1981

D. P. Hutchinson, C. H. Ma, P. A. Staats, and K. L. Vander Sluis, "A Submillimeter-Wave Laser System for Simultaneous Measurement of Electron Density and Faraday Rotation in Tokamak Plasma"

IAEA Technical Committee Meeting on Divertors and Impurity Control in Tokamaks, Garching, Federal Republic of Germany, July 6-9, 1981

L. M. Hively, J. A. Rome, R. H. Fowler, V. E. Lynch, and J. F. Lyon, "Optimization of Bundle Divertors"

H. Howe and A. J. Wootton, "Numerical Simulations of the Bundle Divertor"

R. C. Isler, L. E. Murray, S. Kasai, and J. Sheffield, "Impurity Transport in the ISX-B Tokamak"

R. C. Isler, L. E. Murray, S. Kasai, and J. Sheffield, "The Influence of Neutral Beam Injection on Impurity Transport in ISX-B"

T. C. Jernigan, J. F. Lyon, D. B. Montgomery, J. Sheffield, W. R. Wing, J. A. Rome, L. M. Hively, A. J. Wootton, R. B. Wysor, and T. F. Yang, "The ISX Divertor Program"

P. K. Mioduszewski, P. H. Edmonds, and J. Sheffield, "Pumped Limiter Development on ISX"

Twelfth International Conference on the Physics of Electronic and Atomic Collisions, Gatlinburg, Tennessee, July 15-21, 1981

C. Bottcher, "Numerical Calculation of Electron Impact Ionization"

C. Bottcher and T. G. Heil, "Fully Quantal Studies of Charge Capture by Highly Stripped Ions from Atomic Hydrogen"

R. H. Crandall, "Experiments on Collisions of Electrons and Multicharged Ions"

E. C. Crume, "An Oxygen Atomic Physics Model for Tokamak Transport Simulation"

R. A. Falk, G. H. Dunn, D. C. Gregory, and D. H. Crandall, "Excitation-Autoionization in Electron Impact Ionization of Ti^{+3} and Zr^{+3}"

D. C. Gregory, P. F. Dittner, and D. H. Crandall, "Electron-Impact Ionization of Xe^{3+}"

D. C. Griffin, C. Bottcher, and M. S. Pindzola, "Contributions of Autoionization to Ionization Cross Sections in Ions of the Transitions Series Elements"

J. T. Hogan, "Application of Low Energy (10 eV-2 keV) Ionization ($e + C^{n+}$) and Electron Transfer ($H_0 + C^{n+}$) Data to Calculations of Radiative Cooling and H_0 Transport in Magnetic Fusion Plasmas"

J. T. Hogan, "The Effects of Low Energy Electron Capture Collisions ($H_0 + C^{n+}$) on the Particle and Energy Balance of Tokamak Plasmas"

R. C. Isler, L. E. Murray, and S. Kasai, "Optical Excitation by Charge Exchange of H^0 with O^{8+}"

R. C. Isler, L. E. Murray, and S. Kasai, "Spectral Excitation by Charge Exchange of H^0 with O^{8+} Ions"

B. M. Johnson, D. C. Gregory, K. W. Jones, J. T. Sample D. A. Hutcheon, R. Abegg, and G. J. Basbas, "K-, L-, M-Shell Vacancy Production by 500 MeV Protons"

H. J. Kim, "A Novel Apparatus for Studying Ion-Ion Collisions"

F. W. Meyer and H. J. Kim, "Electron Loss from Atomic Hydrogen in Collisions with N^{+3}"

R. A. Phaneuf, "Electron Capture in Slow C^{+q} + H Collisions"

Seventh International Seminar on Ion-Atom Collisions, Storrs, Connecticut, July 23-24, 1981

F. W. Meyer, "Electron Loss from Rydberg States of Atomic Hydrogen in Fast Collisions with Multicharged Ions"

Second Topical Meeting on Fusion Reactor Materials, Seattle, Washington, August 9-12, 1981

R. Budny and P. Mioduszewski, "First Wall Heat Loading During Disruptions in FED"

B. A. Cramer, "Response and Life Considerations for First Wall Structures in Fusion Reactor Erosion Environments"

K. Farrell and N. H. Packan, "Damage Structure in Nimonic PE16 Alloy Ion Bombarded to High Doses and Gas Levels"

T. A. Gabriel, R. A. Lillie, K. Thoms, and R. L. Childs, "Spectral Tailoring for Fusion Radiation Damage Studies: Where Do We Stand?"

J. R. Haines, B. A. Cramer, J. P. Davisson, and H. C. Mantz, "Material Considerations for the Fusion Engineering Device (FED) Pump Limiter"

J. Kirchner, B. A. Engholm, and the Fusion Engineering Design Center Staff, "Material Considerations in the Design of a Bulk Shield for the Fusion Engineering Device"

H. C. Mantz, J. R. Haines, and B. A. Cramer, "Materials Considerations for the Fusion Engineering Device (FED) Pumped Limiters"

P. Mioduszewski and P. H. Edmonds, "Advanced Limiters for the ISX-C Tokamak"

R. E. Nygren, "Materials Issues in the Fusion Engineering Device"

R. L. Reid, "The Impact of Inboard Shield Thickness on FED Performance and Cost"

Cryogenic Engineering Conference, San Diego, California, August 10-14, 1981

L. Dresner, "Transient Heat Transfer in Superfluid Helium"

S. A. Elrod, J. R. Miller, and L. Dresner, "The Specific Heat of NbTi from 0.0 to 7.5 T Between 4.2 and 20.0 K"

J. W. Lue and J. R. Miller, "Performance of an Internally Cooled Superconducting Solenoid"

J. W. Lue, J. R. Miller, P. L. Walstrom, and W. Herz, "Test of a Cryogenic Helium Pump"

J. R Miller, "The Development of Force-Cooled Superconductors for Use in Large Magnets"

J. R. Miller, S. A. Elrod, J. W. Lue, W. Herz, and K. R. Efferson, "Design, Construction, and Test of High-Capacity, Inertial, Cryogenic Current Leads"

S. W. Schwenterly, P. S. Litherland, E. D. Hudson, and R. S. Lord, "Design Study for Superconducting Main Field Coils for the Oak Ridge Isochronous Cyclotron"

S. W. Schwenterly, "Cryopumping Studies for Fusion Engineering at ORNL"

S. W. Schwenterly and C. M. Fitzpatrick, "Cryogenic Pressure Testing of Demountable Seals for Large Coil Project Applications"

S. S. Shen, "Effect of the Diffusion Barrier on the Magnetic Properties of Practical Nb_3Sn Composites"

S. S. Shen and W. K. McDonald, "Testing Results of Nb_3Sn Composites Made by Modified Jellyroll Method"

P. L. Walstrom, "Steady-State Heat Transfer to Boiling Liquid Helium in Simulated Coil Windings"

Sixth International Conference on Structural Mechanics in Reactor Technology, Paris, France, August 17-21, 1981

B. A. Cramer, "Mechanical and Thermal Design Aspects of the Fusion Engineering Device (FED)"

European Workshop, Computational MHD Models of the Behavior of Magnetically Confined Plasmas, Wildhaus, Switzerland, September 9-11, 1981

V. E. Lynch, B. A. Carreras, H. R. Hicks, J. A. Holmes, and L. Garcia, "Resistive MHD Studies of High β Tokamak Plasmas"

Tenth European Conference on Controlled Fusion and Plasma Physics, Moscow, U.S.S.R., September 14-19, 1981

J. Hogan, "Rotation and Island Effects in Tokamaks with High-Power Neutral Beam Heating"

E. A. Lazarus, "The ISX-B High-Beta Experiment"

E. Lazarus, S. Bates, C. Bush, B. Carreras, J. Dunlap, G. Dyer, P. Edmonds, J. Harris, H. Howe, D. Hutchinson, P. Isler, H. Ketterer, L. Lao, J. Lyon, C. H. Ma, J. T. Mihalczo, M. Murakami, L. Murray, G. Neilson, D. Overbey, V. Paré, J. Saltmarsh, S. Scott, D. Swain, C. Thomas, R. Wieland, J. Wilgen, W. Wing, and A. Wootton, "High Beta Studies with Beam-Heated, Non-Circular Plasmas in ISX-B"

N. A. Uckan, "Status of the Elmo Bumpy Research"

Third COMPUMAG Conference on Electromagnetic Field Computation, Chicago, Illinois, September 15-18, 1981

W. H. Gray, "Stress Analysis of Solenoids that Develop Gaps"

NATO Advanced Summer Institute, Baddeck, Nova Scotia, Canada, September 16-26, 1981

D. H. Crandall, "Electron Impact Ionization of Ions"

Stellarator Workshop, Lebedev Physical Institutute of the U.S.S.R. Academy of Sciences, Moscow, U.S.S.R., September 21-23, 1981

J. H. Harris, T. C. Jernigan, J. F. Lyon, M. B. Baer, B. A. Carreras, R. A. Jory, R. H. Fowler, L. Garcia, R. L. Johnson, E. A. Lazarus, V. E. Lynch, B. E. Nelson, J. A. Rome, and J. Sheffield, "ATF (Advanced Toroidal Facility) Design Studies"

Workshop on Electrode Phenomena, Moscow, U.S.S.R., September 21-23, 1981

P. K. Mioduszewski, "Observations of Unipolar Arcing in ISX"

Third IAEA Meeting on Fusion Reactor Design and Technology, Tokyo, Japan, October 5-16, 1981

T. E. Shannon, "Engineering Aspects of the INTOR Design"

D. Steiner and C. A. Flanagan, "Fusion Engineering Device Design"

D. Steiner and C. A. Flanagan, "Overview of the Fusion Engineering Device (FED) Design"

23rd Annual Meeting of the American Physical Society, Division of Plasma Physics, New York, New York, October 12-16, 1981

S. E. Attenberger, L. M. Hively, and W. A. Houlberg, "Optimized Neutral Beam Heating in Tokamak Reactor Plasmas"

F. W. Baity, O. C. Eldridge, J. H. Mullen, and T. L. Owens, "Effect of ICRH on EBT-S Plasma Parameters"

D. B. Batchelor, R. C. Goldfinger, and H. Weitzner, "Microwave Power Deposition in the Annulus and Core Plasma Components of EBT Devices"

C. Beasley, K. Molvig, and W. I. van Rij, "Numerical Simulation of Finite β Nonlinear Drift Modes"

L. A. Berry, J. C. Glowienka, G. R. Haste, and T. Uckan, "Operating Regimes in the EBT-S Experiment"

L. Bighel, "Plasma Fluctuation Studies in EBT-S"

L. Bighel, R. J. Schmitt, and J. T. Woo, "Plasma Diagnostics Package and Data Acquisition System for EBT-P"

S. K. Borowski, W. A. Houlberg, Y-K. M. Peng, and T. Kammash, "Plasma Initiation and Current Startup in the FED Tokamak"

C. E. Bush, R. C. Isler, L. E. Murray, G. R. Dyer, D. R. Overbey, F. E. Smith, B. Thomas, and M. Murakami, "Impurity Radiation in Neutral Beam Heated ISX-B Plasmas"

M. Caplan, V. Matranga, J. Sandoval, and J. Tancredi, "Operating Characteristics of a 60-GHz, 200 kW Gyrotron"

B. A. Carreras, J. L. Dunlap, J. A. Holmes, V. K. Paré, J. D. Bell, H. R. Hicks, V. E. Lynch, and A. P. Navarro, "MHD Activity in ISX-B: Correlation of Theory and Experiment"

L. A. Charlton, R. A. Dory, J. A. Holmes, G. H. Neilson, J. L. Dunlap, E. A. Lazarus, R. M. Wieland, and D. K. Lee, "MHD Stability of Noncircular ISX-B Plasmas"

J. A. Cobble, D. L. Hillis, L. Bighel, T. Uckan, R. K. Richards, and O. E. Hankins, "Core-Electron Confinement Measurements of EBT-S"

R. J. Colchin, "EBT-S Confinement Studies"

R. J. Colchin, "Status of the ELMO Bumpy Torus (EBT) Experiment"

W. A. Cooper and K. T. Tsang, "Kinetic Effects on Ballooning Stability of Arbitrary Tokamak Equilibria Including an Energetic Species"

E. C. Crume, "An Oxygen Atomic Physics Package for Transport Simlulation"

W. K. Dagenhart, C. D. Croessman, and W. L. Stirling, "H^- Beam Generation Studies with a Cylindrically Focused Surface Converter"

W. A. Davis, "Charge-Exchange Results from Initial ICRH Experiments"

J. L. Dunlap, V. K. Paré, J. D. Bell, A. P. Navarro, E. T. Blair, and W. R. Wing, "MHD Activity in the ISX-B Tokamak"

P. H. Edmonds, J. M. Madison, and P. Mioduszewski, "Results of the Pump Limiter Experiment on ISX"

O. C. Eldridge, F. W. Baity, T. L. Owens, and J. H. Mulien, "Ion Cyclotron Harmonic Heating on EBT-S Theory"

A. M. El Nadi, "The Compressional Alfvén Mode for Realistic EBT Plasmas"

L. C. Emerson, C. E. Bush, R. E. Clausing, W. A. Gabbard, L. Heatherly, A. W. Mullendore, and J. B. Whitley, "In Situ Still and High Speed Cinephotography of the Plasma-Limiter Interactions in ISX-B"

A. C. England, G. R. Dyer, G. Elder, O. C. Eldridge, J. C. Ezell, H. Hsuan, A. G. Kulchar, C. M. Loring, W. K. Russell, and J. B. Wilgen, "Recent Results from Electron Cyclotron Heating at 28 GHz on ISX-B"

C. A. Foster, S. L. Milora, E. A. Lazarus, C. E. Thomas, D. P. Hutchinson, C. H. Ma, C. E. Bush, P. H. Edmonds, W. A. Houlberg, and H. C. Howe, "Pellet Injection Experiments on ISX-B"

L. Garcia, J. D. Callen, B. A. Carreras, P. H. Diamond, and H. R. Hicks, "Multiple Helicity Rippling Modes Calculations"

J. C. Glowienka, D. W. Swain, T. Uckan, and W. B. Ard, "The ELMO Bumpy Torus Proof-of-Principle Device and Program"

R. C. Goldfinger, A. H. Kritz, and D. B. Batchelor, "Lower Hybrid Heating in EBT"

M. R. Gordinier and N. Uckan, "A Global Transport Package for EBT Reactor Design"

J. H. Harris, T. C. Jernigan, J. F. Lyon, B. E. Nelson, R. L. Johnson, and J. Sheffield, "ISX-C: An Advanced Toroidal Facility"

G. R. Haste, "Ring Power Balance in EBT"

H. R. Hicks, B. A. Carreras, J. A. Holmes, and V. E. Lynch, "Nonlinear Stability of Tearing Modes in Tokamak Stellarator Hybrids"

D. L. Hillis and G. R. Haste, "Energetic X-Ray Measurements of the Hot Electron Rings in EBT-S"

S. P. Hirshman and J. C. Whitson, "Spectral Analysis of Nonlinear Mappings"

I. M. Hively and J. A. Rome, "Ripple Optimization of Bundle Divertors"

J. Hogan, "Impurity Charge Exchange Effects: Radiation and Asymmetries"

J. A. Holmes, B. A. Carreras, H. R. Hicks, V. E. Lynch, and K. E. Rothe, "Plasma Shape and q_a Effects on the Nonlinear Evolution of the (m = 1;n = 1) Tearing Mode in Moderate Beta Tokamaks"

R. C. Isler, "The Influence of Neutral-Beam Injection on Impurity Transport in the ISX-B Tokamak"

R. C. Isler and L. E. Murray, "Impurity Transport in the ISX-B Tokamak"

E. F. Jaeger and C. L. Hedrick, "Transport Projections from the Experimentally Observed Ambipolar Potential Scaling in EBT"

R. J. Kashuba and D. G. Swanson, "Mode Conversion of Ion Cyclotron Waves with Oblique Gradients with Respect to the Magnetic Field"

G. G. Kelley and J. T. Hogan, "Halo Neutral Population in Beam-Heated Discharges"

A. H. Kritz, H. Hsuan, D. B. Batchelor, and R. C. Goldfinger, "TORAY – A Ray Tracing Code for the Analysis of Electron Cyclotron Heating in Toroidal Geometry"

A. G. Kulchar, R. E. Clausing, O. C. Eldridge, A. C. England, C. M. Loring, J. E. Simpkins, and J. B. Wilgen, "ECH Preionization and Startup Experiments on ISX-B"

E. A. Lazarus, S. C. Bates, C. E. Bush, J. L. Dunlap, P. H. Edmonds, D. Hutchinson, C. H. Ma, J. T. Mihalczo, M. Murakami, G. H. Neilson, S. C. Scott, D. W. Swain, C. E. Thomas, W. R. Wing, and A. Wootton, "Scaling Studies on β on ISX-B"

V. E. Lynch, R. H. Fowler, R. A. Dory, J. H. Harris, J. F. Lyon, T. C. Jernigan, and J. A. Rome, "Analysis of Helical Coil Systems for the ISX-C Device"

J. F. Lyon, S. D. Scott, S. C. Bates, S. L. Halsted, J. T. Mihalczo, G. H. Neilson, and J. A. Rome, "Studies of Periodic Toroidal Field Ripple Effects on Tokamak Plasmas"

M. M. Menon, H. H. Haselton, D. E. Schechter, C. C. Tsai, G. C. Barber, C. W. Blue, W. K. Dagenhart, R. R. Feezell, W. L. Gardner, E. F. Marguerat, N. S. Ponte, P. M. Ryan, W. L. Stirling, J. H. Whealton, and R. E. Wright, "High Energy (>120 keV) Ion Accelerator Study of a Scaled Advanced Positive Ion Source for Neutral Beam Applications"

J. T. Mihalczo, S. C. Scott, G. R. Dyer, S. L. Halsted, J. F. Lyon, and G. H. Neilson, "Neutron and Charge Exchange Measurements of Ion Temperature in ISX-B"

P. K. Mioduszewski, P. H. Edmonds, and J. Sheffield, "Pump Limiter Studies on ISX"

J. K. Munro, J. Hogan, and G. H. Neilson, "Effects of Flow and Beam-Induced Current on ISX-B Free Boundary Equilibrium"

M. Murakami, S. C. Bates, C. E. Bush, J. L. Dunlap, G. R. Dyer, P. H. Edmonds, D. P. Hutchinson, H. E. Ketterer, E. A. Lazarus, C. H. Ma, J. T. Mihalczo, G. H. Neilson, V. K. Paré, M. J. Saltmarsh, S. D. Scott, D. W. Swain, C. E. Thomas, R. M. Wieland, W. R. Wing, and A. J. Wootton, "Energy Confinement in Beam-Heated ISX-B Plasmas"

L. E. Murray, R. C. Isler, S. Kasai, and T. A. Underwood, "Plasma Rotation Measurements on ISX-B"

G. H. Neilson, D. W. Swain, J. L. Dunlap, G. R. Dyer, P. H. Edmonds, D. P. Hutchinson, E. A. Lazarus, C. H. Ma, M. Murakami, V. K. Paré, M. J. Saltmarsh, C. E. Thomas, R. M. Wieland, and A. J. Wootton, "High Beta and Shaping Experiments in ISX-B"

L. P. Mai, W. C. Brenner, E. M. Iwinski, and G. Gibson, "Bundle Divertor Design for EBT-S"

L. W. Owen, C. L. Hedrick, and L. E. Deleanu, "Nonadiabaticity and High Energy Particle Orbits in EBT"

T. L. Owens, J. H. Mullen, A. L. Henderson, F. W. Baity, and O. C. Eldridge, "Wave Propagation and Coupling Experiments in the Ion Cyclotron Range of Frequencies on EBT"

V. K. Paré, A. P. Navarro, J. L. Dunlap, J. D. Bell, S. C. Bates, and C. W. Nestor, "Two-Dimensional Imaging of X-Ray Emission Density in the ISX-B Tokamak"

Y-K. M. Peng and D. J. Strickler, "Beta Estimates for the Tokamak Fusion Engineering Device (FED)"

R. K. Richards and R. E. Vermillion, "Ion Confinement in EBT-S"

J. A. Rome, "An Author's Guide to Publishing in the Fields of Plasma Physics and Controlled Fusion Energy"

J. A. Rome, R. A. Schill, . . H. Fowler, and V. E. Lynch, "Studies of J-Invariance in Helical Toroidal Devices"

K. E. Rothe, L. E. Deleanu, and J. R. McNally, "Plasma Potential Control Prospects for EBT-R"

P. M. Ryan, G. C. Barber, W. K. Dagenhart, R. R. Feezell, N. S. Ponte, W. L. Stirling, J. H. Whealton, W. L. Gardner, D. E. Schechter, C. C. Tsai, D. H. Thompson, and C. R. Stewart, "40 keV Ion Energy Recovery with Transverse Magnetic Field Electron Blocking"

M. J. Saltmarsh, P. H. Edmonds, and M. Murakami, "Overview of the ISX-B Program"

S. D. Scott, J. F. Lyon, R. H. Fowler, S. L. Halsted, H. E. Ketterer, J. A. Rome, and C. E. Thomas, "A Test of Ripple-Enhanced Neutral Beam Injection on the ISX-B Tokamak"

D. J. Sigmar, K. T. Tsang, and J. C. Whitson, "Poloidal Satellite Coupling in Low Mode Number Alpha Particle Instability"

J. E. Simpkins, R. C. Isler, L. E. Murray, and J. B. Roberto, "Isotopic Exchange Experiments in ISX-B"

J. Smith and B. A. Carreras, "A Study of Linear Resistive Tearing Modes with Toroidal Effects"

D. A. Spong, J. W. Van Dam, H. L. Berk, and M. N. Rosenbluth, "Numerical Solutions of the EBT Radial Eigenmode Problem"

D. S. Stone, "VSWR Measurements in Multimode Transmission Lines"

O. P. Stotler, J. H. Whealton, and J. W. Wooten, "Proton Yield of a Dissociation Gradient Ion Source for Neutral Beam Generation"

D. W. Swain, G. H. Neilson, S. C. Bates, and H. E. Ketterer, "Magnetic Analyses of ISX-B Equilibria"

D. G. Swanson and R. J. Kashuba, "The Effect of Odd Order Derivations in the Mode Conversion-Tunneling Process"

C. E. Thomas, S. L. Milora, E. A. Lazarus, C. A. Foster, S. C. Bates, C. E. Bush, C. R. Dyer, P. H. Edmonds, D. P. Hutchinson, C. H. Ma, D. R. Overbey, and R. K. Richards, "Holographic Interferometry of Large, High Velocity, Solid Hydrogen Pellets in the ISX Tokamak with High Power Neutral Beam Injection"

D. M. Thomas and G. H. Neilson, "Measurements of the Neutral Flux in the Range 50-700 eV in ISX-B"

J. S. Tolliver, E. F. Jaeger, and C. L. Hedrick, "2-D Kinetic Transport Model for EBT"

C. C. Tsai, D. E. Schechter, G. C. Barber, C. W. Blue, W. K. Dagenhart, W. L. Gardner, H. H. Haselton, M. M. Menon, E. F. Marguerat, N. S. Ponte, P. M. Ryan, W. L. Stirling, J. H. Whealton, and R. E. Wright, "Long Pulse (>30 s) Plasma Generator Development of Advanced Positive Ion Sources for Neutral Beam Application"

N. A. Uckan, "Adiabatic Energy Limit in ECH Hot Electron Plasmas"

T. Uckan, R. J. Colchin, W. A. Davis, G. R. Haste, D. L. Hillis, and L. Solensten, "Effect of Ambipolar Potential on Confinement Parameters of the EBT Plasma"

R. Weitzner and D. B. Batchelor, "Ion Cyclotron Resonance Heating"

J. H. Whealton, "Improved Brightness in the APIS Tetrode Ion Source"

J. H. Whealton, "PDX Injector Improvement"

J. H. Whealton, R. W. McGaffey, and J. W. Wooten, "Double Plasma Model for Secondary Production in Electrode Structures"

R. M. Wieland, J. L. Dunlap, H. C. Howe, L. L. Lao, E. A. Lazarus, M. Murakami, G. H. Neilson, V. K. Paré, S. D. Scott, K. A. Stewart, and C. E. Thomas, "High-β Profile Analysis of ISX-B Plasmas"

J. B. Wilgen and D. L. Hillis, "Formation and Decay of a Modulated Electron Ring in EBT-I"

W. R. Wing, E. T. Blair, P. C. Hanna, D. R. Overbey, J. R. Reagan, and K. A. Stewart, "A Data System for ISX-C"

J. W. Wooten, J. H. Whealton, and D. H. McCollough, "Magnetic Blocking Direct Recovery (3-D Calculations)"

A. J. Wootton, S. C. Bates, P. H. Edmonds, H. C. Howe, D. P. Hutchinson, R. C. Isler, H. E. Ketterer, E. A. Lazarus, C. H. Ma, M. Murakami, L. E. Murray, C. E. Thomas, J. B. Wilgen, and W. R. Wing, "Particle Confinement During Neutral Beam Injection in ISX-B"

IAEA Technical Committee Meeting on Radio Frequency Heating in Large Fusion Experiments, Princeton, New Jersey, October 19-22, 1981

A. C. England, O. C. Eldridge, J. C. Ezell, J. C. Jernigan, A. G. Kulchar, C. M. Loring, J. B. Wilgen, K. R. Chu, B. Hui, J. Levine, and M. Read, "RF Heating on ISX-B and ATF at ORNL"

C. M. Loring, "EBT-P Microwave System"

C. M. Loring, "The U.S. Gyrotron Development Program"

D. H. Metzler, "Fusion Engineering Device (FED) Plasma Heating"

Third Neutral Beam Workshop, Gatlinburg, Tennessee, October 19-23, 1981

M. M. Menon and N. S. Ponte, "Energy Dissipation on Ion Accelerator Grids During High Voltage Breakdown"

C. C. Tsai, "Energy Straggling in an Ion Accelerator"

C. C. Tsai, D. E. Schechter, H. H. Haselton, M. M. Menon, P. M. Ryan, and W. L. Stirling, "DC Plasma Generator Development for Neutral Beam Injectors"

U.S.-Japan Cooperative Workshop on Superconductive Energy Storage, Madison, Wisconsin, October 19-23, 1981

S. S. Shen and M. S. Lubell, "Transient Field Losses in Tokamak Coils"

U.S.-Japan Workshop on 3-D MHD Studies for Toroidal Devices, Oak Ridge, Tennessee, October 19-21, 1981

H. R. Hicks, B. Carreras, L. Garcia, J. A. Holmes, and V. E. Lynch, "Resistive Modes in Tokamak-Stellarator Configurations"

J. A. Holmes, B. A. Carreras, L. A. Charlton, H. R. Hicks, and V. E. Lynch, "Resistive Modes in a High β Tokamak"

American Vacuum Society, Tennessee Valley Chapter, Second Annual Symposium and Equipment Exhibit, Knoxville, Tennessee, October 20-22, 1981

P. Mioduszewski, "Vacuum Aspects of Pump Limiter Systems"

Ninth Symposium on Engineering Problems of Fusion Research, Chicago, Illinois, October 26-29, 1981

J. K. Ballou, T. J. McManamy, W. H. Gray, R. L. Brown, and M. S. Lubell, "Design and Construction of an EBT-P Development Coil"

R. J. Barrett and S. L. Thomson, "Tokamak Building Design Considerations for a Large Tokamak Device"

T. V. Baudry and W. H. Gray, "Large Coil Test Stand Structural Analysis"

S. K. Borowski, Y-K. M. Peng, and T. Kammash, "RF Assisted Current Startup in FED"

B. A. Boyd, "EBT-P Data Acquisition System Design"

G. Bronner, G. E. Gorker, and J. G. Murray, "Protection System Proposed for the FED Superconducting Coils"

G. Bronner, G. E. Gorker, J. G. Murray, S. L. Thomson, and H. F. Vogel, "INTOR Power Handling and Conversion"

T. G. Brown, "Design Review of the INTOR Mechanical Configuration"

G. A. Byington, W. D. Shipley, and T. L. Ryan, "Two-Phase Helium-IV Quench Analysis for Superconducting Magnets"

W. D. Cain, T. V. Baudry, J. A. Mayhall, C. J. Hammonds, B. E. Nelson, K. K. Chipley, and W. H. Gray, "The Structural Analysis of ISX-C"

C. E. Childress and J. E. Batey, "QA Engineering for the LCP USA Magnet Manufacturers"

R. Deruy, R. Hooper, B. Hunter, S. Kalsi, S. Kim, J. Schultz, and V. C. Srivastava, "Fusion Engineering Device Magnetic Systems Design"

C. F. Dillow, G. L. Adlon, and J. L. Conlee, "Selection of Vacuum Seals for EBT-P"

L. Dresner, "Thermal Expulsion of Helium from a Quenching Cable-in-Conduit Conductor"

G. R. Dyer, "A Method for Transmitting Analog Data Over a Fiber-Optic Link"

P. H. Edmonds and W. A. Gabbard, "A Facility Approach to Tokamak Operations"

D. T. Erickson, "Bottoms Up Design of the EBT-P Fusion Research Facility"

D. A. Everitt, H. O. Eason, R. L. Livesey, and T. L. White, "Intrinsic Engineering Problems for ELMO Bumpy Torus-Scale (EBT-S)"

G. M. Fuller, B. A. Cramer, J. R. Haines, and J. P. Davisson, "Fusion Engineering Device (FED) First Wall, Armor, and Limiter Design Issues"

G. M. Fuller, J. R. Haines, B. A. Cramer, and J. P. Davisson, "Key Design Issues in the Definition of the FED First Wall and Limiter"

M. R. Gordinier, N. A. Uckan, L. W. Owen, D. K. Lee, and T. Uckan, "Analysis of Field Error Criteria in an EBT Reactor"

G. E. Gorker, B. A. Engholm, W. D. Nelson, and J. G. Murray, "Mechanical Configuration and Shielding for FED Fuel Injectors and Diagnostic Instrumentation"

W. H. Gray, J. K. Ballou, L. A. Fietz, J. W. Lue, J. R. Miller, P. L. Walstrom, and R. L. Brown, "A Comparison Between Experimental and Analytical Electromechanical Strain for Three Superconducting Solenoids"

W. H. Gray, "New Developments in Program STASOL Version 3"

W. H. Gray and W. D. Cain, "On Mechanical Stresses in Solenoids Constructed of Transversely Isotropic Materials"

W. H. Gray, T. J. McManamy, J. K. Ballou, and R. L. Brown, "A Comparison Between Experimental and Analytical Winding Prestrain for a Circular Solenoid"

D. E. Greenwood, R. D. Burris, and K. D. Young, "A CAMAC-Based Inter-Computer Communications System"

D. W. Haas, "The Role of Systems Integration in EBT-P"

W. R. Hamilton and H. F. Imster, "Engineering Overview of EBT-P Device Systems"

T. M. Hellwig and D. A. Bowers, "Thermal Performance of EBT-P Plasma Chamber Concepts"

L. M. Hively, W. A. Houlberg, and S. E. Attenberger, "Optimal Neutral-Beam-Heating Scenario for FED"

R. J. Hooper and B. L. Hunter, "Structural Design Procedures for FED Magnets"

W. A. Houlberg and S. E. Attenberger, "Plasma Engineering Analyses of Tokamak Reactor Operating Space"

B. L. Hunter, T. G. Brown, R. J. Hooper, S. S. Kalsi, J. A. O'Toole, V. C. Srivastava, J. Alcorn, S. H. Kim, R. P. Smith, and L. R. Turner, "Magnet Design for INTOR"

R. L. Johnson, K. K. Chipley, C. J. Hammonds, T. J. Huxford, J. A. Mayhall, J. R. Moore, B. E. Nelson, T. C. Jernigan, J. F. Lyon, and G. H. Neilson, "Engineering Features of ISX-C"

S. S. Kalsi, "Calculation of Transient Current Response of a Set of Coupled Circuits Using Eigenvalue Problem Solving Techniques"

S. S. Kalsi and R. J. Hooper, "Calculations of Eddy Current Losses in Toroidal Field Coil Casing"

C. O. Kemper, "An Automatic Data Acquisition and Communications Computer Network for Fusion Experiments"

J. Kirchner, "Torus Design for the Fusion Engineering Device (FED)"

C. M. Loring, H. O. Eason, and H. Jory, "The Gyrotron — An ECH System Component"

R. V. Lunsford, C. A. Foster, and S. L. Milora, "Pneumatic Hydrogen Pellet Injector Developments"

J. W. Lue and J. R. Miller, "Extended Field Operation of an Internally Cooled Superconducting Magnet"

J. W. Lue and J. R. Miller, "Heated Length Dependence of the Stability of Internally Cooled Superconductors"

J. N. Luton, G. S. Kruse, C. L. Linkenhoker, and M. F. Nishi, "The Pool Boiling Superconducting Coils for the Large Coil Task"

F. S. Malick, W. C. Brenner, and R. B. Chianese, "The Mechanical Design of a Toroidal Divertor for EBT-S"

E. F. Marguerat, H. H. Haselton, M. M. Menon, D. E. Schechter, W. L. Stirling, and C. C. Tsai, "Advanced Design of Positive Ion Sources for Neutral Beam Applications"

J. A. Mayhall, W. D. Cain, C. J. Hammonds, R. L. Johnson, and W. H. Gray, "The Structural Design and Analysis of the Vacuum Vessel, Coil Joints, and Supports for the ISX-C/ATF Tokamak"

J. A. Mayhall, C. J. Hammonds, and R. L. Johnson, "The Structural Design and Analysis of the Vacuum Vessel for the ISX-C Tokamak"

M. M. Menon, "Status and Trends in the Development and Application of Positive Ion Based Neutral Injectors"

M. M. Menon and N. S. Ponte, "Energy Dissipation on Ion Accelerator Grids During High Voltage Vacuum Breakdown"

D. H. Metzler, "Fusion Engineering Device (FED) Plasma Heating"

D. H. Metzler and L. D. Stewart, "INTOR Neutral Beam Injection System Concept"

J. R. Miller, J. W. Lue, and S. S. Shen, "Test of the First Development Coil for ERT-P"

J. R. Miller, J. W. Lue, S. S. Shen, and W. Herz, "Pressure Rise in a Quenching Internally Cooled Superconducting Magnet: Protection of the Coil and Refrigeration Components"

B. E. Nelson, W. D. Cain, K. K. Chipley, and T. J. Huxford, "Design and Analysis of the Toroidal Field Coils for the ISX-C Tokamak"

W. D. Nelson and J. B. Wilgen, "Plasma Diagnostics for FED"

J. A. O'Toole, T. G. Brown, and T. E. Shannon, "Design and Analysis of the INTOR Toroidal Field Coil Structural System"

Y-K. M. Peng, J. F. Lyon, and P. H. Rutherford, "Tokamak FED Plasma Engineering Assessments"

C. C. Queen, R. M. Beckers, M. J. Cole, and A. F. Zuiliger, "Design Description of the ISX-C Neutral Beam System"

C. C. Queen, C. J. Claffey, and A. R. Sadlowe, "Design Description of the Large Coil Test Facility Pulse Coil Support and Transport System"

C. C. Queen and R. O. Hussung, "Design Description of the Large Coil Test Facility Pulse Coil"

R. L. Reid and K. F. Wu, "Global Trade Studies for the Fusion Engineering Device (FED)"

P. H. Sager, G. M. Fuller, B. A. Cramer, J. P. Davisson, J. R. Haines, and J. Kirchner, "FED First Wall/Shield Design"

P. H. Sager, J. Garin, H. Stevens, R. Hager, D. Tobias, and N. Young, "Remote Maintenance Equipment Requirements for FED"

M. J. Saltmarsh, P. H. Edmonds, and the ISX-B Group, "The ISX-B Program"

D. E. Schechter and C. C. Tsai, "Indirectly Heated Cathodes and Duoplasmatron Type Electron Feeds for Positive Ion Surfaces"

R. J. Schmitt, "EBT-P Instrumentation and Control System — Overview"

S. W. Schwenterly, C. M. Fitzpatrick, and W. Court, "Cryogenic Voltage Withstand and Heat Transfer Tests for the General Electric Large Coil Turn Heaters"

T. E. Shannon, "Engineering Features of the INTOR Conceptual Design"

S. S. Shen, R. L. Brown, W. H. Gray, and M. S. Lubell, "A Superconducting Ohmic-Heated Solenoid Concept for ISX-C"

J. F. Shively and D. S. Stone, "Recent Progress in Fusion Gyrotron Development"

G. E. Smith, "Fusion Engineering Device (FED) Configuration and Maintenance"

P. T. Spampinato, "Considerations for Replacing PF Coils on FED"

V. C. Srivastava, "Enhanced Cooling with Helium Channels in the Coil Casing for FED"

D. Steiner, "Overview of the Current FED Baseline"

D. Steiner and C. A. Flanagan, "Overview of the Fusion Engineering Device (FED) Baseline"

D. J. Strickler and Y-K. M. Peng, "The Poloidal Field Coil System of the Fusion Engineering Device"

S. L. Thomson, J. G. Murray, and G. Bronner, "Electromagnetic Effects of Plasma Disruptions in Tokamaks"

N. A. Uckan, D. W. Swain, D. K. Lee, T. Uckan, L. W. Owen, and M. R. Gordinier, "Analysis of Field Error Criteria in an EBT Reactor"

T. L. Weaver, "EBT-P Plasma Heating System Instrumentation and Control Design"

W. R. Wing, "Data System Design Considerations for a Pseudo-Steady-State Device"

R. B. Wysor, D H. Gray, T. C. Jernigan, W. H. Power, J. E. Warwick, J. A. O'Toole, E. J. Rapperport, J. E. Tracey, and T. F. Yang, "Design and Installation of the ISX-B Bundle Divertor"

28th National Vacuum Symposium, American Vacuum Society, Anaheim, California, November 3-6, 1981

S. E. Attenberger, W. A. Houlberg, and S. L. Milora, "Numerical Simulation of Fueling in Tokamaks"

P. H. Edmonds, J. E. Simpkins, and P. Mioduszewski, "Gettering Experience in ISX or Titanium is Good for Your Health"

R. L. Livesey, "Vacuum System Problems of EBT – A Steady-State Fusion Experiment"

S. L. Milora, "Fueling of Magnetic Confinement Devices"

P. K. Mioduszewski and P. H. Edmonds, "Advanced Limiters for ISX"

J. E. Simpkins and P. K. Mioduszewski, "Comparison of Cr and Ti Gettering"

International Conference on Neutron Irradiation Effects, Argonne, Illinois, November 9-12, 1981

R. R. Coltman, Jr., "Organic Insulators and the Copper Stabilizer for Fusion Reactor Magnets"

Winter Meeting of the American Society of Mechanical Engineers, Washington, D.C., November 16-20, 1981

W. H. Gray and T. V. Baudry, "Large-Scale Structural Analysis of the Large Coil Test Facility"

Workshop on the Stability of Superconductors in He I and He II, Saclay, France, November 16-19, 1981

M. S. Lubell, "Stability Aspects of Superconducting Magnets for Tokamaks"

J. R. Miller and J. W. Lue, "Designing Internally Cooled Superconductors for Use in Large Magnets"

Second Workshop on Hot Electron Ring Physics, San Diego, California, December 1-3, 1981

F. W. Baity, D. L. Hillis, J. C. Glowienka, and T. L. Owens, "Enhancement of EBT Ring Parameters During Ion Cyclotron Heating"

D. B. Batchelor, R. C. Goldfinger, and H. Weitzner, "Ray Tracing Studies of Microwave Heating of the Annulus in EBT Devices"

J. C. Glowienka, W. A. Davis, D. L. Hillis, T. Uckan, F. M. Bieniosek, and L. Solensten, "Nonstandard Heating Experiments in EBT"

G. R. Haste, "Formation Criteria for Hot Electrons in EBT"

G. R. Haste, "Hot Electron Rings: Diagnostics Review and Summary of Measurements"

D. L. Hillis, "Hard X-Ray Measurements of the Hot Electron Rings in EBT-S"

S. Hiroe, L. A. Berry, R. J. Colchin, J. C. Glowienka, G. P. Haste, D. L. Hillis, T. Uckan, "Experimental Hot-to-Warm Electron Density Ratio for Instability Threshold in the ELMO Bumpy Torus"

S. Hiroe, T. Kunibe, H. Akiyama, and M. Inutake, "Stabilization of the High-Beta Plasma Instability with the ECH Hot Electron Annulus in a Symmetric Mirror"

L. W. Owen, L. E. Deleanu, and C. L. Hedrick, "Nonadiabaticity and High Energy Particle Orbits in EBT"

D. A. Spong, H. L. Berk, J. W. Van Dam, and M. N. Rosenbluth, "Radial Structure of Instability Modes in the EBT Hot Electron Annulus"

N. A. Uckan, "Hot Electron Ring Physics"

N. A. Uckan, "Ring Temperature Scaling"

T. Uckan and N. A. Uckan, "Synchrotron Emission from the Ring Electrons in EBT"

J. Wilgen and T. Uckan, "Synchrotron Emission Measurements from the Hot Electron Rings in EBT"

Joint Fusion Power Coordinating Committee Meeting, Kurchatov Irstitute, Moscow, U.S.S.R., December 2-5, 1981

J. Sheffield, "Overview of Fusion Programs"

IEEE International Electron Devices Meeting, Washington, D.C., December 7-9, 1981

M. Caplan, V. Matranga, J. Sandoval, and J. Tancredi, "60-GHz, 200-kW Gyrotron"

J. F. Shively and D. S. Stone, "Development of a 200 kW, 60 GHz Gyrotron"

U.S.-Japan Workshop on Heliotron-E Results, Uji, Japan, December 7-11, 1981

J. H. Harris, "Computational Studies of Stellarator-Torsatrons with Applications to Heliotron-E"

M. Murakami, "Neutral Beam Heating and Beta Studies in ISX-B"

Sixth International Conference on Infrared and Millimeter Waves, Miami Beach, Florida, December 7-12, 1981

C. H. Ma, D. P. Hutchinson, P. A. Staats, and K. L. Vander Sluis, "Measurements of Electron Density and Plasma Current Distributions in Tokamak Plasma"

REPORTS AND MEMORANDA

ORNL Reports, Technical Memoranda, and Conference Proceedings

ORNL-5674 *Fusion Energy Division Annual Progress Report for Period Ending December 31, 1980*

ORNL/TM-6566 H. K. Meier and D. J. Sigmar, *Analytic Solution of the Inverse Solov'ev Toroidal Equilibrium*

ORNL/TM-7001 D. B. Batchelor, *A Simple Power Balance Model for Microwave Heating in EBT*

ORNL/TM-7120 W. A. Cooper, *Tensor Pressure Tokamak Equilibrium and Stability*

ORNL/TM-7132 H. R. Hicks, B. Carreras, J. A. Holmes, D. K. Lee, and B. V. Waddell, *3D Nonlinear Calculations of Resistive Tearing Modes*

ORNL/TM-7369 W. H. Gray and T. V. Baudry, *System Software for the NMFECC CRAY-1 Version of TIFTS 4B*

ORNL/TM-7486 C. E. Thomas, *An Experimental Investigation of Solid Hydrogen Pellet Ablation in High-Temperature Plasmas Using Holographic Interferometry and Other Techniques*

ORNL/TM-7487 F. M. Bieniosek, *Study of Plasma Confinement in ELMO Bumpy Torus with a Heavy-Ion Beam Probe*

ORNL/TM-7499 A. P. Navarro, V. K. Paré, and J. L. Dunlap, *LERFCM — A Computer Code for Spatial Reconstruction of Volume Emission from Chord Measurements in Plasmas*

ORNL/TM-7530 A. Komori, *Plasma Fluctuation Measurements in ELMO Bumpy Torus*

ORNL/TM-7552 D. J. Sigmar, *Approach to Ignition of Tokamak Reactors*

ORNL/TM-7555 C. Ruchti, *PLP: A Field Line Plotting Code for Bundle Divertor Design*

ORNL/TM-7574 L. Bighel and T. L. White, *Collective Scattering of Gyrotron Radiation for T_i Measurements on EBT*

ORNL/TM-7584 H. K. Meier, S. P. Hirshman, D. J. Sigmar, and L. L. Lao, *Plateau Diffusion Coefficient for Arbitrary Flux Surface Geometry*

ORNL/TM-7585 N. A. Uckan, C. L. Hedrick, G. R. Haste, F. W. Baity, D. B. Batchelor, F. M. Bieniosek, L. Bighel, S. K. Borowski, J. A. Cobble, R. J. Colchin, R. L. Copeland, W. A. Davis, R. A. Dory, H. O. Eason, J. C. Glowienka, D. L. Hillis, E. F. Jaeger, A. Komori, R. K. Richards, D. A. Spong, T. Uckan, T. L. White, J. B. Wilgen, L. W. Owen, R. C. Goldfinger, L. E. Deleanu, and J. S. Tolliver, *Physics of Hot Electron Rings in EBT: Theory and Experiment*

ORNL/TM-7587 W. H. Gray, *A Guide to Proofing QUME Formatted TED1 Files on the ORNL FED Versatec Printer/Plotters*

ORNL/TM-7588 S. P. Hirshman and D. J. Sigmar, *Neoclassical Transport of Impurities in Tokamak Plasmas*

ORNL/TM-7591 B. A. Carreras, J. A. Holmes, H. R. Hicks, and V. E. Lynch, *Tearing Mode Stability of Tokamak Plasmas with Elliptical Cross Sections*

ORNL/TM-7616 L. L. Lao, S. P. Hirshman, and D. J. Sigmar, *Variational Moment Solutions to the Grad-Shafranov Equation*

ORNL/TM-7636 R. C. Goldfinger, *Formulas and Subroutines for $\vec{B}$, $\vec{A} \cdot \vec{B}$, and ϕ of a Current Loop with Application to Magnetic Fusion Experiments*

ORNL/TM-7665 T. V. Baudry and W. H. Gray, *Using GIFTS on the CRAY-1 for the Large Coil Test Facility Test Stand Design Analysis*

ORNL/TM-7656 C. F. Barnett and J. A. Ray, *Beam Specie Analyzer for Intense Neutral Beams*

ORNL/TM-7666 W. H. Gray and T. V. Baudry, *A Software Enhancement to Produce Report-Quality Graphics from GIFTS*

ORNL/TM-7675 D. H. Crandall, P. M. Hafford, and Y. Itikawa, eds., *U.S.-Japan Workshop on Atomic Collision Data for Fusion*

ORNL/TM-7678 J. A. Holmes, Y-K. M. Peng, and K. E. Rothe, *Equilibrium Evolution on the Resistive Timescale in a Tokamak Reactor*

ORNL/TM-7687 N. A. Uckan, R. G. Spencer, and T. Uckan, *Synchrotron Radiation from the Hot Electron Rings in EBT*

ORNL/TM-7691 J. W. Wooten, J. H. Whealton, D. H. McCollough, R. W. McGaffey, L. J. Drooks, and J. E. Akin, *Ion Extraction and Optics in 3D*

ORNL/TM-7722 J. H. Whealton, R. W. McGaffey, and W. L. Stirling, *Ion Beam Extraction from a Plasma with Aberration Reduction by Method of Mutual Exclusion*

ORNL/TM-7729 L. W. Owen and N. A. Uckan, *Optimization of EBT Reactor Magnetics*

ORNL/TM-7733 H. R. Hicks, B. A. Carreras, J. A. Holmes, and V. E. Lynch, *Nonlinear Analysis of Disruptions in the JIPP T-II Tokamak*

ORNL/TM-7746 D. J. Strickler, Y-K. M. Peng, and T. G. Brown, *Equilibrium Field Coil Concepts for INTOR*

ORNL/TM-7762 S. P. Hirshman and K. Molvig, *Temperature Dependence of the Electron Thermal Conductivity Coefficient Inferred from Neutral Beam Injection*

ORNL/TM-7769 P. Sager, J. Garin, E. R. Hager, P. T. Spampinato, D. Tobias, and N. Young, *Proceedings of FED Remote Maintenance Workshop*

ORNL/TM-7774 R. H. Fowler and J. A. Rome, *The Effects of Toroidal Field Ripple on Injected Tokamaks in the FED Device*

ORNL/TM-7777 C. A. Flanagan, D. Steiner, G. E. Smith, and the FEDC Staff, *Initial Trade and Design Studies for the Fusion Engineering Device*

ORNL/TM-7778 J. Sheffield, *Status of the Tokamak Program*

ORNL/TM-7803 H. C. Howe, *Physics Considerations for the FED Limiter*

ORNL/TM-7807 W. A. Cooper, *Safety Factor Profile Optimization of High n Ideal Ballooning Mode Stability of Tokamaks*

ORNL/TM-7835 J. H. Whealton, *Ion Optics Extraction Arithmetic*

ORNL/TM-7849 J. H. Whealton, J. W. Wooten, and R. W. McGaffey, *Magnetic Blocking Direct Recovery Efficiency*

ORNL/TM-7851 C. C. Tsai, M. M. Menon, P. M. Ryan, D. E. Schechter, W. L. Stirling, and H. H. Haselton, *A Long Pulse Ion Source for Neutral Beam Applications*

ORNL/TM-7857 N. A. Uckan, D. A. Spong, and D. B. Nelson, *Beta Limits in EBT and their Implications for a Reactor*

ORNL/TM-7870 J. H. Whealton, *Primary Ion Tetrode Optics for High Transparency Multibeamlet Neutral Injectors*

ORNL/TM-7879 J. H. Whealton, W. L. Gardner, H. H. Haselton, M. M. Menon, P. M. Ryan, D. E. Schechter, W. L. Stirling, W. K. Dagenhart, N. S. Ponte, G. C. Barber, R. W. McGaffey, and R. E. Wright, *Electrode Design and Performance of the ORNL Postive Ion Sources*

ORNL/TM-7885 J. H. Whealton, *Improvement of Gas Efficiency of Negative Ion Sources*

ORNL/TM-7897 T. Uckan, P. J. Colchin, W. A. Davis, G. R. Haste, D. L. Hillis, and L. Solensten, *Ambipolar Potential and Its Effects on the Confinement Parameters of the EBT Plasma*

ORNL/TM-7901 Y-K. M. Peng, P. H. Rutherford, J. F. Lyon, D. Blackfield, S. K. Borowski, D. R. Cohn, L. M. Hively, J. A. Holmes, W. A. Houlberg, H. C. Howe, P. Mioduszewski, K. E. Rothe, M. Murakami, D. J. Strickler, and M. Ulrickson, *Plasma Assessments for the Fusion Engineering Device (FED)*

ORNL/TM-7912 T. Uckan, F. M. Bieniosek, and L. Solensten, *Field Errors in EBT and their Effects on the Ambipolar Potential*

ORNL/TM-7913 J. A. Rome, J. F. Lyon, and R. H. Fowler, *Using a Constants-of-Motion Space to Clarify Measurements Involving Energetic Ion Orbits in Tokamaks*

ORNL/TM-7957 M. S. Pindzola and D. H. Crandall, *A Compilation of Theoretical Electron-Impact Excitation Cross Sections for Fe Atomic Ions*

ORNL/TM-7989 B. A. Carreras, J. D. Callen, P. W. Gaffney, and H. R. Hicks, *Rippling Modes in the Edge of a Tokamak Plasma*

ORNL/TM-8021 D. A. Spong, *Review of Recent EBT Coupled Ring-Core Stability Theory*

CONF-810511 N. A. Uckan, ed., *Workshop on Ambipolar Potential Formation and Control in Bumpy Tori and Mirrors*

CONF-810512 N. A. Uckan, ed., *EBT Stability Theory: Proceedings of the Workshop*

CONF-811203 N. A. Uckan, ed., *Hot Electron Ring Physics: Proceedings of the Second Workshop*

Subcontractor Reports

ORNL/Sub-7676/1 — **K. H. Carpenter,** *Research Support for Plasma Diagnostics on ELMO Bumpy Torus — Investigation of Diamagnetics for the Hot Electron Rings*

ORNL/Sub-7802/X07/1 — **R. K. Feeney and D. R. Hertling,** *Absolute Experimental Cross Sections for the Electron Impact Single, Double, Triple, and Quadruple Ionization of Cs^+ Ions*

ORNL/Sub-79/21453/S1 — **S. J. Evans, A. L. Nordquist, and G. E. Wendell,** *60 GHz Gyrotron Development Program Alternate Frequency Study*

ORNL/Sub-79/21453/7 — **J. F. Shively, S. J. Evers, S. J. Evans, and D. S. Stone,** *60 GHz Gyrotron Development Program*

WFPS:TME-81-020 — **W. C. Brenner, G. Gibson, E. M. Iwinski, L. P. Mai, F. S. Malick, and D. A. Sink,** *A Study of the Feasibility of Installing a Toroidal or Bundle Divertor in EBT-S*

WFPS:TME-81-026 — **W. C. Brenner, R. Chianese, G. Gibson, F. M. Heck, E. M. Iwinski, A. T. Lee, F. S. Malick, D. A. Sink, and R. W. Stooksberry,** *Engineering Design of a Toroidal Divertor for the EBT-S Fusion Device*

(under subcontract 53Y-72665C) — **McDonnell Douglas Astronautics Company,** *Ion Cyclotron Resonance Heating Study, Phase II. First Semi-annual Report (15 August 1980–15 February 1981)*

Other Reports

DOE/TIC-11600 — **Fusion Engineering Design Center Staff,** *The Fusion Engineering Device. Vol. II: Design Description*

USA/INTOR/81-1 — **W. M. Stacey, M. A. Abdou, J. A. Schmidt, and T. E. Shannon,** *The U.S. Contribution to the International Tokamak Reactor, Phase I, Workshop — Conceptual Design*

MISCELLANEOUS ITEMS

R. J. Barrett and S. L. Thomson, "FED Tokamak Building Design Considerations"

W. R. Becraft, "Scope and Status of the U.S.A. Engineering Test Facility Including Relevant TFTR Research and Development," presentation

T. G. Brown, "Mechanical Configuration Concepts"

M. Caplan and C. Thorington, "Improved Computer Modeling of Magnetron Injection Guns for Gyrotrons"

R. J. Colchin, "The ELMO Bumpy Torus (EBT) Experiment," press release for the American Institute of Physics, New York, New York

D. H. Crandall, C. F. Barnett, and W. L. Wiese, eds., *Atomic Data for Fusion*, bimonthly bulletin, Vol. 7, nos. 1-4, Oak Ridge National Laboratory (1981)

R. Derby, *Vol. V: Technology R&D Requirements for FED Construction*, documentation for Fusion Engineering Device issued by General Atomic Company, San Diego, California

H. H. Haselton, "Outline for Plasma Heating Summary"

S. S. Kalsi and D. B. Montgomery, "Magnetic System Design Concepts," INTOR Committee Review

S. H. Kim, "Heating of Electrons in an Unmagnetized Plasma by the Electromagnetic Wave"

S. H. Kim, "Ionization by Multispecies Absorption in a Plasma"

G. H. Neilson, "Results of Recent High Beta Experiments in Elongated Plasmas in ISX-B," presentation at Columbia University, New York, New York

ORNL, Exxon Nuclear Company, General Atomic Company, General Electric Company, Lawrence Berkeley Laboratory, Lawrence Livermore National Laboratory, Massachusetts Institute of Technology, Princeton Plasma Physics Laboratory, Science Applications, Inc., and TRW Defense and Space Systems, *Plasma Heating Technology Program Plan*

R. L. Reid, "Cost Sensitivity Analysis," INTOR Committee Review

E. Slaughter, Jr., "Lessons Learned from an Explosion in a 50-kV, 50-A dc Power Supply," presentation at the 1981 Joint Electrical Engineering Seminar for Divisions of Union Carbide Corporation, Nashville, Tennessee

F. M. Stickel, "Quality Assurance Approach for the ELMO Bumpy Torus Proof-of-Principle Experiment," presentation at the IEA Fusion Energy Quality Assurance Workshop, Princeton Plasma Physics Laboratory, Princeton, New Jersey, June 2, 1981

L. W. Stratton, J. E. Simpkins, and P. Mioduszewski, "An Investigation of Chromium Gettering for Application in the ISX-B Tokamak," paper submitted to fulfill requirements of ORNL-GLCA/ACM Science Semester

W. A. Uckan and McDonnell Douglas Astronautics Company staff, "Assessment of Alternative Development Paths of the EBT-P Reference Design"

Varian Associates, Inc., "60 GHz Power Source Exceeds 200 Kilowatts Output Power," news release

R. E. Vermillion, "Atomic Spectroscopy on ELMO Bumpy Torus"

LIST OF ABBREVIATIONS

ADIP	Alloy Development for Irradiation Performance
APB	antiphase boundary
APIS	advanced positive ion source
ARE	aspect ratio enhancement
ATF	Advanced Toroidal Facility
BCA	binary collision approximation
CPU	central processing unit
CVF	cavity volume fraction
CW	cold worked
cw	continuous wave
CWTX	Coil Winding Test Experiment
DITE	Divertor and Injection Tokamak Experiment
DNB	diagnostic neutral beam
DOE	Department of Energy
EBR	Experimental Breeder Reactor
EBT	ELMO Bumpy Torus
EBT-I	Initial EBT device and configuration (microwave power is <60 kW at 18 GHz, magnetic field is 5 kG)
EBT-P	EBT Proof of Principle
EBT-S	EBT-Scale device and configuration (microwave power is <200 kW at 28 GHz, magnetic field is 7.2 kG)
ECE	electron cyclotron emission
ECH	electron cyclotron heating
ECRH	electron cyclotron resonant heating
EDS	energy-dispersive spectroscopy
EF	equilibrium field
EPR	Experimental Power Reactor
ETF	Engineering Test Facility
FBR	Fast Breeder Reactor
FCT	flux-conserving tokamak
FDP	Fusion Demonstration Project
FED	Fusion Engineering Device
FEDC	Fusion Engineering Design Center
FIR	far-infrared
FLR	finite Larmor radius
FY	fiscal year
GA	General Atomic Company
GD	General Dynamics-Convair Division
GE	General Electric Company
GEIS	generic environmental impact statement
HFIR	High Flux Isotope Reactor
HFTF	High Field Test Facility
HPTF	High Power Test Facility
HVEM	high voltage electron microscopy
HWHM	half width at half maximum
IAEA	International Atomic Energy Agency
ICH	ion cyclotron heating
ICRF	ion cyclotron range of frequencies
ICRH	ion cyclotron resonant heating
ID	inside diameter
IEA	International Energy Agency
IGC	Intermagnetics General Corporation
INTOR	International Tokamak Reactor
IR	infrared
ISX	Impurity Study Experiment
JAERI	Japan Atomic Energy Research Institute
JET	Joint European Torus

JILA	Joint Institute for Laboratory Astrophysics
JIPP	Institute of Plasma Physics, Nagoya University, Nagoya, Japan
KfK	Kernforschungszentrum Karlsruhe
LANL	Los Alamos National Laboratory
LCP	Large Coil Project
LCT	Large Coil Task
LCTF	Large Coil Test Facility
LIF	laser-induced fluorescence
LHH	lower hybrid heating
LLNL	Lawrence Livermore National Laboratory
LRO	long-range-ordered
LTIF	Low Temperature Irradiation Facility
MCDT	moving coil displacement transducer
MDAC	McDonnell Douglas Astronautics Company
MEA	momentum energy analyzer
METF	Medium Energy Test Facility
MF	multifilamentary
MFE	magnetic fusion energy
MFTF	Mirror Fusion Test Facility
MG	motor-generator
MHD	magnetohydrodynamic
MIS	management-information system
MIT	Massachusetts Institute of Technology
MOA	memorandum of agreement
NBI	neutral beam injection
NBS	National Bureau of Standards
NBT	Nagoya Bumpy Torus
NEPA	National Environmental Policy Act
NMFECC	National Magnetic Fusion Energy Computing Center
NRA	nuclear reaction analysis
NRL	Naval Research Laboratory
OD	outside diameter
OFE	Office of Fusion Energy
OH	ohmic heating
ORIC	Oak Ridge Isochronous Cyclotron
ORNL	Oak Ridge National Laboratory
ORO	Oak Ridge Operations Office
ORR	Oak Ridge Research Reactor
PAG	preferred absorption glide
PCA	prime candidate alloy
PDX	Poloidal Divertor Experiment
PF	poloidal field
PI	preionization
PLT	Princeton Large Torus
POPCON	plasma operation contour
PPPL	Princeton Plasma Physics Laboratory
PVC	polyvinyl chloride
QA	quality assurance
QC	quality control
RA	reduction of area
RBS	Rutherford ion backscattering
rf	radio frequency
RGA	residual gas analysis
rms	root mean square
RPI	Rensselaer Polytechnic Institute
RSIC	Radiation Shielding Information Center
R&D	research and development
SAG	statistical absorption glide
SEM	scanning electron microscopy

SIPA	stress-induced preferred absorption
SMM	submillimeter
SRO	short-range-ordered
SYM	symmetrizing
Symmotron	symmetric modular torsatron
TEM	transmission electron microscopy
TF	toroidal field
TFTR	Tokamak Fusion Test Reactor
TMB	Technical Management Board
TMX	Tandem Mirror Experiment
TPD	Technical Publications Department
TTP	time-temperature-precipitation
UCC-ND	Union Carbide Corporation Nuclear Division
USC	User Service Center
VFA	velocity filter analyzer
VUV	vacuum ultraviolet
0-D	zero-dimensional
1-D	one-dimensional
2-D	two-dimensional
3-D	three-dimensional

FUSION ENERGY DIVISION

JUNE [illegible]

D. B. MORGAN, DIRECTOR
Z. S. BUCHANAN
W. B. JOHNSON
J. SHEFFIELD ASSOCIATE DIRECTOR
A. D. GUTTERY

MANAGEMENT SERVICES SECTION
V. C. KARLOCK[1]
B. J. BEEN

GENERAL ADMINISTRATION AND PROCUREMENT
R. P. JERNIGAN JR.*
D. W. IVEY
J. R. JERNIGAN[2]
F. W. BURNS[2]

PROCUREMENT
J. L. BURICE
S. K. ADKINS
P. L. RAY
R. C. SATTERFIELD

ENGINEERING SERVICES
E. W. WELLS
B. L. STRAUNE
D. R. ALFORD
W. C. BROCK*
R. S. EDWARDS*
J. C. EZELL
H. W. JERNIGAN*
W. K. RUSSELL
D. P. TROOKS
C. K. THOMAS

COMMUNICATIONS AND SPECIAL SERVICES
H. W. JERNIGA*
C. H. COX

FINANCE OFFICE
J. R. HICKEY[3]
R. P. JERNIGAN*
M. V. DUNN*
D. A. FISHER
C. H. JORDAN
C. A. PORTER
E. M. RUCKART

MARK. MENT INFORMATION SYSTEMS
R. K. GRYDER

LIBRARY
C. S. STRICKLER[3,4]
I. E. WEBSTER[4]

FED REPORTS OFFICE
A. S. TRAVIS*[4]

EDITING
A. S. TRAJTS*[4]
D. R. BAUMGARDNER[4]
M. N. JOHNSON

GRAPHICS
M. W. DARNELL[4]
C. H. JOHNSON[4]
J. B. MARTIN[3,4]
J. C. REELEY[4]
S. R. SCHWARTZ[4]
S. S. SCOTT[4]

WORD PROCESSING
E. L. CAGLE[4]
K. M. DOBBS[4]
D. Y. JOHNSON[4]
B. J. McDANIEL*[4]
E. J. SMITH[4]

ADMINISTRATION
B. J. McDANIEL*[4]
D. G. SHARP - XEROX

QUALITY ASSURANCE, SAFETY, AND EMERGENCY PLANNING
R. S. EDWARDS*
W. C. BROCK*

AFFIRMATIVE ACTION
C. E. BUSH*

EBT EXPERIMENTAL SECTION
L. A. BERRY*
R. B. BRYSON

EBT-P PHYSICS
D. W. SWAIN
D. V. JETT
J. C. GLOWIENKA
D. A. RASMUSSEN
T. L. WHITE

EBT-S DIAGNOSTICS AND OPERATIONS
R. J. COLCHIN
F. W. BALTY
J. A. COBBLE
W. A. DAVIS
D. A. EVERITT[5]
A. L. HENDERSON[5]
T. L. OWENS[5]
R. K. RICHARDS
T. UCKAN
G. R. HASTE
L. A. POLLARD[2]
W. A. VOKLEHM[2]
D. W. BIBLE[2]
R. D. BURRIS[2]
D. E. GREENWOOD[2]
S. L. HALL[2]
G. A. HALLOCK[2]
P. HANNA[2]
D. L. HILLIS
L. B. MADDOX[2]
L. SOLERSTEN[2]
J. B. WILGEN
R. E. WINTERBERG[2]
F. D. DONALDSON
R. L. LIVESEY
C. R. SCHAICH
S. HIROE

EBT MICROWAVE TECHNOLOGY AND ENGINEERING
H. O. EASON
D. D. BATES[3]
W. W. McGUFFIN

EBT-P PROJECT
A. L. BOCH
W. C. McCURDY
J. C. McGILL
M. P. REEDY

ENGINEERING
J. D. STOUT[5]
R. A. BROWN[5]
A. Y. BROVERMAN[5]
W. W. FLETCHER[5]
W. R. HAMILTON[5]
R. L. KILBY[5]

BUDGET & CSCS REPORTS
M. V. DUNN*

McDONNELL DOUGLAS ASTRONAUTICS CO
J. H. PFARRMULLER[6] - SITE MANAGER
M. R. CORNER[6]
R. R. ADAMS[6] - MICROWAVE DEVELOPMENT
J. S. BROOKOWICZ[6]
K. W. PRINCE[6]
T. L. MANN[3,6] - MAGNET DEVELOPMENT

GYROTRON PROGRAM
C. M. LORING*

MICROWAVE DEVELOPMENT
C. M. LORING*
H. D. KIMREY
P. A. HOLLIDAY

TOKAMAK EXPERIMENTAL SECTION
W. J. SALTMARSH
J. L. DUNLAP*
G. G. GONZALEZ

MX-B EXPERIMENT
EXPERIMENTAL PROGRAM COORDINATOR
M. MURAKAMI

EXPERIMENT
J. L. DUNLAP*
R. A. FORTNER
L. C. EMERSON[3,1]
P. K. RODUSZEWSKI
G. M. NELSON
V. K. PARE[3]
J. E. SIMPKINS
W. R. WING
A. J. WOOTTON
R. C. ISLER
C. E. BUSH
R. R. KINDSFATHER
P. W. KING
R. A. LANGLEY
E. A. LAZARUS
L. E. MURRAY
C. E. THOMAS
J. F. LYON*
B. L. POPE
S. C. BATES
O. C. ELDRIDGE
A. C. ENGLAND*
J. H. HARRIS*
S. D. SCOTT

MX-B OPERATIONS
P. H. EDMONDS*
G. R. DYER
W. A. GABBARD
J. M. MADISON[3]
J. A. MOORE[5]
J. E. PHELPS[3]
O. C. COLE[3]
S. L. HALSTED
L. A. MAFFINGILL
T. F. RAYBURN
W. J. REDMOND
J. L. YARBER

ATF
DESIGN COORDINATOR
T. C. JERNIGAN*
G. ROBINSON

PHYSICS COORDINATOR
J. F. LYON*
J. H. HARRIS*

PLASMA THEORY SECTION
R. A. DORY
C. L. HEDRICK, JR.*
D. J. SIGMAR*
G. H. WARREN
D. L. COKERS
J. F. COX
D. J. DAIRY

EBT THEORY GROUP
C. L. HEDRICK, JR.*
R. A. UCKAN
D. B. BATCHELOR
J. D. CALLEN*[3,2]
G. L. CHEN
W. B. DORMAN
D. E. HASTINGS
E. F. JAEGER
D. A. SPONG
H. WEITZNER[3,3]

TOKAMAK THEORY GROUP
D. J. SIGMAR*
C. O. BEASLEY, JR.
J. D. CALLEN*[3,2]
B. A. CARRERAS
W. A. COOPER
E. C. CRUME, JR.
P. N. DIAMOND[3,6]
L. GARCIA[3,5]
T. C. HENDER
S. P. HIRSHMAN
J. T. HOGAN
W. A. HOULBERG
H. C. HOWE
K. MOLVIG[3,0]
Y-K. M. PENG*
J. A. ROME

COMPUTING SUPPORT GROUP
C. E. HAMMONS
E. T. BLAIR[3]
R. O. BURRIS[3]
D. N. CLARK[3]
J. E. FRANCIS, JR.
D. E. GREENWOOD[3]
S. L. HALL[3]
R. HARPER[3]
C. O. KEMPER[3]
M. T. KETTERER[3]
S. R. MADDOX[3]
D. R. OVERBEY
J. R. REAGAN[3]
C. R. STEWART
K. A. STEWART
K. G. YOUNG
G. S. MASENGILL

PLASMA TECHNOLOGY SECTION
R. H. MASELTON
P. F. BROWN
G. C. ERICKS

NEUTRAL BEAM INJECTION SYSTEMS - DEVELOPMENT I
W. L. STIRLING*
C. W. BLUE
W. K. DAGENHART*
J. N. WHEALTON
S. C. FORRESTER

NEUTRAL BEAM INJECTION SYSTEMS - DEVELOPMENT II
C. C. TSAI*
M. W. MERON
P. W. RYAN
D. E. SCHECHTER
F. BLUSS

MX-B NEUTRAL BEAMS
W. L. STIRLING*
W. L. GARDNER

NEGATIVE ION DEVELOPMENT
W. L. STIRLING*
W. K. DAGENHART*
C. C. TSAI*

RADIO FREQUENCY HEATING SYSTEMS
W. R. BECRAFT[3,7]
D. J. HOFFMAN
P. K. KORTMAN[3,0]

PELLET FUELING
S. L. MILORA
S. K. COMBS
C. A. FOSTER
D. D. SCHURESKO

ELECTRICAL TECHNOLOGY DEVELOPMENT
N. S. PORTE
G. C. BARBER
R. E. WRIGHT
D. O. SPARKS

CONSULTANTS
W. R. BECRAFT[3,7]
G. G. KELLEY
P. K. KORTMAN[3,0]
J. R. MOELLER[3,9,2]

*DUAL CAPACITY
[1]DIVISION TECHNOLOGY
[2]PART TIME
[3]UCC-ND PURCHASING
[4]INFORMATION DIVISION
[5]UCC-ND ENGINEERING
[6]McDONNELL DOUGLAS
[7]INSTRUMENTATION AN
[8]UCC-ND COMPUTER SC
[9]PRINCETON PLASMA PHYSICS LABORATORY
[10]GENERAL DYNAMICS-C
[11]METALS AND CERAMIC
[12]UNIVERSITY OF WISCO
[13]COURANT INSTITUTE O
NEW YORK UNIVERSITY
[14]UNIVERSITY OF TEXAS
[15]UNIVERSITY OF MADRI
[16]MASSACHUSETTS INSTI
[17]GENERAL ELECTRIC C

ORNL-DWG 82-3873 FED

FUSION ENERGY DIVISION

JUNE 1982

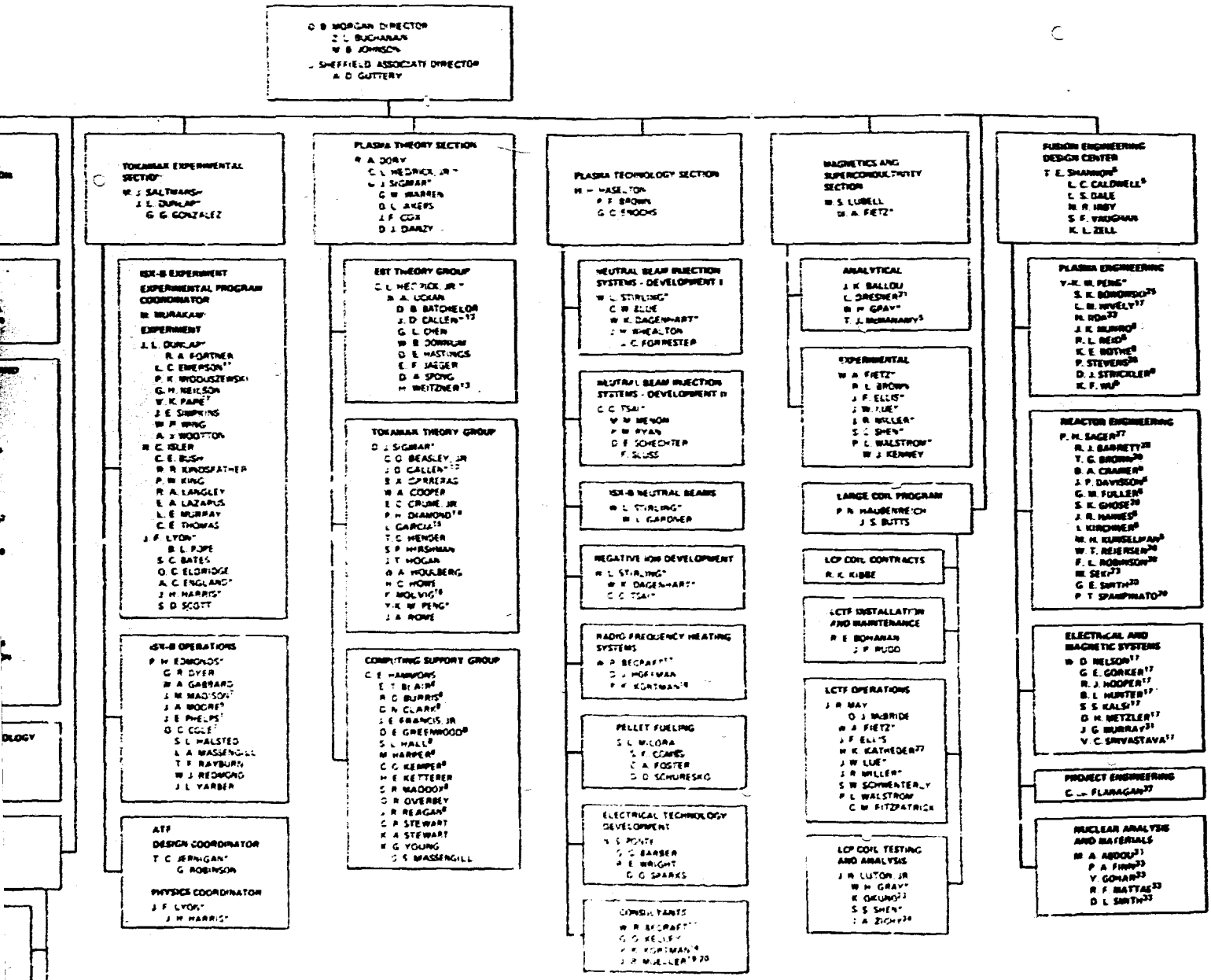

TOTAL CAPACITY
DIVISION TECHNOLOGY UTILIZATION OFFICER
PART TIME
UCC-N PURCHASING
INFORMATION DIVISION
UCC-ND ENGINEERING
MCDONNELL DOUGLAS ASTRONAUTICS COMPANY
INSTRUMENTATION AND CONTROLS DIVISION
UCC-ND COMPUTER SCIENCES
RENSSELAER POLYTECHNIC INSTITUTE
GENERAL DYNAMICS-CONVAIR DIVISION
METALS AND CERAMICS DIVISION
UNIVERSITY OF WISCONSIN
COURANT INSTITUTE OF MATHEMATICS NEW YORK UNIVERSITY
UNIVERSITY OF TEXAS
UNIVERSITY OF MADRID, SPAIN
MASSACHUSETTS INSTITUTE OF TECHNOLOGY
GENERAL ELECTRIC COMPANY
SCIENCE APPLICATIONS, INC
SIGMA ELECTRONICS COMPANY
GRUMMAN AEROSPACE CORPORATION
ON LEAVE OF ABSENCE TO JAPAN ATOMIC ENERGY RESEARCH INSTITUTE
KERNFORSCHUNGSZENTRUM KARLSRUHE, FEDERAL REPUBLIC OF GERMANY
JAPAN ATOMIC ENERGY RESEARCH INSTITUTE, TOKAI, JAPAN
SWISS INSTITUTE FOR NUCLEAR RESEARCH, VILLIGEN, SWITZERLAND
UNIVERSITY OF MICHIGAN
THE UNIVERSITY OF TENNESSEE
GENERAL ATOMIC COMPANY
BURNS & ROE, INC
BECHTEL GROUP, INC
TENNESSEE VALLEY AUTHORITY
PRINCETON PLASMA PHYSICS LABORATORY
WESTINGHOUSE ELECTRIC CORPORATION
ARGONNE NATIONAL LABORATORY

ORNL-5843
Dist. Category UC-20

INTERNAL DISTRIBUTION

1. R. G. Alsmiller, Jr.
2. D. E. Arnurius
3. S. E. Attenberger
4. C. F. Barnett
5. D. B. Batchelor
6. S. C. Bates
7. D. R. Baumgardner
8. C. O. Beasley, Jr.
9. W. R. Becraft
10. J. D. Bell
11-12. L. A. Berry
13. E. E. Bloom
14-15. A. L. Boch
16. S. K. Borowski
17. J. S. Brodkowicz
18. P. F. Brown
19. R. L. Brown
20. N. B. Bryson
21. Z. S. Buchanan
22. J. L. Burke
23. R. D. Burris
24-25. E. L. Cagle
26. J. B. Cannon
27. B. A. Carreras
28. H. P. Carter
29. G. T. Chapman
30. L. A. Charlton
31. G. L. Chen
32. R. G. Clark
33. R. E. Clausing
34. J. A. Cobble
35. R. J. Colchin
36. R. R. Coltman, Jr.
37. T. B. Cook
38. W. A. Cooper
39. D. H. Crandall
40. E. C. Crume, Jr.
41. W. K. Dagenhart
42. W. A. Davis
43. L. E. Deleanu
44-45. R. A. Dory
46-47. J. L. Dunlap
48. H. O. Eason
49. P. H. Edmonds
50. O. C. Eldridge
51. A. C. England
52. D. A. Everitt
53. G. G. Fee
54. D. A. Fisher
55. P. W. Fisher
56. C. A. Flanagan
57. R. H. Fowler
58. W. Fulkerson
59. G. M. Fuller
60. P. W. Gaffney
61. L. Garcia
62. W. L. Gardner
63. S. K. Ghose
64. J. C. Glowienka
65. R. C. Goldfinger
66. G. G. Gonzalez
67. D. H. Gray
68. D. E. Greenwood
69. D. C. Gregory
70. M. L. Grossbeck
71. R. K. Gryder
72. A. D. Guttery
73. P. M. Hafford
74. G. A. Hallock
75. W. R. Hamilton
76. C. E. Hammons
77-78. H. H. Haselton
79. G. R. Haste
80. D. E. Hastings
81-82. P. N. Haubenreich
83. A. L. Henderson
84. J. R. Hickey
85. H. R. Hicks
86. D. L. Hillis
87. S. Hiroe
88. L. M. Hively
89. J. A. Holmes
90. W. A. Houlberg
91. H. C. Howe, Jr.

92. K. E. Jamison
93. D. W. Jared
94. H. W. Jernigan
95. T. C. Jernigan
96-97. M. N. Johnson
98. P. L. Johnson
99. G. G. Kelley
100. R. K. Kibbe
101. H. D. Kimrey
102. R. R. Kindsfather
103. P. W. King
104. C. E. Klabunde
105-106. V. C. Kruzic
107. R. A. Langley
108. D. C. Larson
109. D. K. Lee
110. R. A. Lillie
111. C. T. Liu
112. K. C. Liu
113. R. L. Livesey
114-115. C. M. Loring
116-117. M. S. Lubell
118. J. N. Luton, Jr.
119. V. E. Lynch
120. B. K. Lyon
121. J. F. Lyon
122. C. H. Ma
123. F. C. Maienschein
124. T. L. Mann
125. B. F. Masden
126. B. F. Maskewitz
127. G. S. Massengill
128. J. R. May
129. W. J. McAfee
130. H. C. McCurdy
131. J. C. McGill
132. J. R. McGuffey
133. M. W. McGuffin
134. M. M. Menon
135. D. H. Metzler
136. F. W. Meyer
137. J. T. Mihalczo
138. J. R. Miller
139. P. K. Mioduszewski
140-169. O. B. Morgan
170. J. K. Munro
171. M. Murakami
172. G. H. Neilson
173. B. E. Nelson
174. W. D. Nelson
175. C. W. Nestor, Jr.
176. J. A. O'Toole
177. D. R. Overbey
178. L. W. Owen
179. F. M. Ownby
180. V. K. Paré
181. Y-K. M. Peng
182. J. H. Pfanmuller
183. R. A. Phaneuf
184. N. S. Ponte
185. H. Postma
186. D. A. Rasmussen
187. J. A. Ray
188. T. W. Reddoch
189. J. D. Redman
190. W. L. Reiersen
191. R. K. Richards
192. J. B. Roberto
193. J. A. Rome
194. M. W. Rosenthal
195. W. K. Russell
196. P. M. Ryan
197-198. M. J. Saltmarsh
199. R. T. Santoro
200. C. R. Schaich
201. D. D. Schuresko
202. S. W. Schwenterly
203. J. L. Scott
204. S. D. Scott
205-206. T. E. Shannon
207-208. J. Sheffield
209. D. J. Sigmar
210. J. E. Simpkins
211. E. Slaughter, Jr.
212. L. Solensten
213. P. T. Spampinato
214. D. A. Spong
215. V. C. Srivastava
216. P. H. Stelson
217. C. R. Stewart, Jr.
218. W. L. Stirling
219. W. C. T. Stoddart
220. J. D. Stout
221. D. J. Strickler
222. D. W. Swain
223. C. E. Thomas

224. D. H. Thompson
225. J. S. Tolliver
226. P. F. Tortorelli
227-228. A. S. Travis
229. C. C. Tsai
230. N. A. Uckan
231. T. Uckan
232. W. I. van Rij
233. K. L. Vander Sluis
234. J. M. Vitek
235. R. D. Wall
236. P. L. Walstrom
237. G. M. Warren
238. J. S. Watson
239. J. H. Whealton
240. J. A. White
241. J. C. White
242. R. M. Wieland
243. F. W. Wiffen
244. J. B. Wilgen
245. M. K. Wilkinson
246. J. W. Woods
247. W. L. Wright
248. R. B. Wysor
249. K. G. Young
250. R. A. Zuhr
251-252. Laboratory Records Department
253. Laboratory Records, ORNL-RC
254. Document Reference Section
255-256. Central Research Library
257. Fusion Energy Division Library
258. Fusion Energy Division Publications Office
259. ORNL Patent Office

EXTERNAL DISTRIBUTION

260. S. L. Ackerman, General Dynamics-Convair Division, P.O. Box 80847, San Diego, CA 92138
261. E. Adam, Airco, 100 Mountain Avenue, Murray Hill, NJ 07974
262. S. W. Ahrends, Department of Energy, Oak Ridge Operations Office, P.O. Box E, Oak Ridge, TN 37830
263. Y. Aiyama, Electrotechnical Laboratory, Sakura, Niihari, Ibaraki 305, Japan
264. J. T. Alexander, Department of Energy, Oak Ridge Operations Office, P.O. Box E, Oak Ridge, TN 37830
265. I. Alexeff, Department of Electrical Engineering, The University of Tennessee, Knoxville, TN 37916
266. T. Amano, Institute of Plasma Physics, Nagoya University, Nagoya 464 Japan
267. C. A. Anderson, Westinghouse Electric Corporation, Advanced Reactors Division, P.O. Box 158, Madison, PA 15663
268. J. L. Anderson, CMB-3, MS 348, Los Alamos National Laboratory, P.O. Box 1663, Los Alamos, NM 87545
269. D. J. Anthony, General Electric Company, Building 2, Room 551, 1 River Road, Schenectady, NY 12345
270. W. B. Ard, McDonnell Douglas Astronautics Company, P.O. Box 516, St. Louis, MO 63166
271. V. D. Arp, National Bureau of Standards, Boulder, CO 80302
272. P. L. Auer, Laboratory of Plasma Studies, 312 Upson Hall, Cornell University, Ithaca, NY 14853
273. D. M. Axelrod, Consulting Engineer, Department of Advanced Engineering, United Engineers and Constructors, Inc., 30 S. 17th Street, Philadelphia, PA 19101
274. J. Ayers, EG&G ORTEC, 100 Midland Road, Oak Ridge, TN 37830
275. K. Azuma, The Bank of Tokyo, Nihombashi, P.O. Box 8, Tokyo 103-91, Japan
276. M. Azumi, Plasma Theory Laboratory, Division of Thermonuclear Fusion Research, Japan Atomic Energy Research Institute, Tokai Research Establishment, Tokai, Ibaraki, Japan

277. C. C. Baker, Fusion Power Program, CEN Building, Argonne National Laboratory, 9700 S. Cass Avenue, Argonne, IL 60439
278. D. Baldwin, Lawrence Livermore National Laboratory, P.O. Box 808, Livermore, CA 94550
279. R. G. Bateman, School of Nuclear Engineering, Georgia Institute of Technology, Atlanta, GA 30332
280. J. E. Baublitz, Office of Fusion Energy, Department of Energy, Mail Stop G-256, Washington, DC 20545
281. W. Bauer, Sandia National Laboratories, Livermore, CA 94550
282. J. W. Beal, General Atomic Company, P.O. Box 81608, San Diego, CA 92138
283. D. S. Beard, Office of Fusion Energy, Department of Energy, Mail Stop G-256, Washington, DC 20545
284. G. Bekefi, Massachusetts Institute of Technology, 77 Massachusetts Avenue, Cambridge, MA 02139
285. C. R. Bell, 132 Westlook Circle, Oak Ridge, TN 37830
286. G. Benedict, Department of Energy, Oak Ridge Operations Office, P.O. Box E, Oak Ridge, TN 37830
287. H. L. Berk, Institute for Fusion Studies, University of Texas at Austin, Austin, TX 78712
288. S. E. Berk, Office of Fusion Energy, Department of Energy, Mail Stop G-256, Washington, DC 20545
289. R. A. Berry, Varian Associates, Inc., 611 Hansen Way, Palo Alto, CA 94303
290. R. Beuligmann, General Dynamics-Convair Division, P.O. Box 80847, San Diego, CA 92138
291. Bibliothek, Institut fuer Plasmaphysik, KFA, Postfach 1913, D-5170 Juelich 1, Federal Republic of Germany
292. Bibliothek, Max Planck Institut fuer Plasmaphysik, D-8046 Garching bei Muenchen, Federal Republic of Germany
293. Bibliothèque, Centre des Recherches en Physique des Plasmas, 21 Avenue des Bains, 1007 Lausanne, Switzerland
294. Bibliothèque, Service du Confinement des Plasmas, CEA, B.P. 6, 92 Fontenay-aux-Roses (Seine), France
295. R. J. Bickerton, JET Group, Culham Laboratory, Abingdon, Oxon OX14 3DB, United Kingdom
296. D. Blackfield, Plasma Fusion Center, Massachusetts Institute of Technology, 77 Massachusetts Avenue, Cambridge, MA 02139
297. R. A. Blanken, Office of Fusion Energy, Department of Energy, Mail Stop G-256, Washington, DC 20545
298. S. L. Bogart, Science Applications, Inc., 8400 Westpark Drive, McLean, VA 22102
299. R. W. Boom, 513 Engineering Research Building, University of Wisconsin, Madison, WI 53706
300. R. Botwin, Grumman Aerospace Corporation, Mail Stop C-4705, Bethpage, NY 11714
301. C. M. Braams, FOM-Institut voor Plasma-Fysica, Rijnhuizen, Jutphaas, Netherlands
302. P. Brewington, Department of Energy, Oak Ridge Operations Office, P.O. Box E, Oak Ridge, TN 37830
303. W. B. Briggs, McDonnell Douglas Astronautics Company, P.O. Box 516, St. Louis, MO 63166
304. B. Brunelli, Laboratorio Gas Ionizzati, Casella Postale 65, Frascati (Roma), Italy
305. K. Buchl, Max Planck Institut fuer Plasmaphysik, D-8046 Garching bei Munchen, Federal Republic of Germany
306. S. J. Buchsbaum, Research Communications Principles Division, Bell Telephone Laboratories, Inc., Crawford Corner Road, Holmdel, NJ 07733
307. O. Buneman, Stanford Electronics Laboratories, Stanford University, Palo Alto, CA 94305
308. D. S. Burch, Department of Physics, Oregon State University, Corvallis, OR 97330
309. K. H. Burrell, General Atomic Company, P.O. Box 81608, San Diego, CA 92138
310. P. Caldirola, Laboratorio di Fisica del Plasma ed Elettronica Quantistica del C.N.R., Via Celoria 16, 20133 Milano, Italy
311. J. D. Callen, Department of Nuclear Engineering, University of Wisconsin, Madison, WI 53706
312. K. H. Carpenter, Department of Electrical Engineering, University of Missouri, Rolla, MO 65401

313. P. J. Catto, Science Applications, Inc., 934 Pearl Street, Suite A, Boulder, CO 80302
314. C. T. Chang, Department of Physics, Risø, Roskilde, Denmark
315. R. N. Cherdack, Burns & Roe, Inc., 700 Kinder Kamack Road, Oradell, NJ 07649
316. K. R. Chu, Naval Research Laboratory, Washington, DC 20375
317. T. K. Chu, Princeton Plasma Physics Laboratory, P.O. Box 451, Princeton, NJ 08540
318. A. Clark, National Bureau of Standards, Boulder, CO 80302
319. J. F. Clarke, Associate Director for Fusion Energy, Office of Fusion Energy, Office of Energy Research, Department of Energy, Mail Station G-256, Washington, DC 20545
320. G. Clemens, University Library of Essen, Gustav-Hicking-Strasse 15, D-4300 Essen, Federal Republic of Germany
321. M. Cohen, Office of Fusion Energy, Department of Energy, Mail Stop G-256, Washington, DC 20545
322. D. R. Cohn, Massachusetts Institute of Technology, 77 Massachusetts Avenue, Cambridge, MA 02139
323. P. L. Colestock, Princeton Plasma Physics Laboratory, P.O. Box 451, Princeton, NJ 08540
324. R. W. Conn, Department of Chemical, Nuclear, and Thermal Engineering, 6291 Boelter Hall, University of California, Los Angeles, CA 90024
325. J. R. Conrad, University of Wisconsin, Madison, WI 53706
326. H. Conrads, KFA, Postfach 1913, D-5170 Juelich 1, Federal Republic of Germany
327. T. Consoli, Centre d'Etudes Nucleaires, Avenue des Martyrs 38, Grenoble, France
328. J. G. Cordey, UKAEA, Culham Laboratory, Abingdon, Oxon OX14 3DB, United Kingdom
329. D. N. Cornish, Lawrence Livermore National Laboratory, P.O. Box 808, Livermore, CA 94550
330. J. W. Coursen, Grumman Aerospace Corporation, Mail Stop C-3605, Bethpage, NY 11714
331. E. C. Creutz, National Science Foundation, Washington, DC 20550
332. F. L. Culler, Electric Power Research Institute, P.O. Box 10402, Palo Alto, CA 94303
333. R. A. Dandl, Applied Microwave Plasma Concepts, Inc., 2210 Encinitas Boulevard, Suite F, Encinitas, CA 92024
334. J. N. Davidson, Department of Nuclear Engineering, Georgia Institute of Technology, Atlanta, GA 30332
335. R. C. Davidson, Massachusetts Institute of Technology, 77 Massachusetts Avenue, Cambridge, MA 02139
336. N. A. Davies, Office of Fusion Energy, Department of Energy, Mail Stop G-256, Washington, DC 20545
337. J. C. Davis, Lawrence Livermore National Laboratory, P.O. Box 808, Livermore, CA 94550
338. R. C. Davis, 106 Kingfisher Lane, Oak Ridge, TN 37830
339. W. J. Davis, Sandia National Laboratories, P.O. Box 5800, Albuquerque, NM 87185
340. S. O. Dean, Science Applications, Inc., 2 Professional Drive, Suite 249, Gaithersburg, MD 20760
341-343. R. J. DeBellis, McDonnell Douglas Astronautics Company, P.O. Box 516, St. Louis, MO 63166
344. J. F. Decker, Office of Fusion Energy, Department of Energy, Mail Stop G-256, Washington, DC 20545
345. H. W. Deckman, Advanced Energy Systems Laboratory, Exxon Research and Engineering Company, P.O. Box 8, Linden, NJ 07036
346. H. de la Fuente, Cerrada Rio Rojo 507, Col. Vista Hermosa, Cuernavaca, Morelos, Mexico
347. J. Denavit, Department of Mechanical Engineering, Northwestern University, Evanston, IL 60201
348. Department of Nuclear Engineering Sciences, 202 Nuclear Science Center, University of Florida, Gainesville, FL 32611

349. H. Desportes, STIPE, CEN/Saclay, F91190, Gif-sur-Yvette, France
350. J. M. Deutch, Massachusetts Institute of Technology, 77 Massachusetts Avenue, Cambridge, MA 02139
351. D. A. Dingee, Fusion Programs, Pacific Northwest Laboratories, Battelle Boulevard, P.O. Box 999, Richland, WA 99352
352. Director, Technical Library, Defense Atomic Support Agency, Sandia Base, Albuquerque, NM 87185
353. Documentation S.I.G.N., Departement de la Physique du Plasma et de la Fusion Controlée, Association EURATOM-CEA sur la Fusion, Centre d'Etudes Nucleaires, B.P. 85, Centre du Tri, Grenoble, France
354. T. J. Dolan, Department of Nuclear Engineering, University of Missouri, Rolla, MO 65401
355. G. W. Donaldson, School of Electrical Engineering, University of New South Wales, P.O. Box 1, Kensington, New South Wales, Australia
356. W. F. Dove, Office of Fusion Energy, Department of Energy, Mail Station G-256, Washington, DC 20545
357. R. J. Dowling, Office of Fusion Energy, Department of Energy, Mail Station G-256, Washington, DC 20545
358. L. J. Crooks, Department 621, Bell Telephone Laboratories, Whippany, NJ 07981
359. W. E. Drummond, Department of Physics, University of Texas at Austin, Austin, TX 78712
360. E. Dullni, NB-05/639, Experimentalphysik, Ruhr-Universitaet Bochum, D-4630 Bochum, Federal Republic of Germany
361. G. H. Dunn, Joint Institute for Laboratory Astrophysics, Boulder, CO 80309
362. T. Edelbaum, Charles Stark Draper Laboratories, 75 Cambridge Parkway, Cambridge, MA 02142
363. G. A. Eliseev, I. V. Kurchatov Institute of Atomic Energy, P.O Box 3402, 123182 Moscow, U.S.S.R.
364. W. R. Ellis, Office of Fusion Energy, Department of Energy, Mail Stop G-256, Washington, DC 20545
365. A. M. El-Nadi, Department of Electrical Engineering, Cairo University, Giza, Egypt
366. G. A. Emmert, Department of Nuclear Engineering, University of Wisconsin, Madison, WI 53706
367. H. P. Eubank, Princeton Plasma Physics Laboratory, P.O. Box 451, Princeton, NJ 08540
368. R. W. Fast, Experimental Facilities, National Accelerator Laboratory, P.O. Box 500, Batavia, IL 60510
369. A. Favale, Grumman Aerospace Corporation, Department 930, Plant 5, Bethpage, NY 11714
370. R. Feeney, Georgia Institute of Technology, Atlanta. GA 30332
371. F. R. Fickett, Cryogenics Division, 275.03, Properties of Solids Section, Institute for Basic Standards, National Bureau of Standards, Boulder, CO 80302
372. J. File, Princeton Plasma Physics Laboratory, P.O. Box 451, Princeton, NJ 08540
373. C. R. Finfgeld, Office of Fusion Energy, Department of Energy, Mail Stop G-256, Washington, DC 20545
374. E. von Fischer, Bechtel Group, Inc., P.O. Box 3965, San Francisco, CA 94119
375. H. K. Forsen, Bechtel Group, Inc., Research and Engineering, P.O. Box 3965, San Francisco, CA 94119
376. T. K. Fowler, Lawrence Livermore National Laboratory, P.O. Box 808, Livermore, CA 94550
377. R. L. Freeman, General Atomic Company, P.O. Box 81608, San Diego, CA 92138
378. J. P. Freidberg, Massachusetts Institute of Technology, 77 Massachusetts Avenue, Cambridge, MA 02139
379. J. W. French, Ebasco Services, Inc., Princeton University, P.O. Box 451, Princeton, NJ 08540
380. M. Fujiwara, Institute of Plasma Physics, Nagoya University, Nagoya 464, Japan
381. H. P. Furth, Princeton Plasma Physics Laboratory, P.O. Box 451, Princeton, NJ 08540
382. Y. Furuto, Superconducting Group, Central Research Laboratory, Furukawa Electric Company, Ltd., 9-15, 2-Chome, Futaba, Shinagawaku, Tokyo 141, Japan

383. A. Saines, Combustion Engineering, 1000 Prospect Hill Road, Windsor, CT 06095
384. W. F. Gauster, Neurwaldeggerstrasse 9/2/5, A-1170 Vienna, Austria
385. D. A. Gedcke, EG&G ORTEC, 100 Midland Road, Oak Ridge, TN 37830
386. K. Gentle, Department of Physics, University of Texas at Austin, Austin, TX 78712
387. T. V. George, Office of Fusion Energy, Department of Energy, Mail Stop G-256, Washington, DC 20545
388. A. Gibson, JET Group, Culham Laboratory, Abingdon, Oxon OX14 3DB, United Kingdom
389. G. G. Gibson, Westinghouse Electric Corporation, Advanced Reactors Division, P.O. Box 158, Madison, PA 15663
390. G. von Gierke, Max Planck Institut fuer Plasmaphysik, D-8046 Garching bei Muenchen, Federal Republic of Germany
391. F. C. Gilbert, Division of Military Applications, Department of Energy, Washington, DC 20545
392. H. B. Gilbody, Department of Pure and Applied Physics, Queens University, Belfast, Northern Ireland, United Kingdom
393. J. Gilliland, General Atomic Company, P.O. Box 81608, San Diego, CA 92138
394. R. M. Gilgenbach, JAYCOR, 205 South Whiting Street, Alexandria, VA 22304
395. V. A. Glukhikh, Scientific-Research Institute of Electro-Physical Apparatus, 188631 Leningrad, U.S.S.R.
396. R. Goldston, Princeton Plasma Physics Laboratory, P.O. Box 451, Princeton, NJ 08540
397. B. Gore, Pacific Northwest Laboratories, Battelle Boulevard, P.O. Box 999, Richland, WA 99352
398. M. J. Gouge, Department of Energy, Oak Ridge Operations Office, P.O. Box E, Oak Ridge, TN 37830
399. R. W. Gould, California Institute of Technology, Building 116-81, Pasadena, CA 91125
400. H. Grad, Courant Institute of Mathematical Sciences, New York University, 251 Mercer Street, New York, NY 10012
401. S. Gralnick, Grumman Aerospace Corporation, Bethpage, NY 11714
402. R. J. Gran, Grumman Aerospace Corporation, Bethpage, NY 11714
403. V. L. Granatstein, Naval Research Laboratory, Washington, DC 20375
404. E. Gregory, Airco, 100 Mountain Avenue, Murray Hill, NJ 07974
405. G. Grieger, Max Planck Institut fuer Plasmaphysik, D-8046 Garching bei Muenchen, Federal Republic of Germany
406. H. R. Griem, Department of Physics, University of Maryland, College Park, MD 20742
407. D. C. Griffin, Rollins College, Winter Park, FL 32789
408. R. A. Gross, Department of Mechanical Engineering, Columbia University, New York, NY 10027
409. G. E. Guest, Applied Microwave Plasma Concepts, Inc., 2210 Encinitas Boulevard, Suite F, Encinitas, CA 92024
410. G. M. Haas, Office of Fusion Energy, Department of Energy, Mail Stop G-256, Washington, DC 20545
411. M. P. Hacker, General Atomic Company, P.O. Box 81608, San Diego, CA 92138
412. K. E. Hackett, Massachusetts Institute of Technology, 77 Massachusetts Avenue, Cambridge, MA 02139
413. D. S. Hackley, General Dynamics-Convair Division, P.O. Box 80847, San Diego, CA 92138
414-493. J. M. Haffey, Information Services, Oak Ridge Associated Universities, Badger Road, Oak Ridge, TN 37830
494. O. Hagena, Kernforschungszentrum Karlsruhe GmbH, Postfach 3640, D-7500 Karlsruhe 1, Federal Republic of Germany

495. B. Haizlip, Sandia National Laboratories, P.O. Box 5800, Albuquerque, NM 87185
496. S. M. Hamberger, Institute for Advanced Studies, Australian National University, P.O. Box 4, Canberra, A.C.T. 2000, Australia
497. A. M. Hamende, International Centre for Theoretical Physics, Trieste, Italy
498. R. Hancox, UKAEA, Culham Laboratory, Abingdon, Oxon OX14 3DB, United Kingdom
499. R. Harder, General Atomic Company, P.O. Box 81608, San Diego, CA 92138
500. C. C. Harris, Department of Nuclear Medicine, Duke University, Durham, NC 27706
501. E. G. Harris, Department of Physics, The University of Tennessee, Knoxville, TN 37916
502. A. F. Haught, United Technologies Research Center, Silver Lane, Hartford, CT 06108
503. C. R. Head, Office of Fusion Energy, Department of Energy, Mail Stop G-256, Washington, DC 20545
504. T. G. Heil, Georgia Institute of Technology, Athens, GA 30332
505. W. Heinz, Institut fuer Technische Physik, Kernforschungszentrum Karlsruhe GmbH, Postfach 3640, D-7500 Karlsruhe 1, Federal Republic of Germany
506. C. D. Henning, Lawrence Livermore National Laboratory, P.O. Box 808, Livermore, CA 94550
507. M. W. Heyne, Hughes Aircraft Company, Electron Dynamics Division, 3100 West Lomita Boulevard, Torrance, CA 90509
508. K. W. Hill, Princeton Plasma Physics Laboratory, P.O. Box 451, Princeton, NJ 08540
509. E. Hintz, Institut fuer Plasmaphysik, KFA, Postfach 1913, D-5170 Juelich 1, Federal Republic of Germany
510. T. Hiraoka, Japan Atomic Energy Research Institute, Tokai, Ibaraki, Japan
511. R. L. Hirsch, Exxon Research and Engineering, P.O. Box 101, Florham Park, NJ 07932
512. M. O. Hoenig, Francis Bitter National Magnet Laboratory, 170 Albany Street, Cambridge, MA 02139
513. W. A. Hoffman, Director, Oak Ridge Science Semester, GLCA/ACM, Denison University, Granville, OH 43023
514. P. Hubert, Service des Recherches sur la Fusion Controlée, Centre d'Etudes Nucleaires, B.P. 6, 32 Fontenay-aux-Roses (Seine), France
515. B. Hui, Naval Research Laboratory, Washington, DC 20375
516. H. Hurwitz, Jr., General Electric Company, 1 River Road, Schenectady, NY 12345
517. K. Husimi, Institute of Plasma Physics, Nagoya University, Nagoya 464, Japan
518. W. R. Husinsky, Technical University of Vienna, Vienna, Austria
519. S. Ihara, Energy Division, Electrotechnical Laboratory, Sakura, Niihari, Ibaraki 305, Japan
520. H. Ikegami, Plasma Physics Division, Institute of Plasma Physics, Nagoya University, Nagoya 464, Japan
521. R. Impara, Office of Fusion Energy, Department of Energy, Mail Stop G-256, Washington, DC 20545
522. H. F. Imster, McDonnell Douglas Astronautics Company, P.O. Box 516, St. Louis, MO 63166
523. Institute for Energy Analysis, P.O. Box 117, Oak Ridge, TN 37830
524. M. Iwamoto, Central Research Laboratory, Mitsubishi Electric Corporation, 80 Nakano, Minamishimizu, Amagasaki, Kyogo 660, Japan
525. T. R. James, Office of Fusion Energy, Department of Energy, Mail Stop G-256, Washington, DC 20545
526. G. L. Jahns, General Atomic Company, P.O. Box 81608, San Diego, CA 92138
527. D. L. Jassby, Princeton Plasma Physics Laboratory, P.O. Box 451, Princeton, NJ 08540
528. V. O. Jensen, Department of Physics, Risø, Roskilde, Denmark
529. N. E. Johnson, Science Applications, Inc., P.O. Box 843, Oak Ridge, TN 37830
530. R. A. Johnson, MZ 16-1070, General Dynamics-Convair Division, P.O. Box 80847, San Diego, CA 92138
531. C. K. Jones, Cryogenic Research Laboratory, Westinghouse Electric Corporation, Research and Development Center, 1310 Beulah Road, Pittsburgh, PA 15235

532. R. Jones, Department of Physics, National University of Singapore, Bukit Timah Road, Singapore 10.25
533. R. A. Jump, Department of Energy, Oak Ridge Operations Office, P.O. Box E, Oak Ridge, TN 37830
534. J. Junker, Max Planck Institut fuer Plasmaphysik, D-8046 Garching bei Muenchen, Federal Republic of Germany
535. H. Kakihana, Institute of Plasma Physics, Nagoya University, Nagoya 464, Japan
536. T. Kamimura, Institute of Plasma Physics, Nagoya University, Nagoya 464, Japan
537. S. Kasai, Japan Atomic Energy Research Institute, Tokai Research Establishment, Tokai, Ibaraki, Japan
538. M. Kaufman, Max Planck Institut fuer Plasmaphysik, D-8046 Garching bei Muenchen, Federal Republic of Germany
539. M. Keilhacker, Max Planck Institut fuer Plasmaphysik, D-8046 Garching bei Munchen, Federal Republic of Germany
540. D. W. Kerst, Sterling Hall, University of Wisconsin, Madison, WI 53706
541. C. von Keszycki, Research Center, Building 26, Grumman Aerospace Corporation, Bethpage, NY 11714
542. J. Kim, General Atomic Company, P.O. Box 81608, San Diego, CA 92138
543. K. K. Kim, Department of Electrical Engineering, University of Illinois, Urbana, IL 61801
544. A. Kitsunezaki, JAERI Group, General Atomic Company, P.O. Box 81608, San Diego, CA 92138
545. Y. Kiwamoto, Institute of Applied Physics, Plasma Research Center, University of Tsukuba, Sakura, Niihari, Ibaraki 305, Japan
546. D. Klein, Westinghouse Electric Corporation, Strategic Operations Division, P.O. Box 598, Pittsburgh, PA 15230
547. W. Klose, Kernforschungszentrum Karlsruhe GmbH, Postfach 3640, D-7500 Karlsruhe 1, Federal Republic of Germany
548. H. E. Knoepfel, Laboratorio Gas Ionizzati, Casella Postale 65, Frascati (Roma), Italy
549. C. Kofoed-Hansen, Risø, Roskilde, Denmark
550. A. C. Kolb, Maxwell Laboratories, Inc., 9244 Balboa Avenue, San Diego, CA 92123
551. P. Komarek, Institut fuer Technische Physik, Kernforschungszentrum Karlsruhe GmbH, Postfach 3640, D-7500 Karlsruhe 1, Federal Republic of Germany
552. K. Koyama, Electrotechnical Laboratory, 5-4-1 Mukodaicho, Tanashi, Tokyo, Japan
553. N. A. Krall, JAYCOR, P.O. Box 85154, San Diego, CA 92138
554. R. Kreibel, Department of Physics, Auburn University, Auburn, AL 36830
555. A. H. Kritz, 69 Lillie Street, Princeton, NJ 08540
556. C. A. Kukielka, Science Applications, Inc., P.O. Box 843, Oak Ridge, TN 37830
557. G. Kulcinski, Department of Nuclear Engineering, University of Wisconsin, Madison, WI 53706
558. D. L. Kummer, McDonnell Douglas Astronautics Company, P.O. Box 516, St. Louis, MO 63166
559. K. Kuroda, Hitachi, Ltd., Central Research Laboratory, 1-280, Higa Shiko Igakubo, Kokubunji, Tokyo 185, Japan
560. L. L. Lao, General Atomic Company, P.O. Box 81608, San Diego, CA 92138
561. Laser Fusion Group, Department of Mechanical and Aerospace Science, River Campus Station, University of Rochester, Rochester, NY 14627
562. J. Lassoon, Building R-1, Room 1076, TRW Defense and Space Systems, 1 Space Park, Redondo Beach, CA 92078
563. N. H. Lazar, Building R-1, TRW Defense and Space Systems, 1 Space Park, Redondo Beach, CA 92078
564. E. Lehnert, Royal Institute of Technology, Stockholm 70, Sweden
565. R. Lengye, Max Planck Institut fuer Plasmaphysik, D-8046 Garching bei Muenchen, Federal Republic of Germany

566. L. L. Lengyel, Max Planck Institut fuer Plasmaphysik, D-8046 Garching bei Muenchen, Federal Republic of Germany
567. J. A. Lenhard, Department of Energy, Oak Ridge Operations Office, P.O. Box E, Oak Ridge, TN 37830
568. Library, Culham Laboratory, UKAEA, Abingdon, Oxon OX14 3DB, United Kingdom
569. Library, FOM Institut voor Plasma-Fysica, Rijnhuizen, Jutphaas, Netherlands
570. Library, Institute of Physics, Academia Sinica, Beijing, Peoples' Republic of China
571. Library, Institute of Plasma Physics, Nagoya University, Nagoya 464, Japan
572. Library, International Centre for Theoretical Physics, Trieste, Italy
573. Library, Laboratorio Gas Ionizzati, Casella Postale 65, Frascati (Roma), Italy
574. Library, Plasma Physics Laboratory, Kyoto University, Gokasho Uji, Kyoto, Japan
575. L. M. Lidsky, Department of Nuclear Engineering, Massachusetts Institute of Technology, 77 Massachusetts Avenue, Cambridge, MA 02139
576. R. K. Linford, Los Alamos National Laboratory, P.O. Box 1663, Los Alamos, NM 87545
577. M. Lomer, Director, Culham Laboratory, Abingdon, Oxon OX14 3DB, United Kingdom
578. M. Lotker, Advanced Energy Conversion Research, Northeastern Utilities Service Company, P.O. Box 270, Hartford, CT 06101
579. R. Lucey, JAYCOR, 205 South Whiting Street, Alexandria, VA 22304
580. V. A. Maroni, Chemical Engineering Division, CEN 205, Argonne National Laboratory, Argonne, IL 60439
581. A. Martinelli, Max Planck Institut fuer Plasmaphysik, D-8046 Garching bei Muenchen, Federal Republic of Germany
582. E. A. Mason, Brown University, Providence, RI 02912
583. D. M. Mattox, Division 5834, Sandia National Laboratories, P.O. Box 5800, Albuquerque, NM 87185
584. C. E. Max, Lawrence Livermore National Laboratory, P.O. Box 808, Livermore, CA 94550
585. D. G. McAlees, Exxon Nuclear Company, Inc., C-08777, 777 106th Avenue, NE, Bellevue, WA 98009
586. J. B. McBride, Science Applications, Inc., P.O. Box 2351, La Jolla, CA 92037
587. C. McCoy, Office of Fusion Energy, Department of Energy, Mail Stop G-256, Washington, DC 20545
588. J. E. McCune, 37-391, Massachusetts Institute of Technology, 77 Massachusetts Avenue, Cambridge, MA 02139
589. D. H. McNeill, Princeton Plasma Physics Laboratory, P.O. Box 451, Princeton, NJ 08540
590. D. M. Meade, Princeton Plasma Physics Laboratory, P.O. Box 451, Princeton, NJ 08540
591. A. T. Mense, McDonnell Douglas Astronautics Company, P.O. Box 516, St. Louis, MO 63166
592. C. Mercier, Service des Recherches sur la Fusion Controlée, Centre d'Etudes Nucleaires, B.P. 6, 92 Fontenay-aux-Roses (Seine), France
593. G. Miley, Department of Nuclear and Electrical Engineering, 214 Nuclear Engineering Laboratory, University of Illinois, Urbana, IL 61801
594. R. G. Mills, Princeton Plasma Physics Laboratory, P.O. Box 451, Princeton, NJ 08540
595. S. Miyoshi, Director, Plasma Research Center, Institute of Physics, University of Tsukuba, Sakura, Niihari, Ibaraki, Japan
596. K. Molvig, Massachusetts Institute of Technology, 77 Massachusetts Avenue, Cambridge, MA 02139
597. D. B. Montgomery, Francis Bitter National Magnet Laboratory, 170 Albany Street, Cambridge, MA 02139
598. F. Moon, Department of Theoretical and Applied Mechanics, Cornell University, Ithaca, NY 14850
599. T. J. Morgan, Physics Department, Wesleyan University, Middletown, CT 06457
600. K. G. Moses, JAYCOR, 2811 Wilshire Boulevard, Suite 690, Santa Monica, CA 90403
601. J. H. Mullen, McDonnell Douglas Astronautics Company, P.O. Box 516, St. Louis, MO 63166
602. A. W. Mullendore, Sandia National Laboratories, P.O. Box 5800, Albuquerque, NM 87185

603. C. H. Muller, General Atomic Company, P.O. Box 81608, San Diego, CA 92138
604. M. R. Murphy, Office of Fusion Energy, Department of Energy, Mail Stop G-256, Washington, DC 20545
605. P. Murray, Westinghouse Electric Corporation, 1801 K Street, Washington, DC 20006
606. G. F. Nardella, Office of Fusion Energy, Department of Energy, Mail Stop G-256, Washington, DC 20545
607. A. P. Navarro, Division de Fusion, Junta de Energia Nuclear, Avenida Complutense 22, Madrid (3), Spain
608. J. O. Neff, Program Manager, Department of Energy, Columbus Program Office, Richland Operations, 505 King Avenue, Columbus, OH 43201
609. D. P. Nelson, Office of Fusion Energy, Department of Energy, Mail Stop G-256, Washington, DC 20545
610. M. Nozawa, Japan Atomic Energy Research Institute, Tokai Research Establishment, Tokai, Ibaraki, Japan
611. Oak Ridge Associated Universities, MERT Library, P.O. Box 117, Oak Ridge, TN 37830
612. C. Oberly, Aero Propulsion Laboratory, Power Distribution Branch, Wright-Patterson Air Force Base, OH 45433
613. T. Ogasawara, Department of Physics, College of Science and Engineering, Nihon University, Kanda-Surugadi, Chiyoda, Tokyo, Japan
614. H. Ogiwara, Toshiba Research and Development Center, 1 Komukai Tsohibacho, Saiwai, Kawasaki, Kanagawa 210, Japan
615. T. Ohkawa, General Atomic Company, P.O. Box 81608, San Diego, CA 92138
616. E. Oktay, Office of Fusion Energy, Department of Energy, Mail Stop G-256, Washington, DC 20545
617. R. J. Onega, Nuclear Engineering Group, College of Engineering, Virginia Polytechnic Institute and State University, Blacksburg, VA 24061
618. A. Opdenaker, Reactor Systems and Applications Branch, Office of Fusion Energy, Department of Energy, Mail Stop G-256, Washington, DC 32803
619. B. Outten, Jr., Western Metal Products Company, 1300 Weber Street, Orlando, FL 32803
620. D. Overskei, General Atomic Company, P.O. Box 81608, San Diego, CA 92138
621. D. Palumbo, EURATOM, 51 Rue Belliard, Brussels 5, Belgium
622. R. E. Papsco, Princeton Plasma Physics Laboratory, P.O. Box 451, Princeton, NJ 08540
623. J. Parain, CEN/Saclay, B.P. 2, F91190, Gif-sur-Yvette, France
624. R. R. Parker, Massachusetts Institute of Technology, 77 Massachusetts Avenue, Cambridge, MA 02139
625. P. B. Parks, General Atomic Company, P.O. Box 81608, San Diego, CA 92138
626. L. D. Pearlstein, L-388, Lawrence Livermore National Laboratory, P.O. Box 808, Livermore, CA 94550
627. R. S. Pease, UKAEA, Culham Laboratory, Abingdon, Oxon OX14 3DB, United Kingdom
628. D. L. Pehrson, Lawrence Livermore National Laboratory, P.O. Box 808, Livermore, CA 94550
629. D. Pfirsch, Max Planck Institut fuer Plasmaphysik, D-8046 Garching bei Muenchen, Federal Republic of Germany
630. A. V. Phelps, Joint Institute for Laboratory Astrophysics, University of Colorado, Boulder, CO 80309
631. M. S. Pindzola, Department of Physics, Auburn University, Auburn, AL 36830
632. K. Pinkau, Director, Max Planck Institut fuer Plasmaphysik, D-8046 Garching bei Muenchen, Federal Republic of Germany
633. Plasma Research Laboratory, Australian National University, P.O. Box 4, Canberra, A.C.T. 2000, Australia

634. P. A. Politzer, Department of Nuclear Engineering, Massachusetts Institute of Technology, 77 Massachusetts Avenue, Cambridge, MA 02139
635. R. F. Post, Lawrence Livermore National Laboratory, P.O. Box 808, Livermore, CA 94550
636. J. R. Powell, Department of Applied Sciences, Brookhaven National Laboratory, Upton, Long Island, 11973
637. K. Prelec, Brookhaven National Laboratory, Upton, Long Island, NY 11973
638. F. Prevot, Chef du Service du Confinement des Plasmas, CEA, B.P. 6, 92260 Fontenay-aux-Roses (Seine), France
639. L. K. Price, Department of Energy, Oak Ridge Operations Office, P.O. Box E, Oak Ridge, TN 37830
640. R. E. Price, Office of Fusion Energy, Department of Energy, Mail Stop G-256, Washington, DC 20545
641. D. H. Priester, Office of Fusion Energy, Department of Energy, Mail Stop G-256, Washington, DC 20545
642. J. R. Purcell, General Atomic Company, P.O. Box 81608, San Diego, CA 92138
643. R. V. Pyle, Lawrence Berkeley Laboratory, University of California, Berkeley, CA 94720
644. B. H. Quon, Building R-1, TRW Defense and Space Systems, 1 Space Park, Redondo Beach, CA 90278
645. E. J. Rapperport, Massachusetts Institute of Technology, 77 Massachusetts Avenue, Cambridge, MA 02139
646. M. E. Read, Naval Research Laboratory, Washington, DC 20375
647. P. J. Reardon, Princeton Plasma Physics Laboratory, P.O. Box 451, Princeton, NJ 08540
648. P. H. Rebut, JET Group, Culham Laboratory, Abingdon, Oxon OX14 3DB, United Kingdom
649. Research Information Center, Institute of Plasma Physics, Nagoya University, Nagoya 464, Japan
650. T. C. Reuther, Office of Fusion Energy, Department of Energy, Mail Stop G-256, Washington, DC 20545
651. F. L. Rose, 3910 Benson Hall BF 10, University of Washington, Seattle, WA 98195
652. F. Ring, Lockheed Missile and Space Company, Jackson Plaza, Suite 103, 800 Oak Ridge Turnpike, Oak Ridge, TN 37830
653. M. Roberts, Office of Fusion Energy, Department of Energy, Mail Stop G-256, Washington, DC 20545
654. F. C. Rock, Plasma Physics Laboratory, Department of Physics and Astronomy, Brigham Young University, Provo, UT 84602
655. J. D. Rogers, Los Alamos National Laboratory, P.O. Box 1663, Los Alamos, NM 87545
656. A. Rogister, Institut fuer Plasmaphysik, KFA, Postfach 1913, D-5170 Juelich 1, Federal Republic of Germany
657. R. H. Rohrer, Department of Physics, Emory University, Atlanta, GA 30322
658. W. F. Rolf, Clinch River Breeder Reactor Project, P.O. Box U, Oak Ridge, TN 37830
659. D. J. Rose, Department of Nuclear Engineering, Massachusetts Institute of Technology, 77 Massachusetts Avenue, Cambridge, MA 02139
660. M. N. Rosenbluth, Institute for Fusion Studies, RLM 11.218, University of Texas at Austin, Austin, TX 78712
661. M. L. Rossi, Grumman Aerospace Corporation, Bethpage, NY 11714
662. J. R. Roth, Department of Electrical Engineering, The University of Tennessee, Knoxville, TN 37916
663. P. H. Rutherford, Princeton Plasma Physics Laboratory, P.O. Box 451, Princeton, NJ 08540
664. D. D. Ryutov, Institute of Nuclear Physics, Siberian Branch of the Academy of Sciences of the U.S.S.R., Sovetskaya St. 5, 630090 Novosibirsk, U.S.S.R.
665. G. Sacerdoti, Laboratorio Nazionali, Casella Postale 70, 00044 Frascati (Roma), Italy
666. W. Sadowski, Office of Fusion Energy, Department of Energy, Mail Stop G-256, Washington, DC 20545

667. M. Salvat, Max Planck Institut fuer Plasmaphysik, D-8046 Garching bei Muenchen, Federal Republic of Germany
668. M. M. Satterfield, The Nucleus, 461 Laboratory Road, Oak Ridge, TN 37830
669. Y. Sawada, Heavy Apparatus Engineering Laboratory, Tokyo Shibaru Electric Company, Ltd., 4-2 Chome, Suehiro, Tsurumi, Yokohama, Japan
670. G. A. Sawyer, CTR Division, MS 640, Los Alamos National Laboratory, P.O. Box 1663, Los Alamos, NM 87545
671. G. Schilling, Princeton Plasma Physics Laboratory, P.O. Box 451, Princeton, NJ 08540
672. A. Schlueter, Max Planck Institut fuer Plasmaphysik, D-8046 Garching bei Muenchen, Federal Republic of Germany
673. L. L. Schmid, Pacific Northwest Laboratories, Battelle Boulevard, P.O. Box 999, Richland, WA 99352
674. G. Schmidt, Princeton Plasma Physics Laboratory, P.O. Box 451, Princeton, NJ 08540
675. K. Schmitter, Max Planck Institut fuer Plasmaphysik, D-8046 Garching bei Muenchen, Federal Republic of Germany
676. J. H. Schneider, Joint Research Centre, Ispra Establishment, 21020 Ispra (Varese), Italy
677. B. Schweer, Institut fuer Plasmaphysik, KFA, Postfach 1913, D-5170 Juelich 1, Federal Republic of Germany
678. F. R. Scott, Electric Power Research Institute, P.O. Box 10412, Palo Alto, CA 94303
679. C. M. Sekula, Publications Division, IAEA, Postfach 200, A-1400 Vienna, Austria
680. V. D. Shafranov, I. V. Kurchatov Institute of Atomic Energy, P.O. Box 3402, 123182 Moscow, U.S.S.R.
681. G. Sheffield, Princeton Plasma Physics Laboratory, P.O. Box 451, Princeton, NJ 08540
682. S. Shimamoto, Japan Atomic Energy Research Institute, Tokai Research Establishment, Tokai, Ibaraki, Japan
683. K. Shiraishi, Chief, Physical Metallurgy Laboratory, Japan Atomic Energy Research Institute, Tokai Research Establishment, Tokai, Ibaraki 319-11, Japan
684. J. L. Shohet, Department of Electrical and Computer Engineering, University of Wisconsin, Madison, WI 53706
685. G. Siegel, Tennessee Valley Authority, 1360 Commerce Union Bank Building, Chattanooga, TN 37401
686. SIN Library, CH-5234 Villigen, Switzerland
687. J. Smith, Department of Mathematics, The University of Tennessee, Knoxville, TN 37916
688. M. Soler, Division de Fusion, Junta de Energia Nuclear, Avenida Complutense 22, Madrid (3), Spain
689. M. Spadoni, Laboratorio Nazionali, Casella Postale 70, 00044 Frascati (Roma), Italy
690. I. Spighel, Lebedev Physical Institute, Leninsky Prospect 53, 117924 Moscow, U.S.S.R.
691. J. C. Sprott, University of Wisconsin, Madison, WI 53706
692. W. M. Stacey, School of Nuclear Engineering and Health Physics, Georgia Institute of Technology, Atlanta, GA 30332
693. H. S. Staten, Office of Fusion Energy, Department of Energy, Mail Stop G-256, Washington, DC 20545
694. [illegible] J. Stekly, Magnetics Corporation of America, 179 Bear Hill Road, Waltham, MA 02154
695. [illegible] Stevens, Department of Nuclear Engineering, The University of Tennessee, Knoxville, TN 37916
696. L. D. Stewart, Princeton Plasma Physics Laboratory, P.O. Box 451, Princeton, NJ 08540
697. U. Stiefel, Eidg. Institut fuer Reaktorforschung, 5303 Wurenlingen, Switzerland
698. T. H. Stix, Princeton Plasma Physics Laboratory, P.O. Box 451, Princeton, NJ 08540
699. P. M. Stone, Office of Fusion Energy, Department of Energy, Mail Stop G-256, Washington, DC 20545
700. B. P. Strauss, Magnetics Corporation of America, 179 Bear Hill Road, Waltham, MA 02154

701. W. Sutton, Department of Nuclear Engineering, University of Illinois, Urbana, IL 61807
702. D. Sweetman, UKAEA, Culham Laboratory, Abingdon, Oxon OX14 3DB, United Kingdom
703. K. Tachikawa, Chief, Electric Materials Laboratory, National Research Institute for Metals, 3-12, 2-Chome, Nakameguro, Meguru, Tokyo, Japan
704. J. Tachon, Service des Recherches sur la Fusion Controlée, Centre d'Etudes Nucleaires, B.P. 6, 92 Fontenay-aux-Roses (Seine), France
705. K. Takayama, Institute of Plasma Physics, Nagoya University, Nagoya 464, Japan
706. M. P. Tanaka, Physical Metallurgy Laboratory, Japan Atomic Energy Research Institute, Tokai Research Establishment, Tokai, Ibaraki, Japan
707. J. Tataronis, Department of Electrical and Computer Engineering, University of Wisconsin, Madison, WI 53706
708. C. E. Taylor, Lawrence Berkeley Laboratory, University of California, Berkeley, CA 94720
709. J. B. Taylor, UKAEA, Culham Laboratory, Abingdon, Oxon OX14 3DB, United Kingdom
710. R. J. Taylor, Center for Plasma Physics and Fusion Engineering, University of California, Los Angeles, CA 90024
711. L. E. Temple, Construction Project Management Support Division, ER-15, Department of Energy, Washington, DC 20545
712. D. P. Tewari, Department of Physics, Indian Institute of Technology, New Delhi 110016, India
713. Thermonuclear Library, Japan Atomic Energy Research Institute, Tokai Research Establishment, Tokai, Ibaraki, Japan
714. E. W. Thomas, Department of Physics, Georgia Institute of Technology, Atlanta, GA 30332
715. F. Thomas, Grumman Aerospace Corporation, Bethpage, NY 11714
716. K. Thomassen, Lawrence Livermore National Laboratory, P.O. Box 808, Livermore, CA 94550
717. E. Thompson, UKAEA, Culham Laboratory, Abingdon, Oxon OX14 3DB, United Kingdom
718. M. Thumm, Institut fuer Plasmaforschung, Pfaffenwaldring 31, D-7000 Stuttgart 80, Federal Republic of Germany
719. M. Tillack, Department of Nuclear Engineering, Massachusetts Institute of Technology, 77 Massachusetts Avenue, Cambridge, MA 02139
720. V. T. Tolok, Kharkov Physical-Technical Institute, Academical St. 1, 310108 Kharkov, U.S.S.R.
721. J. E. Tracey, Francis Bitter National Magnet Laboratory, 170 Albany Street, Cambridge, MA 02139
722. M. Trocheris, Service des Recherches sur la Fusion Controlée, Centre d'Etudes Nucleaires, B.P. 6, 92 Fontenay-aux-Roses (Seine), France
723. F. Troyon, Centre des Recherches en Physique des Plasmas, Ecole Polytechnique de Lausanne, 21 Avenue des Bains, 1007 Lausanne, Switzerland
724. J. M. Turner, Office of Fusion Energy, Department of Energy, Mail Stop G-256, Washington, DC 20545
725. D. T. Uchida, Department of Nuclear Engineering, University of Tokyo, Tokyo, Japan
726. K. Uo, Plasma Physics Laboratory, Kyoto University, Gokasho Uji, Kyoto 611, Japan
727. G. Vahala, Department of Physics, College of William and Mary, Williamsburg, VA 23185
728. T. C. Varljen, Westinghouse Electric Corporation, Advanced Reactors Division, P.O. Box 158, Madison, PA 15663
729. R. Varma, Physical Research Laboratory, Navangpura, Ahmedabad, India
730. G. Vécsey, Swiss Institute for Nuclear Research, CH-5324 Villigen, Switzerland
731. D. L. Vieth, Office of Fusion Energy, Department of Energy, Mail Stop G-256, Washington, DC 20545
732. F. L. Vook, Sandia National Laboratories, P.O. Box 5800, Albuquerque, NM 87185
733. F. Waelbroeck, Institut fuer Plasmaphysik, KFA, Postfach 1913, D-5170 Juelich 1, Federal Republic of Germany

734. M. Wakatani, Kyoto University, Gokasho Uji, Kyoto, Japan
735. C. Walters, Technology Division, Building R25, Rutherford Laboratory, Chilton, Didcot, Oxon OX11 0QX, United Kingdom
736. C. N. Watson-Munro, University of Sydney, Wills Plasma Project, Sydney, N.S.W., Australia
737. A. M. Weinberg, Institute for Energy Analysis, P.O. Box 117, Oak Ridge, TN 37830
738. H. Weitzner, Courant Institute of Mathematical Sciences, New York University, 251 Mercer Street, New York, NY 10012
739. P. W. Whitfield, c/o ARAMCO, P.O. Box 8339, Dhahran, Saudi Arabia
740. J. B. Whitley, Sandia National Laboratories, P.O. Box 5800, Albuquerque, NM 87185
741. W. Wilkes, Mound Laboratories, Miamisburg, OH 45432
742. J. W. Willis, Office of Fusion Energy, Department of Energy, Mail Stop G-256, Washington, DC 20545
743. R. R. Winters, Oak Ridge Science Semester, GLCA, Denison University, Granville, OH 43032
744. S. L. Wipf, Q-25, Los Alamos National Laboratory, P.O. Box 1663, Los Alamos, NM 87545
745. J. Wong, Supercon, Inc., 9 Erie Drive, Natick, MA 01760
746. S. K. Wong, General Atomic Company, P.O. Box 81608, San Diego, CA 93128
747. J. T. Woo, Rensselaer Polytechnic Institute, Troy, NY 12181
748. S. B. Woo, Department of Physics, University of Delaware, Newark, DE 19711
749. H. H. Woodson, Department of Electrical Engineering, University of Texas at Austin, Austin, TX 78712
750. W. O. Wuestker, JET Group, Culham Laboratory, Abingdon, Oxon OX14 3DB, United Kingdom
751. M-L. Xue, Institute of Mechanics, Academia Sinica, Beijing, Peoples' Republic of China
752. K. Yamamoto, Japan Atomic Energy Research Institute, 1-1-13 Shinbashi, Minato, Tokyo, Japan
753. T. F. Yang, Francis Bitter National Magnet Laboratory, 170 Albany Street, Cambridge, MA 02139
754. K. Yasukochi, Department of Physics, College of Science and Engineering, Nihon University, Kanada-Surugadai, Chiyoda, Tokyo, Japan
755. H. Yoshikawa, Manager, Materials Engineering, Hanford Engineering Development Laboratory, P.O. Box 1970, Richland, WA 99352
756. S. Yoshikawa, Institute for Advanced Studies, Princeton University, Princeton, NJ 08540
757. J. L. Young, Westinghouse Electric Corporation, 1310 Beulah Road, Pittsburgh, PA 15235
758. B. Zurro, Division de Fusion, Junta de Energia Nuclear, Avenida Complutense 22, Madrid (3), Spain
759. Office of Assistant Manager for Energy Research and Development, Department of Energy, Oak Ridge Operations Office, P.O. Box E, Oak Ridge, TN 37830

760-867. Given distribution as shown in TID-4500, Magnetic Fusion Energy (Distribution Category UC-20)